DESY–PROC–2009–01

Proceedings of the

38th International Symposium on Multiparticle Dynamics ISMD08

September 15-20, 2008
DESY, Hamburg, Germany

Editors: Jochen Bartels, Kerstin Borras, Gösta Gustafson, Hannes Jung, Krzysztof Kutak, Serguei Levonian, Joachim Mnich

Verlag Deutsches Elektronen-Synchrotron

Impressum

Proceedings of the 38th International Symposium on Multiparticle Dynamics (ISMD08)

September 15-20, 2008, Hamburg, Germany

Conference homepage
`http://ismd08.desy.de`

Slides at
`hhttps://indico.desy.de/conferenceOtherViews.py?confId=754`

Online proceedings at
`http://ismd08.desy.de/proceedings.html`

The copyright is governed by the Creative Commons agreement, which allows for free use and distribution of the articels for non-commercial activity, as long as the title, the authors' names and the place of the original are referenced.

Editors:
Jochen Bartels (University Hamburg) , Kerstin Borras (DESY), Gösta Gustafson (University Hamburg, University Lund), Hannes Jung (DESY, University Antwerp), Krzysztof Kutak (DESY), Serguei Levonian (DESY), Joachim Mnich (DESY)
January 2009
DESY-PROC-2009-01
ISBN 978-3-935702-31-7
ISSN 1435-8077

Published by
Verlag Deutsches Elektronen-Synchrotron
Notkestraße 85
22607 Hamburg
Germany

Organizing Committee:

Jochen Bartels (University Hamburg), Kerstin Borras (DESY), Gösta Gustafson (cochair) (University Hamburg, University Lund), Hannes Jung (cochair) (DESY, University Antwerp), Krzysztof Kutak (DESY), Serguei Levonian (DESY), Joachim Mnich (DESY)

Conveners:

Dilute systems:
A. Cooper-Sarkar (Oxford), A. Kulesza (DESY), K. Hatakeyama (Rockefeller)
High density systems in ep, pp and heavy ions:
D. d'Enterria (CERN), T. Csörgő (Budapest), E. Iancu (Saclay)
Interpolation region:
M. Grothe (Wisconsin), M Albrow (FNAL), K. Werner (Nantes)
Strategies and analysis methods:
E. DeWolf (Antwerp), A. Geiser (DESY), M. Sjödahl (Manchester)
New physics:
G. Weiglein (Durham), A. DeRoeck (CERN, University Antwerp)

Advisory Committee:

A. Białas (Cracow), T. Csörgő (Budapest), I. Dremin (Moscow), K. Fiałkowski (Cracow), B. Gary (Riverside), R. Godbole (Bangalore), T. Hallman (Upton), Y. Hama (Sao Paulo), W. Kittel (Nijmegen), T. Kodama (Rio de Janeiro), V. Kuvshinov (Minsk), L. Liu (Wuhan), L. McLerran (Brookhaven), N. Schmitz (Munich), A. Valkarova (Prague), E. De Wolf (Antwerp), N. Xu (Berkeley)

Supported by:

Deutsches Elektronen-Synchroton DESY
Deutsche Forschungsgemeinschaft
SFB 676 (Particles, Strings and the Early Universe)

Preface

The *XXXVIII International Symposium on Multiparticle Dynamics*, ISMD 2008, was held on 15 - 20 September at DESY, Hamburg. This series of symposia attracts participants from different areas, with a common interest in reactions where a large number of particles are produced. Traditionally this has mainly included three communities, hadronic collisions and DIS, high energy heavy ion collisions, and cosmic ray physics. With the increasing accelerator energies, in particular awaiting the startup of the LHC, these communities have been brought even closer. Effects of gluon saturation is not only of interest in heavy ion collisions; saturation and multiple subcollisions are possibly seen at HERA, are essential features at the Tevatron, and will be a major effect in minimum bias and underlying events at the LHC. With the LHC the energy in collider experiments will also become comparable to that in high energy cosmic rays. As the cosmic ray detectors are mostly sensitive to the forward region, the increased forward coverage in the LHC experiments brings these communities closer together.
To further encourage contacts and exchanges of information across the community bounderies, the organizers chose to test a new way to schedule the sessions. Thus five cross-diciplinary sessions were organized in which a predefined set of questions ought to be addressed in the sessions.

- **Dilute systems**
  Conveners: A. Cooper-Sarkar (Oxford), A. Kulesza (DESY), K. Hatakeyama (Rockefeller).
  Topics: High Q^2, structure functions, jets, central production.
  Questions: How well do we know PDFs from HERA and the TeVatron and how well can we predict cross sections at the LHC? Are NLO PDFs all we need? Which PDFs should be used in Monte Carlo event generators? How small in x can we trust the linear evolution equations (BFKL/DGLAP)?

- **High density systems in ep, pp and heavy ions**
  Conveners: D. d'Enterria (CERN), T. Csörgő (Budapest), E. Iancu (Saclay).
  Topics: Saturation, hydrodynamics, CGC, perfect fluids, AdS/CFT.
  Questions: What are the expected effects of multiple interactions and saturation at the LHC? What lesson from heavy ion collisions can shed light on saturation in pp and ep and vice versa? What can heavy ion physics learn from pp and ep? Can ideas from hydrodynamics, classical fields and quenching be used in pp? What from hard QCD calculations can be used in heavy ion physics?

- **Interpolation region**
  Conveners: M. Grothe (Wisconsin), M. Albrow (FNAL), K. Werner (Nantes).
  Topics: Forward production at highest energies, diffraction, glasma.
  Questions: What can cosmic rays say about forward physics at the LHC and vice versa? Transition from dense to dilute systems, as discussed in HI & Cosmic Rays-relevance for pp: forward production, diffractive event (shadow of a dense system) and PDFs?

- **Strategies and analysis methods**
  Conveners: E. DeWolf (Antwerp), A. Geiser (DESY), M. Sjödahl (Manchester).
  Topics: Correlations, heavy quark production, MC techniques.
  Questions: How can forward detectors improve our understanding of QCD effects and identify signals for new physics? Are existing tools sufficient and where should they be improved? How can correlations be used to determine the size of the interaction and phase transitions?

- **New physics**
  Conveners: G. Weiglein (Durham), A. DeRoeck (CERN).
  Topics: Possible signals for Higgs, Susy, etc.
  Questions: Scenarios for new physics: how probable are the different scenarios? How to discriminate new physics from complicated background like multiparton interactions? How to discriminate different scenarios? How well can the LHCexperiments cope with the different scenarios?

The new scheme would not have worked so well without the excellent work by the conveners, who invited good speakers and prepared a very interesting program. This apparently looked attractive, and the symposium had a total of 127 registered participants. An unavoidable consequence of this success was, that it became necessary to include two evening sessions, one of them even with paralell talks.
The program also included a discussion session about the applicability and limitations of collinear factorization, and of linear parton evolution. As a preparation before the real symposium, we had two introductory talks by H. Meyer and L. McLerran.
Another new feature was that all plenary talks were video recorded, and together with the transparencies are available from:
`https://indico.desy.de/conferenceOtherViews.py?confId=754`
Unfortunately, not all presentations during the workshop appear as a writeup in these proceedings. Ch. Anastasiou, H. Büsching and V.V. Khoze were not able to deliver a written version of their contribution. The online version of the proceedings can be found at:
`http://ismd08.desy.de`.
We wish to thank all the participants of ISMD08 for making this symposium so interesting and lively. We thank especially the conveners for their enormous work in the preparation of this symposium. We are in particular indebted to the summary speakers, P. van Mechelen and Y. Kovshegov, who in an excellent way fulfilled their difficult tasks.
Last but not least we wish to thank A. Grabowksy, S. Platz and L. Schmidt for their continuous help and support during all the meeting week. We thank B. Liebaug for the design of the poster. We are grateful to R. Eisberg, O. Knak and S. König for recording the talks and all technical help. We thank M. Mayer, K. Sachs and M. Stein for their help in printing the proceedings. We are grateful to the DESY directorate for financial support of this workshop and for the hospitality which they extended to all participants of the workshop, and to the DFG and the SFB for financial support.

The Organizing Committee:
Jochen Bartels, Kerstin Borras, Gösta Gustafson(cochair), Hannes Jung(cochair), Krzysztof Kutak, Serguei Levonian, Joachim Mnich

Contents

1 Introductory Lecture **1**

A Brief Introduction to the Color Glass Condensate and the Glasma **3**
L. McLerran

2 WG: Dilute systems **19**

Cross section measurements in DIS **21**
K. Papageorgiou

Jet Production at HERA **26**
A. Savin

Extraction of the proton parton density functions using a NLO-QCD fit of the combined H1 and ZEUS inclusive DIS cross sections **31**
G. Li

PDF Constraints From Tevatron Data **36**
M. Lancaster

Small x Resummation - An Overview **41**
Ch. White

Progress in Parton Distribution Functions and Implications for LHC **46**
J. Stirling

Theoretical predictions for the LHC **56**
S. Moch

First physics prospects with the ATLAS detector at LHC **63**
J. Katzy

The Heavy Flavour Content of the Proton **68**
P. Thompson

Update on Neural Network Parton Distributions: NNPDF1.1 **73**
J. Rojo

3 WG: Dense systems **78**

High-energy heavy-ion collisions: from CGC to Glasma **79**
K. Itakura

Particle production and saturation at RHIC and LHC **84**
C. Marquet

Introducing Saturation Effects into Event Generators **89**
E. Avsar

The Ridge, the Glasma and Flow **94**
L. McLerran

Partons and jets at strong coupling from AdS/CFT **99**
E. Iancu

QCD EoS, initial conditions and final state from relativistic hydrodynamics in heavy-ion collisions **104**
M. Nagy

Hydrodynamics & perfect fluids: uniform description of soft observables in Au+Au collisions at RHIC **109**
W. Florkowski, W Broniowski, M. Chojnacki, A. Kisiel

The Remarkable Simplicity and Universality of Multiparticle Production Data **114**
W. Busza

Heavy ions and parton saturation from RHIC to LHC **118**
A. Dainese

Probing the Properties of the Matter Created at RHIC **125**
H. Caines

Relativistic viscous hydrodynamics and AdS/CFT correspondence at finite temperature **130**
R. Baier

AdS/CFT Correspondence in Heavy Ion Collisions **135**
J. L. Albacete, Y. V. Kovchegov, A. Taliotis

Saturation and Confinement: Analyticity, Unitarity and AdS/CFT Correspondence **140**
R. Brower, M. Djuric, C-I Tan

Light, Strange and Charm Hadron Measurements in ep **145**
A. Kropivnitskaya

4 WG: Interpolation Region **150**

Diffractive Production of Jets and Vector Bosons at the Tevatron **151**
K. Hatakeyama

Central Exclusive Production at the Tevatron **156**
M. G. Albrow

Overview on rapidity gap survival predictions for LHC **161**
A.B. Kaidalov

Access to small x Parton Density Functions at the LHC **167**
T. Shears

Theoretical concepts of parton saturation - from HERA to LHC **172**
K. Golec-Biernat

What HERA can tells us about saturation **177**
R. Yoshida

Inclusive diffraction and factorisation at HERA **181**
M. Wing

Exclusive Diffraction and Leading baryons at HERA **186**
D. Wegener

Quasielastic Scattering in the Dipole Model **191**
Ch. Flensburg

Hadronic interaction models in the light of the color glass condensate **197**
S. Ostapchenko

Test of interaction models via accelerator data **203**
T. Pierog

Results of the Pierre Auger Observatory - aspects related to hadronic interaction models **208**
P. Travnicek

$D\overline{D}$ momentum correlations versus relative azimuth as a sensitive probe for thermalization **214**
G. Tsiledakis

Hard Diffraction at the LHC **219**
A. De Roeck

Exclusive photoproduction of dileptons at high energies **225**
M.V.T. Machado

5 WG: Strategies and Analysis Methods **230**

Colour Reconnections and Top Physics **231**
D. Wicke

Heavy Quark Production at HERA as a Probe of Hard QCD **235**
R. Shehzadi

What do we learn from forward detectors at LHC ? **240**
A. Bunyatyan

Recent L3 Results (and Questions) on BEC at LEP **246**
W. J. Metzger

Bose-Einstein or HBT correlations in high energy reactions **251**
T. Csörgő

QCD and Monte Carlo generators **259**
Z. Nagy

On factorization scheme suitable for NLO Monte Carlo event generators **269**
K. Kolar

Review on recent developements in jet finding **274**
J. Rojo

Multi-particle production and TMD distributions **279**
F. Hautmann

Bose-Einstein study of position-momentum correlations of charged pions in hadronic Z^0 decays **286**
C. Ciocca

Squeezed correlations among particle-antiparticle pairs **291**
S.S. Padula

An approach to QCD phase transitions via multiplicity fluctuations and correlations **296**
K. Homma

Antibaryon to Baryon Production Ratios in Pb-Pb and p-p collision at LHC energies of the DPMJET-III Monte Carlo **301**
F.W.Bopp, J.Ranft, R.Engel, S.Roesler

6 WG: New Physics 306

New signatures and challenges for the LHC **307**
M. Strassler

New physics search in the LHCb era **312**
T. Hurth

Searches for Physics beyond the Standard Model **322**
A. Meyer

Discovery potential at the LHC: channels relevant for SM Higgs **327**
I. Tsukerman

Central Exclusive Production of BSM Higgs bosons at the LHC **332**
S. Heinemeyer, V.A. Khoze, M.G. Ryskin, M. Taševský G. Weiglein

A bottom-up strategy for reconstructing the underlying MSSM parameters at the LHC **338**
J.-L. Kneur

Supersymmetry and other beyond the Standard Model physics: Prospects for determining mass, spin and CP properties **343**
W. Ehrenfeld

7 WG: Recent Developments 348

Crossover between hadronic and partonic phases and liquid property of sQGP **349**
M. Xu , M. Yu Meiling, L .Liu

Nuclear Effects in High-p_T Hadron Production at Large x **354**
J. Nemchik, M. Šumbera

The nimbus of away-side jets **360**
I.M. Dremin

Baryon stopping as a test of geometric scaling **365**
Y. Mehtar-Tani, G. Wolschin

Transport Coefficients for Non-Newtonian Fluids and Causal Dissipative Hydrodynamics **370**
T. Kodama, T. Koide

Study of extremely high multiplicity events in the SVD-2 experiment **375**
E. Kokoulina, A. Kutov, V. Ryadovikov

Soft photon production in matter in two particle green's function consideration **380**
A.V. Koshelkin

New Scaling Behavior of low-p_T Hadron Production in proton-(anti)proton collisions at RHIC and Tevatron **385**
M. Tokarev, I. Zborovsk

Strongly Interacting Massive Particles at LHC **390**
O.I. Piskounova, A.B. Kaidalov

Saturation in lepton- and hadron induced reactions **395**
L.L. Jenkovszky

Multi-parton interactions and underlying events from Tevatron to LHC **400**
P. Bartalini, F. Ambroglini, L. Fanò, R. Field, L. Garbini, D. Treleani

Multiplicities and the Underlying Event **406**
D. Kar

Saturation effects in final states due to CCFM with absorptive boundary **411**
K. Kutak, H. Jung

Photoproduction total cross-sections at very high energies and the Froissart bound **416**
Y. N. Srivastava, A. Achilli, R. Godbole, A. Grau, G. Pancheri

Monte Carlo and large angle gluon radiation **421**
G. Marchesini

Production amplitudes in $N = 4$ SUSY and Mandelstam cuts **427**
J. Bartels, L.N. Lipatov

High energy scattering in QCD vs. tiny black holes **433**
L. Álvarez-Gaumé, C. Gómez, A. Sabio Vera, A. Tavanfar, M. A. Vázquez-Mozo

8 Discussion Session 439

Discussion Session **441**
M. Diehl, K. Golec-Biernat, A. Cooper-Sakar, A. De Roeck

Have we seen anything beyond (N)NLO DGLAP at HERA? **443**
A. Cooper-Sarkar

Saturation: what do we need **448**
A. De Roeck, H. Jung

9 Summaries 452

Experimental Summary **453**
P. van Mechelen

Theory Summary **473**
Y. V. Kovchegov

Chapter 1

Introductory Lecture

A Brief Introduction to the Color Glass Condensate and the Glasma

Larry McLerran
RIKEN-BNL Center and Physics Department, Brookhaven National Lab., Upton, NY, 11973
USA
DOI: http://dx.doi.org/10.3204/DESY-PROC-2009-01/26

Abstract
I provide a brief introduction to the theoretical ideas and phenomenological motivation for the Color Glass Condensate and the Glasma.

1 Introduction

The purpose of this talk is to motivate the ideas behind the Color Glass Condensate and the Glasma. As space is limited in such conference proceedings, the references below are not comprehensive, and the reader interested in a fuller documentation and an expanded discussion of the topics below are referred to a few reviews where the original ideas are motivated, and where there are detailed references to the original literature. [1]

The concepts associated with the Color Glass Condensate and the Glasma were generated to address at least three fundamental questions in particle and nuclear physics:

- *What is the high energy limit of QCD?*
- *What are the possible forms of high energy density matter?*
- *How do quarks and gluons originate in strongly interacting particles?*

The Color Glass Condensate is the high energy density largely gluonic matter that is associated with wavefunction of a high energy hadron. [2]- [7] It is the initial state in high energy hadronic collisions, and its components generate the distributions of quarks and gluons measured in high energy deep electron scattering from nuclei. Almost instantaneously after a hadron-hadron collision, the nature of the gluonic matter changes its structure, and the Color Glass Condensate fields are transformed into longitudinal color electric and magnetic fields, the Glasma. [8]- [11] These early stages are shown in Fig. 1. Later, the Glasma decays and presumably thermalizes

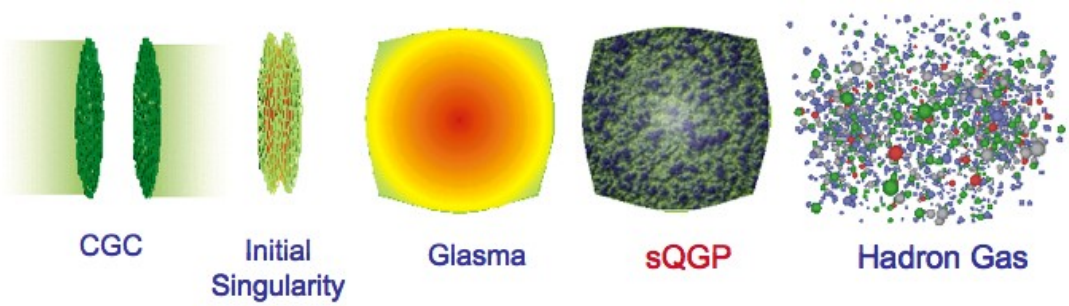


Fig. 1: An artistic conception of high energy hadronic collisions

and forms a Quark Gluon Plasma, which eventually itself decays into hadrons. [12]- [13]

A more detailed picture of the evolution of the matter produced in heavy ion collisions is shown in the space-time diagram of Fig. 2. This picture demonstrates the close correspondence between the physics of hadronic collisions and that of cosomology. There is an initial singularity

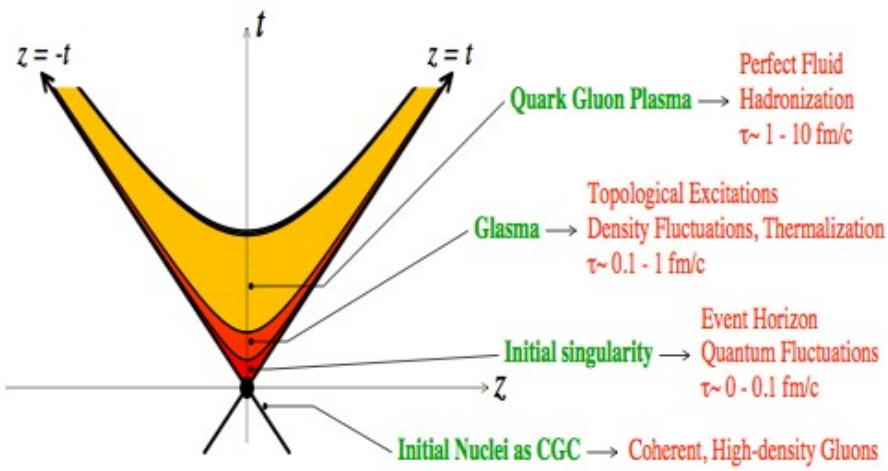


Fig. 2: A space-time diagram for hadronic collisions

and singularity along the light cone. In the expansion, topological excitations are generated, which I will describe later. These excitations have a correspondence with the topological charge changing processes of electroweak theory, which may be responsible for the baryon asymmetry of the universe. [14]- [16] There is a 1+ 1 dimensional analog of Hubble expansion in hadronic collision, which corresponds to that of 3+1 dimensional Hubble flow in cosmology. [17]- [18]

I have purposely not tried to discriminate here between heavy ion collisions and hadronic collisions. Of course the energy density, and the validity of various approximations may depend upon the energy and the nature of particles colliding. The physics should be controlled by the typical density of produced particles, and when the size of the system R becomes large compared to the typical inter-particle separation $d \sim \rho^{-1/3}$, one is justified in taking the large size limit. This should ultimately happen at very high energies since the density of gluons rises as beam energy increases, but it may be greatly enhanced by the use of nuclei.

The reason for this high density of gluons is that the size of a hadron, for example a proton, grows very slowly as a function of collision energy. On the other hand, the number of gluons grows rapidly. The lowest fractional momentum x values probed at some collision energy are typically $x \sim \Lambda_{QCD}/E$, so that the number of gluons at small x is a measure of the number of gluons appropriate for the description of a hadron at energy E. Note that gluons dominate the wavefunction of a hadron for $x \leq 10^{-1}$, shown in Fig. 3. [19]- [25]

These gluons are associated with states in the high energy hadron wavefunction. As shown in Fig. 4, the Fock space components of a nucleon wavefunction have states with 3 quarks, and 3 quarks with arbitrary numbers of gluons and quark-antiquark pairs. The part of the wavefunction with 3 quarks and a few quark-antiquark pairs dominates properties of the nucleon measured in

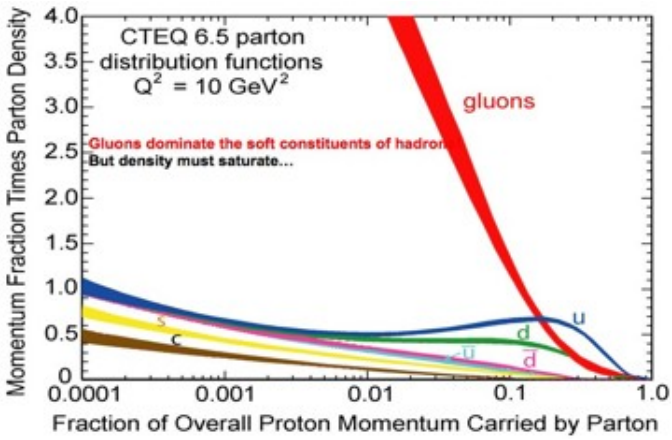


Fig. 3: A distribution of quarks and gluons in a hadron as a function of x

intermediate energy processes and high energy processes at large x. The part with many gluons controls typical high energy processes. These states have a very high density of gluons.

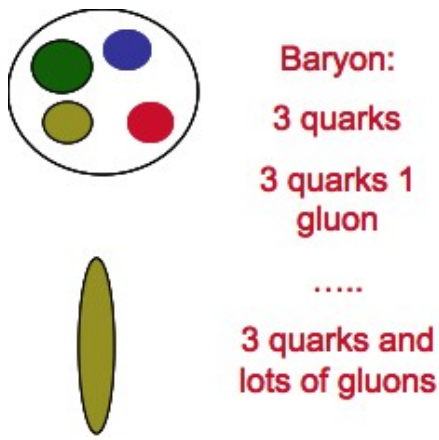


Fig. 4: The Fock space states corresponding to a high energy hadron wavefunction.

Before proceeding further, I want to review some of the kinematic variables useful for the high energy limit. I introduce light cone variables associated with time, energy, longitudinal coordinate and momentum,

$$\begin{aligned} x^{\pm} &= (t \pm z)/\sqrt{2} \\ p^{\pm} &= (E \pm p_Z)/\sqrt{2} \end{aligned} \tag{1}$$

The dot product is $x \cdot p = x_T \cdot p_T - x^+ p^- - x^- p^+$. The uncertainty principle is $x^{\pm} p^{\mp} \geq 1$. A longitudinal boost invariant proper time is $\tau = \sqrt{t^2 - z^2}$ and corresponding transverse mass

is $m_T = \sqrt{p_T^2 + M^2}$. There are several types of rapidity corresponding to different choices of space-time or momentum space variable. Using definitions and the uncertainty principle, we see that up to uncertianties of order one unit of rapidity, all of these rapidity variables are the same,

$$y = \frac{1}{2} ln(p^+/p^-) = ln(p^+/m_T) \sim -ln(x^-/\tau) = -\frac{1}{2} ln(x^+/x^-) = -\eta \tag{2}$$

2 The Color Glass Condensate

The Color Glass Condensate is the matter associated with the high density of gluons appropriate for the description of the wavefunction of a high energy hadron. In the following, I motivate the CGC, and discuss phenomenological implications.

2.1 The Color Glass Condensate and Saturation

As gluons are added to a high energy particle wavefunction, where do they go? The size of a hadron is roughly constant as energy increases. If we add gluons of fixed size then surely at some energy scale these gluons will closely pack the area of a hadron. Repulsive interactions of order α_s will become important and the packing will shutoff when the density is of order $1/\alpha_s$. How can more gluons be packed into the hadron? Resorting to an analogy with hard spheres, we can pack in more gluons if their size is small. They can fit into the holes between the closely packed gluons of larger size. This process can go on forever, packing in gluons of smaller and smaller size as the energy increases. There is a characteristic momentum scale Q_{sat} which corresponds to the inverse size scale of smallest gluons which are closely packed. The saturation momentum, Q_{sat} grows as the energy increases. Note that saturation does not mean the number of gluons stopped growing, only that for gluons of size larger than $1/Q_{sat}$, they have stopped growing.

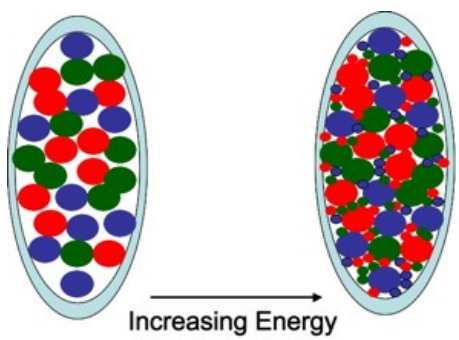


Fig. 5: Gluons being added to the wavefunction of a hadron as energy increases.

We can now understand the name Color Glass Condensate. The word color comes from the color of the gluons. The word condensate comes from the high density of gluons. The phase space density of gluons is

$$\frac{dN}{dyd^2p_Td^2x_T} = \rho \tag{3}$$

There is some effective potential which describes the gluons. At low density, $V \sim -\rho$, since the system wants to increase its density. On the other hand, repulsive interactions balance the inclination to condense, $V_{int} \sim \alpha_s \rho^2$. These contributions balance one another when $\rho \sim 1/\alpha_s$. The phase space density measures the quantum mechanical density of states. When $Q_{sat} >> \Lambda_{QCD}$, the coupling is weak, and the phase space density is large. The gluons are in a highly coherent configuration. The density scaling as the inverse interaction strength $1/\alpha_s$ is characteristic of a number of condensation phenomena such as the Higgs condensate, or superconductivity.

The word glass arises because the gluons evolve on time scales long compared to the natural time scale $1/Q_{sat}$. The small x gluons are classical fields produced by gluons at larger values of x. These fast gluons have their time scale of evolution time dilated relative to their natural one. This scale of time evolution is transferred to the low x gluons. This means that the low x gluons can be approximated by static classical fields, and that different configurations of gluons which contribute to the hadron wavefunction can be treated as a non-intrefering ensemble of fields. These are properties of spin glasses.

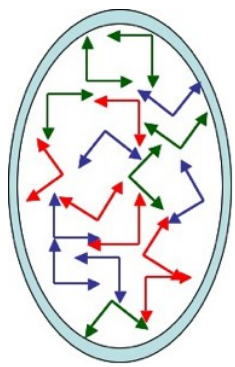


Fig. 6: The color electric and color magnetic fields associated with the Color Glass Condensate.

The configuration of color electric and magnetic fields of the CGC are determined by kinematics. Let the hadron be a thin sheet located a $x^- \sim 0$. The fields will be slowly varying in x^+. Therefore F^{i-} is small, F^{i+} is big and the transverse field strengths F^{ij} are of order one. This means that $\vec{E} \perp \vec{B} \perp \hat{z}$, so that the fields have the form of Lorentz boosted Coulomb fields of electrodynamics. They are shown in Fig. 6. They have random color, polarization and density. The theory of the CGC determines the spectrum of these fluctuations.

2.2 The Renormalization Group

The spectrum of fluctuations is determined by renormalization group arguments. The separation between what we call low x and large x gluons is entirely arbitrary. The way we treat gluons below some separation scale is as classical fields with small fluctuation in the background. For gluons with x larger than the separation scale, we treat them as sources. If we shift the separation scale to a lower value, we need to integrate out the fluctuations at intermediate scales, and they become the sources at high x. This integration is necessary since the fluctuations generate

corrections to the classical theory of the form $\alpha_s ln(x_0/x)$ where x_0 is the separation scale and x is typical of the gluons. If x is too small compared to x_0, then the classical filed treatment does not work. One has to integrate out fluctuations recursively by the method of the renormalization group to generate a theory on the scale of interest. In this way, the fluctuations become new sources for fields at yet lower values of x.

This method of effective field theory was developed to treat the CGC. It was found that the evolution equations are diffusive, and have universal solutions at small x. No matter what hadron one starts with, the matter one eventually evolves to is universal!. The diffusive nature of the evolution means that the number of gluons and the saturation momentum itself never stop growing. At high enough energy, the coupling therefore becomes weak, although because the field strengths are large, the system is non-perturbative.

The renormalization group predicts the dependence of the saturation momentum on energy. [26]- [27] In lowest order, it predicts the power law dependence on x but with too strong a dependence. This is corrected in higher order, and generates a reasonable description about what is known from experiment. [1]

The renormalization group analysis also describes limiting fragmentation and small deviations from in it, in accord with experimental observation. [28]- [29]

2.3 The CGC Provides and Infrared Cutoff

The CGC acts as in infrared cutoff when computing the total multiplicity. [9], [30] For momentum scales $p_T \geq Q_{sat}$ a produced particle sees individual incoherent partons, and the results of ordinary perturbation theory which uses incoherent parton distributions should apply. If the rapidity distribution of gluons in a hadron was roughly constant, then the distribution of gluons would be $dN/d^2p_T dy \sim 1/p_T^2$. At small $p_T \leq Q_{sat}$, the gluon distribution is cutoff since a produced parton sees a coherent field produced by a distribution of sources which is color neutral on the scale $1/Q_{sat}$. This reduces the strength $dN/d^2p_T dy \sim constant/\alpha_s$, up to logarithms. We therefore obtain

$$\frac{dN}{dy} \sim \frac{1}{\alpha_s}\pi R^2 Q_{sat}^2 \tag{4}$$

In hadron-hadron collisions, the $1/p_T^4$ spectrum is also cutoff at $p_T \sim Q_{sat}$, so it too has the form above.

2.4 The Total Cross Section

Assume that the distribution in impact parameter and rapidity factorizes

$$\frac{dN}{dyd^2r_T} = Q_{sat}^2 e^{-2m_\pi r_T} \tag{5}$$

The dependence above in the impact parameter profile is correct at large r_T since the cross section should be controlled by isospin zero exchange. The total cross section measured by some probe is determined by the maximum radius for which $Q_{sat}^2 e^{-2m_\pi b_T} \sim constant$. Using the phenomenological parameterization of the saturation momentum $Q_{sat}^2 \sim e^{\kappa y}$, we see that

$b_T \sim y$, so that the total cross section behaves as

$$\sigma \sim b_T^2 \sim y^2 \sim ln^2(E/\Lambda_{QCD}) \tag{6}$$

The cross section saturates the Froissart bound. [31]- [33] (This becomes modified somewhat when the gluon distribution is computed using a running coupling constant.)

2.5 Qualitative Features of Electron-Hadron Scattering

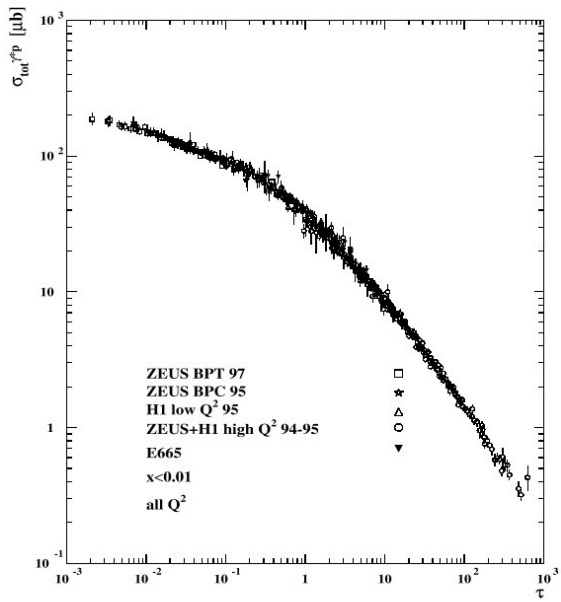


Fig. 7: Geometric Scaling of $\sigma_{\gamma^* p}$

.

The cross section $\sigma^{\gamma^* p}$ is measured in deep inelastic scattering. In the CGC, this cross section is determined by computing the expectation values of electromagnetic currents in the background of the CGC fields. On dimensional grounds, it is only a function of $F(Q^2/Q_{sat}^2)$. In the theory of the CGC, the only energy dependence appears through the dependence of the saturation momentum upon energy. There is no separate energy dependence. This means that the data on deep inelastic scattering should scale in $\tau = Q^2/Q_{sat}^2$ The data on $\sigma^{\gamma^* p}$ for $x \leq 10^{-2}$ is shown in Fig. 7. It clearly demonstrates this scaling. The data for $x \geq 10^{-2}$ does not demonstrate the scaling.

It is a little strange that the data has such scaling for $\tau >> 1$. This region is far from that of saturation. It can nevertheless be shown that for $Q^2 << Q_{sat}^4/\Lambda_{QCD}^2$ that such scaling occurs, although this is the region where a DGLAP analysis is valid. The saturation momentum in this region appears as a result of a boundary condition of the DGLAP evolution. It is also possible to compute the structure functions for deep inelastic scattering in a way which includes both the

effects of the CGC and properly includes DGLAP or BFKL evolution, and good descriptions of the data are obtained. The weakness of this analysis is of course that at Hera energies, the values of Q_{sat}^2 are not so large.

Diffractive deep inelastic scattering may also be analyzed using techniques of saturation and the CGC. One can obtain a good description of diffractive structure functions. The CGC and the impact parameter profile of hadrons are inputs for such computations. [25], [34]- [37]

2.6 The CGC and Shadowing

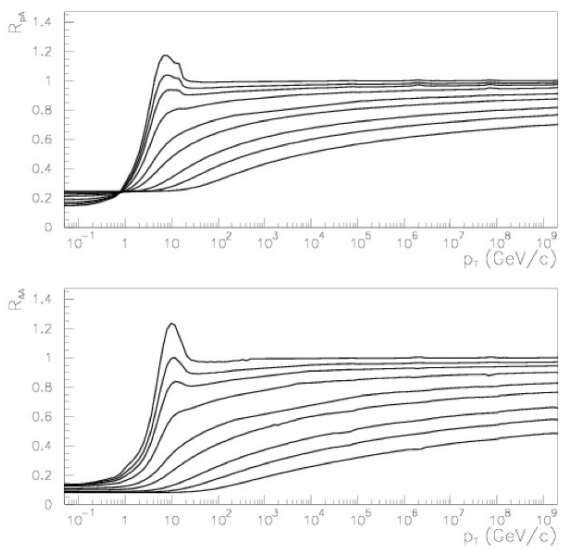


Fig. 8: The ratios R_{pA} and R_{AA} of particles produced in pA and AA collisions to that in pp as a function of the transverse momentum of the produced particle. The curve at the largest value of x is the top curve, and evolution to smaller values of x proceeds by moving further down.

The CGC provides a theory of shadowing for hadron nucleus interactions. [38]- [40] Such shadowing can be measured in lepton-nucleus scattering, pA scattering or AA scattering. There are two competing effects. The first is that the effects of a gluon propagating in a background field are distorted by the background field. Such a field is stronger in a nucleus than in a proton. These fields generate more momentum in the gluon distribution function at intermediate momentum at the expense of gluons at low momentum. This will cause a Cronin peak in the ratios R_{AA} and R_{pA} at intermediate p_T. It can be shown that this effect reflects multiple scattering of a projectile interacting with a target. Such a peak is shown in Fig. 8. Evolution of the distribution function to low values of x is also affected by the CGC. The CGC saturation momentum acts as a cutoff on the evolution equations. Since the saturation momentum is larger for a nucleus than for a proton, as the distribution functions are evolved to smaller values of x, they are overall suppressed in

a nucleus relative to a proton. This is also shown in Fig. 8, where the distribution functions at different values of x are shown as a result of a computation for the CGC.

At RHIC, distributions of particles were measured in dA collisions. [41] In the forward region of such collisions, values of $x \sim 10^{-3}$ of the gold nucleus were measured. At large values of x, a clear Cronin enhancement was found for intermediate p_T. At small x, the distributions were suppressed, as predicted by the CGC. Also at small x, as one increased the associated multiplicity in the collision corresponding to more central collisions, there was less suppression at large x and more suppression at small x. One could describe these observations within the CGC framework. The conclusions from such an analysis are somewhat limited by the kinematic limitations of the energy involved.

3 The Glasma

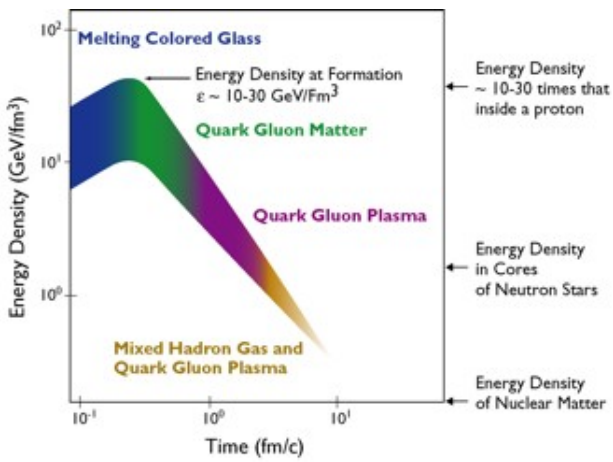


Fig. 9: The various stages of heavy ion collisions.

In Fig. 9, I present the various stages of heavy ion collisions. The times and energy densities on this plot are appropriate for gold-gold collisions at RHIC. The times are measured after the collision is initiated. There is at late times a Quark Gluon Plasma, which is the matter after it has had time to thermalize. Quark Gluon Matter exists at intermediate times when the degrees of freedom are not highly coherent, nor thermalized, and can be thought about as quarks and gluons. The earliest times are when the fields are highly coherent, and most of the energy is in coherent field degrees of freedom, not in the degrees of freedom of incoherent quarks and gluons. The matter at earliest times is called the Glasma, since it is neither a Quark Gluon Plasma, nor a Color Glass Condensate, but has features of both. As we shall see below, almost instantaneously after the collision, the field configurations of the CGC, which are transverse, change into those of the Glasma, which are longitudinal. It is the creation and decay of these Glasma fields which will be the subject of the next subsections.

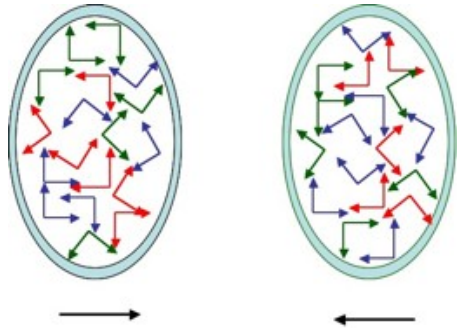


Fig. 10: Colliding sheets of colored glass..

4 Colliding Sheets of Colored Glass

Two hadrons in collision are visualized sheets of colored glass. [8]- [11] They solve classical Yang-Mills equations before and after the collision. These classical fields change their properties dramatically during the collision. Prior to the collision, they are transverse to the direction of motion and confined to the region of thin sheets. In the time it takes light to travel across the thin sheets, the sheets become charged with color electric and color magnetic charge. This results in longitudinal color electric and color magnetic fields between the sheets. The typical strength of these fields is of order Q_{sat}^2/α_S, and the typical variation in the transverse direction is on a size scale $1/Q_{sat}$ These sheets have a large topological charge density since $\vec{E} \cdot \vec{B} \neq 0$. It can be shown that such a description follows from first principles within the formalism of the Color Glass Condensate, and satisfies factorization theorems, similar to those in the parton model. [42]

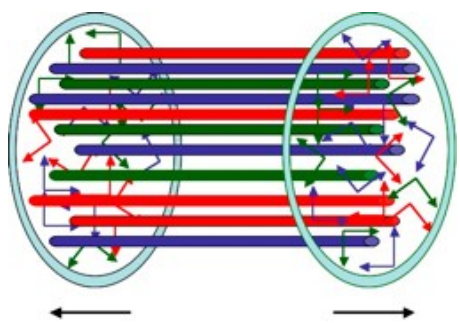


Fig. 11: The Glasma as it appears in early stages of hadronic collisions.

The initial distribution of longitudinal color electric and magnetic fields and their evolution until thermalization is referred to as the Glasma. It has properties such as the coherent strong fields that are similar to the Color Glass Condensate, but it also decays into quarks and gluons which are closer in description to that of a Quark Gluon Plasma. Hence its name. This classical ensemble of flux tubes can decay classically because

$$D_0 \vec{E} \;\; = \;\; \vec{D} \times \vec{B}$$

$$D_0 \vec{B} \;=\; \vec{D} \times \vec{E} \tag{7}$$

Nevertheless, the decay of such flux tubes should generate observable effects in two particle correlations. [43]- [53] Such effects appear to have been observed in the two particle correlations measured at RHIC, and are the subject of my plenary session talk at this meeting.

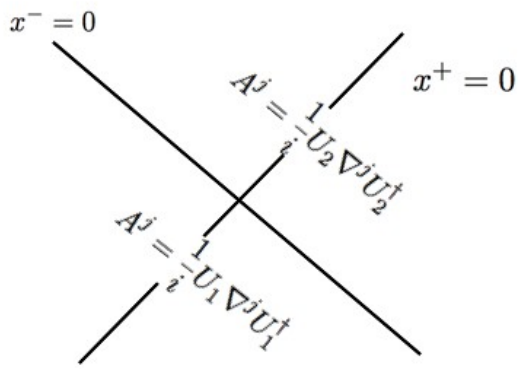


Fig. 12: The vector potential corresponding to a single sheet of colored glass.

How are these Glasma fields formed? The initial vector potential corresponding to single sheet of colored glass is shown in Fig. 12. If we choose a field which is a pure two dimensional gauge transformation of vacuum, but a different gauge transform on either side of the sheet located at $x^- = 0$, the Yang-Mills equations are solved for $x^- \neq 0$. There is a discontinuity at $x^- = 0$, and this discontinuity in the Yang-Mills equations generates the sources of charges corresponding to the Lorentz contracted hadron. The color electric and color magnetic fields generated by this vector potential exist only on the sheets and have $\vec{E} \perp \vec{B} \perp \hat{z}$.

Now consider the collision of two sheets of colored glass as shown in Fig. 13. In the backward lightcone, we use overall gauge freedom to specify $A^\mu = 0$. Within the side light cones, we have A_1 and A_2 chosen so that the correct sources for the hadron are generated along the backward light cone. In the forward light cone we can have the Yang-Mills equation properly generate the source if infinitesimally near the light cone, we take $A = A_1 + A_2$. However, since the sum of two gauge fields which are gauge transforms of vacuum are not a gauge transform of vacuum for non-abelian theories, this field must be taken as an initial condition, so that the fields evolve classically into the forward light cone. This is how the Glasma fields are made, which eventually evolve into the Quark Gluon Plasma.

The fields generated in this way are very slowly varying in rapidity. All of the variation ultimately arises because of the renormalization group evolution of the sources. Therefore, the longitudinal Glasma fields are long range in rapidity. The origin of these long range fields is seen from the Yang-Mills equations, which near the forward light cone become.

$$\begin{aligned} \nabla \cdot E_{1,2} &= A_{2,1} \cdot E_{1,2} \\ \nabla \cdot B_{1,2} &= A_{2,1} \cdot B_{1,2} \end{aligned} \tag{8}$$

It can be shown that the color electric charge and color magnetic charge densities on each sheet are equal in magnitude but opposite in sign. On the average, there is as much strength in color electric field as there is in color magnetic because of the symmetry of the Yang-Mills equation under $E \leftrightarrow B$, and the symmetry of the fields in the Color Glass Condensate.

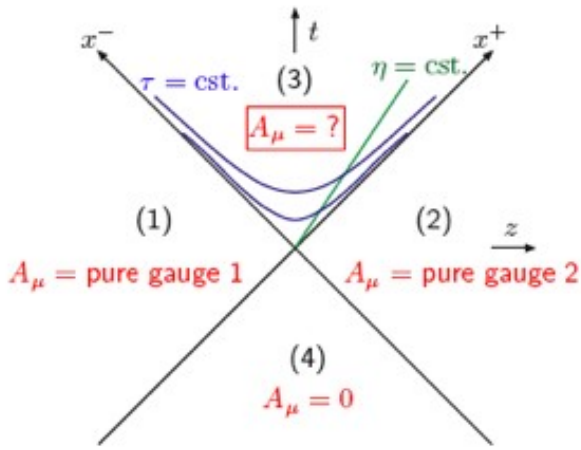


Fig. 13: The vector potential corresponding to the collisions of two sheets of colored glass.

The fields associated with the Glasma will develop turbulent or chaotic modes. [54]- [59] This means that if one starts with the boost invariant field described above, then in a time scale of order $t \sim ln(1/\alpha_S)/Q_{sat}$ small fluctuations which are not boost invariant will grow and begin to dominate the system, This becomes a large effect after the bulk of the Glasma have evaporated, $t \sim 1/Q_{sat}$. There should nevertheless remain a significant component of classical fields until a time of order $t \sim 1/(\alpha_s Q_{sat})$. These instabilities might or might not have something to do with the early thermalization seen at RHIC. They might also generate contributions to transverse flow at early times. This problem is an amusing one since these early time fluctuations may ultimately generate a Kolmogorov spectrum of fluctuations.

4.1 Total Multiplicity in Au-Au Collisions at RHIC

One of the early successes of the CGC-Glasma description was the computation of the rapidity density of produced particles in RHIC Au-Au collisions. [9], [30] The CGC-Glasma provided one of the very few correct predictions for the multiplicity, and as shown in Fig. 14, correctly predicted the dependence of multiplicity upon centrality (and energy).

4.2 Event by Event P and CP Violation

It has been suggested that in RHIC collisions, there might be large event by event CP and P violations. [60]- [62] This can occur by topological charge changing processes generated in the time evolution of the Glasma. These are analogous to the sphaleron transitions which generate

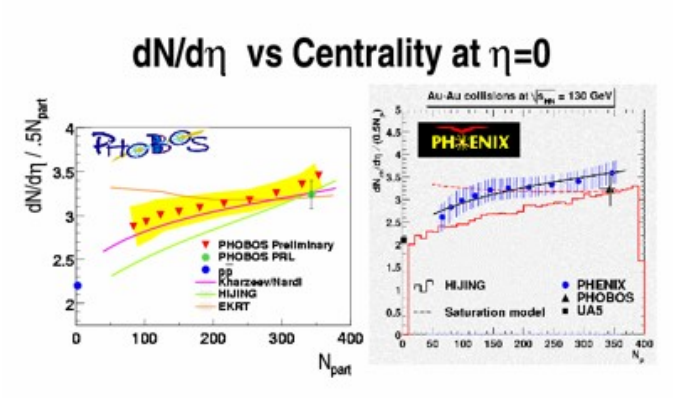


Fig. 14: The multiplicity of produced particles in heavy ion collisions compared to CGC-Glasma expectations

electroweak-baryon number violation in the standard model at temperatures of the order of the electroweak scale. [14]- [16] In QCD, they are associated with anomalous helicity flip processes. Such processes can occur at very early times during the Glasma phase of evolution.

Of course such helicity flip processes take place all the time in the QCD vacuum, since instanton processes are common-place when the coupling is of order one. What makes heavy ion collisions special is that early in the collision, the electromagnetic charges of the nuclei can generate a strong electromagnetic field in off impact parameter zero collisions, and that the high energy density of the Glasma fields makes the coupling small so that effects are computable. The magnetic field decays rapidly in a time of order $1/Q_{sat}$. If there is a net helicity induced by topological charge changing processes in the presence of a magnetic field, then one generates an electromagnetic current parallel to the magnetic field. This is because the magnetic moments align in the magnetic field, and since there is net helicity, this in turn implies a net current. In this way, by measuring the fluctuations in the current, one might measure underlying topological charge changing processes. This effect is called the Chiral Magnetic effect, and is illustrated in Fig. 15.

5 Summary and Conclusions

The Color Glass Condensate and the Glasma are forms of matter predicted by QCD. They provide a successful phenomenology of high energy hadron-hadron and lepton-hadron-collisions. At RHIC and Hera energies, they provide a semi-quantitative framework which describes a wide variety of different processes. The theory underlying the CGC and the Glasma becomes best at the highest energy where the saturation momentum is large and the interaction strength of QCD at that scale $\alpha_s(Q_{sat})$ is correspondingly small. Clearly, experiments at LHC energies can test these ideas. Another way to make the saturation momentum large is of course to use lepton-nucleus collisions where the density is enhanced because of the nucleus. [63]

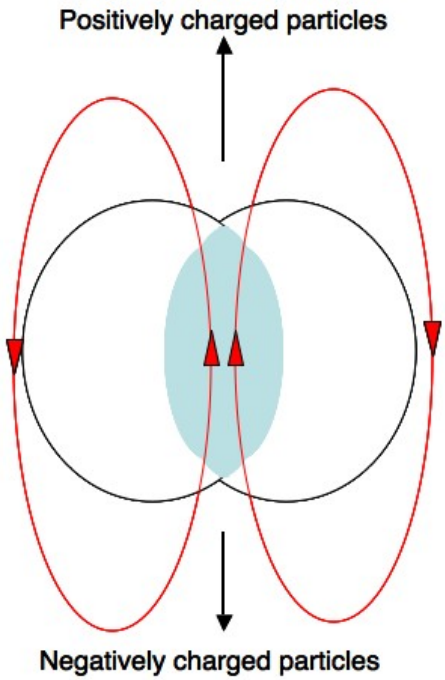


Fig. 15: The chiral magnetic effect as induced by the off impact parameter zero collisio of two heavy ions.

6 Acknowledgments

I thank the organizers of the International Symposium on Miltiparticle Dynamics for their kind hospitality.

This manuscript has been authorized under Contract No. DE-AC02-98CH0886 with the US Department of Energy.

References

[1] E. Iancu and R. Venugopalan, in QGP3, Eds. R. C. Hwa and X. N. Wang, World Scientific, hep-ph/0303204; L. McLerran, arXiv 0807.4095; H. Kowalski and D. Teaney, *Phys. Rev.* **D68** 114005 (2003).

[2] L. McLerran and R. Venugopalan, *Phys. Rev.* **D49** 2233 (1994); **D49** 3352 (1994).

[3] Y. Kovchegov, *Phys. Rev.* **D54** 5473 (1996).

[4] J. Jalilian-Marian, A. Kovner, L. McLerran and H. Weigert, *Phys. Rev.* **D55** (1997), 5414;.

[5] J. Jalilian-Marian, A. Kovner, A. Leonidov and H. Weigert, *Nucl. Phys.* **B504** (1997), 415; *Phys. Rev.* **D59** (1999), 014014.

[6] E. Iancu, A. Leonidov and L. D. McLerran, *Nucl. Phys.* **A692**, 583 (2001); E. Ferreiro E. Iancu, A. Leonidov and L. D. McLerran, *Nucl. Phys.* **A710**,373 (2002); E. Iancu and L. McLerran, *Phys. Lett.* **B510**, 145 (2001).

[7] A. H. Mueller, *Phys.Lett.* **B523**, 243 (2001)

[8] A. Kovner, L. McLerran and H. Weigert, *Phys. Rev.* **D52** 3809 (1995); **D52**, 6231 (1995).

[9] A. Krasnitz and R. Venugopalan, *Nucl. Phys.* **B557** 237 (1999); *Phys. Rev. Lett.* **84** 4309 (2000)

[10] T. Lappi, *Phys. Rev.* **C67** 054903 (2003).

[11] T. Lappi and L. McLerran, *Nucl. Phys.* **A772** 200 (2006).

[12] See the contributions to the RBRC Workshop on New Discoveries at RHIC: The Current Case for the Strongly Interactive QGP, May 2004, *Nuc. Phys.* **A 750** 30 (2005).

[13] See the contributions of the RHIC experiments in I. Arsene et. al. *Nucl. Phys.* **A757** 1 (2005); K. Adcox et. al it Nucl. Phys. **A757** 184 (2005); H. Back et. al. *Nucl. Phys.* **A757** 28 (2005); J. Adams et. al. *Nucl. Phys.* **A757** 102 (2005).

[14] N. Manton, *Phys. Rev.* **D28** 2019 (1983); F. Klinkhammer and N. Manton, *Phys. Rev. D30* 2212 (1984).

[15] V. Kuzmin, V. Rubakov and M. Shaposhnikov, *Phys. Lett.* **B155** 36 (1985).

[16] P. Aronold and L. McLerran, *Phys. Rev.* **D36** 581 (1987); **D37** 1020 (1988).

[17] E. Shuryak, *Phys. Lett.* **B78** 150 (1978); *Sov. J. Nucl. Phys.* **28** 408 (1978); *Yad. Fiz.* **28** 796 (1978); R. Anishetty, P. Koehler and L. McLerran, *Phys. Rev.* **D22** 2793 (1980).

[18] J. D. Bjorken, *Phys. Rev.* **D27** 140 (1983).

[19] J. Breitweg et. al. *Eur. Phys. J.* **67**, 609 (1999).

[20] L. V. Gribov, E. M. Levin and M. G. Ryskin, *Phys. Rept.* **100**, 1 (1983).

[21] A. H. Mueller and Jian-wei Qiu, *Nucl. Phys.* **B268**, 427 (1986); J.-P. Blaizot and A. H. Mueller, *Nucl. Phys.* **B289**, 847 (1987).

[22] L.N. Lipatov, *Sov. J. Nucl. Phys.* **23**, 338 (1976); E.A. Kuraev, L.N. Lipatov and V.S. Fadin, *Sov. Phys. JETP* **45** , 199, (1979); Ya.Ya. Balitsky and L.N. Lipatov, *Sov. J. Nucl. Phys.* **28** 822 (1978).

[23] Y. Kovchegov, *Phys. Rev.* **D60** 034008 (1999); **D61** 074018 (2000).

[24] I. Balitsky, *Nucl. Phys.* **B463** 99 (1996).

[25] K. Golec Biernat, Anna Stasto, and J. Kwiecinski, *Phys. Rev. Lett.* **86** 596 (2001).

[26] E. Iancu, K. Itakura and L. McLerran, *Nucl. Phys.* **A708**, 327 (2002).

[27] A. Mueller and D. Triantafyllopoulos, *Nucl. Phys.* **B640** 331 (2002); D. Triantafyllopoulos, *Nucl. Phys.* **B648** 293 (2003).

[28] B. B. Back. et. al. *Nucl. Phys.* **A757** 28 (2005).

[29] F. Gelis, A. Stasto, and R, Venugopalan, *Eur. Phys. J.* **C48** 489 (2006).

[30] D. Kharzeev, E. Levin and M. Nardi, *Nucl. Phys.* **A747** 609 (2005); T. Hirano and Y. Nara, *Nucl. Phys.* **A743** 305 (2004).

[31] M. Froissart, *Phys. Rev.* **123** 1053 (1961).

[32] A. Kovner and U. Wiedemann, *Phys. Lett.* **B551** 311 (2003).

[33] E. Ferreiro, E. Iancu, K. Itakura and L. McLerran, *Nucl. Phys.* **A710** 373 (2002).

[34] K. Golec-Biernat and M. Wustoff. *Phys. Rev.* **D60** 114023 (1999).

[35] E. Iancu, K. Itakura and S. Munier, *Phys. Lett.* **B590** 199 (2004).

[36] Y. Kovchegov and L. McLerran, *Phys. Rev.* **D60** 054025 (1999).

[37] H. Kowalski, T. Lappi, C. Marquet, and R. Venugopalan, arXiv:0805.4071.

[38] R. Baier, A. Kovner and U. Wiedemann, *Phys. Rev.* **D68** 054009 (2003).

[39] D. Kharzeev, Y. Kovchegov and K. Tuchin, *Phys. Lett.* **B599** 23 (2004).

[40] J. Jalilian-Marian, Y. Nara and R. Venugopalan, *Phys. Lett.* **B577** 54 (2003); *Prog. Part. Nucl. Phys.* **56** 104 (2006); E. Iancu, K. Itakura and D. Triantafyllopoulos, *Nucl. Phys.* **A742** 182 (2004).

[41] I. Arsene et. al.. *Phys. Rev. Lett.* **91** 072305 (2003); **93** 242303 (2004).

[42] F. Gelis, T. Lappi and R. Venugopalan, arXiv:0810.4829 [hep-th]

[43] B. Srivastava et. al. *Intl. J. Mod. Phys.* **E16**, 3371 (2008).

[44] X. N. Wang and M. Gyulassy, *Phys. Rev.* **D44** 3501 (1991).

[45] N. Amelin, M. Braun and C. Pajares, *Z. Phys.* **C63** 507 (1994).

[46] Y. Kovchegov, E. Levin and L. McLerran, *Phys. Rev.* **C63** 024903 (2001); N. Armesto, L. McLerran and C. Pajares, *Nucl. Phys.* **A781**, 201 (2007).

[47] K. Fukushima and Y. Hidaka, arXiv:0806.2143.

[48] A. Dumitru, F. Gelis, L. McLerran and R. Venugopalan, arXiv:0804.3858.

[49] J. Putschke, *J. Phys. G* **34** S679 (2007); J. Adams et. al., *J. Phys.* **G32**, L37 (2006); *Phys. Rev.* **C73** 064907 (2006); **C72** 044902 (2005); M. Daugherity, arXiv:nucl-ex/0611032.

[50] S. Gavin, L. McLerran and G. Moschelli, arXiv:0806.4718 [nucl-th] .

[51] E. Wenger et. al. arXiv:0804.3038

[52] D. Kharzeev, E. Levin and L. McLerran, *Nucl. Phys.* **A748** 627 (2005).

[53] J. Adams et. al. *Phys. Rev. Lett.* **92** 171801 (2004).

[54] S. Mroczynski, *Phys. Lett.* **B214** 587 (1988); **B314** 118 (1993); **B363**, 26 (1997); P. Romatschke and M. Strickland, *Phys. Rev.* **D68** 036004 (2003); **D70** 116006 (2004).

[55] P. Arnold, J. Lenaghan, and G. Moore, *JHEP* **0308** 002 (2003); P. Arnold, J. Lenaghan, G. Moore and L. Yaffe, *Phys. Rev. Lett.* **94** 072302 (2005).

[56] A. Dumitru and Y. Nara, *JHEP* **0509** 041 (2005); A. Dumitru, Y. Nara and M. Strickland, *Phys. Lett.* **B621** 89 (2005).

[57] P. Romatschke and R. Venugopalan, *Phys. Rev. Lett.* **96** 062302 (2006).

[58] H. Fujii and K. Itakura, arXiv:0806.1840; arXiv:0803.0410; A. Iwazaki, arXiv:0804.0188 [hep-ph]

[59] K. Fukushima, F. Gelis, and L. McLerran, *Nucl. Phys.* **A786** 107 (2007).

[60] D. Kharzeev, R. Pisarski and D. Kharzeev, *Phys. Rev. Lett.* **81** 512 (1998).

[61] D. Kharzeev, A. Krasnitz and R. Venugopalan, *Phys. Lett.* **B545** 298 (2002).

[62] D. Kharzeev, L. Mclerran and H. Warringa, *Nucl. Phys.* **A803** 227 (2008).

[63] S. Aronson, proceedings of DIS2007, Munich, Germany, published in Munich 2007, Deep-inelastic scattering, vol 2, 1161.

Chapter 2

Working Group Dilute Systems

Convenors:

Mandy Cooper-Sarkar (Oxford)
Anna Kulesza (DESY)
Ken Hatakeyama (Rockefeller)

Cross section measurements in DIS

K. Papageorgiou
University of the Aegean, Greece

(on behalf of the H1 and ZEUS Collaborations)

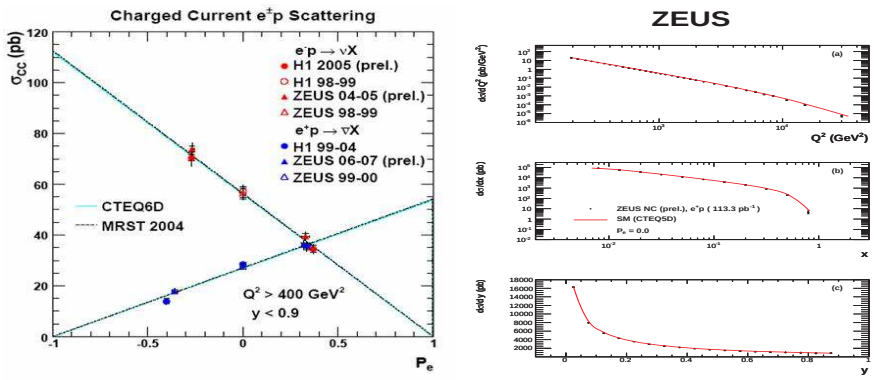
DOI: http://dx.doi.org/10.3204/DESY-PROC-2009-01/36

Abstract

Several topics from the wide field of cross section measurements for Deep Inelastic Scattering (DIS) in ep collissions at HERA are addressed. They include measurements of the Neutral Current (NC) DIS cross section with particular emphasis on the direct determination of the longitudinal proton structure function F_L. Additionally measurements of the Charged Current (CC) e^-p and the Neutral Current (NC) e^+p cross sections from both H1 and ZEUS Collaborations are also presented.

1 Introduction

Studies of the deep inelastic lepton-nucleon scattering has been a very powerfull tool to improve our understanding of the parton structure of the nucleons and also in establishing and testing QCD. The HERA ep collider, having a centre-of-mass energy of 318 GeV in nominal runs, functions like a super microscope with the world's sharpest view of the protons interior, allowing for the first time the direct observation of weak effects in ep DIS at high values of the virtuality Q^2, of the intermediative boson. During the last 3 month's of it's operation (from March to June of 2007), HERA had performed also some special runs with reduced proton beam energies of 460 GeV and 575 GeV dedicated to the direct measurement of the longitudinal polarised structure function F_L. Two different kinds of particle interactions can taken place at HERA: the Neutral Current (NC) and the Charged Current (CC). In the Standard Model (SM), the NC process is mediated by photons or Z- boson, while the CC DIS process is mediated by the exchange of the W-boson. However, at leading order only up and down type of valence quarks contribute to e^-p CC DIS interactions, making these processes valuable for studying flavour specific parton distributions. Chiral structure of weak interactions is directly visible as a function of polarization. The polarization scales linearly with the unpolarised cross section as $\sigma_{CC}^{e^\pm p}(P_e) = (1 \pm P_e)\sigma_{CC}^{e^\pm p}(P_e = 0)$. Measurements of the CC DIS cross section in $e^\pm p$ collissions by both ZEUS [1] and H1 Collaborations revealed a clear and large effect at HERA as depicted in figure 1a. The results are consistent with SM predictions of $\sigma_{CC}^{RH} = 0$ and the absence of RH currents. Measurements of the NC DIS cross sections in e^+p collisions with a longitudinal polarised positron beam, have been previousely published by the ZEUS and the H1 Collaborations [2]. Recent results from ZEUS [3] for the single differential cross sections $\frac{d\sigma}{dQ^2}$,$\frac{d\sigma}{dx}$ and $\frac{d\sigma}{dy}$ for $Q^2 > 185GeV^2$ and $y < 0.95$ based on data corresponding to a luminosity of $L = 113.3pb^{-1}$ at $\sqrt{s} = 318GeV$ and corrected for zero polarization, are presented in figure 1b. Measured cross sections are consistent with SM predictions evaluated using the ZEUS-JETS PDF's.



(a) (b)

Fig. 1: (a) Cross section of CC $e^{\pm}p$ DIS as a function of polarization from the ZEUS (triangles) and the H1 (circles) Collaborations. The results are consistent with SM predictions of $\sigma_{CC}^{RH} = 0$ (b). Single differential NC $e^{+}p$ cross section as a function of Q^2, Bjorken-x and y from the ZEUS Collaboration. The measured cross sections are consistent with SM predictions evaluated using the ZEUS-JETS PDF's.

2 DIS Kinematics

Deep Inelastic Scattering can be described in terms of the kinematical variables x and Q^2. The variable Q^2 is the squared momentum transfer between the lepton and the nucleon and is defined as $Q^2 = -q^2 = -(k - k')^2$, where k and k' denote the four-momenta of the incoming and scattered electron, respectively. The variable x is the Bjorken scaling factor corresponds to the fraction of proton's momentum carried by the struck quark. It is defined by the relation $x = \frac{Q^2}{2P.q}$ where P denotes the four momentum of the incoming proton. The variable $y = \frac{P.q}{P.k}$ is the inelasticity representing the energy fraction transferred from the lepton in the proton rest frame. Bjorken-x and inelasticity are not independent from each other as $Q^2 = sxy$ where s is the total center of mass energy of the ep interaction.
The NC DIS cross section in terms of structure functions can be expressed as following

$$\frac{d^2\sigma(e^{\pm}p)}{dxdQ^2} = \frac{2\pi\alpha^2}{xQ^4} Y_{+}[F_2(x,Q^2) - \frac{y^2}{Y_{+}} F_L(x,Q^2) \pm xF_3(x,Q^2)] \quad (1)$$

where $Y\pm = 1 \pm (1-y)^2$ and x and Q^2 are defined at the hadronic vertex and α is the fine structure constant. In this equation F_2 is the dominant contribution to the cross section for most of the kinematical range and its measurement has been the main ingredient for the PDF's extractions. The H1 and ZEUS Collaborations have presented high statistics measurements of the NC DIS cross section and extracted F_2. The revealed steep rise of F_2 towards low-x values corresponds to the strong scaling violations due to the increase of the gluon density. The data from the two experiments are in very good agreement with each other and with earlier fixed target experiments. In the structure function xF_3 the parity-violating term arising from Z^0 e xchange and has contributions exclusively from the weak force. Experimentally it can be extracted by

measuring the $\frac{d^2\sigma(e^-p)}{dxdQ^2} - \frac{d^2\sigma(e^+p)}{dxdQ^2}$, and is negligible at small Q^2. However, at large y values, the contribution of the longitudinal polarised structure function F_L to the total cross section becomes significant and it cannot be omitted. In addition due to its origin, F_L is directly sensitive to gluon dynamics in the proton and therefore its measurement provides a sensitive test of QCD at low x values.

3 Method for direct F_L measurement

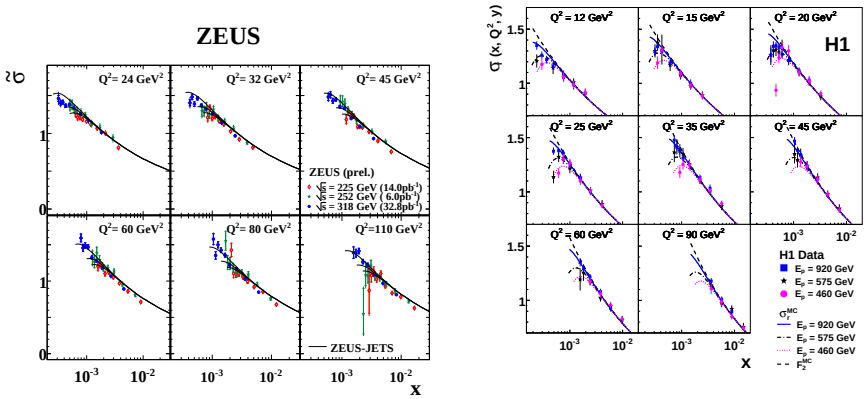
The ep cross section is usually written in the "reduced" form as $\tilde{\sigma}_r = F_2(x,Q^2) - \frac{y^2}{Y_+}F_L(x,Q^2)$, ignoring xF_3 which is negligible at high Q^2. In order to separate F_2 and F_L without any theory assumption one needs to measure the cross section at fixed x and Q^2 and different values of inelasticity, therefore at different beam energies. Then F_L can be extracted as

$$F_L(x,Q^2) = \frac{\tilde{\sigma}_r(x,Q^2,y_1) - \tilde{\sigma}_r(x,Q^2,y_2)}{\frac{y_2^2}{Y_{2+}} - \frac{y_1^2}{Y_{1+}}} \tag{2}$$

The larger the difference in the y values (level arm) or the more measurements of the $\tilde{\sigma}_r$ at intermediate beam energies, the higher the accuracy in the F_L measurement. The experimental challenge in order to measure cross sections at high y values, is related to the identification of the low energy electron in the calorimeter, where a lot of hadronic activity is present. In addition the large photoproduction background at low Q^2 is needed to be controlled and subtracted in order to extract the genuine DIS events. At low y values the high energy electron in the calorimeter is well separated. The DIS events selection criteria for ZEUS experiment, are based on the Uranium Calorimeter for the identification of the electron with energy down to 6 GeV, the use of the CTD and MVD detectors to reject neutrals, and on cuts applied on the z coordinate of the event interaction vertex and also on the longitudinal energy-momemtum variable $E - P_z$ which is calculated using the energy deposits and angles measured with the calorimeter, in order to further reduce the photoproduction background and the radiative corrections. For the H1 Collaboration, the electron identification with energies down to 3GeV relies on the SpaCal and the LAr calorimeter, the use of the CT and BST detectors to reject neutrals, and on cuts applied to the event interaction vertex and to the $E - P_z$ variable as well.

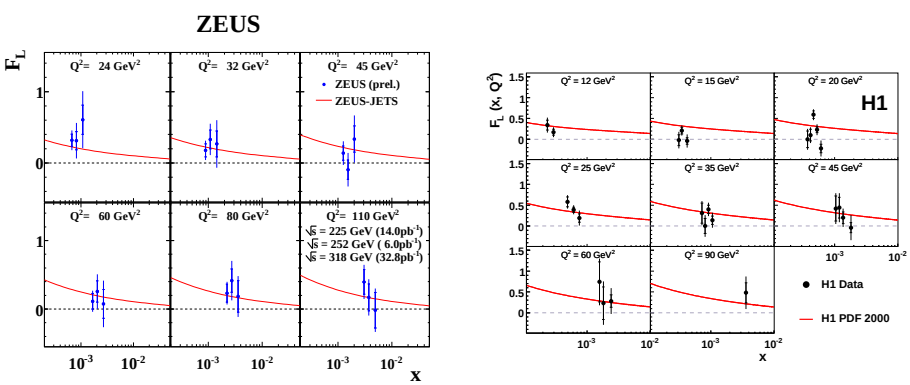
4 Reduced cross section measurement and F_L extraction

Recent measurements of the reduced cross section as a function of x, for various fixed Q^2 values, perfomed separately by the ZEUS [4] and H1 [5] Collaborations and based on data collected at three different center of mass energies ($\sqrt{s} = 318, 252, 225$) GeV), are shown in figures 2a and 2b respectively. The results are compared with the predictions of ZEUS-JETS PDF's and F_2 H1 PDF2000. Visible differences between the data sets and the turn over of the cross sections at low x values are observed, while the cross sections at high-x values are consistent for all data sets. Direct measurements of the longitudinally polarised structure function F_L perfomed for the first time separately by ZEUS [4] and H1 [5] Collaborations, as a function of Bjorken-x for fixed Q^2 values are depicted in figures 3a and 3b respectively. The results are consistent with the prediction of ZEUS-JETS PDF's and H_1 PDF. The x-averaged F_L measurements from the H1 Collaboration [5] as a function of Q^2 values in the range of $12 < Q^2 < 110 GeV^2$, are depicted



(a) ZEUS (b) H1

Fig. 2: Reduced cross section as a function of Bjorken x for various fixed Q^2 values (a) from ZEUS and (b) from $H1$. The lines are predictions using ZEUS-JETS PDF's and $H1$ PDF2000 respectively.



(a) ZEUS (b) H1

Fig. 3: F_L measurements as a function of Bjorken x for various fixed Q^2 values (a) from the ZEUS and (b) from the H1 Collaborations. Lines are predictions using ZEUS-JETS PDF's and H1 PDF2000 respectively.

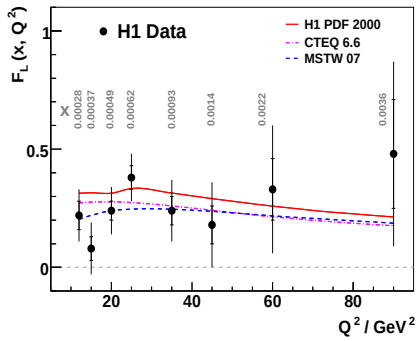


Fig. 4: The x-averaged F_L measurements performed by the H1 Collaboration as a function of the Q^2. The results are consistent with the H1 PDF 2000 fit (red line) and with expectations from other models, CTEQ 6.6 (pink line) and MSTW (blue line) at higher order pertubation theory.

in Figure 4. The results are consistent with the H1 PDF 2000 fit and with the expectations from global parton distribution fits at higher order pertubation theory.

5 Conclusions

The HERA experiments provide unique information on the proton structure over a wide range of Bjorken-x values, an important precision input for physics at LHC. First direct measurements of the longitudinally polarised structure function F_L performed in a new kinematical range of x and Q^2 separately by both the ZEUS ($24 < Q^2 < 110 GeV^2$ and $0.0006 < x < 0.005$) and H1 Collaborations ($12 < Q^2 < 90 GeV^2$ and $0.00024 < x < 0.0036$) are presented here. In general the data are in good agreement with higher order pQCD predictions, although deviations at smaller Q^2 values are visible. The analysis is ongoing, thus it can be expected to further constrain low-x region.

References

[1] ZEUS Collaboration, "Measurement of high-Q^2 charged current deep inelastic scattering cross section with a longitudinally polarised electron beam at HERA", XXXIII International Conference on High Energy Physics, July 26-August 2 , Moscow (Russia).

[2] ZEUS Collaboration, S.Chekanov *et al.*, Phys.Lett. **B637**, 210 (2006).

[3] ZEUS Collaboration, "Measurement of high-Q^2 neutral current deep inelastic e^+p scattering cross sections with longitudinallly polarised electrons at HERA", ZEUS-prel-08-005 (2008).

[4] A. Caldwell, International Workshop on Diffraction in High Energy Physics, DIFFRACTION 2008, 9-14 Sep 2008 , La Londe-les-Maures (France).

[5] H1 Collaboration, Phys.Lett. **B665**, 139 (2008).

Jet Production at HERA

Alexander A. Savin[1] *on behalf of the H1 and ZEUS collaborations*
[1]University of Wisconsin, Madison, Wisconsin 53706, USA

DOI: http://dx.doi.org/10.3204/DESY-PROC-2009-01/37

Abstract

Precise jet measurements at HERA are used to extract α_s value in the regions where the theoretical predictions and data are less affected by uncertainties and to explore regions where the theoretical calculations deviate from the data.

1 Jet measurements and extraction of α_s

Jet production in neutral current (NC) deep-inelastic scattering (DIS) and photoproduction (PHP) at HERA provides an important testing ground for QCD. The strong coupling constant α_s is one of the fundamental parameters of the QCD. High precision in the determination of α_s and consistency in the α_s values obtained in different experiments are achieved by using best available theoretical calculations with experimentally precise measurements in the regions where both are less affected by uncertainties. The HERA combined $\alpha_s(M_Z)$ value [1] is shown in Fig. 1 together with the values obtained by H1 and ZEUS collaborations separately, the 2004 HERA average value, 2006 world average and recent LEP values. The combined value $\alpha_s(M_Z) = 0.1198 \pm 0.0019(exp.) \pm 0.0026(th.)$ was obtained by making a simultaneous fit to H1 and ZEUS data sets, instead of just combining $\alpha_s(M_Z)$ values as it was done for the HERA 2004 average value.

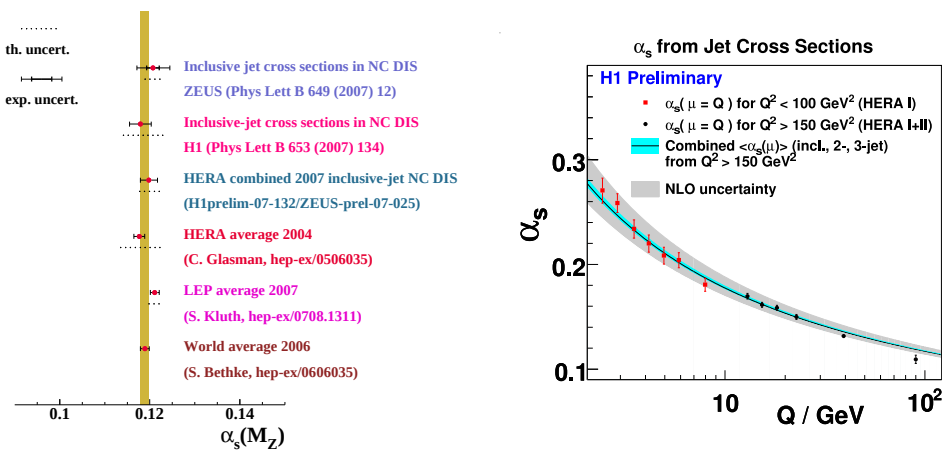


Fig. 1: Measurements of $\alpha_s(M_Z)$ and $\alpha_s(Q)$ at HERA.

A comparison of the combined HERA value to the most recent value of $\alpha_s(M_Z)$ from LEP shows that the central values are compatible within the experimental uncertainty and that

the HERA uncertainty is very competitive with the LEP, which includes an average of many precise determinations.

The precision of the cross-section measurement is directly reflected in the precision of the α_s extraction and can be improved if instead of cross sections the ratios of them are used, since in the cross-section ratios the experimental and theoretical uncertainties partially cancel. Recent H1 measurements in the phase-space region $150 < Q^2 < 15000$ GeV^2 and $0.2 < y < 0.7$, where Q^2 is the virtuality of exchanged boson and y is the inelasticity of the interaction, used most of the data collected by HERA [2]. The data sample corresponds to an integrated luminosity of 395 pb^{-1}. The ratios of the differential inclusive, 2-jet and 3-jet cross sections to the differential NC DIS cross sections were measured. The QCD predictions were calculated using the NLOJET++ program [3]. The predictions were found to describe the data well and all the ratios were fitted simultaneously in order to extract the $\alpha_s(M_Z)$ value, which was found to be $0.1182 \pm 0.0008(exp.)^{+0.0041}_{-0.0031}(scale) \pm 0.0018(PDF)$. The values of α_s as function of Q are shown in Fig. 1. The same plot shows the fitted values of α_s from the recent low-Q^2 measurements (red points, [4]). The error bar denotes the experimental uncertainty of each data point. The solid curve shows the results of evolving $\alpha_s(M_Z)$ only at high $Q^2(Q^2 > 150$ GeV$^2)$, with the inner blue band denoting the correlated experimental uncertainties and the grey band denoting the theoretical uncertainties associated with the renormalisation and factorisation scales, PDF uncertainty and uncertainty in the hadronisation corrections.

A successful extraction of the α_s value in the jet measurements at HERA in a wide kinematic region, including PHP and low-Q^2 DIS, confirms the quality of existing theoretical calculations and their ability to describe the HERA data.

2 Resolved Photoproduction

In PHP at HERA, a quasi-real photon emmitted from the incoming positron or electron can directly take part in the hard interaction, direct PHP, or can act as a source of quarks and gluons with only a fraction of its momentum, x_γ, participating in the hard scatter, resolved PHP. Since x_γ is not directly measurable, a variable $x_\gamma^{\rm obs}$ is used to differentiate between direct- and resolved-photon enriched events.

Figure 2 represents the cross section $d\sigma/d\overline{\eta}$ for direct- and resolved-enriched samples of the dijet photoproduction events measured by the ZEUS experiment [5]. The mean pseudorapidity, $\overline{\eta}$, was calculated for two leading jets with transverse energy, E_T, $E_T^{\rm jet1} > 20$ and $E_T^{\rm jet2} > 15$ GeV.

The next-to-leading-order (NLO) QCD predictions, corrected for hadronisation and using two different photon parton density functions (PDFs) are compared to the data. For, $x_\gamma^{\rm obs} > 0.75$, the NLO QCD predictions describe the data well, with CJK photon PDF better reproducing the shape of the data. At low $x_\gamma^{\rm obs}$ the description is not satisfactory. In this regime the calculations are much more sensitive to the photon PDF, than in the direct photoproduction, but none of the PDFs gives an adequate description of the resolved-enriched data sample. Another issue, which becomes important at low $x_\gamma^{\rm obs}$, is the high-order effects, which will be discussed in details in the next two sections.

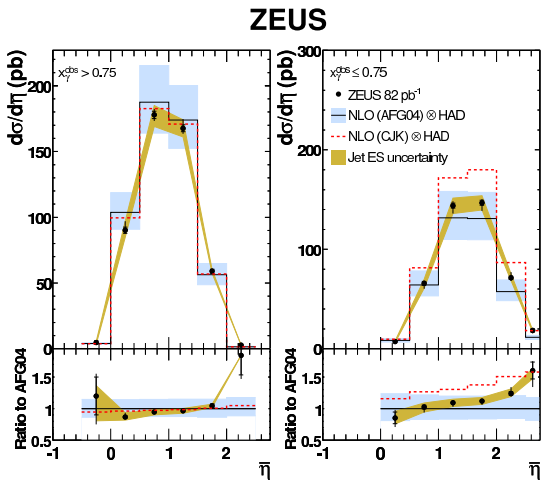


Fig. 2: Measured dijet PHP cross section $d\sigma/d\overline{\eta}$ in direct- and resolved-photon enriched regions, compared to theoretical predictions using different photon PDFs .

3 Forward jets in DIS

A comparison of data on jets produced near the proton direction, forward jets, with NLO QCD calculations has revealed a clear deficit of gluons with sizable transverse momentum, emmitted in these direction. The ZEUS collaboration recently extended the pseudorapidity range of the jets up to 4.3 and performed a measurement in the phase space $0.04 < y < 0.7$, $20 < Q^2 < 100$ GeV^2 and $0.0004 < x_{Bj} < 0.005$ [6].

The measured differential forward-jet cross sections as function of Q^2 and x_{Bj} are shown in Fig. 3a) and b), where they are compared to predictions of the NLOJET++ calculations. The calculations predict lower cross sections than obtained from the data, however they have a large theoretical uncertainty. The leading-order (LO) calculation is also shown, indicating that the contribution of the NLO terms is significant. The difference between data and calculations increases with decreasing x, where the difference between LO and NLO is also increasing. The large contribution of the NLO corrections and the size of the theoretical uncertainty indicate that in this phase-space region the higher-order contributions are important.

The H1 measurement at low-x [7] was performed in region $0.1 < y < 0.7$, $5 < Q^2 < 80$ GeV^2 and $0.0001 < x_{Bj} < 0.01$. The forward jet had to be found in the pseudorapidity range $1.73 < \eta_{jet} < 2.5$ and the "central jet" in the region $-1 < \eta_{jet} < 1$. The cross section as a function of x is presented in Fig. 3 for events which contain two forward and one central jet, where the second forward jet is required to have $\eta_{jet} > 1$. The calculation fails to describe the data at low-x, where the difference between LO and NLO calculations is most pronounced. The data excess provides a strong hint for missing higher-order QCD corrections, i.e. beyond $\mathcal{O}(\alpha_s^3)$, in this forward gluon-radiation-dominated phase space. However, for the process with two radiated gluons, the $\mathcal{O}(\alpha_s^3)$ calculation can only provide a leading order perturbative estimate.

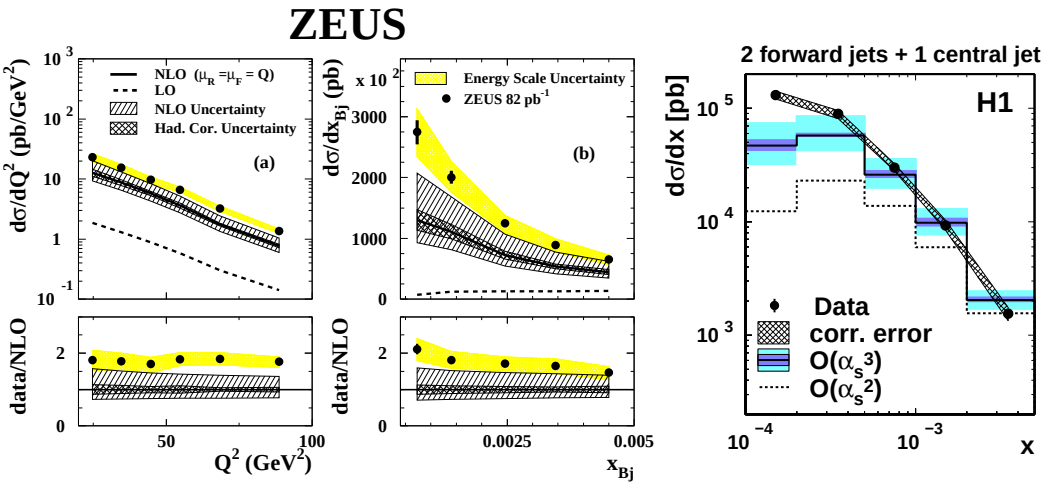


Fig. 3: Forward jets production in DIS.

4 Correlations in multijets at low x_{Bj} in DIS

Inclusive dijet and trijet production in DIS has been measured by the ZEUS collaboration for $10 < Q^2 < 100$ GeV^2 and $10^{-4} < x_{Bj} < 10^{-2}$ [8]. Cross sections, cross section ratios and correlations between the two leading jets provide an important testing ground for studying the parton dynamics in the region of small x_{Bj}.

The dijet and trijet cross sections for events with azimuthal separation between two leading jets, $|\Delta\phi^{jet1,2}_{HCM}|$, less than $2\pi/3$ are presented in Fig. 4. The restriction on the azimuthal separation in dijet sample implicitly requires the presence of at least one other jet, which may or may not be observed in the detector. From the QCD calculation point of view it means that the NLO dijet predictions, at $\mathcal{O}(\alpha_s^2)$, become essentially only LO. Therefore the NLO trijet calculations at $\mathcal{O}(\alpha_s^3)$ were used for comparison with the dijet data sample. An implicit third jet requirement led the trijet NLO calculation to converge even if only two jets are defined. For the trijet data sample the standard trijet NLO procedure was used.

The NLOJET++ calculations at $\mathcal{O}(\alpha_s^2)$ for dijet production underestimate the data, the difference increasing towards low x_{Bj}. The NLOJET++ calculations at $\mathcal{O}(\alpha_s^3)$ are up to about an order of magnitude larger than the $\mathcal{O}(\alpha_s^2)$ calculations and are consistent with the data, thus demonstrating the importance of higher-order corrections in the low-x_{Bj} region. For the trijet sample the calculation works well, since it still provides a proper next-to-leading-order perturbative estimate.

5 Conclusions

The precise study of jet production at HERA demonstrates, that the theoretical predictions are able to successfully describe the data in the regions, where the NLO estimate is available. High-order effects become important in the regions, which are dominated by gluon radiation. The precision in the extraction of α_s at HERA is competitive with those from e^+e^- experiments.

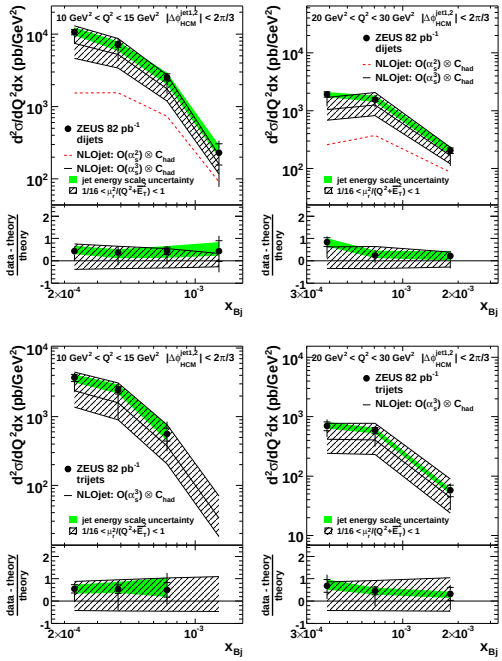


Fig. 4: The dijet and trijet cross sections for events with $|\Delta\phi^{\mathrm{jet}1,2}_{\mathrm{HCM}}| < 2\pi/3$ as a function of x_{Bj} in two Q^2-bins.

References

[1] H1 Collaboration, H1prelim-07-132 (2007);
ZEUS Collaboration, ZEUS-prel-07-025 (2007).

[2] H1 Collaboration, H1prelim-08-031 (2008).

[3] Z. Nagy and Z. Trocsanyi, Phys. Rev. Lett. **87**, 082001 (2001). `hep-ph/0104315`.

[4] H1 Collaboration, H1prelim-08-032 (2008).

[5] ZEUS Collaboration, S. Chekanov *et al.*, Phys. Rev. **D76**, 072011 (2007).

[6] ZEUS Collaboration, S. Chekanov *et al.*, Eur. Phys. J. **C52**, 515 (2007).

[7] H1 Collaboration, F. D. Aaron *et al.*, Eur. Phys. J. **C54**, 389 (2008).

[8] ZEUS Collaboration, S. Chekanov *et al.*, Nucl. Phys. **B786**, 152 (2007).

Extraction of the proton parton density functions using a NLO-QCD fit of the combined H1 and ZEUS inclusive DIS cross sections

Gang LI on behalf of the H1 and ZEUS collaborations
Laboratoire de l'Accélérateur Linéaire, Université Paris-Sud 11
DOI: http://dx.doi.org/10.3204/DESY-PROC-2009-01/38

Abstract
The combined HERA-I data set, of neutral and charged current inclusive cross-sections for e^+p and e^-p scattering, is used as the sole input for a next-to-leading order (NLO) QCD parton distribution function (PDF) fit. The consistent treatment of systematic uncertainties in the joint data set ensures that experimental uncertainties on the PDFs can be calculated without need for an increased χ^2 tolerance. This results in PDFs with greatly reduced experimental uncertainties compared to the separate analyses of the ZEUS and H1 experiments. Model uncertainties, including those arising from parametrization dependence, are also carefully considered. The resulting HERAPDFs have impressive precision compared to the global fits.

1 Introduction

The kinematics of lepton hadron scattering is described in terms of the variables Q^2, the invariant mass of the exchanged vector boson, Bjorken x, the fraction of the momentum of the incoming nucleon taken by the struck quark (in the quark-parton model), and y which measures the energy transfer between the lepton and hadron systems. The differential cross-section for the neutral current (NC) process is given in terms of the structure functions by

$$\frac{d^2\sigma(e^{\pm}p)}{dxdQ^2} = \frac{2\pi\alpha^2}{xQ^4}\left[Y_+F_2(x,Q^2) - y^2F_L(x,Q^2) \mp Y_-xF_3(x,Q^2)\right] ,$$

where $Y_{\pm} = 1 \pm (1-y)^2$. The structure functions F_2 and xF_3 are directly related to quark distributions, and their Q^2 dependence, or scaling violation, is predicted by perturbative QCD. For low x, $x \leq 10^{-2}$, F_2 is sea quark dominated, but its Q^2 evolution is controlled by the gluon contribution, such that HERA data provide crucial information on low-x sea- quark and gluon distributions. At high Q^2, the structure function xF_3 becomes increasingly important, and gives information on valence quark distributions. The charged current (CC) interactions also enable us to separate the flavour of the valence distributions at high-x, since their (LO) cross-sections are given by,

$$\frac{d^2\sigma(e^+p)}{dxdQ^2} = \frac{G_F^2M_W^4}{(Q^2+M_W^2)2\pi x}\left[(\bar{u}+\bar{c}) + (1-y)^2(d+s)\right] ,$$
$$\frac{d^2\sigma(e^-p)}{dxdQ^2} = \frac{G_F^2M_W^4}{(Q^2+M_W^2)2\pi x}\left[(u+c) + (1-y^2)(\bar{d}+\bar{s})\right] .$$

Parton Density Function (PDF) determinations are usually obtained from global NLO QCD fits [1–3], which use fixed target DIS data as well as HERA data. In such analyses, the high statistics HERA NC e^+p data have determined the low-x sea and gluon distributions, whereas the fixed target data have determined the valence distributions. Now that high-Q^2 HERA data on NC and CC e^+p and e^-p inclusive double differential cross-sections are available, PDF fits can be made to HERA data alone, since the HERA high Q^2 cross-section data can be used to determine the valence distributions. This has the advantage that it eliminates the need for heavy target corrections, which must be applied to the $\nu - Fe$ and $\mu - D$ fixed target data. Furthermore there is no need to assume isospin symmetry, i.e. that d in the proton is the same as u in the neutron, since the d distribution can be obtained directly from CC e^+p data. The H1 and ZEUS collaborations have both used their data to make PDF fits [4, 5]. Both of these data sets have very small statistical uncertainties, so that the contribution of systematic uncertainties becomes dominant and consideration of point to point correlations between systematic uncertainties is essential. The ZEUS analysis takes account of correlated experimental systematic errors by the Offset Method, whereas H1 uses the Hessian method [6]. Whereas the resulting ZEUS and H1 PDFs are compatible, the gluon PDFs do have rather different shapes, see Fig. 1, and the uncertainty bands spanned by these analyses are comparable to those of the global fits.

It is possible to improve on this situation since ZEUS and H1 are measuring the same physics in the same kinematic region. These data have been combined them using a theory-free Hessian fit in which the only assumption is that there is a true value of the cross-section, for each process, at each x, Q^2 point [7], [8]. Thus each experiment has been calibrated to the other. This works well because the sources of systematic uncertainty in each experiment are rather different, such that all systemtic uncertainties are re-evaluated. The resulting systematic uncertainties on each of the combined data points are significantly smaller than the statistical errors. In the present paper this combined data set is used as the input to a NLO QCD PDF fit. The consistency of the input data set and its small systematic uncertainties enable us to calculate the experimental uncertainties on the PDFs using the χ^2 tolerance, $\Delta\chi^2 = 1$. This represents a further advantage compared to those global fit analyses where increased tolerances of $\Delta\chi^2 = 50 - 100$ are used to account for data inconsistencies.

For the present HERAPDF0.1 fit, the role of correlated systematic uncertainties is no longer crucial since these uncertainties are relatively small. This ensures that similar results are obtained using either Offset or Hessian methods, or by simply combining statistical and systematic uncertainties in quadrature. For our central fit we have chosen to combine the 43 systematic uncertainties which result from the separate ZEUS and H1 data sets in quadrature, and to Offset the 4 sources of uncertainty which result from the combination procedure. This results in the most conservative uncertainty estimates on the resulting PDFs.

Despite our conservative procedure the experimental uncertainties on the resulting PDFs are impressively small and a thorough consideration of further uncertainties due to model assumptions is necessary. In section 2 we describe the NLO QCD analysis and model assumptions. In section 3 we give results and in section 4 we give a summary.

2 Analysis

The QCD predictions for the structure functions are obtained by solving the DGLAP evolution equations at NLO in the MSbar scheme with the renormalization and factorization scales chosen to be Q^2. The DGLAP equations yield the PDFs at all values of Q^2 provided they are input as functions of x at some input scale Q_0^2. This scale has been chosen to be $Q_0^2 = 4\text{GeV}^2$ and variation of this choice is considered as one of the model uncertainties. The resulting PDFs are then convoluted with NLO coefficient functions to give the structure functions which enter into the expressions for the cross-sections. The choice of the heavy quark masses is, $m_c = 1.4,\ m_b = 4.75\text{GeV}$, and variation of these choices is included in the model uncertainties. For this preliminary analysis, the heavy quark coefficient functions have been caluclated in the zero-mass variable flavour number scheme. The strong coupling constant was fixed to $\alpha_s(M_Z^2) = 0.1176$ [9], and variations in this value of ± 0.002 have also been considered.

The fit is made at leading twist. The HERA data have an invariant mass of the hadronic system, W^2, of $W^2_{min} = 300\text{GeV}^2$ and maximum $x,\ x_{max} = 0.65$, such that they are in a kinematic region where there is no sensitivity to target mass and large-x higher twist contributions. However a minimum Q^2 cut is imposed to remain in the kinematic region where perturbative QCD should be applicable. This has been chosen such that $Q^2_{min} = 3.5\text{GeV}^2$. The variation of this cut is included as one of the model uncertainties.

A further model uncertainty is the choice of the initial parametrization at Q_0^2. The PDFs are parametrized by the generic form

$$xf(x) \quad = \quad Ax^B(1-x)^C(1 + Dx + Ex^2 + Fx^3)\,, \tag{1}$$

and the number of parameters is chosen by saturation of the χ^2, such that parameters D, E, F are only varied if this brings significant improvement to the χ^2. Otherwise they are set to zero.

For our central fit, the PDFs which are parametrized are xu_v, xd_v, xg and $x\bar{U}$, $x\bar{D}$. The normalisation parameters, A, for the d and u valence are constrained to impose the number sum-rules and the normalisation parameter A for the gluon is constrained to impose the momentum sum-rule. The B parameters which constrain the low-x behaviour of the u and d valence distributions are set equal, and the B parameters are also set equal for $x\bar{U}$ and $x\bar{D}$, such that there is a single B parameter for the valence and another different single B parameter for the sea distributions. Assuming that the strange and charm quark distributions can be expressed as x independent fractions, $f_s = 0.33$ and $f_c = 0.15$, of the d and u type sea, gives the further constraint $A(\bar{U}) = A(\bar{D})(1 - f_s)/(1 - f_c)$. The value of $f_s = 0.33$ has been chosen to be consistent with determinations of this fraction using neutrino induced di-muon production. This value has been varied to evaluate model uncertainties. The charm fraction has been set to be consistent with dynamic generation of charm from the start point of $Q^2 = m_c^2$ in a zero-mass-variable-flavour-number scheme. A small variation of the value of f_c is included in the model uncertainties. Saturation of the χ^2 leads us to set the parameters $D, E, F = 0$, for all partons except xu_v for which only $F = 0$.

The results are presented using this parametrization, including six sources of model uncertainty due to variation of: m_c, m_b, f_s, f_c, Q_0^2, Q^2_{min}. Comparison is made to three other classes of parametrization, one based on the ZEUS-JETs parametrization [4], one based on the

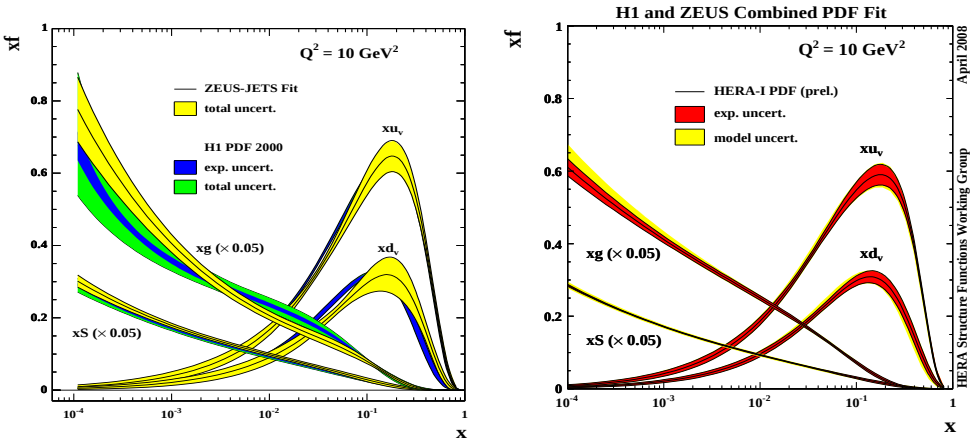


Fig. 1: Left: PDFs from the ZEUS-JETS and H1PDF2000 PDF separate analyses of ZEUS and H1. Right: HERA-PDF0.1 PDFs from the analysis of the combined data set

.

H1 parametrization [5] and one based on the current parametrization but allowing $D \neq 0$ for the gluon. Comparison is also made to results obtained by varying $\alpha_s(M_Z^2)$, see reference [10] for details. Our central choice has less model dependence than the ZEUS-Style parametrization because it has fewer asumptions concerning $\bar{d} - \bar{u}$, and it has less model dependence than the H1-style parametrization in that it does not assume equality of all B parameters. Furthermore, although all types of parametrization give acceptable χ^2 values, the central parametrization has the best χ^2 and it gives the most conservative experimental errors.

3 Results

The total uncertainty of the PDFs obtained from the HERA combined data set is much reduced compared to the PDFs extracted from the analyses of the separate H1 and ZEUS data sets, as can be seen from the summary plots in Fig. 1, where these new HERAPDF0.1 PDFs are compared to the ZEUS-JETS and H1PDF2000 PDFs.

In Fig. 2 we show the HERAPDF0.1 PDFs compared to the CTEQ6.1 PDFs, which also use a zero-mass variable flavour number scheme, and to the preliminary MSTW08 PDFs [11], which use a massive variable flavour number scheme. The precision of the HERAPDF0.1 for the low-x sea and gluon is impressive.

4 Summary

Now that high-Q^2 HERA data on NC and CC e^+p and e^-p inclusive double differential cross sections are available, PDF fits can be made to HERA data alone, since the HERA high Q^2 cross-section data can be used to determine the valence distributions and HERA low Q^2 cross-section data can be used to determine the sea and gluon distributions. The combined HERA-I data set, of neutral and charged current inclusive cross-sections for e^+p and e^-p scattering, has been used as the sole input for a NLO QCD PDF fit in the DGLAP formalism. The consistent treatment of

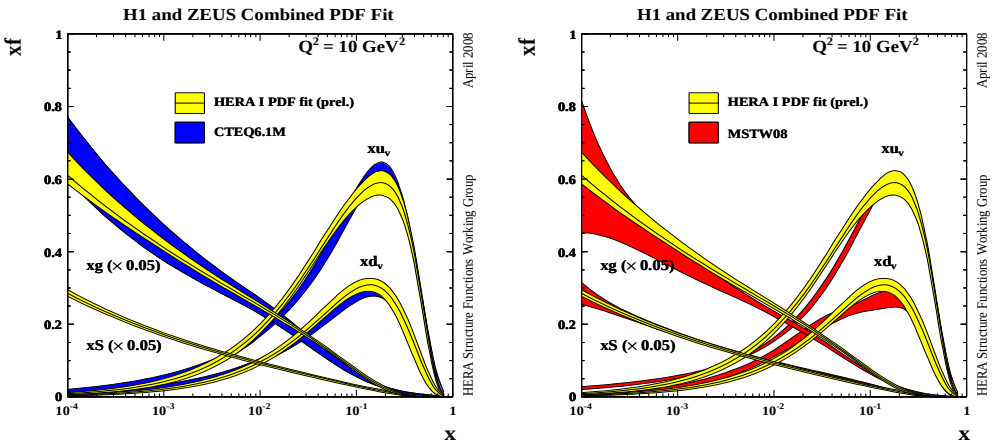


Fig. 2: Left: HERAPDF0.1 at $Q^2 = 10\text{GeV}^2$ compared to the CTEQ6.1 PDFs. Right: HERAPDF0.1 at $Q^2 = 10\text{GeV}^2$ compared to the preliminary MSTW08 PDFs

.

systematic uncertainties in the joint data set ensures that experimental uncertainties on the PDFs can be calculated without need for an increased χ^2 tolerance. This results in PDFs with greatly reduced experimental uncertainties compared to the separate analyses of the ZEUS and H1 experiments. Model uncertainties, including those arising from parametrization dependence, have also been carefully considered. The resulting HERAPDFs have impressive precision compared to the global fits.

References

[1] A. D. Martin et al., Eur. Phys. J **C 44**, 73 (2002).

[2] J. Pumplin et al., JHEP **0207**, 012 (2002).

[3] ZEUS Coll., S. Chekanov et al., Phys. Rev. **D 67**, 012007 (2003).

[4] ZEUS Coll., S. Chekanov et al., Eur. Phys. J **C 42**, 1 (2005).

[5] H1 Coll., C. Adloff et al., Eur. Phys. J **C 30**, 32 (2003).

[6] A. M. Cooper-Sarkar, J. Phys. **G 28**, 2669 (2002).

[7] ZEUS and H1 Collaborations, H1prelim-07-007 (2007).

[8] J. Feltesse, Proceedings of DIS 2008 (2008).

[9] W-M. Yoo et al., J. Phys. **G 33**, 1 (2006).

[10] G. LI, *https://indico.desy.de/getFile.py/access?contribId=38&sessionId=31&resId=0&materialId=slides&confId=*

[11] G. Watt, Proceedings of DIS 2008 (2008).

PDF Constraints From Tevatron Data

Mark Lancaster (on behalf of the CDF and DØ experiments)
UCL, Department of Physics and Astronomy, Gower Street, London, WC1E 6BT, UK
DOI: http://dx.doi.org/10.3204/DESY-PROC-2009-01/39

Abstract
Recent measurements from the CDF and DØ experiments at the Fermilab Tevatron collider that constrain parton distribution functions are presented. These include inclusive jet cross section data and measurements of rapidity distributions in W and Z events.

1 Introduction

The Tevatron $p\overline{p}$ collider presently provides the world's highest energy collisions at a centre of mass energy of 1.96 TeV. Analyses constraining Parton Distribution Functions (PDFs) based on 4 fb^{-1} of integrated luminosity are presently being undertaken and the ultimate constraints are expected to come from datasets of approximately 8 fb^{-1}. The results presented in these proceedings are from $0.2 - 2.0$ fb^{-1} of data taken in 2003-2006. At present PDF constraints are derived from cross section measurements of inclusive jets and the rapidity distributions of W and Z bosons. Ultimately it may be possible to derive PDF constraints from W/Z,γ + jet/heavy-flavour data but to date uncertainties in the underlying QCD calculation have precluded meaningful PDF constraints. In terms of the global PDF fits, the Tevatron provides approximately 10% of the data-points. The data complement that of the HERA and fixed target experiments and provide constraints in the high-Q^2 region which has some overlap with the highest Q^2 HERA data at high x and crucially with the LHC at the Q^2 scale of electroweak symmetry breaking.

2 Inclusive Jet Data

Two Tevatron inclusive jet cross section data are presently included in the PDF global fits : DØ data [1] based on 0.7 fb^{-1} of integrated luminosity with jets reconstructed using the cone algorithm in the kinematic region $50 < E_T < 600$ GeV, $|y| < 2.4$ and CDF data [2] based on 1.0 fb^{-1} of integrated luminosity with jets reconstructed using the k_T algorithm in the kinematic region $54 < E_T < 700$ GeV, $|y| < 2.1$. CDF data [3] with jets reconstructed using the mid-point algorithm are used as a systematic cross-check. In the global PDF fits the jet data have their largest impact in constraining the gluon distribution at high-x ($0.01 < x < 0.5$) which is particularly important for reliably determining the Standard Model background to new physics searches at the LHC. The Tevatron inclusive jet data now have far greater statistical precision than the data used in previous fits from Run-1. The systematics of the procedure used to correct the data back to the parton level is also far better controlled than was the case in Run-1. The CDF data are shown in figure 1 and the DØ data in figure 2.

The systematic uncertainties in these measurements are largest at high E_T with the determination of the jet energy scale providing the largest contribution to the systematic uncertainty. The latest PDF fits provide an excellent fit to the jet data and are found to be most stable when a

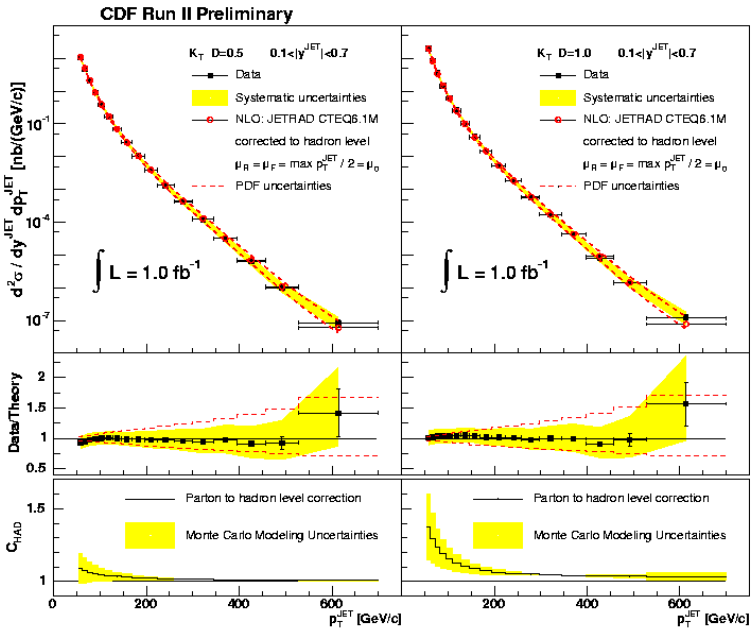


Fig. 1: CDF inclusive jet cross sections compared to NLO predictions.

scale of jet E_T not $E_T/2$ is used. The gluon distribution at high x from the preliminary MSTW analysis [4] is shown in figure 3.

The latest fit is softer at high x compared to previous fits based on the Tevatron Run-1 jet data and the fit is consistent to a fit not including any Tevatron jet data. The fit is also in agreement with the latest CTEQ 6.6 fit [5] and the MSRT 2004 [6] fit. The variance in the gluon distribution is somewhat reduced but more data at high x will be required to reduce the variance below 50% at the highest x values. Further improvements in understanding the jet energy scale from higher statistics control samples will also help reduce the systematic uncertainties in the data.

3 W and Z Rapidity Constraints

The rapidity distributions of W and Z bosons can be measured rather precisely at the Tevatron and to date four measurements have been used to constrain PDFs. They are the DØ measurement [7] of the Z rapidity based on 0.4 fb^{-1} of $Z \to e^+e^-$ data, a preliminary CDF measurement [8] from 2.0 fb^{-1} of $Z \to e^+e^-$ data, a DØ measurement [9] of the W charge asymmetry using $W \to \mu\nu$ events from 0.3 fb^{-1} of data and the CDF measurement [10] of the same quantity using 0.2 fb^{-1} of $W \to e\nu$ data. The latest CDF and DØ data on the W charge asymmetry is not yet included in the global PDF fits since a consistent fit to the the two datasets has not been yet been possible and is under investigation by the collaborations. The Tevatron W and Z data are in principle sensitive to the up and down quark PDFs. However owing to the e_Q^2 weighting

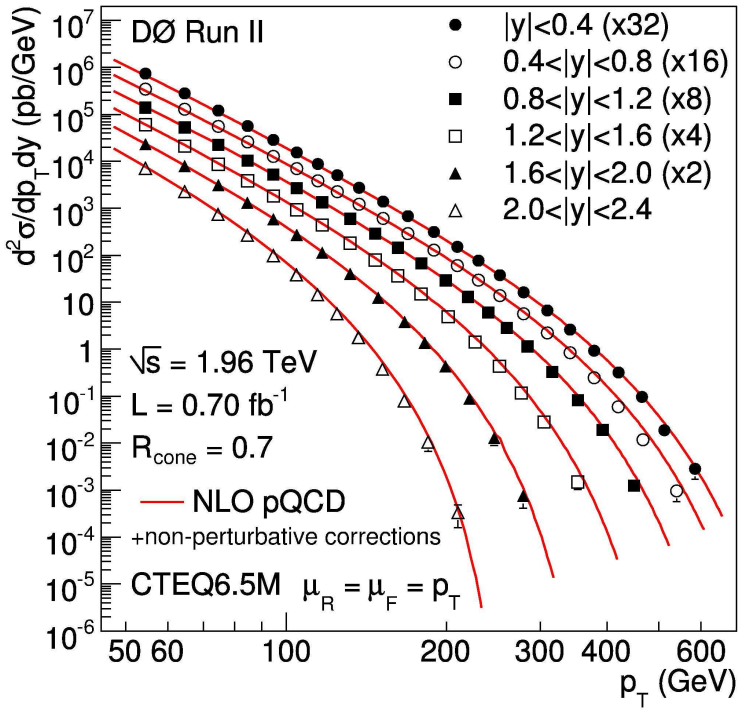


Fig. 2: DØ inclusive jet cross sections compared to NLO predictions.

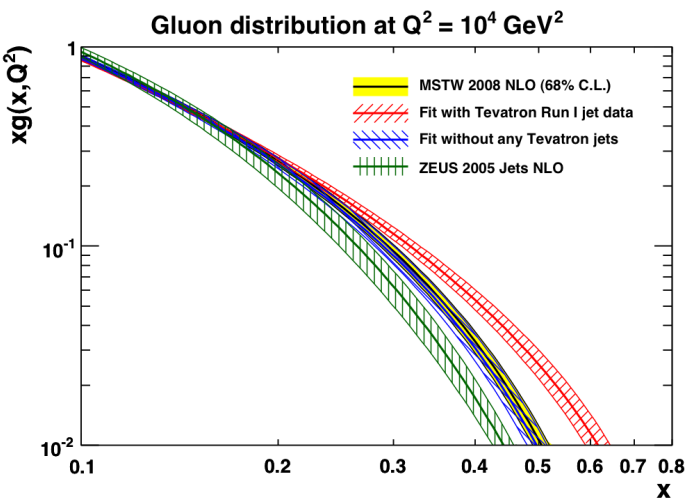


Fig. 3: The gluon distribution at high x from the preliminary MSTW analysis compared to gluon distributions including (or not) the Run-1 Tevatron jet data.

in F_2, the up quark distribution is rather well constrained by the HERA F_2 data and so the Tevatron data mostly provide a constraint on the down valence quark distribution. Z events at high rapidity probe one high x and one low x parton. Both the CDF and DØ data are well described by the latest and previous global PDF fits, with the best description presently provided by the CTEQ6.1 [11] PDFs. The down valence distribution from the preliminary MSTW analysis is shown in figure 4. Previous down valence distributions were rather unstable in the high x region. The new data has allowed the number of constraining parameters to be increased and a more robust distribution to be obtained. The variance on the distribution is now larger but believed to be a more reliable estimate of the uncertainty compared to previous fits. The uncertainty in the high x region, like the gluon, is again significant.

W^+ bosons at the Tevatron are preferentially boosted along the incoming proton direction since the up valence quark carries on average more momentum than the down valence quark. A measurement of the W charge asymmetry as a function of rapidity therefore provides constraints on d/u. Some discrimination between valence and sea quark contributions can be obtained by measuring the charge asymmetry as a function of the lepton E_T since the sea quark contribution is enhanced at low E_T. Published measurements [9, 10, 12] have used the lepton charge asymmetry but recently CDF [13] has unfolded the measurements back to the W rapidity which in principle provides more information since the PDF information is not convoluted with the $V-A$ decay structure. The data is weighted by the two solutions of Y_W based on kinematic constraints informed by the MC. The unfolding is an iterative one to remove the dependence on the MC input parameters, particularly the PDFs.

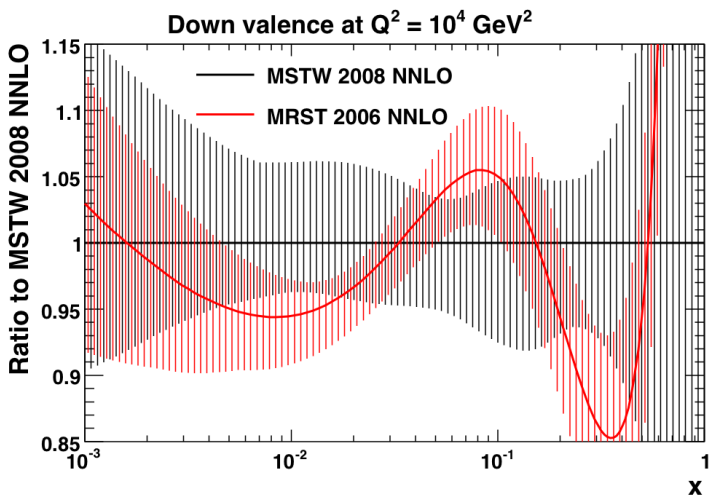


Fig. 4: The down valence quark distribution from the preliminary 2008 MSTW analysis which includes the latest Tevatron Z rapidity data to an older fit without the data.

4 Other Potential Measurements to Constrain PDFs

The measurements presented above are the only Tevatron measurements presently included in global PDF fits. There are a number of other measurements which with greater statistics and improved modeling of the underlying QCD could in principle provide valuable PDF information. These include a measurement of the W cross section ratio at high and low rapidity and measurements of jet + vector boson (W,Z,γ) cross sections where additional flavour information can also be established by tagging bottom and charm jets.

Acknowledgements

I would like to thank Robert Thorne and Graeme Watt of the MSTW team for providing preliminary results from their global PDF fits. The financial support of the Science and Technology Facilities Council is gratefully acknowledged.

References

[1] DØ Collaboration, V. Abazov *et al.,* Phys. Rev. Lett. **101**, 062001 (2008).

[2] CDF Collaboration, A. Abulencia *et al.,* Phys. Rev. **D75**, 092006 (2007).

[3] CDF Collaboration, A. Abulencia *et al.,* hep-ex/0807.2204 (2008) .

[4] G. Watt, A. D. Martin, W. J. Stirling and R. S. Thorne, hep-ph/0806.4890 (2008); and W. J. Stirling in these proceedings .

[5] P. Nadolsky *et al.,* Phys. Rev. **D78** 013004 (2008) .

[6] A.D. Martin, R.G. Roberts, W.J. Stirling and R.S Thorne, Phys. Lett. **B604** 61 (2004).

[7] DØ Collaboration, V. Abazov *et al.,* Phys. Rev. **D76**, 012003 (2007).

[8] CDF Collaboration, http://www-cdf.fnal.gov/physics/ewk/2008/dszdy .

[9] DØ Collaboration, V. Abazov *et al.,* Phys. Rev. **D77**, 0111106(R) (2008).

[10] CDF Collaboration, D. Acosta *et al.,* Phys. Rev. **D71**, 051104 (2005).

[11] J. Pumplin em et al., JHEP **0207** (2002) .

[12] DØ Collaboration, V. Abazov *et al.,* hep-ex/0807.3367 (2008) .

[13] CDF Collaboration, http://www-cdf.fnal.gov/physics/ewk/2007/WChargeAsym/W_Charge_Asymmetry.html .

Small x Resummation - An Overview

Chris White[1]
[1]Nikhef, Kruislaan 409, 1098SJ Amsterdam, The Netherlands.
DOI: http://dx.doi.org/10.3204/DESY-PROC-2009-01/40

Abstract
I provide a summary of BFKL resummation applied to deep inelastic scattering. The origin of the small x problem is described, together with the various approaches that have evolved in recent years for dealing with the issue. Their technical details are briefly compared, and conclusions from global parton fits to scattering data examined.

1 Introduction

As is well known, hadronic cross-sections factorise into the following form:

$$\sigma = f_a(x_a, \mu_F^2) \otimes \hat{\sigma}_{ab} \otimes f_b(x_b, \mu_F^2), \quad a \in \{q, \bar{q}, g\},$$

where $\hat{\sigma}_{ab}$ are perturbatively calculable hard coefficient functions, and f_a non-perturbative parton distribution functions dependent on a longitudinal momentum fraction x and a factorisation scale μ_F. The latter are not calculable in perturbation theory, but evolve with μ_F according to the DGLAP equations:

$$\frac{\partial f_a(x, \mu_F^2)}{\partial \ln \mu_F^2} = \sum_b P_{ab}(x, \mu_F^2) \otimes f_b(x, \mu_F^2),$$

with P_{ab} perturbatively calculable splitting functions. A problem arises at small values of x in that both the splitting functions and hard coefficients contain terms of form $x^{-1}\alpha_S^n \log^m(1/x)$ with $n \geq m-1$. Thus, when x is sufficiently small, each term in the perturbation series diverges even though α_S may be in the perturbative regime. One naïvely expects this to become a problem when:

$$\alpha_S \log\left(\frac{1}{x}\right) \simeq 1 \Rightarrow x \simeq 10^{-2},$$

and we will see later that this back of the envelope reasoning is essentially correct. At small x, one must reorder the perturbation expansion in terms of leading logarithmic (LL), next-to-leading logarithmic (NLL) terms and so on.

In this contribution, we focus on the solution to this problem in deep inelastic scattering, and will be able to answer the following questions. Firstly, how small is small x (i.e. can we confirm the above expectation)? Secondly, what approaches exist to deal with the problem, and how do they differ? Finally, what can scattering data tell us about their validity?

2 The BFKL equation

The small x divergence in deep inelastic scattering can be traced at LL order to ladders of gluon exchanges, with quark mixing at NLL order. The unintegrated gluon 4-point function $f(k^2, Q_0^2)$

which sums up these exchanges can be written as the solution to an integral equation - the BFKL equation [1]- which has the schematic form (up to NLL order)

$$Nf(k^2,Q_0^2) = Nf_I(Q_0^2)+\alpha_S(k^2)\int dk'^2\left[\mathcal{K}_0(k^2,k'^2,Q_0^2) \quad +\alpha_S(\mu^2)\mathcal{K}_1(k^2,k'^2,Q_0^2)\right]f(k'^2),$$

where we have performed a Mellin transform in x, with N the moment variable. Here k^2 and Q_0^2 are transverse momentum scales at the hard and soft ends of the gluon ladder respectively, and $\mathcal{K}_i$ the BFKL kernel, which is currently known exactly up to NLL order [2] and approximately at NNLL order [3]. Solving this equation resums the problem logarithms at the level of the gluon density. This is then related to observable quantities (in this case proton structure functions) using the k_t-factorisation formula [4]

$$\mathcal{F}_i(k^2,N) = \int dk^2 h_i(k,N) f(k^2,Q_0^2),$$

where $h_i(k,N)$ is an impact factor coupling the incoming virtual photon to the gluon ladder. Thus, for physical predictions, one needs a knowledge of both the BFKL kernel to the desired order, and also the impact factors. The latter are known exactly at LL order in DIS [4, 5], and also at approximate NLL order in both the massless [6] and massive cases [7]. It has been known for some time that the LL BFKL formalism is insufficient to describe scattering data, thus any phenomenologically viable resummation approach must satisfy at least the following requirements:

1. Solve the BFKL equation at NLL order (preferably with running α_S).
2. Provide the complete set of splitting functions P_{ab}, and also coefficient functions for the structure functions F_2 and F_L.
3. Match the resummed results to the usual DGLAP results for correct moderate / high x behaviour.
4. Explain why NLO DGLAP appears to work well down to low x.

(strictly speaking one must also add the additional requirement of correctly implementing heavy quarks, as has been shown to be important in fixed order fits to current data). So far only three approaches achieve these aims to a reasonable extent (see also [8] for a recent alternative approach).

3 Resummation approaches

The formalisms which (broadly) satisfy the above requirements are known as the ABF [9], CCSS [10–12] and TW [7, 13, 14] approaches. Here, we summarise the main differences.

Firstly, not all of the approaches use the same factorisation scheme for the parton distributions. ABF present results in the the standard MS-bar scheme to all orders, whereas CCSS and TW present results in schemes which are the conventional MS-bar and DIS schemes respectively up to NLO in the fixed order expansion, but differ slightly from their fixed order counterparts in the resummed terms (ultimately arising from the fact that the regularisation of collinear singularities when solving the BFKL equation takes place in a so-called Q_0-scheme, rather than dimensional regularisation). See the detailed studies in [9, 11, 12] for further details.

	ABF	CCSS	TW
Full set of P_{ab} and C_a (for light flavours)	$\surd$	$\surd$	$\surd$
Resummation of BFKL kernel [15]	$\surd$	$\surd$	$\times$
Factorisation scheme	DIS, MS-bar	MS-bar(NLO+Q_0)	DIS(NLO+Q_0)
Heavy quark effects included	$\times$	$\times$	$\surd$
Global fit carried out	$\times$	$\times$	$\surd$

Table 1: Summary of the ABF, CCSS and TW approaches. See the text for further details.

Secondly, the BFKL kernel is known to contain potentially unstable terms of collinear origin. These can be resummed to all orders in the kernel [15], as is done in the ABF and CCSS approaches. The TW group do not implement this further resummation, although could do so in principle. The latter group also include higher order terms from the impact factors [6, 7], which are not included by the other approaches (consistent with their definition of NLL order).

These and other differences are summarised in table 1. Results for splitting and coefficient functions cannot be directly compared between the approaches due to factorisation scheme ambiguities. However, the main qualitative feature of the resummed splitting functions in all the approaches is a pronounced dip below the NLO DGLAP result at moderate x values, followed by an eventual rise at very small x (see figures 1-2, 5 and 3-4 in [9, 10, 14] respectively).

4 Fits to scattering data

So far, only the TW approach above has been implemented in a global fit to scattering data, although work is in progress involving the other approaches. Nevertheless, the qualitative similarity between the results (i.e. the dip in evolution when resummations are included in the splitting functions) means that similar results to those presented here should presumably be seen in all the approaches.

The dip in the resummed evolution qualitatively changes the shape of the gluon distribution, as seen in figure 1. The gluons agree at high x, as is required by consistent matching of the resummed and fixed order descriptions. At low x (and the input scale for evolution $Q^2 = 1\text{GeV}^2$), the resummed gluon is positive definite and slightly growing as $x \to 0$. This has several phenomenologically desirable features. Firstly, a raised gluon at low x decreases the tension between the Tevatron jet data [16] and the small x HERA data [17]. It also stabilises the longitudinal structure function F_L at low x and Q^2, and consequently reproduces the correct shape for the HERA reduced cross-section data at high inelasticities y.

One notes that the gluon distributions (resulting from a fit to data) move away from each other below $x \sim 10^{-2}$. Thus, this can be taken as an empirically determined upper bound below

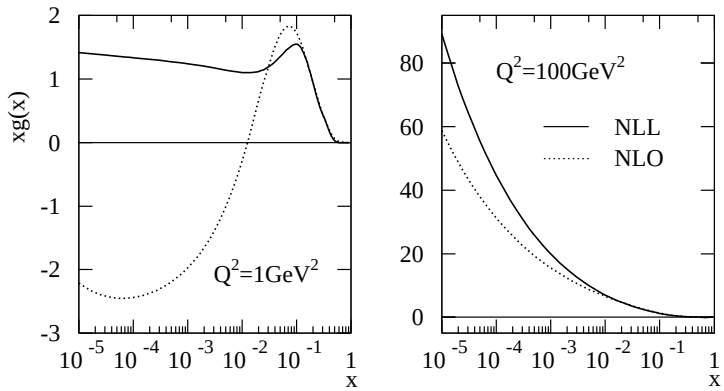


Fig. 1: Gluons obtained in a NLO fit to DIS and related data, with and without NLL small x resummations.

which small x resummation becomes important. Note that this value is in rough agreement with the back of the envelope calculation described in the introduction. It is also clear why NLO DGLAP has worked well down to very low x values ($\sim 10^{-5}$) - the DGLAP splitting function sits roughly in the middle of the resummed dip found in each of the above approaches.

Although the above describes compelling evidence for the need for small x resummation, there are not yet inclusive observables in DIS which defy description using the traditional DGLAP theory. However, resummed and fixed order predictions can be quite different. The case of F_L (shown alongside the recent H1 data [18]) is shown in figure 2 with a current NNLO prediction [19]. One sees from the plot that the two descriptions cannot yet be distinguished, although points at slightly lower Q^2 (thus also lower x) could indeed discriminate between them.

References

[1] I. I. Balitsky and L. N. Lipatov, Sov. J. Nucl. Phys. **28**, 822 (1978);
V. S. Fadin, E. A. Kuraev, and L. N. Lipatov, Phys. Lett. **B60**, 50 (1975).

[2] V. S. Fadin and L. N. Lipatov, Phys. Lett. **B429**, 127 (1998). hep-ph/9802290.

[3] S. Marzani, R. D. Ball, P. Falgari, and S. Forte, Nucl. Phys. **B783**, 143 (2007). 0704.2404.

[4] S. Catani, M. Ciafaloni, and F. Hautmann, Nucl. Phys. **B366**, 135 (1991).

[5] S. Catani and F. Hautmann, Nucl. Phys. **B427**, 475 (1994). hep-ph/9405388.

[6] A. Bialas, H. Navelet, and R. B. Peschanski, Nucl. Phys. **B603**, 218 (2001). hep-ph/0101179.

[7] C. D. White, R. B. Peschanski, and R. S. Thorne, Phys. Lett. **B639**, 652 (2006). hep-ph/0606169.

[8] J. Ellis, H. Kowalski, and D. A. Ross, Phys. Lett. **B668**, 51 (2008). 0803.0258.

[9] G. Altarelli, R. D. Ball, and S. Forte, Nucl. Phys. **B799**, 199 (2008). 0802.0032;
R. D. Ball and S. Forte, Nucl. Phys. **B742**, 158 (2006). hep-ph/0601049;
G. Altarelli, R. D. Ball, and S. Forte, Nucl. Phys. **B742**, 1 (2006). hep-ph/0512237;

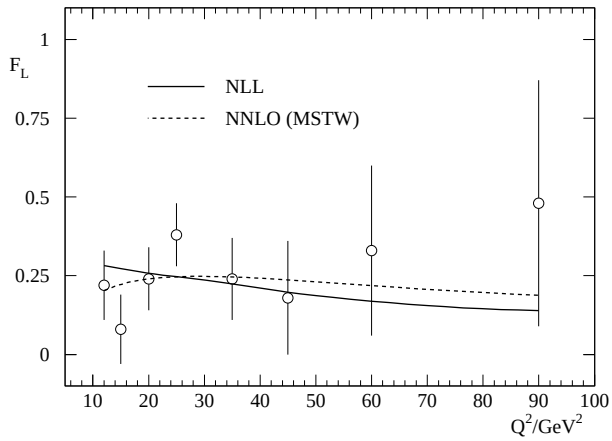


Fig. 2: Resummed prediction for F_L, shown alongside the recent H1 data.

G. Altarelli, R. D. Ball, and S. Forte, Nucl. Phys. **B674**, 459 (2003). hep-ph/0306156;
G. Altarelli, R. D. Ball, and S. Forte, Nucl. Phys. **B621**, 359 (2002). hep-ph/0109178;
G. Altarelli, R. D. Ball, and S. Forte, Nucl. Phys. **B575**, 313 (2000). hep-ph/9911273.

[10] M. Ciafaloni, D. Colferai, G. P. Salam, and A. M. Stasto, JHEP **08**, 046 (2007). 0707.1453.

[11] M. Ciafaloni, D. Colferai, G. P. Salam, and A. M. Stasto, Phys. Lett. **B635**, 320 (2006). hep-ph/0601200.

[12] M. Ciafaloni and D. Colferai, JHEP **09**, 069 (2005). hep-ph/0507106;
M. Ciafaloni, D. Colferai, G. P. Salam, and A. M. Stasto, Phys. Rev. **D68**, 114003 (2003). hep-ph/0307188;
M. Ciafaloni, D. Colferai, and G. P. Salam, JHEP **07**, 054 (2000). hep-ph/0007240;
M. Ciafaloni, D. Colferai, and G. P. Salam, Phys. Rev. **D60**, 114036 (1999). hep-ph/9905566.

[13] R. S. Thorne, Phys. Rev. **D64**, 074005 (2001). hep-ph/0103210;
R. S. Thorne, Phys. Lett. **B474**, 372 (2000). hep-ph/9912284;
R. S. Thorne, Nucl. Phys. Proc. Suppl. **79**, 210 (1999). hep-ph/9906323;
R. S. Thorne, Phys. Rev. **D60**, 054031 (1999). hep-ph/9901331;
C. D. White and R. S. Thorne, Eur. Phys. J. **C45**, 179 (2006). hep-ph/0507244;
C. D. White and R. S. Thorne, Phys. Rev. **D74**, 014002 (2006). hep-ph/0603030.

[14] C. D. White and R. S. Thorne (2007). 0706.2609.

[15] G. P. Salam, JHEP **07**, 019 (1998). hep-ph/9806482.

[16] D0 Collaboration, B. Abbott *et al.*, Phys. Rev. Lett. **86**, 1707 (2001). hep-ex/0011036;
CDF Collaboration, T. Affolder *et al.*, Phys. Rev. **D64**, 032001 (2001). hep-ph/0102074.

[17] H1 Collaboration, C. Adloff *et al.*, Eur. Phys. J. **C30**, 1 (2003). hep-ex/0304003;
H1 Collaboration, C. Adloff *et al.*, Eur. Phys. J. **C21**, 33 (2001). hep-ex/0012053;
H1 Collaboration, C. Adloff *et al.*, Eur. Phys. J. **C19**, 269 (2001). hep-ex/0012052;
ZEUS Collaboration, J. Breitweg *et al.*, Eur. Phys. J. **C7**, 609 (1999). hep-ex/9809005;
ZEUS Collaboration, S. Chekanov *et al.*, Eur. Phys. J. **C21**, 443 (2001). hep-ex/0105090.

[18] H1 Collaboration, F. D. Aaron *et al.*, Phys. Lett. **B665**, 139 (2008). 0805.2809.

[19] A. D. Martin, W. J. Stirling, R. S. Thorne, and G. Watt, Phys. Lett. **B652**, 292 (2007). 0706.0459.

Progress in Parton Distribution Functions and Implications for LHC

W. James Stirling
Department of Physics, University of Cambridge, Cambridge CB3 0HE, UK
DOI: http://dx.doi.org/10.3204/DESY-PROC-2009-01/41

Abstract
Parton distributions functions (pdfs) are an important ingredient for LHC phenomenology. Recent progress in determining pdfs from global analyses is reviewed, and some of the most important outstanding issues are highlighted. Particular attention is paid to the precision with which predictions for LHC 'standard-candle' cross sections can be made, and also to new information that LHC can provide on pdfs.

1 Introduction

High-precision cross-section predictions for both Standard Model and Beyond Standard Model processes at the LHC require high-precision parton distribution functions (pdfs). In some cases, the uncertainty in our knowledge of the pdfs is a significant or even dominant part of the overall uncertainty in the theoretical prediction. Of course, the more accurate the signal and background predictions, the easier it will be to detect new physics. Fortunately the LHC provides a number of 'standard-candle' processes, whose measured cross sections can be used to check the theoretical framework (factorisation, DGLAP evolution etc.). The paradigms are $\sigma(Z)$ and $\sigma(W)$, for which there are realistic prospects of experimental measurements and theoretical predictions accurate at the few % level.

At the same time, the LHC can provide new information on the pdfs themselves. Hadron collider data have always been an important ingredient of pdf global fits. For example, fixed-target Drell-Yan data currently provide (unique) information on high-x sea quarks, Tevatron high-E_T jet data provide direct information on the high-x gluon, and Tevatron W and Z cross sections and distributions provide information on quark distributions complementary to that from deep inelastic scattering. There is every prospect that similar measurements at the LHC will improve our knowledge of pdfs even further.

The basic theoretical tool for precision predictions for hadron colliders such as the Tevatron and the LHC is the QCD factorization theorem for short-distance inclusive processes:

$$\sigma_{AB} \;=\; \int dx_a dx_b \, f_{a/A}(x_a,\mu_F^2)\, f_{b/B}(x_b,\mu_F^2) \;\times\; [\,\hat{\sigma}_0 \;+\; \alpha_S(\mu_R^2)\,\hat{\sigma}_1 \;+\; ...\,]_{ab\to X}\;. \qquad (1)$$

Formally, the cross section calculated to all orders in perturbation theory is invariant under changes in the factorization scale (μ_F) and the renormalization scale (μ_R), the scale dependence of the coefficients $\hat{\sigma}_0, \hat{\sigma}_1, ...$ exactly compensating the explicit scale dependence of the pdfs and the QCD coupling constant. This compensation becomes more exact as more terms are included in the perturbation series. In the absence of a complete set of higher-order corrections,

it is necessary to make a specific choice for the two scales in order to make cross-section predictions. A variation of the scales by a factor of 2 around some 'natural' scale M for the process, i.e. $M/2 < \mu_F, \mu_R < 2M$, is often used to characterise the uncertainty from unknown higher-order terms in the series. The overall theoretical error on a cross section prediction can then be estimated as $\delta\sigma^2_{\rm th} = \delta\sigma^2_{\rm pdf} + \delta\sigma^2_{\rm scl}$.

Almost all the theoretical quantities (subprocess cross sections, coefficient functions and splitting functions) that are needed for a global fit are nowadays known to NNLO in pQCD, and so this will be the *de facto* benchmark for LHC phenomenology. In some cases, e.g. W and Z production, electroweak corrections are also known and can be included. The following table illustrates the relative size of the pdf and scale uncertainties for some standard processes at the LHC, calculated at NNLO[1] in pQCD. Here the pdf uncertainties are taken from the recent MSTW global fit [1, 2], while the scale uncertainty estimates for $t\bar{t}$ and Higgs production are taken from Refs. [3] and [4] respectively. Evidently the pdf uncertainty is a significant issue for Z and $t\bar{t}$ production, but not at present for Higgs production.

process	$\delta\sigma_{\rm pdf}$	$\delta\sigma_{\rm scl}$
$pp \to Z + X$	$\pm 2\%$	$\pm 2\%$
$pp \to t\bar{t} + X$	$\pm 2\%$	$\pm 3\%$
$pp \to H(120\ {\rm GeV}) + X$	$\pm 2\%$	$\pm 15\%$

2 How pdfs are obtained

The method by which pdfs are obtained from a global fit to a variety of 'hard scattering' data is by now well known – a schematic summary is shown in Fig. 1. A typical set of input data (as used, for example, by the MSTW and CTEQ collaborations, see Section 3) is given in the following Table, together with the partons that they constrain.

H1, ZEUS	$F_2^{e^+p}(x,Q^2)$, $F_2^{e^-p}(x,Q^2)$ NC + CC
BCDMS	$F_2^{\mu p}(x,Q^2), F_2^{\mu d}(x,Q^2)$
NMC	$F_2^{\mu p}(x,Q^2), F_2^{\mu d}(x,Q^2), F_2^{\mu n}(x,Q^2)/F_2^{\mu p}(x,Q^2)$
SLAC	$F_2^{e^- p}(x,Q^2), F_2^{e^- d}(x,Q^2)$
E665	$F_2^{\mu p}(x,Q^2), F_2^{\mu d}(x,Q^2)$
CCFR, NuTeV, CHORUS	$F_2^{\nu(\bar{\nu})N}(x,Q^2), F_3^{\nu(\bar{\nu})N}(x,Q^2)$
	$\to$ q, $\bar{q}$ at all x and g at medium, small x
H1, ZEUS	$F_{2,c}^{e^\pm p}(x,Q^2), F_{2,b}^{e^\pm p}(x,Q^2) \to c, b$
E605, E772, E866	Drell-Yan $pN \to \mu\bar{\mu} + X \to \bar{q}\,(g)$
E866	Drell-Yan p,n asymmetry $\to \bar{u}, \bar{d}$
CDF, D0	$W^\pm$ rapidity asymmetry $\to u/d$ ratio at high x
CDF, D0	Z^0 rapidity distribution $\to u, d$
CDF, D0	inclusive jet data $\to g$ at high x
H1, ZEUS	DIS + jet data $\to g$ at medium x
CCFR, NuTeV	dimuon data $\to$ strange sea s, $\bar{s}$

[1] In the case of $t\bar{t}$ production, an approximation to the (as yet uncalculated) full correction has been derived, see [3].

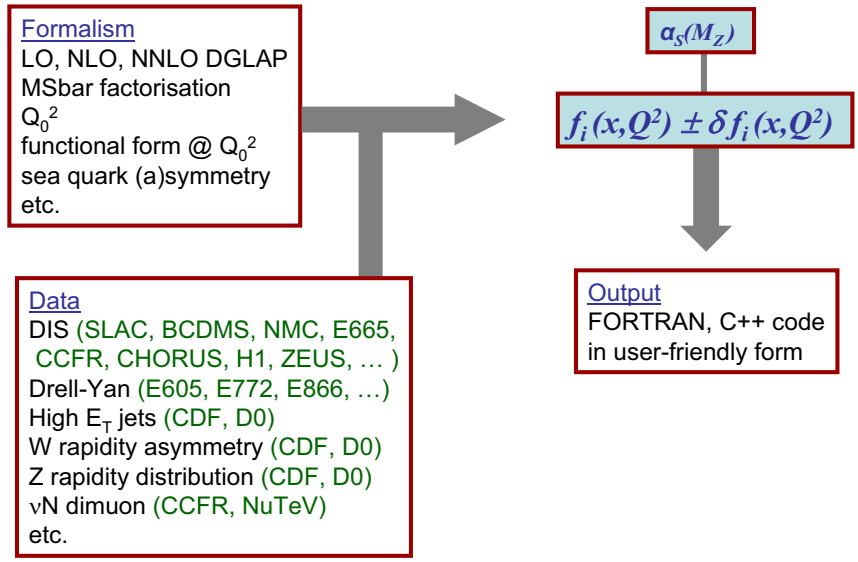


Fig. 1: Anatomy of a pdf global fit.

Over the past 15 years, the quality and quantity of the data has improved enormously, so that nowadays the pdfs are known to very high accuracy, typically to within a few $\%$ over a broad range of x away from $x = 0, 1$. In terms of recent developments, much attention has been focused on the heavy quark (s, c, b) distributions. Until recently, the strange quark distribution was generally parametrised as

$$s(x, Q_0^2) = \bar{s}(x, Q_0^2) = \frac{\kappa}{2}\left[\bar{u}(x, Q_0^2) + \bar{d}(x, Q_0^2)\right] \tag{2}$$

with $\kappa = 0.4 - 0.5$ suggested by (neutrino DIS) data. The suppression was understood as a non-perturbative mass effect. Recent measurements of dimuon production in νN DIS (for example, by CCFR and NuTeV) allow a more-or-less direct determination of both s and $\bar{s}$, via

$$\frac{d\sigma}{dxdy}\left(\nu_\mu(\bar{\nu}_\mu)N \to \mu^+\mu^- X\right) = B_c \mathcal{N}\mathcal{A}\frac{d\sigma}{dxdy}\left(\nu_\mu s(\bar{\nu}_\mu \bar{s}) \to c\mu^-(\bar{c}\mu^+)\right) \tag{3}$$

in the range $0.01 < x < 0.4$. The data appear to slightly prefer $s(x, Q_0^2) \neq \bar{s}(x, Q_0^2)$, both having a different shape to the light sea quark distributions. Generalised parametrisations for s and $\bar{s}$ are therefore used in the most recent global fits.

The charm and bottom quarks are considered sufficiently massive to allow a pQCD treatment, i.e. the distributions are assumed to be generated perturbatively via $g \to Q\bar{Q}$. Two regimes can be distinguished: (i) $Q^2 \sim m_Q^2$ where it is essential to include the *full* m_Q dependence in order to get the correct threshold behaviour, and (ii) $Q^2 \gg m_Q^2$ where the heavy quarks can be treated as essentially massless partons, with large logarithmic contributions of the form $\alpha_S^n \ln^n(Q^2/m_Q^2)$ automatically resummed by the DGLAP equations. The so-called Fixed Flavour Number Scheme (FFNS), in which heavy quarks are not treated as partons, is only valid in region (i), whereas the Zero Mass Variable Flavour Number Scheme (ZM-VFNS), in which

heavy quarks evolve as massless partons from zero at threshold, applies to region (ii) only. In recent years, a more general set of General Mass Variable Flavour Number Schemes (GM-VFNS) have been developed, with the advantage of interpolating smoothly and consistently between the two Q^2 regions, at a given order (up to and including NNLO in practice) in perturbation theory. The two most important points to note are: (i) the definition of a consistent GM-VFNS is tricky and non-unique (not least due to the assignment of $\mathcal{O}(m_Q^2/Q^2)$ contributions), and implementation of an improved treatment of heavy quarks can have a significant knock-on effect on light partons, and (ii) GM-VFNS predictions for the structure functions $F_2^{c\bar{c}}$ and $F_2^{b\bar{b}}$ agree well with measurements at HERA. A more detailed discussion of the treatment of heavy quark pdfs can be found in [5].

Another major advance in recent years has been the treatment of uncertainties in the distribution functions, and most global fit groups produce 'pdfs with errors' sets. These are of course useful in assessing the error on cross-section predictions due to the pdfs themselves. A typical package will consist of a 'best fit' set and $\sim$ 30–40 error sets designed to reflect a $\pm 1\sigma$ variation of all the parameters used to define the starting distributions, as determined by the uncertainties on the data used in the global fit. However, in addition to these 'experimental' uncertainties, there are also uncertainties associated with theoretical assumptions and/or prejudices in the way the global fit is set up and performed. Although these are generally more difficult to quantify, they are often the main reason for the differences between the sets produced by different groups. The following is a non-exhaustive list of the reasons why 'best fit' pdfs and errors can differ:

- different data sets in the fit:
  - — different subselection of data
  - — different treatment of experimental systematic errors
- different choice of:
  - — pQCD order (in DGLAP and cross sections)
  - — factorisation/renormalisation scheme/scale
  - — Q_0^2
  - — parametric form $f_i(x, Q_0^2) = Ax^a(1-x)^b c(x)$ etc., and implicit extrapolation
  - — α_S
  - — treatment of heavy flavours
  - — theoretical assumptions about $x \to 0, 1$ behaviour
  - — theoretical assumptions about sea quark flavour asymmetry
  - — χ^2 tolerance to define $\pm\delta f_i$
  - — evolution, cross-section codes, rounding errors etc.

Note that these can apply both to comparisons of the type CTEQ *vs.* MRST *vs.* ... and to CTEQ6.1 *vs.* CTEQ6.5 etc.

3 Recent progress

There are a number of groups producing pdf sets from global fits to data. In this section we give a very brief summary of these, with references to where more information can be found.

The Martin–Stirling–Thorne–Watt **MSTW** (formerly **MRST**) collaboration produces sets at LO, NLO and NNLO using a 'maximal' set of fitted data as described in the previous section.

The previous MRST2006 sets [6] contained an update of the NNLO fit to include both pdf errors and an improved GM-VFNS treatment of c and b. The new MSTW2008 sets [1, 2] include (i) new data sets in the fit (CHORUS and NuTeV neutrino data and HERA DIS+jet data), (ii) a more sophisticated treatment of s and $\bar{s}$ in which both are allowed to have independent shapes and normalisations, and (iii) an improved treatment of the tolerance procedure to define the error sets (for a summary see [1]).

The **CTEQ** collaboration (Ref. [7] and references therein) produces LO and NLO pdf sets from global fits using roughly the same maximal data set as MSTW/MRST. Earlier this year, the previous (2006) 6.5 set was updated to produce set 6.6. CTEQ6.5 was characterised by the first implementation of a GM-VFNS (the 'SACOT$-\chi$' scheme [8,9]), which had a significant impact on the c and b distributions, a compensating impact on the u and d partons, and a corresponding change in the predictions for $\sigma(W, Z)$. The new 6.6 set has a more sophisticated treatment of the s and $\bar{s}$ pdfs, allowing these to have a more general shape and normalisation than previously. The impact of an additional 'intrinsic charm' contribution is also studied.

Given the similarity of the data fitted and the theoretical framework used, it is no surprise that the pdf outputs from the MSTW and CTEQ analyses are similar. This is illustrated Fig. 2, which compares the latest MSTW2008 and CTEQ6.6 NLO u and g pdfs (with errors) at $Q^2 = 10^4$ GeV^2. Note that the broader CTEQ error band is in part a reflection of a different choice of tolerance in defining the allowed range of $\Delta\chi^2$. The MSTW gluon is smaller at small x, because the parameterisation at $Q_0^2 = 1$ GeV^2 allows the starting distribution to be negative at small x, unlike in the CTEQ (central) fits where the gluon is always constrained to be positive.

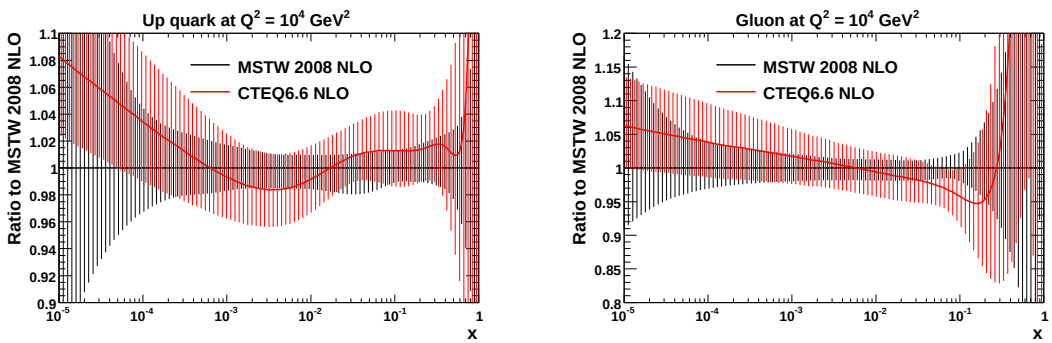


Fig. 2: Comparison of recent MSTW and CTEQ up quark (left) and gluon (right) NLO parton distributions.

Alekhin et al. produce sets at LO, NLO and NNLO. The original 2002 (Alekhin) set [10] was updated first in 2006 [11] (Alekhin–Melnikov–Petriello) and again in 2007 [12] (Alekhin–Kulagin–Petti). The 2002 fit was based on DIS structure function data only (SLAC, BCDMS, NMC, E665, H1, ZEUS). The 2006 AMP version added E605 and E866 Drell-Yan data, and CHORUS, CCFR and NuTeV neutrino structure function and dimuon data. Unlike the CTEQ and MSTW/MRST fits, the Alekhin fit does not include Tevatron high-E_T jet data, nor a complete GM-VFNS treatment of heavy quarks, and this accounts for much of the differences between the resulting parton distributions.

Both the **H1** and **ZEUS** collaborations have produced pdf sets in the past based on their own HERA DIS data supplemented by other DIS data. The most recent H1 (2003) set added BCDMS data to H1 structure function data to give a broad coverage in x and Q^2. The ZEUS (2005) set was based on ZEUS data (both inclusive structure function and DIS+jet data) only. The two collaborations also had different treatments of pdf errors: offset (ZEUS) *vs.* Hessian (H1). Recently H1 and ZEUS have joined together to produce a combined pdf set, HERAPDF0.1, details of which can be found in the talk by Gang Li [13]. Differences between the previous H1 and ZEUS fitting procedures have been resolved, and experimental and model uncertainties have been carefully considered. However this fit uses only HERA inclusive cross section NC and CC $e^{\pm}p$ data, and therefore there are small but significant differences in both quark and gluon differences in comparison with MSTW and CTEQ, which can in large part be traced to the influence of Tevatron and fixed-target Drell-Yan data in the latter global fits.

The **NNPDF** (Neural Net) collaboration [15] uses neural net technology in the fit to avoid having to choose a particular parametric form at Q_0^2. The new (NLO) set, NNPDF1.0, is based on a Monte Carlo approach, with neural networks used as unbiased interpolants. The method is designed to provide a faithful and statistically sound representation of the uncertainty on parton distributions. The fit is performed to a restricted 'DIS only' data set in a ZM-VFNS scheme for the heavy quarks. The absence of Drell-Yan and neutrino dimuon data from the fit means that the detailed flavour structure of the quark sea is not well determined (and therefore neither are the predictions for W and Z cross sections at the LHC, see Section 4 below). The absence of Tevatron High-E_T jet data from the fit is another signficant source of difference between NNPDF and CTEQ/MSTW. A recent update (NNPDF1.1 [16]) introduces independent parametrisations for the strange pdfs.

Finally, there have been a number of other studies of pdfs designed for particular purposes or to investigate different theoretical frameworks. For example, the 'dynamical parton model' approach (see [14] and references therein) attempts to describe DIS and other data from a set of valence-like partons evolved upwards in Q^2 from a low starting scale. A reasonable fit is obtained, although the total χ^2 is signficantly larger than in a (standard) fit in which the small-x parameters are unconstrained.

4 Parton distributions at the LHC

There are a number of LHC standard-candle processes, $\sigma(W^{\pm}, Z^0, t\bar{t}, \mathrm{jets}, ...)$, that can be used to probe and test pdfs, typically in the range $x \sim 10^{-2\pm1}$, $Q^2 \sim 10^{4-6}$ GeV^2 (see Fig. 3), which is where most New Physics signals (Higgs, SUSY, etc.) are expected. The total W and Z cross sections provide a particularly important point of comparison between the various pdf sets. A number of factors are relevant, including (i) the rate of evolution from the Q^2 of the fitted DIS data to $Q^2 \sim 10^4$ GeV^2, driven mainly by α_S and the gluon distribution, and (ii) the mix of quark flavours, since F_2 and $\sigma(W, Z)$ probe *different* combinations of quark flavours. A very precise measurement of cross section *ratios* at LHC (e.g. $\sigma(W^+)/\sigma(W^-)$ and $\sigma(W^{\pm})/\sigma(Z)$) will allow these subtle quark flavour effects to be explored.

By way of example, we show in Fig. 4 a selection of predictions for $\sigma(W^{\pm})$ and $\sigma(Z)$ LHC cross sections [2]. The error ellipses correspond to the MSTW2008 NLO and NNLO pdf

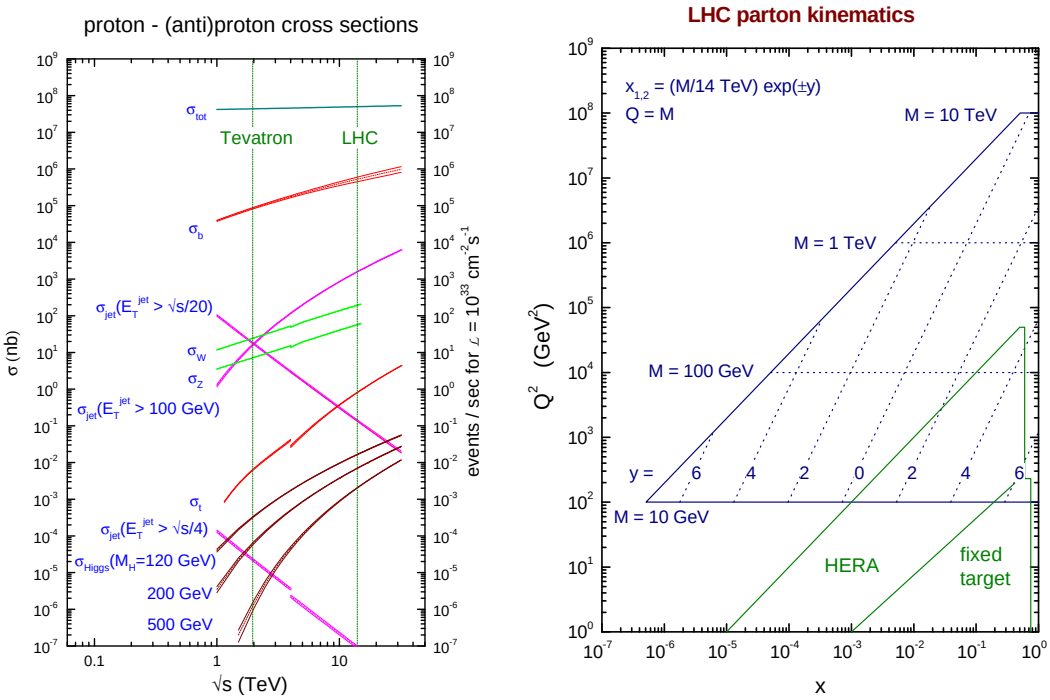


Fig. 3: Standard Model cross section predictions at hadron-hadron colliders (left), and the parton x, Q^2 region probed by the production of a heavy object of mass M and rapidity y at the LHC (right).

sets. Note that the cross section ratios are determined more precisely than the absolute cross sections themselves. In the case of the W^+/W^- cross section ratio, the overall uncertainty is of order 1%, and comes mainly from the uncertainty in the u/d ratio at the relevant x and Q^2 values. Note that the change in the cross sections going from MRST2004 to MRST2006 is due to an improvement in the heavy flavour prescription [6] discussed earlier, which mainly affects the charm distribution, while the predictions are relatively stable in going from MRST2006 to MSTW2008. The CTEQ6.6 and CTEQ6.5 predictions are very similar, but both are significantly higher than the CTEQ6.1 predictions. Again, this is mainly due to a different treatment of s, c, b quarks in the fit. The CTEQ6.6 LHC predictions are about $+2\%$ higher than MSTW2008, because of slight differences in the quark (u, d, s, c) distributions, but overall the predictions agree reasonably well within the quoted uncertainties. Care is however needed in comparing predictions based on different orders of QCD perturbation theory (NLO, NNLO, NNLL-NLO, ...), since the higher-order contributions to the cross sections are not negligible.

The error ellipses on the MSTW W and Z predictions come from the new 'dynamical tolerance' treatment of pdf uncertainties described in [1]. There is an additional uncertainty of the same size from scale variation (quantified in the usual way by varying the scales from $M/2$ to $2M$). Combining these, we predict a total ('1σ') uncertainty of $\sim \pm 4\%$ on the total W and Z

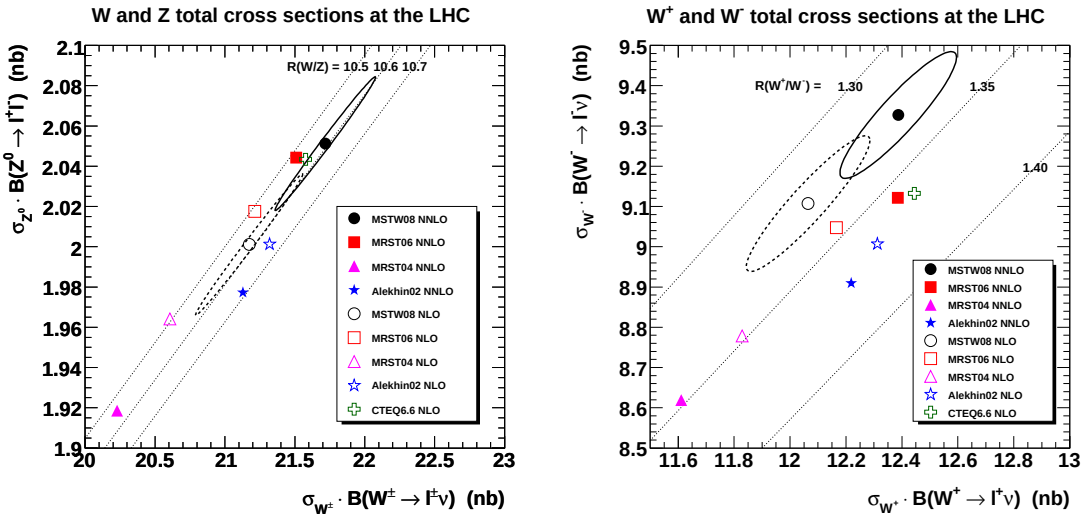


Fig. 4: $W^{\pm}$ *vs.* Z (left) and W^{+} *vs.* W^{-} (right) total cross sections at the LHC calculated using various past and present pdf sets at NLO and NNLO. The 1σ error ellipses are shown for the MSTW 2008 NLO and NNLO pdfs.

cross sections at LHC, and these could therefore be useful in calibrating the machine luminosity. A more complete discussion of the role of higher-order corrections in cross-section predictions at the LHC can be found in Refs. [17, 18].

It is clear from Fig. 3 that in order to probe very small x at the LHC we need to produce relatively light objects at forward rapidity, since then $x \sim (M/\sqrt{s})\exp(-y) \ll 1$. The simplest process to use for this purpose is Drell-Yan (DY) lepton pair production. At the LHC this requires good detection of low p_T leptons in the forward region. Interestingly, this is precisely the region that will be accessible to LHCb [19]. Translating the detector acceptance for muon pairs into the (x, Q^2) plane gives the 'LHCb' region shown in Fig. 5. There are two main impacts of such a measurement: (i) quark distributions can be measured in the perturbative domain at smaller x values than at HERA, and (ii) DGLAP evolution over 1–2 orders of magnitude in Q^2 can be tested by comparing pdf measurements at the same (small) x value at HERA and LHCb. Detailed studies are underway to quantify the improvement in pdf precision at small x resulting from the inclusion of such LHCb data in the global fit.

5 Summary

In the past few years there has been progress in our understanding of parton distribution functions, and convergence of the various approaches used to determine them. The main distinguishing features of the currently available 'precision' pdf sets are (i) how heavy quarks are treated, (ii) how the tolerance for determining pdf error sets is defined, and (iii) whether the Tevatron high$-E_T$ jet data are included in the fit. If they are, then the high-x gluon is slightly larger than the gluon derived from fits which are based on structure function data only. In the context of a *full* NNLO global pdf analysis, the NNLO ($\mathcal{O}(\alpha_S^4)$) corrections to the high$-E_T$ jet cross section are still the most important missing ingredient, although their quantitative impact on the current

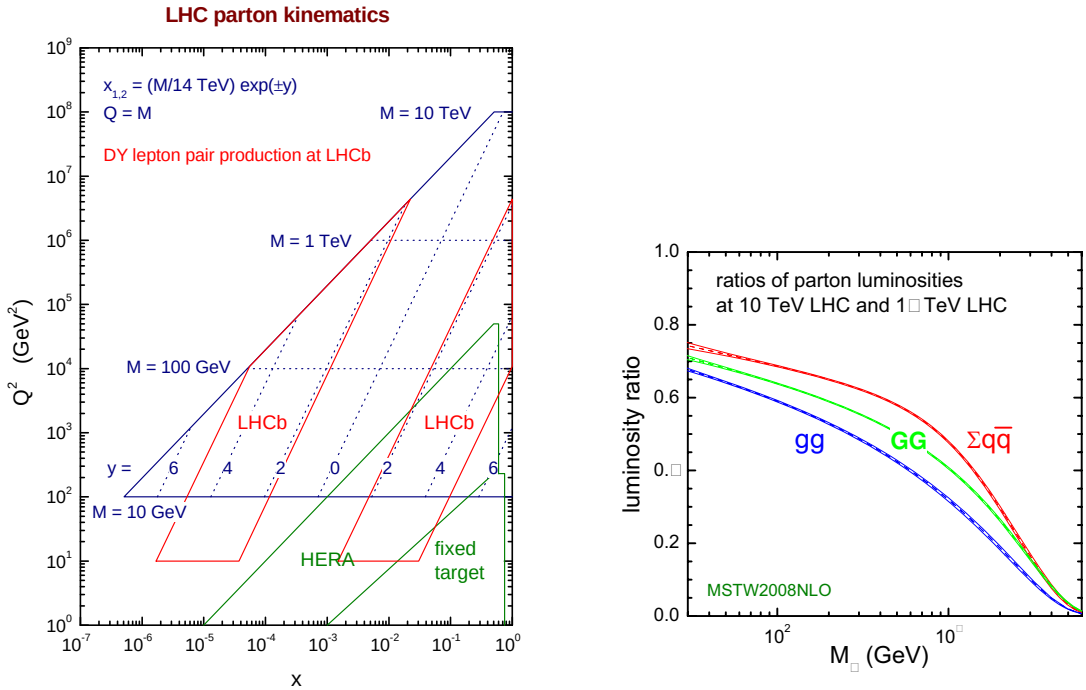


Fig. 5: The parton (x, Q^2) region probed by Drell-Yan lepton pair production in LHCb (left), and the ratio of $\sum q\bar{q}$, gg and GG ($G = g + 4/9 \sum(q + \bar{q})$) parton luminosities at 10 TeV and 14 TeV LHC (right).

partial-NNLO analysis is not expected to be large.

The situation regarding the treatment of heavy quark flavour (c, b) distributions is now quite satisfactory, with GM-VFNS generally accepted as the correct procedure. Within this framework, there is good agreement with HERA data on F_2^c and F_2^b. However, it is important to remember that pQCD-generated heavy flavour distributions may not be the whole story. The issue of additional *intrinsic* heavy flavour contributions, dominant at high x where the structure function data are sparse, is still an open question.

Early data from the LHC will be important for benchmarking a number of Standard Model standard-candle cross sections. In the case of $\sigma(W)$ and $\sigma(Z)$, the (NNL0) cross sections are predicted to approximately $\pm 4\%$ [2]. Note that such cross sections are not much smaller at $\sqrt{s} = 10$ TeV energy, since they tend to sample small-x partons that are not changing rapidly with x. This is illustrated in the right-hand figure in Fig. 5, which shows the ratio of the parton luminosities at 10 TeV and 14 TeV for $\sum q\bar{q}$ (relevant for W, Z, etc. production), gg (relevant for Higgs, $t\bar{t}$ etc. production), and GG (with $G = g + 4/9 \sum_q (q + \bar{q})$, relevant for high$-E_T$ dijet production) initial states.

Looking further ahead, a number of LHC measurements have the potential to constrain the pdfs even further. The most interesting appears to be the cross section for relatively low-mass Drell-Yan lepton pairs produced at large rapidity, which may be able to provide information on quark distributions at very small $x \sim 10^{-5} - 10^{-6}$, outside the domain currently accessible at HERA. The LHCb detector appears well suited to this measurement.

Acknowledgements

Useful discussions with and input from my MSTW collaborators Alan Martin, Robert Thorne and Graeme Watt are gratefully acknowledged.

References

[1] G. Watt, A. D Martin, W. J. Stirling and R. S. Thorne, *Proceedings of 16th International Workshop on Deep Inelastic Scattering and Related Subjects (DIS 2008), London, England, April 2008*, arXiv:0808.4890[hep-ph].

[2] A. D. Martin, W. J. Stirling, R. S. Thorne and G. Watt, in preparation.

[3] S. Moch and P. Uwer, Phys. Rev. D **78** (2008) 034003.

[4] R. V. Harlander and W. B. Kilgore, Phys. Rev. Lett. **88**, 201801 (2002).

[5] R. S. Thorne and W. K. Tung, arXiv:0809.0714 [hep-ph].

[6] A. D. Martin, W. J. Stirling, R. S. Thorne and G. Watt, Phys. Lett. B **652** (2007) 292.

[7] P. M. Nadolsky *et al.*, Phys. Rev. D **78** (2008) 013004.

[8] S. Kretzer, H. L. Lai, F. I. Olness and W. K. Tung, Phys. Rev. D **69** (2004) 114005.

[9] W. K. Tung, S. Kretzer and C. Schmidt, J. Phys. G **28** (2002) 983.

[10] S. Alekhin, Phys. Rev. D **68** (2003) 014002.

[11] S. Alekhin, K. Melnikov and F. Petriello, Phys. Rev. D **74** (2006) 054033.

[12] S. Alekhin, S. Kulagin and R. Petti, arXiv:0810.4893 [hep-ph].

[13] Gang Li, these proceedings.

[14] P. Jimenez-Delgado and E. Reya, arXiv:0810.4274 [hep-ph].

[15] J. Rojo, these proceedings; R. D. Ball *et al.*, Nucl. Phys. B **809** (2009) 1.

[16] J. Rojo *et al.*, arXiv:0811.2288 [hep-ph].

[17] S. Moch, these proceedings.

[18] Ch. Anastasiou, these proceedings.

[19] T. Shears, these proceedings.

Theoretical predictions for the LHC

S. Moch
Deutsches Elektronensynchrotron DESY, Platanenallee 6, D–15738 Zeuthen, Germany
DOI: http://dx.doi.org/10.3204/DESY-PROC-2009-01/55

Abstract
We review the status of QCD predictions for the Large Hadron Collider. We include recent theoretical developments for cross sections calculations to higher orders and discuss various Standard Model reactions such as $W^{\pm}/Z$-boson, Higgs boson or top quark production.

1 Introduction

The Large Hadron Collider LHC is built to explore the energy frontier as it operates at a center-of-mass energy of $\sqrt{s} = 14$ TeV. It will realize a major leap forward in collision energy compared to all other colliders thus far and it allows searches for the Higgs boson and tests of proposed extensions of the Standard Model, such as supersymmetry or models with large extra dimensions. The experimental signatures of many of the new physics scenarios are characterized by a high multiplicity of particles in the final state. They consist of multiple jets, leptons and missing transverse energy, see Fig. 1.

The cross sections for Standard Model scattering processes such as the production of b-quarks, $W^{\pm}$ and Z-bosons, multiple jets and top quarks at LHC are large. These Standard Model reactions lead to similar final states as those encountered for instance in the decay of the Higgs-boson. Thus, the challenge for theory at LHC is to provide precise predictions for the known physics, i.e. the Standard Model background in order to extract and identify signs of any kind of new physics. In particular, the theoretical predictions have to match or exceed the accuracy of the LHC data. To quote numbers, let us consider some rough estimates. The total cross section for W-boson production amounts to $\sigma_W \sim 150$ nb. With a branching ratio BR$(W \to e + \mu) \sim 20\%$ this leaves approximately 300M leptonic events at a luminosity of 10 fb^{-1} or, in other words, a production rate of 30 Hz in the initial low luminosity run. Likewise, for Z-boson production we

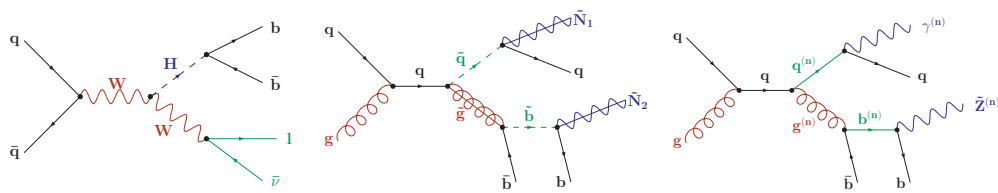


Fig. 1: Sample of Feynman diagrams for different physics scenarios at LHC with multiple jets, leptons and missing transverse energy. Left: Higgs-strahlung $q\bar{q} \to W(Z)H$ in the dominant decay mode $H \to b\bar{b}$. Middle: neutralino pair-production $\tilde{N}^0_{1,2}$ in the Minimal Supersymmetric Standard Model (with R-parity). Right: pair-production of excited Kaluza-Klein-modes $\gamma^{(n)}, Z^{(n)}$ in a model with large extra dimensions.

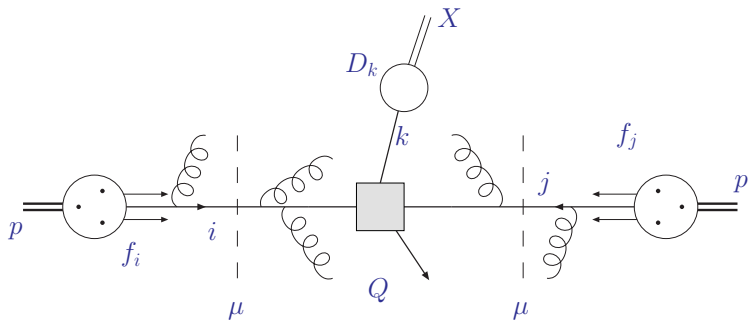


Fig. 2: Factorization for the hard-scattering cross sections in Eq. (1) in the QCD improved parton model.

have $\sigma_Z \sim 50$ nb and with BR$(Z \to ee + \mu\mu) \sim 6.6\%$ a total of 33M leptonic events at 10 fb^{-1}. For the low luminosity run this implies a rate of 3.5 Hz. In comparison, the typical rates for new physics signals are often of order $\sigma_{\text{new physics}} \sim \mathcal{O}(1-10)$ pb.

For precision predictions, much of the physics is actually dominated by the gauge theory of the strong interactions, Quantum Chromodynamics (QCD) and its perturbative formulation is an essential and established part of our theory toolkit. See e.g. Ref. [1] for a recent review on hard QCD at LHC. The basic prerequisite is QCD factorization which rests on the ability to separate dynamics from different scales. This is sketched schematically in Fig. 2.

QCD factorization allows a proton-proton scattering cross section of some hadronic final state X to be written as,

$$\begin{aligned}\sigma_{pp\to X} &= \sum_{ijk} \int dx_1\, dx_2\, dz\, f_i(x_1,\mu^2)\, f_j(x_2,\mu^2) \\ &\quad \times \hat{\sigma}_{ij\to k}\left(x_1, x_2, z, Q^2, \alpha_s(\mu^2), \mu^2\right)\, D_{k\to X}(z,\mu^2)\,, \end{aligned} \tag{1}$$

where Q is the hard scale and details of the integration range in the convolution depend on the kinematics of the hard scattering process under consideration.

The parton luminosity $f_i \otimes f_j$ $(i,j = q,\bar{q},g)$ is given as a convolution of the parton distribution functions (PDFs) in the proton. The latter depend on the parton momentum fractions x_1, x_2 and on the factorization scale μ. The PDFs are universal and have to be determined by fits to reference processes at low scales μ. The scale μ of the PDFs then has to be evolved from those of the reference processes to the one appropriate for applications at LHC. As the LHC probes the energy frontier this implies a scale evolution over two to three orders, see e.g. Ref. [2] for the current status of the parton luminosity. This evolution (μ-dependence) of the PDFs is governed by the perturbatively calculable splitting functions P_{ij}, now known through next-to-next-to-leading order (NNLO) in QCD [3, 4]. The (hard) parton cross section $\hat{\sigma}_{ij\to k}$ $(i,j,k = q,\bar{q},g)$ describes how the constituent partons from incoming protons interact at short distances of order $\mathcal{O}(1/Q)$. It is calculable in perturbative QCD as a series in the strong coupling constant α_s at leading order (LO) in QCD or, including quantum corrections, at next-to-leading order (NLO) or even NNLO. $\hat{\sigma}_{ij\to k}$ is the main quantity of interest in discussing the accuracy

process ($V \in \{\gamma, W^\pm, Z\}$)	background to	reference
$pp \to VV + 1\,\text{jet}$	$t\bar{t}H$, new physics	$WW + 1\,\text{jet}$ [5, 6]
$pp \to H + 2\,\text{jets}$	H production by vector boson fusion (VBF)	$H + 2\,\text{jets}$ [7]
$pp \to t\bar{t}b\bar{b}$	$t\bar{t}H$	$q\bar{q} \to t\bar{t}b\bar{b}$ [8]
$pp \to t\bar{t} + 2\,\text{jets}$	$t\bar{t}H$	
$pp \to VVb\bar{b}$	VBF $\to VV$, $t\bar{t}H$, new physics	
$pp \to VV + 2\,\text{jets}$	VBF $\to VV$	
$pp \to V + 3\,\text{jets}$	various new physics signatures	
$pp \to VVV$	SUSY trilepton	ZZZ [9], WWZ [10]

Table 1: Scattering processes at LHC for which the radiative corrections to NLO in QCD are needed.

of theoretical predictions at LHC. For completeness, we mention that X may denote any final state, e.g. hadrons, mesons or jets. The transition from the perturbative hard partons k in Eq. (1) to the observed particles is again non-perturbative and $D_{k\to X}$ can therefore be a fragmentation function or also a jet algorithm. Here the interface with showering algorithms (based on a Monte Carlo approach) becomes particularly crucial.

Physical observables like the cross section $\sigma_{pp\to X}$ in Eq. (1) cannot depend on the factorization scale, which implies that any dependence on μ in $\sigma_{pp\to X}$ has to vanish at least to the order in α_s considered.

$$\frac{d}{d\ln\mu^2}\sigma_{pp\to X} = \mathcal{O}(\alpha_s^{l+1})\,. \tag{2}$$

This variation defines the commonly adopted approach to quantify uncertainties in theoretical predictions based on the scale variation.

Let us now turn to hard parton scattering cross sections $\hat{\sigma}_{ij\to k}$. As mentioned, there exist various levels of accuracy for predictions building on exact matrix elements. At LO, we have at our disposal many highly automated programs for tree level calculations in the Standard Model, in its minimal supersymmetric extension (MSSM) or in other BSM models, which allow easy interfacing of LO calculations with parton shower Monte Carlos. These LO estimates based on exact matrix elements seem mandatory in search scenarios for studies of distributions, e.g. in p_T or the (pseudo-)rapidity (η) and for assessing the effects of kinematical cuts.

However, any LO prediction has large theoretical uncertainties, typically estimated by the scale variation, Eq. (2). Consider, for instance, the cross section for $pp \to W + 4$ jets, which is of $\mathcal{O}(\alpha_s^4)$ at LO. From a variation of the coupling of $\Delta(\alpha_s^{\rm LO}) \simeq 10\%$ one can roughly estimate a cross section uncertainty of $\Delta(\sigma^{\rm LO}) \simeq 40\%$. Thus, one needs to go beyond the Born approximation for scattering processes where quantum corrections at NLO may have an impact on the signal significance. Given the high multiplicity of final state particles at LHC (see Fig. 1) there exists a number of key processes at LHC which need to be known to NLO in QCD (see e.g. Ref. [11]). These are summarized in Tab. 1 and the computation of these radiative corrections is presently a very active field of research.

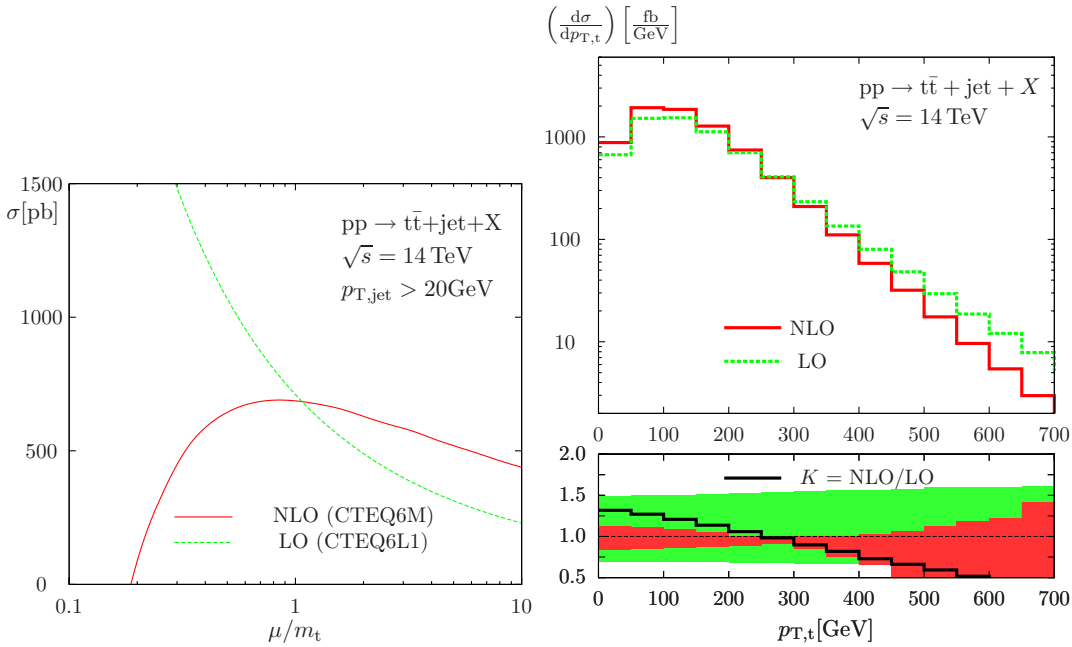


Fig. 3: The scale dependence of the LO and NLO cross sections for $t\bar{t}+1$ jet production at LHC (left) and the transverse-momentum distribution of the top-quark $p_{T,t}$ along with the K-factor and the scale variation in the range $m_t/2 \leq \mu \leq 2m_t$.

Let us illustrate the effects of NLO radiative corrections in QCD with the results of the recent impressive state-of-the-art calculation for $t\bar{t}+$ jet production [12, 13]. Fig. 3 displays the much improved scale dependence and shows that the perturbative corrections are moderate for the nominal scale choice of the order of the top-quark mass, $\mu \simeq m_t$. It also shows the NLO differential distribution in the transverse momentum of the top-quark for this reaction along with the kinematics dependence of the K-factor and the uncertainty band due to the scale variation in the commonly adopted range $m_t/2 \leq \mu \leq 2m_t$. From Fig. 3 it is clearly visible, that the NLO corrections (i.e. the K-factor) are not a uniform function of the transverse momentum p_T.

Finally, there is of course demand for fully differential QCD predictions to NNLO for hadron collider processes. Currently, this scope has been achieved e.g. for the di-lepton pair production in Drell-Yan [14] or Higgs production in gluon fusion [15]. However, it remains a challenge for many other reactions which can potentially be measured very precisely at LHC, such as Higgs production in vector boson fusion, top-pair production and to $V+1$ jet, where $V \in \{\gamma, W^{\pm}, Z\}$. However, also electroweak corrections become important once such an accuracy of a few percent is needed for an observable. As an example of the prospects at NNLO let us focus on the total cross section for top-quark pair-production, where currently complete NLO QCD predictions exist [16–18]. Based on soft gluon resummation though, it is possible to derive approximate NNLO results for the total cross section which combine the complete logarithmic dependence on the heavy quark velocity $\beta = \sqrt{1-4m^2/s}$ near threshold $s \simeq 4m^2$ with the complete two-loop Coulomb corrections as well as the exact dependence on the factorization

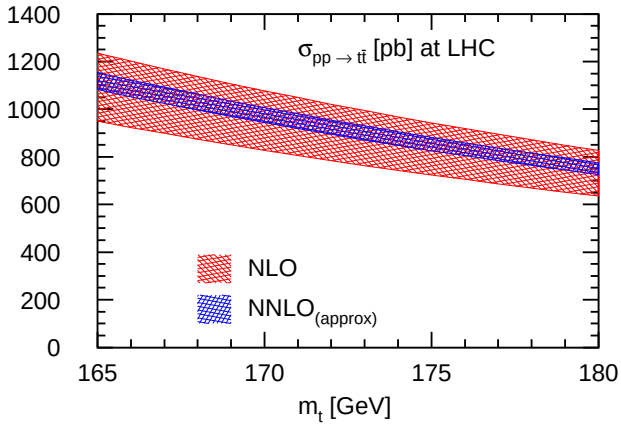


Fig. 4: The NLO and $\mathrm{NNLO}_{\mathrm{approx}}$ QCD prediction for the $t\bar{t}$ total cross section for LHC with $\sqrt{s} = 14$ TeV. The bands denote the total uncertainty from PDF and scale variations for the MRST06nnlo set according to Eq. (3).

scale at NNLO [19]. For phenomenology, this provides a very good approximation to the unknown exact NNLO result, because the parton luminosity in the convolution (1) emphasizes the threshold region pf phase space, i.e. it gives much weight to parton energies of order $\hat{s} \simeq 4m^2$.

At this level of accuracy, it is interesting to account for both the scale variation according to Eq. (2) and the PDF uncertainty. We define the range as

$$\sigma(\mu = 2m_t) - \Delta\sigma_{PDF}(\mu = 2m_t) \;\leq\; \sigma(\mu) \;\leq\; \sigma(\mu = m_t/2) + \Delta\sigma_{PDF}(\mu = m_t/2)\,, \qquad (3)$$

where $\Delta\sigma_{PDF}$ is computed from the variation of the cross section with respect to the parameters of the global fit of PDFs. The NLO QCD corrections provide the first instance where a meaningful error can be determined in this way. In Fig. 4 we plot the uncertainty range (3) comparing NLO and NNLO accuracy. The latter enters in the approximation based on the soft corrections as detailed above. The residual scale dependence of σ_{NNLO} is 2%, which corresponds to a reduction by a factor of two compared to NLO. At LHC σ_{NNLO} leads only to a small shift of a few percent in the central value and the total $\mathrm{NNLO}_{\mathrm{approx}}$ band is about 6% for CTEQ6.6 PDFs [20] and about 4% for the MRST06nnlo PDF set [21], which exhibits a drastic reduction of the scale uncertainty and much improved perturbative stability as compared to the prediction based on NLO QCD.

2 Summary

We have briefly reviewed some aspects of the theoretical framework of hard QCD at LHC. Precision predictions rely on knowledge of the parton luminosity as well as the rates for the corresponding partonic subprocess. Improving the theoretical accuracy for the latter is currently a active field of research and a lot of ongoing activity is concentrated on processes with multiparticle production to higher orders for both, the (new physics) signal and the background at LHC with massive particles and jets.

We have illustrated the present status of perturbative QCD predictions with a few examples from top quark production and we have tried to convey the message that QCD theory is ready to meet the challenges of LHC.

Let us finish with a disclaimer. All aspects of Higgs production are covered extensively e.g. in Ref. [22]. Moreover, we have left out a detailded discussion of all aspects of W- and Z-boson production. We have also omitted details of specific hadronic final states, e.g. jet algorithms, b-quark (b-jet) production or aspects of b-quark fragmentation as well as parton showers in Monte Carlo simulations and any computational details of higher order radiative corrections. We have also skipped any discussion of resummation approaches meant to improve fixed order perturbation theory, be it threshold logarithms of Sudakov type or $\ln(p_T)$-terms in transverse momentum. For all these remaining aspects as well as a broader coverage, the interested reader is referred e.g. to Refs. [1, 23, 24] and to the numerous references therein.

Acknowledgments

I would also like to thank the organizers for the invitation to the *XXXVIII International Symposium on Multiparticle Dynamics (ISMD 2008)* where I have enjoyed the nice atmosphere during conference.

References

[1] S. Moch, J. Phys. G **35** (2008) 073001 [arXiv:0803.0457 [hep-ph]].

[2] W. J. Stirling, these proceedings.

[3] S. Moch, J. A. M. Vermaseren and A. Vogt, Nucl. Phys. B **688** (2004) 101 [arXiv:hep-ph/0403192].

[4] A. Vogt, S. Moch and J. A. M. Vermaseren, Nucl. Phys. B **691** (2004) 129 [arXiv:hep-ph/0404111].

[5] S. Dittmaier, S. Kallweit and P. Uwer, Phys. Rev. Lett. **100** (2008) 062003 [arXiv:0710.1577 [hep-ph]].

[6] J. M. Campbell, R. Keith Ellis and G. Zanderighi, JHEP **0712** (2007) 056 [arXiv:0710.1832 [hep-ph]].

[7] J. M. Campbell, R. K. Ellis and G. Zanderighi, JHEP **0610** (2006) 028 [arXiv:hep-ph/0608194].

[8] A. Bredenstein, A. Denner, S. Dittmaier and S. Pozzorini, JHEP **0808** (2008) 108 [arXiv:0807.1248 [hep-ph]].

[9] A. Lazopoulos, K. Melnikov and F. Petriello, Phys. Rev. D **76** (2007) 014001 [arXiv:hep-ph/0703273].

[10] V. Hankele and D. Zeppenfeld, Phys. Lett. B **661** (2008) 103 [arXiv:0712.3544 [hep-ph]].

[11] C. Buttar *et al.*, arXiv:hep-ph/0604120.

[12] S. Dittmaier, P. Uwer and S. Weinzierl, Phys. Rev. Lett. **98** (2007) 262002 [arXiv:hep-ph/0703120].

[13] S. Dittmaier, P. Uwer and S. Weinzierl, arXiv:0810.0452 [hep-ph].

[14] C. Anastasiou, K. Melnikov and F. Petriello, Nucl. Phys. B **724** (2005) 197 [arXiv:hep-ph/0501130].

[15] S. Catani and M. Grazzini, Phys. Rev. Lett. **98** (2007) 222002 [arXiv:hep-ph/0703012].

[16] P. Nason, S. Dawson and R. K. Ellis, Nucl. Phys. B **303** (1988) 607.

[17] W. Beenakker, H. Kuijf, W. L. van Neerven and J. Smith, Phys. Rev. D **40** (1989) 54.

[18] M. Czakon and A. Mitov, arXiv:0811.4119 [hep-ph].

[19] S. Moch and P. Uwer, Phys. Rev. D **78** (2008) 034003 [arXiv:0804.1476 [hep-ph]].

[20] P. M. Nadolsky *et al.*, Phys. Rev. D **78** (2008) 013004 [arXiv:0802.0007 [hep-ph]].

[21] A. D. Martin, W. J. Stirling, R. S. Thorne and G. Watt, Phys. Lett. B **652** (2007) 292 [arXiv:0706.0459 [hep-ph]].

[22] Ch. Anastasiou, these proceedings.

[23] J. M. Campbell, J. W. Huston and W. J. Stirling, Rept. Prog. Phys. **70** (2007) 89 [arXiv:hep-ph/0611148].

[24] L. J. Dixon, arXiv:0712.3064 [hep-ph].

First physics prospects with the ATLAS detector at LHC

Judith Katzy on behalf of the ATLAS Collaboration
DESY, Hamburg, Germany

DOI: http://dx.doi.org/10.3204/DESY-PROC-2009-01/56

Abstract

The status of the ATLAS detector at the time of the first circulating LHC beam is presented. We report on the physics prospects for the early data with center of mass energies of 10 TeV and 14 TeV and integrated luminosities of 10 pb^{-1} up to 1 fb^{-1}.

1 Introduction

ATLAS (A Toroidal LHC ApparatuS) is one of the two general purpose detectors built to probe proton-proton collisions at 14 TeV. Here we present the status and physics start-up plans as of October 2008. The paper is organized as follows: The ATLAS detector concept and status is explained. Detector studies with data taken before proton-proton collisions are described and the plans for early physics are outlined.

1.1 The ATLAS detector

The ATLAS detector presents the typical large acceptance concentric collider detector structure. The inner tracking detectors (ID) surround the beam pipe. They consist of cylindrical layers (in the barrel part) and disks (in the forward parts) of silicon pixel with $0.8 \cdot 10^8$ channels and silicon strips with $6 \cdot 10^6$ channels, followed by a Transition Radiation Tracker (TRT) used for tracking and particle identification (e/π separation) with a momentum resolution of $\sigma(p_T)/p_T = 5 \cdot 10^{-4}\ p_T$ + 0.01. The ID covers the acceptance region of $|\eta| < 2.5$ and is immersed in a 2 Tesla magnetic field.

An electromagnetic lead-liquid argon sampling calorimeter system with accordion shape (LAr) is housed in a barrel and two endcap cryostats. The endcap cryostats also contain a hadronic sampling calorimeter with copper absorbers as well as the forward calorimeters with electromagnetic and hadronic sections made out of copper and tungsten absorbers respectively. The liquid argon calorimeter is complemented by barrel and extended barrel tile calorimeters (TileCal) using scintillating tiles with iron absorbers. The electromagnetic calorimeter has 180000 channels including longitudinal segmentation. Its energy resolution in the barrel and endcap regions is $\sigma(E)/E$ = 10%/$\sqrt{(}E) \bigoplus 0.7\%$. The hadronic energy resolution is $\sigma(E)/E \simeq 50\%/\sqrt{(}E) \bigoplus$ 3% in the Iron-Tiles and $\sigma(E)/E \simeq 100\%/\sqrt{(}E) \bigoplus 10\%$ in the copper/tungsten part. The LAr is fully installed and has been operated steadily since May 2008 with only 0.02% dead channels. The calorimetry is surrounded by the large air-core toroid muon system which includes precision tracking chambers with a standalone momentum resolution of $\Delta p_T/p_T < 10\%$ up to 1 TeV and additional trigger chambers.

For luminosity measurements, LUCID, a Cherenkov detector, is situated at 17 m from the interaction point close to the beam pipe. Two additional calorimeters will be placed at 140 and 240 m respectively. A detailed description of the full detector can be found at [1].

1.2 Pre-Collision data

Test beam measurements have been performed from May-November 2004 at the CERN H8 beam line with a vertical slice of the full detector corresponding to about 1% of the full size. The detector was put into magnetic fields between 0-1.4T strength. The response of the detector to particles was measured for $e^{+/-}, \pi^{+/-}, \mu, p, \gamma$ in energy ranges between 1-350 GeV. In total $9 \cdot 10^7$ events were collected. Both this and previous testbeam data was used in tuning the GEANT4 simulation of the ATLAS detector.

Since spring of 2008 cosmic data have been collected with the components installed in ATLAS. The rate of cosmic events crossing the inner detector is 15 Hz. A wealth of information can be extracted from these events for alignment, detector timing, pulse shape analysis and energy calibration. For example, the uniformity of the response of the LAr electromagnetic calorimeter has been cross-checked at the 3% level [2].

2 Collisions: A physics roadmap

One of the main goals with first collisions will be to calibrate the detectors in-situ using well known physics samples. The measurement of known Standard Model signals will serve also to validate and tune MC generators. At the same time, one should be prepared for surprises of very striking new physics signatures. A few examples of analysis are described in this section. A recent and exhaustive review of the physics potential of ATLAS can be found in reference [3].

At the time of the talk initial collisions at 10TeV were planned with an integrated luminosity of up to few pb^{-1}. After the LHC accident on September 19, 2008 the schedule has been revised and a clear decision on the start-up beam energy has not been taken at the time of writing. However, 10 TeV collisions are still likely expected first and are therefore considered here together with the physics capabilities of low luminosity 14 TeV samples.

2.1 Minimum-Bias and underlying event

About 2/3 of the total pp cross-section can be measured with to the so-called minimum bias trigger configuration which basically selects the non-single-diffractive events. There are large uncertainties in the extrapolation of the charged particle multiplicity produced in Minimum-Bias events from Tevatron to LHC energies, as shown in Figure 1. It is important to measure this cross-section, as Minimum-Bias events are the source of pile-up at higher luminosity. Up to about 20 events per bunch crossing are expected at design luminosity. They will need to be well understood to do precision physics. These measurements are best done with early data at low instantaneous luminosity. The expected p_T spectrum of the particles is soft with the cross-section peaking at 250 MeV. To increase the precision of the measurement, the reconstruction of tracks for these events can be extended down to 150 MeV.

2.2 W/Z Boson Production

The Z and W Boson cross-sections can be measured for leptonic decays with an initial robust analysis. The analysis is based on leptons with $p_T > 20$ GeV ($p_T > 25$ GeV for W) at $|\eta| < 2.5$. Lepton trigger and reconstruction efficiencies are extracted using the tag-and-probe method [3]. The overall efficiency for the signal is expected to be close to 70% (80%) for the Z (W) analysis, resulting in about 25,000 expected signal events and 100 expected background events for an integrated luminosity of 50 pb^{-1} for $Z \rightarrow \mu\mu$, see Figure 2. The expected errors of the cross-section are 0.8% (statistical) and 3% (systematic). An additional uncertainty will come from the uncertainty of the luminosity, which is estimated to be 10% at that stage. For $W \rightarrow \mu\nu$ 300,000 selected events are expected with 20,000 background, resulting in expected errors on the cross-section of 0.2% (statistical) and 3% (systematic). The precision of the measurement of W and Z will be quickly dominated by systematic effects and a final precision of 1-2% will be already reachable with 1fb^{-1}.

Due to the relatively high rate and the clean final state, the samples of Z and W boson with leptonic decays will be used to determine detector efficiencies like lepton trigger and reconstruction efficiencies, optimize the tau reconstruction and calibrate the energy scale of the calorimeters with progressively increasing precision. These studies can already start with 10 TeV collisions as the production cross-section is reduced by only 30%.

2.3 Inclusive Jet measurements

When measuring inclusive QCD jet cross-sections, one quickly enters into new territory. With an integrated luminosity of 20 pb^{-1} at 14 TeV, 10 jets of 2 TeV are expected, an energy beyond the reach of the Tevatron. The achievable precision of the measurement will depend on the level of understanding of the Jet Energy Scale at that time. Initially, a jet scale precision of 5-10% with a resultion of 60-75%/$\sqrt{(E)} \pm 7$% is expected at central rapidity. It should be noted that the reconstruction of the jet energy scale and resolution depends strongly on the underlying event and the simulation of the hadronic shower and can therefore not be measured with test beams. Study of the high-p_T tails of the inclusive jet cross-section is sensitive to New Physics e.g. quark compositeness or contact interactions.

2.4 Top

At the LHC, the dominant $t\bar{t}$ pair production process is gluon-gluon fusion with a cross-section about 100 times larger than at the Tevatron, whereas backgrounds are expected to rise only by about a factor 10. The cross-section for the gold-plated semi-leptonic decay $t\bar{t} \rightarrow bW\bar{b}W \rightarrow blvbjj$ with l= e,μ, is of the order of 250 pb at 14 TeV. A robust analysis has been developed to establish a clear signal with the first data [3]. It relies solely on the measurement of four jets (3 jets with $p_T > 40$ GeV and 1 with $p_T > 20$ GeV), one isolated electron or muon with $p_T > 20$ GeV (including trigger) and Missing $E_T > 20$ GeV. It does not make use of the full b-tagging capability, since precise alignment of the inner detector may not be available in the early days. With an integrated luminosity of 100 pb^{-1}, about 500 reconstructed hadronic top decays are expected over background composed mainly of internal combinatorics within $t\bar{t}$ events and W+jets events. Thanks to the over-constrained kinematics of the $t\bar{t}$ system, it will be possible

to measure b-tagging performance and Missing E_T and to calibrate the light jet energy scale. The $t\bar{t}$ cross-section will also be measured in the di-lepton channel. With 100 pb^{-1} the cross-section can be measured with an uncertainty of 5-10%, dominated by systematics and excluding the uncertainty on luminosity.

3 Early discovery

New heavy states forming a narrow resonance decaying into opposite sign dileptons are predicted in many extensions of the Standard Model: grand unified theories, technicolor, little Higgs models, and models including extra dimensions [3]. The signature of these events is a mass peak in the invariant mass distribution of opposite sign dileptons on top of the Drell-Yan spectrum. The sensitivity to this clear signature rises with decreasing mass of the resonance, a resonance peak around 1 TeV (which is unreachable by the Tevatron experiments) could be discovered with as little as 100 pb^{-1}.

Super Symmetry (SUSY) is the second candidate for early discovery at the LHC. Relatively large cross-sections are predicted for squark pair-, squarkgluino- and gluino pair production. These processes would have spectacular signatures with events with many jets, high p_T leptons and missing E_T. The best experimental signature would be events with 4 jets plus one lepton. R-parity conserving SUSY can be found with 1 fb^{-1} if the gluino and squark masses are O(1TeV). However, it would still require a good understanding of the background. Conversely, if gluinos and squarks are much heavier they might still be found at the LHC eventually, but it will be difficult to study them in detail.

3.1 Higgs

In the Standard Model, the electroweak symmetry is spontaneously broken via the Higgs mechanism. The Higgs boson is the only piece of the Standard Model that has not been observed experimentally and its possible discovery is one of the main goals of the LHC.

The Higgs boson couples preferentially to heavy particles and this determines its production mechanisms and decay modes. At LHC, gluon fusion, $gg \rightarrow H$, dominates, followed by vector boson fusion, $qq \rightarrow qqH$, with two forward quark jets and lack of color exchange between those quarks. Other mechanisms are associated production with weak gauge bosons, $qq \rightarrow WH/ZH$, or heavy quarks, $qq, gg \rightarrow ttH$. They are relevant for low mass Higgs searches, i.e. at $m_H < 130$ GeV. For this range, the $b\bar{b}$ decay mode dominates but is difficult to exploit because of the large background from jets. Below 140 GeV the $H \rightarrow \gamma\gamma$ decay mode is one of the interesting channels that can be exploited both in inclusive analysis or optimized for specific associated production mechanisms. Sensitivity to low mass Higgs comes also from $H \rightarrow \tau\tau$ in the vector boson fusion mode.

The most favorable decay modes are WW and ZZ when kinematically allowed. The most powerful channel with the cleanest signature is $H \rightarrow ZZ^* \rightarrow 4l$ with good discovery potential in the range $130 < m_H < 600$ GeV, except in the mass region around $2m_W$. A Standard Model Higgs boson with mass above 130 GeV might be discovered with 5 fb^{-1}. Eventually, the full mass range will be explored at the LHC. More data may be needed if the mass is close to the direct LEP bound of 114.4 GeV. If the Higgs is discovered its mass can be determined to a

precision of 0.1%.

3.2 Summary

The LHC operation is about to start. During the last five years, all the elements of the ATLAS detector have been progressively installed in the cavern, the last ones in July 2008. Overall the detector is ready and functioning well with full solid angle coverage and only a very small fraction of dead channels. Many dedicated combined commissioning runs recording cosmic ray events have taken place in the last two years, helping in pre-calibrating the detector and having the full chain ready for data taking. With first collisions the most urgent task will be to understand the detector in detail and perform first measurements of Standard Model physics: minimum-bias events, QCD jets, W/Z and top pair production. These measurements will test the Standard Model in a much extended kinematic region and provide important first constraints on the MC generators. One should be open to the possibility of finding new physics if Nature has chosen a scenario which would provide spectacular signatures at LHC energies. We will progressively study the TeV scale in more detail with increased statistics looking for hints of the Higgs and of many possible phenomena beyond the Standard Model.

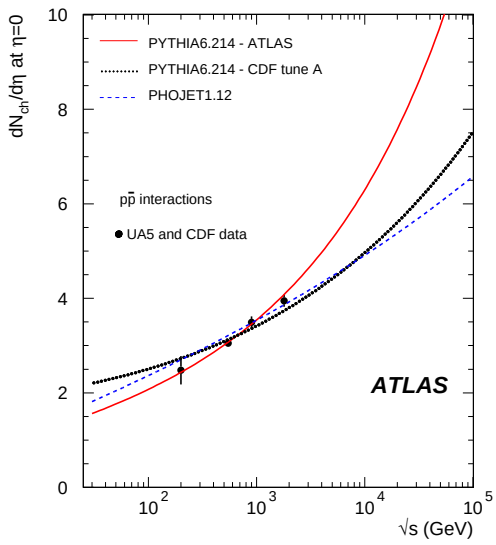


Fig. 1: Charged particle multiplicity in minimum bias events. Predictions for LHC.

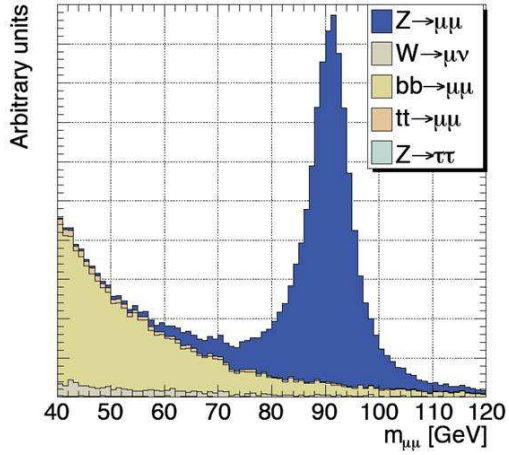


Fig. 2: Di-muon invariant mass distribution in the $Z \rightarrow \mu\mu$ channel for signal and background for 50 pb^{-1}

.

References

[1] ATLAS Collaboration, *"The Atlas Experiment at the CERN Large Hadron Collider"*. JINST S08003, 2008 .

[2] D.Dannheim for ATLAS Collaboration, *"Commissioning and Performance of the ATLAS Liquid Argon Calorimeter", talk and proceedings at ICHEP08* ATL-LARG-PROC-2008-001, 2008 .

[3] ATLAS Collaboration, *"Expected Performance of the ATLAS Experiment, Detector, Trigger and Physics"* CERN-OPEN-2008-020, 2008 .

The Heavy Flavour Content of the Proton

Paul D. Thompson
University of Birmingham, UK

DOI: http://dx.doi.org/10.3204/DESY-PROC-2009-01/57

Abstract

Recent measurements on heavy flavour production at HERA using the H1 and ZEUS experiments are presented. The cross sections for charm and beauty production in deep-inelastic scattering (DIS) using the HERA II data sample are shown. The results are based on various experimental methods including the reconstruction of D mesons, the measurement of semi-leptonic processes, measurements of the impact parameter, in the transverse plane, of tracks to the primary vertex and the reconstruction of the secondary vertex in the vertex detectors. The measurements are compared with the predictions of next-to-leading order (NLO) quantum chromodynamics (QCD).

1 Introduction

In perturbative QCD calculations, the production of heavy quarks at HERA proceeds dominantly via the direct photon-gluon fusion (PGF) process $\gamma g \rightarrow c\bar{c}$ ($\gamma g \rightarrow b\bar{b}$), where the photon interacts with a gluon from the proton to produce a pair of heavy quarks in the final state. Therefore, the measurement of processes involving heavy flavour production provides a test of the understanding of the QCD production mechanism and information on the gluon content of the proton. The presence of the heavy quark mass M provides an additional 'hard' scale to the momentum transfer of the exchanged boson Q and the transverse momentum of the heavy quark p_T meaning the perturbative series has to be treated in different ways depending on the relative magnitude of M, Q and p_T. At small scales ($Q, p_T \sim M$) the mass of the heavy quark is taken into account via the 'massive' PGF matrix element. At high scales ($Q, p_T \gg M$) the quark's mass may be neglected and it is treated as a 'massless' parton. The latest sets of global parton density functions (PDFs) from the MRST and CTEQ fitting groups (MRST08, CTEQ6.6) are based on heavy flavour schemes which aim to interpolate between the 'massive' behaviour at low Q^2 and 'massless' behaviour at high Q^2. The measurement of the inclusive contribution of processes involving charm and beauty to the proton structure function $F_2^{c\bar{c}}$ and $F_2^{b\bar{b}}$ allow to test these so-called "General Mass" schemes. The understanding of the gluon and heavy quark distributions in the region of low Bjorken x has important implications for the measurement of standard model and new physics processes at hadron colliders such as the Tevatron and LHC.

Recent measurements on charm and beauty production at HERA using the H1 and ZEUS experiments are presented here with the focus being on the DIS kinematic region. Many of the results presented in this paper utilise the full HERA II data sample and thus offer a significant improvement in precision compared with the previous HERA I results.

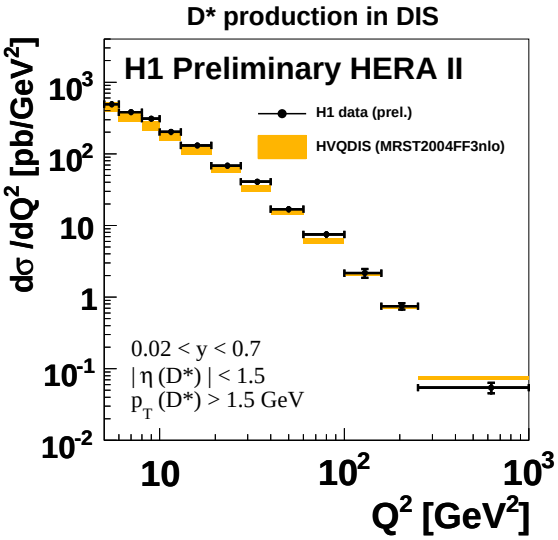


Fig. 1: The differential D^* cross section in DIS for $d\sigma/dQ^2$ as measured by the H1 collaboration

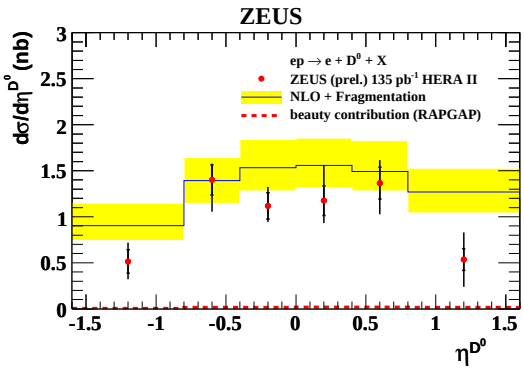


Fig. 2: The differential D^0 cross section in DIS for $d\sigma/d\eta$ as measured by the ZEUS collaboration.

2 Analysis Techniques

Charm quarks contribute around $20-30\%$ of the inclusive DIS cross section. Charmed hadrons are predominantly detected by reconstructing the decay products of $D^{*\pm}$, $D^{\pm}$, $D_s^{\pm}$ or D^0 mesons in the central tracking detectors of H1 and ZEUS. For $D^{*\pm}$ measurements the "Golden Decay" chain $D^* \rightarrow K\pi\pi_{\rm slow}$ is most often used. The signal to background ratio of the measurements can be improved by using information on the decay length significance of the secondary vertex as reconstructed by the silicon vertex detectors of the experiments.

In contrast to the rather large contribution of charm quarks to the total DIS cross section, beauty quarks contribute only a few $\%$, and an order of magnitude less at low values of Q^2. Therefore, the detection of beauty hadrons is very challenging. To extract signals use is made of the properties of beauty hadrons; their semi-leptonic decays, their relatively large mass and long lifetime. In semi-leptonic decays the large transverse momentum of the lepton w.r.t. the jet axis ($p_T^{\rm rel}$ method) may be used to tag events containing beauty quarks. This information can also be combined with information from the silicon vertex detectors, for example by measuring the large displacements from the primary vertex (impact parameter) of the lepton track. In analyses without the lepton requirement the impact parameter significance of all tracks with hits in the silicon vertex detectors can be combined with information from the position of the secondary vertex through use of a neural network. The c, b and light quark fractions in the data are extracted using a simultaneous fit of simulated reference distributions, obtained from Monte Carlo simulation, to the measured distributions.

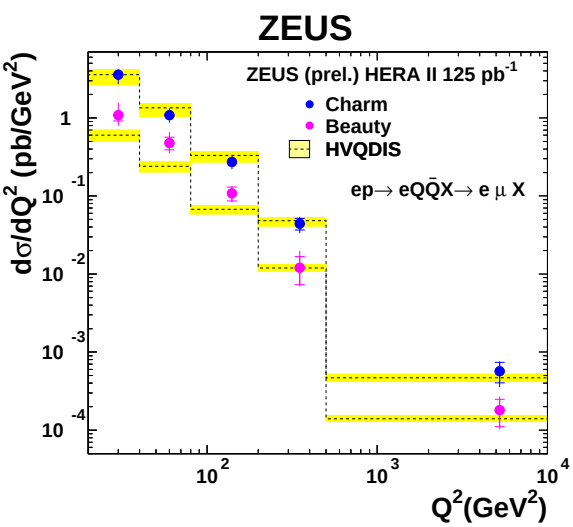


Fig. 3: The inclusive charm and beauty differential cross section in DIS for $d\sigma/dQ^2$ as measured by the ZEUS collaborationusing events with semi-muonic decays.

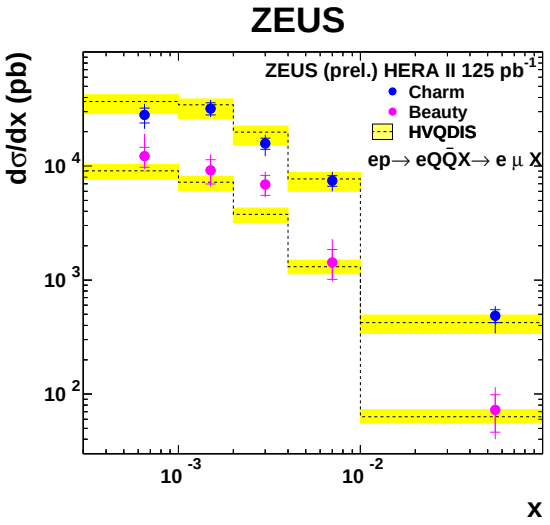


Fig. 4: The inclusive charm and beauty differential cross section in DIS for $d\sigma/dx$ as measured by the ZEUS collaborationusing events with semi-muonic decays.

3 Results

3.1 D Meson Cross Sections

The cross sections for the production of various D mesons have been made in DIS by H1 and ZEUS. The H1 collaboration have measured the $D^{*\pm}$ cross section in the range $5 < Q^2 < 1000$ GeV^2, $0.02 < y < 0.7$, $p_T(D^{*\pm}) > 1.5$ GeV and $-1.5 < \eta(D^{*\pm}) < 1.5$ [1]. The cross section is shown as a function of Q^2 in figure 1. The 'massive' NLO QCD prediction of HVQDIS [2] is shown to give an adequate description of the data over the full Q^2 range, including the high Q^2 region where the massive scheme may not be expected to be applicable.

The ZEUS collaboration have measured $D^{*\pm}$,$D^{\pm}$ and D^0 production cross sections in DIS using HERA II data samples [3–5]. The measurements of $D^{\pm}$ [4] and D^0 [5] mesons were improved by using lifetime information from the ZEUS Micro Vertex Detector. The D^0 meson cross section as a function of $\eta(D^0)$ is shown in figure 2. The cross section is reasonably well described by the prediction of massive NLO QCD.

3.2 Charm Fragmentation

The D meson cross sections described above can be measured in double differential $x - Q^2$ bins and the results used to extrapolate in p_T and η, using HVQDIS, to the full phase space in order to measure the charm structure function $F_2^{c\bar{c}}(x, Q^2)$. As well as the extrapolation it is also important to understand the fragmentation of charmed quarks into D mesons. The process is usually modelled using the convolution of the hard scattering cross section with a non-perturbative fragmentation function $D_c^{D^*}(z)$ where $z = E_{D^*}/E_c$. There exist a number of single parameter

fragmentation functions which have been tuned to e^+e^- data. A recent publication on HERA I data by the H1 collaboration [6] found that these fragmentation functions were able to describe D^* data for events where there was a jet with $p_T > 3$ GeV in the centre-of-mass frame. For events without a jet the hadron level approximations to the fragmentation function were much less well described by the standard fragmentation parameters.

3.3 Inclusive Heavy Flavour Cross Sections in DIS

The inclusive cross section of charm and beauty quarks at HERA has been measured by the ZEUS collaboration [7]. The measurement was made using the semi-leptonic decay of heavy hadrons into muons in the range $Q^2 > 20$ GeV^2, $0.01 < y < 0.7$, $p_T(\mu) > 1.5$ GeV and $-1.6 < \eta(\mu) < 2.3$. The heavy flavour contributions were extracted by simultaneous fits to the missing transverse momentum, $p_T^{\rm rel}(\mu)$ and the muon impact parameter distributions. The relatively low cut on the transverse momentum of the lepton allows the inclusive charm and beauty cross sections to be extracted. These are shown as a function of x and Q^2 in figure 3. The data are reasonably well described by the predictions of massive NLO QCD, with the beauty data tending to be somewhat higher than the QCD prediction at low values of Q^2. The measurements can be extrapolated to the full phase space in order to evaluate the charm and beauty structure functions.

The H1 collaboration have analysed the inclusive production of charm and beauty quarks in DIS [8] using the impact parameter of tracks and the output of a neural network. The analysis makes use of the full available HERA II data sample. The inclusive 'reduced' beauty cross section in DIS $\tilde{\sigma}^{b\bar{b}}$ ($\tilde{\sigma}^{b\bar{b}} \simeq F_2^{b\bar{b}}$) is shown as a function of x for different values of Q^2 in figure 5. The data from the ZEUS collaboration using semi-muonic samples are also shown. The data between the different methods are in reasonable agreement, although the ZEUS results tend to be higher than H1 at low Q^2. The fully inclusive measurements are compared in the figure with the latest GM scheme predictions of MSTW and CTEQ, and are found to be generally well described. The massive FFNS prediction is also seen to be able to describe the data. The measurements were also found to be described by the NNLO predictions of MSTW.

The charm structure function $F_2^{c\bar{c}}$ is shown as a function of Q^2 for different values of x in figure 6. The data span a large range in the Q^2 and x plane. The $F_2^{c\bar{c}}$ measurements from the different experimental methods discussed above (i.e. from inclusive silicon vertex information and extrapolated from D meson and semi-muonic cross sections) are found to be in good agreement. The HERA II heavy flavour data have significantly improved in precision compared with HERA I. The precision of the HERA charm data would further improve if the data from the different methods and experiments is combined. The theoretical predictions based on the massive scheme give a reasonable description of the data across the x and Q^2 plane with the largest difference between CTEQ5F3 and MRST2004FF being in the region $Q^2 < 2m_c^2$ which is due to the different PDF inputs in this region.

4 Conclusion

Measurements of the heavy flavour content of the proton in DIS at HERA have been presented. The extraction of the inclusive cross sections $F_2^{b\bar{b}}$ and $F_2^{c\bar{c}}$ allow the comparison of different

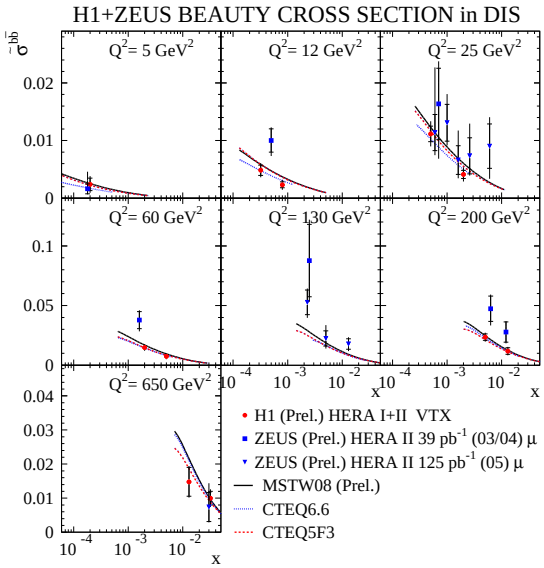


Fig. 5: The measured reduced cross section $\tilde{\sigma}^{b\bar{b}}$ shown as a function of x for 5 different Q^2 values.

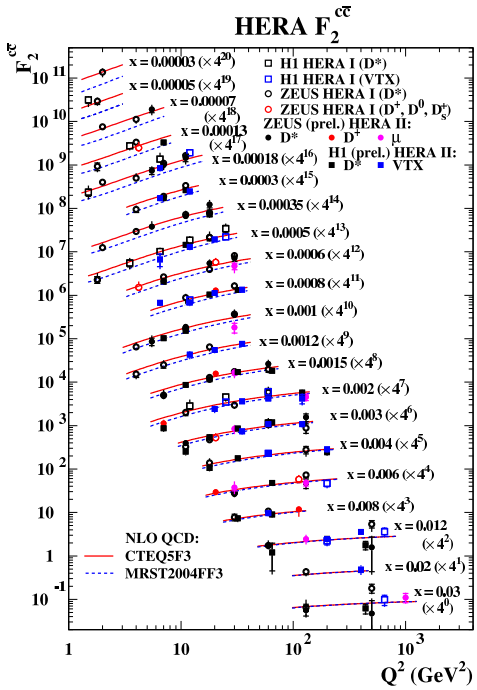


Fig. 6: The measured $F_2^{b\bar{b}}$ shown as a function of Q^2 for various x values.

experimental techniques. The cross sections are found to be well described by the predictions of perturbative QCD at NLO and NNLO.

References

[1] H1 Collaboration, "Dstar production at low Q2 with the H1 detector", contribution to the 16th International Conference on Deep-inelastic Scattering (DIS08), London UK, April 2008 (H1 prelim-08-072) ; H1 Collaboration, "Dstar production at high Q2 with the H1 detector", contribution to the 34th International Conference on High Energy Physics, Philadelphia USA, July 2008 (H1 prelim-08-074)

[2] B. W. Harris and J. Smith, Phys. Rev. D **57** (1998) 2806 [hep-ph/9706334].

[3] ZEUS Collaboration, "$F_2^{c\bar{c}}$ from $D^{\pm}$ mesons in DIS", contribution to the 15th International Conference on Deep-inelastic Scattering (DIS07), Munich Germany, April 2007 (ZEUS-prel-07-008)

[4] ZEUS Collaboration, "$F_2^{c\bar{c}}$ from $D^{\pm}$ mesons in DIS using 2005 $e-p$ data", contribution to the 15th International Conference on Deep-inelastic Scattering (DIS07), Munich Germany, April 2007 (ZEUS-prel-07-009)

[5] ZEUS Collaboration, "D^0 meson cross sections in DIS using HERA II data" (ZEUS-prel-07-034).

[6] *et al.* [H1 Collaboration], arXiv:0808.1003 [hep-ex].

[7] ZEUS Collaboration, "Charm and Beauty in DIS from muons", contribution to the 34th International Conference on High Energy Physics, Philadelphia USA, July 2008 (ZEUS-prel-08-007).

[8] H1 Collaboration, "Dstar production at high Q2 with the H1 detector", contribution to the 34th International Conference on High Energy Physics, Philadelphia USA, July 2008 (H1 prelim-08-074).

Update on Neural Network Parton Distributions: NNPDF1.1

Juan Rojo[1,3]*, Richard D. Ball*[2]*, Luigi Del Debbio*[2]*, Stefano Forte*[3]*, Alberto Guffanti*[4]*,*
José I. Latorre[5]*, Andrea Piccione*[3]*, and Maria Ubiali*[2]
[1] LPTHE, CNRS UMR 7589, Universités Paris VI-Paris VII,
F-75252, Paris Cedex 05, France
[2] School of Physics and Astronomy, University of Edinburgh,
JCMB, KB, Mayfield Rd, Edinburgh EH9 3JZ, Scotland
[3] Dipartimento di Fisica, Università di Milano and INFN, Sezione di Milano,
Via Celoria 16, I-20133 Milano, Italy
[4] Physikalisches Institut, Albert-Ludwigs-Universität Freiburg
Hermann-Herder-Straße 3, D-79104 Freiburg i. B., Germany
[5] Departament d'Estructura i Constituents de la Matèria, Universitat de Barcelona,
Diagonal 647, E-08028 Barcelona, Spain
DOI: http://dx.doi.org/10.3204/DESY-PROC-2009-01/58

Abstract
We present recent progress within the NNPDF parton analysis framework. After a brief review of the results from the DIS NNPDF analysis, NNPDF1.0, we discuss results from an updated analysis with independent parametrizations for the strange and anti-strange distributions, denoted by NNPDF1.1. We examine the phenomenological implications of this improved analysis for the strange PDFs.

Introduction PDFs and their associated uncertainties will play a crucial role in the full exploitation of the LHC physics potential. However, it is known that the standard approach to PDF determination [1, 2] suffers from several drawbacks, mainly related to the lack of control on the bias introduced in the choices of specific PDF parametrizations and flavour assumptions, as well as to the difficulty in providing a consistent statistical interpretation of PDFs uncertainties in the presence of incompatible data.

Motivated by this situation, a novel method has been introduced which combines a MC sampling of experimental data with neural networks as unbiased interpolators for the PDF parametrization. This method, proposed by the NNPDF Collaboration, was first successfully applied to the parametrization of DIS structure functions [3, 4] and more recently to the determination of PDFs [5,6]. In this contribution we present recent results within this NNPDF analysis framework.

The NNPDF1.0 analysis NNPDF1.0 [6] was the first DIS PDF analysis from the NNPDF Collaboration. The experimental dataset used in the NNPDF1.0 analysis consists of all relevant fixed target and collider deep-inelastic scattering data: structure functions from NMC, SLAC and BCDMS, CC and NC reduced cross-sections from HERA, direct $F_L(x, Q^2)$ from H1 and neutrino CC reduced cross sections from CHORUS.

In NNPDF1.0, five PDFs are parametrized with neural networks at the initial evolution scale, which is taken to be $Q_0^2 = m_c^2 = 2\,\text{GeV}^2$: $\Sigma(x, Q_0^2)$, $V(x, Q_0^2) \equiv (u_v + d_v + s_v)(x, Q_0^2)$,

$T_3(x,Q_0^2) \equiv (u+\bar{u}-d-\bar{d})(x,Q_0^2)$, $\Delta_S(x,Q_0^2) \equiv (\bar{d}-\bar{u})(x,Q_0^2)$, and $g(x,Q_0^2)$. The strange distributions are fixed by the additional assumption:

$$s(x,Q_0^2) = \bar{s}(x,Q_0^2) = C_S/2\left(\bar{u}(x,Q_0^2)+\bar{d}(x,Q_0^2)\right) \ . \tag{1}$$

The fraction of (symmetric) strange over non-strange sea is taken to be $C_S = 0.5$, as suggested by di-muon data. While recent analysis (see [7] and references therein) suggest a somewhat smaller central value, Eq. 1 is a very crude approximation and therefore uncertainties in C_S are expected to be rather large, as the new NNPDF1.1 analysis confirms below.

The overall normalization of $g(x), \Delta_S(x)$ and $g(x)$ is fixed by imposing the momentum and valence sum rules. The NNPDF NLO evolution program employs a hybrid N-space and x-space method [5], whose accuracy has been checked with the Les Houches benchmark tables [8], obtained from a comparison of the HOPPET [9] and PEGASUS [10] evolution programs.

The NNPDF1.0 gluon and singlet PDFs are shown in Fig. 1, compared with the results of other sets. We observe that our analysis produces results consistent with those obtained by other collaborations [1, 2] while our error bands tend to get bigger in the region where data do not constrain PDFs behavior. Interestingly, this happens without any error blow-up from the use of large tolerance factors [1, 2] in the PDF error definition.

The NNPDF1.1 analysis NNPDF1.1 is an update of the previously described NNPDF1.0 analysis which introduces independent parametrizations in the strange PDF sector and a randomization of the preprocessing. The motivations for this update are twofold. First of all, the stability analysis of [6], were the preprocessing exponents were varied their optimal values, indicated that uncertainties might have been slightly underestimated for some PDFs in some restricted $x-$regions, like for example the valence PDF in the large-x region. On the other hand, the restrictive assumptions on the strange distributions Eq. 1 should also lead to an uncertainty underestimation for some PDFs and some observables, especially those directly sensitive to the strange sector.

Instead of the simplified assumptions in Eq. 1, in NNPDF1.1 both $s_+(x,Q_0^2)$ and $s_-(x,Q_0^2)$ are parametrized with independent neural networks. The architecture is the same as in [6], so that each PDF is described by 37 free parameters. The $s_-(x)$ distribution is forced to satisfy the strange valence sum rule following the method of [6]. These strange PDFs are mostly constrained in our analysis by the CHORUS data as well as by the HERA CC data.

Another improvement in NNPDF1.1 with respect to NNPDF1.0 is a randomization of the preprocessing exponents, which were kept fixed at their optimal values in [6]. In the present analysis for each replica the PDF preprocessing exponents are allowed to vary at random within a given range, which is given in Table 1. This range is determined as the range in which variations of the preprocessing exponents produce no deterioration of the fit quality, see Table 11 in [6].

In Fig. 1 we show the results from the NNPDF1.1 analysis for the $\Sigma(x)$, $g(x)$,$s_+(x)$ and $s_-(x)$ distributions compared to other PDF sets, including NNPDF1.0. First of all, we observe that the central values for both PDFs are reasonably close between NNPDF1.0 and NNPDF1.1, thus ensuring the validity of the flavour assumptions in the former case. Second, we see that the uncertainties in $s_+(x)$ are large, so that all other PDF sets are included within the NNPDF1.1

PDF	m	n
$\Sigma(x,Q_0^2)$	$[2.7,3.3]$	$[1.1,1.3]$
$g(x,Q_0^2)$	$[3.7,4.3]$	$[1.1,1.3]$
$T_3(x,Q_0^2)$	$[2.7,3.3]$	$[0.1,0.4]$
$V_T(x,Q_0^2)$	$[2.7,3.3]$	$[0.1,0.4]$
$\Delta_S(x,Q_0^2)$	$[2.7,3.3]$	$[0,0.01]$
$s_+(x,Q_0^2)$	$[2.7,3.3]$	$[1.1,1.3]$
$s_-(x,Q_0^2)$	$[2.7,3.3]$	$[0.1,0.4]$

Table 1: The range of variation of the preprocessing exponents used in NNPDF1.1.

error band, which turns out to be much larger than for NNPDF1.0, since there the strange sea was fixed by Eq. 1. The situation for the strange valence PDF $s_-(x)$ is similar: it turns out to be completely unconstrained from the present data set (see Fig. 1), with central value compatible with zero.

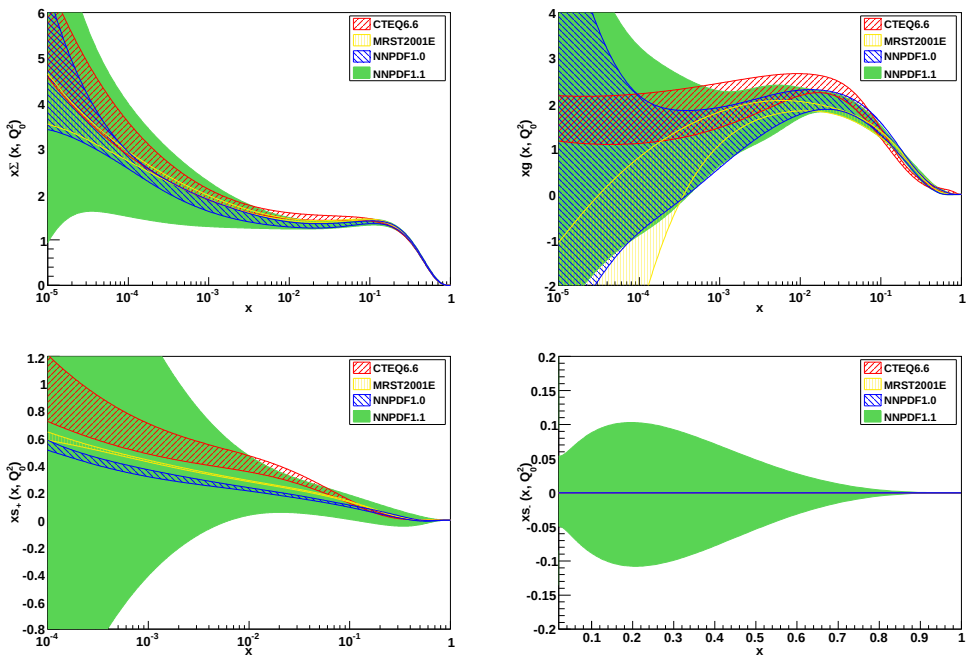


Fig. 1: The NNPDF1.1 PDFs compared with other PDF sets, including NNPDF1.0.

The PDFs from the NNPDF1.1 analysis are seen to be reasonably stable with respect the NNPDF1.0 ones (see $\Sigma(x)$ and $g(x)$ in Fig. 1), which is an important result since both two new input PDFs and a randomization of the preprocessing have been incorporated in the new analysis. This stability is quantified by the stability estimators [5], shown in Table 1. The only differences turn out to be for the uncertainty in $V(x)$ and on the singlet PDF $\Sigma(x)$ in the extrapolation region. The uncertainty in $V(x)$, which was known to be underestimated by a factor 1.5-2 in

	Data	Extrapolation
$\Sigma(x,Q_0^2)$	$5\,10^{-4} \le x \le 0.1$	$10^{-5} \le x \le 10^{-4}$
$\langle d[q]\rangle$	1.6	1.0
$\langle d[\sigma]\rangle$	3.5	2.7
$g(x,Q_0^2)$	$5\,10^{-4} \le x \le 0.1$	$10^{-5} \le x \le 10^{-4}$
$\langle d[q]\rangle$	2.9	3.3
$\langle d[\sigma]\rangle$	1.5	1.5
$T_3(x,Q_0^2)$	$0.05 \le x \le 0.75$	$10^{-3} \le x \le 10^{-2}$
$\langle d[q]\rangle$	1.3	0.9
$\langle d[\sigma]\rangle$	1.4	2.6
$V(x,Q_0^2)$	$0.1 \le x \le 0.6$	$3\,10^{-3} \le x \le 3\,10^{-2}$
$\langle d[q]\rangle$	2.2	2.4
$\langle d[\sigma]\rangle$	5.3	5.3
$\Delta_S(x,Q_0^2)$	$0.1 \le x \le 0.6$	$3\,10^{-3} \le x \le 3\,10^{-2}$
$\langle d[q]\rangle$	1.0	1.4
$\langle d[\sigma]\rangle$	1.9	1.6

Table 2: Stability estimators which compare parton distributions from NNPDF1.0 and NNPDF1.1.

NNPDF1.0 [6], now has correspondingly increased by the expected factor, mainly due to the absence of assumptions on the valence strange PDF $s_-(x)$, as can be seen in Fig. 2. A comparable increase in uncertainty is observed in the extrapolation region of $\Sigma(x)$, which can be attributed to the extra flexibility induced by the presence of the independent $s_+(x)$ PDF.

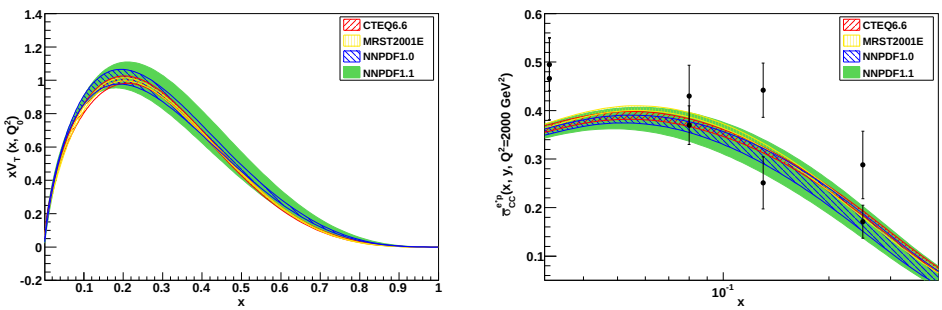


Fig. 2: The valence PDF $V(x,Q_0^2)$ (left) and the the CC reduced cross section $\widetilde{\sigma}_{\rm CC}$ from HERA (right).

As a consequence of the large uncertainties for $s_-(x)$, the uncertainties in the CC DIS observables turn out to be larger than in NNPDF1.0, as can be seen in Fig. 2. This result indicates that the previously determined uncertainties in those observables had been somewhat underestimated, as it should be obvious by the crude assumptions concerning the strange distributions, Eq. 1, introduced in NNPDF1.0.

We can further study the features of the determined strange PDFs by computing their moments. As done for example in [11], the magnitude of the strange sea can be characterized by the following ratio of second moments:

$$K_S(Q^2) \equiv \frac{\int_0^1 dx\; x\; s_+\left(x,Q^2\right)}{\int_0^1 dx\; x\left(\bar{u}\left(x,Q^2\right)+\bar{d}\left(x,Q^2\right)\right)} = -0.1 \pm 1.7\;, \quad Q^2 = 20\;{\rm GeV}^2\;, \qquad (2)$$

consistent within errors with the value $C_S = 0.5$ used in Eq. 1. On the other hand, the strange asymmetry can be characterized by the second moment of the s_- distribution, which turns out to

be:

$$\langle x \rangle_{s_-} \equiv \int_0^1 dx\, x s_- \left(x, Q_0^2\right) = -0.001 \pm 0.04\,, \tag{3}$$

that is, consistent with zero within uncertainties. This quantity has important physical implications, for example related the determination of the Weinberg angle and the NuteV anomaly [12]. Both results for the strange PDF moments, Eqns. 2 and 3, further confirm the implicit NNPDF1.0 assumption that, in the absence of further experimental data, a PDF analysis without independent parametrizations for s_+ and s_- can perfectly describe all available inclusive DIS measurements.

Our results for the moments of the strange PDFs can be compared with related studies of the strange content of the nucleon (see for example [11] and references therein). We observe that our results are compatible with previous determinations of these moments, albeit with large uncertainties. These indicate that a quantitative determination of the strange and anti-strange distributions (and the associated moments) requires a dedicated study which includes experimental data directly sensitive to the strange PDFs. The obvious example is dimuon production from neutrino DIS [7], which is provided in a form in which it can be consistently incorporated into a NLO PDF analysis.

Outlook The NNPDF1.0 DIS analysis is the first parton set within the NNPDF framework and is available through the LHAPDF library. The updated NNPDF1.1 analysis includes two main improvements: independent parametrizations for the strange PDFs and a randomization of the preprocessing.

Acknowledgments This work has been partially supported by the grant ANR-05-JCJC-0046-01 (France), an INFN fellowship, as well as by grants PRIN-2006 (Italy), and by the European network HEPTOOLS under contract MRTN-CT-2006-035505.

References

[1] A. D. Martin, R. G. Roberts, W. J. Stirling, and R. S. Thorne, Eur. Phys. J. **C28**, 455 (2003). hep-ph/0211080.

[2] P. M. Nadolsky *et al.*, Phys.Rev.D **78** 013004 (2008), arxiv:0802.0007.

[3] S. Forte, L. Garrido, J. I. Latorre, and A. Piccione, JHEP **05**, 062 (2002). hep-ph/0204232.

[4] NNPDF Collaboration, L. Del Debbio, S. Forte, J. I. Latorre, A. Piccione, and J. Rojo, JHEP **03**, 080 (2005). hep-ph/0501067.

[5] NNPDF Collaboration, L. Del Debbio, S. Forte, J. I. Latorre, A. Piccione, and J. Rojo, JHEP **03**, 039 (2007). hep-ph/0701127.

[6] NNPDF Collaboration, R. D. Ball *et al.* (2008). arxiv:0808.1231.

[7] D. A. Mason (2006). FERMILAB-THESIS-2006-01.

[8] M. Dittmar *et al.* (2005). hep-ph/0511119.

[9] G. P. Salam and J. Rojo (2008). arxiv:0804.3755.

[10] A. Vogt, Comput. Phys. Commun. **170**, 65 (2005). hep-ph/0408244.

[11] H. L. Lai *et al.*, JHEP **04**, 089 (2007). hep-ph/0702268.

[12] S. Davidson, S. Forte, P. Gambino, N. Rius, and A. Strumia, JHEP **02**, 037 (2002). hep-ph/0112302.

Chapter 3

Working Group Dense Systems

Convenors:

D. d'Enterria (CERN)
T. Csörgő (Budapest)
E.Iancu (Saclay)

High-energy heavy-ion collisions: from CGC to Glasma

Kazunori Itakura
KEK, 1-1 Oho, Tsukuba, Ibaraki, 305-0801, Japan
DOI: http://dx.doi.org/10.3204/DESY-PROC-2009-01/27

Abstract
I present an overview of recent theoretical developments towards "first principle" description of heavy-ion collisions at high energies.

1 Introduction

Relativistic heavy-ion collisions are multi-step phenomena which necessarily entail transition from high to low energy densities, or, equivalently from perturbative to non-perturbative kinematical regions (see Fig. 1). Thus, it is quite difficult to describe *all* the steps within the first-principle (i.e., QCD-based) calculations even though the collision energy is taken to be high enough. Nevertheless, we believe that at least the first two steps (the initial condition and the earliest stage well before thermalization) allow a firm QCD-based description because, as I will explain later, these two essentially occur around a large semi-hard momentum scale. From the viewpoint of high energy QCD, the initial condition and the earliest stage after the collision are respectively described by the Color Glass Condensate (CGC) [1] and the Glasma [2]. In this talk, I overview the recent developments towards understanding the dynamics of CGC and Glasma, and discuss a possible scenario of the heavy-ion collisions at high energy. In particular, unstable dynamics of the Glasma provides a novel mechanism for early thermalization.

2 Initial conditions : CGC

2.1 What is the CGC?

Consider one nucleus that is moving very fast in the z direction. When the scattering energy is quite high, what we measure is not a simple valence structure of each nucleon, but a state with a huge number of gluons that are emitted either directly from the valence partons or successively from (already emitted) gluons. Such a highly dense gluonic state is now called the CGC, and is indeed observed experimentally through the electron deep inelastic scattering off a proton. We

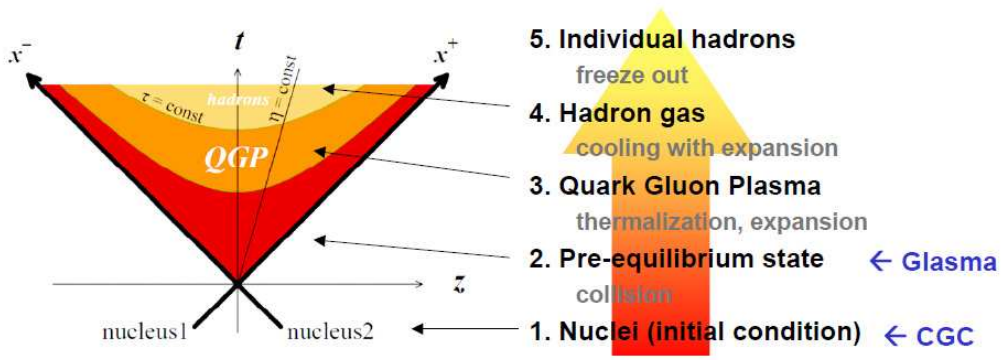


Fig. 1: Relativistic heavy-ion collision in the high energy limit

describe the CGC by separating the whole degrees of freedom into large and small x partons (x is the fraction of momentum carried by a parton). Large x partons are distributed on a Lorentz contracted nucleus and their motion is very slow compared to the time scale of the collision. Thus we treat them altogether as a *static* color source $\rho^a(x_\perp)$. We also assume that ρ^a can be taken as random reflecting the unpredictable configuration of partons at the moment of collision. Small x partons (mostly gluons) are then regarded as a coherent radiation field created by the color source (large x partons). Hence, we investigate the following stochastic Yang-Mills equation:

$$(D_\nu F^{\nu\mu})^a = \delta^{\mu+}\rho^a(x_\perp)\,. \tag{1}$$

We further introduce a weight function $W[\rho]$ (that is however a priori unknown) to control the randomness of the source $\rho^a(x_\perp)$. These are the basic strategies of CGC (see Ref. [1] for details).

Most of gluons in CGC have relatively large transverse momentum called the saturation momentum, $Q_s \gg \Lambda_{\rm QCD}$ whose inverse corresponds to a typical transverse 'size' of gluons when they fill up the transverse disk and start to interact with each other. One can compute in QCD the energy (or x) and atomic mass number A dependences of Q_s as

$$Q_s^2(x,A) \propto A^{1/3}(1/x)^\lambda\,, \quad \lambda \simeq 0.3\,, \tag{2}$$

which is surprisingly consistent with the scale Q_s^2 determined from experimental data through the geometric scaling. Since $Q_s(x,A)$ grows with increasing energy ($x \sim \ln 1/s \to 0$), the weak-coupling treatment becomes better and better with increasing energy, where $\alpha_s(Q_s) \ll 1$.

Another important feature of CGC is that, as a result of the large number of gluons, it has a strong gauge field $A \sim Q_s/g$ and thus strong color electric and magnetic fields $E, B \sim Q_s^2/g$. This is the region where we cannot ignore the nonlinear terms in the interaction. Therefore, CGC is a weakly-coupled many body system of gluons which shows coherent and nonlinear behavior.

2.2 CGC as the initial condition of heavy-ion collision

Let us now consider the collision of two nuclei in the center of mass frame where both nuclei can be equally treated as CGCs [3] (see Fig. 1). In this case, the right-hand-side in eq. (1) is replaced by $J^\mu = \delta^{\mu+}\delta(x^-)\rho_1(x_\perp) + \delta^{\mu-}\delta(x^+)\rho_2(x_\perp)$ with ρ_1 (ρ_2) being a color source of the right (left) moving nucleus 1 (2). Before the collision, classical gauge fields belonging to each nucleus are created by these color sources. What is truly nontrivial occurs in the forward light cone ($x^\pm > 0$), where we expect real gluon emissions and non-equilibrium transition towards QGP. We describe the very early stage of time evolution by solving *source free* Yang-Mills equations in the forward light cone, with the initial condition specified by the CGC fields of each nucleus.

Note also that the created matter which locates in between two (passed) nuclei will expand in the longitudinal direction almost at the speed of light, and we expect that it is a good approximation to describe the solution to the Yang-Mills equation by a boost invariant field. Namely, we consider the solution in the following form:

$$A^\pm = \pm x^\pm \alpha(\tau, x_\perp), \quad A^i = \alpha_3^i(\tau, x_\perp)\,, \tag{3}$$

where $\tau = \sqrt{2x^+x^-} > 0$ is the proper time. Indeed, this expression gives a solution independent of *rapidity* $\eta = \frac{1}{2}\ln(x^+/x^-)$ which can be easily seen if one defines vector fields in the (τ,η)

coordinates: $A_\eta = x^+A^- - x^-A^+ = -\tau^2\alpha(\tau, x_\perp)$. The initial condition for the fields α and α_3^i is specified at $\tau = 0+$ by using the CGC fields of each nucleus, α_1 and α_2:

$$\alpha|_{\tau=0} = \frac{ig}{2}[\alpha_1^i, \alpha_2^i]\,, \quad \alpha_3^i|_{\tau=0} = \alpha_1^i + \alpha_2^i\,, \tag{4}$$

and for the time derivatives

$$\partial_\tau\alpha|_{\tau=0} = \partial_\tau\alpha_3^i|_{\tau=0} = 0. \tag{5}$$

Obviously, *the initial condition is completely determined by the CGC fields of each nucleus* which depend only on transverse coordinates, $\alpha_{1,2}^i(x_\perp)$.

3 Pre-equilibrium stages : Glasma

Unlike the CGC, the gluonic matter created after the collision shows strong time dependence of the field as a result of rapid expansion in the longitudinal direction (recall that the CGC is static, i.e., x^+-independent). Thus, to identify such a unique nature of the created matter, we now use a new name "Glasma" meaning the transitional state between 'glass' and 'plasma' [2]. Glasma is a rapidly expanding and interacting gluon field. Immediately after the collision, it will still remember the properties of CGC, and most of the gluons will have transverse momenta of the order of Q_s. Namely, the Glasma can still be treated as a weak coupling system.

3.1 Stable dynamics : boost-invariant Glasma

The first attempts towards understanding nonlinear dynamics of the Glasma were numerically done in real-time simulations of classical Yang-Mills fields on the lattice. Most of the simulations were performed in the boost-invariant case. Obtained physical quantities such as the gluon transverse momentum spectra and the energy density were found to be reasonable enough. More recently, such numerical results have driven people to think of the analytic aspects of the Glasma. The most important recognition is the emergence of a *flux tube structure* (Fig. 2, left). Before the collision, each CGC has purely transverse $\mathbf{E}$ and $\mathbf{B}$ that are orthogonal to each other $\mathbf{E}\cdot\mathbf{B} = E_\perp \cdot B_\perp = 0$. However, just after the collision, the field strength instantaneously becomes purely *longitudinal*. Indeed, the z-components at $\tau = 0+$ are explicitly given by

$$E^z|_{\tau=0^+} = -ig[\alpha_1^i, \alpha_2^i]\,, \qquad B^z|_{\tau=0^+} = ig\epsilon_{ij}[\alpha_1^i, \alpha_2^j]\,, \tag{6}$$

with $\alpha_{1,2}$ being the CGC fields, while all the transverse components are vanishing. Such longitudinally extended fields in between two receding nuclei remind us of the Lund string model, but

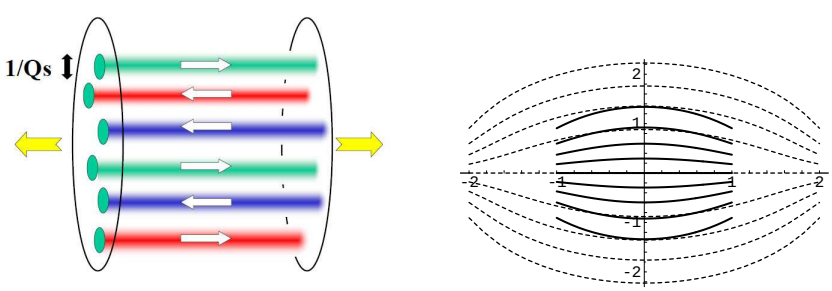


Fig. 2: Flux tube structure of the Glasma (left) and how the flux tube expands in time (right)

there are two significant differences. First, reflecting the CGC structures of the colliding nuclei, transverse coherence length of the flux tubes should be of order $1/Q_s$, instead of $1/\Lambda_{\rm QCD}$ as in the Lund model. This is so because the Glasma flux tube is a perturbative object while the Lund model simulates nonperturbative dynamics of string breaking. Second, the Glasma flux tube can have a magnetic field in it while the Lund model treats only electric flux tubes. In fact, even a purely magnetic flux tube is possible if one takes the same color structure for the same spatial components α_1^i and α_2^i ($i = x, y$) but different for different components.

Dynamics of an isolated flux tube can be reasonably understood within Abelian approximation [4]. If one looks deeply inside of the flux tube, the field strengths may be large, but are regular and homogeneous. Thus one can gauge-transform the field so that it is directed to the third color component. On the other hand, if one looks well outside of the flux tube, the field is weak enough, and one can ignore nonlinear effects. Hence, if the field profile is not singular in the tube and decays rapidly outside the tube, Abelian approximation is expected to be reasonable enough. In this approximation, one can easily solve the Yang-Mills equation even in expanding geometry, and can compute the time dependence of *E* and *B* for a simple profile such as a Gaussian. The right panel of Fig. 2 shows how a single flux tube evolves in the actual time t (not in τ). Since the Glasma flux tube is essentially 'perturbative', it expands outwards and the strength in the tube decays rapidly in time (in contrast, a nonperturbative flux tube does not expand in the transverse direction and the strength inside the tube does not change). Lastly, we note that the τ dependence of each component of the field strength computed in this simple picture is remarkably consistent with the numerical result reported in Ref. [2].

3.2 Unstable dynamics : boost-noninvariant Glasma

It should be noticed that the boost-invariant Glasma cannot say anything about thermalization because boost invariance means eternal absence of nontrivial p_z dependence. Therefore, even isotropization (a necessary condition for thermalization) never occurs with boost invariant solutions. Of course this is a serious problem in the CGC-glasma description of the heavy-ion collision, and people have been investigating this both numerically [5] and analytically [4, 6, 7]. Below, I explain one of the recent findings of analytic approaches that *the rapidity-dependent fluctuation undergoes Nielsen-Olesen instability and can grow exponentially* [4].

We perform a stability analysis of the system against rapidity-dependent perturbations $a_{i,\eta}$:

$$A_i = \mathcal{A}_i(\tau, x_\perp) + a_i(\tau, \eta, x_\perp)\,, \quad A_\eta = \mathcal{A}_\eta(\tau, x_\perp) + a_\eta(\tau, \eta, x_\perp)\,, \tag{7}$$

where $\mathcal{A}_i$ and $\mathcal{A}_\eta$ are boost-invariant background fields given in eq. (3). Coupling between $\mathcal{A}_{i,\eta}$ and $a_{i,\eta}$ is present due to the nonlinear interaction in the non-Abelian gauge theory. For simplicity, we replace the background fields by τ-independent and spatially constant electric/magnetic fields, and consider the SU(2) group.[1] The first simplification was done because we expect that the time scale of instability is much shorter than that of the background field, and because we consider the region deep inside of the flux tube. In Ref. [4], the cases with either electric or magnetic field were explicitly shown, but one can similarly discuss the case where both are present [9].

[1] Generalization to SU(3) should be straightforward [9]. We have two constant background fields (directed to the 3rd and 8th color components).

When we have both electric and magnetic fields, the linearized equation for the fluctuation[2] $\tilde{a}_+^{(\pm)}$ which is the Fourier component having the third color charge $(\pm)$ and positive spin $+$ is given by [9]

$$\frac{1}{\tau}\partial_\tau(\tau\partial_\tau\tilde{a}_+^{(\pm)}) + \left\{\frac{1}{\tau^2}\left(\nu \pm \frac{gE}{2}\tau\right)^2 + (2n+|m|+1\mp m\pm 2)gB\right\}\tilde{a}_+^{(\pm)} = 0\,, \qquad (8)$$

where m and ν, respectively, are the orbital angular momentum and the momentum conjugate to the rapidity (a similar equation holds for negative spin $-$). Note that the term $\pm 2gB$ originates from the anomalous magnetic moment.

When we have only the electric field ($E \neq 0,\ B = 0$), the situation is similar to the Schwinger mechanism. Massless charged fluctuations are infinitely accelerated, but there is no amplification of the field (no instability). On the other hand, when we have only the magnetic field ($E = 0,\ B \neq 0$), the fluctuation forms Landau levels, and the lowest level ($n = 0$) becomes unstable. This is the *Nielsen-Olesen instability* which is known for non-expanding Yang-Mills systems [8]. Indeed, the explicit form of the solution is given by the modified Bessel function $I_{i\nu}(\sqrt{gB}\tau)$, which asymptotically shows divergent behavior:

$$I_{i\nu}(\sqrt{gB}\tau) \sim \mathrm{e}^{\sqrt{gB}\tau}\Big/\sqrt{2\pi\sqrt{gB}\tau}.$$

Note that the magnetic field given by the CGC can be strong $\sqrt{gB} \sim Q_s$. Therefore, we conclude that the mode with ν grows exponentially with the time scale given by $\tau_{\mathrm{grow}} = 1/Q_s$.

In relation to the early thermalization problem in RHIC, extensive investigation is performed for the plasma instability scenario. However, being formulated in a kinetic equation, it is applicable only after $\tau \sim 1/Q_s$ and thus cannot say anything about the very early stage of heavy-ion collisions $\tau < 1/Q_s$. This is the place where the *Glasma* instabilities play a unique important role. As we discussed, the characteristic time scale of the Glasma instabilities is $1/Q_s$. This implies that the system begins to show unstable behavior well before the kinetic description can be applicable.

References

[1] For a review, see E. Iancu and R. Venugopalan, "*The color glass condensate and high energy scattering in QCD*," arXiv:hep-ph/0303204.

[2] T. Lappi and L. McLerran, Nucl. Phys. A772 (2006) 200.

[3] A. Kovner, L. McLerran and H. Weigert, Phys. Rev. D **52** (1995) 3809; *ibid.* 6231.

[4] H. Fujii and K. Itakura, Nucl. Phys. A809 (2008) 88.

[5] P. Romatschke and R. Venugopalan, Phys. Rev. Lett. **96** (2006) 062302; Phys. Rev. D **74** (2006) 045011.

[6] S. G. Matinyan, B. Muller and D. H. Rischke, Phys. Rev. C **57** (1998) 1927, K. Fukushima, Phys. Rev. C **76** (2007) 021902 [Erratum-ibid. C **77** (2007) 029901].

[7] A. Iwazaki, "*Decay of Color Gauge Fields in Heavy Ion Collisions and Nielsen-Olesen Instability*," arXiv:0803.0188 [hep-ph].

[8] S. J. Chang and N. Weiss, Phys. Rev. **D20** (1979) 869, N. K. Nielsen and P. Olesen, Nucl. Phys. **B144** (1978) 376.

[9] H. Fujii, K. Itakura, and A. Iwazaki, in preparation.

[2] Here, we do not discuss the fluctuation a_η because it is stable.

Particle production and saturation at RHIC and LHC

Cyrille Marquet
Institut de Physique Théorique, CEA/Saclay, 91191 Gif-sur-Yvette cedex, France
Department of Physics, Columbia University, New York, NY 10027, USA
E-mail: cyrille@phys.columbia.edu

DOI: http://dx.doi.org/10.3204/DESY-PROC-2009-01/28

Abstract

The Color Glass Condensate picture of the nuclear wave function at small-x successfully predicted the suppressed production of high-p_T particles at forward rapidities in deuteron-gold collisions at RHIC. This triggered more efforts which resulted in theoretical improvements and predictions for different observables which will provide further phenomenological tests. I review recent theoretical developments and discuss the resulting predictions.

1 Saturation and the Color Glass Condensate

When probing small distances inside a hadron or nucleus with a hard process, one resolves their partonic constituents. Increasing the energy of the scattering process at a fixed momentum transfer allows to probe lower-energy partons, with smaller energy fraction x. As the parton densities in the hadronic/nuclear wavefunction grow with decreasing x, they eventually become so large that a non-linear (yet weakly-coupled) regime is reached, called saturation, where partons do not interact with the probe independently anymore, but rather behave coherently.

The Color Glass Condensate (CGC) is an effective theory of QCD [1] which aims at describing this part of the wave function. Rather than using a standard Fock-state decomposition, it is more efficient to describe it with collective degrees of freedom, more adapted to account for the collective behavior of the small-x gluons. The CGC approach uses classical color fields:

$$|h\rangle = |qqq\rangle + |qqqg\rangle + \cdots + |qqqg\ldots ggg\rangle + \ldots \quad \Rightarrow \quad |h\rangle = \int D\mathcal{A}\, \Phi_{x_A}[\mathcal{A}]\, |\mathcal{A}\rangle\,. \quad (1)$$

The long-lived, large-x partons are represented by a strong color source $\rho \sim 1/g_S$ which is static during the lifetime of the short-lived small-x gluons, whose dynamics is described by the color field $\mathcal{A} \sim 1/g_S$. The arbitrary separation between the field and the source is denoted x_A.

The CGC wavefunction $\Phi_{x_A}[\mathcal{A}]$ is the fundamental object of this picture, it is mainly a non-perturbative quantity, but the x_A evolution can be computed perturbatively. Requiring that observables are independent of the choice of x_A, a functional renormalization group equation can be derived. In the leading-logarithmic approximation which resums powers of $\alpha_S \ln(1/x_A)$, the JIMWLK equation describes the evolution of $|\Phi_{x_A}[\mathcal{A}]|^2$ with x_A. The information contained in the wavefunction, on gluon number and gluon correlations, can be expressed in terms of n-point correlators, probed in scattering processes. These correlators consist of Wilson lines averaged with the CGC wavefunction, and resum powers of $g_S\mathcal{A}$.

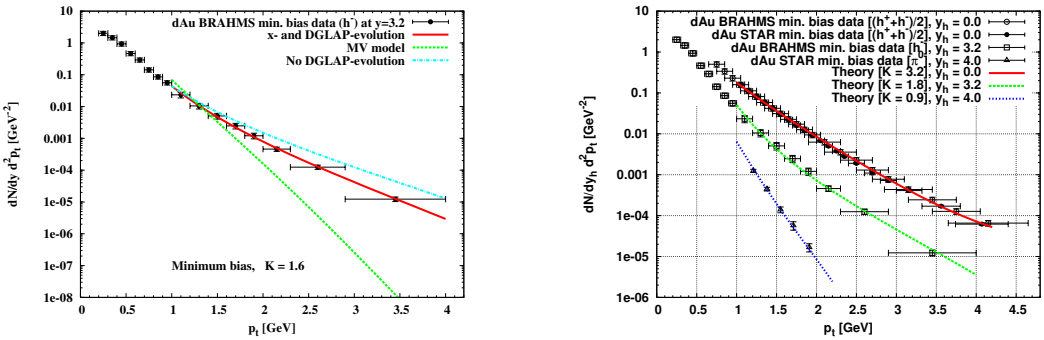


Fig. 1: Forward particle production in d+Au collisions at RHIC. The left plot shows the importance of including both the large-x DGLAP evolution of the dilute deuteron and the small-x CGC evolution of the dense nucleus. The right plots shows the excellent description of the spectra shapes, and the K factors needed to obtain the normalization.

The JIMWLK equation reduces to a hierarchy of equations for the correlators. Most of the phenomenology uses a mean-field approximation which significantly simplifies the high-energy QCD evolution: it reduces the hierarchy to a single closed non-linear equation for the two-point function $\langle S_{\mathbf{xy}}\rangle_{x_A} = 1 - \langle T_{\mathbf{xy}}\rangle_{x_A}$, the Balitsky-Kovchegov (BK) equation [2, 3]. It reads

$$\frac{d\langle S_{\mathbf{xy}}\rangle_x}{d\ln(1/x)} = \frac{\bar{\alpha}}{2\pi}\int d^2\mathbf{z}\, M_{\mathbf{xyz}}\Big(\langle S_{\mathbf{xz}}\rangle_x\langle S_{\mathbf{zy}}\rangle_x - \langle S_{\mathbf{xy}}\rangle_x\Big)\,, \quad M_{\mathbf{xyz}} = \frac{(\mathbf{x}-\mathbf{y})^2}{(\mathbf{x}-\mathbf{z})^2(\mathbf{z}-\mathbf{y})^2}\,, \qquad (2)$$

with $\bar{\alpha} = \alpha_S N_c/\pi$. All the correlators can then be expressed in terms of the solution of this equation. Finally, the Fourier transform of the dipole correlator $\int d^2\mathbf{x}d^2\mathbf{y}\, e^{i\mathbf{k}.(\mathbf{x}-\mathbf{y})}\langle T_{\mathbf{xy}}\rangle_{x_A}/(\mathbf{x}-\mathbf{y})^2$ is an (all-twist) unintegrated gluon density. It determines forward particle production [4], while more exclusive final states involve more complicated correlators. Solving eq. (2) reveals the existence of an intrisic momentum scale in the nuclear wave function: the saturation scale $Q_s(x)$ which characterizes the transition from the dilute regime $k > Qs$ to saturation regime $k < Q_s$.

One of the most important progress is the recent calculation of the next-to-leading evolution equation [5, 6]. Concerning how the running coupling should be included, two schemes have been proposed by Balitsky (B) and Kovchegov and Weigert (KW). The following substitution should be done in formula (2), with $R^2(\mathbf{x},\mathbf{y},\mathbf{z})$ given in [6]:

$$\frac{\bar{\alpha}}{2\pi}M_{\mathbf{xyz}} \overset{KW}{\to} \frac{N_c}{2\pi^2}\left[\frac{\alpha_s((\mathbf{x}-\mathbf{z})^2)}{(\mathbf{x}-\mathbf{z})^2} + 2\frac{\alpha_s((\mathbf{x}-\mathbf{z})^2)\alpha_s((\mathbf{z}-\mathbf{y})^2)}{\alpha_s(R^2(\mathbf{x},\mathbf{y},\mathbf{z}))}\frac{(\mathbf{x}-\mathbf{z})\cdot(\mathbf{z}-\mathbf{y})}{(\mathbf{x}-\mathbf{z})^2(\mathbf{z}-\mathbf{y})^2} + \frac{\alpha_s((\mathbf{z}-\mathbf{y})^2)}{(\mathbf{z}-\mathbf{y})^2}\right] \qquad (3)$$

$$\downarrow B$$

$$\frac{N_c\,\alpha_s((\mathbf{x}-\mathbf{y})^2)}{2\pi^2}\left[M_{\mathbf{xyz}} + \frac{1}{(\mathbf{x}-\mathbf{z})^2}\left(\frac{\alpha_s((\mathbf{x}-\mathbf{z})^2)}{\alpha_s((\mathbf{z}-\mathbf{y})^2)}-1\right) + \frac{1}{(\mathbf{z}-\mathbf{y})^2}\left(\frac{\alpha_s((\mathbf{z}-\mathbf{y})^2)}{\alpha_s((\mathbf{x}-\mathbf{z})^2)}-1\right)\right]\,. \qquad (4)$$

At next-to-leading order, there remains a discrepancy between the linear part of the BK equation and the BFKL equation. Running coupling corrections to particle production have also been investigated [7]. Another important recent theoretical development is the inclusion of Pomeron loops in the evolution [8], and the derivation of potential consequences at very high energies [9,10]. Concerning phenomenology at present colliders, there was however no significant impact.

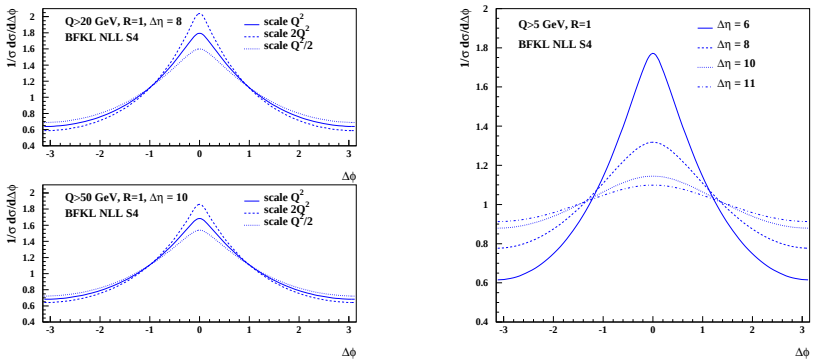


Fig. 2: Angular correlations of Mueller-Navelet jets in the NLL-BFKL framework. Left plots: for standard Tevatron (top) and LHC (bottom) kinematics, the renormalization scale uncertainty is indicated (with $Q^2 = k_1 k_2$). Right plot: predictions for CDF (miniplugs) kinematics. The $\Delta\Phi$ distribution is peaked around $\Delta\Phi = 0$, which is indicative of jet emissions occuring back-to-back, and the $\Delta\Phi$ distribution flattens with increasing $\Delta\eta$ or with R deviating from 1.

2 Forward particle production in pA collisions

Forward particle production in pA collisions allows to investigate the non linear QCD dynamics of high-energy nuclei with a probe well understood in QCD. Indeed, while such processes are probing small-momentum partons in the nuclear wavefunction, only high-momentum partons of the proton contribute to the scattering ($\sqrt{s}x_p = ke^y$ and $\sqrt{s}x_A = ke^{-y}$). The dilute hadron contributes via standard parton distribution functions while the CGC is described by its unintegrated gluon distribution. It was not obvious that the CGC picture (1), which requires small values of x_A, would be relevant at present energies. However, it has been the case for many observables in the context of HERA [11] and RHIC [12]. One of the most acclaimed successes is the prediction that the yield of high-p_T particles at forward rapidities in d+Au collisions is suppressed compared to A pp collisions, and should decrease when increasing the rapidity.

In Fig.1 the $dAu \to hX$ p_T spectra computed in the CGC approach [13] is compared to RHIC data, and the description of the slope is impressive. The need of K factors to describe the normalization could be expected since this is a leading-order based calculation. Improving the calculation with the next-leading evolution has yet to be done. While the suppression was predicted in the CGC approach, other postdictions later offered alternative descriptions. The idea is that the value of x probed in the deuteron is so high that large-x effects could be responsible for the suppression [14]. This would not happen in pA collisions at the LHC, with a smaller x_p.

While the CGC framework was quite successful in describing single inclusive particle production at forward rapidities, the focus should now shift towards more exclusive observables like two-particle production $pA \to h_1 h_2 X$. In particular the correlations in azimuthal angle between the produced hadrons should be suppressed compared to pp collisions [15]. By contrast with single particle production, in two-particle production the CGC cannot be described only by its unintegrated gluon distribution, the so-called k_T-factorization framework is not applicable. This means that more tests could be done, probing the CGC structure deeper. The second d+Au run at RHIC gives the opportunity to carry out such measurements.

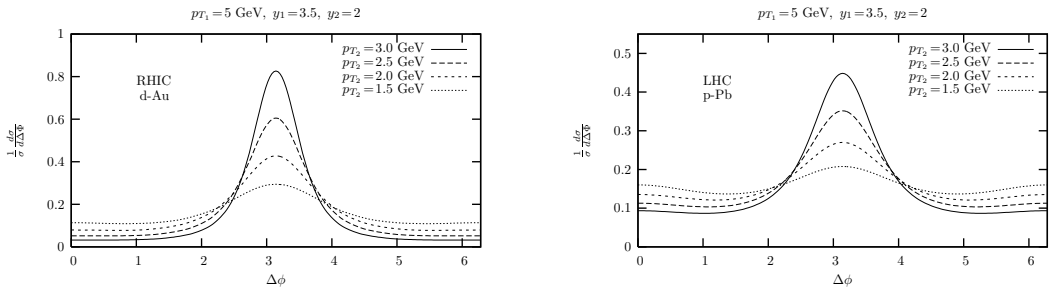


Fig. 3: Two-particle production at forward rapidities in pA collisions. The $\Delta\phi$ spectrum is displayed at RHIC (left) and LHC (right) energies. When varying p_{T_2} at fixed y_2, the correlation in azimuthal angle is suppressed as p_{T_2} gets closer to the saturation scale. At the LHC, smaller values of x_A are probed, and the azimuthal angle correlation is more suppressed as indicated by the vertical axis. The peak is also less pronounced.

3 Selected predictions for the LHC

Mueller-Navelet jets [16] in hadron-hadron scattering are two jets produced in each of the forward directions. In the high-energy regime, in which the jets are separated by a large rapidity interval, this process is sensitive to the small-x QCD evolution. An interesting observable is the azimuthal decorrelation of the jets as a function of their rapidity separation $\Delta\eta = y_1 - y_2$ and of the ratio of their transverse momenta $R = k_2/k_1$ [17]. Predictions are shown in Fig.2, for Tevatron and LHC kinematics, where $\Delta\Phi = \pi - \phi_1 + \phi_2$ is the relative azimuthal angle between the two jets. The curves are obtained in the linear regime, using next-to-leading logarithmic (NLL) BFKL evolution. At higher energies, saturation effects will also be relevant [18].

Coming back to forward particle production in pA collisions, predictions for the process $pA \to h_1 h_2 X$ are shown in Fig.3, for RHIC and the LHC [19]. k_1, k_2 and y_1, y_2 are the transverse momenta and rapidities of the final state hadrons, and the azimuthal angle spectra are displayed. It is obtained that the perturbative back-to-back peak of the azimuthal angle distribution (which is recovered for very large momenta) is reduced by initial state saturation effects. As the momenta decrease closer to the saturation scale ($Q_s \simeq 2$ GeV), the angular distribution broadens. But at RHIC energies, saturation does not lead to a complete disappearance of the back-to-back peak.

Finally, predictions for the total charged-particle multiplicity in AA collisions at the LHC are shown in Fig.4. Two approaches are compared: in the first, k_T-factorization is assumed but the evolution of the unintegrated gluon densities is accurately obtained from the next-leading BK equation [20]; in the second, the x evolution is only parametrized but multiple scatterings are correctly taken into account by solving classical Yang-Mills equation [21]. While full next-leading treatment of both multiple scatterings and small-x evolution is desirable, the numbers obtained are similar, which indicates that the uncertainties in both approaches are under control.

References

[1] E. Iancu and R. Venugopalan (2003). hep-ph/0303204.

[2] I. Balitsky, Nucl. Phys. **B463**, 99 (1996). hep-ph/9509348.

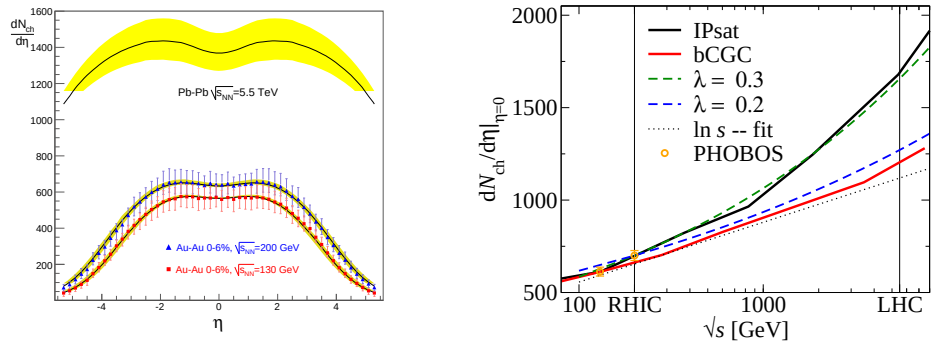


Fig. 4: The charged-particle multiplicity in AA collisions at RHIC and the LHC. In both approaches a few parameters are fixed to reproduce RHIC data, such as the initial value of Q_s. Then the small-x evolution determines the multilicity at the LHC. The predictions are similar, around 1400 charged particles at mid rapidity for central collisions.

[3] Y. V. Kovchegov, Phys. Rev. **D60**, 034008 (1999). hep-ph/9901281;
Y. V. Kovchegov, Phys. Rev. **D61**, 074018 (2000). hep-ph/9905214.

[4] C. Marquet, Nucl. Phys. **B705**, 319 (2005). hep-ph/0409023.

[5] I. Balitsky, Phys. Rev. **D75**, 014001 (2007). hep-ph/0609105;
I. Balitsky and G. A. Chirilli, Phys. Rev. **D77**, 014019 (2008). 0710.4330.

[6] Y. V. Kovchegov and H. Weigert, Nucl. Phys. **A784**, 188 (2007). hep-ph/0609090.

[7] Y. V. Kovchegov and H. Weigert, Nucl. Phys. **A807**, 158 (2008). 0712.3732.

[8] D. N. Triantafyllopoulos, Acta Phys. Polon. **B36**, 3593 (2005). hep-ph/0511226;
G. Soyez, Acta Phys. Polon. **B37**, 3477 (2006). hep-ph/0610436.

[9] Y. Hatta, E. Iancu, C. Marquet, G. Soyez, and D. N. Triantafyllopoulos, Nucl. Phys. **A773**, 95 (2006). hep-ph/0601150.

[10] E. Iancu, C. Marquet, and G. Soyez, Nucl. Phys. **A780**, 52 (2006). hep-ph/0605174.

[11] C. Marquet, AIP Conf. Proc. **828**, 157 (2006). hep-ph/0510176.

[12] J. Jalilian-Marian and Y. V. Kovchegov, Prog. Part. Nucl. Phys. **56**, 104 (2006). hep-ph/0505052.

[13] A. Dumitru, A. Hayashigaki, and J. Jalilian-Marian, Nucl. Phys. **A765**, 464 (2006). hep-ph/0506308;
A. Dumitru, A. Hayashigaki, and J. Jalilian-Marian, Nucl. Phys. **A770**, 57 (2006). hep-ph/0512129.

[14] B. Z. Kopeliovich, J. Nemchik, I. K. Potashnikova, M. B. Johnson, and I. Schmidt, Phys. Rev. **C72**, 054606 (2005). hep-ph/0501260;
L. Frankfurt and M. Strikman, Phys. Lett. **B645**, 412 (2007).

[15] D. Kharzeev, E. Levin, and L. McLerran, Nucl. Phys. **A748**, 627 (2005). hep-ph/0403271.

[16] A. H. Mueller and H. Navelet, Nucl. Phys. **B282**, 727 (1987).

[17] A. Sabio Vera, Nucl. Phys. **B746**, 1 (2006). hep-ph/0602250;
A. Sabio Vera and F. Schwennsen, Nucl. Phys. **B776**, 170 (2007). hep-ph/0702158;
C. Marquet and C. Royon (2007). 0704.3409.

[18] C. Marquet and R. B. Peschanski, Phys. Lett. **B587**, 201 (2004). hep-ph/0312261;
C. Marquet, R. B. Peschanski, and C. Royon, Phys. Lett. **B599**, 236 (2004). hep-ph/0407011;
C. Marquet and C. Royon, Nucl. Phys. **B739**, 131 (2006). hep-ph/0510266;
E. Iancu, M. S. Kugeratski, and D. N. Triantafyllopoulos, Nucl. Phys. **A808**, 95 (2008). 0802.0343.

[19] C. Marquet, Nucl. Phys. **A796**, 41 (2007). 0708.0231.

[20] J. L. Albacete, Phys. Rev. Lett. **99**, 262301 (2007). 0707.2545.

[21] T. Lappi, J. Phys. **G35**, 104052 (2008). 0804.2338.

Introducing Saturation Effects into Event Generators

Emil Avsar
Institut de Physique Théorique de Saclay
DOI: http://dx.doi.org/10.3204/DESY-PROC-2009-01/50

Abstract
We present the results of a numerical study on applying an absorptive boundary on the BFKL equation mimicking the full BK equation solution for $k_\perp$ above the saturation momentum. It is explained how this strategy can be used to introduce saturation effects into event generators based on the linear small x dynamics.

During the past years there has been much progress in our understanding of the high energy, or small-x, region of QCD. The QCD analysis of the dynamics in this region suggest that one reaches a new state of matter referred to as the Color Glass Condensate (CGC) [1] in which the energy, or x, evolution of the relevant physical processes is highly nonlinear. Although theoretically well motivated, it is not really clear that the physics of the CGC has been observed at present collider experiments. There are a few hints at saturation at HERA, but the problem is that one has been looking for saturation effects mostly in inclusive observables such as F_2, for which the expected signatures of saturation, such as geometric scaling, can be mimicked by the linear evolution as well. Besides, analytical estimates often involve many approximations and large uncertainties. It should be emphasized that the question of whether or not saturation effects are already important at colliders is not an academic one. If in fact the nonlinear physics is important then the extraction of our PDFs, based on the linear collinear factorization, is wrong and since the PDFs will be used for almost all the physics analyses in LHC, the problem could potentially be very severe. It is therefore very important to estimate the size of the expected nonlinear corrections.

Although the theory of the nonlinear dynamics is generally understood, detailed calculations are often very difficult. The small-x evolution of a hadron wavefunction in the CGC formalism is governed by the JIMWLK equation which can be rewritten as a Langevin equation which generates an infinite hierarchy of evolution equations for the scattering amplitudes T^k. Having a Langevin formulation, the JIMWLK evolution equation is amenable for a numerical study. Although a numerical simulation of the JIMWLK equation exists, one is still quite far from building an event generator from which properties of exclusive final states as observed in experiments could be studied. At the present we therefore have to conclude that we are far from building an event generator based on the full nonlinear dynamics[1]

In this talk we describe how one can introduce saturation effects into event generators based on the linear evolution without knowing the full details of the nonlinear evolution. Although the analytic ideas apply naturally to the BFKL and the nonlinear BK [5, 6] equations, we shall ultimately be interested in modifying the CASCADE [7] event generator which is based

[1] A possibility could be to use the much simpler dipole model. Investigations on this possibility have been reported in a series of papers [2–4], but there is yet no final result.

on the CCFM [8] evolution equation. We will study the effects of saturation for $k_\perp$ above the saturation momentum $Q_s(x)$, where we can rely on $k_\perp$-factorization on which both the CCFM and BFKL evolutions are based. At first sight it might sound strange to look for the signatures of saturation above Q_s, since Q_s is supposed to mark the border between the nonlinear and the linear evolutions. It is, however, not true that saturation effects abruptly set in below Q_s while being negligible above it. The nonlinear evolution which certainly dominates the physics below Q_s can still modify what happens at $k_\perp$ above[2] Q_s, where one would naively think that the linear evolution would be valid.

In discussing saturation, it is convenient to work with the unintegrated gluon density $\phi(x, k_\perp)$, which in light-cone gauge can be defined as the expectation value of the Fock space number operator $\langle a_k^\dagger a_k \rangle$. This gluon density is related to the scattering amplitude $T(x, r_\perp)$ via the relation

$$T(x, r_\perp) = r_\perp^2 \int \frac{d^2k_\perp}{(2\pi)^2} e^{-i\mathbf{k}_\perp \cdot \mathbf{r}_\perp} \phi(x, k_\perp). \tag{1}$$

Although the unintegrated gluon density which enters the $k_\perp$-factorization is a different quantity, the BFKL equation is identical in both definitions. For BK, the nonlinear term will look different whether one uses ϕ or the $k_\perp$-factorizable gluon density. However, our analysis will not give a correct treatment of the $k_\perp \leq Q_s(x)$ region anyhow, so it does therefore not matter which quantity we choose. As the nonlinear term written for ϕ (see below) is much simpler, we shall use ϕ as our unintegrated gluon density in what follows, which thus is not the $k_\perp$-factorizable density.

The BK equation is written in terms of ϕ as

$$\partial_Y \phi(Y, k) = \int \frac{dk'^2}{k'^2} \bar{\alpha}_s(max(k^2, k'^2)) \left\{ \frac{k'^2\phi(Y, k') - k^2\phi(Y, k)}{|k^2 - k'^2|} + \frac{k^2\phi(Y, k)}{\sqrt{4k'^4 + k^4}} \right\} - \\ -\bar{\alpha}_s(k^2)\phi^2(Y, k) \tag{2}$$

where as usual $Y \equiv \ln 1/x$ and $\bar{\alpha}_s \equiv \frac{N_c\alpha_s}{\pi}$. Here we have introduced a running α_s which should be seen as a phenomenological modification of the leading order equation for which α_s is fixed. The linear part of this equation is the BFKL equation. What we shall do below is to solve the BFKL and BK equations numerically. We will also solve the BFKL equation in the presence of an absorptive boundary which mimics the full BK equation above Q_s. We now describe this procedure.

A few years ago it was suggested by Mueller and Triantafyllopoulos [9] that one could obtain the correct Y dependence of Q_s, and also the correct form for $T(Y, r)$, above Q_s (for r this means $r \leq Q_s^{-1}$) by simply studying the linear evolution in the presence of an absorptive boundary. The fact that the essential information of the nonlinear evolution can be obtained without knowing the details of it is suggested (for fixed α_s) by a correspondence between small-x QCD and statistical physics. However, one should also be aware that this formal correspondence is of limited relevance for phenomenology since the usual scales for Y and $k_\perp$ involved are

[2]How far up in $k_\perp$ the effects of saturation are visible for a given x is of course not entirely clear. The numerical analysis is therefore important.

typically much beyond what is studied at colliders. We shall discuss phenomenological issues more below. The idea of the absorptive boundary can be outlined as follows.

To control the approach towards the saturation region one can in BFKL follow the evolution along lines of constant amplitude[3] T. In particular when T is close to, but strictly below unity, the line of constant amplitude can be identifed with Q_s. A saddle point approximation then determines the anomalous dimension which determines the behaviour of T near the saturation boundary. However, even though one follows lines of constant amplitude with T strictly below unity, one has to be careful since the diffusive nature of the BFKL solution means that there may be "paths" contributing to the solution and which pass through the saturation region. For such paths the BFKL equation does not give the correct treatment. The idea is therefore to endow BFKL with an absorptive boundary such that all those paths are cut out from the solution. As one is throwing out some of the contributions to the BFKL saddle point solution, the definition of the lines of constant amplitude are also modified. It then turns out that Q_s behaves as (for fixed α_s)

$$\ln Q_s^2 = C + cY - \frac{3}{2\gamma_s}\ln Y \tag{3}$$

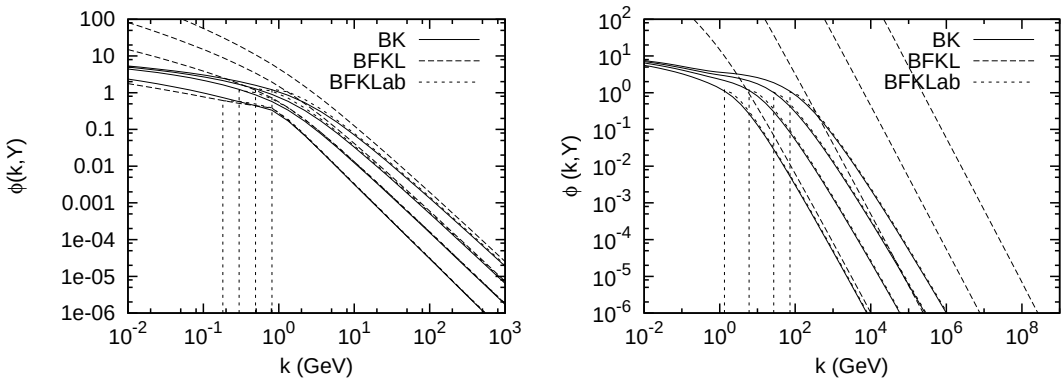
where C is some constant (depending on α_s) and $c \approx 4.9$ and $\gamma_s \approx 0.63$. If one had just studied the lines of constant amplitude for the original BFKL solution one would instead of the term $\frac{3}{2\gamma_s}\ln Y$ get $\frac{1}{2\gamma_s}\ln Y$. The difference between these two terms represents the modification due to the nonlinear physics.

More specifically the absorptive boundary is applied as follows. Pick first a line of constant amplitude $Q_c(Y)$ so that $T(Y, Q_c^{-1}(Y)) = const$ where the constant can be any number much less than unity (actually Q_c is chosen such that T becomes a constant *after* the boundary has been applied). Then the BFKL saddle point solution is forced to vanish at some point $\rho \equiv \ln 1/(\Lambda r)^2 = \rho_c - \Delta$ where $\rho_c \equiv \ln(Q_c/\Lambda)^2$. The form of the BFKL solution is such that T will increase from the point $\rho = \rho_c$ down to some $\rho = \rho_s$ after which it will decrease to zero at $\rho = \rho_c - \Delta$. The point of the maximum, ρ_s, can then be identified with the saturation momentum[4] . The parameter Δ can in turn be determined by requiring the consistency constraint that $T(Y, \rho_s) = b$, for some $b < 1$. This procedure gives Q_s as written above.

In the numerical simulation we shall proceed in the same way. Thus we define some critical value c, corresponding to $\phi(Y, k_c) = c$ such that ϕ is forced to vanish for all $k^2 \leq k_c^2 \cdot \exp(-\Delta)$. The value $\phi(Y, k) = 0$ is, however, not a fixed point for the BFKL evolution which is nonlocal in k as can be seen from (2), and we therefore do not allow points where ϕ has been set to zero to evolve again. One should notice that neither the analytical nor the numerical procedure with the absorptive boundary gives the correct treatment of the dynamics below Q_s. The numerical simulation is important for a detailed analysis, and especially for phenomenology as lower Y values, which are the ones important for phenomenology, are not completely controlled by the analytical treatment.

[3] In [9] the analysis was done in coordinate space for T. However, the corresponding analysis in momentum space for ϕ is basicly the same so in the end we shall apply the boundary for the linear part of equation (2).

[4] This is just a convention. Any line of constant amplitude will give a valid definition. It turns out that $\rho_s - \rho_c$ is just a constant, which appears as the constant C in (3). The overall normalization of Q_s cannot be determined from theory.



In figure 1 we show the solutions to BK, BFKL and BFKL with absorptive boundary condition (BFKLab) respectively. In the left plot we have the values $Y = 2, 4, 6$ and 8 respectively while in the right plot we have $Y = 10, 20, 30$ and 40. The results for BFKLab have been obtained for a specific set of values of the parameters Δ and c. Generally we see that we have to choose the critical value c to be around 0.1-0.5 to match the full BK solution. It turns out that larger critical values match more smoothly with equations whose nonlinear term are cubic, quartic and so on, as opposed to BK which has a quadratic nonlinear term.

We thus see that the BFKLab solution mimics the full BK solution very well, and not only for high values for Y, but also for small values where the analytic arguments are much more uncertain. A very important consequence of the saturation mechanism, which has been known for some time, is that the evolution with a running α_s becomes much more stable and sensible. Note that for the completely linear case the solution is very unstable and we see that at around $Y = 20$ the linear curve is nowhere close to the nonlinear one, even at very high $k_\perp$. Here we have regulated the singularity in the running α_s by replacing the argument k^2 with $k^2 + k_0^2$. For the BFKL solution we used $k_0^2 = 2$ GeV^2 while for BK and BFKLab we have $k_0^2 = 0.5$ GeV^2. If for BFKL we choose this lower cutoff then the solution is even more unstable and deviates earlier from the nonlinear solutions. Thus the result depends very sensitively on the nonperturbative cutoff. For BFKLab the solution is completely stable and we have checked that there is essentially no dependence at all on k_0. This is in strong contrast to BFKL, and is an important consequence of the nonlinear physics. This problem appears also for CCFM which like BFKL shows a diffusive behaviour in $k_\perp$. In event generators based on the linear physics one has therefore a quite strong dependence on the soft cut.

We have just described how one can economically introduce saturation effects into the linear small-x evolution. This method is very suitable for use in a Monte Carlo (MC) event generator. The only issue we face now is to go from BFKL to CCFM as there are no event generators based on BFKL. The CCFM formalism is suitable for the study of exclusive final states and is implemented in the CASCADE event generator. Although BFKL and CCFM are different formalisms there are nevertheless great similarities between the two. We have here no space to enter a detailed discussion on CCFM. As one of the most important similarities we shall however mention the following two points.

Numerical studies [10] have shown that CCFM, just like BFKL, shows a broadening of $k_\perp$. Infact this should come as no surprise. Denoting the momenta of the emitted real gluons by $q_\perp$ and that of the t-channel propagators by $k_\perp$, one is in CCFM free to go up and down in $k_\perp$ with the standard $d^2q_\perp/q_\perp^2$ bremstrahlung spectrum. In CCFM we also have angular ordering which prevents real gluons with very low momenta $q_\perp$ to be emitted, but this does not put much constraint on the virtual propagators $k_\perp$ which can again perform a random walk. The second point is that the CCFM gluon density grows as $\exp(\lambda Y)$ where to leading order $\lambda \approx 0.5$ just like in BFKL. Therefore the problem of unitarity is still there for CCFM, and in particular this shows that Q_s extracted from CCFM should be very similar to that extracted from BFKL. We are currently investigating a numerical solution of the CCFM equation.

In the MC program (for an early application see the talk by K. Kutak), the gluon distribution is first constructed by the standard forward evolution. The gluon ladder is then constructed via the backward evolution approach, starting from the hard scattering process. The unitarity constraint can be applied to the first step using the same strategy. This will give us a $k_\perp$ distribution which is cut below Q_s (which can be determined once the distribution is known). In the backward evolution one should then also make sure for consistency that no real gluon with $q_\perp < Q_s$ is emitted, as such gluons would have undergone saturation effects (basicly multiple scatterings).

In the application to event generators, the scales involved are not as large as the ones showed in figure 1, neither for $k_\perp$ nor for Y. In fact for $k_\perp$ the phenomenologically relevant part occupies a very small window in the figure. Here it can potentially be difficult to see any deviation from the linear physics, especially after full energy-momentum conservation is introduced. The precise choice of c and Δ can also be important in such a small window. We will come back to these issues in a lengthier paper.

Acknowledgements

I am grateful to my collaborator Edmond Iancu, and to Gösta Gustafson, Hannes Jung and Krzysztof Kutak for useful discussions.

References

[1] E. Iancu, A. Leonidov and L. McLerran arxiv: hep-ph/0202270, (2002).

[2] E. Avsar, G. Gustafson and L. Lönnblad JHEP **07**, 062 (2005).

[3] E. Avsar, G. Gustafson and L. Lönnblad JHEP **01**, 012 (2007).

[4] E. Avsar, G. Gustafson and L. Lönnblad JHEP **12**, 012 (2007).

[5] I. Balitsky, Nucl. Phys. **B463**, 99 (1996).

[6] Y. Kovchegov, Phys. Rev. **D60**, 034008 (1999).

[7] H. Jung and G. Salam Eur. Phys. J. **C19**, 351 (2001).

[8] S. Catani, F. Fiorani and G. Marchesini Nucl. Phys. **B336**, 18 (1990).

[9] A. Mueller and D. Triantafyllopoulos Nucl. Phys. **B640**, 331 (2002).

[10] J. Kwiecinski, A. Martin and P. Sutton Phys. Rev. **D52**, 1445 (1995).

The Ridge, the Glasma and Flow

Larry McLerran
RIKEN-BNL Center and Physics Department, Brookhaven National Lab., Upton, NY, 11973 USA
DOI: http://dx.doi.org/10.3204/DESY-PROC-2009-01/30

Abstract
I discuss the ridge phenomena observed in heavy ion collisions at RHIC. I argue that the ridge may be due to flux tubes formed from the Color Glass Condensate in the early Glasma phase of matter produced in such collisions

1 The Color Glass Condensate and the Glasma

The Color Glass Condensate is the matter which composes the low x part of a hadron wavefunction at high energy. [1] It is an ensemble of color electric and color magnetic fields which are in the form of Lienard-Wiechart potentials, $\vec{E} \perp \vec{B} \perp \hat{z}$, where $\hat{z}$ is in the direction of the beam.

These fields change their character after the collisions, where in a very short time, $t \sim Q_{sat}^{-1} e^{-\kappa/\alpha_S}$, longitudinal color electric and magnetic fields are produced. There are both color electric and magnetic fields because of the duality of QCD under $E \leftrightarrow B$, and the symmetry of the fields in the CGC under this transformation. Since there is both a longitudinal electric and magnetic field, these fields carry topological charge. They have a variation in the transverse size scale of $\Delta r_\perp \sim Q_{sat}^{-1}$, and may be thought of as an ensemble of flux tubes. This ensemble of flux tubes is the Glasma. [2]

Flux tubes have a long extent in longitudinal coordinate and therefore should have a long range in rapidity. If a system undergoes 1 dimensional Hubble flow until a time τ_F, and has an extent in rapidity $y = ln\{(t+z)/(t-z)\}$, then it must have been produced at a time before $\tau_i = \tau_f e^{-y/2}$. (For example, if τ_f is a nuclear size, and y is the total rapidity, then τ_i is the Lorentz contracted nuclear size in the center of mass frame.)

The multiplicity of flux tubes is

$$\frac{dN_{FT}}{dy} \sim R^2/R_{FT}^2 \sim Q_{sat}^2 R^2 \tag{1}$$

where R is the radius of the nucleus, and R_{FT} is the radius of the fluxtube. The flux tube is composed of high intensity color fields, and when these flux tubes decay their multiplicty per flux tube per unit rapidity should be of order $1/\alpha_S$, a factor typical of classical fields. This yields the familiar Kharzeev-Nardi formula for the multiplicity of initially produced gluons, [3]

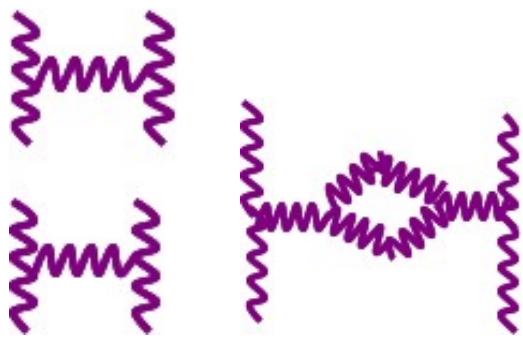
$$\frac{dN_{gluons}}{dy} \sim \frac{1}{\alpha_S} Q_{sat}^2 R^2 \tag{2}$$

2 Flux Tubes and Long Range Rapidity Correlations

To compute the long range rapidity correlation associated with a flux tube, one needs an expression for the two gluon emission amplitude. The leading order classical contribution is given by Fig. 1a. [4] Note that if this were emission from purely classical source, then the connected two particle emission amplitude,

$$\frac{d^2N}{d^2p_T^1 dy^1 d^2p_T^2 dy^2} = \left\langle \frac{dN}{d^2p_T^1 dy^1}\frac{dN}{d^2p_T^2 dy^2}\right\rangle - \left\langle \frac{dN}{d^2p_T^1 dy^1}\right\rangle\left\langle \frac{dN}{d^2p_T^2 dy^2}\right\rangle \tag{3}$$

would vanish. In emission from a Glasma, on the other hand, one has to average the sources,



a b

Fig. 1: a: The diagram contributing to the two particle correlation induced by the classical field. b: The short range correlation which arises as a quantum correction to the long range classical correlation.

which are treated as a stochastic variable. If the sources are Gaussian correlated, then one of the contractions of the sources from the nuclei indeed contributes to the disconnected diagram, but there are remaining contributions associated with the different contractions of the sources. [4] These contributions are associated with quantum interference in the two gluon emission amplitude, and may be difficult to precisely model in simulations which have flux tubes as sources of gluons. (In experiment, the disconnected contribution is subtracted by the effects of mixed events, since a disconnected contribution corresponds to no event by event correlation.)

In Fig. 1b, the correlated two particle emission amplitude is shown. This arises as a quantum correction to the classical emission. It has a short range correlation in rapidity, and a correction to the long range term. (In fact there can in principle be an interference between the classical two particle emission and the quantum correction.) Note that the classical contribution of Fig. 1a, is of order $1/\alpha_S^2$, since it arises from the amplitude squared corresponding to two classical fields. The quantum correction is of order 1.

Star has measured the forward backward asymmetry in heavy ion collisions. [5] The forward backward correlation strength is defined to be

$$b = \frac{< N_F N_B > - < N_F >< N_B >}{< N_B^2 > - < N_B >^2} \tag{4}$$

If the separation in rapidity for the forward backward correlation is large, the numerator should measure the strength of the long range correlation, but the denominator is a sum over short and long range pieces. This gives, [6]- [8]

$$b = \frac{1}{1 + \kappa \alpha_S^2} \tag{5}$$

Since α_S should decrease as centrality increases, this correlation strength should increase as a function of centrality. The measured strength of the correlation is indeed very strong for central

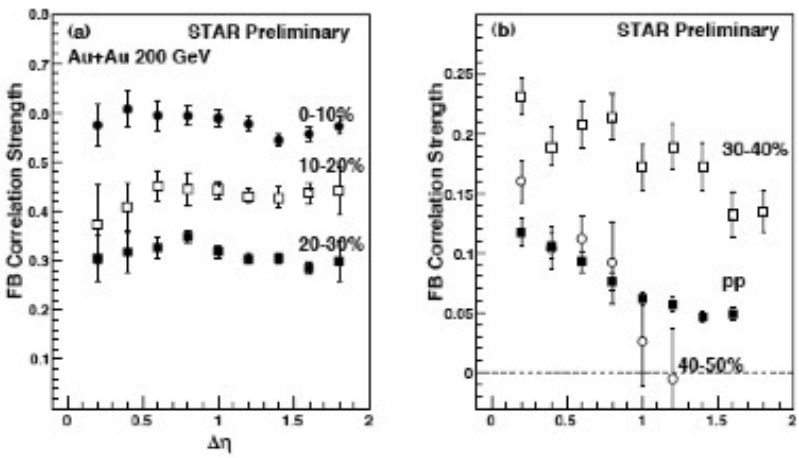


Fig. 2: The forward backward correlation strength measured for Gold-Gold collisions in STAR

collisions. It is also claimed that the correlation is much larger than can be expected from impact parameter fluctuations.

The STAR experiment has also measured directly the two particle correlation. If one plots the correlation as a function of the azimuthal angle between the two particles, and the rapidity between the two particles, a structure elongated in rapidity and collimated in angle appears. This is the so called ridge. It appears either when one or particles have a lower momentum cutoff or when the momenta is integrated over.

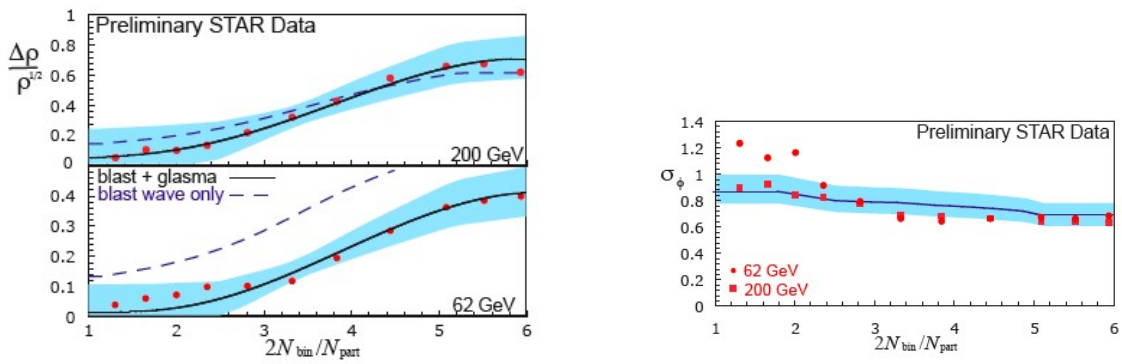
In the Glasma description, the two particle correlation should be very strong since essentially all the produced particles arise from flux tubes. It should also be noted that the two particle correlation predicted by the Glasma extends into the hard regime. As pointed out by Shuryak, at high momenta, the Glasma flux tubes are the fragmentation jets which appear when one perturbatively computes hard scattering. [10] When two high p_T particles are produced, the charges which induce the scattering are scattered out of the beam, leaving image charges in the fragments of the receding hadrons which produced the jets. The color fields associated with these image charges are responsible for the beam fragmentation jets, arising from the decay of the flux tube.

One of the interesting features of the ridge is the collimation in azimuthal angle. As pointed out by S. Voloshin, [11] this may arise from flow effects. The position in the transverse plane of the colliding nuclei for a flux tube is localized. This structure acquires transverse momentum due to radial flow. The flowing flux tube, when it decays its distribution of decay products will be preferentially along the direction of motion of the flux tube. The amplitude of the flux tube distribution will also acquire a non-trivial dependence upon centrality from flow.

With Sean Gavin, we estimated these flow effects for the Glasma using a blast wave model to incorporate the effects of flow. [9] We describe the ridge which is integrated over the energies of both the particles in the two particle correlation function. Detail of the experimental method for extracting the ridge are given in the Quark Matter 2008 contribution of STAR presented by Daugherity. [12]

$$\frac{d^2N}{d^2p_T^1 dy^1 d^2p_T^2 dy^2} = \left\langle \frac{dN}{d^2p_T^1 dy^1}\frac{dN}{d^2p_T^2 dy^2} \right\rangle - \left\langle \frac{dN}{d^2p_T^1 dy^1} \right\rangle \left\langle \frac{dN}{d^2p_T^2 dy^2} \right\rangle \tag{6}$$

In Fig. 3 a, the dependence on the amplitude of the ridge as a function of centrality is shown.



a b

Fig. 3: a: The amplitude for the ridge as a function of centrality at two different energies. The formula without a factor of $1/\alpha_S$ which arises in the Glasma description is shown as dashed line. b: The angular width of the ridge as a function of centrality

The red points are data. The solid line is our description. There is a one parameter ambiguity due to an overall normalization for the emission amplitude, which is not yet computed. The dashed line curve, is fit to the data not including a factor of $1/\alpha_S$ which arises from the classical field description of the ridge. In Fig. 3b, the angular width of the ridge is shown as a function of centrality.

At this meeting, Takeshi Kodama informed me that the SPHERIO collaboration from Brazil have seen the ridge in their computations. This arises because of the string-like configurations in the initial state. An excellent talk has been presented at the meeting RANP 2008 by Jun Takahashi. [13]

Clearly the next stage of theoretical analysis of the ridge will be to expand upon the SPHERIO treatment of the ridge. Some effort need be taken to properly account for the interference diagrams in the two particle correlation function which yield the ridge. In addition, one needs to understand the effect of energy-momentum conservation, and how it appears in the backward direction from the ridge.

3 Acknowledgements

I thank the organizers of the International Symposium on Miltiparticle Dynamics for their kind hospitality. I also thank Takeshi Kodama for telling me of the recent results from SPHERIO. I thank my colleagues Adiran Dumitru, Sean Gavin, Francois Gelis, Geroge Moschelli and Raju Venugopalan for their efforts and keen insight during our collaboration.

References

[1] L. McLerran and R. Venugopalan, *Phys. Rev.* **D49** 2233 (1994); **D49**, 3352 (1994); E. Iancu, A. Leonidov and L. McLerran, *Nucl. Phys.* **A692** 583 (2001); E. Ferreiro, E. Iancu, A. Leonidov and L. Mclerran, *Nucl. Phys.* **A703** 489 (2002).

[2] A. Kovner, L. McLerran and H. Weigert, *Phys. Rev.* **D52** 6231 (1995); **D52**, 3809 (1995); A. Kovner and R. Venugopalan, *Nucl. Phys.* **B557** 237 (1999); *Phys. Rev. lett.* **84** 4309 (2000); *Phys. Rev. lett.* **84** 4309 (2000); A. Krasnitz and R. Venugopalan, *Phys. Rev. Lett.* **87** 192302 (2001); L. McLerran and T. Lappi, *Nucl. Phys.* **A772** 200 (2006).

[3] D. Khrazeev and M. Nardi, *Phys. Lett.* **B507** 121 (2001)

[4] A. Dumitru, F. Gelis, L. McLerran and R. Venugopalan, *Nucl. Phys.* **A810** 91 (2008).

[5] B. Srivastava for the STAR Collaboration, *J. Phys.* **G35** 104140 (2008).

[6] Y. Kovchegov, E. Levin and L. McLerran, *Phys. Rev.* **C63** 024903 (2001).

[7] N. Armesto, L. McLerran and C. Pajares,]it Nucl. Phys. **A781** 201 (2007).

[8] K. Fukushima and Y. Hidaka, *Nucl. Phys.* **A813** 171 (2008) .

[9] S. Gavin, L. McLerran and G. Moschelli, arXiv:0806.4718[nucl-th]

[10] E. Shuryak, *Phys. Rev.* **C76** 047901 (2007).

[11] S. Voloshin, *Phys. Lett.* **B632** 490 (2006).

[12] A. Daugherity for the STAR Collaboration (and references therein), *J. Phys.* **G35** 104090 (2008).

[13] J. Takahashi, see `http://omnis.if.ufrj.br/~ranp/ranp/`

Partons and jets at strong coupling from AdS/CFT

Edmond Iancu
Institut de Physique Théorique de Saclay, F-91191 Gif-sur-Yvette, France
DOI: http://dx.doi.org/10.3204/DESY-PROC-2009-01/32

Abstract
Calculations using the AdS/CFT correspondence can be used to unveil the short–distance structure of a strongly coupled plasma, as it would be seen by a 'hard probe'. The results admit a natural physical interpretation in terms of parton evolution in the plasma: via successive branchings, essentially all partons cascade down to very small values of the longitudinal momentum fraction x and to transverse momenta smaller than the saturation momentum $Q_s \sim T/x$. This picture has some striking consequences, like the absence of jets in electron–proton annihilation at strong coupling, of the absence of particle production at forward and backward rapidities in hadron–hadron collisions.

1 Introduction

One of the most interesting suggestions emerging from the experimental results at RHIC is that the deconfined, 'quark–gluon', matter produced in the early stages of an ultrarelativistic nucleus–nucleus collision might be strongly interacting. This observation motivated a multitude of applications of the AdS/CFT correspondence to problems involving a strongly–coupled gauge plasma at finite temperature and/or finite quark density. While early applications have focused on the long–range and large–time properties of the plasma, so like hydrodynamics, more recent studies have been also concerned with the response of the plasma to a 'hard probe' — an energetic 'quark' or 'current' which probes the structure of the plasma on space–time scales much shorter than the characteristic thermal scale $1/T$ (with T being the temperature).

From the experience with QCD one knows that the simplest hard probe is an electromagnetic current. In deep inelastic scattering (DIS), the exchange of a highly virtual space–like photon between a lepton and a hadron acts as a probe of the hadron parton structure on the resolution scales set by the process kinematics: if Q^2 is (minus) the photon virtuality and s is the invariant photon–hadron energy squared, then the photon couples to quark excitations having transverse momenta $k_\perp \lesssim Q$ and a longitudinal momentum fraction $x \sim Q^2/s$. Also, the partonic fluctuation of a space–like current can mimic a quark–antiquark 'meson', which is nearly on–shell in a frame in which the current has a high energy. Furthermore, the decay of the time–like photon produced in electron–positron annihilation is the simplest device to produce and study hadronic jets in QCD. Thus, by studying the propagation of an energetic current through the plasma one has access to quantities like the plasma parton distributions, the meson screening length, or the energy loss and the momentum broadening of a jet.

At strong coupling and large number of colors $N_c \gg 1$, the AdS/CFT correspondence allows one to study the propagation of an Abelian '$\mathcal{R}$–current' through the finite–temperature plasma described by the $\mathcal{N} = 4$ supersymmetric Yang–Mills (SYM) theory. (For a recent review

and more references see [1].) In this context, DIS has been first addressed for the case of a dilaton target, in Refs. [2,3]. These studies led to an interesting picture for the partonic structure at strong coupling: through successive branchings, all partons end up by 'falling' below the 'saturation line', i.e., they occupy — with occupation numbers of order one — the phase–space at transverse momenta below the saturation scale $Q_s(x)$, which itself rises rapidly with $1/x$. Such a rapid increase, which goes like $Q_s^2(x) \sim 1/x$ and hence is much faster than in perturbative QCD, comes about because the high–energy scattering at strong coupling is governed by a spin $j \simeq 2$ singularity (corresponding to graviton exchange in the dual string theory), rather than the usual $j \simeq 1$ singularity associated with the gluon exchange at weak coupling.

In Refs. [4], this partonic picture has been extended to a finite–temperature SYM plasma in the strong 't Hooft coupling limit $\lambda \equiv g^2 N_c \to \infty$ (meaning $N_c \to \infty$). The results of these analyses will be briefly described in what follows.

2 Deep inelastic scattering at strong coupling from AdS/CFT

The strong coupling limit $\lambda \to \infty$ in the $\mathcal{N} = 4$ SYM gauge theory corresponds to the semiclassical, 'supergravity', approximation in the dual string theory, which lives in a ten–dimensional curved space–time with metric $AdS_5 \times S^5$. The finite–temperature gauge plasma is 'dual' to a black hole in AdS_5 which is homogeneous in the four Minkowski dimensions and whose AdS radius r_0 is proportional to the temperature: $r_0 = \pi R^2 T$, with R the curvature radius of AdS_5. The interaction between the $\mathcal{R}$–current J_μ and the plasma is then described as the propagation of a massless vector field A_μ which obeys Maxwell equations in the AdS_5 Schwarzschild geometry. The fundamental object to be computed is the retarded current–current correlator,

$$\Pi_{\mu\nu}(q) \,\equiv\, i \int \mathrm{d}^4 x \, \mathrm{e}^{-iq\cdot x} \, \theta(x_0) \, \langle [J_\mu(x), J_\nu(0)] \rangle_T \,, \tag{1}$$

whose imaginary part determines the cross–section for the current interactions in the plasma, i.e., the plasma structure functions in the *space–like* case $Q^2 \equiv -q^\mu q_\mu > 0$ ('deep inelastic scattering') and the rate for the current decay into 'jets' in the *time–like* case $Q^2 < 0$ ('e^+e^- annihilation'). The imaginary part arises in the supergravity calculation via the condition that the wave A_μ has no reflected component returning from the horizon. Physically, this means that the wave (current) can be absorbed by the black hole (the plasma), but not also regenerated by the latter. The classical solution $A_\mu(r)$ is fully determined by this 'no–reflected–wave' condition near the horizon together with the condition that the fields take some prescribed values at the Minkowsky boundary: $A_\mu(r \to \infty) = A_\mu^{(0)}$. The current–current correlator is then obtained as

$$\Pi_{\mu\nu}(q) \,=\, \frac{\partial^2 \mathcal{S}_{\rm cl}}{\partial A_\mu^{(0)} \partial A_\nu^{(0)}} \,, \tag{2}$$

where $\mathcal{S}_{\rm cl}$ denotes the classical action density (the Maxwell action evaluated on the classical solution), and is bilinear in the boundary fields $A_\mu^{(0)}$.

In what follows we shall focus on the space–like current, i.e., on the problem of DIS off the plasma [4]. (The corresponding discussion of a time–like current can be found in the second paper in Ref. [4]; see also the related work in Ref. [5].) We choose the current as a plane–wave

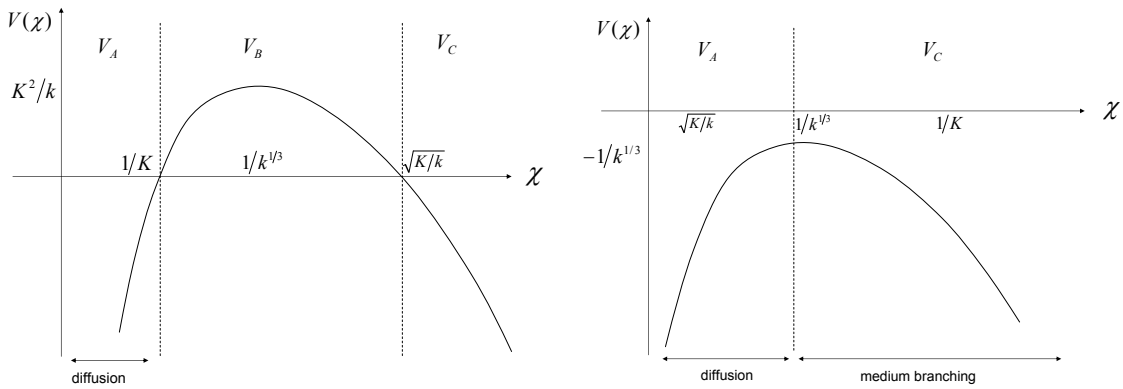


Fig. 1: *The potential in the effective Schrödinger equation describing the propagation of the space–like Maxwell wave in AdS_5–BH. Left: low energy, or large x ($x \gg T/Q$). Right: high energy, or small x ($x \lesssim T/Q$)*

propagating in the z direction in the plasma rest frame: $J_\mu(x) \propto \mathrm{e}^{-i\omega t+iqz}$. Also, we asume the high–energy and large–virtuality kinematics: $\omega \gg Q \gg T$. The physical interpretation of the results can be facilitated by choosing a different definition for the radial coordinate on AdS_5: instead of r, it is preferable to work with the inverse coordinate $\chi \equiv \pi R^2/r$, which via the UV/IR correspondence corresponds (in the sense of being proportional) to the transverse size L of the partonic fluctuation of the current. Then, the AdS_5 boundary lies at $\chi = 0$ and the black–hole horizon at $\chi = 1/T$.

Via a suitable change of function, the Maxwell equations for A_μ can be rewritten as a pair of time–independent Schrödinger equations — one for the longitudinal modes, the other one for the transverse ones. Then, the dynamics can be easily understood by inspection of the respective potential, as illustrated in Fig. 1 for two different regimes of energy. (Note that in plotting the potential in these figures we are using the dimensionless variables $K \equiv Q/T$ and $k \equiv q/T$; also, χ is multiplied by T.) The dynamics depends upon the competition between, on one hand, the virtuality Q^2, which acts as a potential barrier preventing the Maxwell wave A_μ to penetrate deeply inside AdS_5, and, on the other hand, the product ωT^2, which controls the strength of the interactions between this wave and the black hole. (We recall that the gravitational interactions are proportional to the energy density of the two systems in interaction.) The relevant dimensionless parameter is $Q^3/\omega T^2$, which can be also rewritten as xQ/T, where $x \equiv Q^2/2\omega T$ (the Bjorken variable for DIS) has the physical meaning of the longitudinal momentum fraction of the plasma 'parton' struck by the current.

Specifically, in the high–Q^2 regime at $Q^3/\omega T^2 \gg 1$, or $x \gg T/Q$, the interaction with the plasma is relatively weak and the dynamics is almost the same as in the vacuum: the wave penetrates in AdS_5 up to a maximal distance $\chi_0 \sim 1/Q$ where it gets stuck against the potential barrier. Physically, this means that the current fluctuates into a pair of partons (say, a quark–antiquark 'meson') with transverse size $L \sim 1/Q$. At finite temperature, however, the potential barrier has only a finite width — it extends up to a finite distance $\chi_1 \sim (1/T)\sqrt{Q/\omega}$ —, so there is a small, but non–zero, probability for the wave to cross the barrier via tunnel effect. Physically, this means that the plasma structure function at large x is non–vanishing, but extremely small

(exponentially suppressed) : $F_2(x,Q^2) \,\propto\, xN_c^2Q^2\,\exp\{-(x/x_s)^{1/2}\}$ for $x \gg x_s \equiv T/Q$. In other terms, when probing the plasma on a transverse resolution scale Q^2, one finds that there are essentially no partons with momentum fraction x larger than $T/Q \ll 1$.

Where are the partons then ? To answer this question, let us explore smaller values of Bjorken's x, by increasing the energy ω at fixed Q^2 and T. Then the barrier shrinks and eventually disappears; this happens when ω is large enough for $\chi_1 \sim \chi_0$, a condition which can be solved either for x (thus yielding $x \sim x_s = T/Q$), or for Q, in which case it yields the *plasma saturation momentum* : $Q_s^2(x,T) \sim T^2/x^2$. For higher energies, meaning $x < x_s$, the barrier has disappeared and the Maxwell wave can propagate all the way down to the black hole, into which it eventually falls, along a trajectory which coincides with the 'trailing string' of a heavy quark [6]. Physically, this means that the current has completely dissipated into the plasma. We interpret this dissipation as *medium–induced branching* : the current fragments into partons via successive branchings, with a splitting rate proportional to a power of the temperature. This branching continues until the energy and the virtuality of the partons degrade down to values of order T. The lifetime of the current (estimated as the duration of the fall of the Maxwell wave into the black hole) is found as $\Delta t \,\sim\, \omega/Q_s^2 \,\propto\, \omega^{1/3}$ — a result which agrees with a recent estimate of the 'gluon' lifetime in Ref. [7]. Since the current is tantamount to a 'meson' with size $1/Q$ and rapidity $\gamma = \omega/Q$, our analysis also implies an upper limit on the transverse size of this 'meson' before it melts in the plasma: $L_{\max} \sim 1/Q_s \sim 1/\sqrt{\gamma}\,T$. This limit is consistent with the meson screening length computed in Refs. [8]. The saturation momentum Q_s turns out to also be the scale which controls the energy loss [4, 6] and the transverse momentum broadening [9, 10] of a parton moving into the plasma. For instance, the rate for the energy loss of a heavy quark reads (in the ultrarelativistic limit $\gamma \gg 1$) [4, 10]

$$-\frac{\mathrm{d}\omega}{\mathrm{d}t} \,\sim\, \sqrt{\lambda}\,Q_s^2\,, \tag{3}$$

where one should keep in mind that the saturation scale in the r.h.s. is itself a function of ω, and hence of time: $Q_s^2 \sim (\omega T^2)^{1/3}$. Eq. (3) may be viewed as the time–dependent generalization of the 'drag force' first computed in Refs. [6].

The complete absorbtion of the current by the plasma is tantamount to the 'black disk' limit for DIS: in this high–energy, or small–x, regime the structure function is not only non–zero, but in fact it reaches its maximal possible value allowed by unitarity. This value is found as $F_2(x,Q^2) \,\sim\, xN_c^2Q^2$ for $x \sim x_s$, a result with a natural physical interpretation: for a given resolution Q^2, essentially all partons have momentum fractions $x \lesssim T/Q \ll 1$ and occupation numbers $n \sim \mathcal{O}(1)$. This is similar to parton saturation in pQCD, except that, now, the occupation numbers at saturation are of order one, rather than being large ($n \sim 1/g^2N_c$), as it was the case at weak coupling.

This result has interesting consequences for a (hypothetic) high–energy hadron–hadron collision, in which these partons would be liberated: Since there are no partons carrying large longitudinal momenta, there will be no 'forward/backward jets' in the wake of the collision, that is, no hadronic jets following the same directions of motion as the incoming hadrons. Rather, all particles will be produced at central rapidities and will be isotropically distributed in the transverse space. Similar conclusions hold for a *time–like* virtual photon decaying in the vacuum [4], that is, for the analog of electron–positron annihilation at strong coupling (see Fig. 2): unlike

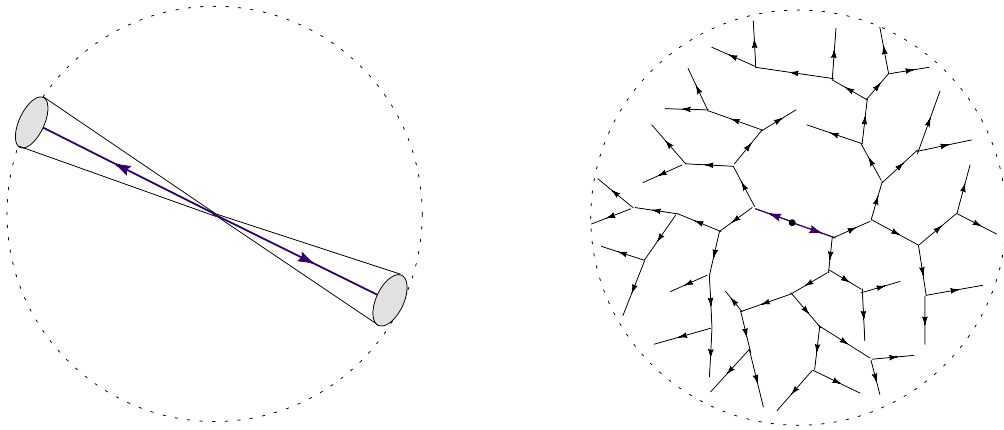


Fig. 2: *Final state produced in e^+e^- annihilation: (left) weak coupling; (right) strong coupling.*

at weak coupling, where the typical final state involves a pair of back–to–back hadronic jets, at strong coupling the original pair of partons undergoes a rapid branching process leading to an isotropic distribution of matter in the detector. Similar results have reached in Refs. [11]. This picture for the final state looks quite different from that predicted by perturbative QCD and observed in actual high–energy experiments. Such a discrepancy suggests that much caution should be taken when trying to extrapolate results from AdS/CFT to QCD.

References

[1] D. Son and A. Starinets, `arXiv:0704.0240 [hep-th]`.

[2] J. Polchinski and M. J. Strassler, *JHEP* **05** (2003) 012.

[3] Y. Hatta, E. Iancu, and A. H. Mueller, *JHEP* **01** (2008) 026.

[4] Y. Hatta, E. Iancu, and A. H. Mueller, *JHEP* **01** (2008) 063; *JHEP* **05** (2008) 037.

[5] P.M. Chesler, K. Jensen, and A. Karch, `arXiv:0804.3110 [hep-th]`.

[6] C. P. Herzog et al, *JHEP* **07** (2006) 013; S. S. Gubser, *Phys. Rev.* **D74** (2006) 126005.

[7] S. S. Gubser, D. R. Gulotta, S. S. Pufu, F. D. Rocha, `arXiv:0803.1470 [hep-th]`.

[8] K. Peeters et al, *Phys. Rev.* **D74** (2006) 106008; H. Liu et al *Phys. Rev. Lett.* **98** (2007) 182301; M. Chernicoff et al *JHEP* **09** (2006) 068; E. Caceres et al *JHEP* **10** (2006) 011.

[9] J. Casalderrey-Solana and D. Teaney, *JHEP* **04** (2007) 039; *Phys. Rev.* **D74** (2006) 085012; S. S. Gubser, *Phys. Rev.* **D76** (2007) 126003.

[10] F. Dominguez et al, `arXiv:0803.3234 [nucl-th]`; A.H. Mueller, `0805.3140 [hep-ph]`.

[11] D. M. Hofman and J. Maldacena, *JHEP* **05** (2008) 012.

QCD EoS, initial conditions and final state from relativistic hydrodynamics in heavy-ion collisions

Márton Nagy
MTA KFKI Research Institute for Particle and Nuclear Physics, Budapest, Hungary
DOI: http://dx.doi.org/10.3204/DESY-PROC-2009-01/33

Abstract
Some recent developments in exact results in relativistic hydrodynamics is reviewed. We discuss phenomenological applications in high-energy collisions and theoretical features of the solutions. We compare the method of numerical modelling to the strategy based on exact solutions. We argue that the efforts made and progress achieved in this seemingly purely theoretical topic is of interest for phenomenology.

1 Introduction

Nowadays one of the primary challenges to physics is to understand the phase structure of strong interactions. An important goal of heavy-ion physics is thus to interpret the results of high-energy collider experiments. It is a hard task, since one needs to follow the time-evolution of the created matter in order to see the collective properties. The mean free path is small if temperature is high, (as first noted by Fermi [1]), so the idea arises naturally to use hydrodynamics for this end. Hydrodynamics is almost the only way which dynamically connects the initial conditions with the final state. As the first results from the RHIC particle accelerator appeared, lots of models failed to describe the measurements. However, many successful models were based on hydrodynamics, and this in-turn led to a firm understanding that the created matter is an almost perfect liquid [2]. A typical feature of the measured soft hadronic observables was the appearance of different scalings. The strength of hydrodynamics lies in the fact that it relies only on the simple assumption of local thermal equilibrium and local energy-momentum conservation, and no physical scales are present, this leads to an easy explanation of scalings.

The equations of relativistic hydrodynamics: In this subsection we briefly review the well-known equations of perfect fluid relativistic hydrodynamics. The metric is $g^{\mu\nu}$, $u^\mu = \gamma(1, \mathbf{v})$ is the four-velocity field, $\mathbf{v} = v\mathbf{n}$ is the three-velocity. The pressure is denoted by p, the energy density by ε, the temperature by T, and the entropy density by σ. In high energy collisions, σ is large compared to the net baryonic charge density, so in the following we will not take conserved charges into account. The fundamental equations are obtained by Landau's argumentation, which starts from the conservation of energy-momentum and entropy density, expressed as

$$\partial_\nu(\sigma u^\nu) = 0 \quad , \quad \partial_\nu T^{\mu\nu} = 0 \quad , \quad T^{\mu\nu} = (\varepsilon + p)u^\mu u^\nu - pg^{\mu\nu}. \tag{1}$$

This form of the $T_{\mu\nu}$ energy-momentum tensor specifies the perfectness of the fluid. The Euler equation and the energy equation follow as

$$(\varepsilon + p)u^\nu \partial_\nu u^\mu = \left(g^{\mu\rho} - u^\mu u^\rho\right)\partial_\rho p, \tag{2}$$

$$(\varepsilon + p)\partial_\nu u^\nu + u^\nu \partial_\nu \varepsilon = 0. \tag{3}$$

These equations have to be supplemented by an equation of state (EoS), which connects p, T, and ε, in order to have a closed set of equations. Assuming $\varepsilon = \kappa(T)p$, the κ factor is $1/c_s^2$, the inverse speed of sound. In most exact solutions one uses $\kappa = const.$

Exact vs. numerical solutions: Having the hydrodynamical equations, we can either solve them numerically or investigate them analytically. They are nonlinear, and thus it is hard to find even particular analytic solutions. So obviously, the main advantage of the numerical approach is that in this way one can in principle use any type of initial conditions, and calculate the corresponding final state observables. On the other hand, the similar advantage of the analytic approach is also obvious: if one finds a suitable analytic solution, then one can map not only a single initial condition but a manifold of them, and constrain its parameters. Also, many classes of exact solutions are parametric solutions, naturally explaining scalings. So our point is that analytic hydrodynamical solutions can also yield important insight into the dynamics. The interest in this direction has somewhat revived in the last few years; we will first summarize the historical results, then some recent developments.

2 Historic results

The most important and seminal two relativistic hydrodynamical solutions, the Landau-Khalatnikov solution and the Hwa-Bjorken solution had great impact in the application of relativistic hydrodynamics to high-energy phenomena.

The Landau-Khalatnikov solution: The idea of relativistic hydrodynamics stems mostly from Landau. He also elaborated on Fermi's idea on the applications [3,4], and Khalatnikov gave the first analytic solution to the relativistic hydrodynamical equations [5]. This solution is an 1+1 dimensional, implicit, complicated one. We just highlight the main notions and steps. What is needed, is the expression of the T temperature and Ω fluid rapidity, defined as $v = \tanh\Omega$, as a function of t and r, the time and spatial coordinate, or of $x_+ = t+r$ and $x_- = t-r$, the lightcone coordinates. Rearranging the hydrodynamical equations a bit, one arrives at the conclusion that the key to the solution is a potential, $\Phi(x_+, x_-)$, with $\partial_+\Phi = Te^{\Omega}$, $\partial_-\Phi = Te^{-\Omega}$, and Φ can be calculated from its Legendre-transform $\chi\left(Te^{\Omega}, Te^{-\Omega}\right) = \Phi - x_+Te^{\Omega} - x_-Te^{-\Omega}$, which satisfies the linear Khalatnikov-equation:

$$\partial_\theta^2\chi\left(\theta,\Omega\right) + \left(\kappa-1\right)\partial_\theta\chi\left(\theta,\Omega\right) - \kappa\partial_\Omega^2\chi\left(\theta,\Omega\right) = 0, \tag{4}$$

where $\theta = \ln T$ was used. Now the solution of this equation can be written up with integral-formulas using the Green-function formalism (see e.g. [6]); the essence of the Landau-Khalatnikov-solution is the fully stopped finite piece of matter initial condition. It yields approximately Gaussian rapidity distribution for the produced particles, which is a realistic prediction.

The Hwa-Bjorken solution: Contrasted to the Landau-Khalatnikov solution, the Hwa-Bjorken solution (originally formulated by Hwa [7], discussed by many others, rediscovered and fully exploited by Bjorken [8]) provides an over-simplified picture of the 1+1 dimensional dynamics. It uses the τ and η Rindler-coordinates: the time t and spatial coordinate r is expressed as $t = \tau\cosh\eta$, $r = \tau\sinh\eta$. The core assumption (valid at infinite collision energies) is the boost-invariance, i.e. that σ and T are independent of η, and indeed, the simple

$$v = r/t \quad , \quad \sigma_0/\sigma = \tau_0/\tau \tag{5}$$

forms give an accelerationless solution of the hydrodynamical equations. The expression of the temperature depends on the actual value of κ. This solution leads to a flat rapidity distribution, thus although it can be used approximately to various estimates, it needs a correction.

3 Recent results

Nonrelativistic models: Although relativistic effects are more than essential in high-energy experiments, the nonrelativistic case also deserves a brief summary here: the equations are much simper, and allow for more exact solutions [9–13]. A pretty general family is described in Ref. [11], with a self-similar ellipsoidal velocity and temperature profile. It contains some of the other solutions as special cases. It serves as a base of the Buda-Lund model, which is successful in describing particle spectra, correlations, and their scalings [14, 15].

It is also worthwhile to mention this exact solution because (as far as we know) this is the only one which can be generalized for arbitrary temperature-dependent speed of sound: if one assumes Gaussian density profile and spatially constant temperature, then one gets a parametric solution for any $\kappa(T)$ function. This result — though non-relativistic — is unique, and makes possible to use any QCD-inspired EoS. One would naturally look for similar relativistic solutions.

Relativistic accelerationless solutions: The generalization of the Hwa-Bjorken solution to arbitrary number of spatial dimensions seems a straightforward direction of development, although it was a formidable task [16, 17]. These solutions are also the relativistic equivalents of the nonrelativistic solutions mentioned in the previous subsection. They have an accelerationless, spherically symmetric velocity profile: $v = \mathbf{r}/t$. The pressure is $p = nT$, with some conserved charge n. Ellipsoidal profiles are allowed in the forms of n and T as

$$n = n_0 \left(\frac{\tau_0}{\tau}\right)^3 \frac{1}{\mathcal{T}(S)} \quad , \quad T = T_0 \left(\frac{\tau_0}{\tau}\right)^{3\frac{1}{\kappa}} \mathcal{T}(S) \quad , \quad S = \frac{1}{t^2}\left(\frac{x^2}{A^2} + \frac{y^2}{B^2} + \frac{z^2}{C^2}\right), \qquad (6)$$

where $\mathcal{T}$ is an arbitrary function of the ellipsoidal scaling variable S, with principal axes A, B, and C in the directions x, y, and z. In Ref. [17] other generalizations are also found, e.g. to hyperbolic profiles, and Ref. [18] shows a slight generalization, where even the velocity field can show more general, ellipsoidal symmetry, but still without any acceleration. Other important accelerationless solutions were presented in Refs. [19, 20].

Accelerating solutions: There were no known examples of exact explicit and accelerating solutions until recently an interesting class of spherically symmetric solutions emerged [21, 22]: as a generalization of the Hwa-Bjorken solution, one finds that the

$$v = \tanh(\lambda\eta) \quad , \quad p = p_0 \left(\tau_0/\tau\right)^{\lambda d(\kappa+1)/\kappa} \cosh^{-(d-1)\Phi_\lambda}(\eta/2) \qquad (7)$$

expressions are indeed solutions of the hydrodynamical equations, for certain values of the real parameters λ, d, Φ_λ and κ: κ is the (constant) inverse speed of sound, d is the number of spatial dimensions, λ is a parameter of the solution; for $\lambda = 1$ the Hwa-Bjorken solution is recovered, for $\lambda \neq 1$ the solution is accelerating. The Φ_λ parameter is introduced because for some choices of λ the pressure depends on η as well. The allowed parameter sets are listed in Table 1. They have many interesting properties; for a detailed explanation, see Ref. [22]. The $\kappa = 1$, $d = 1$ solutions, on the other hand, allow to an easy approximate calculation of the rapidity distribution [22].

Case	λ	d	κ	ϕ_λ
(a)	2	$\in \mathbb{R}$	d	0
(b)	$\frac{1}{2}$	$\in \mathbb{R}$	1	$\frac{\kappa+1}{\kappa}$
(c)	$\frac{3}{2}$	$\in \mathbb{R}$	$\frac{4d-1}{3}$	$\frac{\kappa+1}{\kappa}$
(d)	1	$\in \mathbb{R}$	$\in \mathbb{R}$	0
(e)	$\in \mathbb{R}$	1	1	0

Table 1: Allowed parameters for the family of accelerating solutions of Eq. (7).

These distributions qualitatively agree with the observed peaked (Gaussian) structure, and the λ parameter can be extracted from a fit to measured data with acceptable statistical significance, thus these solutions serve as a means to improve Bjorken's original estimate [8] of the initial energy density: the work done by the fluid (because of acceleration) and the shift in the estimated origin of the trajectories caused by the presence of acceleration leads to the conclusion that the Bjorken estimate needs to be corrected by a factor greater than 1: for $\sqrt{s_{NN}} = 200$GeV Au+Au collisions, from rapidity distributions measured by the BRAHMS collaboration, one gets not less than a factor of 2.0 ± 0.1 correction, and taking the softness of the EoS into account, a conjectured correction factor of 2.9 ± 0.2 [21]. This result is important in the interpretation of experimental data in terms of advanced estimates of the initial energy densities. A somewhat less important estimate can also be made more precise: the life-time of the reaction increases by about 20% with taking the acceleration into account in this way [21]. It should be noted that in the case of stiff EoS, $\kappa = 1$, not only these solutions with the λ parameter, but the general explicit solution can be obtained [22] because of an analogy to a linear wave-equation. For multi-dimensional flows, this idea resulted in a broad class of new general solutions [23], although only for this particular EoS, and it is not clear how these results could be generalized for any other.

Harmonic flows in $1+1$ *dimensions:* Another recent approach toward new solutions was a generalization of the Bjorken ansatz (the boost invariance) to a harmonic ansatz: $\partial_+\partial_-\Omega = 0$. A new class of solutions is obtained when substituted into the hydrodynamical equations [24]:

$$p = p_0 \exp\left\{ -\frac{(1+\kappa)^2}{4\kappa}\left(l_+^2 + l_-^2\right) + \frac{\kappa^2-1}{2\kappa} l_+ l_- \right\} \quad , \quad \Omega = \frac{1}{2}\left(l_+^2 - l_-^2\right). \tag{8}$$

The notations are

$$l_\pm(x_\pm) = \sqrt{\ln F_\pm} \quad , \quad z_\pm = h \int^{F_\pm} \frac{dx}{\sqrt{\ln x}}, \tag{9}$$

where h is an arbitrary constant. This solution, although not fully explicit, is very interesting, since it interpolates between the Landau and the Bjorken pictures (fixed h, $l_\pm \to \infty$, and $h \to 0$, respectively). If one calculates the entropy density per unit rapidity, which is proportional to the observable particle distribution, it depends on the assumed freeze-out surface, but in general it is approximately Gaussian [24]. More general expressions for the entropy flow $\frac{\mathrm{d}S}{\mathrm{d}n}$, based partially on the Khalatnikov method, were discussed recently in Ref. [6].

4 Summary: where we are now and where to go

The interest in the numerical simulations of relativistic hydrodynamics is steadily growing: it seems obvious to almost everyone that hydrodynamics is the correct tool to describe high-energy collective phenomena. We see now that a similar common interest begins to arise towards exact solutions. With simple examples we tried to demonstrate that there are many new and interesting solutions, and that these are of phenomenological importance: if one has a solution with a few adjustable fit parameters, it gives invaluable insight into the dynamics and yields advanced estimates for the initial conditions (such as energy density, life-time).

Finding exact solutions to the hydrodynamical equations, however, is a difficult problem, and needs lots of effort. For instance, there is no known solution in more than one spatial dimensions with a little bit general equation of state. Similarly, no accelerating solutions are known which go beyond spherical symmetry. The quest for such solutions (e.g. for an ellipsoidally symmetric one) might lead to a more accurate description of the observables, and thus test the perfectness of the fluid and the used equation of state.

The support of OTKA T49466 and T73143 grants is gratefully acknowledged. We thank to the organizers of ISMD 2008 for their kind hospitality and support.

References

[1] E. Fermi, Prog. Theor. Phys. **5**, 570 (1950).
[2] PHENIX Collaboration, K. Adcox *et al.*, Nucl. Phys. **A757**, 184 (2005). nucl-ex/0410003.
[3] L. D. Landau, Izv. Akad. Nauk SSSR Ser. Fiz. **17**, 51 (1953).
[4] S. Z. Belenkij and L. D. Landau, Nuovo Cim. Suppl. **3S10**, 15 (1956).
[5] I. M. Khalatnikov, Zhur. Eksp. Teor. Fiz. **27**, 51 (1953).
[6] G. Beuf, R. Peschanski, and E. N. Saridakis (2008). 0808.1073.
[7] R. C. Hwa, Phys. Rev. **D10**, 2260 (1974).
[8] J. D. Bjorken, Phys. Rev. **D27**, 140 (1983).
[9] T. Csörgő, Central Eur. J. Phys. **2**, 556 (2004). nucl-th/9809011.
[10] S. V. Akkelin, T. Csörgő, B. Lukács, Y. M. Sinyukov, and M. Weiner, Phys. Lett. **B505**, 64 (2001). hep-ph/0012127.
[11] T. Csörgő, Acta Phys. Polon. **B37**, 483 (2006). hep-ph/0111139.
[12] P. Csizmadia, T. Csörgő, and B. Lukács, Phys. Lett. **B443**, 21 (1998). nucl-th/9805006.
[13] T. Csörgő, S. V. Akkelin, Y. Hama, B. Lukács, and Y. M. Sinyukov, Phys. Rev. **C67**, 034904 (2003). hep-ph/0108067.
[14] M. Csanád, T. Csörgő, and B. Lörstad, Nucl. Phys. **A742**, 80 (2004). nucl-th/0310040.
[15] T. Csörgő and B. Lörstad, Phys. Rev. **C54**, 1390 (1996). hep-ph/9509213.
[16] T. Csörgő, F. Grassi, Y. Hama, and T. Kodama, Phys. Lett. **B565**, 107 (2003). nucl-th/0305059.
[17] T. Csörgő, L. P. Csernai, Y. Hama, and T. Kodama, Heavy Ion Phys. **A21**, 73 (2004). nucl-th/0306004.
[18] Y. M. Sinyukov and I. A. Karpenko (2005). nucl-th/0505041.
[19] T. S. Biró, Phys. Lett. **B474**, 21 (2000). nucl-th/9911004.
[20] T. S. Biró, Phys. Lett. **B487**, 133 (2000). nucl-th/0003027.
[21] T. Csörgő, M. I. Nagy, and M. Csanád, Phys. Lett. **B663**, 306 (2008). nucl-th/0605070.
[22] M. I. Nagy, T. Csörgő, and M. Csanád, Phys. Rev. **C77**, 024908 (2008). 0709.3677.
[23] M. S. Borshch and V. I. Zhdanov, SIGMA. **3**, 116 (2007). 0709.1053.
[24] A. Bialas, R. A. Janik, and R. B. Peschanski, Phys. Rev. **C76**, 054901 (2007). 0706.2108.

Hydrodynamics & perfect fluids: uniform description of soft observables in Au+Au collisions at RHIC †

Wojciech Florkowski[1,2‡], *Wojciech Broniowski*[1,2], *Mikolaj Chojnacki*[1], *Adam Kisiel*[3,4]
[1]The H. Niewodniczański Institute of Nuclear Physics,
Polish Academy of Sciences, PL-31342 Kraków, Poland,
[2]Institute of Physics, Jan Kochanowski University, PL-25406 Kielce, Poland,
[3]Faculty of Physics, Warsaw University of Technology, PL-00661 Warsaw, Poland,
[4]Department of Physics, Ohio State University, 1040 Physics Research Building,
191 West Woodruff Ave., Columbus, OH 43210, USA

DOI: http://dx.doi.org/10.3204/DESY-PROC-2009-01/34

Abstract

It is argued that the use of the initial Gaussian energy density profile for hydrodynamics leads to much better uniform description of the RHIC heavy-ion data than the use of the standard initial condition obtained from the Glauber model. With the modified Gaussian initial conditions we successfully reproduce the p_T-spectra, v_2, and the pionic HBT radii (including their azimuthal dependence). The emerging consistent picture of hadron production hints that a solution of the long standing RHIC HBT puzzle has been found.

1 Introduction

Relativistic hydrodynamics of the perfect fluid may be considered as the standard framework for the description of the intermediate stages of relativistic heavy-ion collisions [1–7]. However, despite the clear successes in reproducing the particle transverse-momentum spectra and the elliptic flow coefficient v_2, the typical approach based on the relativistic hydrodynamics cannot reproduce correctly the pion correlation functions. In particular, the ratio of the so called HBT radii $R_{\rm out}$ and $R_{\rm side}$ comes out too large, exceeding the experimentally measured value by about 20-50%. Very recently, we have found [8] that the consistent description of the soft hadronic observables may be achieved within the hydrodynamic model if one makes a modification of the initial conditions – the initial energy profile obtained in most cases from the optical Glauber model should be replaced by the Gaussian profile.

Our framework consists of the recently developed 2+1 boost-invariant inviscid hydrodynamics [9–11] linked to the statistical-hadronization model THERMINATOR [12]. The initial eccentricity is obtained from the Monte-Carlo Glauber model GLISSANDO [13]. The simulations done with GLISSANDO include the eccentricity fluctuations [14–22]. In each simulated event the distribution of sources (a mixture of the wounded-nucleon contributions and the binary-collision points) is first rotated to the principal-axes frame and then histogrammed. As a result one obtains the two-dimensional profile that takes into account the fluctuations of the principal

† Supported in part by the Polish Ministry of Science and Higher Education, grants N202 153 32/4247 and N202 034 32/0918, and by the U.S. NSF Grant No. PHY-0653432.

‡ speaker

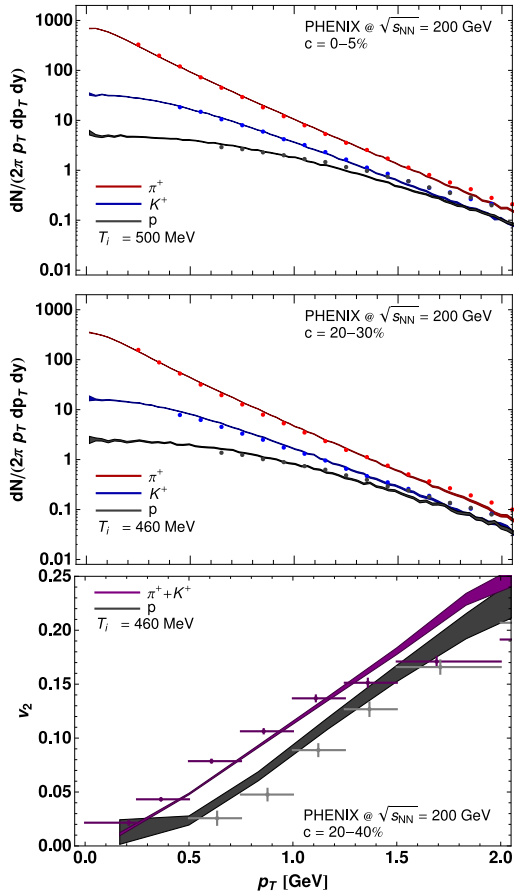


Fig. 1: The transverse-momentum spectra of pions, kaons and protons for the centrality bin c = 0-5% (upper panel), c = 20-30% (middle panel), and the elliptic flow coefficient v_2 for c = 20-40% (lower panel), plotted as functions of the transverse momentum and compared to the RHIC Au+Au data.

axes with respect to the reaction plane. This procedure determines the initial energy distribution in the transverse plane which is parameterized as the two-dimensional Gaussian and used as the initial condition for the hydrodynamics. The main characteristic of the hydrodynamic stage is the use of the realistic equation of state which interpolates between the lattice simulations of full QCD and the hadron-gas model. The final stage of the evolution is described with the help of the Monte-Carlo thermal model THERMINATOR which simulates hadron emission from the freeze-out hypersurface delivered by the hydrodynamic calculation. We assume the single freeze-out scenario [23, 24] with the universal final temperature T_f =145 MeV. Besides the final temperature our model has essentially two additional parameters: the initial temperature T_i, fixing the absolute normalization of the spectra, and the initial time for the start of hydrodynamics τ_0 =0.25 fm. Of course, for each centrality class we fix the geometric parameters a and b (i.e., the widths of the initial Gaussian energy distribution) by the GLISSANDO simulations as explained above.

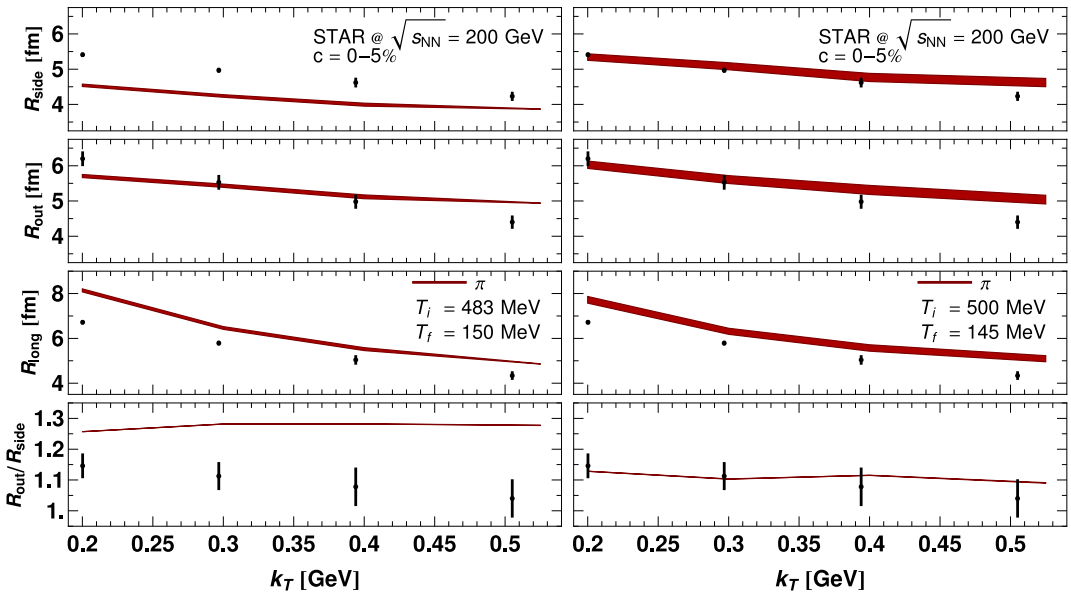


Fig. 2: The pion HBT radii $R_{\rm side}$, $R_{\rm out}$, $R_{\rm long}$, and the ratio $R_{\rm out}/R_{\rm side}$ for central collisions, shown as the functions of the average momentum of the pair and compared to the RHIC Au+Au data.

2 Results

In Fig. 1 we show our results describing the transverse-momentum spectra of pions, kaons, and protons for the centrality classes c = 0-5% and c = 20-30%. Fig. 1 presents also our results describing the elliptic flow coefficients v_2 for the centrality class c = 20-40%, plotted as functions of the transverse momentum. The spectra and the elliptic flow are compared to the RHIC data [25, 26]. We observe a very good agreement between the model predictions and the data. The small excess of the theoretical proton v_2 above the data may be attributed to the lack of rescattering in the final state.

In Fig. 2 we present our results on the pion HBT radii $R_{\rm side}$, $R_{\rm out}$, $R_{\rm long}$, and the ratio $R_{\rm out}/R_{\rm side}$ for central collisions, compared to the RHIC data [27]. The left panel shows our best results obtained with the traditional Glauber initial condition [28], while the right panel shows the results obtained with the Gaussian initial condition [8]. One can see that a very good agreement between the data and the theoretical model predictions is achieved in the case where the Gaussian initial condition is used. In particular, the ratio $R_{\rm out}/R_{\rm side}$ is well reproduced. We note that the calculation of the radii does not introduce any extra parameters. All the characteristics of the emitting source were already fixed by the fits to the spectra and v_2.

Finally, in Fig. 3 the results describing the azimuthal dependence of the HBT radii are plotted [29]. Here $R^2(\phi) = R_0^2 + 2R_2^2\cos(2\phi)$. Again, we observe a very good agreement between the data and our model for different centralities and different average momenta of the pion pairs k_T.

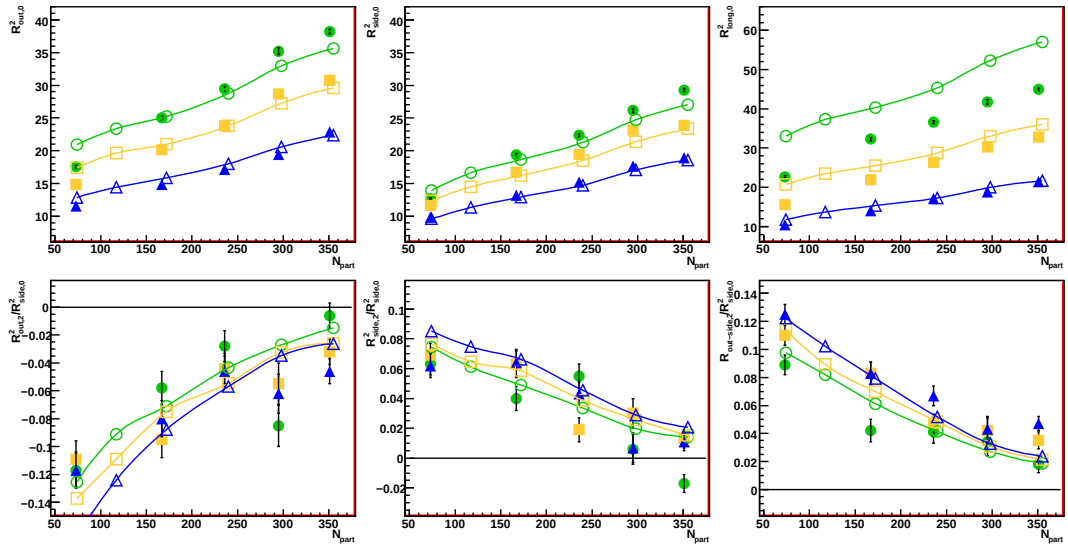


Fig. 3: Results for the RHIC HBT radii and their azimuthal oscillations. For each value of $N_{\rm part}$ on the horizontal axis the experimental points (filled symbols) and the model results (empty symbols) are plotted. The points from top to bottom at each plot correspond to k_T contained in the bins 0.15-0.25 GeV (circles), 0.25-0.35 GeV (squares), and 0.35-0.6 GeV(triangles). The top panels show $R^2_{\rm out,0}$, $R^2_{\rm side,0}$, and $R^2_{\rm long,0}$, the bottom panels show the magnitude of the allowed oscillations divided conventionally by $R^2_{\rm side,0}$.

3 Conclusions

The results presented above indicate that it is possible to achieve a uniform description of the RHIC heavy-ion data collected at the highest beam energies in the soft hadronic sector using the hydrodynamics of perfect fluid with the Gaussian initial condition for the energy density. In particular, it is possible to describe the transverse-momentum spectra and the elliptic flow coefficient v_2 simultaneously with two-particle observables such as the HBT correlation radii (the preliminary results show also that the correlations of the non-identical particles are well reproduced in our model). Our finding shows that there exists a solution to the long standing RHIC HBT puzzle understood as the impossibility of the consistent description of the spectra and the HBT radii in a single hydrodynamic approach.

The use of the Gaussian initial profile leads to a faster development of the initial transverse flow which makes the system evolution shorter. At the same time the transverse size of the system at freeze-out is slightly larger (as compared to the standard Glauber scenario). These two effects put together lead to the desired reduction of the ratio $R_{\rm out}/R_{\rm side}$. Another important effect helping to describe correctly the data consists of the use of the semi-hard equation of state (with no soft point leading to the extended duration of hadronization) and of the adoption of the single freeze-out scenario which also reduces the emission time, hence, decreasing the radius $R_{\rm out}$.

Of course, the open question remains to find the microscopic mechanism leading to the Gaussian initial conditions. Needless to say, this problem goes far beyond the straightforward application of the hydrodynamics that were discussed here. Alternatively, one may think of other modifications of the initial conditions, such as introducing the initial transverse flow [9,

30, 31] or separating the system into a thermalized core and an outer mantle/corona consisting of independent NN collisions [32–34]. Yet another direction is to study the effects of viscosity [35].

References

[1] D. Teaney, J. Lauret, and E. V. Shuryak, Phys. Rev. Lett. **86**, 4783 (2001).

[2] T. Hirano and K. Tsuda, Phys. Rev. **C66**, 054905 (2002).

[3] P. F. Kolb and U. Heinz (2003). in Quark-Gluon Plasma 3, edited by R.C. Hwa and X.-N. Wang (World Scientific, Singapore, 2004), p. 634, nucl-th/0305084.

[4] P. Huovinen (2003). in Quark-Gluon Plasma 3, edited by R.C. Hwa and X.-N. Wang (World Scientific, Singapore, 2004), p. 600, nucl-th/0305064.

[5] K. J. Eskola, H. Honkanen, H. Niemi, P. V. Ruuskanen, and S. S. Rasanen, Phys. Rev. **C72**, 044904 (2005).

[6] Y. Hama *et al.*, Nucl. Phys. **A774**, 169 (2006).

[7] C. Nonaka and S. A. Bass, Phys. Rev. **C75**, 014902 (2007).

[8] W. Broniowski, M. Chojnacki, W. Florkowski, and A. Kisiel, Phys. Rev. Lett. **101**, 022301 (2008).

[9] M. Chojnacki, W. Florkowski, and T. Csorgo, Phys. Rev. **C71**, 044902 (2005).

[10] M. Chojnacki and W. Florkowski, Phys. Rev. **C74**, 034905 (2006).

[11] M. Chojnacki and W. Florkowski, Acta Phys. Polon. **B38**, 3249 (2007).

[12] A. Kisiel, T. Taluc, W. Broniowski, and W. Florkowski, Comput. Phys. Commun. **174**, 669 (2006).

[13] W. Broniowski, M. Rybczynski, and P. Bozek (2007). arXiv:0710.5731 [nucl-th].

[14] M. Miller and R. Snellings (2003). nucl-ex/0312008.

[15] R. S. Bhalerao, J.-P. Blaizot, N. Borghini, and J.-Y. Ollitrault, Phys. Lett. **B627**, 49 (2005).

[16] PHOBOS Collaboration, S. Manly *et al.*, Nucl. Phys. **A774**, 523 (2006).

[17] S. A. Voloshin (2006). nucl-th/0606022.

[18] R. Andrade, F. Grassi, Y. Hama, T. Kodama, and J. Socolowski, O., Phys. Rev. Lett. **97**, 202302 (2006).

[19] PHOBOS Collaboration, B. Alver *et al.*, Phys. Rev. Lett. **98**, 242302 (2007).

[20] Y. Hama *et al.* (2007). 0711.4544.

[21] B. Alver *et al.*, Phys. Rev. **C77**, 014906 (2008).

[22] S. A. Voloshin, A. M. Poskanzer, and R. Snellings (2008). 0809.2949.

[23] W. Broniowski and W. Florkowski, Phys. Rev. Lett. **87**, 272302 (2001).

[24] W. Broniowski, A. Baran, and W. Florkowski, Acta Phys. Polon. **B33**, 4235 (2002).

[25] PHENIX Collaboration, S. S. Adler *et al.*, Phys. Rev. **C69**, 034909 (2004).

[26] PHENIX Collaboration, S. S. Adler *et al.*, Phys. Rev. Lett. **91**, 182301 (2003).

[27] STAR Collaboration, J. Adams *et al.*, Phys. Rev. **C71**, 044906 (2005).

[28] M. Chojnacki, W. Florkowski, W. Broniowski, and A. Kisiel, Phys. Rev. **C78**, 014905 (2008).

[29] A. Kisiel, W. Broniowski, M. Chojnacki, and W. Florkowski (2008). 0808.3363.

[30] M. Gyulassy, Y. M. Sinyukov, I. Karpenko, and A. V. Nazarenko, Braz. J. Phys. **37**, 1031 (2007).

[31] Y. Sinyukov (2008). talk presented at Quark Matter 2008, Jaipur, India, 4-10 February 2008.

[32] P. Bozek, Acta Phys. Polon. **B36**, 3071 (2005). nucl-th/0506037.

[33] F. Becattini and J. Manninen, J. Phys. **G35**, 104013 (2008). 0805.0098.

[34] P. Bozek (2008). 0811.1918.

[35] S. Pratt and J. Vredevoogd (2008). 0809.0516.

The Remarkable Simplicity and Universality of Multiparticle Production Data

Wit Busza
Massachusetts Institute of Technology

DOI: http://dx.doi.org/10.3204/DESY-PROC-2009-01/35

Abstract

A discussion is given of the remarkable simplicity and universality of multiparticle production data at high energies, in particular in heavy ion collisions.

The question is raised if the reason for this simplicity and universality is trivial or profound and consequences for LHC are considered.

In this talk I will present no new results. It is aimed at those of you who are not experts on heavy ion collisions but who are interested in soft collisions, in particular in the phenomenology and mechanism of multiparticle production in pp and e^+e^- collisions. I want to bring to your attention the fact that there exists today a vast amount of high quality data on multiparticle production in relativistic heavy ion collisions [1–4] and that these data exhibit great similarity to the pp and e^+e^- data [1, 5], and that therefore trends observed in AA data may throw light on our understanding of soft processes in general and not just in AA collisions.

The most remarkable feature of multiparticle production data is its simplicity and universality [6, 7]. It is probably fair to state that as a rule the data exhibit features and trends that are much simpler than the explanations.

In our current understanding of the multiparticle production process in e^+e^-, pp, pA, and AA collisions there are some similarities but overall our picture of each process is quite different. In e^+e^- for example we view the initially produced virtual photon as evolving, through sequential pair production and radiation, into a system of partons that fragment (and/or combine) into the multihadron final state. On the other hand, in the highest energy head-on (central or small impact parameter) heavy ion collisions, the conventional picture is that, viewed in the center of mass frame, two Lorentz contracted disks collide. Each is essentially a dense wall of low momentum strongly interacting gluons together with their sources, the high momentum weakly interacting partons. The gluon walls are the so-called colored glass condensate or CGC [8]. In a very short time ($\leq \frac{1fm}{c}$) after the collision the two gluon walls stop each other and produce a hot equilibrated strongly interacting system with high pressure. At RHIC energies there is general consensus [9] that at the time of equilibration the temperature, pressure and energy density of the system are higher than the critical values obtained in lattice QCD calculations for the hadronic/partonic phase transition. There is also general consensus that the hot system is more like a strongly interacting liquid with extremely low value of the ratio of viscosity to entropy, then that of a weakly interacting gas. The final multihadron state is the last stage of this system as it expands and cools.

The surprising fact is that most of the global trends observed in the collision of all these systems and at all energies are the same. Bringing these trends to your attention is the main aim of my talk.

Before discussing the heavy ion data, I wish to point out that the most extensive set of AA data on multiparticle production of particles into almost the full 4π solid angle comes from the PHOBOS experiment at RHIC [1]. In PHOBOS only charged particles are measured and for the majority of these only the polar and azimuthal angles. Thus only $\frac{d^2N}{d\eta d\phi}$, the particle density in pseudorapidity η and azimuthal angle ϕ space, is measured. In this talk I will not distinguish between rapidity and pseudorapidity. The two are almost identical for particles with speed close to that of light except for polar angles close to zero. Nevertheless it should be remembered that pseudorapidity distributions do distort true rapidity distributions, and conclusions based on pseudorapidity distribution might sometimes be misleading.

The first universal trend worth pointing out is that in AA collisions, as in e^+e^- and pp, for all impact parameter and colliding systems studied, the mid rapidity particle density $\frac{dN}{d\eta}$ increases linearly with the logarithm of the energy of the collision [1], with no signs of any change in the trend as the energy increases. This is despite the fact that the energy range studied to date covers energies low enough where the conditions are such that the initial energy density must be well below critical and furthermore dominated by baryons, and high enough that, almost certainly the initial energy density is above critical and the system created is essentially baryon free.

As proof that this observed simple rate of increase of particle density is neither obvious nor well understood is the observation that the predictions of various authors [10] for the expectations at LHC differ by more than a factor of 2.

At mid rapidity not only does the particle density increase with energy as $ln\sqrt{s}$ ($\sqrt{s}$ is the nucleon-nucleon center of mass energy) but also the amplitude of azimuthal anisotropy of particle production [11], ie. of v_2, the second Fourier coefficient in $\frac{d^2N}{d\phi d\eta} = N_0(1 + 2v_2 cos2\phi)$ with v_1 and higher coefficients neglected.

One of the most prominent universal features of all multiparticle production data is "extended longitudinal scaling" [1], an extended (in rapidity) version of "limiting fragmentation". Plotting $\frac{dN}{d\eta}$ as a function of η, boosted to the rest frame of either of the two colliding systems, we find that as $\sqrt{s}$ increases, $\frac{dN}{d\eta}(\eta)$ is independent of $\sqrt{s}$ for a bigger and bigger range of η. Extended longitudinal scaling appears to be valid not only for $\frac{dN}{d\eta}(\eta)$ but also for $v_2(\eta)$ [1]. An instructive way of visualizing and obtaining an intuitive understanding of extended longitudinal scaling is to consider the outcome of the collision of two beams, say yellow and blue, whose energies can be set independently. Extended longitudinal scaling would manifest itself as follows. For a given energy of the yellow beam, as the energy of the blue beam is increased $\frac{dN}{d\eta}$ and v_2 increases until it reaches a maximum value. Once this value is reached, increasing the blue beam energy further, even to infinity, has no effect on $\frac{dN}{d\eta}$ or v_2. The maximum values of these quantities (ie. point on the limiting curve) can be increased only by increasing the energy of the yellow beam. This phenomenon is seen for all colliding systems and is a direct manifestation of some kind of universal saturation phenomenon.

It is interesting to note that the limiting curve for $\frac{dN}{d\eta}$, to within the precision of the data, is a straight line with $\frac{dN}{d\eta}$ close to zero at a value of η corresponding to one of the colliding systems at rest. This fact, together with the fact that the difference of rapidity between the colliding systems $\sim ln\sqrt{s}$ and also $\frac{dN}{d\eta}|_{y=0} \sim ln\sqrt{s}$ (with $\sqrt{s}$ in GeV), imply that the shape of the $\frac{dN}{d\eta}(\eta)$ distributions are independent of energy. This similarity of $\frac{dN}{d\eta}(\eta)$ distributions at all energies, to

fairly high precision, is seen in e^+e^-, pp, pA, and AA collisions. From these facts it also follows that the total charged particle multiplicity increases linearly with $ln^2\sqrt{s}$ (with $\sqrt{s}$ in GeV), which again is consistent with observation for all colliding systems studied [7].

Another prominent feature in AA collisions is that the energy dependence and system dependence are to a large degree independent of each other. For example, at all energies, the total charged particle multiplicity scale in the same linear manner with the total number N_{part} of nucleons participating in the collision [1](the so-called participant scaling first observed in pA collisions [12]), and the fractional increase with N_{part} of the mid rapidity particle density is independent of the energy [1,13]. These two features are quite surprising. Naively one would expect the fraction of soft and hard collisions to change with energy and therefore so also the N_{part} dependence. Furthermore it is hard to understand what mechanism gives rise to the apparent number conservation of produced particles per participant under conditions when the distribution with rapidity of the produced particles changes significantly. For example, how is it that by changing the impact parameter of the collision one exchanges, one for one, a 100 GeV particle for one 1 GeV particle (the energy being conserved through increases in transverse momentum of many particles)?

Below I give other examples of facts that can be simply stated but that have no simple explanations.

In both AA and in pp there are hard collisions. There is one difference: in AA per nucleon-nucleon collision fewer high transverse momentum particles are produced. This is the so-called "jet quenching" phenomenon [14]. All theoretical estimates, based on the hypothesis that jet-quenching is due to energy loss of the recoiling parton in the high density medium, predict a weak P_t dependence of the suppression of the high P_t particles. In reality the suppression, up to the highest P_t values measured ($\leq 20\frac{GeV}{c}$), seems to be independent of P_t [15]. Furthermore the magnitude of this suppression is not that different from the suppression of the high $x_{Feynmann}$ forward particles in pA collisions at all energies studied [16]. In both cases, as a first approximation, one can qualitatively explain the data with the simple assumption that the central part of the nucleus is totally absorbing and only particles originating along the periphery of the nucleus survive.

A final example is the striking observation that for a given impact parameter of an AA collision at a given energy, if $\frac{v_2}{n}$ is plotted as a function of $\frac{KE}{n}$, where n is the number of valence quarks in the produced particle and KE is its kinetic energy, the data for all produced particles fall on a universal curve [17]. This is taken as evidence of the existence in the intermediate state of a system with quark degrees of freedom followed by coalescence. This interpretation of the general features of this data is highly plausible, however it is difficult to understand why all the data fall with such high precision on one curve.

To conclude, through this talk I have attempted, on the one hand to bring to your attention the fact that there exists a large body of very high quality data on multiparticle production in AA collisions, and on the other, to point out the interesting curiosity that on the whole the data is simpler and more universal than the current explanations of it.

I do not understand this fact and I am intrigued by it. Is the remarkable simplicity and universality of the data an accident? If not, is it trivial or profound? Is it possible that we are

simply wrong or missing something fundamental in our current interpretation of the facts?

In the not too distant future, multiparticle production data in PbPb collisions will become available at an energy 27 times higher than the highest energy data at RHIC. The trends discussed in this talk, when extrapolated to LHC energies suggest that the following will be seen at LHC [7, 10]: 1) extended longitudinal scaling and N_{part} scaling, 2) for PbPb collisions with N_{part}=386 (top 3% centrality) at $\sqrt{s}$=5500 GeV, $N_{charged}$=15000 $\pm$ 1000, 3) for PbPb collisions at $\sqrt{s}$=5500 GeV, for the 40% most central collisions, v_2=0.075 $\pm$ 0.005, 4) $\frac{v_2}{n}$ will continue to be a universal function of $\frac{KE}{n}$, 5) the suppression of high P_t hadrons at mid rapidity, will continue to be independent of P_t (with $R_{AA} \sim 0.2$ for the most central PbPb collisions), 6) for non-single-diffractive pp collisions at $\sqrt{s}$= 14000 GeV (10000 GeV), $N_{charged}$=70$\pm$8 (65$\pm$8), 7) for inelastic pp collisions at $\sqrt{s}$ = 14000 GeV (10000 GeV), $N_{charged}$=60$\pm$10 (56$\pm$9).

If most of these extrapolations turn out to be consistent with LHC data, more than ever it will become crucial that a coherent explanation can be found for the continued simplicity and universality of the data.

On the other hand, if some or all of the results turn out to be very different from these extrapolations, it will be a strong indication of the onset of new physics at LHC.

References

[1] PHOBOS Collaboration, B. B. Back *et al.,* Nucl. Phys. **A757**, 28 (2005). nucl-ex/0410022.

[2] STAR Collaboration, J. Adams *et al.,* Nucl. Phys. **A757**, 102 (2005). nucl-ex/0501009.

[3] BRAHMS Collaboration, I. Arsene *et al.,* Nucl. Phys. **A757**, 1 (2005). nucl-ex/0410020.

[4] PHENIX Collaboration, K. Adcox *et al.,* Nucl. Phys. **A757**, 184 (2005). nucl-ex/0410003.

[5] UA5 Collaboration, G. J. Alner *et al.,* Z. Phys. **C33**, 1 (1986).

[6] W. Busza, Acta Phys. Polon. **B35**, 2873 (2004). nucl-ex/0410035.

[7] W. Busza, J. Phys. **G35**, 044040 (2008). 0710.2293.

[8] L. McLerran. Talk given at ISMD08;
K. Itakura. Talk given at ISMD08.

[9] E. . Rischke, D. and e. . Levin, G. Prepared for Workshop on New Discoveries at RHIC: The Current Case for the Strongly Interactive QGP, Brookhaven, Upton, New York, 14-15 May 2004.

[10] E. . Armesto, N. *et al.,* J. Phys. **G35**, 054001 (2008). 0711.0974.

[11] NA49 Collaboration, C. Alt *et al.,* Phys. Rev. **C68**, 034903 (2003). nucl-ex/0303001.

[12] W. Busza *et al.,* Phys. Rev. Lett. **34**, 836 (1975);
W. Busza *et al.* Invited paper presented at Topical Meeting on High Energy Collisions involving Nuclei, Trieste, Sep 9-14, 1974.

[13] PHOBOS Collaboration, B. B. Back *et al.,* Phys. Rev. **C74**, 021902 (2006).

[14] PHENIX Collaboration, K. Adcox *et al.,* Phys. Rev. Lett. **89**, 212301 (2002). nucl-ex/0204005.

[15] PHENIX Collaboration, A. Adare *et al.* (2008). 0801.4020.

[16] D. S. Barton *et al.,* Phys. Rev. **D27**, 2580 (1983).

[17] PHENIX Collaboration, A. Adare *et al.,* Phys. Rev. Lett. **98**, 162301 (2007). nucl-ex/0608033;
STAR Collaboration, J. Adams *et al.,* Phys. Rev. Lett. **92**, 052302 (2004). nucl-ex/0306007.

Heavy ions and parton saturation from RHIC to LHC

A. Dainese
INFN - Laboratori Nazionali di Legnaro, Legnaro (Padova), Italy
DOI: http://dx.doi.org/10.3204/DESY-PROC-2009-01/52

Abstract
The phenomenology of gluon saturation at small parton momentum fraction, Bjorken-x, in the proton and in the nucleus is introduced. The experimentally-accessible kinematic domains at the nucleus–nucleus colliders RHIC and LHC are discussed. Finally, the saturation hints emerging from measurements at RHIC and the perspectives for LHC are described.

1 Introduction: small-x gluons in the proton and in the nucleus

In the collinear factorization approach of perturbative QCD, the parton distribution functions (PDFs) of the proton are determined through global fits obtained using the DGLAP scale evolution equations [1–3]. The HERA ep deep inelastic scattering (DIS) data on the proton structure function $F_2(x, Q^2)$ as a function of the parton momentum fraction Bjorken-x and of the squared momentum transfer Q^2, and, especially, the Q^2 slope, $\partial F_2(x, Q^2)/\partial \ln Q^2$, in the small-$x$, $3 \times 10^{-5} \lesssim x \lesssim 5 \times 10^{-3}$, and small-$Q^2$ region, $1.5 \lesssim Q^2 \lesssim 10$ GeV^2, set rather stringent constraints on the small-x gluon distribution $xg(x, Q^2)$. In this kinematic region, the gluon distribution exhibits a strong rise towards low x and the agreement of the global fits with the HERA $F_2(x, Q^2)$ data is not as good as it is at larger values of x and Q^2 [4]. In particular, the gluon density xg tends to rise faster than what suggested by the data. This is due to the fact that the kernels of the DGLAP equations only describe splitting of one parton into two or more, so that the resulting evolution is linear in the PDFs. At low Q^2, the small-x gluon density may increase to the point where gluon fusion, $\mathrm{gg} \to \mathrm{g}$, becomes significant. Within the DGLAP framework, this phenomenology can be accounted for in an effective way by including nonlinear corrections in the evolution equations, that is, negative terms of order $\mathcal{O}(g^2)$, $\mathcal{O}(g^3)$, etc... that tame the evolution towards small x. The first nonlinear corrections, the GLRMQ terms, were derived in Ref. [5,6]. A more accurate description of the small-x nonlinearities is achieved in the framework of k_{t}-factorization, in which the BK equation [7, 8] is used to evolve the PDFs as a function of x for fixed transverse momentum squared, k_{t}^2, of the gluon. Both approaches to nonlinear gluon dynamics, in DGLAP and in BK, suggest that one can expected potentially-measurable effects in pp collisions at LHC energy, for example in heavy-flavour production [9].

In the case of proton–nucleus and nucleus–nucleus collisions, where nuclei with large mass number A are involved, the nonlinear effects are enhanced by the larger density of gluons per unit transverse area of the colliding nuclei. The high density of gluons at small x and small Q^2 induces a suppression of the observed hard scattering yields with respect to expectations based on a scaling with the number of binary nucleon–nucleon collisions. This reduction affects the kinematic region dominated by small-x gluons: low transverse momentum p_{t} and forward rapidity y, since, at leading order, we have $x \sim p_{\mathrm{t}} \exp(-y)/\sqrt{s_{\mathrm{NN}}}$. The effect, indicated as

nuclear shadowing, is usually accounted for in terms of a modification of the parton distribution functions of the nucleon in the nucleus, $f_i^{\rm A}(x,Q^2)$, with respect to those of the free nucleon, $f_i^{\rm N}(x,Q^2)$:

$$R_i^{\rm A}(x,Q^2) = \frac{f_i^{\rm A}(x,Q^2)}{f_i^{\rm N}(x,Q^2)} \tag{1}$$

where $i = {\rm q_v}, {\rm q_{sea}}, {\rm g}$ for valence quarks, sea quarks, and gluons. We have shadowing, $R_{\rm g}^{\rm A} < 1$, for $x \lesssim 5 \times 10^{-2}$. However, as we will discuss in the following, the strength of the reduction is constrained by existing experimental data only for $x \gtrsim 10^{-3}$.

The use of nuclear-modified parton distribution functions allows high-density effects at small x to be accounted for within the framework of perturbative QCD collinear factorization. However, factorization is expected to break down when the gluon phase-space becomes *saturated*. In these conditions, in the collision with an incoming projectile parton, the partons in the target nuclear wave function at small x would act coherently, not independently as assumed with factorization. In the limit, they may form a Colour Glass Condensate (CGC) [10]: a system, that can be describe in analogy to a spin glass, where gluons (colour charges) have large occupation number, as in a condensate. The relevant parameter in the CGC is the so-called saturation scale $Q_{\rm S}^2$, defined as the scale at which the transverse area of the nucleus is completely saturated and gluons start to overlap. This happens when the number of gluons, $\sim {\rm A}\, xg(x,Q_{\rm S}^2)$, multiplied by the typical gluon size, $\sim 1/Q_{\rm S}^2$, is equal to the transverse area, $\sim \pi R_{\rm A}^2$. Thus:

$$Q_{\rm S}^2 \sim \frac{{\rm A}\, xg(x,Q_{\rm S}^2)}{\pi R_{\rm A}^2} \sim \frac{{\rm A}\, xg(x,Q_{\rm S}^2)}{{\rm A}^{2/3}} \sim {\rm A}^{1/3} x^{-\lambda} \sim {\rm A}^{1/3} (\sqrt{s_{\rm NN}})^{\lambda} e^{\lambda y}\,, \quad \text{with } \lambda \approx 0.3. \tag{2}$$

$Q_{\rm S}^2$ grows at forward rapidity, at high c.m.s. energy , and it is enhanced by a factor about 6 ($200^{1/3}$) in the Au or Pb nucleus, with respect to the proton. Saturation affects the processes in the region $Q^2 \lesssim Q_{\rm S}^2$, where gluon recombination dominates and factorization may start to become invalid.

2 Exploring the saturation region

Figure 1, elaborated from Ref. [11], shows the experimental acceptances in the plane (x, Q^2) for: the nuclear DIS (lepton–nucleus) experiments NMC, SLAC-E139, FNAL-E665, EMC; the nuclear Drell-Yan (lepton–nucleus) experiment FNAL-E772; the RHIC (dAu) experiments BRAHMS and PHENIX; the experiments in preparation at LHC, ALICE, ATLAS, CMS, LHCb.

The current knowledge of the nuclear modification of the PDFs is based on the nuclear DIS data, reaching down to $x \gtrsim 10^{-3}$. As it can be seen from the figure, the LHC will give access to an unexplored small-x domain of QCD. There are several model extrapolations of the amount of nuclear shadowing in this region, with $R_g^{\rm Pb}(x,Q^2)$ ranging from 0.1 to 0.8 at $x \sim 10^{-4}$ and $Q^2 \sim 2\ {\rm GeV}^2$ (see e.g. Ref. [12]).

The estimated values of the saturation scale in heavy-ion collisions at RHIC and LHC are reported in the figure. For a Au nucleus probed at RHIC energy, $\sqrt{s_{\rm NN}} = 200\ {\rm GeV}$, the estimated saturation scale is $Q_{\rm S}^2 \sim 2\ {\rm GeV}^2$: processes that involve gluons at $x < 10^{-3}$–10^{-2} are affected. For a Pb nucleus probed at LHC energy, $\sqrt{s_{\rm NN}} = 5.5\ {\rm TeV}$, the estimated saturation scale is $Q_{\rm S}^2 \sim$

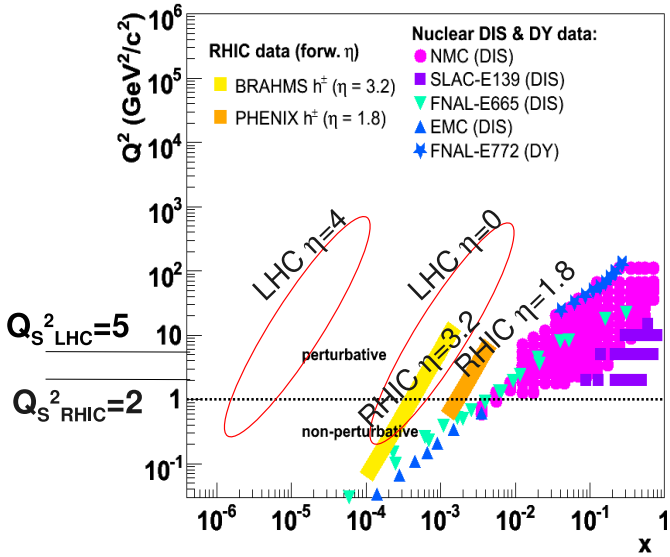


Fig. 1: The kinematic regions in x and Q^2 explored by nuclear DIS and Drell-Yan experiments, by RHIC experiments, and by experiments in preparation at LHC. Elaborated from a compilation in Ref. [11].

$5\ \mathrm{GeV}^2$: processes that involve gluons at $x < 10^{-4}$–10^{-3} are affected. The line at $Q^2 = 1\ \mathrm{GeV}^2$ shows the lower limit of applicability of the perturbative QCD approach. At variance from RHIC, where the perturbative region and the saturation region have little overlap, at the LHC it will be possible to explore the saturation region with perturbative probes, like heavy quarks, and $\mathrm{c\overline{c}}$ in particular. This means that discrepancies between charm production measurements close to the threshold and perturbative predictions could signal the onset of saturation effects. We will further discuss this point in Section 4.2. Another very promising approach to the investigation of small-x effects is by measuring hard process (jets, heavy quarks, weak-interaction vector bosons) in the forward rapidity region (see Section 4.1).

3 Hints of saturation at RHIC

Two experimental observations in heavy-ion collisions at RHIC support the saturation predictions of a reduced parton flux in the incoming ions due to nonlinear QCD effects. On one hand, the measured hadron multiplicities (see e.g. Ref. [13]), $\mathrm{d}N_{\mathrm{ch}}/\mathrm{d}\eta \approx 700$, are significantly lower than the $\mathrm{d}N_{\mathrm{ch}}/\mathrm{d}\eta \approx 1000$ values predicted by minijet [14] or Regge [15] models, but are well reproduced by CGC approaches [16]. Assuming parton–hadron duality, hadron multiplicities at mid-rapidity rise proportionally to Q_{S}^2 times the transverse (overlap) area [17], a feature that accounts naturally for the experimentally-observed factorization of $\sqrt{s_{\mathrm{NN}}}$- and centrality-dependences in $\mathrm{d}N_{\mathrm{ch}}/\mathrm{d}\eta$ (Fig. 2, left). The second possible manifestation of CGC-like effects in the RHIC data is the BRAHMS observation [18] of suppressed yields of semi-hard hadrons ($p_{\mathrm{t}} \approx$ 2–4 GeV/c) in dAu relative to pp collisions at forward rapidities (up to $\eta \approx 3.2$, Fig. 2, right). Hadron production at such small angles is sensitive to partons in the Au nucleus with

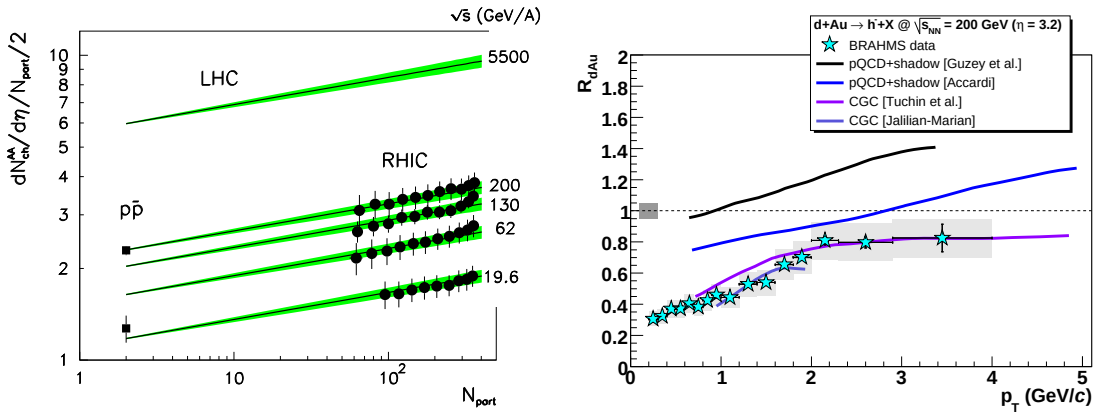


Fig. 2: Hints of saturation at RHIC. Left: Normalized $\mathrm{d}N_{\mathrm{ch}}/\mathrm{d}\eta$ as a function of c.m.s. energy and centrality (given in terms of the number of nucleons participating in the collision, N_{part}) measured by PHOBOS in Au–Au [13] compared with saturation predictions [17]. Right: Nuclear modification factor $R_{\mathrm{dAu}}(p_{\mathrm{t}})$ for negative hadrons at η = 3.2 in dAu at $\sqrt{s_{\mathrm{NN}}}$ = 200 GeV: BRAHMS data [18] compared to pQCD [19, 20] and CGC [21, 22] predictions.

$x^{\mathrm{min}} \sim p_{\mathrm{t}} \exp(-\eta)/\sqrt{s_{\mathrm{NN}}} \sim 10^{-3}$ [19]. The observed nuclear modification factor, $R_{\mathrm{dAu}} \approx 0.8$, cannot be reproduced by pQCD calculations [19, 20] that include the same nuclear shadowing that describes the dAu data at $\eta = 0$, but can be described by CGC approaches that parametrise the Au nucleus as a saturated gluon wavefunction [21, 22].

4 Perspectives for LHC

4.1 Accessing the small-x region with hard processes at forward rapidity

The four LHC experiments —i.e. the two general-purpose and high-luminosity ATLAS and CMS detector systems as well as the heavy-ion-dedicated ALICE and the heavy-flavour-oriented LHCb experiments— have all detection capabilities in the forward direction very well adapted for the study of low-x QCD phenomena with hard processes in collisions with proton and ion beams (see e.g. Ref. [23] for more details):

- Both CMS and ATLAS feature hadronic calorimeters in the range $3< |\eta| <5$ which allow them to measure jet cross-sections at very forward rapidities. Both experiments feature also zero-degree calorimeters (ZDC, $|\eta| \gtrsim 8.5$ for neutrals), which are a basic tool for neutron-tagging "ultra-peripheral" Pb–Pb photoproduction interactions. CMS has an additional electromagnetic/hadronic calorimeter (CASTOR, $5.3 < |\eta| < 6.7$) and shares the interaction point with the TOTEM experiment providing two extra trackers at very forward rapidities (T1, $3.1 < |\eta| < 4.7$, and T2, $5.5 < |\eta| < 6.6$) well-suited for DY measurements.
- The ALICE forward muon spectrometer at $2.5 < \eta < 4$, can reconstruct J/ψ and Υ (as well as Z^0) in the di-muon channel, as well as statistically measure single inclusive heavy-quark production via semi-leptonic (muon) decays. ALICE counts also on ZDCs in both

sides of the interaction point for forward neutron triggering of Pb–Pb photoproduction processes.

- LHCb is a single-arm spectrometer covering rapidities $1.8 < \eta < 4.9$, with very good particle identification capabilities designed to accurately reconstruct charm and beauty hadrons. The detector is also well-suited to measure jets, $Q\overline{Q}$ and $Z^0 \to \mu\mu$ production in the forward hemisphere.

4.2 Probing small-x gluons with heavy quarks

As already mentioned, at LHC it will be possible to probe the saturation region with perturbative probes, such as heavy quarks. The x regime relevant for charm production in heavy-ion collisions at LHC ($x \gtrsim 2m_{\rm c}\exp(-y)/\sqrt{s_{\rm NN}}$) extends down to $x \sim 10^{-4}$ already at central rapidity $y = 0$ and down to $x \sim 10^{-6}$ at forward rapidity $y \approx 4$ [24]. Charm (and beauty) production cross sections at small $p_{\rm t}$ and forward rapidity are thus expected to be significantly affected by parton dynamics in the small-x region. As an example, the EKS98 parametrisation [25] of the PDFs nuclear modification, shown in Fig. 3 (centre) for $Q^2 = 5\ {\rm GeV}^2$, predicts a reduction of the charm (beauty) cross section at NLO of about 35% (20%) in Pb–Pb at 5.5 TeV and 15% (10%) in pPb at 8.8 TeV [24].

The comparison of heavy-quark production in pp and pPb collisions (where final-state effects, such as parton energy loss, are not expected to be present) is regarded as a sensitive tool to probe nuclear PDFs at LHC energy. The ratio of invariant-mass spectra of dileptons from heavy-quark decays in pPb and pp collisions would measure the nuclear modification $R_{\rm g}^{\rm Pb}$ [26]. Another promising observable in this respect is the nuclear modification factor of the D meson $p_{\rm t}$ distribution, defined as:

$$R^{\rm D}_{\rm pA(AA)}(p_{\rm t},\eta) = \frac{1}{\langle N_{\rm coll}\rangle} \times \frac{{\rm d}^2N^{\rm D}_{\rm pA(AA)}/{\rm d}p_{\rm t}{\rm d}\eta}{{\rm d}^2N^{\rm D}_{\rm pp}/{\rm d}p_{\rm t}{\rm d}\eta}\,. \tag{3}$$

In Fig. 3 (right) we show the sensitivity of $R^{\rm D}_{\rm pPb}$ to different shadowing scenarios, obtained by varying the modification of the PDFs in the Pb nucleus (displayed, for gluons, by the curves labeled 'a', 'b', 'c' and 'EKS98' in the left panel of the same figure). The ALICE experiment will be able to measure D meson production down to almost zero transverse momentum, at central rapidity [27]. As shown by the projected experimental uncertainties on the $\rm D^0$ nuclear modification factor in pPb, reported in the left panel of Fig. 3, this measurement is expected to be sensitive to the level of nuclear shadowing at LHC.

Charmonium production at low $p_{\rm t}$ and forward rapidity is another promising probe of small-x gluons at LHC. All four LHC experiments are expected to have good capability for J/ψ reconstruction in the central and in the forward rapidity region. In particular, ALICE will provide a measurement via di-muons in $2.5 < y < 4$ down to $p_{\rm t} \approx 0$ [27], which probes the poorly-known region $x < 10^{-5}$ where current PDF parametrisations have large uncertainties. Figure 4 shows the J/ψ rapity-differential cross section at NLO from the Color Evaporation Model [30], in $2.5 < y < 4$ with different PDF sets, compared to the projected precision of the ALICE measurement [29].

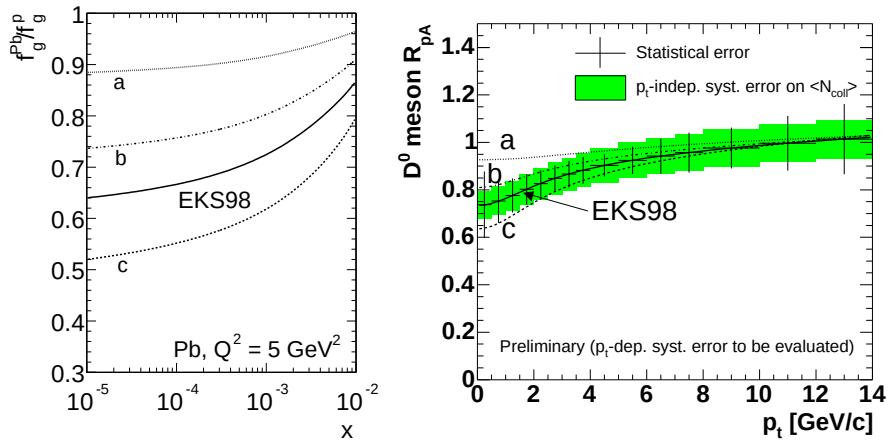


Fig. 3: Charm production in p–Pb at LHC. Left: EKS98 [25] parametrisation for the modification of the gluon PDF in a Pb nucleus at $Q^2 = 5\ \mathrm{GeV}^2 \simeq 4\,m_c^2$, along with three other different scenarios. Right: corresponding $R_{\mathrm{pA}}^{\mathrm{D}}$ in p–Pb at $\sqrt{s_{\mathrm{NN}}} = 8.8$ TeV and expected sensitivity of the ALICE experiment with the $\mathrm{D}^0 \to \mathrm{K}^-\pi^+$ measurement at central rapidity ($|\eta| < 0.9$), with one year of data taking at nominal LHC luminosity [28].

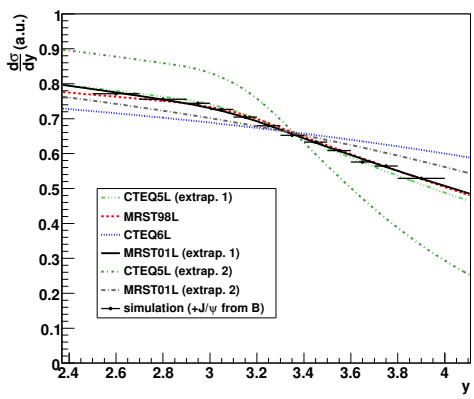


Fig. 4: J/ψ production in pp at LHC. Cross section as a function of rapidity as predicted using different PDF sets (details in the text) , compared to the projected precision of the measurement of the ALICE experiment [29].

.

5 Summary

We have discussed how gluons nonlinear evolution and the phonomenology of saturation are expected to set on at small x in the hadrons, and how these effects are enhanced by the higher transverse gluon density in large nuclei. The study of this almost unexplored regime can provide fundamental insight on the high-energy limit of QCD. We have described the experimental indications of the onset of saturation in heavy-ion collisions at RHIC. The LHC, as a heavy-ion collider, will be a unique laboratory for the investigation of the saturation regime with perbura-

tive probes, such as forward rapidity hard processes and heavy quarks at low momentum and/or forward rapidity.

Acknowledgements: I am grateful to the organizers of the International Symposium on Multiparticle Dynamics 2008 for the invitation and support. I warmly thank D. d'Enterria for stimulating discussions and for providing useful material for the preparation of this contribution, and K. Kutak for valuable comments on the manuscript.

References

[1] Y. L. Dokshitzer, Sov. Phys. JETP **46**, 641 (1977).

[2] V. N. Gribov and L. N. Lipatov, Sov. J. Nucl. Phys. **15**, 438 (1972).

[3] G. Altarelli and G. Parisi, Nucl. Phys. **B126**, 298 (1977).

[4] A. D. Martin, R. G. Roberts, W. J. Stirling, and R. S. Thorne, Eur. Phys. J. **C35**, 325 (2004).

[5] L. V. Gribov, E. M. Levin, and M. G. Ryskin, Nucl. Phys. **B188**, 555 (1981).

[6] A. H. Mueller and J.-w. Qiu, Nucl. Phys. **B268**, 427 (1986).

[7] I. Balitsky, Nucl. Phys. **B463**, 99 (1996).

[8] Y. Kovchegov, Phys. Rev. **D60**, 034008 (1999).

[9] J. Baines *et al.* (2006). hep-ph/0601164.

[10] E. Iancu and R. Venugopalan, World Scientific, Singapore. hep-ph/0303204.

[11] D. G. d'Enterria, Eur. Phys. J. **A31**, 816 (2007). hep-ex/0610061.

[12] K. J. Eskola, H. Paukkunen, and C. A. Salgado, JHEP **07**, 102 (2008). 0802.0139.

[13] B. B. Back *et al.*, Nucl. Phys. **A757**, 28 (2005). nucl-ex/0410022.

[14] M. Gyulassy and X.-N. Wang, Comput. Phys. Commun. **83**, 307 (1994). nucl-th/9502021.

[15] A. Capella, U. Sukhatme, C.-I. Tan, and J. Tran Thanh Van, Phys. Rept. **236**, 225 (1994).

[16] L. D. McLerran and R. Venugopalan, Phys. Rev. **D50**, 2225 (1994). hep-ph/9402335.

[17] N. Armesto, C. A. Salgado, and U. A. Wiedemann, Phys. Rev. Lett. **94**, 022002 (2005). hep-ph/0407018.

[18] I. Arsene *et al.*, Nucl. Phys. **A757**, 1 (2005). nucl-ex/0410020.

[19] V. Guzey, M. Strikman, and W. Vogelsang, Phys. Lett. **B603**, 173 (2004). hep-ph/0407201.

[20] A. Accardi, Acta Phys. Hung. **A22**, 289 (2005). nucl-th/0405046.

[21] D. Kharzeev, Y. Kovchegov, and K. Tuchin, Phys. Lett. **B599**, 23 (2004).

[22] J. Jalilian-Marian, Nucl. Phys. **A748**, 664 (2005). nucl-th/0402080.

[23] D. G. d'Enterria (2006). hep-ph/0610061.

[24] N. Carrer and A. Dainese (2003). hep-ph/0311225.

[25] K. J. Eskola, V. J. Kolhinen, and C. A. Salgado, Eur. Phys. J. **C9**, 61 (1999). hep-ph/9807297.

[26] A. Accardi *et al.* (2004). hep-ph/0308248.

[27] B. Alessandro *et al.*, J. Phys. **G32**, 1295 (2006).

[28] R. Grosso, PhD Thesis, Università di Trieste (2004).

[29] D. Stocco, PhD Thesis, Università di Torino (2008).

[30] M. Bedjidian *et al.* (2003). hep-ph/0311048.

Probing the Properties of the Matter Created at RHIC.

Helen Caines
Physics Department, Yale University, New Haven, CT, U.S.A
DOI: http://dx.doi.org/10.3204/DESY-PROC-2009-01/53

Abstract
I discuss the use of high momentum particles as calibrated probes of the medium created in heavy-ion collisions at RHIC. Since high Q^2 processes only happen in the first stages of the collisions the scattered partons must pass through the produced medium before leaving the collision region. Their modifications, with respect to those from p-p collisions, due to this interaction with the medium provides valuable information on the properties of the medium.

1 Introduction

At RHIC there is strong evidence that heavy-ion collisions at $\sqrt{s_{NN}}$ = 200 GeV produce a strongly coupled plasma whose constituents are quarks and gluons - known as the strongly coupled Quark-Gluon Plasma, sQGP. A number of striking discoveries were made within the first three years of RHIC's operations and are detailed in the four experiment's "white papers" [1–4]. Having established that a sQGP is created we are now in the process of determining the properties of this new state of matter. One technique we are using to probe the medium is that of comparing the products of hard scattered partons in p-p to those in A-A. Parton-parton scatterings with high Q^2 occur during the initial stages of the interactions at RHIC energies. Since the production takes place at an early stage we have direct access to the hot and dense core of the reaction. In p-p collisions the jet cross-section can be directly calculated from pQCD. In Au-Au collisions the hard scattered partons must first traverse the hot and dense medium created before escaping the collision region. By observing the suppression and modification patterns of the fragmentation products in Au-Au compared to those in p-p we can learn about the properties of the sQGP.

2 The p-p Baseline

Before examining the Au-Au data, we needed to ensure that we can indeed describe the jet properties in p-p collisions at $\sqrt{s_{NN}}$ =200 GeV. Measurements of the total jet cross-section [5] and the identified particle p_T spectra (for example [6,7]) show that there is remarkable agreement to the data confirming that hard processes with light quarks and gluons are a well calibrated probe. Recently preliminary charged particle fragmentation functions as a function of jet energy have also been reported [8]. Figure 1 shows the ξ=log(E^{jet}/p^{hadron}) distributions compared to PYTHIA (v6.4) [9] for reconstructed leading jet energies of 30-40 GeV, using two different radii for the jet finding midpoint cone algorithm. The PYTHIA simulations were passed through the experiment's GEANT detector response simulators. The overall agreement indicates that next-to-leading order corrections are not very large, since these effects are not included in the PYTHIA simulation.

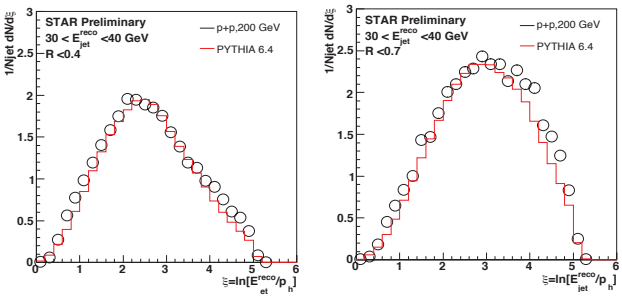


Fig. 1: Preliminary charged particle dN/dξ distributions for leading jets reconstructed with energies from 30-40 GeV. The left plot is for jet cone radii of R=0.4, the right for R=0.7. Only statistical errors are shown.

3 Nuclear Modification Factors and Di-hadron Correlations

Having convinced ourselves that we have a well calibrated probe via jet studies in p-p we turn our attention to the heavy-ion data. Before attempting full jet reconstruction we first looked at the inclusive high p_T particle spectra. At high p_T it is expected that particle production is dominated by fragmentation of hard scattered partons. If these partons do not interact with the medium the particle production rate should scale with the number of binary nucleon-nucleon collisions (N_{bin}) in the initial interaction. In this case the nuclear modification factor, $R_{AA}(p_T)$ (defined as the yields in A-A divided by the N_{bin} scaled p-p yields), at high p_T should be unity. If however the partons lose energy interacting with the sQGP the R_{AA} at high p_T should be suppressed.

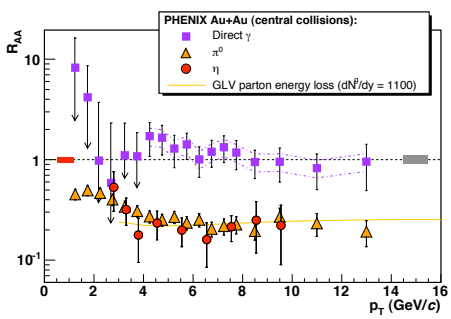


Fig. 2: The R_{AA} of direct γ, π^0, and η for central Au-Au events at $\sqrt{s_{NN}}$ = 200 GeV. The solid curves show the predictions from model calculations incorporating parton energy loss.

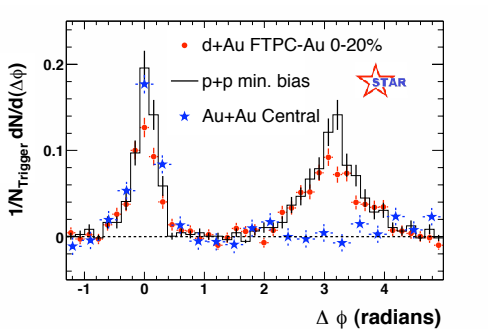


Fig. 3: Di-hadron correlations for p-p, d-Au, and Au-Au collisions at $\sqrt{s_{NN}}$ =200 GeV. p_T^{trig} = 4 GeV/c and $p_T^{ass} > 2$ GeV/c.

The measured R_{AA} for π^0, η, and direct γ are shown in Fig. 2 for central Au-Au collisions at $\sqrt{s_{NN}}$ =200 GeV [10]. The π^0 and η shown a large suppression of a factor five while the photons follow N_{bin} scaling. This scaling of the γ is predicted since they carry no color charge and have mean-free paths (or attenuations lengths) larger than the size of the medium. All hadrons measured to date, including those from heavy flavor decays, show an equivalent suppression at

high p_T for central data. The level of suppression decreases for peripheral collisions.

The theoretical description that is emerging to describe the R_{AA} results is that the partons undergo significant gluon radiation which is induced by their traversing a dense colored medium. The mean parton energy loss is proportional to the gluon density of the sQGP and dependent on the distance that the parton travels through it. Several theoretical models have been suggested to describe the data either via the gluon density or the transport coefficient $\hat{q}$, which is the mean k_T^2 transferred to the medium per unit length, see for example [11–14]. While all models are based on induced gluon radiation they differ in the methods used to calculate the energy loss. The obtained values of $\hat{q}$ calculated via these models vary between $\hat{q} \approx$ 1-13 [15]. Different observables are therefore required to uniquely identify those properties of the medium that cause the R_{AA} suppression as a function of N_{part}. Di-hadron correlations are one such measurement. These correlations are made by studying the distributions of the azimuthal difference, $\Delta(\phi)$, of all associated particles with $p_T > p_T^{ass}$ with respect to trigger particles with $p_T > p_T^{trig}$. Hadrons resulting from the fragmentation of the same parton will form a peak at $\Delta(\phi)$=0 while those associated with the backwards scattered parton form a peak at $\Delta(\phi)=\pi$. In p-p and d-Au collisions these two peaks are clearly observed (Fig. 3). In the most central Au-Au data however, the back scattered (away-side) peak disappears [16], indicated by the blue stars in Fig. 3. The fact that the away-side peak is evident in d-Au collisions means that the jet quenching signal observed in Au-Au is clearly not an intial but a final state effect due to the sQGP.

The near- and away-side peak particle yields were measured as a function of the number of participants, N_{part}, for Au-Au and Cu-Cu events at $\sqrt{s_{NN}}$ = 200 GeV. For the near-side the particle yield per trigger is the same for Au-Au and Cu-Cu collisions, independent of N_{part}, and the same as that measured for d-Au collisions. This suggests that the near-side peak is the result of unmodified vacuum fragmentation. The away-side yield is the same in Cu-Cu and Au-Au for a fixed N_{part} but the yields fall strongly as the centrality increases [17]. Both [11] and [14] have tried to describe these results. Neither group describes the low N_{part} behavior on the away-side well but they do show reasonable agreement with the shape of the N_{part} suppression in Au-Au. The authors of [14] also matches the data independence on colliding species while [11] predicted a stronger suppression at a fixed N_{part} for the Cu-Cu data.

Since these di-hadron correlations are not performed on an event-by-event basis we cannot calculate true fragmentation functions. Instead we approximate an average fragmentation function by calculating $z_T = p_T^{ass}/\, p_T^{trig}$. This Au-Au di-hadron fragmentation function, $D_{AA}(z_T)$, is then compared to that from p-p collisions. The away-side $D_{AA}(z_T)$ for Au-Au and Cu-Cu for different centralities are shown in the left panel of Fig. 4. The right panel shows the away-side I_{AA}, the binary scaled yield of particles in the jet correlation ratio of Au-Au to p-p data, as a function of z_T. Several interesting effects emerge from these plots. First the similarity of the Cu-Cu and Au-Au data for the same N_{part} is preserved as a function of z_T. Second the suppression of the more central events is not a shape modification but a uniform suppression over the measured range of z_T. This suggests that what we are observing on the away-side is energy loss of the parton *in* the medium followed by vacuum fragmentation *outside* of the medium, albeit with a reduced jet energy.

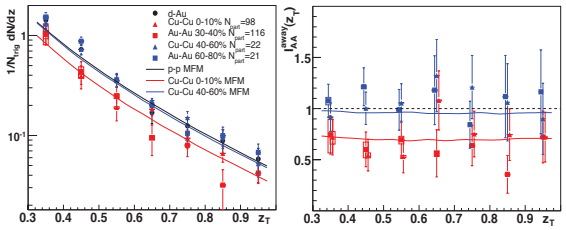


Fig. 4: Left: Away-side di-hadron fragmentation functions for Au-Au and Cu-Cu collisions at $\sqrt{s_{NN}}$ = 200 GeV. 6 $< p_T^{trig} <$ 10 GeV/c and 3 GeV/c $< p_T^{ass} < p_T^{trig}$. Right: The away-side I_{AA} as a function of z_T, from [17].

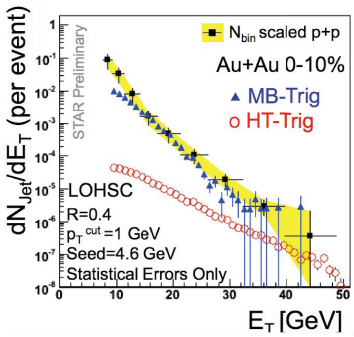


Fig. 5: Leading jet yields per event as a function of E_T for the most central Au-Au events at $\sqrt{s_{NN}}$ = 200 GeV compared to p-p events at the same energy. See text for more details.

4 Full Jet Reconstruction

With the full instrumentation and operation of the barrel calorimeter STAR now has the neutral and charged energy available allowing them to perform, for the first time in heavy-ion collisions, full jet reconstruction. Several new strategies had to adopted to control the large background from the softer particles in Au-Au event. It has been shown by CDF that $\sim$ 80 % of a given jet's energy is contained within a cone radius of R=0.3 [18]. Therefore to *find* the jets a small cone radius can be used. Finally the bulk of the background has p_T less than 2 GeV/c, and thus only tracks and calorimeter towers with p_T or $E_T >$ 1-2 GeV are assigned to jets. A correction is then applied to the reconstructed jet energy to account for the removed jet particles. This correction is calculated assuming PYTHIA fragmentation. The background from the Au-Au events is estimated by removing all the particles in the identified jet's cone and averaging over the rest of the event. The precision of this reconstruction is therefore strongly dependent on the event-by-event fluctuations and region-to-region correlations, such as elliptic flow, of this background [19, 20].

Figure 5 shows the resulting jet energy spectra for Au-Au and p-p events at $\sqrt{s_{NN}}$ = 200 GeV. The black circles show the N_{bin} scaled p-p data, the yellow band indicates the systematic error on this data. The blue triangles show the 0-10% centrality Au-Au data from a minimum bias trigger, only statistical errors are shown. These data have been corrected for efficiency, acceptance, and energy resolution. The open red circles show the uncorrected high tower trigger Au-Au dataset. This high tower trigger selected events online where at least one tower of the calorimeter had an energy greater than 7.5 GeV deposited in it. Therefore this data is extremely biased. This result is not corrected and is shown to indicate the potential jet energy reach of the data when all the corrections and biases have been accounted for. A comparison of the minimim bias and scaled p-p data shows that, within the currently large statistical and systematic uncertainties, the cross-section for hard processes scales with N_{bin} as predicted. The suppressions observed through the nuclear modification factors and di-hadron analysis are indeed likely due to energy loss of the scattered partons and not a reduction of the number of initial hard scatterings.

5 Summary

At RHIC we have much evidence that a strongly coupled deconfined state of quarks and gluons is created in the more central Au-Au collisions. We are now moving from the discovery phase into one of quantitative analysis of the properties of this medium. Studies of the nuclear modification factors and di-hadron correlations as a function of centrality and colliding species show that there is significant energy loss of hard scattered partons as they pass through the sQGP. However, the fragmentation functions themselves appear to be that of vacuum fragmentation in the ranges measured. Several models have been developed to try to describe our observations. However, they virtually all fail in describing all the details of the measurements now available. There is also the need for more selective experimental data. To this end an exciting new avenue of study has been opened with the first preliminary result on full jet reconstruction being announced. The measured Au-Au jet energy spectrum shows no strong suppression indicating that fully reconstructed jets indeed allow for the identification of all the particles resulting from the parton's fragmentation. Thus the observed high p_T single and di- hadron suppressions are likely due to a modification of this fragmentation both as a function of z=p^{had}/E^{jet} and particle composition. Studies are underway to try to quantify these effects. We can expect great progress in the future in high p_T correlation/jet studies due to the upgrades occurring at both STAR and PHENIX and the proposed RHIC luminosity upgrade. Finally there is the commencement of the LHC in 2009 where hard scatterings are much more prevalent and a new regime will begin.

References

[1] BRAHMS Collaboration, I. Arsene *et al.*, Nucl. Phys. **A757**, 1 (2005). nucl-ex/0410020.

[2] PHENIX Collaboration, K. Adcox *et al.*, Nucl. Phys. **A757**, 184 (2005). nucl-ex/0410003.

[3] PHOBOS Collaboration, B. B. Back *et al.*, Nucl. Phys. **A757**, 28 (2005). nucl-ex/0410022.

[4] STAR Collaboration, J. Adams *et al.*, Nucl. Phys. **A757**, 102 (2005). nucl-ex/0501009.

[5] STAR Collaboration, B. I. Abelev *et al.*, Phys. Rev. Lett. **97**, 252001 (2006). hep-ex/0608030.

[6] STAR Collaboration, J. Adams *et al.*, Phys. Lett. **B637**, 161 (2006). nucl-ex/0601033.

[7] PHENIX Collaboration, S. S. Adler *et al.*, Phys. Rev. Lett. **91**, 241803 (2003). hep-ex/0304038.

[8] STAR Collaboration, M. Heinz (2008). 0809.3769.

[9] T. Sjostrand, S. Mrenna, and P. Skands, JHEP **05**, 026 (2006). hep-ph/0603175.

[10] PHENIX Collaboration, S. S. Adler *et al.*, Phys. Rev. Lett. **96**, 202301 (2006). nucl-ex/0601037.

[11] A. Dainese, C. Loizides, and G. Paic, Eur. Phys. J. **C38**, 461 (2005). hep-ph/0406201.

[12] M. Gyulassy, P. Levai, and I. Vitev, Nucl. Phys. **B571**, 197 (2000). hep-ph/9907461.

[13] S. Wicks, W. Horowitz, M. Djordjevic, and M. Gyulassy, Nucl. Phys. **A784**, 426 (2007). nucl-th/0512076.

[14] H. Zhang, J. F. Owens, E. Wang, and X.-N. Wang, Phys. Rev. Lett. **98**, 212301 (2007). nucl-th/0701045.

[15] PHENIX Collaboration, A. Adare *et al.*, Phys. Rev. **C77**, 064907 (2008). 0801.1665.

[16] STAR Collaboration, C. Adler *et al.*, Phys. Rev. Lett. **90**, 082302 (2003). nucl-ex/0210033.

[17] STAR Collaboration, O. Catu, J. Phys. **G35**, 104088 (2008).

[18] *http: //www-cd.fnal.gov/physics/new/qcd/qcd.html*.

[19] STAR Collaboration, J. Putschke (2008). 0809.1419.

[20] STAR Collaboration, S. Salur (2008). 0810.0500.

Relativistic viscous hydrodynamics and AdS/CFT correspondence at finite temperature

Rudolf Baier
Fakultät für Physik, Universität Bielefeld, D-33501 Bielefeld, Germany
DOI: http://dx.doi.org/10.3204/DESY-PROC-2009-01/54

Abstract
Second-order viscous hydrodynamics in conformal field theories at high temperature is reviewed and the transport coefficients in strong-coupling are given obtained from gauge-gravity duality. Results for bulk physics are compared with RHIC data.

1 Introduction

I start with a definition: a fluid which has no shear stresses, viscosity or heat conduction is called a PERFECT FLUID, i.e. it looks isotropic in its rest frame, and a quotation: "Top physics story of 2005 is the RHIC discovery of the strongly interacting quark-gluon plasma (called sQGP), which behaves almost like a perfect fluid, with very low viscosity" [1].

Today it is still a crucial story, however, its content needs to be carefully tested!

This talk is based on the work by R. Baier, P. Romatschke, D. T. Son, A. O. Starinets and M. A. Stephanov on "Relativistic viscous hydrodynamics, conformal invariance, and holography" [2], and by M. Luzum and P. Romatschke on "Conformal relativistic viscous hydrodynamics: applications to RHIC results at $\sqrt{s(NN)} = 200$ GeV" [3].

2 Hydrodynamics

Relativistic hydrodynamics [4] is written in terms of the energy momentum tensor:

$$T^{\mu\nu} = T^{\mu\nu}_{perfect} + \Pi^{\mu\nu} = (\epsilon + p)u^\mu u^\nu + p g^{\mu\nu} + \Pi^{\mu\nu} \,, \tag{1}$$

where ϵ is the energy density, p the pressure and u^μ the fluid velocity which fulfills $u_\mu u^\mu = -1$. In the following only shear viscosity terms are kept and no net charge in the system is assumed. The symmetric shear tensor $\Pi^{\mu\nu}$ satisfies $u_\mu \Pi^{\mu\nu} = 0, \;\; \Pi^\mu_\mu = 0$. The evolution equations are given by the local conservation law (geometric covariant derivative ∇_μ): $\nabla_\mu T^{\mu\nu} = 0$.

To be noted: in case of interactions present in the system, e.g. in underlying QCD dynamics, a non-vanishing $\Pi^{\mu\nu}$ is present. The main question to be answered is: is the contribution by $\Pi^{\mu\nu}$ large or small?

2.1 Approximation

To first-order in gradients with respect to u^μ, the shear tensor reads

$$\Pi^{\mu\nu} = -2\eta < \nabla^\mu u^\nu > \equiv -\eta \sigma^{\mu\nu} \,, \tag{2}$$

with η the shear viscosity, and

$$\sigma^{\mu\nu} \equiv (\nabla^\mu u^\nu + \nabla^\nu u^\mu) - \frac{2}{3}\Delta^{\mu\nu}\nabla_\alpha u^\alpha \ , \ \ \Delta^{\mu\nu} = g^{\mu\nu} + u^\mu u^\nu \ . \tag{3}$$

The projection $\Delta^\mu_\alpha \nabla_\beta T^{\alpha\beta} = 0$ leads to the relativistic Navier-Stokes equation in first-order theory

$$(\epsilon + p) u^\alpha \nabla_\alpha u^\mu = \nabla^\mu p - \Delta^\mu_\alpha \nabla_\beta \left[-2\eta < \nabla^\alpha u^\beta > \right] , \tag{4}$$

which is a parabolic differential equation: the time derivative is of first order ($u^\alpha \nabla_\alpha \equiv D \rightarrow \partial/\partial t$), while the space derivative is of second order (∇^2): "Relativistic first-order dissipative theory is highly pathological, and therefore should be discarded in favor of the second-order one" [5].

To see this problem differently, apply a small linear perturbation in the first-order theory, e.g. in the transverse mode $\delta u_\perp$, to find a diffusion equation in the shear channel with a Gaussian solution, which propagates outside the light-cone.

A minimal modification beyond the diffusion equation by introducing a relaxation time $\tau_\pi > 0$ leads to a hyperbolic equation,

$$[\tau_\pi \partial_t^2 + \partial_t - \frac{\eta}{(\epsilon + p)} \partial_x^2] \ \delta u_\perp = 0 \ , \tag{5}$$

which becomes second-order in gradients [6].

2.2 Conformal hydrodynamics

Going much beyond the above conjecture, having CFT in mind, a new result has been obtained [2, 7]: *all* second-order terms have been classified by conformal symmetry. Starting from the Weyl transformations: $g^{\mu\nu} \rightarrow e^{2\omega(x)} \ g^{\mu\nu}$, $T^{\mu\nu} \rightarrow e^{6\omega} \ T^{\mu\nu}$, ... the constitutive relation of causal viscous hydrodynamics expressed by the derivative expansion to second-order is derived:

$$\begin{aligned} \Pi^{\mu\nu} = & - \eta\sigma^{\mu\nu} + \eta\tau_\pi \left[\langle D\sigma^{\mu\nu\rangle} + \frac{1}{3}\sigma^{\mu\nu}(\nabla_\alpha u^\alpha) \right] \\ & + \kappa \left[R^{<\mu\nu>} - 2u_\alpha R^{\alpha<\mu\nu>\beta} u_\beta \right] + \lambda_1 \sigma^{<\mu}{}_\lambda \sigma^{\nu>\lambda} + \lambda_2 \sigma^{<\mu}{}_\lambda \Omega^{\nu>\lambda} + \lambda_3 \Omega^{<\mu}{}_\lambda \Omega^{\nu>\lambda} , \end{aligned} \tag{6}$$

where $R^{\alpha\beta\gamma\delta}$ is the Riemann tensor, and $R^{\alpha\beta}$ is the Ricci tensor, present in case of curved spaces. $\Omega^{\alpha\beta}$ denotes the antisymmetric vorticity tensor. An independent elegant derivation of this result introducing a Weyl-covariant formalism can be found in [8].

2.3 Müller-Israel-Stewart theory

Keeping just one term in the derivative expansion at second-order, namely

$$\Pi^{\mu\nu} = -\eta\sigma^{\mu\nu} + \eta \ \tau_\pi \ \langle D\sigma^{\mu\nu\rangle} \ , \tag{7}$$

defines the Müller-Israel-Stewart theory [11, 12]. In [2] it is remarked that it does not match with AdS/CFT $\mathcal{N} = 4$ SYM and that therefore all second-order terms in Eq. (6) consistent with conformal symmetry have to be included into the shear tensor.

3 AdS/CFT correspondence

Following Maldacena [9] a strongly coupled quantized conformal gauge theory in $d = 4$ dimensions ($\mathcal{N} = 4$ SYM with $8N_c$ (1 gauge and 6 scalar) bosons and ($4N_c$) Weyl fermions), which is obviously NOT QCD, is dual to a weakly coupled classical supergravity (type IIB) in $d = 10$ dimensions (on $AdS_5 \times S^5$) via a holographic property based on the near extremal black $D3-$ brane metric with horizon $r = r_0$,

$$ds^2 = \frac{r^2}{R^2}(-f(r)dt^2 + d\vec{x}^2) + \frac{R^2}{r^2 f(r)}dr^2, \;\; f(r) = 1 - \frac{r_0^4}{r^4}\,, \tag{8}$$

where the radial (bulk) coordinate is bounded by $r_0 \leq r < \infty$, with the gauge theory on the boundary at ∞. $D3-$ branes are dynamical walls on which strings can end: the theory of open strings is living on $D3-$branes $\Longleftrightarrow$ the gravity theory of fields is living in the space curved by the branes. The Hawking temperature is given by $T = \frac{r_0}{\pi R^2}$.

The hydrodynamic transport coefficients are calculated in the limit of large 't Hooft coupling $\lambda = g_{YM}^2 N_c$, $N_c \to \infty$, $g_{YM}^2 << 1$, i.e. the string coupling $g_s = \frac{g_{YM}^2}{4\pi} << 1$ is small, implying no loops and small curvature $\frac{l_s^4}{R^4} = \frac{1}{\lambda} << 1$. The radius R of curvature is large compared to the string scale l_s, implying classical gravity.

The rather involved AdS/CFT-gravity calculations [2, 7], e.g. from the sound channel dispersion for momentum $\omega, k << T$, leads up to $O(k^3)$, etc.:

$$\frac{\eta}{s} = \frac{1}{4\pi}, \;\; \tau_\pi = \frac{2 - \ln 2}{2\pi T}, \;\; \kappa = \frac{\eta}{\pi T} = 2\lambda_1\,, \;\; \lambda_2 = -\frac{\ln 2}{2\pi T}\eta\,, \;\; \lambda_3 = 0\,. \tag{9}$$

The essence of the calculation is to consider the quasi-normal modes in order to relate the gravitational perturbations to a black hole/brane to the ones of a hydrodynamic system, e.g. see figures in [10].

4 Heavy-ion collisions

4.1 Ambiguities

Heavy-ion collisions require beyond well-understood hydrodynamics, which consists of a set of differential equations:

- initial conditions, i.e. equilibration time and distribution of energy density [13],
- a QCD equation of state,
- a hadronisation prescription.

4.2 Results

The main results obtained in [3] using the code based on viscous conformal hydrodynamics [2] are:

- viscous hydrodynamics simulation give a good description of RHIC data, including the elliptic flow v_2, with (s.. entropy density)

$$\frac{\eta}{s} = 0.1 \pm 0.1(theory) \pm 0.08(experiment)\,, \tag{10}$$

- the modest estimate is: $\frac{\eta}{s} < 0.5$,
- an early thermalisation time τ_0 is questioned, but $\tau_0 < 2\ fm$,
- weak dependence on the values of the second-order parameters $\tau_\pi, \lambda_1, ...$
  This is a consequence of the interplay between small gradients and the values of the parameters, which are at weak coupling: $\frac{\eta/s}{\tau_\pi T} = 1/6 = 0.167,\ \kappa = \lambda_1 = \lambda_3 = 0,\ \lambda_2 = -2\tau_\pi\eta$, and are not very different from the ones for $\lambda >> 1:\ \ \frac{\eta/s}{\tau_\pi T} = 0.383\ (1 - 3.52\ \lambda^{-3/2} + ...)$ (including corrections [14]).

These results imply for the viscosity: near equilibrium there is an estimate

$$\frac{\eta}{s} \simeq \hbar\ \frac{mean\ free\ path\ \lambda_f}{deBroglie\ wavelength}\ , \tag{11}$$

which allows to distinguish between

- a dilute system (QFT $->$ kinetic theory $->$ hydro):
  with the scale $\lambda_f\ \rightarrow \frac{\eta}{s} >> \hbar$, e.g. pQCD $(N_f = 0)$ [15]

$$\frac{\eta}{s} \simeq 3.8 \frac{1}{g^4 \ln(2.8/g)} \simeq O(1)\ \ for\ g = 2.5\ , \tag{12}$$

  BUT with $\ln(2.8/g) \simeq O(1) : \frac{\eta}{s} \simeq 0.1 \quad \rightarrow$ is sensitive to the constant under the log !
- a strongly coupled system (QFT $->$ hydro):
  the only scale is $1/T\ \rightarrow \frac{\eta}{s} = \frac{\hbar}{4\pi} \simeq 0.08$, which is the KSS bound [16, 17].

The modest estimate given above, however, does not rigorously exclude a perturbative QCD plasma versus a sQGP. A related statement follows from the estimates of the thermalisation time; for pQCD see [18].

5 Conclusions

There is excitement in the heavy-ion community about the beautiful ideas of the gauge/gravity correspondence, which strongly helps to gain intuition into STRONG COUPLING phenomena.

But one may ask for more [19], e.g. "Is there an experiment whose outcome could cast strong doubts on the relevance of AdS/CFT to understand QCD" ? One answer maybe jet physics [20].

For me one of the most challenging questions of the theory is related to the detailed microscopic mechanism for the rather RAPID EQUILIBRATION of matter in RHIC collisions.

Acknowledgements

I would like to thank P. Romatschke for fruitful discussions, H. Jung and the conveners of the session "Dense Systems" for the invitation, and DESY for financial support.

References

[1] T. D. Lee, arXiv:hep-ph/0605017.

[2] R. Baier, P. Romatschke, D. T. Son, A. O. Starinets and M. A. Stephanov, JHEP **0804** (2008) 100 [arXiv:0712.2451 [hep-th]].

[3] M. Luzum and P. Romatschke, Phys. Rev. **C78** (2008) 034915 [arXiv:0804.4015 [nucl-th]].

[4] see: J. Y. Ollitrault, Eur. J. Phys. **29** (2008) 275 [arXiv:0708.2433 [nucl-th]].

[5] W. A.Hiscock and L. Lindblom, Phys. Rev. D **31** (1985) 725.

[6] T. Koide, G. S. Denicol, Ph. Mota and T. Kodama, Phys. Rev. C **75** (2007) 034909 [arXiv:hep-ph/0609117]; T. Kodama, talk at this Symposium.

[7] S. Bhattacharyya, V. E. Hubeny, S. Minwalla and M. Rangamani, JHEP **0802** (2008) 045 [arXiv:0712.2456 [hep-th]].

[8] R. Loganayagam, JHEP **0805** (2008) 087 [arXiv:0801.3701 [hep-th]].

[9] J. M. Maldacena, Adv. Theor. Math. Phys. **2** (1998) 231 [Int. J. Theor. Phys. **38** (1999) 1113] [arXiv:hep-th/9711200]; O. Aharony, S. S. Gubser, J. M. Maldacena, H. Ooguri and Y. Oz, Phys. Rept. **323** (2000) 183 [arXiv:hep-th/9905111].

[10] M. Natsuume, Prog. Theor. Phys. Suppl. **168** (2007) 372; M. Natsuume, arXiv:0807.1394 [nucl-th].

[11] I.-Shih Liu, I. Müller and T. Ruggeri, Ann. Phys. **169** (1986) 191.

[12] W. Israel, Ann.Phys. **100** (1976) 310; W. Israel and J.M. Stewart, Phys. Lett. **58A** (1976) 213 and Ann.Phys. **118**, (1979) 341.

[13] see also W. Florkowski, talk at this Symposium.

[14] A. Buchel and M. Paulos, Nucl. Phys. B **805** (2008) 59 [arXiv:0806.0788 [hep-th]].

[15] P. Arnold, G. D. Moore and L. G. Yaffe, JHEP **0305** (2003) 051 [arXiv:hep-ph/0302165].

[16] G. Policastro, D. T. Son and A. O. Starinets, Phys. Rev. Lett. **87** (2001) 081601 [arXiv:hep-th/0104066].

[17] P. Kovtun, D. T. Son and A. O. Starinets, Phys. Rev. Lett. **94** (2005) 111601 [arXiv:hep-th/0405231].

[18] R. Baier, A. H. Mueller, D. Schiff and D. T. Son, Phys. Lett. B **502** (2001) 51 [arXiv:hep-ph/0009237]; Phys. Lett. B **539** (2002) 46 [arXiv:hep-ph/0204211].

[19] P. Jacobs [ALICE EMCal Collaboration], CERN Cour. **48N5** (2008) 27.

[20] E. Iancu, talk at this Symposium.

AdS/CFT Correspondence in Heavy Ion Collisions[†]

Javier L. Albacete[1], *Yuri V. Kovchegov*[2][‡], *Anastasios Taliotis*[2]
[1]ECT*, Strada delle Tabarelle 286, I-38050, Villazzano (TN), Italy,
[2]Department of Physics, The Ohio State University, Columbus, OH 43210, USA

DOI: http://dx.doi.org/10.3204/DESY-PROC-2009-01/29

Abstract

We construct a model of high energy heavy ion collisions as two ultrarelativistic shock waves colliding in AdS_5. The metric in the forward light cone after the collision is constructed perturbatively through expansion in graviton exchanges. We conclude that shock waves corresponding to physical energy-momentum tensors of the nuclei must completely stop almost immediately after the collision in AdS_5, which, on the field theory side, corresponds to complete nuclear stopping due to strong coupling effects, likely leading to Landau hydrodynamics. We propose using zero-net energy shock waves, which continue moving along their light cones after the collision, as a possible way to model the collision which may lead to Bjorken hydrodynamics at late proper times.

1 General Setup: Expansion in Graviton Exchanges

Our goal is to describe the isotropization (and thermalization) of the medium created in heavy ion collisions assuming that the medium is strongly coupled and using AdS/CFT correspondence to study its dynamics. We want to construct a metric in AdS_5 which is dual to an ultrarelativistic heavy ion collision as pictured in Fig. 1. Throughout the discussion we will use Bjorken approximation of the nuclei having an infinite transverse extent and being homogeneous (on the average) in the transverse direction, such that nothing in our problem would depend on the transverse coordinates x^1, x^2.

We start with a metric for a single shock wave moving along a light cone [2]:

$$ds^2 = \frac{L^2}{z^2}\left\{-2\,dx^+\,dx^- + \frac{2\,\pi^2}{N_c^2}\,\langle T_{--}(x^-)\rangle\,z^4\,dx^{-\,2} + dx_\perp^2 + dz^2\right\}. \qquad (1)$$

Here $x^\pm = \frac{x^0 \pm x^3}{\sqrt{2}}$, z is the coordinate describing the 5th dimension such that the boundary of the AdS space is at $z = 0$, and L is the curvature radius of the AdS space. According to holographic renormalization [3], $\langle T_{--}(x^-)\rangle$ is the expectation value of the energy-momentum tensor for a single ultrarelativistic nucleus moving along the light-cone in x^+-direction in the gauge theory.

The metric in Eq. (1) is an exact solution of Einstein equations in AdS_5: $R_{\mu\nu} + \frac{4}{L^2}\,g_{\mu\nu} = 0$. It can also be represented perturbatively as a single graviton exchange between the source nucleus

[†] This talk was based on [1].
[‡] speaker

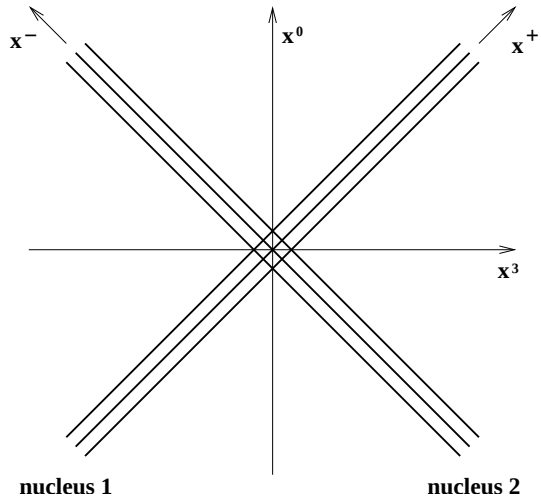


Fig. 1: The space-time picture of the ultrarelativistic heavy ion collision in the center-of-mass frame. The collision axis is labeled x^3, the time is x^0.

at the AdS boundary and the location in the bulk where we measure the metric/graviton field. This is shown in Fig. 2, where the solid line represents the nucleus and the wavy line is the graviton propagator. Incidentally a single graviton exchange, while being a first-order perturbation of the empty AdS space, is also an exact solution of Einstein equations. This means higher order tree-level graviton diagrams are zero (cf. classical gluon field of a single nucleus in covariant gauge in the Color Glass Condensate (CGC) formalism [4]).

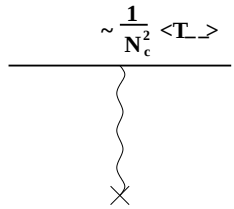


Fig. 2: A representation of the metric (1) as a graviton (wavy line) exchange between the nucleus at the boundary of AdS space (the solid line) and the point in the bulk where the metric is measured (denoted by a cross).

Now let us try to find the geometry dual to a collision of two shock waves with the metrics like that in Eq. (1). Defining $t_1(x^-) \equiv \frac{2\pi^2}{N_c^2} \langle T_{1\,--}(x^-)\rangle$ and $t_2(x^+) \equiv \frac{2\pi^2}{N_c^2} \langle T_{2\,++}(x^+)\rangle$ we write the metric resulting from such a collision as

$$ds^2 = \frac{L^2}{z^2}\Big\{ -2\,dx^+\,dx^- + dx_\perp^2 + dz^2 + t_1(x^-)\,z^4\,dx^{-\,2} + t_2(x^+)\,z^4\,dx^{+\,2} + \text{higher order graviton exchanges}\Big\} \qquad (2)$$

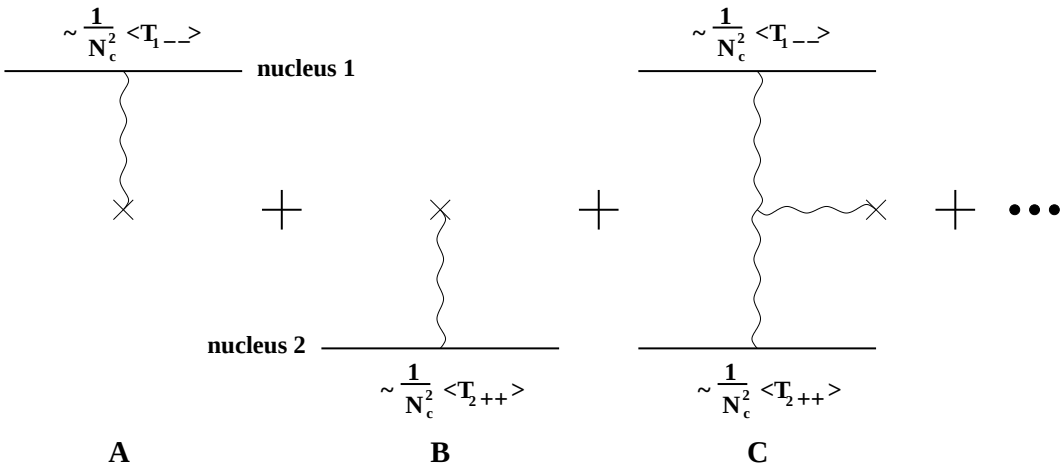


Fig. 3: Diagrammatic representation of the metric in Eq. (2). Wavy lines are graviton propagators between the boundary of the AdS space and the bulk. Graphs A and B correspond to the metrics of the first and the second nucleus correspondingly. Diagram C is an example of the higher order graviton exchange corrections.

The metric of Eq. (2) is illustrated in Fig. 3. The first two terms in Fig. 3 (diagrams A and B) correspond to one-graviton exchanges which constitute the individual metrics of each of the nuclei, as shown in Eq. (1). Our goal below is to calculate the next order correction to these terms, which is shown in the diagram C in Fig. 3. Fig. 3 illustrates that construction of dual geometry to a shock wave collision in AdS_5 consists of summing up all tree-level graviton exchange diagrams, similar diagrammatically to the classical gluon field formed by heavy ion collisions in CGC [5]. While classical gluon fields lead to free-streaming final state [6], their AdS graviton "dual" is likely to lead to a hydrodynamic final state for the gauge theory like the one found in [2].

2 Perturbative Solution of Einstein Equations

To solve Einstein equations perturbatively in graviton exchanges we write

$$g_{\mu\nu} \,=\, g^{(0)}_{\mu\nu} + g^{(1)}_{\mu\nu} + g^{(2)}_{\mu\nu} + \dots \,. \tag{3}$$

Here $g^{(0)}_{\mu\nu}$ is the metric of the empty AdS_5 space with non-zero components

$$g^{(0)}_{+-} = g^{(0)}_{-+} = -\frac{L^2}{z^2}, \quad g^{(0)}_{ij} = \delta_{ij}\,\frac{L^2}{z^2}, \;\; i,j = 1,2, \qquad g^{(0)}_{zz} = \frac{L^2}{z^2}. \tag{4}$$

$g^{(1)}_{\mu\nu}$ is the first perturbation of the empty AdS_5 space due to the two nuclei

$$g^{(1)}_{--} = t_1(x^-)\,L^2\,z^2, \quad g^{(1)}_{++} = t_2(x^+)\,L^2\,z^2 \tag{5}$$

with all the other components zero.

We want to find the next non-trivial correction $g^{(2)}_{\mu\nu}$. By the choice of Fefferman-Graham coordinates one has $g_{z\mu} = g_{\mu z} = 0$ exactly for $\mu \neq z$ and $g_{zz} = L^2/z^2$. Hence the non-trivial

components of $g^{(2)}_{\mu\nu}$ are those for $\mu, \nu = 0, \ldots, 3$. Due to translational and rotational invariance of the nuclei in the transverse direction $g^{(2)}_{ij} \sim \delta_{ij}$. We thus parametrize the unknown components of $g^{(2)}_{\mu\nu}$ as

$$g^{(2)}_{--} = \tfrac{L^2}{z^2}\, f(x^+, x^-, z), \quad g^{(2)}_{++} = \tfrac{L^2}{z^2}\, \tilde{f}(x^+, x^-, z),$$
$$g^{(2)}_{+-} = -\tfrac{1}{2}\, \tfrac{L^2}{z^2}\, g(x^+, x^-, z), \quad g^{(2)}_{ij} = \tfrac{L^2}{z^2}\, h(x^+, x^-, z)\, \delta_{ij} \tag{6}$$

with f, $\tilde{f}$, g and h some unknown functions. Imposing causality we require that functions f, $\tilde{f}$, g and h are zero before the collision, i.e., that before the collision the metric is given only by the empty AdS space and by the contributions of the two nuclei (5). Also, according to general properties of $g_{\mu\nu}$ outlined in Sect. 1 (see [3]), we demand that f, $\tilde{f}$, g and h go to zero as z^4 when $z \to 0$.

Linearizing Einstein equations in f, $\tilde{f}$, g, and h we solve the obtained system of differential equation to obtain [1]

$$h(x^+, x^-, z) \,=\, h_0(x^+, x^-)\, z^4 + h_1(x^+, x^-)\, z^6 \tag{7}$$

where h_0 and h_1 are determined by the causal solutions of the following equations

$$(\partial_+\, \partial_-)^2\, h_0(x^+, x^-) \,=\, 8\, t_1(x^-)\, t_2(x^+), \tag{8}$$

$$\partial_+\, \partial_-\, h_1(x^+, x^-) \,=\, \frac{4}{3}\, t_1(x^-)\, t_2(x^+). \tag{9}$$

f, $\tilde{f}$, and g are easily expressed in terms of $h(x^+, x^-, z)$ from Eq. (7) (see [1]).

3 Nuclear Stopping and How One May Avoid It

Imagine a collisions of two shock waves whose energy-momentum tensors are given by smeared delta-functions

$$t_1(x^-) \,=\, 2\,\pi^2\, \frac{\mu}{a}\, \theta(x^-)\, \theta(a - x^-), \;\; t_2(x^+) \,=\, 2\,\pi^2\, \frac{\mu}{a}\, \theta(x^+)\, \theta(a - x^+). \tag{10}$$

Here for a shock wave moving in the x^+-direction $\mu \propto p^+\, \Lambda^2\, A^{1/3}$ and $a \,\propto\, R\, \frac{\Lambda}{p^+} \,\propto\, \frac{A^{1/3}}{p^+}$, where the nucleus of radius R has A nucleons in it with N_c^2 valence gluons each. p^+ is the light cone momentum of each nucleon and Λ is the typical transverse momentum scale. Using the solution found in Sect. 2 along with holographic renormalization we find the "$--$" component of the energy-momentum tensor of a shock wave after the collision at $x^- = a/2$ and for $x^+ \gg a$:

$$\langle T_{--}(x^+ \gg a, x^- = a/2) \rangle \,=\, N_c^2\, \frac{\mu}{a} - 4\,\pi^2\, N_c^2\, \mu^2\, x^{+\,2}. \tag{11}$$

The first term on the right of Eq. (11) is due to the original shock wave while the second term describes energy loss due to graviton emission.

Eq. (11) shows that $\langle T_{--} \rangle$ of a nucleus becomes *zero* at light-cone times

$$x^+ \,\sim\, \frac{1}{\sqrt{\mu\, a}} \,\sim\, \frac{1}{\Lambda\, A^{1/3}}. \tag{12}$$

Indeed zero $\langle T_{--} \rangle$ would mean a complete *stopping* of the shock wave and the corresponding nucleus. At larger x^+ the energy-momentum tensor component in Eq. (11) becomes negative: one can show that higher order graviton exchanges become important at this light cone time likely preventing $\langle T_{--} \rangle$ from becoming negative. As the shock wave can loose all of its energy by emitting a single graviton as shown in Fig. 3C, it is highly unlikely that higher order graviton exchanges/emissions would prevent the shock wave from stopping. We thus conclude that the collision of two nuclei at strong coupling leads to a necessary stopping of the two nuclei shortly after the collision. If the nuclei stop completely in the collision, the strong interactions between them are almost certain to thermalize the system, probably leading to Landau hydrodynamics [7].

However, in the real-life heavy ion collisions the nuclei interact weakly at the early stages of the collisions and continue moving along their light cones after the collision. While finding a dual theory describing these weak coupling effects in the framework of the AdS/CFT correspondence is very hard, we suggest mimicking them by using zero-net energy shock waves with

$$t_1(x^-) \,=\, \Lambda_1^2\, \delta'(x^-), \;\; t_2(x^+) \,=\, \Lambda_2^2\, \delta'(x^+) \tag{13}$$

in the shock waves metric of Eq. (2). $\delta'(x)$ denotes the derivative of a delta-function and Λ_1 and Λ_2 are the transverse momentum scales describing the two nuclei. One can then show [1] that the lowest order non-trivial graviton exchange of Fig. 3C leads to the following energy density ϵ and transverse p and longitudinal p_3 pressure components for the produced medium at early times:

$$\epsilon(\tau) \,=\, \frac{N_c^2}{\pi^2}\, 4\, \Lambda_1^2\, \Lambda_2^2, \;\; p(\tau) \,=\, \frac{N_c^2}{\pi^2}\, 4\, \Lambda_1^2\, \Lambda_2^2, \;\; p_3(\tau) \,=\, -\frac{N_c^2}{\pi^2}\, 4\, \Lambda_1^2\, \Lambda_2^2. \tag{14}$$

(One can prove [1] that graviton expansion of Fig. 3 corresponds to expansion in $\Lambda_1^2\, \tau^2$ and $\Lambda_2^2\, \tau^2$ for the energy-momentum tensor of the gauge theory: hence the lowest order diagram (Fig. 3C) gives the dominant contribution to $T_{\mu\nu}$ at early times.) One can see from Eq. (14) that the energy density of the strongly coupled medium starts out as a constant at early times, a conclusion which has been reached earlier in [8]. The energy-momentum tensor components in Eq. (14) are also similar to those found in CGC at early times [9], and may serve as a starting point for a possible evolution of the strongly-coupled system towards Bjorken hydrodynamics [10].

This research is sponsored in part by the U.S. Department of Energy under Grant No. DE-FG02-05ER41377.

References

[1] J. L. Albacete, Y. V. Kovchegov, and A. Taliotis, JHEP **07**, 100 (2008). 0805.2927.

[2] R. A. Janik and R. B. Peschanski, Phys. Rev. **D73**, 045013 (2006). hep-th/0512162.

[3] S. de Haro, S. N. Solodukhin, and K. Skenderis, Commun. Math. Phys. **217**, 595 (2001). hep-th/0002230.

[4] Y. V. Kovchegov, Phys. Rev. **D55**, 5445 (1997). hep-ph/9701229.

[5] A. Kovner, L. D. McLerran, and H. Weigert, Phys. Rev. **D52**, 3809 (1995). hep-ph/9505320.

[6] A. Krasnitz, Y. Nara, and R. Venugopalan, Nucl. Phys. **A717**, 268 (2003). hep-ph/0209269.

[7] L. D. Landau, Izv. Akad. Nauk SSSR Ser. Fiz. **17**, 51 (1953).

[8] Y. V. Kovchegov and A. Taliotis, Phys. Rev. **C76**, 014905 (2007). 0705.1234.

[9] T. Lappi, Phys. Lett. **B643**, 11 (2006). hep-ph/0606207.

[10] J. D. Bjorken, Phys. Rev. **D27**, 140 (1983).

Saturation and Confinement: Analyticity, Unitarity and AdS/CFT Correspondence

Richard Brower [1], *Marko Djuric* [2], *Chung-I Tan* [3†]
[1] Boston University, Boston, MA 02215, USA,
[2] Brown University, Providence, RI 02912, USA,
[3] Brown University, Providence, RI 02912, USA.

Abstract
In $1/N_c$ expansion, analyticity and crossing lead to crossing even and odd ($C = \pm 1$) vacuum exchanges at high-energy, the *Pomeron* and the *Odderon*. We discuss how, using *String/Gauge duality*, these can be identified with a reggeized *Graviton* and the anti-symmetric *Kalb-Ramond fields* in AdS background. With confinement, these Regge singularities interpolate with glueball states. We also discuss unitarization based on eikonal sum in AdS.

1 Forward Scattering, Gauge/String Duality and Confinement

The subject of near-forward high energy scattering for hadrons has a long history. We focus here on the recent developments based on Maldacena's weak/strong duality, relating Yang-Mills theories to string theories in (deformed) Anti-de Sitter space [1–5]. For conformally invariant gauge theories, the metric of the dual string theory is a product, $AdS_5 \times W$, $ds^2 = \left(\frac{r^2}{R^2}\right)\eta_{\mu\nu}dx^\mu dx^\nu + \left(\frac{R^2}{r^2}\right)dr^2 + ds^2_W$, where $0 < r < \infty$. For the dual to $\mathcal{N} = 4$ supersymmetric Yang-Mills theory the AdS radius R is $R^2 \equiv \sqrt{\lambda}\alpha' = (g^2_{\rm YM}N)^{1/2}\alpha'$, and W is a 5-sphere of this same radius. We will ignore fluctuations over W and also assume that $\lambda \gg 1$, so that the spacetime curvature is small on the string scale, and $g^2_{YM} \ll 1$ so that we can use string perturbation theory. (See [3, 4] for more references.)

The fact that 5-dim description enters in high energy collision can be understood as follows. In addition to the usual LC momenta, $p_\pm = p^0 \pm p^z$ (2d), and transverse impact variables, $\vec{b}$ (2d), there is one more "dimension": a "resolution" scale specified by a probe, e.g., $1/Q^2$ of virtual photon in DIS, (see Fig. 1a.) Because of conformal symmetry, these 5 coordinates transform into each others, leaving the system invariant. In the strong coupling limit, conformal symmetry is realized as the $SL(2, C)$ isometries of Euclidean AdS_3 subspace of AdS_5, where r can be identified with Q^2.

The traditional description of high-energy small-angle scattering in QCD has two components — a soft Pomeron Regge pole associated with exchanging tensor glueballs, and a hard BFKL Pomeron at weak coupling. On the basis of gauge/string duality, a coherent treatment of the Pomeron was provided [1]. These results agree with expectations for the BFKL Pomeron at negative t, and with the expected glueball spectrum at positive t, but provide a framework in which they are unified [6].

One important step in formulating the dual Pomeron involves the demonstration [7] that in exclusive hadron scattering, the dual string theory amplitudes at wide angle, due to the red-shifted local-momenta, $s \to \tilde{s} = (R/r)^2 s$ and $t \to \tilde{t} = (R/r)^2 t$, give the power laws that are expected in a gauge theory. It was also noted that at large s and small t that the classic Regge form of the scattering amplitude

† speaker

should be present in certain kinematic regimes [7, 8]. Equally important is the fact that, with confinement, transverse fluctuations of the metric tensor G_{MN} in AdS acquire a mass and can be identified with a tensor glueball [9, 10]. It was suggested in [10] that, at finite λ, this will lead to a Pomeron with an intercept below 2. That is, Pomeron can be considered as a *Reggeized Massive Graviton*.

The *dual Pomeron* was subsequently identified as a well-defined feature of the curved-space string theory [1]. For a conformal theory in the large N_c limit, a dual Pomeron can always be identified with the leading eigenvalue of a Lorentz boost generator M_{+-} of the conformal group [3]. The problem reduces to finding the spectrum of a single J-plane Schrödinger operator. In the strong coupling limit, conformal symmetry requires that the leading $C = +1$ Regge singularity is a fixed J-plane cut. For ultraviolet-conformal theories with confinement deformation, the spectrum exhibits a set of Regge trajectories at positive t, and a leading J-plane cut for negative t, the cross-over point being model-dependent. (See Fig. 1b.) For theories with logarithmically-running couplings, one instead finds a discrete spectrum of poles at all t, with a set of slowly-varying and closely-spaced poles at negative t.

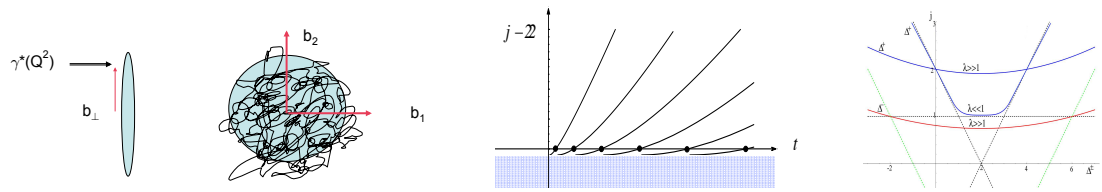


Fig. 1: (a) Intuitive picture for AdS^5 kinematics. (b) Schematic representation of J-plane singularity structure. (c) Schematic form of Δ-j relation for $\lambda << 1$ and $\lambda >> 1$ for $C = +1$ and $\lambda >> 1$ for $C = -1$.

2 Conformal Pomeron, Odderon and Analyticity

At high-energy, analyticity and crossing lead to $C = \pm 1$ vacuum exchanges, the *Pomeron* and the *Odderon*. The qualitative picture for Pomeron exchange in weak coupling [11] has been understood for a long time, in leading order expansion in g^2_{YM} and all order sum in $g^2_{YM} log(s/s_0)$. In the conformal limit, both the weak-coupling BFKL Pomeron and Odderons correspond to J-plane branch points, e.g., the BFKL Pomeoron is a cut at $j_0^{(+)}$, above $j = 1$. Two leading Odderons have been identified. (See [4, 12] for more references.) Both are branch cuts in the J-plane. One has an intercept slightly below 1 [13], and the second has an intercept precisely at 1 [14]. These are summarized in Table 1.

In the strong coupling limit, conformal symmetry dictates that the leading $C = +1$ Regge singularity is a fixed J-plane cut at $j_0^{(+)} = 2 - 2/\sqrt{\lambda} + O(1/\lambda)$. As λ increases, the "conformal Pomeron" moves to $j = 2$ from below, approaching the AdS graviton. We have recently shown [4] that the strong coupling *conformal odderons* are again fixed cuts in the J-plane, with intercepts specified by the AdS mass squared, m^2_{AdS}, for Kalb-Ramond fields [15],

$$j_0^{(-)} = 1 - m^2_{AdS}/2\sqrt{\lambda} + O(1/\lambda) \; . \tag{1}$$

Interestingly, two leading *dual odderons* can be identified, parallel the weak-coupling situation. One solution has $m^2_{AdS,(1)} = 16$. There is also a second solution where $m^2_{AdS,(2)} = 0$. We outline below how these features emerge in *Gauge/String duality*.

	Weak Coupling	Strong Coupling
$C=+1$: Pomeron	$j_0^{(+)} = 1 + (\ln 2)\ \lambda/\pi^2 + O(\lambda^2)$	$j_0^{(+)} = 2 - 2/\sqrt{\lambda} + O(1/\lambda)$
$C=-1$: Odderon	$j_{0,(1)}^{(-)} \simeq 1 - 0.24717\ \lambda/\pi + O(\lambda^2)$ $j_{0,(2)}^{(-)} = 1 + O(\lambda^3)$	$j_{0,(1)}^{(-)} = 1 - 8/\sqrt{\lambda} + O(1/\lambda)$ $j_{0,(2)}^{(-)} = 1 + O(1/\lambda)$

Table 1: Pomeron and Odderon intercepts at weak and strong coupling, with $\lambda = g_{YM}^2 N_c$ the 't Hooft coupling.

2.1 Flat-Space Expectation for $C = \pm 1$ Sectors

String scattering in 10-d flat-space at high energy leads to a crossing-even and crossing-odd amplitudes,

$$\mathcal{T}_{10}^{(\pm)}(s,t) \to f^{(\pm)}(\alpha' t)(\alpha' s)^{\alpha_\pm(t)}\ , \tag{2}$$

where $\alpha_+(t) = 2 + \alpha' t/2$ and $\alpha_-(t) = 1 + \alpha' t/2$ respectively. That is, at $t = 0$, a massless state with integral spin is being exchanged, e.g., for $C = +1$, one is exchanging a massless spin-2 particle, the ubiquitous graviton. Of course, the coefficient functions, $f^{(\pm)}(\alpha' t)$, are process-dependent.

Massless modes of a closed string theory can be identified with transverse fluctuations coming from a left-moving and a right-moving level-one oscillators, e.g., states created by applying $a_{1,I}^\dagger \tilde{a}_{1,J}^\dagger$ to the vacuum, i.e., $a_{1,I}^\dagger \tilde{a}_{1,J}^\dagger |0; k^+, k_\perp\rangle$, with $k^2 = 0$. Since a 10-dim closed string theory in the low-energy limit becomes 10-dim gravity; these modes can be identified with fluctuations of the metric G_{MN}, the anti-symmetric Kalb-Ramond background B_{MN} [15], and the dilaton, ϕ, respectively. It is important to note that we will soon focus on AdS^5, i.e., one is effectively working at $D = 5$. With $D = 5$, the independent components for G_{MN} and B_{MN} are 5 and 3 respectively, precisely that necessary for having (massive) states with spin 2 and 1 [10]. For oriented strings, it can be shown that the symmetric tensor contributes to $C = +1$ and the anti-symmetric tensor contributes to $C = -1$.

2.2 Diffusion in AdS for Pomeron and Odderon

Let us next introduce diffusion in AdS. We will restrict ourselves to the conformal limit. Regge behavior is intrinsically non-local in the transverse space. For flat-space scattering in 4-dimension, the transverse space is the 2-dimensional impact parameter space, $\vec{b}$. In the Regge limit of s large and $t < 0$, the momentum transfer is transverse. Going to the $\vec{b}$-space, $t \to \nabla_b^2$, and the flat-space Regge propagator, for both $C = \pm 1$ sectors, is nothing but a diffusion kernel, $\langle\ \vec{b}\ |\ (\alpha' s)^{\alpha_\pm(0) + \alpha' t \nabla_b^2/2}\ |\ \vec{b}'\ \rangle$, with $\alpha_+(0) = 2$ and $\alpha_-(0) = 1$ respectively. In moving to a ten-dimensional momentum transfer $\tilde{t}$, we must keep a term coming from the momentum transfer in the six transverse directions. This extra term leads to diffusion in extra-directions, i.e., for $C = +1$, $\alpha'\tilde{t} \to \alpha'\Delta_P \equiv \frac{\alpha' R^2}{r^2}\nabla_b^2 + \alpha'\Delta_{\perp P}$. The transverse Laplacian is proportional to R^{-2}, so that the added term is indeed of order $\alpha'/R^2 = 1/\sqrt{\lambda}$. To obtain the $C = +1$ Regge exponents we will have to diagonalize the differential operator Δ_P. Using a Mellin transform, $\int_0^\infty d\tilde{s}\ \tilde{s}^{-j-1}$, the Regge propagator can be expressed as $\tilde{s}^{2+\alpha'\tilde{t}/2} = \int \frac{dj}{2\pi i}\ \tilde{s}^j\ G^{(+)}(j) = \int \frac{dj}{2\pi i}\ \frac{\tilde{s}^j}{j - 2 - \alpha'\Delta_P/2}$ where $\Delta_P \simeq \Delta_j$, the tensorial Laplacian. Using a spectral analysis, it leads to a J-plane cut at $j_0^{(+)}$.

A similar analysis can next be carried out for the $C = -1$ sector. We simply replace the Regge kernel by $\tilde{s}^{1+\alpha' \tilde{t}/2} = \int \frac{dj}{2\pi i}\ \tilde{s}^j\ G^{(-)}(j) = \int \frac{dj}{2\pi i}\ \tilde{s}^j (j - 1 - \alpha' \Delta_O/2)^{-1}$. The operator $\Delta_O(j)$ can be fixed by examining the EOM at $j = 1$ for the associated super-gravity fluctuations responsible for this exchange, i.e., the anti-symmetric Kalb-Ramond fields, B_{MN}. One finds two solutions,

$$G^{(-)}(j) = \frac{1}{[j - 1 - (\alpha'/2R^2)(\Box_{Maxwell} - m^2_{AdS,i})]}\ , \tag{3}$$

$i = 1, 2$, where $\Box_{Maxwell}$ stands for the Maxwell operator. Two allowed values are $m^2_{AdS,1} = 16$ and $m^2_{AdS,2} = 0$. A standard spectral analysis then lead to a branch-cut at $j_0^{(-)}$, given by Eq. (1).

2.3 Regge and DGLAP Connection

It is also useful to explore the conformal invariance as the isometry of transverse AdS_3. Upon taking a two-dimensional Fourier transform with respect to $q_\perp$, where $t = -q_\perp^2$, one finds that $G^{(\pm)}$ can be expressed simply as

$$G^{(\pm)}(z, x^\perp, z', x'^\perp; j) = \frac{1}{4\pi z z'} \frac{e^{(2-\Delta^{(\pm)}(j))\xi}}{\sinh \xi}\ , \tag{4}$$

where $\cosh \xi = 1 + v$, $v = [(x^\perp - x'^\perp)^2 + (z - z')^2]/(2zz')$ the AdS_3 chordal distance, and $z = R^2/r$, and $\Delta^{(\pm)}(j) = 2 + \sqrt{2}\ \lambda^{1/4} \sqrt{(j - j_0^{(\pm)})}$ is a J-dependent effective AdS_5 conformal dimension [1,3,4]. The $\Delta - j$ curve for $\Delta^{(\pm)}$ is shown in Fig. 1c. A related discussion on $\Delta(j)$ can be found in [16].

For completeness, we note that, for both $C = +1$ and $C = -1$, it is useful to introduce Pomeron and Odderon kernels in a mixed-representation,

$$\mathcal{K}^{(\pm)}(s, z, x^\perp, z', x'^\perp) \sim \left(\frac{(zz')^2}{R^4}\right) \int \frac{dj}{2\pi i}\ \left[\frac{(-\tilde{s})^j \pm (\tilde{s})^j}{\sin \pi j}\right] G^{(\pm)}(z, x^\perp, z', x'^\perp; j)\ . \tag{5}$$

To obtain scattering amplitudes, we simply fold these kernels with external wave functions. Eq. (5) also serves as the starting point for eikonalization.

3 Unitarity, Absorption, Saturation and the Eikonal Sum

For simplicity, we will focus here on the $C = +1$ sector, assuming all crossing odd amplitudes vanish. It has been shown in Refs. [**?**, 2, 3] that, in the strong coupling limit, a 2-to-2 amplitude, $A(s, t)$, in the near-forward limit can be expressed in terms of a "generalized" eikonal representation,

$$A_{2\to 2}(s, t) = \int dz dz' P_{13}(z) P_{24}(z') \int d^2b\ e^{-ib^\perp q_\perp} \widetilde{A}(s, b^\perp, z, z')\ , \tag{6}$$

where $\widetilde{A}(s, b^\perp, z, z') = 2is \left[1 - e^{i\chi(s, b^\perp, z, z')}\right]$, and $b^\perp = x^\perp - x'^\perp$ due to translational invariance. The probability distributions for left-moving, $P_{13}(z)$, and right moving, $P_{14}(z)$ particles are products of initial (in) and final (out) particle wave functions. The eikonal, χ, can be related to the strong coupling Pomeron kernel [1, 3], and can be expressed as the inverse Mellin transform of $G^{(+)}(j, x^\perp - x'^\perp, z, z')$.

We note the salient feature of eikonal scattering locally in transverse AdS_3, and the near-forward field-theoretic amplitude is obtained from a bulk eikonal amplitude after convolution. It is useful to

focus our attention on the properties of the bulk eikonal formula $\widetilde{A}(s, b^{\perp}, z, z')$ itself. For χ real, it is elastic unitary. On the other hand, when χ is complex, (with $\mathrm{Im}\chi > 0$), one has inelastic production. Absorption and saturation can now be addressed in this context. It is also important to note that, for Froissart bound, confinement is crucial. Discussion on these and related issues can be found in Ref. [3].

We end by pointing out one unique feature of strong coupling – the eikonal is predominantly real. To simplify the discussion, let us consider the second order contributions to the imaginary part of the elastic amplitude. The AGK cutting rule for the imaginary part of the elastic amplitude generalizes to

$$\cos(j_0\pi)|\chi|^2 = \left[1 - 2\sin^2(j_0\pi/2) - 2\sin^2(j_0\pi/2) + 2\sin^2(j_0\pi/2)\right]|\chi|^2 \tag{7}$$

where the first term on the right is due to the elastic scattering, the last term is due to two-cut-Pomeron contribution, and the second and the third are due to one-cut-Pomeron contributions. The tradition weak coupling approach to diffraction scattering has $j_0 \simeq 1$, leading to a net negative contribution: $-1 = 1 - 2 - 2 + 2$. This leads to absorption, already dominant at second order. However, for extreme strong coupling, one has $j_0 \simeq 2$, leading to a positive cut contribution: $1 = 1 - 0 - 0 + 0$. This is consistent with scattering being predominantly elastic. However, the real world is neither strictly weak coupling nor strong coupling. For $j_0 \simeq 1.5$, one finds the two-Pomeron contribution vanishes: $0 = 1 - 1 - 1 + 1$. That is, what used to be the dominant correction to elastic scattering now vanishes. Clearly, these issues deserve further examination. For applications of [1–5] for DIS, see [17].

References

[1] R. C. Brower, J. Polchinski, M. J. Strassler, and C.-I. Tan, JHEP **12**, 005 (2007). hep-th/0603115.

[2] R. C. Brower, M. J. Strassler, and C.-I. Tan (2007). arXiv:0707.2408 [hep-th].

[3] R. C. Brower, M. J. Strassler, and C.-I. Tan (2007). 0710.4378.

[4] R. C. Brower, M. Djuric, and C.-I. Tan (2008). 0812.0354.

[5] L. Cornalba, M. S. Costa, J. Penedones, and R. Schiappa (2007). hep-th/0611122;
L. Cornalba, M. S. Costa, J. Penedones, and R. Schiappa, Nucl. Phys. **B767**, 327 (2007). hep-th/0611123;
L. Cornalba, M. S. Costa, and J. Penedones (2007). arXiv:0707.0120 [hep-th].

[6] E. Levin and C.-I. Tan, "Proc. for International Symposium on Multiparticle Dynamics", Santiago, Spain, July 1992, and "Workshop on Small-x and Diffractive Physics at Tevatron", FNAL, Sept. 1992 (1992). hep-ph/9302308.

[7] J. Polchinski and M. J. Strassler, Phys. Rev. Lett. **88**, 031601 (2002). hep-th/0109174.

[8] R. C. Brower and C.-I. Tan, Nucl. Phys. **B662**, 393 (2003). hep-th/0207144.

[9] R. C. Brower, S. D. Mathur, and C.-I. Tan, Nucl. Phys. **B574**, 219 (2000). hep-th/9908196.

[10] R. C. Brower, S. D. Mathur, and C.-I. Tan, Nucl. Phys. **B587**, 249 (2000). hep-th/0003115.

[11] L. N. Lipatov, Sov. J. Nucl. Phys. **23**, 338 (1976);
E. A. Kuraev, L. N. Lipatov, and V. S. Fadin, Sov. Phys. JETP **45**, 199 (1977);
I. I. Balitsky and L. N. Lipatov, Sov. J. Nucl. Phys. **28**, 822 (1978).

[12] C. Ewerz (2005). hep-ph/0511196.

[13] R. A. Janik and J. Wosiek, Phys. Rev. Lett. **82**, 1092 (1999). hep-th/9802100;
M. A. Braun (1998). hep-ph/9805394.

[14] J. Bartels, L. N. Lipatov, and G. P. Vacca, Phys. Lett. **B477**, 178 (2000). hep-ph/9912423.

[15] M. Kalb and P. Ramond, Phys. Rev. **D9**, 2273 (1974).

[16] D. M. Hofman and J. Maldacena, JHEP **05**, 012 (2008). 0803.1467.

[17] E. Levin, J. Miller, B. Z. Kopeliovich, and I. Scmidt (2008). 0811.3586;
Y. Hatta, E. Iancu, and A. H. Mueller (2007). arXiv:0710.2148 [hep-th];
L. Cornalba and M. S. Costa (2008). 0804.1562.

Light, Strange and Charm Hadron Measurements in ep Collisions as a Baseline for Heavy-Ion Physics

Anna Kropivnitskaya (for the H1 and ZEUS Collaborations)
Institute for Theoretical and Experimental Physics, Moscow, Russia
DOI: http://dx.doi.org/10.3204/DESY-PROC-2009-01/75

Abstract
An overview of the recent results on hadron spectroscopy from the electron-proton collider experiments H1 and ZEUS at HERA is presented. Production of particles with light and strange quarks is measured and the results are compared to RHIC data and to predictions of Monte Carlo models. The investigation of exotic states in the strangeness sector is reviewed. Measurements in the charm sector cover studies of the radially and orbitally excited charm states.

1 Introduction

High energy particle collisions which give rise to large multiplicities of produced hadrons provide an opportunity to study the hadronisation process, in which quarks and gluons convert to colourless hadrons. Since most hadrons are produced with low transverse momentum, the theory of perturbative quantum chromodynamics (pQCD) is not applicable to describe hadronisation. The production of long-lived hadrons and resonances at high energies was studied in detail in electron-positron (e^-e^+) collisions at LEP using Z^0 decays [1]. The measurements using high energy hadronic interactions were restricted to long-lived and heavy quark hadrons. Recently, the production of the hadronic resonances $\rho(770)^0$, $K^*(892)^0$ and $\phi(1020)$ was measured in heavy-ion and proton-proton (pp) collisions at RHIC [2]. The electron-proton (ep) collider HERA allows the study of particle production in quasi-real photon-proton (γp) collisions, where the nuclear density is much lower than at RHIC. This is particularly interesting, because the γp centre-of-mass energy at HERA is about the same as for colliding nucleons at RHIC.

2 Generic Shape of Hadronic Spectra

Particle production in γp, pp and AuAu collisions has several properties. The transverse momentum (p_T) charged particle spectra [3] are described by a power law distribution

$$\frac{1}{\pi}\frac{d^2\sigma}{dp_T^2 dy} = \frac{A}{(E_{T_0} + E_T^{kin})^n} \ , \tag{1}$$

where y is rapidity, $E_T^{kin} = \sqrt{m_0^2 + p_T^2} - m_0$ is the transverse kinetic energy, m_0 is the nominal resonance mass, A is a normalisation factor and E_{T_0} and n are free parameters. At low E_T^{kin} the power law function (1) is behaving like a Boltzmann exponential distribution $\exp(-E_T^{kin}/T)$ with $T = E_{T_0}/n$. This exponential behaviour of the hadronic spectra was interpreted within a thermodynamic picture of hadroproduction [4]. In this framework the parameter T plays the role

of the temperature at which hadronisation takes place. At high E_T^{kin} the constant E_{T_0} becomes negligible.

In figure 1, some features for the charged particle spectra are shown. In pp the T increases and n decreases with increasing s. When comparing hadron production in γp, pp and AuAu at fixed s the parameters T and n increase with the complexity of the collisions.

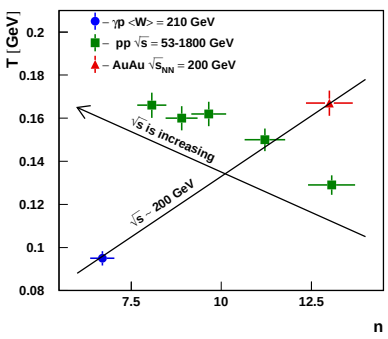


Fig. 1: Fit parameters $T = E_{T_0}/n$ and n from power law distribution of charged particle spectra.

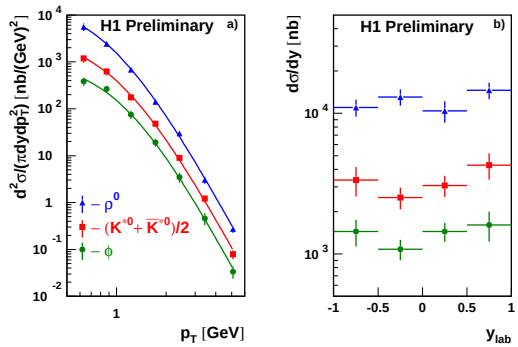


Fig. 2: The measured differential non-diffractive cross-sections for ρ^0, K^{*0} and ϕ mesons.

3 Inclusive Photoproduction of $\rho^0(770)$, $K^*(892)^0$ and $\phi(1020)$ Mesons

First measurements of inclusive non-diffractive photoproduction of ρ^0, K^{*0} and ϕ mesons at HERA are presented by the H1 collaboration. In figure $2a$), the invariant differential cross sections for the production of these resonances as a function of transverse momentum are presented together with a power law fit (1) as for the charged particle spectrum. In figure $2b$), the differential cross sections as a function of rapidity (y_{lab}) are observed to be flat, within errors in the visible range. It is observed that these resonances with their different masses, lifetimes and strangeness content are produced with about the same value of the average transverse kinetic energy. This observation supports a thermodynamic picture of hadronic interactions.

In figure 3, a modification of the shape of ρ^0 resonance produced in γp collisions at HERA is described by taking into account Bose-Einstein correlations (BEC) in the Monte Carlo model. A similar effect is observed in pp and heavy-ion collisions at RHIC [2] and in e^+e^- annihilation at LEP [5], using Z^0 decays.

The cross section ratios $R(K^{*0}/\rho^0)$, $R(\phi/\rho^0)$ and $R(\phi/K^{*0})$ are estimated. In figure 4, the $R(\phi/K^{*0})$ is compared to results obtained in pp and heavy-ion collisions by the STAR experiment at RHIC [2]. The ratio $R(\phi/K^{*0})$ measured in γp interactions is in agreement with pp results. A tendency of ϕ meson production to be more abundant in AuAu collisions is observed, but an increased accuracy is required to reach firm conclusions.

4 K^0_S, Charged $K^*(892)$ Mesons and Λ Baryon Production in DIS

The H1 collaboration has studied K^0_S and Λ production in the DIS within the photon virtuality range $2 < Q^2 < 100$ GeV^2 [6] as a function of event variables and final state particle variables.

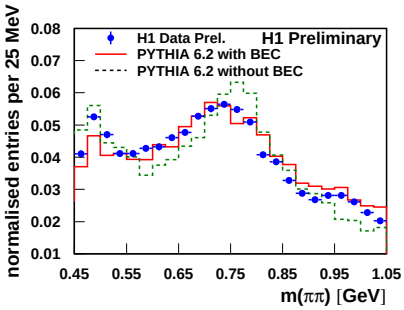


Fig. 3: The unlike-sign mass spectrum with the like-sign spectrum subtracted.

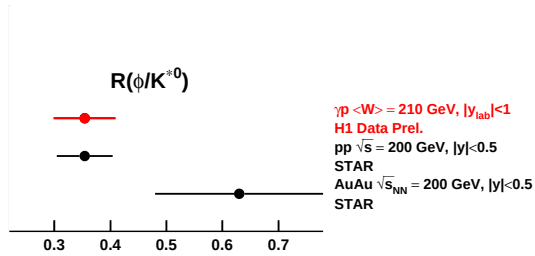


Fig. 4: The ratio $R(\phi/K^{*0})$ of the total cross-sections.

The cross section of K^0_S and Λ as a function of p_T are presented in figures 5 and 6 correspondingly. The overall features of the data are reproduced by colour dipole model (CDM) based predictions, when using the strangeness suppression factor $\lambda_s = 0.3$ and applying model parameters tuned to LEP e^+e^- data. However, the predictions fail to describe the details of the distributions in various regions of the phase space, in particular at low p_T, low x and large positive rapidity. There was no asymmetry observed between Λ and $\overline{\Lambda}$, which indicates a similar production process for baryons and antibaryons.

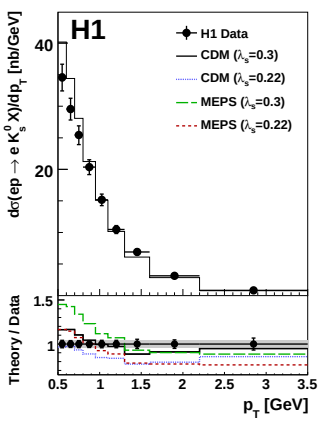


Fig. 5: The differential production cross section for K^0_S as a function of p_T.

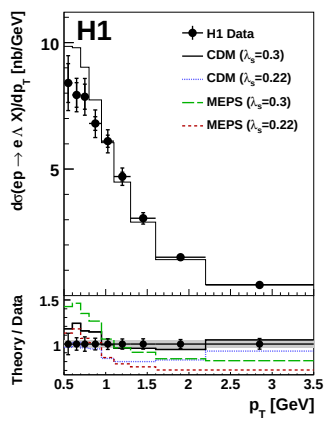


Fig. 6: The differential production cross section for Λ as a function of p_T.

The H1 collaboration has reported the observation of charged $K^*(892)$ mesons in the DIS kinematic region $5 < Q^2 < 100$ GeV^2 [7]. The invariant mass spectrum is shown in figure 7. The cross sections for the $K^{*\pm}$ production are measured as a function of the transverse momentum, pseudorapidity, photon virtuality, Feynman-x and the centre-of-mass energy of the hadronic final state. The measured cross sections are in agreement with DJANGOh1.4 (CDM) and RAPGAP3.1 (MEPS) Monte Carlo model predictions. This is consistent with the results of the K^0_S and Λ measurements.

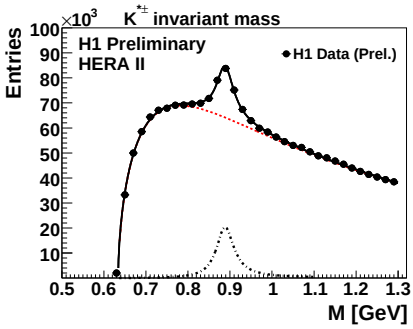


Fig. 7: The measured $K^0_S\pi^\pm$ invariant mass spectrum.

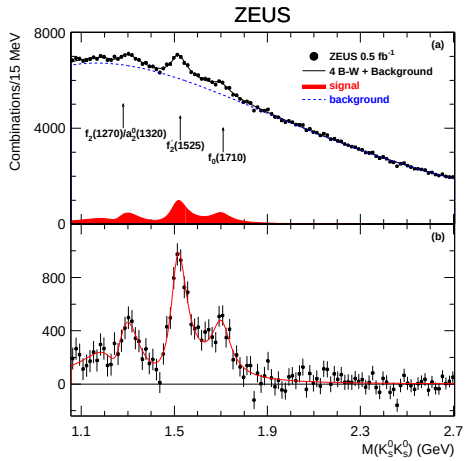


Fig. 8: (a) The measured $K^0_SK^0_S$ invariant mass spectrum. (b) The background-subtracted $K^0_SK^0_S$ invariant mass spectrum.

5 Exotic States in the Strangeness Sector

The $K^0_SK^0_S$ final state was studied with the ZEUS detector [8]. In figure 8, the measured invariant mass distribution is shown. Three enhancements which correspond to $f_2(1270)/a^0_2(1320)$, $f'_2(1525)$ and $f_0(1710)$ were observed. No state heavier than the $f_0(1710)$ is seen. The invariant distribution was fitted taking into account the interference pattern predicted by SU(3) symmetry arguments. The measured masses of the $f'_2(1525)$ and $f_0(1710)$ states are slightly below the PDG values [9], while the widths are consistent with the PDG values [9]. The $f_0(1710)$ state, which has a mass consistent with the lower lying $J^{PC} = 0^{++}$ glueball candidate, is observed with a five standard deviation statistical significance. However, if this state is the same as that seen in $\gamma\gamma \to K^0_SK^0_S$ [10], it is unlikely to be a pure glueball state, since photons can couple in partonic level only to charged objects.

6 Charmed Particle Production

ZEUS studied excited charm and charm-strange mesons. The signals are reported [11] of $D_1(2420)^0$, $D^*_2(2460)^0$ and $D_{s1}(2536)$ mesons in the decay chains D^0_1, $D^{*0}_2 \to D^{*\pm}\pi^\mp$, $D^\pm\pi^\mp$ and $D^\pm_{s1} \to D^{*\pm}K^0_S$, $D^0K^\pm$. The measured masses are in reasonable agreement with the world average values [9] while the measured D^0_1 width is above the world average value.

The measured D^0_1 helicity parameter is $h(D^0_1) = 5.9^{+3.0}_{-1.7}(\text{stat.})^{+2.4}_{-1.0}(\text{syst.})$, which is inconsistent with the prediction of $h = 0$ for a pure S-wave decay of the 1^+ state, and is consistent with the prediction of $h = 3$ for a pure D-wave decay. The measured D^+_{s1} helicity parameter is $h(D^+_{s1}) = -0.74^{+0.23}_{-0.17}(\text{stat.})^{+0.06}_{-0.05}(\text{syst.})$, which is inconsistent with the prediction of $h = 3$ for a pure D-wave decay of the 1^+ state, and is barely consistent with the prediction of $h = 0$ for a pure S-wave decay. Both D- and S-wave seem to contribute to the $D^+_{s1} \to D^{*+}K^0_S$ decay. These measurements are consistent with e^+e^- results.

No radially excited $D^{*\prime+}(2640)$ meson was observed. The best upper limit on the charm

branching fraction is estimated to $f(c \to D^{*\prime +}) \cdot \mathcal{B}_{D^{*\prime +} \to D^{*+}\pi^+\pi^-} < 0.4\%$ (95% C.L.).

7 Summary

Production of particles consisting of light and strange quarks was measured and compared to the RHIC data and to the predictions of Monte Carlo models. The ratio $R(\phi/K^{*0})$ measured in γp interactions is in agreement with pp results. A tendency of ϕ meson production to be more abundant in AuAu collisions is observed, but an increased accuracy is required to reach firm conclusions. The overall features of the strange particle production are well described by theoretical models. However, there are still many details that need improvements, in particular concerning the treatment of the non-pertubative effects. The $K^0_S K^0_S$ final state spectrum shows clear evidence for the $f_0(1710)$ state, consistent with the lowest lying $J^{PC} = 0^{++}$ glueball candidate. Excited charm and charm-strange mesons were observed and their helicity structure were studied.

8 Acknowledgements

The support of the Helmholtz Association in the framework of the Helmholtz-Russian-Joint-Research Group (HRJRG-002) and ISMD08 Committees is gratefully acknowledged. I would like to thank Andrey Rostovtsev for useful discussions.

References

[1] A. Boehrer, (Siegen U.), Phys. Rept. **291**, 107, and references herein (1997).

[2] STAR Collaboration, J. Adams *et al.,* Phys. Rev. Lett. **92**, 092301 (2004);
STAR Collaboration, C. Adler *et al.,* Phys. Rev. **C71**, 064902 (2005);
STAR Collaboration, J. Adams *et al.,* Phys. Lett. **B612**, 181 (2005).

[3] H1 Collaboration, I. Abt *et al.,* Phys. Lett. **B328**, 176 (1994);
H1 Collaboration, C. Adloff *et al.,* Eur. Phys. J. **C10**, 363 (1999);
PHENIX Collaboration, S. Adler *et al.,* Phys. Rev. **C69**, 034909 (2004);
UA1 Collaboration, C. Albajar *et al.,* Nucl. Phys. **B335**, 261 (1990);
CDF Collaboration, F. Abe *et al.,* Phys. Rev. Lett. **61**, 1819 (1988);
British-Scandinavian Collaboration, B. Alper *et al.,* Nucl. Phys. **B87**, 19 (1975).

[4] R. Hagedorn, Nuovo Cim. Suppl. **3**, 147 (1965).

[5] OPAL Collaboration, P. D. Acton *et al.,* Z. Phys. **C56**, 521 (1992);
ALEPH Collaboration, D. Busculic *et al.,* Z. Phys. **C69**, 379 (1996).

[6] H1 Collaboration, A. Aktas *et al.,* DESY-08-095; *Contribution 847 to Int. Conf. in HEP, ICHEP08, Philadelphia, USA, Aug 2008.*

[7] H1 Collaboration, A. Aktas *et al., Contribution 867 to Int. Conf. in HEP, ICHEP08, Philadelphia, USA, Aug 2008.*

[8] ZEUS Collaboration, S. Chekanov *et al.,* Phys. Rev. Lett. **101**, 112003 (2008).

[9] W.-M. Y. *et al.* (Particle Data Group), J. Phys. **G33**, 1 (2006).

[10] TASSO Collaboration, M. Althoff *et al.,* Phys. Lett. **B121**, 216 (1983);
L3 Collaboration, M. Acciarri *et al.,* Phys. Lett. **B501**, 173 (2001).

[11] ZEUS Collaboration, S. Chekanov *et al.,* DESY-08-093; *Contribution 243 to Int. Conf. in HEP, ICHEP08, Philadelphia, USA, Aug 2008.*

Chapter 4

Working Group Interpolation Region

Convenors:

M. Grothe (University Wisconsin, Madison)
M. Albrow (FNAL)
K. Werner (Nantes)

Diffractive Production of Jets and Vector Bosons at the Tevatron

Kenichi Hatakeyama , for the CDF Collaboration
Rockefeller University

DOI: http://dx.doi.org/10.3204/DESY-PROC-2009-01/21

Abstract
Recent results on diffractive dijet and vector boson production and exclusive dijet production from the Collider Detector at Fermilab (CDF) experiment are presented.

1 Introduction

CDF Collaboration performed various measurements on inclusive diffraction and exclusive production using $p\bar{p}$ collision data from the Fermilab Tevatron collider collected in Run I (1992–1996) and Run II (2001–). One of the important results from the Run I studies is the observation of the QCD factorization breakdown in hard single diffractive (SD) processes [1–5]; the rate of hard SD processes, in which one of the incoming proton or antiproton is scattered quasielastically and a hard partonic scattering (such as dijet production) occurs, was found to be lower than theoretical predictions by a factor of $\mathcal{O}(10)$. In [4, 5], the diffractive structure function $F^D(Q^2, x, \xi, t)$ was measured using SD dijet events and found to be suppressed with respect to the one measured in ep collisions at HERA by $\mathcal{O}(10)$, where ξ is the fractional momentum loss of the diffracted (anti)proton and t is the four-momentum transfer squared. This suppression is similar to the one observed in soft diffractive processes with respect to the Regge theory predictions, and is generally attributed to additional color exchanges in the same $p\bar{p}$ collision which spoil the diffractive rapidity gap [6–8].

Another important result from the Run I diffractive studies is from a study on F^D using double pomeron exchange (DPE) dijet events [9], $p + \bar{p} \rightarrow p + jjX + \bar{p}$. The diffractive structure function F^D measured in DPE dijet events was found to be approximately equal to expectations from HERA. This observation is consistent with the expectations from, *e.g.*, the gap probability renormalization model [8]. The main goal of the Run II diffractive studies is to study the characteristics of diffractive events more in detail with help of the upgraded detectors and larger statistics in order to deepen our understanding of diffractive exchange and the QCD nature of the pomeron.

In addition, there has been an increased interest in studies on *exclusive* events, mainly due to a possibility of finding the Higgs boson in exclusive events at the Large Hadron Collider (LHC). Exclusive events in pp ($p\bar{p}$) collisions contain nothing but the leading proton and (anti)proton and the object(s) of interest such as dijet, diphoton, dielectron, and most importantly the Higgs boson, as shown in Fig. 1. We do not expect to observe the exclusive Higgs production at the Tevatron; however, we can study other exclusive processes that can provide a calibration for theoretical predictions of exclusive Higgs production at the LHC.

The recent Run II studies on hard diffraction and exclusive dijet production are presented below. Studies on exclusive dilepton, diphoton, and charmonium states are presented in [10].

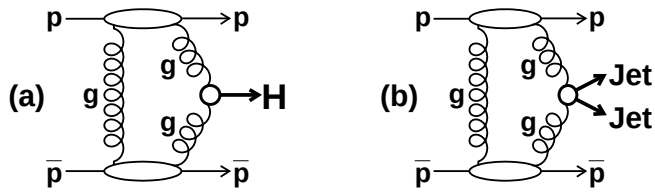


Fig. 1: Diagrams for exclusive production of (left) Higgs and (right) dijet production.

2 Diffractive Dijet Production

The diffractive structure function F^D was studied using Run II SD dijet data using a similar way to that used in Run I studies [4, 5], *i.e.*, by taking a ratio of SD to non-diffractive (ND) dijet rates as a function of x, which is in leading-order QCD approximately equal to the ratio of diffractive to ND structure function.

One of the major challenges in Run II diffractive studies is the rejection of multiple $p\bar{p}$ interaction events, in which diffractive rapidity gaps are spoiled by overlapping $p\bar{p}$ interactions (overlaps) and the hard scattering cannot be associated with the diffracted leading (anti)proton accurately. This rejection was done by reconstructing ξ from the calorimeter towers by $\xi^{cal} = \sum_{\rm towers} E_T^i \eta^i / \sqrt{s}$; $\xi^{cal} \sim \xi^{RP} < 0.1$ in SD events without overlaps, while $\xi^{cal} > 0.1$ in events with overlaps, where ξ^{RP} refers to the ξ value reconstructed based on the information from the Roman pot (RP) detector which detects the diffracted antiproton.

The high statistics Run II data allowed the SD/ND dijet ratio measurement in Q^2 up to 10^4 GeV^2, and no appreciable Q^2 dependence was observed. Also in the Run II study, the t distribution in SD dijet events was measured up to $Q^2 \sim 4500$ GeV^2, and no dependence of the shape of the t distribution on Q^2 was found.

3 Diffractive W/Z Production

CDF studied diffractive W/Z production using the Run II data recently. The study of diffractive W/Z production is important to determine the quark content of the pomeron; the production by gluons is suppressed by a factor of α_s and it can also be identified by an additional jet.

In Run I, CDF studied diffractive W production by identifying diffractive events using rapidity gaps [2], and found the fraction of W events which are diffractive to be $[1.15 \pm 0.51({\rm stat}) \pm 0.20({\rm syst})]$%. In addition, the gluon content of the pomeron was determined to be $[54^{+16}_{-14}]$% in combination with results on diffractive dijet and b-quark production [1, 3]. D0 made measurements on diffractive W production and also Z production [11], and reported the fractions of W and Z events with a rapidity gap to be $[0.89^{+0.19}_{-0.17}]$% and $[1.44^{+0.61}_{-0.52}]$% [11], respectively. These fractions are not corrected for the gap acceptance correction A_{gap}, *i.e.*, the fraction for diffractive events that satisfy the experimental definitions of the rapidity gaps. The estimate on A_{gap} ranges from 0.2 to 1.0 depending on the diffractive models considered.

In the new CDF Run II measurement, the RP detector is used to detect the leading antiproton in diffractive W/Z events. The RP detector provides an accurate ξ measurement, and also eliminates the ambiguity associated with A_{gap}. As in diffractive dijet production, ξ can be recon-

structed from both the energy depositions in the calorimeters (ξ^{cal}) and hits in the RP detector (ξ^{RP}). The ξ^{cal} distributions in W/Z events with a leading antiproton are shown in Fig. 2. The diffractive W and Z candidate events without overlaps are selected by requiring $\xi^{cal} < \xi^{RP}$ and $\xi^{cal} < 0.1$, respectively.

In diffractive $W \to l\nu$ events without overlaps, the difference between ξ^{cal} and ξ^{RP} is related to missing E_T ($\not\!\!E_T$) and η_ν as $\xi^{RP} - \xi^{cal} = \frac{\not\!\!E_T}{\sqrt{s}} e^{-\eta_\nu}$, which allows to determine the neutrino kinematics, and consequently the W kinematics. The reconstructed W mass is shown in Fig. 2.

The fractions of W and Z events which are diffractive are measured to be $[0.97 \pm 0.05(\mathrm{stat}) \pm 0.11(\mathrm{syst})]\%$ and $[0.85 \pm 0.20(\mathrm{stat}) \pm 0.11(\mathrm{syst})]\%$ in $0.03 < \xi < 0.10$ and $|t| < 1$ GeV/c. The measured diffractive W fraction is consistent with the Run I CDF result when corrected to the ξ and t range in this measurement.

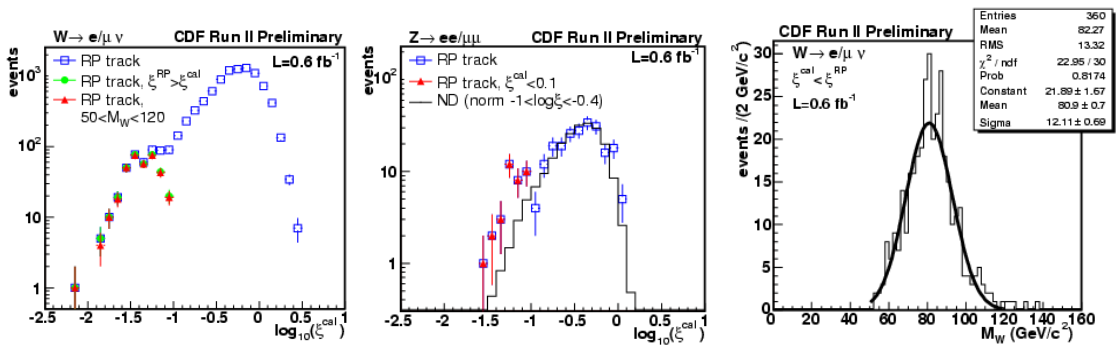


Fig. 2: Calorimeter distribution in W (left) and Z (center) events with a Roman-pot track. (right) Reconstructed W mass in diffractive W candidate events.

4 Rapidity Gaps between Very Forward Jets

The double diffractive (DD) dissociation refers to a class events in which two colliding particles dissociate into clusters of particles (including jets in the case of hard DD events) with a large rapidity gap between them. Measurements on DD events were made by CDF [12–15] and D0 [16] in Run I in $p\bar{p}$ collisions at $\sqrt{s} = 1800$ and 630 GeV. Recently, CDF reported new preliminary results on events with a rapidity gap between forward jets from the Run II data. In CDF II, the miniplug (MP) calorimeters covering $3.5 \lesssim |\eta| \lesssim 5.1$ allow a study of very forward jets with a larger rapidity gap between them than in Run I. Figure 3 (left) shows the kinematic characteristics of the leading two jets in an event both in MPs with $E_T > 2$ GeV and $\eta_1\eta_2 < 0$. Since these jets are in a very forward region, they have high energies despite their relatively low E_T's.

The dependence of the gap fraction $R_{gap} = N_{gap}/N_{all}$ was studied as a function of $\Delta\eta = \eta_{max} - \eta_{min}$ in these MP dijet events in a similar way as in [15]. $\eta_{max(min)}$ is the pseudorapidity of the tower closest to $\eta = 0$ in the proton(antiproton) outgoing direction. The comparison of R_{gap} as a function of $\Delta\eta$ in min-bias events and MP dijet events with $E_T^{jet1,2} > 2$ GeV and $E_T^{jet1,2} > 4$ GeV is shown in Fig. 3. A rapidity gap in $|\eta| < 1.1$ (CCAL gap) is always required.

The event fraction with a central rapidity gap is about 10% in soft events, while it is about 1% in dijet events, which is consistent with the results from Run I [12–16]. It is interesting to note that the shape of the R_{gap} distribution is similar between the soft and hard events. A study on the azimuthal decorrelation between the two leading jets in these forward dijet events is underway in order to investigate the effect of the Muller-Navelet jets [17].

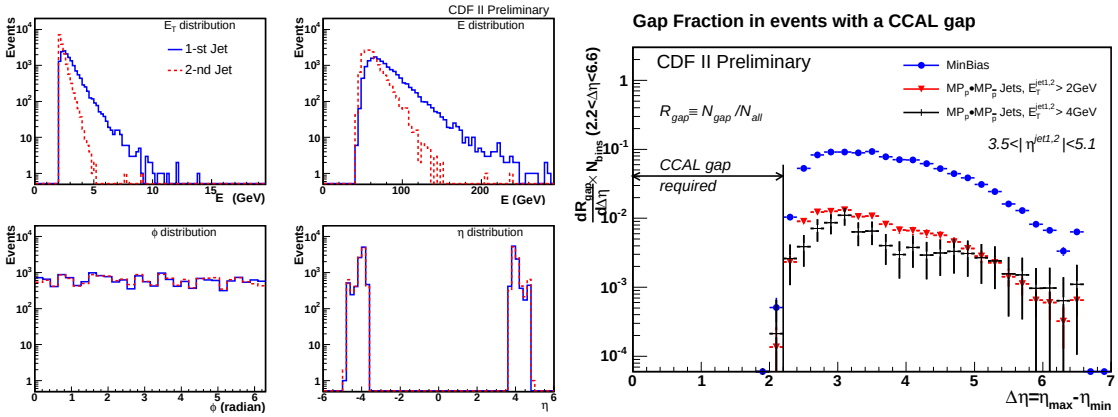


Fig. 3: (left) Kinematic distributions for the two leading jets in an event, both in the MP calorimeters. (right) The gap fraction R_{gap} vs. $\Delta\eta$ for min-bias and MP dijet events of $E_T^{jet1,2} > 2$ GeV and $E_T^{jet1,2} > 4$ GeV.

5 Exclusive Dijet Production

The exclusive dijet production was first searched for by CDF in Run I data, and the limit of $\sigma_{excl} < 3.7$ nb (95% CL) was placed [9]. In the Run II search [18], first a sample of inclusive DPE dijet events is selected. The exclusive signal is then searched for examining dijet mass fraction R_{jj} which is the ratio of dijet mass M_{jj} to system mass M_X. This observable should be sensitive to how much the event energy is concentrated in the dijet. The R_{jj} of exclusive dijet events is expected to be peaked around $R_{jj} \sim 0.8$ and have a long tail toward lower values due to hadronization effects causing energy leak from jet cones and also the presence of gluon radiations in the initial and final states. Figure 4 shows R_{jj} distributions for data, inclusive DPE dijet Monte Carlo (MC) events from the POMWIG Monte Carlo with various sets of pomeron structure functions, and the non-DPE events. The data clearly show an excess at high R_{jj} over the non-DPE background events and inclusive DPE predictions. The shape of the excess is well described by exclusive dijet MC based on two models (ExHuME [19], DPEMC [20]); however, the measured cross section disfavors DPEMC. Predictions by Khoze *et al.* [21] are found to be consistent with data within its factor of 3 uncertainty.

6 Summary

The long-standing diffractive program at CDF has substantially improved our understanding of diffractive processes. In Run II, the measurements on diffractive dijets and the diffractive structure function are extended to $Q^2 \sim 10^4$ GeV^2, and the measurement of diffractive W/Z production was made using the RP detector. The study on events with a rapidity-gap between forward

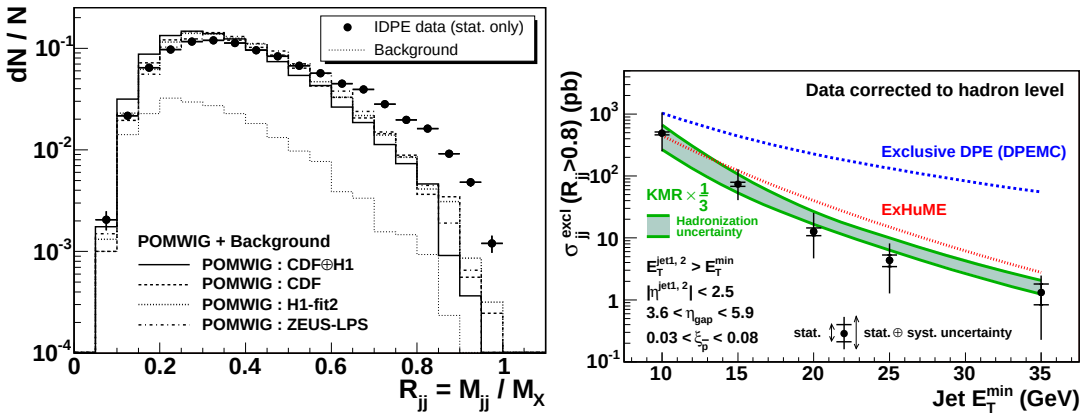


Fig. 4: (left) Dijet mass fraction R_{jj} in inclusive DPE dijet data (left). An excess over predictions at large R_{jj} is observed as a signal of exclusive dijet production. (right) The measured cross section for exclusive dijet production compared to predictions.

jets is underway. In addition, CDF reported a first observation of exclusive dijet production which provides a valuable calibration for the predictions on exclusive Higgs production at the LHC.

References

[1] CDF Collaboration, F. Abe *et al.*, Phys. Rev. Lett. **79**, 2636 (1997).

[2] CDF Collaboration, F. Abe *et al.*, Phys. Rev. Lett. **78**, 2698 (1997).

[3] CDF Collaboration, A. Affolder *et al.*, Phys. Rev. Lett. **84**, 232 (2000).

[4] CDF Collaboration, A. Affolder *et al.*, Phys. Rev. Lett. **84**, 5043 (2000).

[5] CDF Collaboration, A. Affolder *et al.*, Phys. Rev. Lett. **88**, 151802 (2002).

[6] E. Gotsman, E. Levin, and U. Maor, Phys. Rev. D **60**, 094011 (1999).

[7] A. B. Kaidalov, V. A. Khoze, A. D. Martin, and M. G. Ryskin, Eur. Phys. J. **C21**, 521 (2001).

[8] K. Goulianos. `hep-ph/0203141`.

[9] CDF Collaboration, A. Affolder *et al.*, Phys. Rev. Lett. **85**, 4215 (2000).

[10] M. Albrow, these proceedings.

[11] D0 Collaboration, V. Abazov *et al.*, Phys. Lett. B **574**, 169 (2003).

[12] CDF Collaboration, F. Abe *et al.*, Phys. Rev. Lett. **74**, 855 (1995).

[13] CDF Collaboration, F. Abe *et al.*, Phys. Rev. Lett. **80**, 1156 (1998).

[14] CDF Collaboration, F. Abe *et al.*, Phys. Rev. Lett. **81**, 5278 (1998).

[15] CDF Collaboration, A. Affolder *et al.*, Phys. Rev. Lett. **87**, 141802 (2001).

[16] D0 Collaboration, S. Abachi *et al.*, Phys. Rev. Lett. **76**, 734 (1996).

[17] C. Marquet and C. Royon. `arXiv:0704.3409`.

[18] CDF Collaboration, T. Aaltonen *et al.*, Phys. Rev. D **77**, 052004 (2008).

[19] J. Monk and A. Pilkington, Comput. Phys. Commun. **175**, 232 (2006).

[20] M. Boonekamp and T. Kucs, Comput. Phys. Commun. **167**, 217 (2005).

[21] V. A. Khoze, A. D. Martin, and M. G. Ryskin, Eur. Phys. J. C **14**, 525 (2000).

Central Exclusive Production at the Tevatron

Michael G. Albrow
on behalf of the CDF Collaboration.
Fermi National Accelerator Laboratory,
P.O.Box 500, Wilson Road, Batavia, IL 60510, USA

DOI: http://dx.doi.org/10.3204/DESY-PROC-2009-01/22

Abstract
In CDF we have observed several exclusive processes: $\gamma\gamma \to e^+e^-$ and $\mu^+\mu^-$, $\gamma + I\!P \to J/\psi, \psi(2S)$, and $I\!P + I\!P \to \chi_c$. The cross sections agree with QED, HERA photoproduction data, and theoretical estimates of $gg \to \chi_c$ with another gluon exchanged to screen the color. This observation of exclusive χ_c, together with earlier observations of exclusive dijets and exclusive $\gamma\gamma$ candidates, support some theoretical predictions for $p + p \to p + H + p$ at the LHC. Exclusive dileptons offer the best means of precisely calibrating forward proton spectrometers.

1 Central Exclusive Production

Central exclusive production at the Tevatron is the process $p + \bar{p} \to p + X + \bar{p}$, where "+" means a rapidity gap Δy exceeding 3 units, and X is a simple system fully measured. Exchanges (t-channel) over such large gaps must be color singlets with spin J [or Regge intercept $\alpha(0)] \geq$ 1.0. Only photons γ and pomerons $I\!P$ qualify, apart from W and Z bosons which always cause the proton to break up. The gluon g would qualify apart from its color, but if another gluon is exchanged that can be cancelled, and $I\!P = gg$ is often a good approximation. It cannot be exact; QCD forbids a pure gg state, and a $q\bar{q}$ component certainly grows as Q^2 increases. The $I\!P$ has C = +1; in QCD one should also have a ggg state with C = -1, the odderon [1] O, not yet observed. The central masses M_X are roughly limited to $M_X \lesssim \frac{\sqrt{s}}{20}$ with the outgoing protons having Feynman $x_F > 0.95$. Hence $M_X \lesssim 3$ GeV at the CERN ISR [2], appropriate for glueball spectroscopy, where $M(\pi^+\pi^-)$ shows a broad $f_0(600)$, a narrow $f_0(980)$ and still unexplained structure possibly associated with $f_0(1710)$, a glueball candidate. The study of X = hadrons, e.g. $\phi\phi$ and $D^\circ\bar{D}^\circ$ to name two channels among many, has not been studied above ISR energies, but CDF is a perfect place to do it and hopefully it will be done.

At the LHC M_X can reach $\approx$ 700 GeV, into the electroweak sector, and we can have $X = Z, H, W^+W^-, ZZ$, slepton pairs $\tilde{l}\tilde{l}$, etc. Measuring the forward protons after 120m of 8T dipoles, in association with the central event, as the FP420 [4] proponents hope to do at ATLAS and CMS, one can measure M_X with $\sigma(M_X) \approx 2$ GeV per event [5], and for a state such as H, also its width if $\Gamma(H) \gtrsim 3$ GeV/c^2. There are scenarios (e.g. SUSY) in which FP420 could provide unique measurements, e.g. if there are two nearby states both decaying to $b\bar{b}$ or to W^+W^-. The quantum numbers of X are $J^{PC} = 0^{++}$ or 2^{++} (and these are distinguishable) for $I\!P I\!P$ production. Two-photon collisions $\gamma\gamma \to l^+l^-, W^+W^-, \tilde{l}\tilde{l}$ become important at the LHC thanks to the intense high momentum photons, orders of magnitude more than at the Tevatron,

giving > 50 fb for W^+W^- as a continuum background to $H \to W^+W^-$. $H \to ZZ$ does not have this background.

While there is a gold mine of physics in $p+X+p$ at the LHC, we need to show that (a) the cross sections are within reach, and (b) one can build the spectrometers with resolution $\sigma(M_X) \approx$ 2 GeV/c^2 and calibrate their momentum scale *and resolution*, to measure $\Gamma(H)$, and perhaps to distinguish nearby states. Both these issues are addressed by CDF in a "TeV4LHC" spirit, and they are also very interesting in their own right. The calculation of cross sections (e.g. [6]) involves, in addition to $\sigma(gg \to X)$, the unintegrated gluon distribution $g(x_1, x_2)$, rapidity gap survival probability (no other parton interactions), and the Sudakov factor (probability of no gluon radiation producing hadrons). The Durham group predicts $\sigma(SMH)$ for $p + H + p$ at the LHC = $3^{\times 3}_{\div 3}$ fb. At the Tevatron $p + H + \bar{p}$ is out of reach, but the process $p + \chi_c(\chi_b) + \bar{p}$ is identical as far as QCD is concerned, as is $p+\gamma\gamma+\bar{p}$. Measuring these constrains the SMH cross section. In CDF we have looked for both exclusive $\gamma\gamma$ [7] and χ_c [8], without however having detectors able to see the p and $\bar{p}$. Instead we added forward calorimeters ($3.5 < |\eta| < 5.1$) and beam shower counters BSC ($5.5 < |\eta| < 7.4$). If these are all empty there is a high probability that both p and $\bar{p}$ escaped intact with small $|t|$. We also measured [9] exclusive dijets.

For the exclusive $\gamma\gamma$ search we triggered on events with two electromagnetic (EM) clusters with $E_T > 4$ GeV in the central calorimeter, with a veto on signals in the BSC. This killed pile-up events and enabled us to take data without prescaling the trigger. We required all other detectors to be consistent with only noise; then our *effective* luminosity is only about 10% of the delivered luminosity. We found [7] 3 events with exactly two back-to-back EM-showers (assumed to be photons) with $M(\gamma\gamma) > 10$ GeV/c^2. From wire proportional chambers at the shower maximum we concluded that two were perfect $p + \bar{p} \to p + \gamma\gamma + \bar{p}$ candidates and one was also consistent with being a $p + \bar{p} \to p + \pi^\circ\pi^\circ + \bar{p}$ event. The Durham prediction [10] was $0.8^{\times 3}_{\div 3}$ events, clearly consistent. We have since accumulated more data, with a lower threshold, now being analysed.

With the above trigger we also found [11] 16 $p + \bar{p} \to p + e^+e^- + \bar{p}$ events, with $M(e^+e^-) > 10$ GeV/c^2 (up to 38 GeV/c^2), the QED $\gamma\gamma \to e^+e^-$ process [12]. Exclusive 2-photon processes had not previously been observed in hadron-hadron collisions; the cross section agrees with the precise theory prediction. This process has been suggested as a means of calibrating the LHC luminosity; then it must be done in the presence of pile-up, and one will need to know the acceptance etc. at the few % level. More interesting for FP420 is that measurement of an exclusive lepton pair gives both forward proton momenta, with a precision dominated by the incoming beam momentum spread ($\frac{\delta p}{p} \approx 10^{-4}$, or 700 MeV). One can do this with pile-up, selecting dileptons with no associated tracks on the l^+l^- vertex and $\Delta\phi \approx \pi$. One can also cut on $p_T(l^+l^-)$ (correlated with $\Delta\phi$), but $\Delta\phi$ has better resolution. In CDF we found that a cut $\pi - \Delta\phi < \frac{0.8GeV}{M(l^+l^-)}$ rads is suitable for QED-produced pairs. For each pair one can predict ξ_1 and ξ_2, and, if a proton is in the FP420 acceptance, compare ξ_i and ξ_{420}. This can also possibly map the acceptance A($\xi, t \approx$0), as the cross section shape is known from QED, and the (Coulomb) protons have very small t.

CDF also used a "muon+track" trigger, again with BSC veto, to study $p + \bar{p} \to p + \mu^+\mu^- + \bar{p}$ with 3 GeV/c^2 $< M(\mu\mu) <$4 GeV/c^2. This is a very rich region, with the J/ψ and $\psi(2S)$ vector mesons that can only be produced exclusively by photoproduction $\gamma + I\!P \to \psi$, or

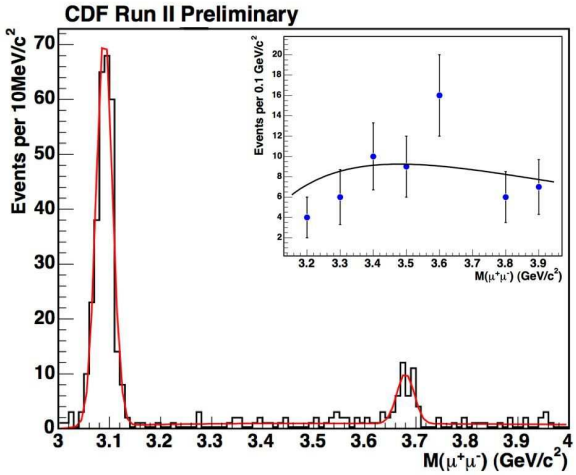


Fig. 1: Exclusive dimuon mass spectrum in the charmonium region, together with the sum of two Gaussians and the QED continuum, shown in the inset, excluding the 3.65 - 3.75 GeV/c^2 bin ($\psi(2S)$). All line shapes are predetermined, with the normalization free.

possibly by odderon exchange: $O + I\!P \to \psi$. We know what to expect for photoproduction from HERA, so an excess would be evidence for the elusive O. The spectrum [8] is shown in Fig. 1, together with the sum of three components: the vector mesons and a continuum, $\gamma\gamma \to \mu^+\mu^-$, which is again consistent with QED. These central exclusive spectra are exceptionally clean; in fact the biggest background ($\approx$ 10%) is the identical process but with an undetected $p \to p^*$ dissociation. The J/ψ and $\psi(2S)$ cross sections $\frac{d\sigma}{dy}|_{y=0}$, are (3.92$\pm$0.62)nb and (0.54$\pm$0.15)nb, agreeing with expectations [13, 14]. Thus we do not have evidence for O exchange, and put a limit $\frac{O}{\gamma} < 0.34$ (95% c.l.), compared with a theory prediction [15] 0.3 - 0.6.

While the QED and photoproduction processes in Fig. 1 should hold no surprises, their agreement with expectations validates the analysis. We required no EM tower with $E_T^{EM} >$ 80 MeV. If we allow such signals (essentially γ's) the number of J/ψ events jumps from 286 to 352, while the number of $\psi(2S)$ only increases from 39 to 40. The spectrum of EM showers is shown in Fig. 2. These extra J/ψ events are very consistent with being $\chi_{c0}(3415) \to J/\psi + \gamma$, from $I\!P I\!P \to \chi_c$, with about 20% of the γ being not detected (giving a background of 4% under the exclusive J/ψ). We measure $\frac{d\sigma}{dy}(\chi_c)|_{y=0}$ = (75$\pm$14)nb. The existence of this process implies that $p + H + p$ must happen at the LHC (assuming H exists), as the QCD physics is qualitatively identical. The χ_c cross section agrees with predictions: 150nb [16] and $130^{\times 4}_{\div 4}$nb [6]. It is therefore likely that $\sigma(p + p \to p + SMH + p)$ is of order 0.5-5 fb, within reach of FP420. In SUSY models the cross section can be much higher [4].

We are looking for $p+\bar{p} \to p+\Upsilon+\bar{p}$ (by photoproduction, or by $O+I\!P$), and $I\!P+I\!P \to \chi_b$. The Υ should be measurable in the presence of pile-up using $n_{ass} = 0$, $\Delta\phi$ and p_T cuts (n_{ass} is the number of additional tracks on the dilepton vertex). We have candidate events, with the $\Upsilon(1S), (2S)$ and $(3S)$ states resolved; cross sections are now being determined. The $\chi_b \to \Upsilon+\gamma$

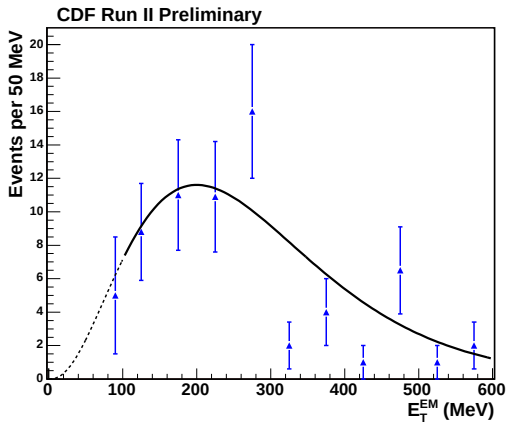


Fig. 2: The E_T spectrum of electromagnetic showers associated with J/ψ, together with an empirical function to estimate the fraction under the 80 MeV cut. These are $\chi_{c0}(3415)$ candidates.

probably can not be studied in the presence of pile-up, and it is challenging. We have also made a search [17] for exclusive Z, allowed only through photoproduction: $\gamma + I\!P \rightarrow Z$. In the Standard Model the (integrated) cross section at the Tevatron is too small to see, $\sigma_{excl}(Z)$ = 0.3fb [14] or 1.3fb [18], before branching fractions. In White's pomeron theory [19] the cross section is expected to be much larger, but a quantitative prediction is lacking. Our search uses both e^+e^- and $\mu^+\mu^-$ pairs with $M(l^+l^-) > 40$ GeV/c^2. There are 8 exclusive candidates with $\sigma(p + \bar{p} \rightarrow p + (\gamma\gamma \rightarrow l^+l^-) + \bar{p}) = 0.24^{+0.13}_{-0.10}$ pb (for $|\eta(\mu)| < 4.0$), agreeing with σ(QED) = 0.256 pb. All the events have $\pi - \Delta\phi < 0.013$(rad) and $p_T(\mu^+\mu^-) < 1.2$ GeV/c. Only one event had a $\bar{p}$ in the acceptance of the Roman pots when they were operational, and a track was observed, showing that the event was exclusive, and that at the LHC such $l^+l^- + p$ events will be available for calibration. If we remove the requirement that the BSC should be empty there are 4 additional events, interpreted as $p \rightarrow p^*$ dissocation. One of them has $M(\mu^+\mu^-) \approx M(Z)$ and a larger $\Delta\phi$ and p_T than the others, but we cannot claim it to be truly exclusive. We put a limit on exclusive $\sigma_{excl}(Z) < 0.96$ pb at 95% c.l. Clearly it will be interesting to look for exclusive $p + Z + p$ at the LHC. In early running of the LHC, when bunch crossings without pile-up are not yet rare, it is important to measure these exclusive processes, to the extent possible without complete forward coverage. In CMS we have plans to add forward shower counters [20] around the beam pipe to help tag rapidity gaps, together with the ZDC and forward hadron calorimeters. With large forward gaps in both directions, a trigger on two EM showers with $E_T > 4$ GeV should be possible, hopefully observing $\Upsilon \rightarrow e^+e^-, \gamma\gamma \rightarrow e^+e^-$, $I\!P I\!P \rightarrow \gamma\gamma$, and $\chi_b \rightarrow \Upsilon + \gamma \rightarrow e^+e^-\gamma$. Clean single interactions are surely needed for the χ_b and $I\!P I\!P \rightarrow \gamma\gamma$; both channels are excellent tests of $p + H + p$. One may even hope that when exclusive Higgs production is measured, the coupling ggH can be derived by comparing the three cross sections!

References

[1] See e.g. C.Ewerz, The odderon in Quantum Chromodynamics, hep-ph/0306137 (2003), and references therein.

[2] T.Akesson *et al.* (AFS Collaboration), Nucl.Phys. **B264**, 154 (1986).

[3] At this meeting such a study was initiated by the Kiev group (V.Aushev, L.Jenkovszky et al.).

[4] M.G.Albrow *et al.*, The FP420 R&D project, Higgs and new physics with forward protons at the LHC, arXiv:0806.0302 [hep-ex].

[5] M.G.Albrow and A.Rostovtsev, Searching for the Higgs at hadron colliders using the missing mass method, hep-ph/0009336.

[6] V.A.Khoze *et al.*, Eur.Phys.J. C**35**, 211 (2004); V.A.Khoze, A.D.Martin and M.G.Ryskin, Eur.Phys.J. C**14**, 525 (2000); A.De Roeck *et al.*, Eur.Phys.J. **C25**, 391 (2002).

[7] A.Abulencia *et al.*, (CDF Collaboration), Phys.Rev.Lett. **99**, 242001 (2007).

[8] T.Aaltonen *et al.*, (CDF Collaboration) Observation of exclusive charmonium production and $\gamma\gamma \to \mu^+\mu^-$ in $p\bar{p}$ collisions at $\sqrt{s}$ = 1.96 TeV; paper in preparation.

[9] T.Aaltonen *et al.*, (CDF Collaboration) Phys.Rev. **D77**, 052004 (2008).

[10] V.A.Khoze *et al.*, Eur.Phys.J. C**38**, 475 (2005).

[11] A.Abulencia *et al.* (CDF Collaboration), Phys.Rev.Lett. **98**, 112001 (2007).

[12] J.Vermaseren, LPAIR, Nucl.Phys. **B229**, 347 (1983).

[13] E.g. S.Klein and J.Nystrand, Phys.Rev.Lett. **92**, 142003 (2004).

[14] L.Motyka and G.Watt, Phys.Rev. **D78**, 014023 (2008).

[15] A.Bzdak *et al.*, hep-ph/07021354 (2007).

[16] F.Yuan, Phys.Lett. **B510**, 155 (2001).

[17] CDF Collaboration, Search for exclusive Z boson production; paper in preparation.

[18] V.P.Goncalves and M.V.T.Machado, Eur.Phys.J. **C53**, 33 (2008)

[19] A.R.White, Phys.Rev. **D72**, 036007 (2005). White does not claim that photoproduced Z have to be exclusive.

[20] M.Albrow *et al.*, Forward physics with rapidity gaps at the LHC, arXiv:0811:0120[hep-ex].

Overview on rapidity gap survival predictions for LHC

A.B. Kaidalov
Institute of Theoretical and Experimental Physics,Moscow, Russia
DOI: http://dx.doi.org/10.3204/DESY-PROC-2009-01/23

Abstract
An important role of unitarity effects related to multipomeron exchanges in diffractive processes is emphasized. A general technique to calculate these effects is presented. Role of interactions between pomerons is investigated. Recent theoretical models, which take into account these interactions are reviewed and consequences for survival probabilities of hard diffractive processes at LHC energies are discussed.

1 Introduction

Diffractive processes at high energies are usually described by pomeron exchange in the t-channel (see for example review [1]). An increase with energy of the total interaction cross sections indicates that an intercept of the pomeron is larger than unity. An exchange by a Regge pole with $\Delta \equiv \alpha_P(0) - 1 > 0$ leads to the violation of the s-channel unitarity. Therefore, multipomeron exchanges in the t-channel are very important for such "supercritical" pomeron. They restore unitarity and make theory consistent with Froissart bound.

Unitarity effects, related to the multipomeron exchanges, are especially important for inelastic diffractive processes and strongly reduce their cross sections. Inelastic diffractive processes correspond to configurations of final hadrons with one or several rapidity gaps. Reduction of cross sections in comparison with the born (Regge pole) approximation is usually called gap survival probability, because it determines a probability not to fill the gap by produced hadrons. Knowledge of the gap survival probability is important for experimental investigation of diffractive processes at LHC, and in particular for searches of the Higgs boson in the central exclusive double pomeron production.

I shall give a short review of recent developments in theory of diffractive processes at high energies and shall discuss the role of interactions between pomerons for survival probabilities of rapidity gaps.

2 General method for calculation of multi-pomeron cuts

A general method for calculation of multi-pomeron contributions to amplitudes of diffractive processes has been formulated by V.N. Gribov [2]. I shall illustrate it using as an example a contribution of two-pomeron exchange to the process of elastic scattering. Using analyticity and unitarity properties for pomeron-particle scattering amplitudes the total contribution can be expressed as the sum over all intermediate diffractive states as shown in Fig.1

An account of elastic intermediate states for n-pomeron exchange amplitudes leads to the eikonal formula in the impact parameter space:

$$\mathrm{Im}\, T \;=\; 1 \;-\; e^{-\Omega/2}, \tag{1}$$

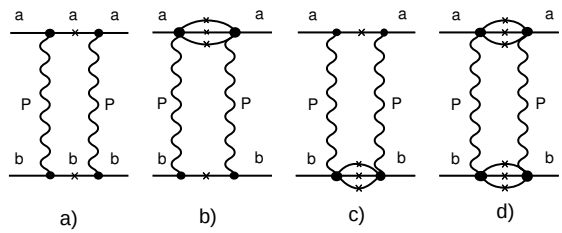


Fig. 1: Two-pomeron exchange diagram as a sum over all possible diffractive states.

where the eikonal Ω is the Fourier transform of the pomeron pole exchange.

Low mass diffractive states are often approximated by several resonance states. In this case the same method leads to eq. 1 with Ω being a matrix, whose elements correspond to transitions between different diffractive states. The simplest treatment is a diagonalization of this matrix. Thus an account of the low mass diffraction in the Gribov's method is equivalent to the Good-Walker [3] approach to inelastic diffraction.

In the eikonal approximation a probability not to fill the gap is equal to $e^{-\Omega}$ and the survival probability is:

$$S^2 \;=\; \frac{\int\, |\mathcal{M}(s,b)|^2\, e^{-\Omega(b)}\, d^2b}{\int\, |\mathcal{M}(s,b)|^2\, d^2b}, \tag{2}$$

This expression is easily generalized to the case of several channels. The same eq. 2 is valid for each diagonal state and it is necessary to sum over all diagonal states (with corresponding weights).

The quantity Ω increases with energy as s^{Δ} and becomes large at very high energy. According to eq. 2 cross sections of inelastic diffractive processes become negligible at small impact parameter and are concentrated at the edge of interaction region at $b > 1$ fm. Note that models based on perturbative QCD are not valid in this peripheral region.

The value of S^2 is not universal: it depends on dependence of a matrix element $\mathcal{M}(s,b)$ on impact parameter b.

3 Unitarity effects for hard diffraction

The condition for masses M of hadronic states produced in diffractive process (by the pomeron exchange) is $M^2 \ll s$. Thus very large masses can be generated at very high energies and heavy states can be produced (jets, heavy quarks, W and Z bosons, Higgs meson etc.) They represent an interesting class of hard diffractive processes, where the subprocess of a heavy state production can be calculated using QCD perturbation theory. The simplest inclusive diffractive process is a diffractive dissociation of a highly virtual photon. In this case the photon interacts with a quark and a study of these processes at HERA gave a possibility to determine the distribution of quarks and gluons in the pomeron. These distributions and QCD factorization can be used to predict cross sections of hard inclusive diffractive processes in hadronic interactions. Note, however, that multi-pomeron contributions violate both Regge and QCD factorization and strongly

modify predictions based on a single pomeron exchange. CDF data [4] show that cross section of diffractive dijet production at Tevatron is about an order of magnitude smaller as compared to the prediction based on QCD factorization and partonic distributions extracted from HERA data. Calculation of gap survival probability in the two-channel eikonal model [5] allows to reproduce the observed suppression.

It is interesting that the same suppression is observed for double gap (double pomeron exchange) events at Tevatron [6]. This observation is in accord with a dominance of eikonal-type rescatterings [7].

4 Large mass diffraction and interactions of pomerons

So far we have considered the low mass excitations in diffractive intermediate states of Fig.1. We know that large mass excitations constitute a large fraction of diffraction cross section. The large mass behavior of the pomeron-particle amplitudes is described by the triple-pomeron and multi-pomeron diagrams (Fig.2).

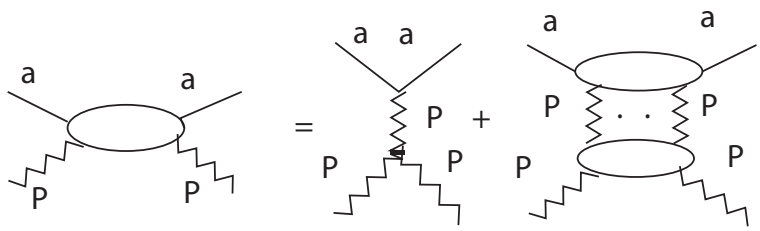


Fig. 2: Diagrams for the pomeron-particle scattering amplitudes at large M^2.

It is clear that for very large masses it is not enough to consider the triple-pomeron contribution only. An important theoretical question is: what is the structure of the vertices for n pomeron to m pomeron transitions? The simplest approximation is to assume an eikonal-type structure for the pomeron-particle amplitudes at large M^2:

$$g_{mn} = cg^{m+n} \tag{3}$$

where c and g are some functions of t. This behavior of vertices follows from multiperipheral model and is natural from the t-channel unitarity point of view. It was used in [8] to sum all diagrams with interactions of pomerons. This model leads to a good description of total, elastic and single diffraction dissociation cross sections (σ_{SD}) in $pp(p\bar{p})$ interactions [8] with $\Delta \approx 0.2$. It is worth to note that without multi-pomeron effects σ_{SD} has too fast increase with energy and exceeds experimentally observed cross section by a factor ~ 10.

More recently the same structure of multi-pomeron vertices has been used for the description of diffractive processes [9] and, assuming validity of AGK cutting rules, for multiparticle production at high energies [10].

Investigation of asymptotic behavior of diffractive processes in reggeon field theory has started already in seventies. Most of these investigations were based on the version of the theory with a triple-pomeron interaction only [11]. It is not clear that for supercritical pomeron

such theory is consistent with s and t- channel unitarity. One dimensional version of this theory leads to a decrease of total cross section as $s \to \infty$. More recent studies [12, 13], based on partonic interpretation of reggeon field theory, indicate that it is necessary to take into account 4P-interaction to make this theory consistent.

5 Recent estimates of survival probabilities

In this section I shall review recent models for diffractive processes, which take into account interactions between pomerons, and shall discuss predictions of these models for survival probabilities of hard diffractive processes.

The Durham group (KMR) has recently made a new fit to the data on cross sections of diffractive processes [14, 15]. All $n \to m$ pomeron transition were taken into account in the framework of a partonic model, which leads to the behavior $g_{mn} \sim nmg^{n+m}$, which is somewhat different from the one discussed above in the eikonal approximation. Summation of diagrams was performed by numerical solution of a system of highly nonlinear equations for amplitudes. Formulas for cross sections of different inelastic diffractive processes were obtained using some probabilistic arguments (and not cutting rules as in the standard approach). In this model it is possible to obtain a reasonable description of total cross section for pp-interaction, its elastic cross section in the diffraction cone region and cross sections of single and double diffraction. The result for an intercept of the pomeron is sensitive to details of the model. In particular in one dimensional version of the model with $\alpha\prime = 0$ values of Δ close to 0.5 were obtained [14], while in a more accurate treatment, which takes into account transverse degrees of freedom [15], Δ decreases to values close to 0.3.

In the treatment of diagrams with interactions between pomerons it is necessary to take into account that the notion of the pomeron exchange is meaningful for large rapidity gaps only (usual choice $y > y_0$, with $y_o = ln(10) = 2.3$). Thus a cutoff at small rapidities for each pomeron line should be introduced. This leads to a natural limitation to the number n of the t-channel iterations of pomeron exchanges (or number of gaps) at each initial energy: $n < ln(s/s_0)/y_0$ with $s_0 = 1\ GeV^2$. This threshold effect was taken into account in ref.[8] and should be accounted for in all realistic calculations with pomeron interactions. It plays an important role in calculations of survival probabilities (see below). I believe that introduction of this effect in KMR calculation will further decrease the value of Δ.

A different approach was used by the Tel-Aviv group (GLM)[16]. Arguments based on a small value of the pomeron slope were used to justify applicability of perturbative QCD (pQCD) for diffractive processes. Motivated by pQCD the authors used the triple-pomeron interaction only with maximal number of pomeron loops. The last assumption may be reasonable for interaction of very small dipoles, but is difficult to justify for interaction of protons. One dimensional approximation was used in calculations. Besides the diagrams with pomeron loops two-channel eikonal model was used. I have emphasized above that inelastic diffractive processes are concentrated at the edge region of large impact parameters and that nonperturbative effects (for example two-pion cut in the pomeron trajectory and residues) are important in this region. The fit to total pp-interaction cross section, differential cross section of elastic scattering and inelastic diffraction was performed in the model [16] and parameters of the pomeron were determined. The value

$\Delta = 0.33$ for the intercept of the pomeron was found. Note that the threshold effects, discussed above, has not been taken into account in this model.

Let us discuss the common features and the differences in results of these two models. A general feature of models, which take into account interactions between pomerons ("enhanced" diagrams), is a slower increase with energy of total cross sections. For example predictions of both KMR and GLM models for the total cross section of pp interaction at LHC energy are close to 90 mb, which is substantially smaller than in models without these interactions. Same effect exists in the model of ref.[8], though the corresponding cross section is closer to 100 mb. Values of the pomeron intercept is substantially higher than in the eikonal-type models. Our experience for models with pomeron interactions [8] indicates that for values of the pomeron intercept $\Delta > 0.2$ the models become rather unstable: results for cross sections are sensitive to details of models.

There is a significant difference in predictions of KMR and GLM models for low and large mass contributions to the single diffraction dissociation cross sections. For example at Tevatron energies predictions of the KMR model for low-mass diffraction and high-mass diffraction are 4,4 mb and 6.5 mb correspondingly, while in GLM model the corresponding numbers are 8.6 and 1.2 mb. It is difficult to understand how it was possible to describe the CDF data on high-mass diffraction in both models with so different values of high-mass cross sections? The form of the mass distribution for low mass diffraction, proposed in GLM model (RRP-term, production of very large masses $\sim s^{1/2}$ by secondary reggeons) seems to me unacceptable.

The largest difference in KMR and GLM models is in predictions for survival probabilities. In ref.[14] the change in S^2 due to enhanced diagrams has not been calculated and calculation [17] in a simplified model, which takes into account threshold effects, show that for DPE Higgs production at LHC this change is small. On the other hand in GLM model a modification of survival probabilities due to enhanced diagrams is very strong: for DPE Higgs production at LHC it decreases the probability calculated in the two channel eikonal model by a factor ≈ 16. This is important for experiments, planned to observe DPE Higgs production at LHC. For DPE processes at Tevatron GLM model predicts a decrease of survival probability by a factor 3.5. This does not agree with CDF data [6] (see above). Thus a controversy in theoretical predictions for suppression of hard diffractive processes due to enhanced diagrams [5, 18, 19] is in my opinion still not resolved.

In view of large uncertainties in predictions of theoretical models for survival probabilities of diffractive processes it is worth to summarize what we know about these probabilities from experiment. A comparison of CDF data on diffractive dijet production [4] with prediction based on QCD factorization and survival factor of two channel eikonal model show that extra suppression due to enhanced diagrams does not exceed 50%. Similar estimate follows from CDF data on DPE dijet production [6, 20].

Thus up to energies of Tevatron interaction between pomerons play a minor role in hard diffractive processes. This is to a large extent related to the phase-space limitations. For soft diffraction enhanced diagrams are important and lead to a change of parameters of the "bare" pomeron in reggeon theory. At LHC the effects of enhanced diagrams will be observable in hard diffractive processes. Their influence on survival probabilities can be studied, in particular, in diffractive production of jets (with not too large masses).

I thank E. Gotsman, E. Levin, A.D. Martin and S. Ostapchenko for useful discussions. This work was partially supported by the grants RFBR 0602-72041-MNTI, 0602-17012, 0802-00677a and NSh-4961,2008.2.

References

[1] A.B. Kaidalov, Phys. Rep. **50**, 157 (1979).

[2] V.N. Gribov, Sov. Phys. JETP **19**, 483 (1969).

[3] M.L. Good and W.D. Walker, Phys. Rev. **126**, 1857 (1960).

[4] CDF Collaboration: T. Affolder et al., Phys. Rev. Lett. **84**, 5043 (2000).

[5] A.B. Kaidalov,V.A. Khoze,A.D. Martin and M.G. Ryskin, Eur. Phys. J. **C21**, 521 (2001).

[6] CDF Collaboration, T.Affolder et al., Phys.Rev.Lett. **85**, 4215 (2000).

[7] A.B. Kaidalov, V.A. Khoze, A.D. Martin and M.G. Ryskin, Phys. Lett. **B559**, 235 (2003).

[8] A.B. Kaidalov, L.A. Ponomarev, K.A. Ter-Martirosyan, Sov. J. Nucl. Phys. **44**, 486 (1986).

[9] S. Ostapchenko, Phys. Lett. **B636**, Phys. Rev. **D74**, 014026 (2006).

[10] S. Ostapchenko, Phys. Rev. **D77**, 034009 (2008).

[11] D. Amati, L. Caneschi, and R. Jengo, Nucl. Phys. **B101**, 397 (1976);
D. Amati, G. Marchesini, M. Ciafaloni and G. Parisi, Nucl. Phys. **B114**, 483 (1976).

[12] K. Boreskov, in *Multiple facets of quantization and supersymmetry*, p.322; arXiv:hep-ph/0112825.

[13] S. Bondarenko et al., Eur. Phys. J. **C50**, 593 (2007).

[14] M.G. Ryskin, A.D. Martin and V.A. Khoze, Eur. Phys. J. **C54**, 199 (2008).

[15] A.D. Martin, talk at Conf. Diffraction 08, September 2008.

[16] E. Gotsman, E. Levin, U. Maor, J.S. Miller, arXiv:hep-ph/0805.2799.

[17] A.D. Martin, V.A. Khoze and M.G. Ryskin, arXiv:hep-ph/0803.3939.

[18] J. Bartels, S. Bondarenko, K. Kutak, L. Motyka, Phys. Rev. **D73**, 093004 (2006).

[19] L. Frankfurt, C.E. Hyde, M. Strikman, C. Weiss, arXiv:hep-ph/0710.2942;0808.0182.

[20] K. Hatakeyama, talk at ISMD 2008.

Access to small x Parton Density Functions at the LHC

Tara Shears, on behalf of the LHC collaborations.
University of Liverpool

DOI: http://dx.doi.org/10.3204/DESY-PROC-2009-01/24

Abstract
Predictions for particle production at the LHC employ parton density functions extrapolated to lower x and higher Q^2 regions than have been tested experimentally. In these proceedings studies of low mass Drell-Yan, forward jet and J/ψ production, and their sensitivity to small x, are summarised. Features of the LHC experiments conducive to making these measurements are compared.

1 Introduction

The Large Hadron Collider (LHC) at CERN will operate at a centre of mass energy of $\sqrt{s} = 14$ TeV. Measurements made of particle production will access an unexplored kinematic region. Predicted cross-sections for such processes rely on assumptions for parton momentum fraction (x) extrapolated to untested regions.

The parton density functions (PDFs) that describe the momentum fraction carried by individual partons are based on measurements made at HERA, the Tevatron and fixed target experiments. These cover only a fraction of the x-Q^2 region accessed at the LHC (where Q^2 is the scale of the hard interaction). In order to describe LHC data the PDFs must be evolved up in Q^2 and down in x. Measurements taken at the LHC can therefore be used to test the DGLAP and BFKL evolution schemes used to achieve this.

These proceedings describe how certain measurements made at the LHC can probe the small x region of the proton. Smaller values of x are probed in measurements of low mass particle production, or forward (high rapidity) particle production. Section 2 describes the features of the LHC experiments relevant to these analyses. Section 3 summarises studies which have been carried out so far. Conclusions are given in section 4.

2 The LHC experiments

Four experiments, ALICE, ATLAS, CMS and LHCb, detect proton proton collisions at the LHC (heavy ion collisions will not be considered here). ATLAS and CMS have been designed to instrument as much of the solid angle around the collision point as possible, whereas the coverage of the ALICE and LHCb experiments is determined by sensitivity to heavy ion and heavy quark processes respectively. The pseudorapidity coverage of the major detector components of the four experiments is summarised in table 1.

3 Preliminary physics studies

Studies of low invariant mass Drell-Yan production, forward jet and forward particle production have been carried out by the experiments and will be presented in the following subsections. Note

Detector	ALICE	ATLAS	CMS	LHCb
Tracking	$-0.9 < \eta < 0.9$	$-2.5 < \eta < 2.5$	$-2.5 < \eta < 2.5$ $3.1 <\mid \eta \mid < 4.7$ $5.2 <\mid \eta \mid < 6.5$	$1.8 < \eta < 4.9$
EM calorimeters	$-0.9 < \eta < 0.9$	$-4.5 < \eta < 4.5$	$-6.5 < \eta < 6.5$	$1.8 < \eta < 4.9$
Had calorimeters	$\mid \eta \mid > 8.5$	$\mid \eta \mid < 4.5, \mid \eta \mid > 8.1$	$\mid \eta \mid < 6.5$	$1.8 < \eta < 4.9$
Muon chambers	$-4 < \eta < -2.5$	$\mid \eta \mid < 2.7$	$\mid \eta \mid < 2.5$	$1.8 < \eta < 4.9$
Counters	$-3.4 < \eta < 5$ $-6.1 < \eta < -5$ $\mid \eta \mid > 8.1$	$5 < \eta < 6.1$		
Triggers	$Pt(\mu) > 1(2)$ GeV	$Pt(\mu) > 4(10)$ GeV	$Pt(\mu) > 3.5$ GeV	$Pt(\mu) > 1$ GeV

Table 1: Pseudorapidity coverage of the main components of each LHC experiment: tracking; electromagnetic and hadronic calorimetry; muon chambers; particle counters; example transverse momentum (Pt) trigger thresholds for muons. For the last category, numbers in brackets refer to thresholds imposed during high luminosity running.

that these studies are preliminary and represent an incomplete survey of all measurements sensitive to small x. For example, measurements of forward W and Z boson production at LHCb [1], and exclusive upsilon production at CMS [2] will not be described here.

3.1 Low mass Drell Yan production

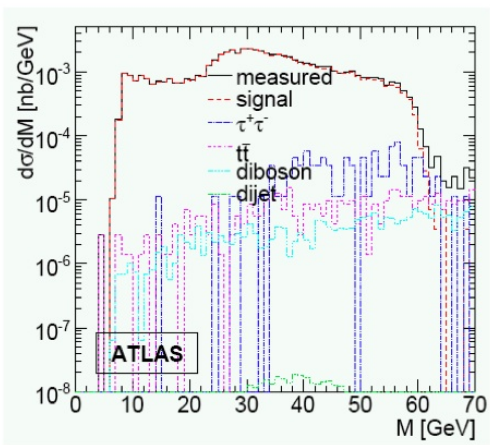
The ATLAS, CMS and LHCb collaborations have performed studies of low invariant mass Drell-Yan production.

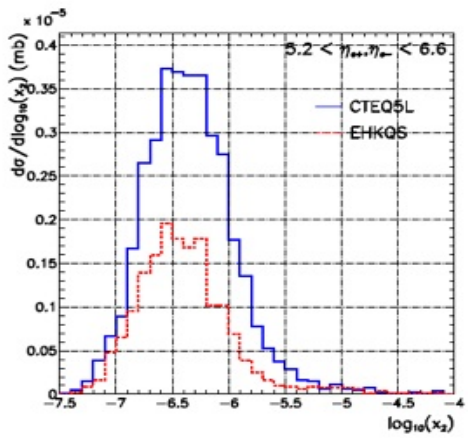
ATLAS has studied $\gamma^* \rightarrow e^+e^-$ production, where the final state electrons lie within the pseudorapidity region $\mid \eta \mid < 2.5$ [3]. Events are triggered by requiring an electron candidate of at least 10 GeV transverse momentum within the angular acceptance. Candidates are reconstructed by requiring two oppositely charged electrons which both have transverse momentum exceeding 10 GeV within $\mid \eta \mid < 2.5$. In addition, the missing transverse energy of the event must not exceed 30 GeV. The selection efficiency depends on mass, and is about 1% for invariant masses around 8 GeV. Figure 1 shows the invariant mass spectrum of selected events, with background estimates overlaid. Note that the dijet background contains significant statistical uncertainty. Systematic errors have been investigated and are thought to be small. The largest, due to PDF uncertainty, arises from the acceptance correction. With 50 pb^{-1} of data analysed the statistical error of an inclusive cross-section measurement, for masses between 8 and 60 GeV, is about 7%, and values of x down to 10^{-4} can be probed.

CMS has studied the same production channel in the forward rapidity region ($5.2 <\mid \eta \mid < 6.5$) [4]. Events are triggered by requiring a large electromagnetic (> 300 GeV) and small hadronic (< 5 GeV) energy deposit in the calorimeter, and at least one charged track found by the TOTEM tracking stations. Candidate events must also satisfy a minimum invariant mass cut m(ee)> 4 GeV. Studies are preliminary - no backgrounds or systematic error have yet been considered. Figure 1 shows the values of x probed as a function of differential cross-section, for predictions using PDFs which include an estimate of saturation (EHKQ6) and which do not (CTEQ5L). Values of x approaching 10^{-6} can be probed. The measurement is sensitive to the

saturation effects included in the PDF set tested.

LHCb has studied the production of $\gamma^* \rightarrow \mu^+\mu^-$ events inside the experimental acceptance of $1.8 < \eta < 4.9$ [1]. Events can be triggered by requiring two muon candidates, of summed transverse momentum exceeding 1.6 GeV. This requirement is 70% efficient for invariant masses m($\mu\mu$) >8 GeV. Candidate events are then chosen by requiring that both muons have low impact parameter and a high degree of isolation. These requirements are combined in a likelihood. Backgrounds from bottom and charm semi-leptonic decays, and kaons and pions misidentified as muons, have been considered. Figure 1 illustrates the likelihood shapes for these different contributions, shown as a function of differential cross-section. A full evaluation of systematic error is ongoing. Purities of 70% are thought to be achievable at invariant masses of 8-10 GeV, which would probe values of x approaching 10^{-6}. The statistical error is estimated at 1% if $100pb^{-1}$ of data are analysed.





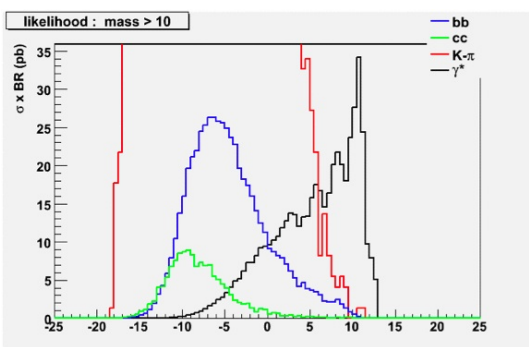


Fig. 1: (Top left) Invariant mass of $\gamma^* \rightarrow e^+e^-$ events analysed at ATLAS. Background contributions are shown by the coloured lines. (Top right) Range of x probed in forward $\gamma^* \rightarrow e^+e^-$ production with the CMS detector. Two theoretical predictions are shown: EHK6, which includes a treatment of saturation; CTEQ5, which does not. (Bottom left) Selection likelihood shapes for signal and major backgrounds for $\gamma^* \rightarrow \mu^+\mu^-$ with the LHCb experiment.

3.2 Forward jet production

CMS have studied jet production in the region $3 <| \eta |< 5$ [4]. Events can be triggered by requiring a transverse energy deposit exceeding 10 GeV in the HF calorimeter. Jets are defined using a cone algorithm, with radius R= $\sqrt{\Delta\phi^2 + \Delta\eta^2} = 0.5$. A candidate jet must have transverse energy exceeding 20 GeV. Figure 2 shows that values of x can be probed down to 10^{-5}. However, this measurement requires careful systematic error evaluation. Studies indicate that, unlike measurements of Drell-Yan production, accuracy is limited by the uncertainty in jet energy correction, which could contribute up to 30% systematic error in low transverse energy jets, where the smallest x is probed.

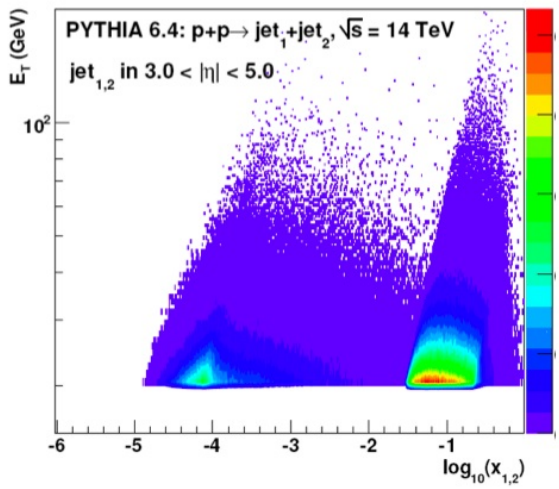


Fig. 2: Range of x probed in forward jet production with CMS, shown as a function of the transverse energy of the jet.

3.3 Forward J/ψ production

The ALICE experiment can probe small x through measurements of forward muon production. Figure 3 shows the region of x accessible when J/ψ production is measured within the confines of the ALICE muon detector. No studies have yet been performed, but the figure suggests it may be possible to probe values of x approaching 10^{-6}.

4 Conclusions

Measurements made of low invariant mass particle production at the LHC, particularly at forward rapidities, probe the small x region of the proton. These measurements can be used to test the evolution of the parton density functions to small x. Studies carried out by the LHC experiments indicate that it may be possible to probe values of x down to 10^{-6}.

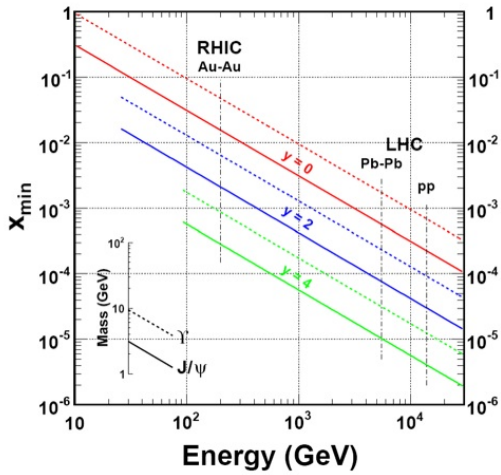


Fig. 3: Range of x probed in Υ (dotted line) and J/ψ (solid line) production with the ALICE experiment, shown for data taken at different centre-of-mass energies. Values of x probed at rapidities of 0, 2 and 4 are shown by the red, blue and green lines.

5 Acknowledgements

The author would like to thank the LHC collaborations, and particularly Monika Grothe, Tom Lecompte and Karel Safarik, for helpful discussions and input.

References

[1] R. McNulty,"Potential PDF sensitivity at LHCb", Proceedingsof the XVI International Workshop on Deep-Inelastic Scattering and Related Topics, April 7-11, 2008 London, England **doi:10.3360/dis.2008.29**.

[2] The CMS collaboration, **CMS PAS DIF-07-001** (2008).

[3] The ATLAS collaboration, **ATL-COM-2008-064** (2008).

[4] The CMS collaboration, **CERN/LHCC 2006-039/G-124**, (2006).

Theoretical concepts of parton saturation - from HERA to LHC

Krzysztof Golec-Biernat
Institute of Nuclear Physics Polish Academy of Sciences, Cracow, Poland,
Institute of Physics, University of Rzeszów, Rzeszów, Poland

DOI: http://dx.doi.org/10.3204/DESY-PROC-2009-01/66

Abstract
We present a short summary of parton saturation concepts as seen in deep inelastic scattering.

1 Introduction

The deep inelastic scattering (DIS) experiments, in which leptons probe nucleons with the help of electroweak bosons, reveal that nucleons consist of partons. These are colored quarks of Quantum Chromodynamics (QCD) which carry approximately half of the nucleon's momentum. The missing half is provided by gluons to which the electroweak bosons do not couple. Thus, although not directly probed, gluons are extremally important for the description of the nucleon structure. Quantitatively, this is summarized by the DGLAP evolution equations of QCD which govern the dependence of the quark and gluon distributions in a nucleon on a scale Q^2 (identified in DIS with photon's virtuality $q^2 = -Q^2$). The sign of the logarithmic derivative, $\partial F_2/\partial \log Q^2$, at different values of the Bjorken variable x is determined by the relative contribution of quarks to gluons. In the limit $x \to 0$, studied intensively by the experiments at HERA, the deep inelastic processes are dominated by a strongly rising gluon distribution. Therefore, in the small-x limit, gluonic systems inside the nucleon are predominantly studied. The description of processes in such systems, using perturbative QCD (pQCD), is the aim of this presentation.

2 Collinear factorization versus k_T-factorization

In the electron–proton DIS, the measured proton structure functions, F_T and F_L, are related to the parton distributions through the collinear factorization formula resulting from pQCD:

$$F_{T,L}(x,Q^2) = \sum_{i=q,\bar{q},g} \{C^{(i)}_{T,L} \otimes f_i)\}(x,Q^2) + \sum_{n=1} \frac{\Lambda^{(n)}_{T,L}(x,\alpha_s)}{Q^{2n}} \tag{1}$$

where $\otimes$ indicates integral convolution in parton longitudinal momentum fractions, $\alpha_s = \alpha_s(Q^2)$ is the running strong coupling constant, $C^{(i)}_{T,L}(z,\alpha_s)$ are perturbatively computed coefficient functions and $f_i(x,Q^2)$ are quark, antiquark and gluon distributions (multiplied by x). The Q^2-dependence of the parton distributions is determind by the DGLAP evolution equations [1] with initial conditions which are fitted to data. The first term on the r.h.s. of eq. (1) provides the leading twist-2 description with logarithmic dependence on Q^2 while the remaining terms, called higher twists, seem to be suppressed for large Q^2. In the standard analysis, a global fit of the leading twist formula to the HERA data on $F_2 = F_T + F_L$, together with cross sections of other hard processes, leads to the determination of the parton distributions shown in Fig. 1. A

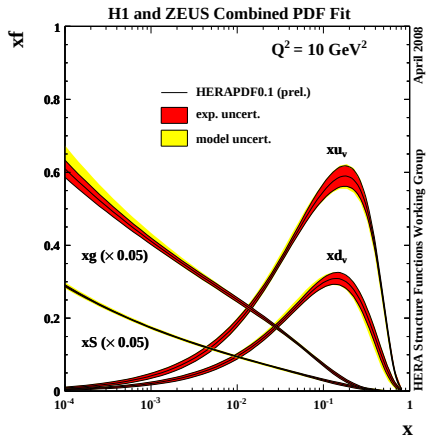


Fig. 1: *Parton distributions from a global fit to the HERA data as functions of x for fixed $Q^2 = 10\ \mathrm{GeV}^2$.*

distinct feature of this determination is a strong rise of the gluon and sea quark distributions for $x \to 0$.

A closer theoretical examination of the small-x scattering reveals that for not too high Q^2, the higher twist terms cannot be neglected since they are enhanced by powers of $\alpha_s \log(1/x)$, when the smallness of α_s is compensated by a large logarithm of x. The relevant resummation of such terms in the leading (LO) and next-to-leading (NLO) logarithmic approximation leads to the BFKL approach to the structure functions with the following k_T-factorized form [2]:

$$F_2(x,Q^2) = Q^2 \int \frac{d^2k_T}{k_T^4}\, \Phi(k_T^2/Q^2, \alpha_s(k_T))\, f(x,k_T) \tag{2}$$

where the impact factor $\Phi(k_T^2/Q^2, \alpha_s(k_T))$ describes the interaction of the virtual photon with a gluon with nonzero transverse momentum k_T. In the LO this is the process: $\gamma^*(Q^2)g(k_T) \to q\bar{q}$. The function $f(x,k_T)$ is called unintegrated gluon distribution which obeys the BFKL equation [3] and is related to the gluon distribution $g(x,Q^2)$ through the formula

$$xg(x,Q^2) = \int \frac{d^2k_T}{k_T^2}\, f(x,k_T)\, \theta(|k_T| < Q^2)\,. \tag{3}$$

From the solution of the BFKL equation, the small-x limit is dominated by the gluon distribution with the power-like rise, $f(x,k_T) \sim x^{-\lambda}$ and $\lambda \approx 0.3$. There is a general agreement, based on the experience with the Froissart-Martin bound, that such a rise of the gluon distribution, and in consequence F_2, violates unitarity and eventually must be tamed. The BFKL solution is also plagued by diffusion to infrared, namely, the k_T-integration in the pQCD formula (2) is quickly dominated by the contribution from the soft momenta region, $k_T \approx \Lambda_{QCD}$, where the Landau pole of $\alpha_s(k_T)$ is encountered. A cure for these problems is absolutely necessary.

3 Parton saturation

The taming of the power-like rise of the gluon distribution $xg(x,Q^2)$ was addressed for the first time by Gribov, Levin and Ryskin in [4] in the double logarithmic approximation. Summing fan

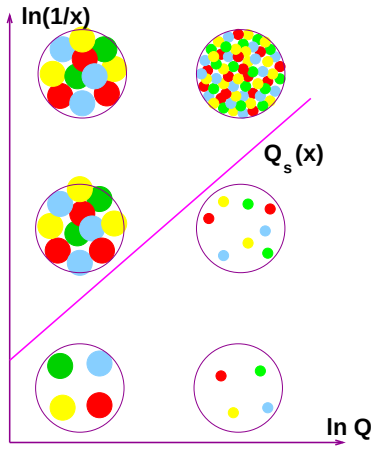


Fig. 2: *Saturation line in the* (x, Q^2)*-plane.*

diagrams, which take into account the fusion of t-channel gluons, the linear DGLAP equation for the gluon distribution receives a negative, nonlinear term,

$$\frac{\partial^2 xg(x,Q^2)}{\partial \ln(1/x) \partial \ln Q^2} = \overline{\alpha}_s xg(x,Q^2) - \frac{\alpha_s^2}{\pi^2 R^2} \frac{[xg(x,Q^2)]^2}{Q^2}\,, \tag{4}$$

where $\overline{\alpha}_s = N_c \alpha_s/\pi$ and the parameter R controls the strength of the nonlinearity. With such a modification, the gluon distribution saturates for $x \to 0$, and so does the structure function. This result was extended in [5] by including nonlinear modifications for the sea quark distributions. A crucial feature introduced by the nonlinearity is an x-dependent saturation scale $Q_s^2(x)$, defined as a value of Q^2 for which the nonlinear term in eq. (4) is comparable with the linear one:

$$xg(x,Q_s^2)\,\frac{\alpha_s(Q_s^2)}{Q_s^2} \;\sim\; \pi R^2\,. \tag{5}$$

Therefore, saturation effects are important when the number of gluons per unit of rapidity, xg, times the gluon-gluon interaction cross section, α_s/Q^2, approaches the geometric size of the nucleon or a gluonic system inside the nucleon ("hot spot"). In such a case, a simple additive treatment of parton emission breaks down and gluons start to annihilate. Since from (5) $Q_s^2 \sim xg$ and $xg \sim x^{-\lambda}$ before the saturation limit is reached, we find that $Q_s^2 \gg \Lambda_{QCD}^2$ for sufficiently small x, and the presented approach based on perturbative QCD is justified . This is schematically illustrated in Fig. 2 where two regions separated by the saturation line, $Q^2 = Q_s^2(x)$, are shown. Below this line, in the dilute region, the linear evolution equations are valid, while approaching the line, the saturation region is entered with nonlinear equations describing parton saturation.

Eq. (4) is a rather crude approximation since it is valid in the extreme case, $x \to 0$ and $Q^2 \to \infty$. In the k_T-factorization approach the latter limit is relaxed and only large logarithms $\log(1/x)$ are relevant. Summing BFKL pomeron fan diagrams with triple pomeron vertices in the leading logarithmic approximation and in the limit of large number of colors N_c, the Balitsky-

Kovchegov (BK) equation for the unintegrated gluon density $\phi(x, k_T)$ is found[1] [6, 7]:

$$\partial_Y \phi(x, k_T) \, = \, \overline{\alpha}_s \, \chi(-\partial_L) \, \phi \, - \, \overline{\alpha}_s \, \phi^2 \tag{6}$$

where $Y \, = \, \log(1/x)$ is rapidity, $L \, = \, \log k_T^2$ and χ is the BFKL characteristic function. This nonlinear equation generalizes the linear BFKL equation. The properties of its solutions were intensively studied both analytically [8] and numerically [9]. The most fruitful approach is based on the relation to the known from statistical physics Fisher-Kolmogorov equation, which admits travelling wave solutions. In our language, it means that the BK solution develops a saturation scale, $Q_s(x) \sim x^{-\lambda}$ with known value of λ [8], such that for small x we have

$$\phi(x, k_T) = \phi(k_T/Q_s(x)) \, . \tag{7}$$

This property, called geometric scaling, was observed in the data from HERA [10]. Looking more carefully, for $k_T \gg Q_s(x)$ the gluon distribution $\phi \sim 1/k_T^2$, while for small transverse momenta, $\Lambda_{QCD} \ll k_T < Q_s(x)$, the behaviour changes to logarithmic, $\phi \sim \ln(Q_s(x)/k_T)$. This is the illustration of the transition to saturation, when both the power-like growth in x and infrared diffusion in k_T of the gluon distribution are tamed, see again Fig. 2 with $Q^2 \equiv k_T^2$.

4 Color dipole approach and beyond

A more intuitive approach to parton saturation is provided by the color dipole approach [11, 12]. In the target rest frame, the DIS at small x can be formulated as the eikonal scattering of a color quark-antiquark dipole, formed by the splitting $\gamma^* \, \to \, q\bar{q}$, on the target color field. The dipole scattering amplitude $N(\mathbf{x}, \mathbf{y})$ is given by two Wilson lines collinear to quarks' velocity u

$$N(\mathbf{x}, \mathbf{y}) = 1 - \frac{1}{N_c} \mathrm{Tr} \, U(\mathbf{x}) U^\dagger(\mathbf{y}) \, , \qquad U(\mathbf{x}) = \mathrm{P} \exp \left\{ ig \int_{-\infty}^{\infty} d\lambda \, u \cdot A(\lambda u + \mathbf{x}) \right\} \tag{8}$$

where $\mathbf{x}$ and $\mathbf{y}$ are two dimensional vectors of the quark transverse positions, conserved during the collision, and A is a target color field. The deviation of the classcal quark trajectory from the light-like line defines the change of N with rapidity Y, which leads to the new BK equation for the dipole scattering amplitude [6]. Its solutions fulfil the unitarity bound, $N \, \leq \, 1$. When the dependence on the impact parameter, $\mathbf{b} = (\mathbf{x} + \mathbf{y})/2$ is neglected, the new equation is equivalent to eq. (6) after Fourier transforming of $N/\mathbf{r}^2$ with respect to $\mathbf{r} = \mathbf{x} - \mathbf{y}$. The BK equation in the transverse space was also obtained in the Mueller's dipole approach [12] in which the $q\bar{q}$ dipole develops a system of dipoles (by radiating soft gluons in the large N_c approximation) which subsequently multiply interact with a large nucleus target [7].

The dipole scattering amplitude is the basic ingredient in the computation of the nucleon structure functions at small x. In the last ten years, this amplitude was also modelled using the properties of the BK solutions such as color transparency, $N \sim r^2$ for a small dipole size $r = |\mathbf{r}|$; geometric scaling, $N = N(rQ_s(x))$; and the unitarity bound, $N \, \leq \, 1$. A recent comprehensive review on the dipole models of DIS processes is presented in [13].

The BK equation describes unitarity corrections in the asymmetric configuration when the target is extended and dense and the projectile is small and dilute. In a more symmetric

[1] ϕ is related to the unintegrated gluon density f from Section 2 by $f(x, k) \sim k^2 \nabla_k^2 \phi(x, k)$.

configuration, e.g. in the pp scattering at LHC, the BK equation is no longer sufficient, which means that in the diagrammatic approach closed pomeron loops have to be taken into account besides fan diagrams. An interesting attempt in this direction was made in [14] where pomeron loops were modelled as color reconnections in the dipole cascades. The resulting scattering amplitudes respect the target-projectile symmetry and describe reasonable well the existing total and diffractive cross sections in the $p\overline{p}$ scattering. The pomeron loops were also studied in a statistical approach, based on the stochastic Fisher-Kolmogorov equation, finding a new kind of scaling called diffusive scaling [15]. Recently, high energy factorization theorems for the gluon production in heavy nucleus collisions were proven in the color glass condensate approach [16].

Acknowledgements This work has been supported by the Polish grant no. N N202 249235 and by the Research Training Network HEPTools (MRTN-2006-CT-035505).

References

[1] V. N. Gribov and L. N. Lipatov, Sov. J. Nucl. Phys. **15**, 438 (1972);
G. Altarelli and G. Parisi, Nucl. Phys. **B126**, 298 (1977);
Y. L. Dokshitzer, Sov. Phys. JETP **46**, 641 (1977).

[2] S. Catani, M. Ciafaloni, and F. Hautmann, Phys. Lett. **B242**, 97 (1990);
S. Catani, M. Ciafaloni, and F. Hautmann, Nucl. Phys. **B366**, 135 (1991);
J. C. Collins and R. K. Ellis, Nucl. Phys. **B360**, 3 (1991).

[3] V. S. Fadin, E. A. Kuraev, and L. N. Lipatov, Phys. Lett. **B60**, 50 (1975);
L. N. Lipatov, Sov. J. Nucl. Phys. **23**, 338 (1976);
E. A. Kuraev, L. N. Lipatov, and V. S. Fadin, Sov. Phys. JETP **45**, 199 (1977);
I. I. Balitsky and L. N. Lipatov, Sov. J. Nucl. Phys. **28**, 822 (1978).

[4] L. V. Gribov, E. M. Levin, and M. G. Ryskin, Phys. Rept. **100**, 1 (1983).

[5] A. H. Mueller and J.-w. Qiu, Nucl. Phys. **B268**, 427 (1986).

[6] I. Balitsky, Nucl. Phys. **B463**, 99 (1996). hep-ph/9509348.

[7] Y. V. Kovchegov, Phys. Rev. **D60**, 034008 (1999). hep-ph/9901281;
Y. V. Kovchegov, Phys. Rev. **D61**, 074018 (2000). hep-ph/9905214.

[8] S. Munier and R. B. Peschanski, Phys. Rev. Lett. **91**, 232001 (2003). hep-ph/0309177;
S. Munier and R. B. Peschanski, Phys. Rev. **D69**, 034008 (2004). hep-ph/0310357;
S. Munier and R. B. Peschanski, Phys. Rev. **D70**, 077503 (2004). hep-ph/0401215.

[9] N. Armesto and M. A. Braun, Eur. Phys. J. **C20**, 517 (2001). hep-ph/0104038;
K. J. Golec-Biernat, L. Motyka, and A. M. Stasto, Phys. Rev. **D65**, 074037 (2002). hep-ph/0110325.

[10] A. M. Stasto, K. Golec-Biernat, and J. Kwiecinski, Phys. Rev. Lett. **86**, 596 (2001). hep-ph/0007192.

[11] N. N. Nikolaev and B. G. Zakharov, Z. Phys. **C49**, 607 (1991).

[12] A. H. Mueller, Nucl. Phys. **B415**, 373 (1994);
A. H. Mueller and B. Patel, Nucl. Phys. **B425**, 471 (1994). hep-ph/9403256;
A. H. Mueller, Nucl. Phys. **B437**, 107 (1995). hep-ph/9408245.

[13] L. Motyka, K. Golec-Biernat, and G. Watt (2008). 0809.4191.

[14] E. Avsar, G. Gustafson, and L. Lonnblad, JHEP **07**, 062 (2005). hep-ph/0503181;
E. Avsar, G. Gustafson, and L. Lonnblad, JHEP **01**, 012 (2007). hep-ph/0610157;
E. Avsar, G. Gustafson, and L. Lonnblad, JHEP **12**, 012 (2007). 0709.1368.

[15] A. H. Mueller and A. I. Shoshi, Nucl. Phys. **B692**, 175 (2004). hep-ph/0402193;
S. Munier, Nucl. Phys. **A755**, 622 (2005). hep-ph/0501149;
E. Iancu, A. H. Mueller, and S. Munier, Phys. Lett. **B606**, 342 (2005). hep-ph/0410018.

[16] F. Gelis, T. Lappi, and R. Venugopalan (2008). 0804.2630;
F. Gelis, T. Lappi, and R. Venugopalan (2008). 0807.1306.

What HERA can tells us about saturation

R. Yoshida
Argonne National Laboratory, 9700 S. Cass Ave, Argonne, IL. 60439, U.S.A.
DOI: http://dx.doi.org/10.3204/DESY-PROC-2009-01/67

Abstract
Indications of gluon saturation in the proton in the HERA data are briefly discussed.

1 Saturation at HERA?

In 1992, HERA began to explore the proton structure below x of 10^{-3} for the first time. Many expected that at such low x the description of the proton structure function F_2 using the DGLAP equations will break down; this was a reasonable assumption based on the presence of terms of the type $\alpha_s log(1/x)$ in the DGLAP splitting functions. We expected the behavior of F_2 at low x to be described by BFKL equations, and perhaps observe saturation, i.e. that parton recombination processes will begin to be important as the gluon density increases at low x. The naive expectation at that time was that we may observe some type of flattening, even a turning down, of the rising gluon at low x visible at a fixed Q^2 as we probed lower and lower in x, as shown in Fig. 1(left).

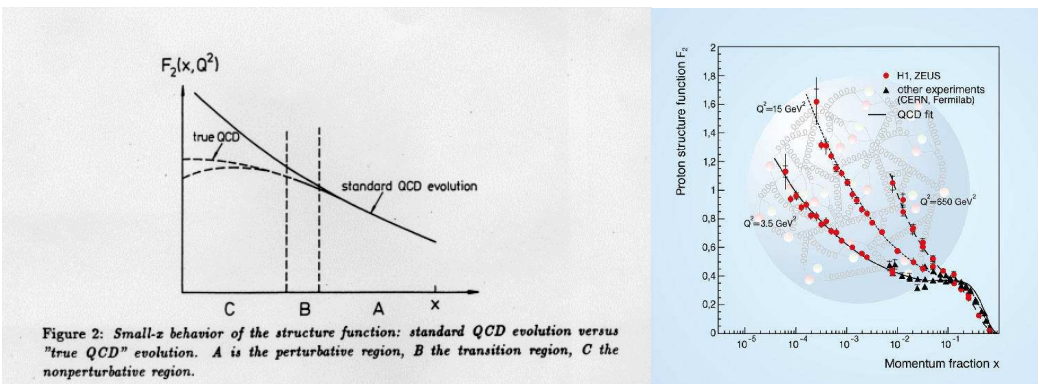


Fig. 1: Left: A figure from the 1991 HERA Workshop Proceeding showing the qualitative features expected in the HERA measurements of F_2. The region marked A is perturbative (including BFKL). In region B, non-linear recombination (saturation) effects become noticeable. Region C is the non-perturbative region. Right: F_2 as actually measured at HERA shown with the results of a perturbative QCD (DGLAP) fit.

HERA stopped data taking in 2007; a precision down to a few percent has been reached in the measurement of F_2 in large areas of the measureable phase space. The DGLAP description of the F_2 structure function to the lowest measured x has been excellent as shown in Fig. 1(right).

While DGLAP failed below Q^2 of 1 GeV [1], where the applicability of perturbative QCD is suspect in any case, there seemed to be no room in the data for any low-x effects, let alone saturation. Most HERA experimentalists considered then that saturation not to have been observed

in the HERA data; this is also the case today. On the other hand, there are several indications in the HERA data that DGLAP may not be the whole story.

2 Diffractive DIS and the Saturation Model

One of the surprises at HERA has been the observation of diffractive deep inelastic scattering (diffractive DIS). While pQCD analyses in terms of diffractive (or Pomeron) structure functions have had successes in fitting the data (see for example [2]), it is not obvious how a description of the total DIS cross-section (F_2) in terms of DGLAP evolution is reconciled with the characteristics of diffractive DIS. In particular, the fact the diffractive DIS is a constant fraction of the total DIS cross-section as a function of x at a fixed Q^2 is difficult to understand.

In 1998, the saturation model of Golec-Biernat and Wuestoff [3] was introduced. In this model, both the DIS and diffractive DIS are formulated in terms of the cross-section of a color dipole (from the virtual photon) and a proton. The measurements at HERA (both diffractive and inclusive DIS) were qualitatively well-described in this model only if HERA data were probing the region in which the dipole-proton cross-section had saturated, i.e. become constant as a function of the dipole radius. The model implies that at Q^2 of 2-5 GeV^2, and at x of 10^{-5}, HERA has sensitivitiy to saturation effects.

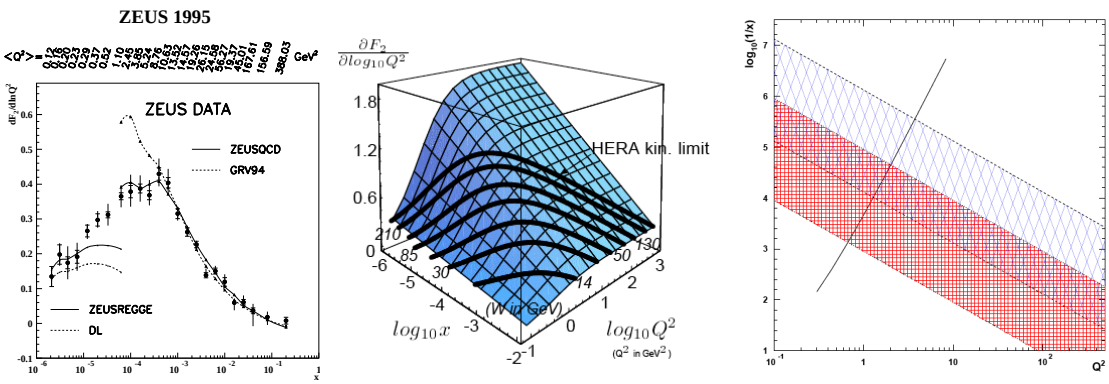


Fig. 2: Left: $dF_2/dlnQ^2$ as a function of x and changing Q^2 (scale at the top). Center: $dF_2/dlnQ^2$ as a function of x and Q^2 from the paramerized F_2 of D. Haidt. Right: Critical-line of saturation from the original paper of GBW.

3 Perturbative–non-peturbative boundary

Real photon-proton cross-section, as all hadronic cross-sections at high energy, obey the expectations of Pomeron exchange in the Regge framework. The cross-section rises slowly as a function of the cms energy. On the other hand, in DIS, interpreted as a collision of a virtual photon and a proton, the cross-section rises rapidly – corresponding to the increasing gluon density in the proton. The two behaviors must match together in the Q^2, x plane if physics is to remain smooth. Indeed it is possible to see where this transition takes place by looking at the derivative $dF_2/dlnQ^2$ as a function of x (and Q^2) as shown in Fig. 2(left) [4]. The shape of the Fig. 2(left) plot can be understood by visualizing $dF_2/dlnQ^2$ in the x and Q^2 plane in any reasonable

model [5] that interpolates between the Regge behavior at Q^2 = 0 and in the DIS region as shown in Fig. 2(center). The Fig. 2(left) plot shows $dF_2/dlnQ^2$ essentially at a fixed W.

It should be noted then that the "critical line" (shown in Fig. 2(right)) in the Golec-Biernat–Wuestoff (GBW) model [3] that signifies the onset of saturation effects is at more-or-less the same position as the fold that can be seen in Fig. 2(center). It should also be noted that this behavior is very difficult to observe for F_2 as a function of x at a fixed Q^2 in the manner shown in Fig. 1.

If satuation in the model of GBW is taken seriously, it appears that the HERA data, at about Q^2 of 2-5 GeV^2 at x^{-5} is indeed in the saturation region. It also appears that the saturation transition-line is, perhaps unsurprisingly, related also to the boundary of Regge-like and pQCD-like behavior of F_2. Unfortunately, the Q^2 range at which HERA data could be observing saturation phenomena may be already too low for perturbative QCD to be strictly applicable.

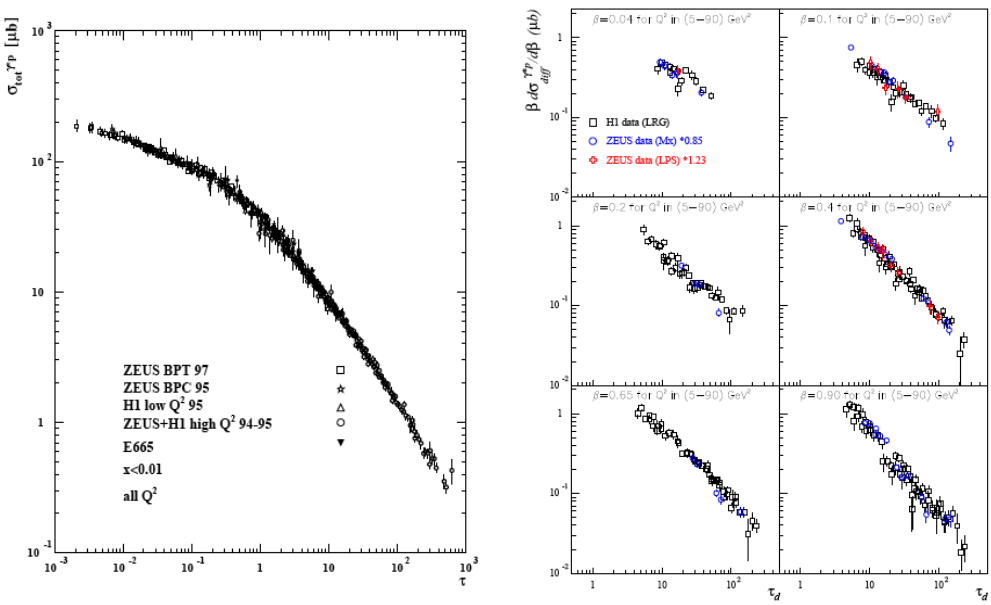


Fig. 3: Left: geometric scaling of F_2. Right: geometric scaling of diffractive DIS.

4 Geometric scaling

The saturation model predicts a behavior called geometric scaling of the cross-sections [6]. If cross-sections scale geometrically, they become a funcition only of $\tau = Q^2/Q_s^2(x)$ rather than x and Q^2 separately. This behavior for both inclusive DIS (F_2) and diffractive DIS [7] are shown in Fig. 3. Other exclusive DIS cross-sections which are expected to have the same behavior indeed show this behavior. These include exclusive Vector Meson production in DIS and Deeply Inelastic Compton Scattering.

It is somewhat curious, however, that geometric scaling behavior appears to extend to much higher x and Q^2 than would be expected from our understanding of the saturation region.

5 What does it all mean?

We've seen that DGLAP evolution describes F_2 at HERA very well. On the face of it, this precludes any type of saturation effect observable at HERA. On the other hand, saturation models based on the dipole picture give an elegant and simultaneously (qualitatively) correct description of low-x F_2, low-Q^2 F_2, diffractive DIS, VM production, DVCS and other phenomena (see, for example, C. Marquet in these proceedings) which are otherwise described by rather separate theoretical treatments. Furthermore, the saturation models match onto experimental and theoretical ideas at RHIC (see, for example L. McLerran in these proceedings).

While how saturation models correspond to more rigorous theoretical ideas such as BK, JIMWLK and BFKL is becoming clearer (see, for example, C. Marquet and C. White in these proceedings), there are also still quite a number of theoretical objections to the model to be found in the literature.

If indeed saturation is being observed at HERA, is appears to be in the regions of Q^2 at the edge of applicability of perturbative QCD. However, since it is likely that whatever physics governs the behavior of F_2 is continuous, DGLAP cannot then be the sole explanation of what is being measured at HERA – this is in apparent contraditions to the good description of F_2 using DGLAP alone.

The most precise F_2 at HERA in the low to medium Q^2 region will come from the HERA Structure Function Working Group soon. It maybe that this data will help in beginning to answer the question of whether saturation has been observed at HERA.

6 Acknowlegements

I would like to thank the organizers of ISMD08 for the invitation to speak, and the pleasant and efficient atmosphere at the symposium. This work was supported by the U.S. Department of Energy, Office of Science, under contract DE-AC02-06CH11357.

References

[1] ZEUS Collaboration, Phys. Rev. D **67**, 012007 (2003).

[2] A. Martin, M. Ryskin, and G. Watt, Phys. Lett. B **644**, 131 (2007).

[3] K. Golec-Biernat and M. Wusthoff, Phys. Rev. D **59**, 014017 (1999).

[4] ZEUS Collaboration, Eur. Phys. J. C **7**, 609 (1999).

[5] D. Haidt, Nucl.Phys.Proc.Suppl. **79**, 186 (1999).

[6] A. Stasto, K. Golec-Biernat, and J. Kwiecinski, Phys. Rev. Lett. **86**, 596 (2001).

[7] C. Marquet and L. Schoeffel, Phys. Lett. B **639**, 471 (2006).

Inclusive diffraction and factorisation at HERA

M. Wing
University College London, DESY and Universität Hamburg

Abstract
In this article, recent measurements of diffraction in deep inelastic scattering are presented along with QCD fits to extract the partonic structure of the exchange. These so-called diffractive parton density functions can then be used in predictions for other processes to test factorisation in diffraction. This is an important verification of QCD and has significance for predicting exotic signals such as diffractive Higgs production at the LHC.

1 Introduction

Diffraction in deep inelastic scattering (DIS) has long been a subject of great interest since the discovery of the first striking events at the beginning of the HERA programme [1, 2]. The final state of a diffractive ep collision at HERA contains a high energy scattered electron measured in the detector and a proton which remains intact and exits through the beam-pipe, sometimes to be detected in proton spectrometers along the proton beam-line. In addition the event consists of hadronic activity in the main detector, but with none in the direction of the proton. This dearth of hadronic activity in the proton direction constitutes the striking experimental signature which caused great surprise in the early years. Along with this so-called large rapidity gap (LRG), the hadronic final state has a very low invariant mass, M_X, compared to non-diffractive DIS. All three signatures are used to isolate diffractive events. The techniques complement each other with detection of the final-state proton providing the cleanest signature but also with much lower statistics and a more restricted kinematic range. The LRG and M_X methods are similar in range and statistics but have different background contaminations.

Such events can be understood in terms of the exchange of a colourless object, sometimes known as the Pomeron, which develops a structure. The virtual photon emitted from the electron collides with a parton in this colourless object producing a hard collision. Figure 1 shows this process along with relevant kinematic variables. The cross section for diffractive processes can be factorised into the convolution of the Pomeron flux, $f_{I\!P}$, as suggested by Regge theory, diffractive parton density functions (dPDFs), $f_{i/I\!P}$, and the hard scatter between one of the partons from the diffractive exchange and the photon, $\sigma_{ep\to eXp} \sim f_{I\!P} \otimes f_{i/I\!P} \otimes \sigma_{i\gamma\to jk}$.

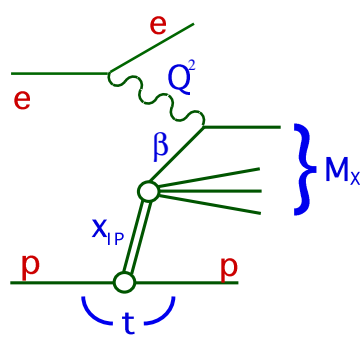


Fig. 1: Schematic of diffraction in DIS.

There are several motivations to study the nature of diffractive processes and learn more about QCD, *viz*: diffractive processes constitute a large fraction of inclusive cross section; the transition from "soft" to "hard" regimes [3]; the appli-

cability of the factorisation approach; and the potential for major discoveries such as the Higgs boson produced in diffractive processes at the LHC which relies on the above understanding.

This article reviews the most recent measurements of inclusive diffraction in DIS and the extraction of dPDFs from such data. Factorisation is then tested through comparison of dPDFs (convoluted with an appropriate programme to calculate the hard scatter) for jet production in DIS and photoproduction as well as at the Tevatron.

2 Inclusive diffraction in DIS

The ZEUS collaboration has recently published results on inclusive diffraction in DIS using all three methods [4,5]. The data from the M_X method extend the previous results [6] to higher photon virtuality, Q^2, and, in the region of overlap, with increased precision. The data using the LRG method is a significant update over previous ZEUS measurements with this method. It covers the same kinematic range as the data from the M_X method and complements the previously released data using the LRG method from the H1 collaboration [7]. Similarly, the data where the proton is tagged using the leading proton spectrometer (LPS) complement previous measurements [8,9].

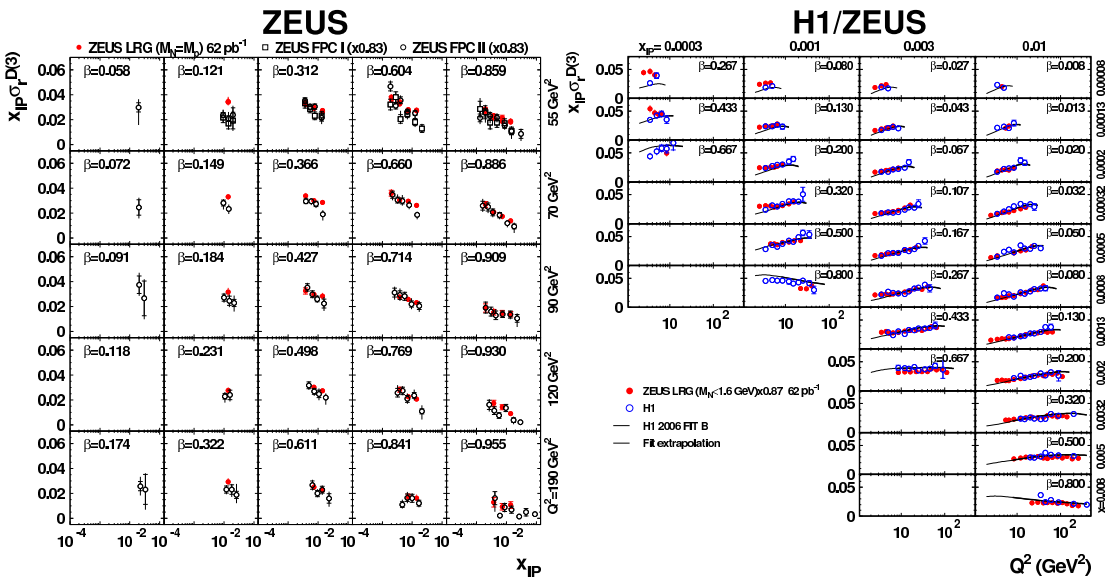


Fig. 2: Comparison of the reduced cross section in inclusive diffractive DIS as a function of (left) $x_{I\!P}$ for fixed β and Q^2 for the LRG and M_X methods and (right) Q^2 for fixed $x_{I\!P}$ and β for H1 and ZEUS data using the LRG method.

A comparison of the ZEUS measurements of the inclusive reduced cross section using the LRG and M_X methods is shown in Fig. 2 (left) for the high-Q^2 data as a function of the Pomeron momentum fraction, $x_{I\!P}$, at fixed Q^2 and fixed Pomeron momentum fraction carried by the parton in the hard scatter, β. The data using the M_X method are scaled to account for the residual background from proton dissociation in which a proton breaks up into a low-mass nucleon. Some differences between the methods (more marked at lower Q^2, not shown) as a function of $x_{I\!P}$ are observed which can be attributed to the suppression of Reggeon and pion trajectories at high $x_{I\!P}$ in the M_X method. Also at lower Q^2, the two measurements have a

somewhat different Q^2 dependence with the data from the M_X method decreasing faster with the Q^2 than those from the LRG data. However the overall agreement between the two data sets is reasonable.

The measurements of the reduced cross section from both H1 and ZEUS collaborations using the LRG method are compared in Fig. 2 (right) as a function of Q^2 for fixed $x_{I\!P}$ and β. To enable a comparison in shape, the ZEUS data have been normalised to the H1 data within the uncertainty in the relative normalisation of the two measurements. Overall the (qualitative) agreement is good and work is ongoing to combine the measurements which will give a quantitative measure of their compatibility and possibly lead to a significantly improved determination of the cross section. Already from these data it can be seen that at fixed β, the Q^2 dependence is different for different $x_{I\!P}$ values. This effect, also seen in the results using the M_X method, means that the data cannot be described by a single factorisable Regge contribution, $f_{I\!P}$.

Results in which a forward-going proton was tagged not only provide a clean measure of diffraction, but also as a result allow the determination of the residual background from proton dissociation, which is independent of all kinematic variables, in the other data samples. This and other results of these measurements are discussed in the relevant publications [5, 8, 9].

3 Extraction of dPDFs

The H1 collaboration pioneered fits in next-to-leading-order (NLO) QCD to the dPDFs. The inclusive data presented in the previous section was fit [7] and found to be dominated ($\sim$70%) by the gluon density in the diffractive exchange. However at large longitudinal momentum fraction, $z_{I\!P}$, of the parton relative to the diffractive exchange, the data lack constraining power. Although the quark contribution is stable, the gluon density can vary considerably when choosing different parametrisations. This residual uncertainty (larger than other theoretical and experimental uncertainties) needed further input and was reduced by considering jet production in DIS and simultaneously fitting [10] these and the inclusive data.

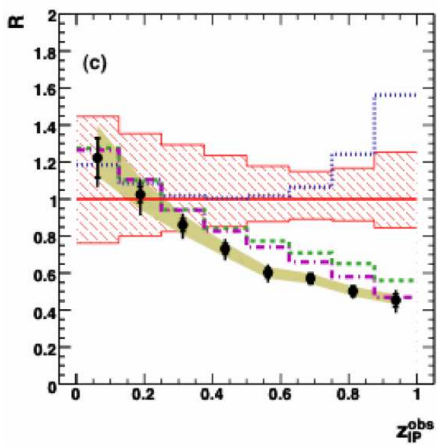


Fig. 3: Ratio of ZEUS data to NLO QCD theory as a function of $z_{I\!P}^{\rm obs}$ for different dPDFs: a ZEUS fit to LPS and charm data (solid line); a H1 fit to inclusive LRG data, H1 fit 2006 - A (dotted line) and H1 fit 2006 - B (dashed line); and a fit to inclusive data from Martin et al., MRW 2006 (dot-dashed line).

Figure 3 shows data from ZEUS on jet production, similar to that used by H1 in the NLO QCD fit for the dPDFs. The ratio of the measured cross section to NLO QCD predictions with different dPDFs is shown as a function of the experimental estimator of $z_{I\!P}$. The data show clear sensitivity to the choice of dPDF with the theoretical predictions differing by up to a factor of 3 coming from the weak constraints on the gluon density. There is also a clear preference for two of the dPDFs, MRW 2006 and H1 fit 2006 B, where the latter is one of the above two parametrisations derived from fits to inclusive data. The good description of the data by these

two parametrisations also demonstrates the applicability of factorisation in diffractive DIS. These results demonstrate that jet data can be used in NLO QCD fits to further constrain the dPDFs.

An NLO QCD fit was performed for the jet data as a function of the variable $z_{I\!P}$ at different scales and in combination with the inclusive data. The resulting parton densities for quark and gluons are shown in Fig. 4 in comparison to the previous fits to the inclusive data only. The new parametrisation of the gluon density follows that of H1 fit 2006 B and is now similarly well constrained in comparison with the quark density over the whole kinematic range.

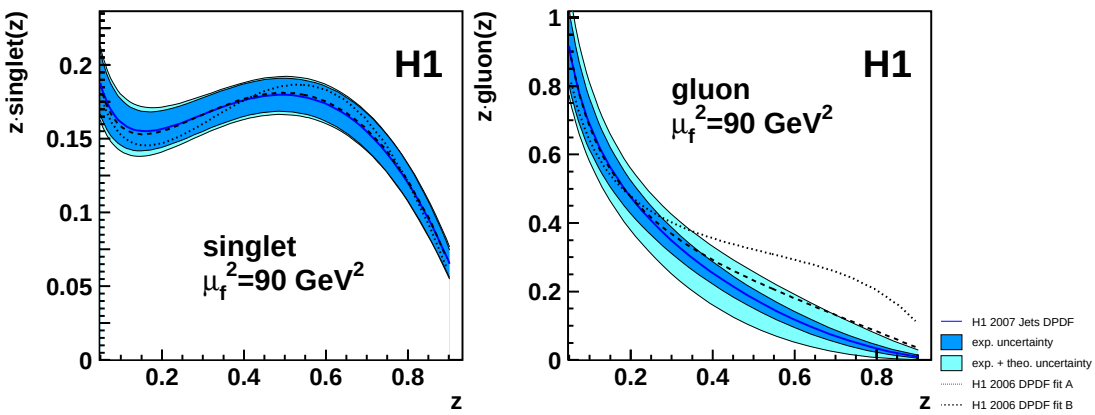


Fig. 4: Comparison of dPDFs for the quark and gluon densities when simultaneously fitting inclusive and jet data (bands) and when fitting inclusive only (lines).

4 Diffractive jet photo/hadroproduction

It has long been observed that when dPDFs are compared to Tevatron data [11], the rate is over-estimated by about a factor of 10. Explanations of this factorisation breaking exist [12] which predict secondary (multiple) interactions between the remnants which destroy the rapidity gap signature of diffraction. It might also be expected for this to occur in photoproduction in which the almost-real photon develops a structure and can effect a hadronic collision. A useful variable to isolate such interactions is x_γ which is the fraction of the photon's momentum participating in the hard scatter. High values, the direct process, indicate the photon was point-like whereas lower values, the resolved process, indicate that the photon developed some structure. However, as can be seen in Fig. 5 and also confirmed by ZEUS data [13], no dependence of a suppression factor is seen as a function of x_γ. There are indications of an overall suppression factor which (also) depends on the jet transverse energy.

5 Discussion

At first sight the situation in photoproduction and hadroproduction seems contradictory. However, it should be noted that the nature and rate of secondary interactions in the two processes is almost certainly different. From inclusive jet photoproduction data [14], secondary interactions are expected, but almost certainly not at the same rate as in hadroproduction. It should be remembered that in photoproduction, part of the resolved collisions look like the collision of a structured, vector-meson like, object with a proton. However, there is also the perturbative point-like splitting of the photon, which is fully calculable in QCD [15], in which the photon is not a

structured object in the same way as for the vector meson model. This is in contrast the obvious structured objects in hadroproduction.

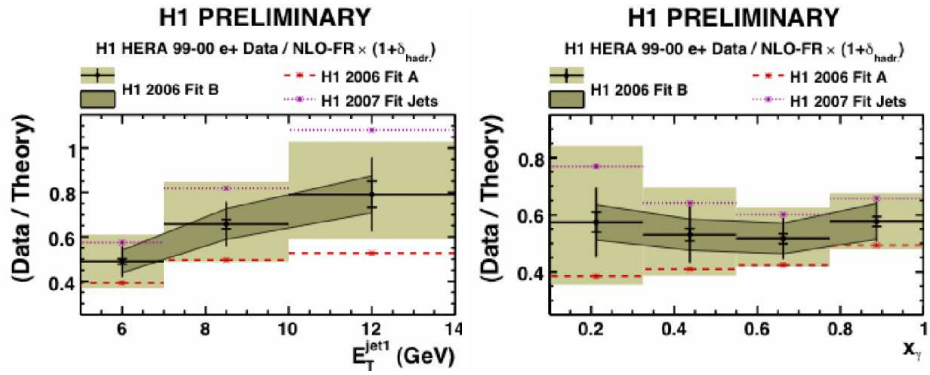


Fig. 5: Ratio of data to theory in jet photoproduction as a function of E_T^{jet1} and x_γ.

In summary, new measurements of inclusive diffraction have been made and new determinations of the partonic structure of the diffractive exchange calculated. These new parton densities demonstrate the applicability of factorisation in deep inelastic scattering, but do not change the situation in hadroproduction where models of secondary interactions are invoked to alleviate this breaking of factorisation. The situation in photoproduction is less clear cut, but also does not contradict the results in DIS or in hadroproduction. Further improvements will be made with the analysis of more inclusive and jet data and combination of data sets from the two collaborations.

Acknowledgements

M. Albrow, M. Diehl and J. Chyla are acknowledged for their questions which contributed to the above discussion. The Alexander von Humboldt Stiftung is also gratefully acknowledged.

References

[1] ZEUS Collaboration, M. Derrick *et al.*, Phys. Lett. **B315**, 481 (1993).
[2] H1 Collaboration, T. Ahmed *et al.*, Nucl. Phys. **B429**, 477 (1994).
[3] D. Wegener, *these proceedings*.
[4] ZEUS Collaboration, S. Chekanov *et al.*, Nucl. Phys. **B800**, 1 (2008).
[5] ZEUS Collaboration, S. Chekanov *et al.*, ZEUS-PUB-08-010 (2008).
[6] ZEUS Collaboration, S. Chekanov *et al.*, Nucl. Phys. **B713**, 3 (2005).
[7] H1 Collaboration, A. Aktas *et al.*, Eur. Phys. J. **C48**, 715 (2006).
[8] ZEUS Collaboration, S. Chekanov *et al.*, Eur. Phys. J. **C38**, 43 (2004).
[9] H1 Collaboration, A. Aktas *et al.*, Eur. Phys. J. **C48**, 749 (2006).
[10] H1 Collaboration, A. Aktas *et al.*, JHEP **0710**, 042 (2007).
[11] CDF Collaboration, T. Affolder *et al.*, Phys. Rev. Lett. **84**, 5043 (2000).
[12] A. Kaidalov *et al.*, Phys. Lett. **B559**, 235 (2003).
[13] ZEUS Collaboration, S. Chekanov *et al.*, Euro. Phys. J. **C55**, 177 (2008).
[14] ZEUS Collaboration, J. Breitweg *et al.*, Euro. Phys. J. **C1**, 109 (1998).
[15] E. Witten, Nucl. Phys. **B120**, 189 (1977).

Exclusive Diffraction and Leading baryons at HERA

D. Wegener *
Institute of Physics, TU Dortmund
DOI: http://dx.doi.org/10.3204/DESY-PROC-2009-01/69

Abstract
Recent results on elastic vector meson production are presented and compared to QCD based model predictions. M_V, Q^2, t provide a hard scale. The processes can be described by dipole and 2–gluon exchange models. Leading neutron and proton production data have been measured and are compared to model predictions. Moreover the conditional structure function $F_2^{LN(3)}$ is derived from the neutron data.

1 Exclusive diffraction

1.1 Exclusive vector meson production – predictions

The production of vector mesons in the process $ep \to eVp$ according to the factorization theorem can be described as a three step process, if a hard scale exists: the photon fluctuates into a $q\bar{q}$ pair, carrying the fractional longitudinal momenta z and 1–z respectively. It is followed by the interaction of the dipole with the proton parametrized by the dipole cross section σ_{dip} and finally the recombination into a vector meson. The amplitude for the process is given by the expression $A = \Psi_\gamma \bigotimes \sigma_{dip} \bigotimes \Psi_V$. While Ψ_γ is calculable in QED, Ψ_V is defined by models or parton–hadron duality [1].
The dipole cross section is assumed to be universal in the sense that it permits to describe with the same parameter set the processes $ep \to eX, epX, eVp$. For the latter process $\bar{Q}^2 = z(z-1)(Q^2+M_V^2)$ provides a universal scale. While for longitudinal photons $q\bar{q}-$pairs with fractional longitudinal momenta $z \approx (1-z) \approx \frac{1}{2}$ dominate, i.e. the extension of the dipole is $r^{-2} \approx \frac{1}{4}(Q^2+M_V^2)$, transverse photons contribute up to $z = 0,1$, hence reliable pQCD calculations of A_T are only possible at higher Q^2 [1]. Vertex factorization holds in the sense that at fixed t elastic and inelastic diffraction display the same Q^2 and W dependence.
In pQCD, σ_{dip} can be modelled in LO by the exchange of two gluons and as a gluon ladder in LL $\frac{1}{x}$ respectively [3, 4]. Hence the vector meson production cross section depends on the gluon distribution according to $\sigma_{VM} \sim [xg(x)]^2 \sim W^\delta$ since $x \approx \frac{Q^2}{W^2}$. Because of the steep rise of g(x) for decreasing x, δ is expected to increase for large Q^2. At low Q^2 the Regge model predicts $\delta \approx 0.2$.

1.2 Hard scales

The measured cross section for the process $\gamma p \to Vp$ as a function of the total energy W is shown in fig.1a. The $\rho^0-, \omega-$ and $\phi-$meson cross sections increase with W with an exponent δ comparable with the total cross section, for the heavy quarkonium states $\psi(1S), \psi(2S)$ and $\Upsilon(1S)$ as predicted by pQCD [1] the increase is steeper. The dipole model ascribes the steeper

*representing the H1 and ZEUS collaboration, supported by the BMBF, FRG under contract number 05H16PEA

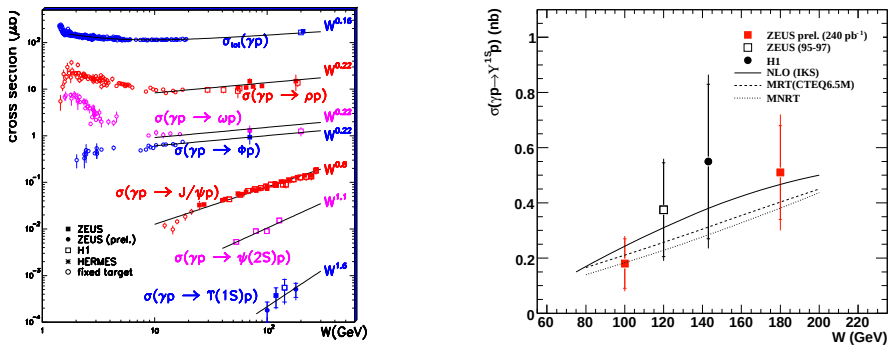


Fig. 1: Photoproduction cross section of vector mesons as function of cms energy W (a) and for $\Upsilon(1S)$ compared with model predictions(b) [2]

rise of the $\psi(2S)$ cross section to the zero of the wave function and correspondingly a smaller dipole. In summary the mass of the heavy quarkonium states provides a hard scale; indeed, as demonstrated by fig.1b, pQCD models reproduce the W–dependence of $\sigma(\gamma p \to \Upsilon(1S)p)$.
If flavour factors are taken into account [5], the cross section for the process $ep \to eVp$ displays an universal dependence on $Q^2 + M_V^2$. This is predicted by the dipole model [1] since the cross sections are expected to depend only on the dipole size. The t–dependence of the cross section at low t can be parametrized by an exponential $\frac{d\sigma}{dt} \sim exp(b \cdot t)$, where b is an universal function of $Q^2 + M_V^2$ (fig.2a); moreover the slope levels off for $Q^2 + M_V^2 \approx 5\ GeV^2$ as predicted by the dipole model [1], where $b = b_{dip} \bigoplus b_{nucl}$ and $b_{dip} \to 0$ for large Q^2. The point like photon probes the gluon distribution of the proton which turns out to be smaller than the proton radius.
Measuring the W–dependence of the production cross section for different Q^2 intervals, $\delta(Q^2)$ can be determined. It increases with Q^2 (fig.2b) as expected for a hard process. The data are compatible with predictions based on 2–gluon exchange and the dipole model respectively [7]. Figs.1–2 demonstrate that $Q^2 + M_V^2$ provides an universal hard scale.
Moreover the momentum transfer t at the proton vertex supplies a hard scale as shown in fig.3a, where the t dependence of $\frac{d\sigma}{dt}$ for the process $\gamma p \to \rho Y$ is plotted. At large t the data are described by a power law with a power characteristic for a hard process [9]. This result can be generalized, since factorization of the processes at the two vertices have been shown to hold for a plethora of elastic and inelastic diffractive reactions [6, 10].
Measurements of the DVCS process $\gamma^* p \to \gamma p$ are less sensitive to model assumptions since the final state is calculable. The measured values of $\delta(Q^2) \approx 0.8$ [11] are compatible with the expectations for a hard process. The dimensionless variable $S(Q^2) = \sqrt{\frac{\sigma_{DVCS} \cdot Q^4 \cdot b(q^2)}{1+\rho^2}}$ allows the study of the Q^2-dependence and $R(Q^2) = \frac{ImA(\gamma^* p \to \gamma p)}{ImA(\gamma^* p \to \gamma^* p)} = \frac{\sqrt{\pi \cdot \sigma_{DVCS} \cdot b(Q^2)}}{\sigma_T(\gamma^* p \to X) \cdot \sqrt{1+\rho^2}}$ provides direct information on the general parton distributions (GPD). ρ is the ratio of the real to imaginary part of the DVCS scattering amplitude. Recent results [11] are shown in fig.3b and compared to model calculations based on GPD's [12]. The expected skewing effect of 2–gluon exchange is observed (fig. 3b).

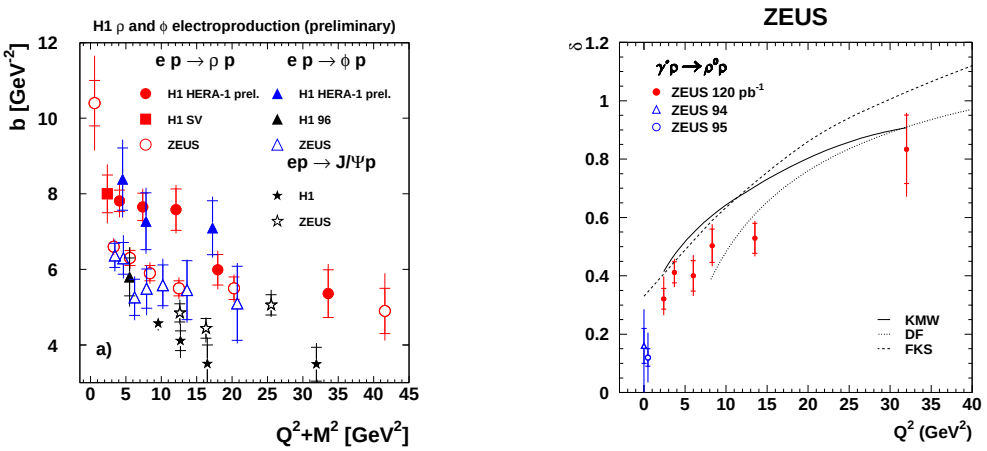


Fig. 2: (a) Slope b of the t-distribution for the process $ep \rightarrow epV$ as function of Q^2 [6] and (b) Q^2 dependence of $\delta(Q^2)$ [7]

.

1.3 Helicity amplitudes

The analysis of the angular distribution for the processes $ep \rightarrow e\rho^0 p, e\Phi p$ allows to determine 15 spin density matrix elements (SDME) and 6 helicity amplitudes $T_{\lambda_\gamma \lambda_V}$ respectively [13]. If the helicity of the virtual photon is transfered to the vector meson, single as well as double flip amplitudes should vanish and only 5 SDME should contibute. Moreover pQCD predicts $T_{00} > T_{11} > T_{01} > T_{10}, T_{1-1}$. Recent results are shown in fig.4 [6]. The five SDME expected to be nonzero,if SCHC holds, are indeed so; they agree with the predictions of a pQCD based model [14]. Except for $r^5_{00} \sim T_{10}\dot{T}^*_{00}$, all other spin–flip SDME are compatible with zero as predicted by SCHC. The SDME $r^4_{00} = \frac{\sigma_L}{\sigma tot}$, where $\sigma_{tot}(\sigma_L)$ are the total production cross section for unpolarized and longitudinal photons respectively, is shown in fig.4 (left upper corner) as function of Q^2. A leveling off is observed for $Q^2 \approx 10\ GeV^2$.

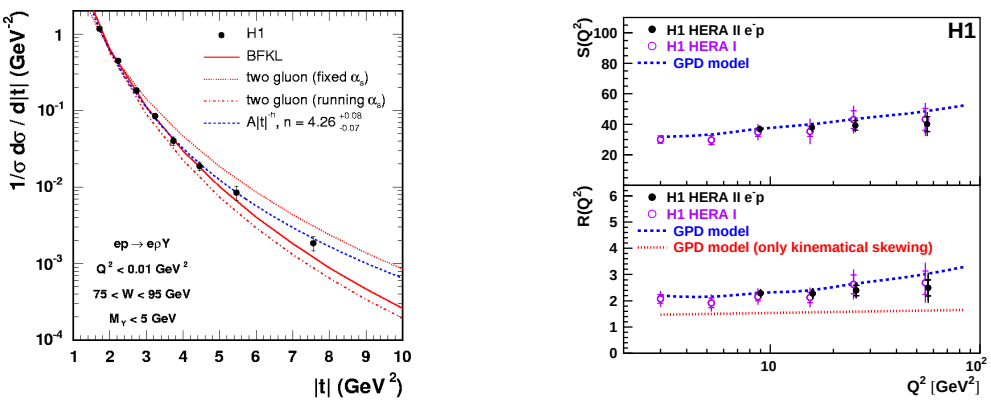


Fig. 3: (a) t-distribution for the process $\gamma p \rightarrow \rho X$ [8] and (b) plot of dimensionless variables S and R as function of Q^2 [11]

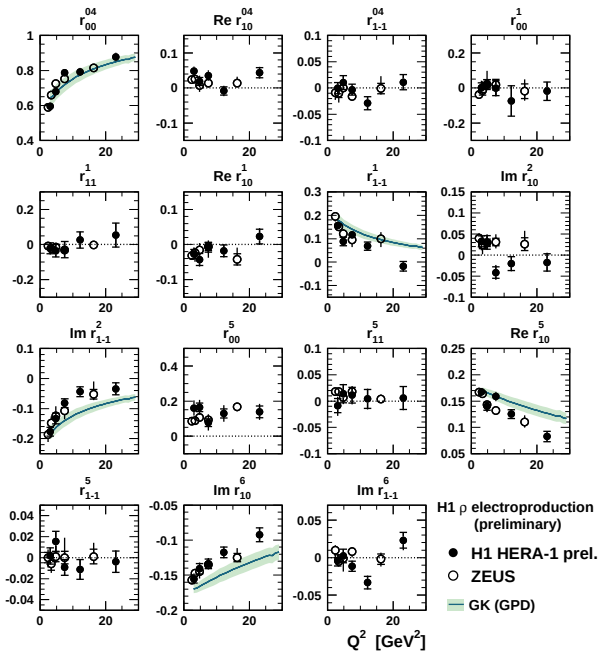


Fig. 4: Q^2-dependence of SDME [6] compared to pQCD predictions [14]

2 Leading baryons in $ep \to eNX$

Studying this process allows a test of the applicability of standard fragmentation models to the semi-inclusive process; moreover the principle of limiting fragmentation [15], postulating the factorization of the photon and proton vertex, can be checked by comparing baryon production in the process $\gamma p \to NX$ and $\gamma^* p \to NX$. The interpretation of the data in the spirit of Regge exchange allows the $\pi-$flux to be factorized from the inclusive scattering of the electron on the $\pi-$meson: $\frac{d^2\sigma}{dx_L dt} = f_{\pi/p}(x_L, t) \cdot \sigma_{\gamma^*\pi}((1-x_L)W, Q^2)$. Moreover the influence of absorption and migration due to rescattering effects can be studied, being of interest for models describing the gap survival probability in diffractive processes at LHC [16].

In fig.5a data [18] for the process $ep \to enX$ are compared with the prediction of different fragmentation models. None describes the data (see also fig. 5b), only the RAPGAP Monte Carlo with $\pi-$exchange reproduces their shape [18]. As demonstrated by fig.5b, a mixture of DJANGO and RAPGAP with $\pi-$exchange allows to reproduce the data. In the interval $0.5 < x_L < 0.9$ $\pi-$exchange dominates. Note, however, that the ratio $r = \frac{\sigma(ep\to epX)}{\sigma(ep\to enX)} \approx 2$ while for $\pi-$exchange $r = \frac{1}{2}$ is expected [18], hence the Regge model with isospin 1 exchange only is not sufficient.

The cross sections for the processes $\gamma p \to n + X$ are suppressed in comparison to those of the reaction $ep \to enX$ (fig.5a), indicating absorption and migration. In the interval $x_L > 0.5$ absorption models [16, 17], based on multi–Pomeron exchange, describe this suppression reasonably, if one considers the different W-dependence of the processes. Kaidalov et al. [16] have shown that migration processes are of importance for $x_L < 0.5$.

Finally H1 [19] has derived the ratio of structure functions $F_2^{LN(3)}(x, Q^2, x_L)/F_2(x, Q^2)$ (fig.5c). This ratio turns out to be constant over a broad interval of x and Q^2 for $0.37 < x_L < 0.82$, which

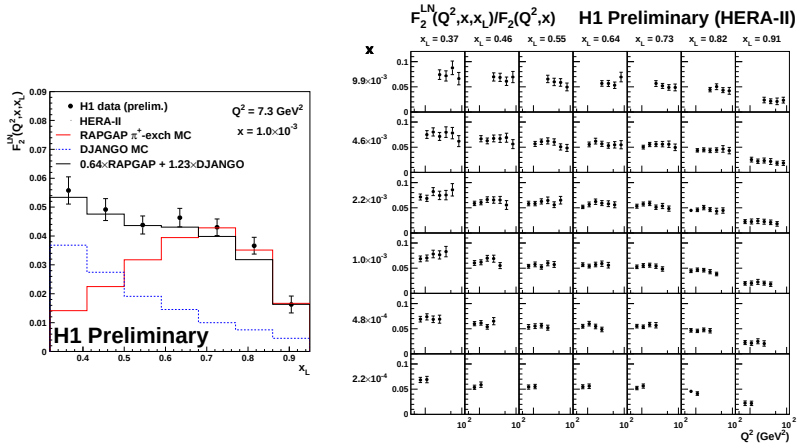


Fig. 5: (a) Ratio of normalized cross sections of photo– and electroproduction of leading neutrons as function of x_L [18], (b) conditional structure function $F_2^{LN(3)}$ as function of x_L [19] and (c) ratio of $F_2^{LN(3)}(x, Q^2, x_L)/F_2(x, Q^2)$ as function of the kinematical variables [19]

nourishes the hope that the structure function $F_2^{\pi}(x, Q^2)$ can be constrained by these data.

References

[1] I. P. Ivanov, N.N. Nikolaev, A.A. Savin, Phys. Part. Nucl. **37** 1 (2006) .

[2] ZEUS Collaboration, J.T. Maltan, Int. workshop on DIS, London 2008 .

[3] M.G. Ryskin, Z. Phys. **C57**, 89 (1993).

[4] S. Brodsky,L. Frankfurt,J.F. Gunion,A.H. Mueller,M. Strikmann, Phys. Rev. **D50**, 3134 (1994).

[5] H1 Collaboration, C. Adloff *et al.*, Phys. Lett. **B483**, 360 (2000).

[6] H1 Collaboration, contr. to DIS2008 H1prelim-08-013 .

[7] ZEUS Collaboration, S. Chekanov *et al.*, PMC Physics. **A1**, 6 (2007).

[8] H1 Collaboration, F.D. Aaron *et al.*, Phys. Lett. **B638**, 422 (2006).

[9] W. Geist, D. Drijard, A. Putzer, R. Sosnowski, D. Wegener, Phys. Rep **197**, 264 (1990).

[10] K. Goulianos, Phys. Rep **101**, 169 (1983).

[11] H1 Collaboration, F.D. Aaron *et al.*, Phys. Lett. **B659**, 796 (2008).

[12] A. Freund, Phys. Rev **D68**, 096006 (2003).

[13] K. Schilling, G. Wolf, Nucl. Phys. **B61**, 381 (1973).

[14] S.V. Goloskokov,P. Kroll, Eur.Phys.J **C53**, 367 (2008).

[15] J. Benecke, T.T. Chou, C.N. Yang, E. Yen, Phys. Rev. **D41**, 2330 (1990).

[16] A.B. Kaidalov, V.A. Khoze, A.D. Martin, M.G. Ryskin, Eur.Phys. J. **C47**, 385 (2006).

[17] U. D'Alesio, H.J. Pirner, Eur.Phys. J. **A7**, 109 (2000).

[18] ZEUS Collaboration, S. Chekanov *et al.*, Nucl. Phys. **B776**, 1 (2007).

[19] H1 Collaboration, H1 contribution to ICHEP2008, H1prelim-08-111

.

Quasielastic Scattering in the Dipole Model

Christoffer Flensburg[†]
Dept. of Theoretical Physics, Sölvegatan 14A, S-223 62 Lund, Sweden
DOI: http://dx.doi.org/10.3204/DESY-PROC-2009-01/70

Abstract
A series of previous papers [1] develops a dipole model in initial state impact parameter space that includes subleading effects such as running α_s, unitarity, confinement and saturation. Here some recent work [2] is presented, where the model is applied to a new set of data: vector meson production in $\gamma^\star p$, DVCS and $d\sigma/dt$ in pp. This allows us to tune a more realistic model of the proton wavefunction from the pp data, and confirm the predictive power of the model in high Q^2 of DVCS and vector meson production. For low Q^2 vector meson resonances dominate the photon wavefunction, making our predictions depend on a tuned parametrisation in this range.

1 Why Dipoles?

To calculate cross sections for hadronic particles it is important to understand the evolution in the initial state. In a high energy collision, each of the two incoming particles will emit gluons before meeting and interacting. Enumerate the possible initial states with i, j and give each state a probability w_i such that $\sum_i w_i = 1$. With a scattering probability p_{ij} between state i and j the total interaction probability can be expressed as

$$T_{\text{tot}}(\mathbf{b}) = 2\sum_{ij} w_i w_j p_{ij}. \tag{1}$$

That means that the expectation value of p_{ij}, weighted by w_i can be measured. Similarly the diffractive, including elastic, cross section is

$$T_{\text{diff}}(\mathbf{b}) = \sum_{ij} w_i w_j p_{ij}^2. \tag{2}$$

To get both these cross sections right, not only the expectation value of p_{ij} with respect to w_i is required, but also the fluctuations. That is, it is possible to measure if the cross section is dominated by frequently occuring states with a low interaction probability, giving a low $T_{\text{diff}}/T_{\text{tot}}$, or by rare states with a high interaction probability, giving a high $T_{\text{diff}}/T_{\text{tot}}$. Also the elastic interaction probability can be written in this way as

$$T_{\text{el}}(\mathbf{b}) = \left(\sum_{ij} w_i w_j p_{ij}\right)^2. \tag{3}$$

[†] In collaboration with Gösta Gustafson and Leif Lönnblad

This makes the form of the impact parameter profile important since the more spread out the interaction probability is, the smaller the elastic cross section will be.

These arguments show that to describe all the above cross sections, it is important to have a good description of the fluctuations, both in $\mathbf{b}$ and w_i.

2 Our Model

Our model uses colour dipoles in impact parameter space, based on the model by Mueller [3]. One of the reasons to do the calculations in impact parameter space is that each emission is on a shorter timescale than the previous ones, essentially freezing their transverse position. Each incoming particle is represented by a dipole state (for example the photon is represented as a single dipole), which is then evolved in rapidity before colliding. The evolution is equivalent to leading order BFKL, and we have made corrections for higher order effects.

2.1 Evolution

Each dipole is emitting gluons, forming two new dipoles with a probability density of

$$\frac{d\mathcal{P}}{dY} = \frac{\bar{\alpha}(r_<)}{2\pi r_{\max}^2} d^2z \left(\frac{\mathbf{x}-\mathbf{z}}{|\mathbf{x}-\mathbf{z}|} K_1(\frac{|\mathbf{x}-\mathbf{z}|}{r_{\max}}) - \frac{\mathbf{y}-\mathbf{z}}{|\mathbf{y}-\mathbf{z}|} K_1(\frac{|\mathbf{y}-\mathbf{z}|}{r_{\max}}) \right)^2 \tag{4}$$

where $\mathbf{x}$ and $\mathbf{y}$ are the transverse positions of the partons in the original dipole, while $\mathbf{z}$ is the position of the emitted gluon. $r_<$ is the size of the smallest of the three involved dipoles (the original one, and the two new ones), and is setting the scale for the **running coupling constant** for the emission. Also **confinement** is included in this emission density, which takes form in the modified Bessel functions K_1 which fall off exponentially for large arguments. The confinement scale is set by $r_{\max}$, corresponding to a gluon mass $1/r_{\max}$ in a screened Yukawa potential.

Energy conservation is accounted for by approximating the $\mathbf{p_T}$ of the partons as twice the inverse dipole size, from which p_+ can be calculated. Allowing only emissions that respect energy-momentum conservation gives a cutoff for emitting too small dipoles, that is, too large $\mathbf{p_T}$, cutting away the poles in the emission probability (4).

Apart from the 1 to 2 emission above, the model also includes a 2 to 2 dipole swing, where dipoles of the same colour may recombine, changing the colour flow, but not the momenta. The swing favours small dipoles over large dipoles, which reduces the cross section and gives a **saturation** effect.

2.2 Interaction and Cross sections

To find the cross section, the interaction probability of two evolved states of dipoles is calculated for a given impact parameter. The probability that a dipole i from one state will interact with a dipole j in the other state is

$$f_{ij} = \frac{\alpha_s^2}{8} \left(\log \left(\frac{(\mathbf{x}_i - \mathbf{y}_j)^2 (\mathbf{y}_i - \mathbf{x}_j)^2}{(\mathbf{x}_i - \mathbf{x}_j)^2 (\mathbf{y}_i - \mathbf{y}_j)^2} \right) \right)^2, \tag{5}$$

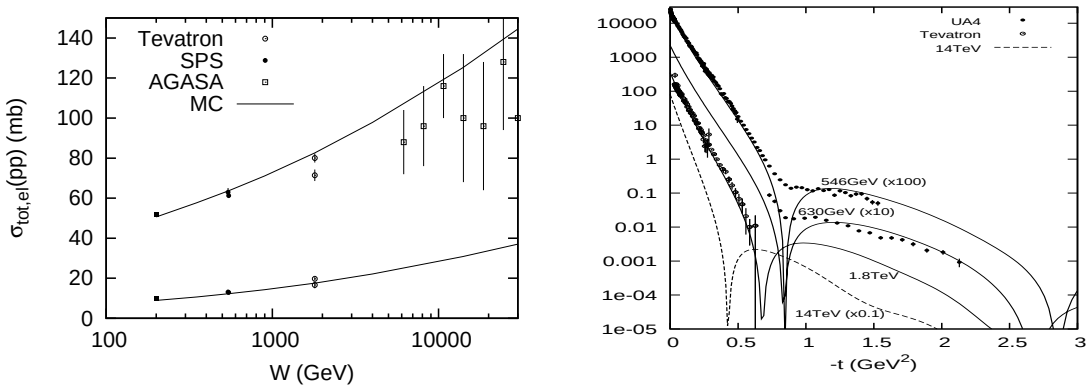


Fig. 1: Left: The total and elastic pp cross section. Right: Differential $d\sigma/dt$ cross section in pp. Data from [4].

with $\mathbf{x}_i$, $\mathbf{y}_i$ the transverse positions of the partons of dipole i. This is then corrected for confinement, which introduces Bessel functions as was done for the emission probability (4). Using this, the total interaction probability of the two dipole states can be calculated in the **unitarised** form,

$$T(b) = 1 - e^{-\sum f_{ij}}. \tag{6}$$

This is again using the fact that the interactions are taking place during a short timescale, freezing the transverse positions of the partons. This evolution and interaction can be simulated in a Monte Carlo program to determine the interaction probability numerically. Integrating over the impact parameter then gives the total cross section, and modifications to the order of integration as in section 1 yields diffractive and elastic cross sections.

3 Results

By tuning the two evolution parameters Λ_{QCD} and $r_{\max}$ and the proton wavefunction we can describe the total and elastic pp cross section (fig 1). The tuned proton wavefunction is an equilateral triangle of dipoles with a radius of 3 GeV^{-1}. It should be noted that once the cross section is tuned for a total and elastic cross section at a given energy, the energy dependence of the cross sections depends very weakly on the tuning, so it is a direct result of the evolution in our model. The fourier transform of the elastic amplitude then gives also $\sigma(t)$. As the elastic amplitude is calculated through the optical theorem, only the imaginary part is included, which causes a dip to 0 amplitude at a certain t. With the real part included, this dip would be smoothed out. The fact that it is possible to describe the energy dependence of the cross sections, as well as following $\sigma(t)$ over many orders of magnitude is a sign of the predictive power of the model.

It is possible to calculate also $\gamma^\star p$ using the virtual photon dipole wavefunction. For high Q^2 the wavefunction can be calculated perturbatively and the cross section as function of Q^2 and W is predicted directly from the pp tuning. The results agree with data (dotted line in fig 2), showing that the model can predict data without being tuned to it.

For low Q^2 (below 5-10 GeV^2) the photon wavefunction will have important soft contributions. Confinement suppresses too large dipoles, which can be taken into account by shrinking

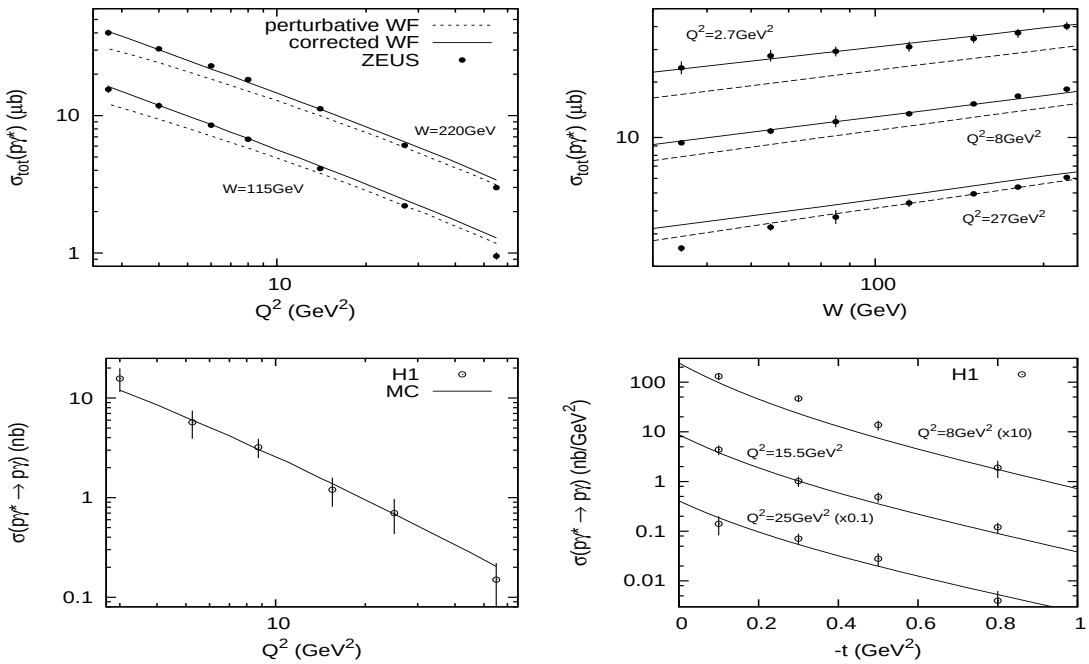


Fig. 2: Top: Total $\gamma^\star p$ as function of Q^2 (left) and W (right). Bottom: DVCS for $W = 82$ GeV as function of Q^2 (left) and t (right). Data from [5, 6]

large dipoles coming out from the perturbative wavefunction. This can be compared to the confinement used in the evolution and can be estimated using the confinement scale $r_{\max}$ from the evolution. The most important effect is when the quark-antiquark pair propagates as a vector meson, boosting the wavefunction at mesonic dipole sizes. This vector meson resonance is not well understood quantitatively, so it had to be parametrised and tuned to low Q^2 total $\gamma^\star p$ cross section data. The result with both soft effects included in the photon wavefunction is shown in the full line in fig 2.

Once the photon wavefunction was determined, also for low Q^2, the deeply virtual Compton scattering (DVCS) cross section can be calculated, using a $Q^2 = 0$ photon wavefunction for the outgoing particle. The results agree with data in Q^2, W and t dependence as can be seen in the plots in fig 2, further confirming the predictive power of our model.

By replacing the outgoing $Q^2 = 0$ photon wavefunction with a vector meson wavefunction, we can also calculate vector meson production cross sections. The vector meson wavefunction cannot be calculated perturbatively, but there are several models that estimate it, using normalisation and decay width to fix parametrisations. We used the DGKP [7] and the Boosted Gaussian [8] models in our calculations. For the light vector mesons, the Q^2 and W dependence on the total cross section agrees well with data, specially for the Boosted Gaussian model (fig 3). Also the t dependence agrees for high Q^2, while for lower Q^2, the slope is too steep. This is not surprising, as the vector meson dominance of the photon wavefunction dominates in this range. It was tuned only to the total cross section in $\gamma^\star p$, and we can not expect this parametrisation to correctly describe also the impact parameter profile that determines the t dependence. Possibly,

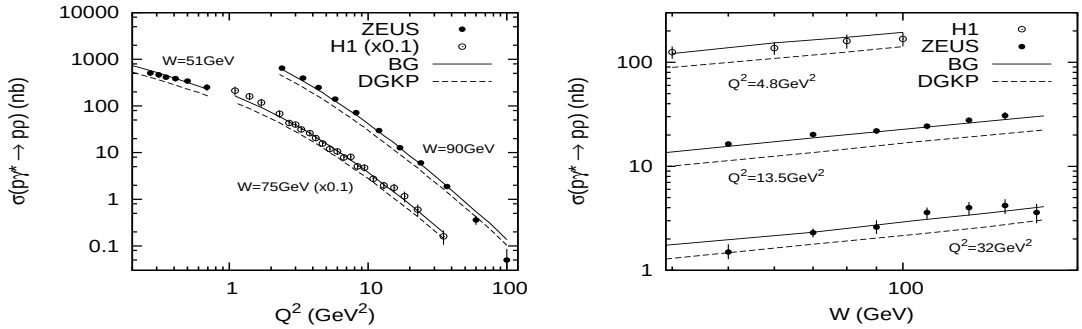


Fig. 3: Rho production as function of Q^2 (left) and W (right). Data from [9, 10]

this is also the case in DVCS, but since the available experimental data for t dependence does not go below $Q^2 = 8$ GeV^2, it is not observed. Moreover, the vector meson wavefunctions are approximative parametrisations, and they may yield incorrect t distributions.

Also ψ production can be calculated with this method, however, the results are not as good. One source of uncertainty is the vector meson resonance correction to the photon wavefunction, which would have to be retuned for a charm pair fluctuating into a ψ. More work is needed to achieve reliable results for heavy quark vector mesons.

4 Conclusions and outlook

Our dipole model has proven to describe a wide selection of data in both pp and in $\gamma^\star p$ collisions. The pp data and the total $\gamma^\star p$ cross section has been used for tuning the parameters of the evolution and the wavefunctions, while other aspects, like DVCS and the energy dependence of all processes, have been found without tuning, showing good predictive power of the model. For low Q^2 there are soft effects in the photon wave functions that we do not understand quantitatively, mainly the vector meson resonance.

Looking forward, we are currently working on using the information in the evolved states to determine not only the cross section, but also the exclusive final state. The evolution gives us the particles, their momenta, and even their colour connections. Some of the partons that have not collided will, however, have spacelike momenta and have to be reabsorbed as virtual fluctuations.

References

[1] Avsar, Emil and Gustafson, Gösta and Lönnblad, Leif, JHEP **07**, 062 (2005). `hep-ph/0503181`;
Avsar, Emil and Gustafson, Gösta and Lönnblad, Leif, JHEP **01**, 012 (2007). `hep-ph/0610157`;
Avsar, Emil and Gustafson, Gösta and Lönnblad, Leif, JHEP **12**, 012 (2007). `0709.1368`.

[2] Flensburg, Christoffer and Gustafson, Gösta and Lönnblad, Leif (2008). `0807.0325`.

[3] A. H. Mueller, Nucl. Phys. **B415**, 373 (1994);
A. H. Mueller and B. Patel, Nucl. Phys. **B425**, 471 (1994). `hep-ph/9403256`;
A. H. Mueller, Nucl. Phys. **B437**, 107 (1995). `hep-ph/9408245`.

[4] CDF Collaboration, F. Abe *et al.*, Phys. Rev. **D50**, 5518 (1994).

[5] ZEUS Collaboration, S. Chekanov *et al.*, Nucl. Phys. **B713**, 3 (2005). `hep-ex/0501060`.

[6] H1 Collaboration, F. D. Aaron *et al.*, Phys. Lett. **B659**, 796 (2008). `0709.4114`.

[7] H. G. Dosch, T. Gousset, G. Kulzinger, and H. J. Pirner, Phys. Rev. **D55**, 2602 (1997). hep-ph/9608203.

[8] J. R. Forshaw, R. Sandapen, and G. Shaw, Phys. Rev. **D69**, 094013 (2004). hep-ph/0312172.

[9] H1 Collaboration, C. Adloff *et al.*, Eur. Phys. J. **C13**, 371 (2000). hep-ex/9902019.

[10] ZEUS Collaboration, S. Chekanov *et al.*, PMC Phys. **A1**, 6 (2007). 0708.1478.

Hadronic interaction models in the light of the color glass condensate

S. Ostapchenko[1,2]
[1]Institutt for fysikk, NTNU Trondheim, Norway,
[2]D. V. Skobeltsyn Institute of Nuclear Physics, Moscow State University, Russia
DOI: http://dx.doi.org/10.3204/DESY-PROC-2009-01/71

Abstract
Implementation of screening and saturation effects in cosmic ray interaction models is reviewed in comparison with the corresponding treatment of the color glass condensate approach. A feasibility of developing a color glass-based hadronic Monte Carlo generator is discussed, underlying the related and yet unsolved problems. Finally, existing contradictions between model predictions and high energy cosmic ray data are considered and the potential of the color glass condensate approach to resolve the remaining puzzles is analyzed.

1 Introduction

Nowadays hadronic Monte Carlo (MC) generators have a wide range of applicability both in collider and in cosmic ray (CR) fields. In the latter case, among the crucial requirements to the MC models is the corresponding predictive power, due to the necessity to extrapolate such models from accelerator energies up to the highest ones studied with cosmic rays. Traditionally, CR interaction models are developed in the Reggeon Field Theory (RFT) framework [1]: the scattering process is described as a multiple exchange of composite states – Pomerons, each one corresponding to an independent parton cascade. Depending on parton virtualities, one distinguishes "soft" and "semihard" contributions to the Pomeron exchange amplitude, corresponding to whether all the partons are soft, $|q^2| < Q_0^2$, Q_0^2 being a virtuality cutoff for the pQCD being applicable, or a part of the underlying cascade enters the perturbative domain (some $|q^2| > Q_0^2$). Applying the Abramovskii-Gribov-Kancheli (AGK) cutting procedure [2] to the corresponding elastic scattering diagrams, one obtains various interaction cross sections and relative probabilities for particular hadronic final states, which are then employed in the MC procedures.

2 Screening and saturation effects in MC models

Crucial differences between present hadronic MC generators are related to how they treat nonlinear interaction effects emerging in the high parton density regime. The latter appear naturally when considering hadron-hadron and, especially, nucleus-nucleus scattering in the limit of high energies and small impact parameters, where a large number of parton cascades develops in parallel, being closely packed in the interaction volume. In the QCD framework, the corresponding dynamics is described as merging of parton ladders, leading to the saturation picture: at a given virtuality scale parton density can not exceed a certain value; going to smaller momentum fractions x, further parton branching is compensated by merging of parton cascades [3]. Importantly, at smaller x, the saturation is reached at higher and higher virtuality scale $Q^2_{\rm sat}(x)$.

The approach has been further developed in the large N_c-based color glass condensate (CGC) framework, where detailed predictions for the $Q^2_{\rm sat}(x)$ behavior have been derived [4].

In MC generators one usually attempts to mimic the saturation picture in a phenomenological way. Standard method, employed e.g. in the SIBYLL model [5], is to treat the virtuality cutoff Q^2_0 between soft and semihard parton processes as an effective energy-dependent saturation scale: $Q^2_0 = Q^2_{\rm sat}(s)$ and to neglect parton (and hadron) production at $|q^2| < Q^2_0(s)$. The parameters of the corresponding $Q^2_0(s)$ parametrization are usually tuned together with the other model parameters by fitting the measured proton-proton cross section.

A more sophisticated procedure has been applied in the EPOS model [6], where effective saturation effects, being described by a set of parameters, depend on energy, impact parameter, types of interacting hadrons (nuclei). The corresponding mechanism influences not only the configuration of the interaction (how many processes of what type occur) but also the energy partition between multiple scattering processes and the hadronization procedure, the relevant parameters being fitted both with cross section and with particle production data.

An alternative approach has been employed in the QGSJET-II model [7] which provides a microscopic treatment of nonlinear effects in the RFT framework by describing the latter with help of enhanced diagrams [8] corresponding to Pomeron-Pomeron interactions. In particular, the procedure proposed in [9] allowed one to resum contributions of dominant enhanced graphs to the scattering amplitude to all orders in the triple-Pomeron coupling. Furthermore, to treat secondary particle production the unitarity cuts of the corresponding diagrams have been analyzed and a procedure has been worked out to resum the corresponding contributions for any particular final state of interest [10], which allowed one to implement the algorithm in the MC generator and to sample various configurations of the interaction in an iterative fashion. The main drawback of the approach is the underlying assumption that Pomeron-Pomeron coupling is dominated by soft ($|q^2| < Q^2_0$) parton processes. Thus, in contrast to the perturbative CGC treatment, the model has no dynamical evolution of the saturation scale: the saturation may only be reached at the Q^2_0 scale; at $|q^2| > Q^2_0$ parton evolution is described by purely linear DGLAP formalism.

3 Prospects for CGC-based MC generators

A promising framework for the development of a new generation of hadronic MC models is the color glass condensate scheme. Indeed, it seems very attractive to fully exploit the recent progress in the theoretical understanding of low-x QCD and to have a larger part of the kinematic space being described by perturbative methods, compared to present day MC generators. The ultimate goal for such a procedure is to enhance the predictive power, which is of utmost importance for model applications at the LHC and, especially, at the highest CR energies. However, to achieve this ambitious goal a number of key developments is still missing in the approach.

Let us recall that what one basically needs are coherent predictions for elastic scattering amplitude, hence, for total and inelastic cross sections, and for relative probabilities of various configurations of hadronic final states. The latter can be specified in different ways, e.g., as configurations of final (s-channel) partons, which can be resolved from each other (by imposing a cutoff on the parton virtuality or on some suitable angular scale) and which can then be mapped into secondary hadron production patterns, using, for example, string fragmentation procedures.

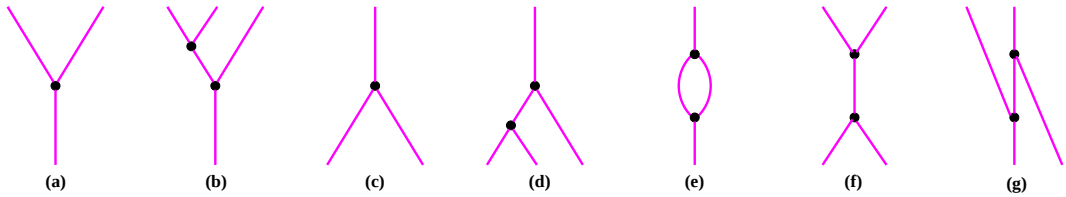


Fig. 1: Enhanced Pomerons diagrams up to the second order in G_{3P}.

When describing the scattering amplitude in the framework which treats Pomeron-Pomeron interactions, it is extremely important to have a complete resummation of all significant contributions of the kind, since diagrams with different numbers of Pomerons contribute with altering signs and since more complicated topologies become generally important when moving to higher energies. Meanwhile, most of the present applications of the CGC scheme are based on the Balitsky-Kovchegov (BK) approach [11], which is just the QCD analog of the Schwimmer model, corresponding to taking into consideration the diagrams of "fan" type only. Despite ongoing progress in accounting for contributions of more complicated diagrams, the full CGC evolution kernel remains unknown. Should one actually expect significant corrections to the BK approach? The affirmative answer comes already from considering the simplest enhanced diagrams up to the second order in the triple-Pomeron coupling, as depicted in Fig. 1.[1] Indeed, in addition to the "fan" type diagrams of Fig. 1 (a), (c) and Fig. 1 (b), (d), which are proportional to $G_{3P}\, s^{2\Delta_P}$ and $G_{3P}^2\, s^{3\Delta_P}$ correspondingly, one has the contributions of graphs of Fig. 1 (e-g), whose weights are proportional to $G_{3P}^2\, s^{2\Delta_P} \,/\, (\lambda_P + 2\lambda_{3P})$ (e), $G_{3P}^2\, s^{2\Delta_P}$ (f), and $G_{3P}^2\, s^{3\Delta_P}$ (g). Here λ_P is the slope and Δ_P the effective energy exponent (intercept minus unity) of the Pomeron exchange amplitude, whereas G_{3P} and λ_{3P} are the residue and the slope for the triple-Pomeron vertex. While the graph of Fig. 1 (f) is sub-leading in the high energy limit compared to the ones of Fig. 1 (b) and (d), this is not the case for the diagram of Fig. 1 (g). More delicate issue is the contribution of the "loop" diagram of Fig. 1 (e), which formally is also sub-leading. However, taking into account the smallness of both the BFKL Pomeron slope and of the one for the triple-Pomeron coupling, it appears to be *at least competitive* with the lowest order ones of graphs Fig. 1 (a), (c).

The fundamental problem of the CGC approach is related to the predicted too quick expansion of the black disk towards large impact parameters, the scattering slope rising with energy in a power-like way, in a contradiction with the unitarity [12]. It appears that the scheme works well in the region of the impact parameter space where the saturation scale is well-defined and fails outside that region. Though phenomenological approaches have been proposed to cure the problem by suppressing the emission of nonperturbative large size dipoles [13], it is not clear yet if the approach is suitable enough for the description of peripheral hadronic collisions.

Finally, to obtain probabilities for different hadronic final states, a necessary ingredient for a self-consistent MC procedure, one has to deal with unitarity cuts of elastic scattering diagrams. Till present, no systematic analysis of the kind has been performed in the CGC framework. As a possible alternative one may consider the "black box" strategy: developing a phenomenological MC model on the basis of the CGC predictions for *inclusive* gluon spectra. However, such

[1] For the sake of simplicity, here we restrict ourselves to the triple-Pomeron vertex only.

a model would have a very limited range of applicability, the basic correlations of hadronic observables being driven by the chosen *ad hoc* prescriptions rather than by the underlying theory.

4 UHECR puzzles

An interesting application of hadronic MC generators is related to the studies of very high energy cosmic rays. Those are generally detected using an indirect method: studying the development of nuclear-electro-magnetic cascades, extensive air showers (EAS), initiated by primary cosmic ray (PCR) particles in the atmosphere. Among the basic EAS observables is the shower maximum position $X_{\max}$ – the depth in the atmosphere (in g/cm^2) where maximal number of ionizing particles is observed, as well as total numbers of charged particles N_e and muons N_μ at ground level. The former depends mainly on the inelastic cross section for the primary particle interaction with air and on the corresponding inelasticity – the relative energy difference between the initial and the most energetic secondary particle. In turn, N_μ depends on the development of the nuclear cascade in the atmosphere, being mainly (but not only) related to the multiplicity of pion-air interactions. Hadronic MC models are employed in the simulation of EAS development, the results being compared to experimental data and used to infer the properties of PCR, like the energy spectrum and the elemental composition.

It appears that present day models behave reasonably well in CR applications up to the energies of the order of 10^9 GeV lab. For example, the results of the KASCADE-Grande Collaboration on the EAS muon content are well bracketed by the corresponding predictions for primary protons and iron nuclei (the two extreme PCR mass groups), if the `QGSJET-II` model is employed in the analysis [14]. However, the situation proved to be much more confusing in what concerns the properties of ultra-high energy cosmic rays (UHECR), with energies in excess of $10^9 \div 10^{10}$ GeV lab. The correlations between the measured UHECR arrival directions and the positions of near-by Active Galactic Nuclei (AGN), reported recently by the Pierre Auger Collaboration [15], give a strong support to the proton dominance of the PCR composition, if the angular size of the mentioned correlations is considered. On the other hand, the results of the very same collaboration on the PCR composition indicate that the latter is a mixture of protons and heavier nuclei: the measured $X_{\max}$ position is well in between model predictions for primary protons and iron nuclei [16]. Even more confusing are the Pierre Auger results for the EAS muon number: using three independent, although indirect, analysis methods, the inferred N_μ appeared to be 60% higher than predicted by `QGSJET-II` for p-induced air showers [17].

A possible explanation of the latter puzzle has been proposed in `EPOS` framework: a substantial enhancement of (anti-)baryon production in the model resulted in a significant increase of the predicted N_μ [18]. However, the model proved to be unable to resolve the above-discussed contradiction: the inferred N_μ appears to be some $20 \div 50$% (depending on the method) higher than expected for proton-induced EAS, if `EPOS` is employed in the simulation procedure [17].

A question arises if a potential CGC-based MC model could provide a coherent description of the Pierre Auger data. For the predicted EAS characteristics for p-induced air showers to be consistent with the Pierre Auger results, $X_{\max}$ has to be moved deeper in the atmosphere while N_μ has to be significantly enhanced, desirably for muon energies in excess of $5 \div 10$ GeV. The former may be achieved by increasing proton-air inelastic cross section or, alternatively, by en-

hancing the interaction inelasticity. In principle, a quick expansion of the black disk may provide the necessary enhancement of $\sigma^{\rm inel}_{p-{\rm air}}$, apart from the fact that the process can not be consistently described within the perturbative framework. In turn, a high inelasticity may be obtained if one assumes an independent fragmentation of constituent quarks of the incident proton, when the latter go through a dense gluon cloud of the target nucleus [19]. More difficult would be to obtain a significantly higher N_μ than, e.g., in `QGSJET-II`, which will require a substantial increase of pion-air multiplicity. The main feature of the CGC approach is a dynamical treatment of the saturation effects, whereas in `QGSJET-II`, parton saturation may only be reached below the cutoff scale Q_0^2. Additional saturation effects for $|q^2| > Q_0^2$ should generally lead to a suppression of the average parton density, hence, to a reduction of the multiplicity and of the N_μ predicted. However, one still has the freedom in the normalization of the saturation parton density, which is defined up to a constant factor. The latter circumstance, in combination with a quicker expansion of the high parton density towards large impact parameters may, in principle, allow one to achieve a very significant enhancement of secondary particle multiplicity, hence, of EAS muon content. It is worth stressing, however, that the main question is whether such properties come out as *natural predictions* of the color glass condensate approach. The answer will, probably, not come until a coherent CGC-based MC model emerges on the market.

Acknowledgments

The author would like to acknowledge fruitful discussions with A. Kaidalov and K. Itakura and the support of the European Commission under the Marie Curie IEF Programme (grant 220251).

References

[1] V. Gribov, Sov. Phys. JETP **26**, 414 (1968).

[2] V. Abramovskii, V. Gribov, and O. Kancheli, Sov. J. Nucl. Phys. **18**, 308 (1974).

[3] L. Gribov, E. Levin, and M. Ryskin, Phys. Rep. **100**, 1 (1983).

[4] J. Jalilian-Marian *et al.*, Nucl. Phys. **B504**, 415 (1997);
E. Iancu, A. Leonidov, and L. Mclerran, Nucl. Phys. **A692**, 583 (2001).

[5] R. Fletcher *et al.*, Phys. Rev. **D50**, 5710 (1994);
R. Engel *et al.*, Proc. of 26-th Int. Cosmic Ray Conf. (Salt Lake City) **v. 1**, 415 (1999).

[6] K. Werner, F.-M. Liu, and T. Pierog, Phys. Rev. **C74**, 044902 (2006).

[7] S. Ostapchenko, Phys. Rev. **D74**, 014026 (2006);
S. Ostapchenko, AIP Conf. Proc. **928**, 118 (2007).

[8] J. Cardi, Nucl. Phys. **B75**, 413 (1974);
A. Kaidalov, L. Ponomarev, and K. Ter-Martirosyan, Sov. J. Nucl. Phys. **44**, 468 (1986).

[9] S. Ostapchenko, Phys. Lett. **B636**, 40 (2006).

[10] S. Ostapchenko, Phys. Rev. **D77**, 034009 (2008).

[11] I. Balitsky, Nucl. Phys. **B463**, 99 (1996);
Y. Kovchegov, Phys. Rev. **D60**, 034008 (1999).

[12] A. Kovner and U. Wiedemann, Phys. Lett. **B551**, 311 (2003).

[13] E. Ferreiro *et al.*, Nucl. Phys. **A710**, 373 (2002);
E. Avsar, JHEP **0804**, 033 (2008).

[14] KASCADE-Grande Collaboration, V. de Souza *et al.*, Proc. of 30-th Int. Cosmic Ray Conf. (Merida) (2007).

[15] Pierre Auger Collaboration, J. Abraham *et al.,* Science **318**, 938 (2007).

[16] Pierre Auger Collaboration, M. Unger *et al.,* Proc. of 30-th Int. Cosmic Ray Conf. (Merida) (2007).

[17] Pierre Auger Collaboration, F. Schmidt *et al.,* Proc. of 15-th Int. Symp. on Very High Energy Cosmic Ray Interactions (Paris) (2008).

[18] T. Pierog and K. Werner, Phys. Rev. Lett. **101**, 171101 (2008).

[19] H. Drescher, A. Dumitru, and M. Strikman, Phys. Rev. Lett. **94**, 231801 (2005).

Test of hadronic interaction models via accelerator data

T. Pierog
Forschungszentrum Karlsruhe, Institut für Kernphysik, Germany
DOI: http://dx.doi.org/10.3204/DESY-PROC-2009-01/72

Abstract
At high energy, cosmic rays can only be studied by measuring the extensive air showers they produce in the atmosphere of the Earth. Although the main features of air showers can be understood within a simple model of successive interactions, detailed simulations and a realistic description of particle production are needed to calculate observables relevant to air shower experiments. Currently hadronic interaction models are the main source of uncertainty of such simulations. We will study how accelerator data can constrain the different hadronic models available for extensive air shower simulations.

1 Cosmic rays and hadronic interactions

Due to the steeply falling energy spectrum of cosmic rays, direct detection by satellite- or balloon-borne instruments is only possible up to about $\sim 10^{14}$ eV. Fortunately, at such high energy, the cascades of secondary particles produced by cosmic rays reach the ground and can be detected in coincidence experiments. The cascades are called extensive air showers (EAS) and are routinely used to make indirect measurements of high energy cosmic rays.

As a consequence of the indirect character of the measurement, detailed simulations of EAS are needed to extract information on the primary particle from shower observables. Whereas electromagnetic interactions are well understood within perturbative QED, hadronic multiparticle production cannot be calculated within QCD from first principles. Differences in modeling hadronic interactions, which cannot be resolved by current accelerator data, are the main source of uncertainty of EAS predictions [1, 2]. In this article, we will discuss the relation between hadronic multiparticle production and EAS observables and the constrains given by accelerator data.

2 Heitler's Model

Thanks to a simple Heitler model generalized for hadronic showers [3, 4], one can extract the main observables of hadronic interactions needed to understand the development of air showers.

In this kind of toy model, a hadronic interaction of a charged particle with energy E will produce $N_{\rm tot}$ new particles with energy $E/N_{\rm tot}$, with $N_{\rm EM}$ particles (π^0 mainly) transferring their energy to the electromagnetic channel. Introducing a characteristic energy ($E_0 = 150\,\text{GeV}$), where pions are assumed to decay into muons, the number of muons for a shower with primary energy E_0 after n generations is given as [5]

$$N_\mu = \{N_{\rm tot} - N_{\rm EM}\}^n = \left(\frac{E_0}{E_{\rm dec}}\right)^{1+\ln R/\ln N_{\rm tot}}, \qquad (1)$$

with $R = (N_{\rm tot} - N_{\rm EM})/N_{\rm tot}$. The muon number depends therefore strongly on R, which is understandable since $N_{\rm EM}$ counts particles giving all their energy to the electromagnetic channel – not producing muons.

Usually these kind of toy models consider only pions as secondary particles resulting in $R = 2/3$. In this case the muon number depends only on $N_{\rm tot}$, as does $\rm X_{max}$ [5], as

$$X_{\rm max} = \lambda_{\rm had} + \lambda_{\rm EM} \cdot \ln\left(\frac{E_0}{N_{\rm tot} E_c}\right), \tag{2}$$

with $\lambda_{\rm had}$ being the hadronic interaction path length, and with $E_c = 85$ MeV being the critical energy (where particles disappearing from the shower). Let us now be a bit more realistic, and consider all kinds of hadrons, including (anti)baryons. Particle production in hadronic interactions is model dependent, and so is the precise value of R. With R being less than 1 and $N_{\rm tot} >> 1$, the muon number depends very sensitively on the ratio R.

Thus this simple approach allows us to extract the main observables which lead the EAS development, namely:

- cross section
- multiplicity (and inelasticity)
- (anti)baryon production

We will compare the commonly used hadronic interaction models for EAS simulations to accelerator data for these observables.

3 Accelerator data

Hadronic interaction models

There are several hadronic interaction models commonly used to simulate air showers. For high energy interactions ($E_{\rm lab} \gtrsim 100$ GeV), the models studied here are EPOS 1.6 [6,7], QGSJET 01 [8], QGSJET II [9, 10], and SIBYLL 2.1 [11–13]. The physics models and assumptions are discussed in, for example, [14].

Cross section

As seen Sec. 2, the cross section is very important for the development of air showers and in particular for the depth of shower maximum. As a consequence, the number of electromagnetic particles at ground is strongly correlated to this observable (if the shower maximum is closer to ground, the number of particles is higher).

The proton-proton scattering total cross section is typically used as an input to fix basic parameters in all hadronic interaction models. Therefore, as shown in Fig. 1 lefthand-side, it is very well described by all the models at low energy, where data exist. And then it diverges above 2 TeV center-of-mass (cms) energy because of different model assumptions. In all the figures EPOS 1.6 is represented by a full (blue) line, QGSJET II by a dashed (red) line, QGSJET 01 by a dash-dotted (black) line and SIBYLL 2.1 by a dotted (green) line.

From p-p to proton-air interactions, the Glauber model is used in all models but with different input parameters depending on nuclear effects (none in SIBYLL 2.1, strong in QGSJET II).

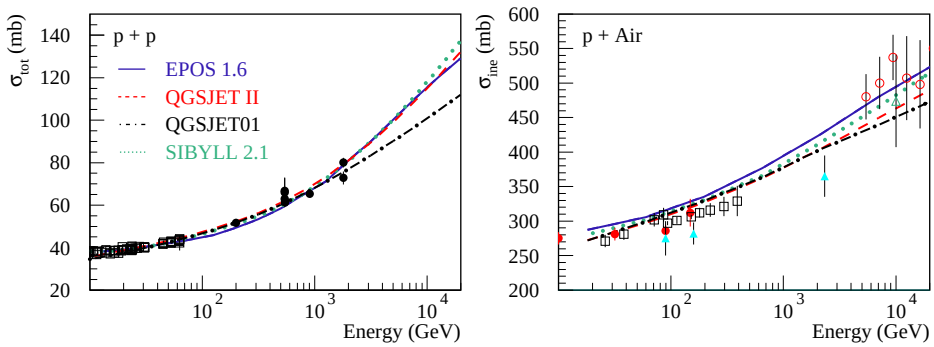


Fig. 1: Total cross section of p-p collision (lefthand-side) and inelastic proton-air cross section (righthand-side) as calculated with EPOS 1.6 (full line), QGSJET II (dashed line), QGSJET 01 (dash-dotted line) and SIBYLL 2.1 (dotted line). Points are data from accelerator [15] and cosmic ray experiment [16–19].

So comparing the models to each other Fig. 1 righthand-side, differences appear even at low energy where the p-p cross section are similar. And at high energy the spread is again larger. Furthermore, the simulated cross sections seem all to increase faster than the measured one, even at low energy ($<$ 1 Tev) where direct measurement of single hadrons from cosmic rays can be done at ground [16–19] (almost accelerator like measurement since proton flux is known).

Multiplicity

According to eq. 2, the multiplicity plays a similar kind of role as the cross section, but with a weaker dependence (log). On the other hand, the predictions from the models have much larger differences.

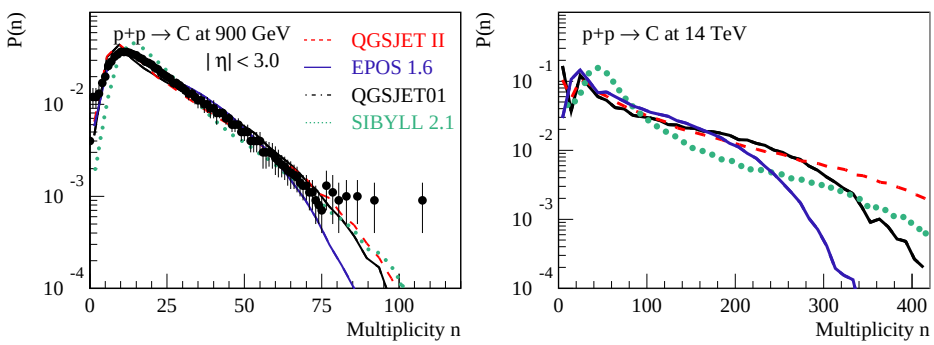


Fig. 2: Multiplicity distribution of $\overline{p}$-p collision at 900 GeV cms energy (lefthand-side) and 14 TeV (righthand-side) as calculated with EPOS 1.6 (full line), QGSJET II (dashed line), QGSJET 01 (dash-dotted line) and SIBYLL 2.1 (dotted line). Points are data [20].

As shown in Fig. 2, going from 900 GeV cms energy (lefthand-side), where models agree with the UA5 data [20], to 14 TeV (LHC) (righthand-side), the discrepancy can be larger than a

factor of 2 in the tail of the distribution (and the shape is different). The EPOS model predicting much smaller multiplicity than QGSJET II.

The multiplicity distribution of charged particles is a very good test of the fundamental property of the hadronic interaction models and it should be one of the first result of the LHC experiments.

(Anti)Baryon production

In the forward region, the number of (anti)baryons is very important for the number of muons produced in EAS, because it changes the ratio R of eq. 1. The process is well described in [21], where it is also shown that the number of antiprotons on the projectile side of π-carbon collision can only be reproduced correctly by the EPOS model. This is due to a more sophisticated remnant treatment in this model which allows baryon number transfer between the inner part of the collision and the forward (or backward) region. This can be tested with other data like the lambda rapidity distribution published by the NA49 collaboration [22] and shown on the lefthand-side of Fig. 3. We can see that in EPOS a large number of lambdas are in the central region and not at large rapidity any more (cf QGSJET 01).

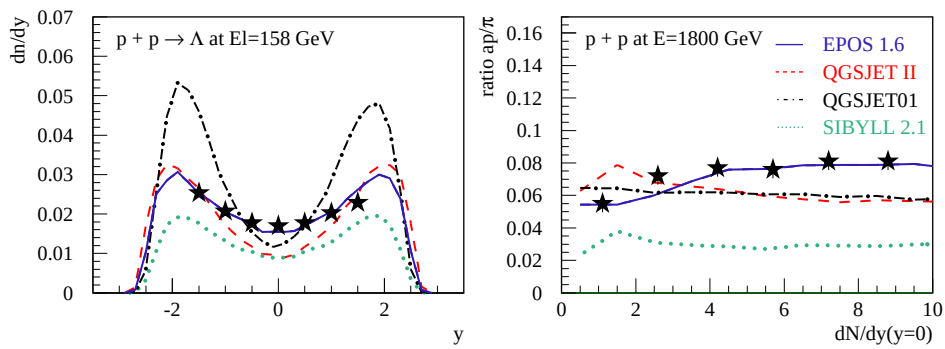


Fig. 3: Lambda rapidity distribution of p-p collision at 158 GeV lab energy (lefthand-side) and ratio of anti-proton over pion in $\overline{p}$-p scattering at 1.8 TeV cms energy as a function of the plateau height (righthand-side) as calculated with EPOS 1.6 (full line), QGSJET II (dashed line), QGSJET 01 (dash-dotted line) and SIBYLL 2.1 (dotted line). Points are data [22, 23].

Another particularity of the (anti)baryons is that their production increase faster with the energy that the pion production. In other words, the ratio $\overline{p}/\pi$ increase with energy. At the highest measured energy (TEVATRON [23]), we can see on the righthand-side of Fig. 3, that only EPOS described correctly this ratio as a function of the event multiplicity. Other models are too low. This explain why air showers simulated with EPOS contain more muons. Measurement of (anti)baryon distributions at LHC will be very important to constrain muon number in air showers.

4 Summary

Using a simple toy model, it was shown that EAS development is driven by a limited number of fundamental observables like the proton (and pion) air cross section, the multiplicity (and inelasticity) and the number of (anti)baryon in proton (and pion) air interactions. Unfortunately these quantities are well measured only at low energy ($\sim$100 GeV lab) in proton (or pion) nucleus scattering. The cross section and multiplicity are measured up to 2 TeV cms energy in (anti)proton-proton collisions, but nevertheless the hadronic models commonly used for EAS simulations show big differences in their extrapolation already at LHC energies. The discrepancy is even larger if we consider hadron-nucleus collisions. Situation is even worth for the forward distributions of (anti)baryons (important for muons), which are not measured at all at collider energies. In that case, the models disagree with each other already at low energy. This probably explain why none of these hadronic interaction models can consistently reproduce all results from an experiment like KASCADE [24], even if the energies involved are in the range of accelerator data.

References

[1] J. Knapp, D. Heck, and G. Schatz. FZKA-5828.

[2] J. Knapp, D. Heck, S. J. Sciutto, M. T. Dova, and M. Risse, Astropart. Phys. **19**, 77 (2003). astro-ph/0206414.

[3] W. Heitler, *The Quantum Theory of Radiation*, third editionth edn. Oxford University Press, London, 1954.

[4] J. Matthews, Astropart. Phys. **22**, 387 (2005).

[5] T. Pierog, R. Engel, and D. Heck, Czech. J. Phys. **56**, A161 (2006). astro-ph/0602190.

[6] H. J. Drescher, M. Hladik, S. Ostapchenko, T. Pierog, and K. Werner, Phys. Rept. **350**, 93 (2001). hep-ph/0007198.

[7] K. Werner, F.-M. Liu, and T. Pierog, Phys. Rev. **C74**, 044902 (2006). hep-ph/0506232.

[8] N. N. Kalmykov, S. S. Ostapchenko, and A. I. Pavlov, Nucl. Phys. Proc. Suppl. **52B**, 17 (1997).

[9] S. Ostapchenko, Phys. Lett. **B636**, 40 (2006). hep-ph/0602139.

[10] S. Ostapchenko, Phys. Rev. **D74**, 014026 (2006). hep-ph/0505259.

[11] R. S. Fletcher, T. K. Gaisser, P. Lipari, and T. Stanev, Phys. Rev. **D50**, 5710 (1994).

[12] J. Engel, T. K. Gaisser, T. Stanev, and P. Lipari, Phys. Rev. **D46**, 5013 (1992).

[13] R. Engel, T. K. Gaisser, T. Stanev, and P. Lipari. Prepared for 26th International Cosmic Ray Conference (ICRC 99), Salt Lake City, Utah, 17-25 Aug 1999.

[14] S. Ostapchenko, Czech. J. Phys. **56**, A149 (2006). hep-ph/0601230.

[15] Particle Data Group Collaboration, C. Caso *et al.*, Eur. Phys. J. **C3**, 1 (1998).

[16] H. H. Mielke, M. Foeller, J. Engler, and J. Knapp, J. Phys. **G20**, 637 (1994).

[17] G. b. Yodh, S. c. Tonwar, T. k. Gaisser, and R. w. Ellsworth, Phys. Rev. **D27**, 1183 (1983).

[18] M. Honda *et al.*, Phys. Rev. Lett. **70**, 525 (1993).

[19] R. M. Baltrusaitis *et al.*, Phys. Rev. Lett. **52**, 1380 (1984).

[20] UA5 Collaboration, R. E. Ansorge *et al.*, Z. Phys. **C43**, 357 (1989).

[21] T. Pierog and K. Werner, Phys. Rev. Lett. **101**, 171101 (2008). astro-ph/0611311.

[22] NA49 Collaboration, T. Susa, Nucl. Phys. **A698**, 491 (2002).

[23] E735 Collaboration, T. Alexopoulos *et al.*, Phys. Rev. **D48**, 984 (1993).

[24] A. Haungs *et al.*, Czech. J. Phys. **56**, A241 (2006).

Results of the Pierre Auger Observatory - aspects related to hadronic interaction models

Petr Travnicek for the Pierre Auger Collaboration[†]
Institute of Physics of the Academy of Sciences of the Czech Republic, Na Slovance 2 CZ-182 21 Praha 8, Czech Republic

DOI: http://dx.doi.org/10.3204/DESY-PROC-2009-01/73

Abstract

The southern part of the Pierre Auger Observatory in Argentina is now fully completed and already provides world unique data samples of the cosmic ray showers in the energy range from 10^{18} eV till above 10^{20} eV. In order to avoid a strong dependency on MC simulations for energy calibration, the experiment combines two techniques: surface detector arrays and fluorescence telescopes. However, the interpretation of some measured quantities such as mean shower maximum in terms of chemical composition of cosmic rays, naturally depends on MC simulations and models of hadronic interactions at extremely high energies. This contribution describes selected results of the Pierre Auger Observatory and pinpoints several issues where the models of hadronic interactions play a very important role or can be even tested at energies far from the reach of current accelerators.

1 Introduction

The existence of Ultra High Energy Cosmic Rays (UHECR) is difficult to explain either by present scenarios of acceleration mechanisms in astronomical objects or by models suggesting that these particles originate e.g. from decays of super-heavy dark matter. UHECR thus attract attention of both astrophysicists and particle physicists.

UHECR are supposed to be mostly protons or heavier nuclei that quickly lose energy as they interact with relict photons at energies above the pion production threshold $E_{TH} \sim 6\times10^{19}$ eV (GZK mechanism [1]). Consequently, events observed when the particles hit the Earth atmosphere have to originate from distances close to us (within $\sim$ 100 Mpc) and the flux of these particles has to be suppressed above the GZK threshold. This expectation is however in contradiction with previous measurements of the AGASA experiment [2]. All the above-mentioned mysteries of UHECR and more that were presented e.g. in Ref. [3] were the basic motivations for construction of the Pierre Auger Observatory (PAO), the world largest cosmic ray detector.

Already during the construction phase the PAO was able to take data and the collaboration reported many results such as an estimate of upper limit on the cosmic-ray photon and diffuse tau neutrino flux [4–6] or the highlighted analysis of correlation of the highest-energy cosmic rays with the positions of nearby active galactic nuclei [7, 8]. In this contribution we rather focus

[†] see `www/auger.org/admin` for full author list

on energy calibration, spectrum and composition studies and examples how PAO can test the validity of hadronic interaction models at extreme energies.

2 Experimental setup and measurement principle

The southern site of the PAO is situated in the Argentinian province Mendoza, close to the city of Malargüe. It consists of 3000 km^2 surface detector arrays and a set of 24 fluorescence telescopes. The surface detector stations are water Cerenkov tanks each equipped by 3 photomultipliers. Six fluorescence telescopes occupy one fluorescence detector building. In total four of these buildings are located on the array border on small hills and thus overlook the interior of the array. In the year 2008 the southern part of the Observatory was fully completed with successful operation of all four fluorescence detector buildings and by fulfilling the original aim of 1600 deployed and working surface detector stations.

The essential part of the project is to build the northern counterpart of the existing south experiment. The suitable site was already chosen in Colorado, USA. Not only the full sky coverage but also the interesting and encouraging results obtained from the southern site and subsequent new scientific questions emerging from the data are the main motivations for the northern Observatory.

When a cosmic ray particle hits the Earth atmosphere, it interacts at high altitudes with a nucleus of the atmospheric gas and many new particles are created in the forward direction. Secondary particles then continue to interact with other atmospheric nuclei and the extensive air shower is formed. Decays of secondary neutral pions feed the electromagnetic shower and decays of charged mesons form the muon component. The surface array measures the shower lateral profile on the ground and surface detector stations are sensitive to both electromagnetic and muon components. The fluorescence telescopes register the longitudinal profile of the fluorescence light induced along the air shower by de-excitations of N_2 molecules excited by the passage of the electromagnetic shower. The measured light intensity is proportional to the energy that shower particles lose in the atmosphere. The fluorescence detectors thus provide calorimetric measurement of the shower energy estimated as $E_{FD} = k \int_0^\infty \frac{dE}{dX} dX$, where X is the atmospheric depth and k is the correction factor taking into account missing energy due to neutrinos and energetic muons. Fluorescence telescopes can, however, operate only during the nights with low Moon-light intensity. Since the majority of the measured showers is detected only by surface Cerenkov stations, the conversion of the surface detector signal to shower energy has to be used for these events.

3 Energy calibration of surface detector signals and cosmic ray energy spectrum

The signal at about 1000 m from the shower core (S(1000)) is on average the ideal parameter to measure the shower energy from the surface detector data [9] . The chosen distance to shower core is mostly given by the requirement of good reconstruction quality and it is defined by the geometry of the array. Having the optimal energy estimator determined, the correction to the signal attenuation for different zenith angles has to be estimated. This is done from the real data avoiding any Monte Carlo simulations. For each shower the signal parameter S38=S(1000)/CIC(θ) is calculated. This parameter is defined as the S(1000) signal of the same shower if its zenith

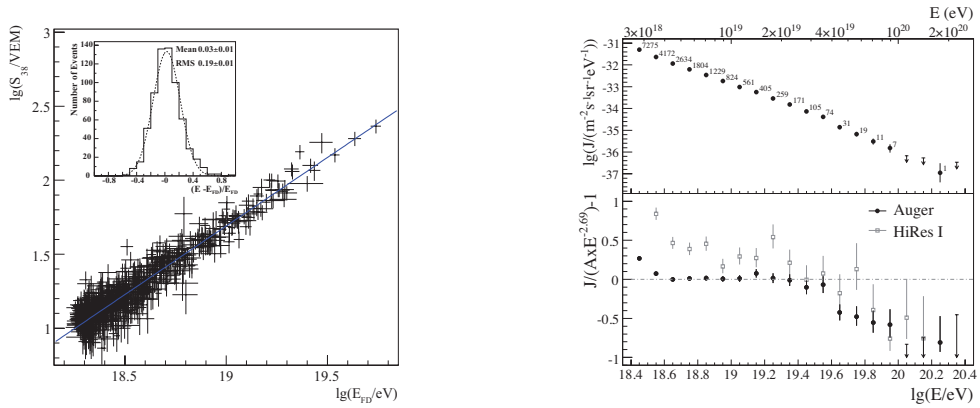


Fig. 1: *(left)* Correlation between $\lg S_{38^\circ}$ and $\lg E_{FD}$ for the 661 hybrid events used in the fit. The full line is the best fit to the data. The fractional differences between the two energy estimators are shown in the inset. *(right)* Upper panel: The differential flux J as a function of energy, with statistical uncertainties. Lower Panel: The fractional differences between Auger and HiResI data compared with an energy spectrum $J \sim \mathrm{E}^{-2.69}$.

angle θ would be 38°. The crucial part is thus to estimate the signal attenuation curve CIC(θ) from the real data. This is done by requiring the isotropic distribution of the events above a given energy (i.e. above a given S38). Since the surface detector is flat and the trigger efficiency approaches unity (>99%) above 3×10^{18} eV it is natural to expect that the distribution of number of events above some energy is flat in $\cos^2(\theta)$. The constant intensity cut given in the number of events in each $\cos^2(\theta)$ bin is chosen and the CIC(θ) is then found from the real data so that the dN/d($\cos^2(\theta)$) is constant as required. It was shown that the shape of the CIC(θ) curve does not depend on the chosen value of the cut.

At this stage the last step of the energy calibration is applied. It is the relation of the S38 parameter to the measured energy from the fluorescence detectors. The calibration curve is shown in Fig. 1 (left) showing nice correlations of the two parameters. The correction to the missing energy applied to the measured calorimetric energy of the fluorescence detectors is the only step where the models of hadronic interaction enter the calibration procedure. The differences between the corrections for different models and primaries are on the level of a few percent [10]. The total uncertainty of the fluorescence energy measurement is about 22%. While the largest part is given by the uncertainty of fluorescence yield (15 %), the missing energy uncertainty is only about 4 %.

Having the conversion of S(1000) to S38 and finally to the shower energy estimated, the cosmic ray energy spectrum can be constructed [11]. The spectrum is plotted in Fig. 1 (right) together with the HiResI data [12]. At the confidence level of 6 standard deviations the flux $J \sim E^{\alpha=-2.69}$ stops to continue with the same slope α above the energy 4×10^{19} eV.

4 Mass composition, shower maximum

While the estimated energy spectrum depends only slightly on the models of hadronic interactions, the analyzes of cosmic ray composition are essentially based on these models. In order

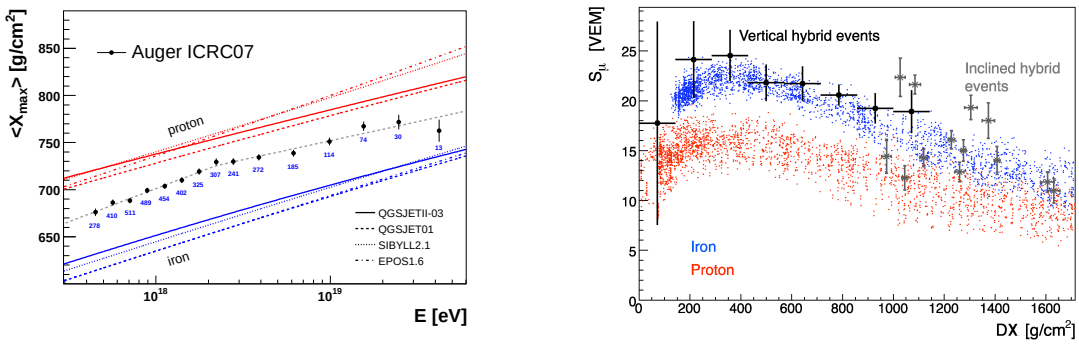


Fig. 2: *(left)* $< X_{max} >$ as a function of energy compared to predictions from hadronic interaction models. The dashed line denotes a fit with two constant elongation rates (slopes k of $< X_{max} > \sim k \lg(E/eV)$) and a break-point. *(right)* Reconstructed and predicted (energy scale $E_{MC} = 1.3 E_{\rm FD}$) muon tank signal contribution in dependence on the distance of the shower maximum to ground for vertical and inclined hybrid events.

to obtain information about the composition of comic rays, the PAO studies shower parameters sensitive to the mass of the primary particle. One of the most powerful parameters is the position of the shower maximum measured by the fluorescence detectors.

As the shower passes through the atmosphere, the electromagnetic component evolves and increases its size until the particle energy is lower than critical energy in the air. At this point the shower reaches its maximum and this position is defined as the amount of traversed matter X_{max}. The shower initiated by heavy nucleus with N nucleons can be roughly approximated as N proton sub-showers at energies N times lower. These sub-showers thus penetrate less the atmosphere than the proton shower at the same total energy resulting to smaller average X_{max} value. Also the shower to shower fluctuations of X_{max} would be smaller for the heavy primary particle because the "averaging" occurs between these N sub-showers. The average value of X_{max} is related to the mean logarithmic mass via: $< X_{max} >= D_{\rm p}[\ln(E/E_0) - < \ln A >] + {\rm c}_p$, where $D_{\rm p}$ denotes the 'elongation rate' of a proton, and ${\rm c}_p$ is the average depth of a proton with reference energy E_0.

The dependency of the average measured X_{max} on energy is plotted in Fig. 2 (left) with the prediction of various interaction models [13]. The measurements favor a mixed composition at all energies. However, a more precise interpretation of Fig. 2 in terms of chemical composition is ambiguous due to uncertainties of hadronic interactions. At low energies the data suggests moderate lightening of primary cosmic rays. At high energies EPOS model seems to favor transition from the light to the heavy component. When compared to QGSJETII model, the experimental data seem to follow an almost constant composition in the same energy region.

5 Tests of hadronic interaction models

Since for the composition analysis the knowledge of hadronic interactions is essential, the question appears, whether and how the interaction models can be tested using the data.

One of the possible tests [14] requires the assumption of so called shower universality of the electromagnetic component. It is based on the natural expectation that due to huge amount of

particles in the shower, the details of the initial hadronic interaction are quickly washed out. The resulting electromagnetic component can be thus parametrized using global shower parameters such as energy, zenith angle and distance of the detector to shower maximum. It was shown that to the level of about 15% the signal from the electromagnetic component at given distances to shower maximum is in fact same for proton and iron primary particles as well as for different interaction models [14].

For the muon signal the situation is quite different and showers initiated by heavier primaries at given energy yield larger muon signals than those originated by light primaries. However, it is important that the ratio of the signal for a combination of given model and primary particle to some reference prediction (e.g. for protons in QGSJETII model) is constant as a function of the distance to the shower maximum. This leads to the parametrization of the total signal in terms of the equation:

$$S_{MC}(E,\theta,DX,N_{\mu}^{REL}) = S_{EM}(E,\theta,DX) + N_{\mu}^{REL} S_{\mu}^{QGSJETII,p}(10^{19}eV,\theta,DX),$$

where DX is distance of the detector to the shower maximum, θ is the zenith angle, E is energy of the primary particle and N_{μ}^{REL} is the relative muon normalization with respect to the prediction of the QGSJETII model at $10^{19}eV$ for protons. The constant intensity method similar to what was already described is section 3 can be used to find the muon normalization factor so that the distribution of real events satisfies:

$$\frac{dN}{d(\cos^2(\theta))}_{S(1000)>S_{MC}(E,\theta,DX,N_{\mu}^{REL})} = const.$$

In other words, the question is asked, how the Monte Carlo simulations have to be modified in terms of N_{μ}^{REL} so that the predicted attenuation curve is the same as the attenuation curve measured.

For the bulk of the surface detector events the position of the shower maximum is unknown and the measured $< X_{max} >$ as described in Sec. 4 must be taken and $DX = X_{GR}\sec(\theta) - - < X_{max} >$, where X_{GR} is the vertical atmospheric depth of the ground position. S_{MC} is then function of only 3 parameters, $S_{MC} = S_{MC}(E,\theta,N_{\mu}^{REL})$. The shower to shower fluctuations of X_{max} are taken into account at the end of the analysis. It was shown that $N_{\mu}^{REL} = 1.45 \pm 0.11(\mathrm{stat})^{+0.11}_{-0.09}(\mathrm{sys})$ [15]. About 50 % more muons are thus needed so that proton primaries with QGSJETII model simulate properly the measured signal attenuation. The prediction of the same model but with iron nuclei gives $N_{\mu}^{REL} \sim 1.39$ with respect to the proton prediction. Hence, either the muon numbers in the model have to be adjusted or particles as heavy as iron or even heavier form the entire primary particle flux (which is quite improbable and also contradicts the shower maximum studies presented in Sec. 4). The advantage of this method is that after N_{μ}^{REL} is found the energy scale $S38_{MC}(10^{19}eV, 38^{\circ}, N_{\mu}^{REL} = 1.45)$ can be estimated. A 30% shift between the FD and Monte Carlo energy scale was found [15].

Other model tests can be done with smaller statistics on hybrid events where the shower profile is measured by the fluorescence detector (so the energy and X_{max} are known). The muon signal can be then calculated as a difference of the measured signal in the surface detectors and the electromagnetic signal recorded by fluorescence telescopes.

Also inclined events can be analyzed. The electromagnetic signal of these showers on ground is marginal and the measured surface detector signal is caused directly by the muons. Both analyzes agree with the value N_{μ}^{REL} obtained from the constant intensity method. The evolution of the muon signal as a function of the distance to the shower maximum for hybrid and inclined events is plotted in Fig.2 (right) together with the prediction of the QGSJETII model [15].

6 Conclusions

The hybrid approach of the PAO means that the crucial results such as the energy spectrum or anisotropy studies are independent on models of hadronic interactions. However, these models are essential to interpret shower parameters sensitive to primary particle mass in terms of the UHECR composition. Many magnitudes above the energy of current accelerators, the models of hadronic interaction can be tested using the data of the PAO.

Acknowledgments

The author would like to thank D. Nosek, T. Pierog, R. Smida, F. Schmidt and J.Ridky from the Pierre Auger collaboration for their comments and help with preparation of the contribution. The contribution was prepared with the support of grants of the Czech Republic GACR 202/06/P006, MSMT-CR LA08016 and MSMT-LC527.

References

[1] K. Greisen, Phys. Rev. Lett. **16** (1966) 748.
G. T. Zatsepin and V. A. Kuzmin, JETP Lett. **4** (1966) 78 [Pisma Zh. Eksp. Teor. Fiz. **4** (1966) 114]. .

[2] M. Takeda *et al.*, Phys. Rev. Lett. **81** (1998) 1163 .

[3] H Meyer, these proceedings, “Cosmic Rays and high energy collisons at HERA, Tevatron and LHC” .

[4] J. Abraham *et al.* [Pierre Auger Collaboration], Astropart. Phys. **27** (2007) 155 .

[5] J. Abraham *et al.* [Pierre Auger Collaboration], Astropart. Phys. **29** (2008) 243 .

[6] J. Abraham *et al.* [The Pierre Auger Collaboration], Phys. Rev. Lett. **100** (2008) 211101 .

[7] J. Abraham *et al.* [Pierre Auger Collaboration], Science **318** (2007) 938 .

[8] J. Abraham *et al.* [Pierre Auger Collaboration], Astropart. Phys. **29** (2008) 188 [Erratum-ibid. **30** (2008) 45] .

[9] D. Newton, J. Knapp and A. A. Watson, Astropart. Phys. **26** (2007) 414 [arXiv:astro-ph/0608118]. Phys. Rev. Lett. **101** (2008) 061101 .

[10] T. Pierog, R. Engel, D. Heck, S. Ostapchenko and K. Werner, P roceedings of the 30th International Cosmic Ray Conference (ICRC 2007), Merida, Yucatan, Mexico, 3-11 Jul 2007. arXiv:0802.1262 [astro-ph] .

[11] J. Abraham *et al.* [Pierre Auger Collaboration], Phys. Rev. Lett. **101** (2008) 061101 .

[12] R.U. Abbasi *et al.* , Phys. Rev. Lett. **100**, 10 1101 (2008) .

[13] M. Unger [The Pierre Auger Collaboration], arXiv:0706.1495 [astro-ph]. Proceedings of the 30th International Cosmic Ray Con ference (ICRC 2007), Merida, Yucatan, Mexico, 3-11 Jul 2007 .

[14] F. Schmidt, M. Ave, L. Cazon and A. S. Chou, Astropart. Phys. **29** (2008) 355 .

[15] R. Engel [Pierre Auger Collaboration], Proceedings of the 30th International Cosmic Ray Conference (ICRC 2007), Merida, Yucatan, Mexico, 3-11 Jul 2007.

.

$D\overline{D}$ momentum correlations versus relative azimuth as a sensitive probe for thermalization

G. Tsiledakis[†]*and K. Schweda*
University of Heidelberg Physikalisches Institut, D-69120 Heidelberg, Germany
DOI: http://dx.doi.org/10.3204/DESY-PROC-2009-01/80

Abstract
In high-energy nuclear collisions at LHC, where a QGP might be created, the degree of thermalization at the partonic level is a key issue. Due to their large mass, heavy quarks are a powerful tool to probe thermalization. We propose to measure azimuthal correlations of heavy-quark hadrons and their decay products. Changes or even the complete absence of these initially existing azimuthal correlations in $Pb-Pb$ collisions might indicate thermalization at the partonic level. We present studies with PYTHIA for $p-p$ collisions at 14 TeV using the two-particle transverse momentum correlator $\langle\overline{\Delta}p_{t,1}\overline{\Delta}p_{t,2}\rangle$ as a sensitive measure of potential changes in these azimuthal correlations. Contributions from transverse radial flow are estimated.

1 Introduction

Ultra-relativistic heavy ion collisions offer the unique opportunity to probe highly excited (dense) nuclear matter under controlled laboratory conditions. The compelling driving force for such studies is the expectation that at high enough temperature and/or density hadrons dissolve into a new form of elementary particle matter, the Quark Gluon Plasma (QGP), where quarks and gluons are deconfined. An essential difference between elementary particle collisions and nuclear collisions is the development of collective motion in the latter. The collective flow of all hadrons, especially the multistrange hadrons ϕ and Ω, has been experimentally measured [1] at RHIC and suggest that collective motion develops in the early partonic stage. Presently, the degree of thermalization at the parton level is a crucial issue.

The observables related to heavy-quark hadrons are of particular interest in the study of thermalization [2]. Heavy quarks remain massive in a QGP and can only be pair-created in the early stage of the collisions contrary to light quarks which obtain their small bare masses in the deconfined phase when chiral symmetry is partially restored. In the subsequent evolution of the medium, the number of heavy quarks is conserved because the typical temperature of the medium is much smaller than the thresholds for thermal heavy quark (c, b) production. These heavy quarks participate in collective motion provided their interactions at the partonic level occur at high frequency. Thus, collective motion of heavy-quark hadrons will be a useful tool for studying the early thermalization of light quarks in high-energy nuclear collisions.

[†] speaker

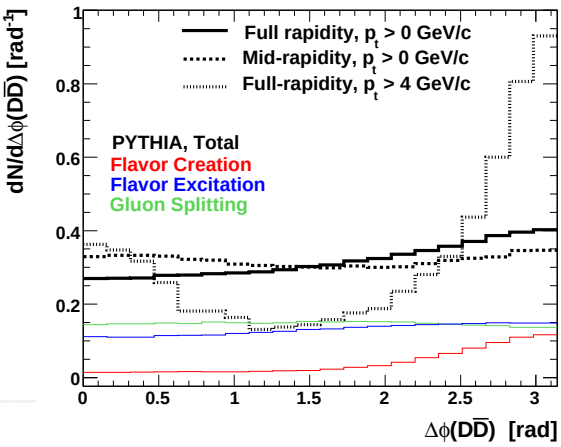


Fig. 1: (Colour online) Distribution in relative azimuth $\Delta\phi$ of $D\overline{D}$ pairs from $p-p$ collisions at $\sqrt{s}$ = 14 TeV as calculated by PYTHIA (v. 6.406), at full rapidity (solid line), and mid-rapidity (dashed line). Contributions from flavor creation, flavor excitation and gluon splitting to the full rapidity distribution are also shown as well as the $p_t > 4$ GeV/c range (dotted line).

1.1 $D\overline{D}$ angular correlations

Since heavy quarks are pair-created by initial hard scattering processes, each quark-antiquark pair is correlated in relative azimuth $\Delta\phi$ due to momentum conservation. In elementary collisions, these correlations survive the fragmentation process to a large extent and hence are observable in the distribution of D and $\overline{D}$ mesons. The observation of broadened angular correlations of heavy-quark hadron pairs in high-energy heavy-ion collisions would be an indication of thermalization at the partonic stage (among light quarks and gluons) since the hadronic interactions at a late stage in the collision evolution cannot significantly disturb the azimuthal correlation of $D\overline{D}$ pairs [3]. As a result, a visible decrease or the complete absence of such correlations, would indicate frequent interactions of heavy quarks and other light partons in the partonic stage in nucleus-nucleus collisions at RHIC and LHC energies.

Concerning $p-p$ collisions, the Monte Carlo event generator PYTHIA [4] reproduces well the experimentally observed correlations of D mesons, measured at fixed target energies [5]. Fig. 1 shows the calculated correlation for $p-p$ collisions at LHC energies ($\sqrt{s}$ = 14 TeV) where the PYTHIA (v. 6.406) parameters were tuned to reproduce the NLO predictions [6, 7] (with the option MSEL=1). The calculations at leading order (LO) which contain only flavor creation processes ($q\overline{q} \rightarrow Q\overline{Q}$, $gg \rightarrow Q\overline{Q}$) lead to back-to-back $D\overline{D}$ pairs. Next-to-leading order (NLO) contributions like flavor excitation ($qQ \rightarrow qQ, gQ \rightarrow gQ$) and gluon splitting ($g \rightarrow Q\overline{Q}$) which become dominant at high energy, do not show explicit angular correlation leading to a strongly suppressed back-to-back correlation. At mid-rapidity, the $D\overline{D}$ correlation in $p-p$ collisions at LHC energies has a rather flat angular distribution [8]. Thus, the measurement of these correlations and their modifications in $Pb-Pb$ collisions is challenging. We introduce the two-particle transverse momentum correlator as a sensitive measure of heavy-quark correlations.

2 Employing the two-particle transverse momentum correlator

The strong transverse momentum dependence of the $D\overline{D}$ correlation leads to a $\Delta\phi$ distribution peaked at 180° for high p_t D mesons, as one would expect for back-to-back pairs stemming from hard scatterings of partons (Fig. 1). For this purpose, an additional measure is introduced. The

occurence of non-statistical fluctuations of the event-by-event mean transverse momentum M_{pt} goes along with correlations among the transverse momenta of particles. Such correlations can be calculated employing the two-particle transverse momentum correlator [9, 10] for D and $\overline{D}$ respectively.

$$\langle \Delta p_{t,1}, \Delta p_{t,2} \rangle^{(D\overline{D})} = \frac{1}{\sum_{k=1}^{n_{\rm ev}} N_k^{\rm pairs}} . C_k \tag{1}$$

where C_k is the p_t convariance:

$$C_k = \sum_{i=1}^{N_k} \sum_{j=1}^{N_k} (p_{ti} - \overline{p_t}^{(D)})(p_{tj} - \overline{p_t}^{(\overline{D})}) \tag{2}$$

where p_{ti} and p_{tj} are the p_t for i^{th} and j^{th} track in an event of D and $\overline{D}$ respectively, $\overline{p_t}$ is the inclusive mean transverse momentum of all tracks from all events of D and $\overline{D}$, $\sum_{k=1}^{n_{\rm ev}} N_k^{\rm pairs}$ the total number of $D\overline{D}$ pairs and n_{ev} the total number of $p-p$ collisions. It is also possible

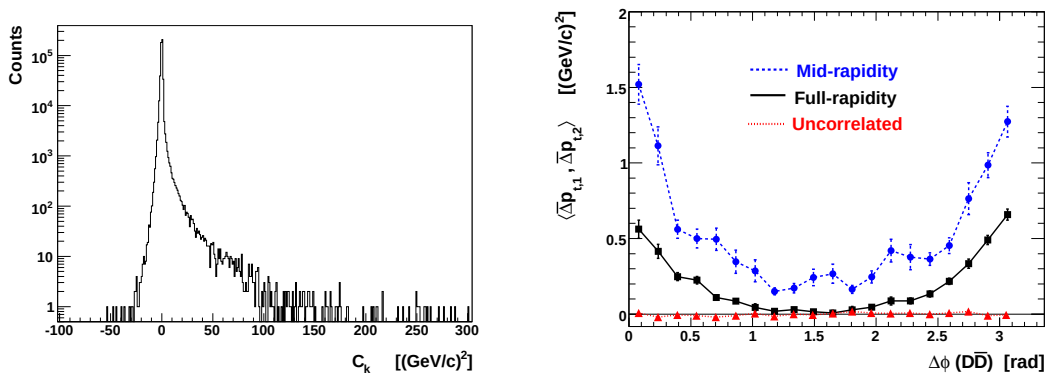


Fig. 2: (Colour online) Distribution of the p_t convariance C_k for $D\overline{D}$ pairs from $p-p$ collisions at $\sqrt{s}$ = 14 TeV as calculated by PYTHIA (v. 6.406) (left panel) and their momentum correlator $\langle \Delta p_{t,1}, \Delta p_{t,2} \rangle$ as a function of $\Delta\phi$ at full rapidity, mid-rapidity and for background using the mixed event method (right panel).

to study the scale dependence of p_t correlations in azimuthal space by calculating the correlator in bins of the azimuthal separation $\Delta\phi$ of particle pairs. For the case of independent particle emission from a single parent distribution, $\langle \Delta p_{t,1}, \Delta p_{t,2} \rangle$ vanishes. Fig. 2 (left panel) shows the distribution of the p_t convariance C_k for $D\overline{D}$ pairs. The mean of this distribution reveals a strong correlation with $\langle \Delta p_{t,1}, \Delta p_{t,2} \rangle = 0.199 \pm 0.006$ GeV$^2/c^2$, which corresponds to the normalized dynamical fluctuation Σ_{pt} [11] of $\sim$ 30% in $\overline{p_t}$. This is a strong correlation when compared to $\sim$ 1% that was measured for unidentified charged particles in central collisions at SPS and RHIC [11–13]. The $D\overline{D}$ momentum correlator $\langle \Delta p_{t,1}, \Delta p_{t,2} \rangle$ as a function of relative azimuth angle $\Delta\phi$ is shown in Fig. 2 (right panel). Using particles from different $p-p$ collisions, which are physically uncorrelated (mixed event method), results in a value of $\langle \Delta p_{t,1}, \Delta p_{t,2} \rangle$ consistent with zero, as expected. Applying the correlator to $D\overline{D}$ mesons from the same $p-p$ collision, a rich structure is observed. At full rapidity, the most pronounced features are a strong peak at

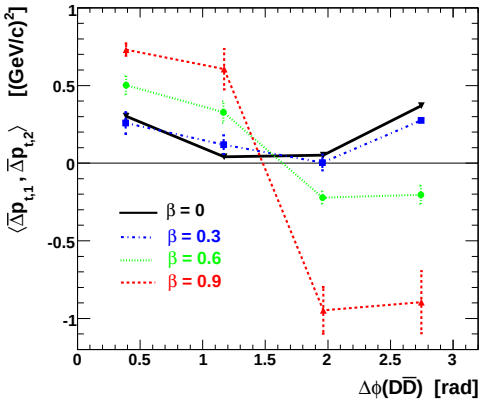


Fig. 3: (Colour online) The momentum correlator $\langle \Delta p_{t,1}, \Delta p_{t,2} \rangle$ of $D\overline{D}$ pairs from $p-p$ collisions at $\sqrt{s}$ = 14 TeV as calculated by PYTHIA (v. 6.406), as a function of their relative azimuth $\Delta\phi$ at full rapidity for various collective flow velocities β.

small angles due to gluon splitting, while flavor creation of $c\overline{c}$-quark pairs results in a peak of similar magnitude at large angles. At mid-rapidity the signal is even enhanced, due to the harder p_t spectrum of $D\overline{D}$ meson-pairs.

Our tests show that a realistic amount of elliptic flow does not change these correlations. Concerning the radial flow contribution, it is assumed that the expansion produces an additional momentum $p_{t,f} = \gamma m \beta$, where γ is the Lorentz factor, β is the profile velocity and m is the mass of the D meson. By adding this radial flow component [14] vectorially to the momentum vector produced by PYTHIA, we evaluate the $\langle \Delta p_{t,1}, \Delta p_{t,2} \rangle$ as a function of $\Delta\phi$. As it is shown in Fig. 3, strong radial flow will further increase the same side momentum correlations of $D\overline{D}$ pairs and might lead to strong anti-correlations at large angles.

As we have shown, the initial correlations of $c\overline{c}$ pairs survive the fragmentation process. However, direct reconstruction of D mesons from topological decays suffer from small efficencies resulting in low statistics. Therefore, we investigated semileptonic decays of D mesons and performed an analogous analysis. Our results indicate that dileptons from $D\overline{D}$ decay preserve the original $D\overline{D}$ angular p_t correlation to a large extent. Fig. 4 shows the momentum correlator $\langle \Delta p_{t,1}, \Delta p_{t,2} \rangle$ of e^+e^- pairs from $D\overline{D}$ decay, as a function of of their relative azimuth $\Delta\phi$ at full rapidity, where the away-side peak at large angles is sizeable (right panel). The correlation is given by $\langle \Delta p_{t,1}, \Delta p_{t,2} \rangle = 0.007 \pm 0.001$ GeV$^2/c^2$, which corresponds to the normalized dynamical fluctuation Σ_{pt} of $\sim 12\%$.

3 Conclusions and outlook

In summary, the $D\overline{D}$ momentum correlations versus relative azimuth in $p-p$ collisions at $\sqrt{s}$ = 14 TeV were investigated. The two-particle transverse momentum correlator $\langle \overline{\Delta} p_{t,1} \overline{\Delta} p_{t,2} \rangle$ is a sensitive measure to carefully address these correlations. Our measure has a high sensitivity leading to strong $D\overline{D}$ back-to-back correlation and helps to identify and disentangle different contributions to the observed correlation pattern. We demonstrated that the correlation of generated $c\overline{c}$ pairs survives the fragmentation process and even semileptonic decay to electrons (positrons) to a large extent. Thus, measurements of these correlations seem feasible with the upcoming collisions from LHC.

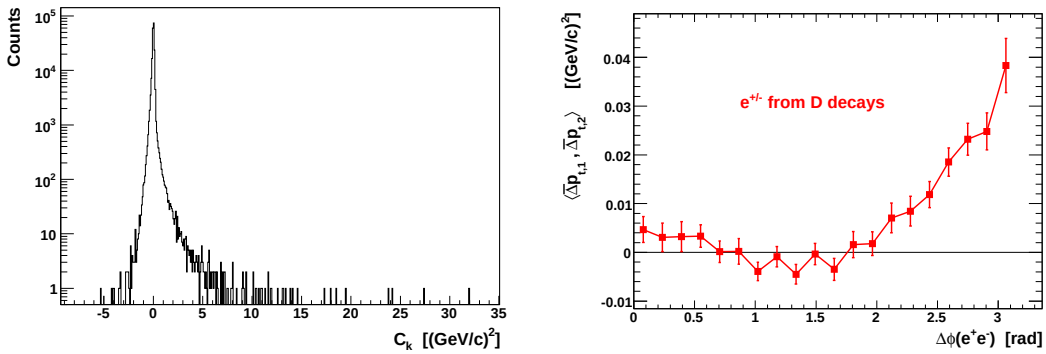


Fig. 4: (Colour online) Distribution of the p_t convariance C_k for e^+e^- pairs from $D\overline{D}$ decays from $p-p$ collisions at $\sqrt{s}$ = 14 TeV as calculated by PYTHIA (v. 6.406) (left panel) and their momentum correlator $\langle \Delta p_{t,1}, \Delta p_{t,2} \rangle$ as a function of $\Delta\phi$ at full rapidity (right panel).

References

[1] K.H. Ackermann *et al.* (STAR collaboration), Phys. Rev. Lett. **86**, 402 (2001); C. Adler *et al.* (STAR collaboration), Phys. Rev. Lett. **89**, 132301 (2002); J. Adams *et al.* (STAR collaboration), Phys. Rev. Lett. **95**, 122301 (2005); B.I. Abelev *et al.* (STAR collaboration), Phys. Rev. C **69**, 054907 (2004).

[2] E.L Bratkovskaya *et al.*, Phys. Rev. Lett. **86**, 402 (2001).

[3] X. Zhu *et al.*, Phys. Lett. B **647**, 366 (2007).

[4] T. Sjöstrand *et al.*, Comput. Phys. Commun **135**, 238 (2001).

[5] C. Lourenço and H.K. Wöhri, Phys. Rep. **433**, 127 (2006).

[6] N. Carrer and A. Dainese (ALICE Collaboration), arXiv:hep-ph/0311225.

[7] E. Norrbin and T. Sjöstrand, Eur. Phys. J. C **17**, 137 (2000).

[8] X. Zhu *et al.*, Phys. Rev. Lett. **100**, 152301 (2008).

[9] J. Adams *et al.* (STAR collaboration), Phys. Rev. C **72**, 044902 (2005).

[10] D. Adamova *et al.* (CERES collaboration), Nucl. Phys. A **811**, 179 (2008).

[11] D. Adamova *et al.* (CERES collaboration), Nucl. Phys. A **727**, 97 (2003).

[12] H. Sako *et al.* (CERES collaboration), J. Phys. G **30**, S1371 (2004).

[13] M. Rybczinski *et al.* (NA49 collaboration), J. Phys. Conf. Ser. **5**, 74 (2005).

[14] E. Cuautle and G. Paić, AIP Conf. Proc. **857**, 175 (2006).

Hard Diffraction at the LHC

Albert De Roeck
CERN, 1211 Geneva 23 Switzerland and University of Antwerp
DOI: http://dx.doi.org/10.3204/DESY-PROC-2009-01/82

Abstract
A short review is given on the opportunities for hard diffractive and forward physics measurements at the LHC.

1 Introduction

The Large Hadron Collider (LHC) [1], is a proton-proton collider being installed in the Large Electron Positron (LEP) tunnel at the CERN Laboratory (the European Laboratory for Particle Physics near Geneva, Switzerland). It will be a unique tool for fundamental physics research and the highest energy accelerator in the world for many years following its completion. The LHC will provide two proton beams, circulating in opposite directions, at an energy of 7 TeV each (center-of-mass $\sqrt{s} = 14$ TeV). These beams upon collision will produce an event rate about 100 times higher than that presently achieved at the Tevatron $p\bar{p}$ collider. The first collisions at 14 TeV are now expected for summer/fall 2009.

Apart from the discovery potential the LHC will be also a pivotal instrument to study QCD at the highest energies. Diffraction is an important component in hadronic collisions, and the LHC will shed new light on these still relatively poorly understood interactions. The type of diffractive collisions, or collisions with rapidity gaps expected at the LHC, is shown in Fig. 1 (left).

Diffractive collisions are usually pictured as the result of a diffractive exchange (aka pomeron). In this language the high energy of the LHC beams effectively leads to "pomeron beams" with an energy close to a TeV, allowing to study partonic collisions with fractional momenta of the partons in the "pomeron" of 10^{-3}, and p_T^2 transfers of more than 1 $(\mathrm{TeV}/c)^2$. The gap dynamics is presently not fully understood and events with multi-gaps will allow new insights.

2 Detectors for Diffraction

Diffractive events can be tagged by recording rapidity gaps in the events or by detecting the forward proton. The central detector of the CMS and ATLAS experiments have an acceptance in pseudorapidity η, of roughly $|\eta| < 2.5$ for tracking information and $|\eta| < 5$ for calorimeter information.

CMS plans to install a calorimeter that would cover the η range up to $\eta = 6.5$. At the time of this symposium a part of CASTOR was installed as shown in Fig.1 (right). In conjunction with the T2 detector of TOTEM, which has roughly the same acceptance in η, charged particles like electrons can be measured in this forward region. A view of this instrumented region is given in Fig. 2 (left).

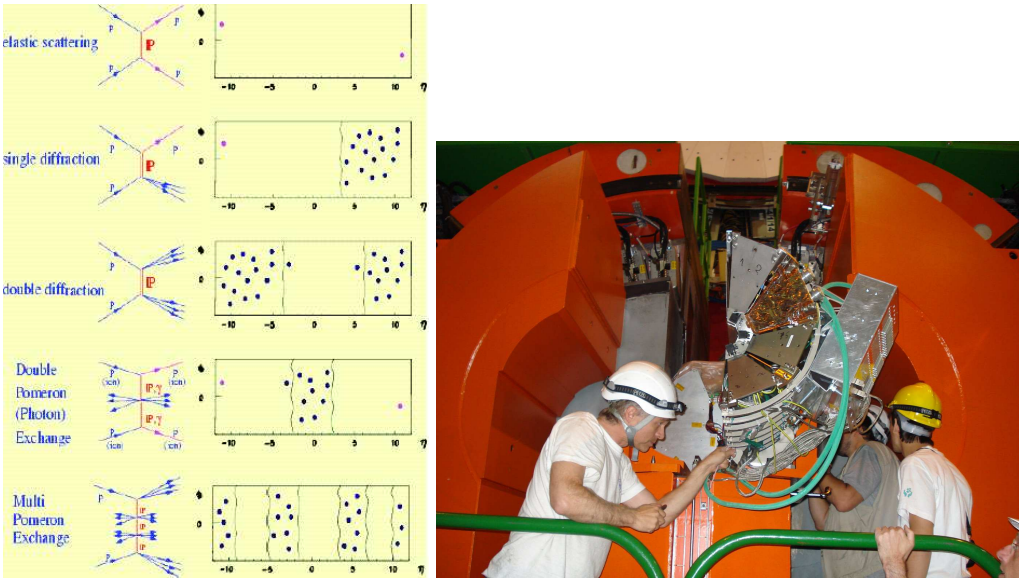


Fig. 1: (Left) Rapidity gap configurations for diffractive events at the LHC; (Right) Installation of part of the CASTOR detector.

CMS is studying the option to include scintillators or GEMs at places among the beamline up to 60-70m or so, to study the particle production in the forward region and backgrounds of the machine, as detailed in [4].

Several of the LHC experiments will have so called Zero Degree Calorimeters (ZDCs). These detectors are located at 140m from the interaction point, where the proton beams are separated in their own beampipe. Finally, TOTEM and ATLAS plan to install Roman Pots that would allow to detect protons which lot 1% to 10% of the total incident energy. A common data taking between TOTEM and CMS –which use the same interaction point– is foreseen [5].

3 FP420

The FP420 project proposes to complement the experiments CMS and ATLAS by installing additional near-beam detectors at 420m away from the interaction region [6]. The presence of these detectors will allow to measure exclusive production of massive particles, such as the Higgs particle, as discussed in the next section.

The aims of the FP420 R&D study are

- Redesign the area of the machine around 420m. Right now this area contains a connecting cryostat, but no magnet elements.
- Study the mechanics, stability and services for detectors at 420m
- Design and test tracking detectors to operate close to the beam
- Design fast timing detectors (with O(10) psec resolution)
- Study RF pickup, integration, precision alignment, radiation and resolution issues for the

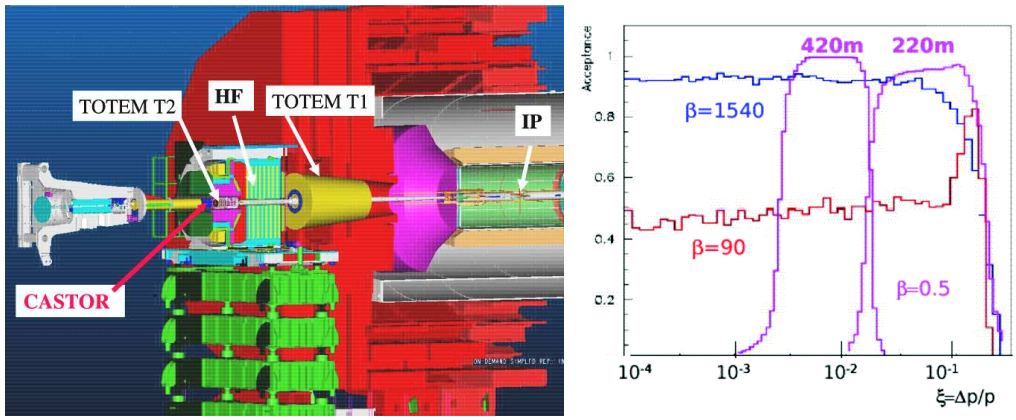


Fig. 2: (Left) Schematics of the CMS forward region. (Right) ξ acceptance of the Roman Pots of TOTEM and detectors at 420m.

FP420 setup.

- Study trigger, event selection, and pile-up issues.
- Study the operation of FP420 detectors at the highest LHC luminosity.

The FP420 project has members from ATLAS, CMS, and "independent" physicists, with excellent contacts with the LHC machine group. In the emerging design the principle of FP420 is based on moving "pockets" which contain tracking and timing detectors. The tracking detectors that are developed are 3D silicon pixel detectors, which are radiation hard and can detect particles close to the edge. Timing detectors include both gas and crystal radiators. The first test beam results of all these detector types are very encouraging and a full pocket beam-test was performed October 2007. Discussions on the implementation of FP420 in the ATLAS and CMS experiments have started. More technical details on FP420 can be found in [7].

4 Diffraction and QCD

The acceptance for diffractive physics with tagged protons is given in Fig. 2(right), for TOTEM and for detectors at 420m. Similar numbers hold for the ATLAS RPs. It shows that special runs with high β^* optics allow to detect protons over essentially the whole ξ range, but this corresponds essentially to luminosities below 10^{31} cm^{-1} s^{-1}. At the nominal high luminosity β^* detectors at 220m (TOTEM or RP220) and detectors at 420m are complementary on the region they cover. Physics topics include QCD and diffraction.

With special optics and rather short running time (perhaps a week) processes with cross sections of μbarns are accessible, while with high luminosity processes with nbarn and pbarn cross sections can be studied. As an example for jet events, generator studies show that with about 300 nb^{-1} about 60000 SD events and 2000 DPE events are produced with jets having an E_T larger than 20 GeV. With 100 pb^{-1} we have 500000 and 30000 events with jets with an E_T larger than 50 GeV. Low luminosities will allow initial studies while high luminosity samples will allow for detailed t, M_x, p_T dependence studies.

An extensive program of two photon physics and photon-proton physics becomes accessible as well. In particular the study of the processes $\gamma\gamma \to WW$ and ZZ is of interest and can give precise measurements of the anomalous couplings. The QED processes $\gamma\gamma \to \mu\mu, ee$ can be precise monitors of the luminosity. Two photon processes can also be used to search for chargino pair production.

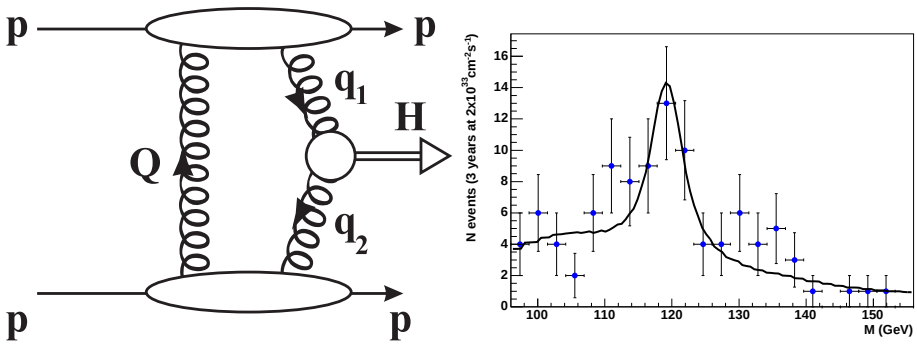


Fig. 3: (Left) Diagram for the CEP process; (Right) A typical mass fit for 3 years of data taking at 2×10^{33} cm^{-2} s^{-1} (60 fb^{-1}). The significance of the fit is 3.5σ and uses only events with both protons tagged at 420m.

5 Central exclusive Higgs production

Central exclusive Higgs (CEP) production $pp \to p + H + p$ is of special interest. The diagram is shown in Fig. 3 (left). One of the key advantages of CEP is that the $gg \to b\bar{b}$ process is strongly suppressed in LO, hence the decay $H \to b\bar{b}$ has less background and becomes potentially observable. The Higgs to b-quark Yukawa coupling is otherwhise very difficult to access at the LHC. The inclusive $H \to b\bar{b}$ channel is not accessible due to the too large QCD backgrounds. Recently, the ttH channel was analysed with detailed simulation in [8] and found not to be accessible even with 60 fb^{-1}. Also the WH associated channel was found to be marginally observable in the $b\bar{b}$ decay mode.

The cross section for CEP of Higgs bosons has been subject of many discussions over the last years, in particular during the HERA/LHC workshops [9], but now generally the calculations of [10] are taken as a reference. Note that there are still some issues and concerns on the CEP soft survival probability at the LHC and the uncertainties in the PDFs. Generator level calculations, including detector and trigger cuts, and estimates of selection efficiencies, show that the decay channels $H \to b\bar{b}$ and $H \to WW$ are accessable. Eg. $M_H = 120$ GeV/c^2 gives about 11 events with O(10) events background for 30 fb^{-1} in the $b\bar{b}$ decay mode. For M_H above 140 GeV/c^2 about 5-6 events with no appreciable background for 30 fb^{-1} in the WW decay mode [11] will be observed, using channels with at least one leptonic decay. There are however challenges: the signals from detectors at 420m cannot be used to trigger the events at the first trigger level in neither ATLAS nor CMS. Hence the event will have to be triggered at the first level with the information of the central detector. At the next trigger level the signals of FP420 can be used. While this is no problem for the WW decay channel, it is a challenge for the $b\bar{b}$ channel.

Several additional selection cuts for a low mass Higgs-like object decaying into jets can be used, but generally, with di-jet thresholds of O(40) GeV and these additional cuts, the rate at the first level for this trigger is very high: O(10) kHz. The usage of the FP420 information can however strongly reduce that rate at the next level, so this is not necessarily a show stopper. But in any case, studies both using detailed [5] and fast [12] simulations show that the measurement of the SM Higgs decay into $b\bar{b}$ will be very challenging, even with the highest luminosities.

The rate is much larger for MSSM Higgs production, thus leading to a much more favourable signal to background ratio than for the SM Higgs. The cross section can be a factor 10 or more larger than the SM model one. This has recently been explored in a systematic way in [13]. Fig. 3 (right) shows an example of a signal for 60 fb^{-1} after acceptance cuts, trigger efficiencies etc., for a MSSM Higgs with a cross section that is a factor 8 enhanced w.r.t the the SM Higgs, based on the so called m_h^{max} scenario [14], with $m_A = 120$ GeV and $\tan\beta = 40$. A clear signal over background is observable.

A detailed study of the backgrounds to this diffractive process was presented in [5]. At high luminosity, ie. 10^{33} cm^{-2}s^{-1} and higher, the pile-up is considerable, coming mainly from soft single diffractive interactions. Several techniques such as correlations between the detectors at 420/220m, vertices, event multiplicities and especially fast timing are essential to reduce the pile-up background. Rapidity gaps can obviously not be used due to the many interactions per bunch crossing.

To a very good approximation the central system in CEP is constrained to be a colour singlet, $J_Z = 0$ state, and, due to the strongly constrained three particle final state, the measurement of azimuthal correlations between the two scattered protons will allow to determine the CP quantum numbers of the produced central system [15]. Hence this is a way to get information on the spin of the Higgs, and is added value to the LHC measurements.

Other searches for new physics in the channel are possible as well. It has been pointed out that the mass of long lived gluinos, as predicted in split SUSY models, can be determined with CEP events to better than 1%, with 300 fb^{-1} for masses up to 350 GeV [16]. More spectacular are the predictions presented in [17], where a very high cross section of CEP WW and ZZ events is expected, in a color sextet quark model.

6 Conclusion

The LHC is coming on line, with the first 14 TeV collisions to be expected in summer/fall 2009.

Already with the first data the LHC will allow for novel measurements on hard diffraction, from jets to W, Z and heavy flavor production. When forward proton tagging systems are used, like FP420, a different way to study the Higgs will become accessible. In all, forward and diffractive physics is now well in the blood of the LHC experiments.

References

[1] The LHC Study Group: *The Large Hadron Collider Conceptual Design*, CERN-AC-95-05 (1995).

[2] Lippmaa, E. et al., Felix Collaboration, *FELIX: A full acceptance detector at the LHC*,CERN-LHCC, http://www.cern.ch/FELIX/Loi/letofin.html, 97 (1997).

[3] Ageev, A. et al., J. Phys **G28**, (2002), R117.

[4] M. Albrow et al., arXiv:0811.0120 2008.

[5] M. Albrow et al. (CMS& TOTEM) *Prospects for diffractive and forward physics at the LHC*. CERN-LHCC-2006-039, CERN-LHCC-G-124, CERN-CMS-NOTE-2007-002, Dec 2006. 156pp.

[6] M.G. Albrow et al. *FP420: An R& D proposal to investigate the feasibility of installing proton tagging detectors in the 420-m region at LHC*, CERN-LHCC-2005-025, Jun 2005.

[7] M.G. Albrow et al., *FP420 R&D report*, to appear.

[8] CMS Collaboration *CMS physics : Technical Design Report v.2 : Physics performance* CERN-LHCC-2006-021 (2006); J. Phys. G: Nucl. Part. Phys. **34** (2007) 995, doi:10.1088/0954-3899/34/6/S01.

[9] S. Alekhin et al., *Proceedings of the HERA-LHC workshop*, CERN-2005-014, DESY-PROC-2005-01 (2005), hep-ph/0601013 and hep-ph/0601012.

[10] V.A Khoze, A.D. Martin and M.G. Ryskin, Eur. Phys. J. C. **23** (2002) 311.

[11] Cox, B. E. et al. Eur.Phys.J. C **45** (2006) 401, hep-ph/0505240.

[12] B.E. Cox, F.K. Loebinger, A.D. Pilkington, MAN-HEP-2007-15, Sep 2007, arXiv:0709.3035 [hep-ph]

[13] S. Heinemeyer et al., DCPT-07-80, IPPP-07-40, Aug 2007, arXiv:0708.3052

[14] M.S. Carena, S. Heinemeyer, C.E.M. Wagner and G. Weiglein, Eur. Phys. J. C **26** (2003) 601.

[15] V.A Khoze, A.D. Martin and M.G. Ryskin, Eur. Phys. J. C **34** (2004) 327, hep-ph/0401078.

[16] P.J. Bussey, T.D. Coughlin, J. R. Forshaw, A.D. Pilkington, JHEP **0611** (2006) 027.

[17] A.R. White, Phys. Rev. D **72** (2005) 036007.

[18] Koji Terashi for the CDF collaboration. FERMILAB-CONF-07-148-E, Proceedings of 42nd Rencontres de Moriond on QCD Hadronic Interactions, La Thuile, Italy, 17-24 Mar 2007, arXiv:0705.3804.

Exclusive photoproduction of dileptons at high energies

M.V.T. Machado
Centro de Ciências Exatas e Tecnológicas, Universidade Federal do Pampa
Campus de Bagé, Rua Carlos Barbosa. CEP 96400-970. Bagé, RS, Brazil
DOI: http://dx.doi.org/10.3204/DESY-PROC-2009-01/83

Abstract
The exclusive photoproduction of lepton pairs on nucleon and nucleus target is investigated within the high energy color dipole approach, where the main physical quantity is the dipole-target elastic scattering amplitude that captures the main features of the dependence on the atomic number A, on energy and on momentum transfer t. These calculations are input in predictions for electromagnetic interactions in pp and AA collisions to be measured at the LHC.

The physics of large impact parameter interactions [1] at the LHC and Tevatron has raised great interest as these electromagnetic interactions in pp and AA collisions extend the physics program of photon induced processes beyond the energies currently reached at DESY-HERA. This can happen in a purely electromagnetic process through a two-photon interactions or in an interaction between a photon from one of the nuclei and the other "target" nucleus. These ultraperipheral collisions (UPCs) are a good place to constraint the photonuclear cross sections as the dominant processes in UPCs are photon-nucleon (nucleus) interactions. Electromagnetic interactions can also be studied with beams of protons or anti-protons, but there is then no Z^2-enhancement in the photon flux in contrast to AA collisions. Several analysis are currently being done at Tevatron focusing on such processes. For instance, the CDF Collaboration is analyzing the exclusive production of muon pairs, $p\overline{p} \to p\overline{p} + \mu^+\mu^-$, at lower invariant masses [2]. The two main contributions to these events are, as with heavy-ion beams, $\gamma\gamma \to \mu^+ + \mu^-$ and $\gamma + IP \to J/\Psi(\text{or } \Psi')$, followed by the meson decay into a dilepton pair.

In this contribution, we summarize the results presented in Ref. [4], where the high energy color dipole approach [3] is used to study the exclusive photoproduction of lepton pairs. The motivation to consider the color dipole formalism is due to the fact that the electromagnetic deeply virtual Compton scattering (DVCS) cross section at high energies is nicely reproduced in several implementations of the dipole cross section at low x [8–11]. The present process at small t and large timelike virtuality of the outgoing photon shares many features of DVCS. Simple models for the elementary dipole-hadron scattering amplitude that captures main features of the dependence on atomic number A, on energy and on momentum transfer t were considered. Our investigation is complementary to conventional partonic description of timelike Compton scattering (TCS) [5], $\gamma p \to \gamma^* + p$, which considers the relevant generalized parton distributions (GPDs). It should be noticed that the TCS process has so far only been studied at LO in the collinear factorization framework in terms of the quark GPDs and sub-processes initiated by gluons have not been considered [5]. This approach has been recently considered to make predictions for the relevant kinematics for LHC [6, 7] and a detailed investigation of competing processes (like the Bethe-Heitler contribution) and possible interference term is presented.

1 TCS process within the color dipole approach

In the color dipole picture [3], the scattering process $\gamma p \to \gamma^* p$ is assumed to proceed in three stages: first the incoming real photon fluctuates into a quark–antiquark pair, then the $q\bar{q}$ pair scatters elastically on the proton, and finally the $q\bar{q}$ pair recombines to form a virtual photon (which subsequently decays into lepton pairs). The amplitude for production of the exclusive final state such as a virtual photon in TCS, is given by [8, 9, 11]

$$\mathcal{A}^{\gamma p\to\gamma^* p}(x,Q,\Delta) = \sum_f \sum_{h,\bar{h}} \int d^2\vec{r} \int_0^1 dz\, \Psi^*_{h\bar{h}}(r,z,Q)\, \mathcal{A}_{q\bar{q}}(x,r,\Delta)\, \Psi_{h\bar{h}}(r,z,0)\,, \tag{1}$$

where $\Psi_{h\bar{h}}(r,z,Q)$ denotes the amplitude for a photon to fluctuate into a quark–antiquark dipole with helicities h and $\bar{h}$ and flavour f. The quantity $\mathcal{A}_{q\bar{q}}(x,r,\Delta)$ is the elementary amplitude for the scattering of a dipole of size $\vec{r}$ on the proton, $\vec{\Delta}$ denotes the transverse momentum lost by the outgoing proton (with $t=-\Delta^2$), x is the Bjorken variable and Q^2 is the photon virtuality.

As one has a real photon at the initial state, only the transversely polarized overlap function contributes to the cross section. The expression for the overlap function can be found for instance in Ref. [11]. In our numerical calculations we use still the space-like kinematics and we expect not a large deviation from the correct kinematics. However, the approximation we have considered to estimate the cross section should be taken with due care. It should be noticed that some corrections to this exclusive process are needed. For TCS one should use the off-diagonal gluon distribution, since the exchanged gluons carry different fractions x and x' of the proton's (light-cone) momentum. The skewed effect can be accounted for, in the limit that $x' \ll x \ll 1$, by multiplying the elastic differential cross section by a correction factor [12]. We quote Ref. [4] for details.

In the numerical calculations we consider the non-forward saturation model of Ref. [9] (MPS model), which has the advantage of giving directly the t dependence of the elastic differential cross section without the necessity of considerations about the impact parameter details of the process. It is based on the studies about the growth of the dipole amplitude towards the saturation regime in the geometric scaling regime [13]. The geometric scaling property can be extended to the case of non zero momentum transfer [14], provided $r\Delta \ll 1$, where the elementary dipole amplitude now reads as:

$$\mathcal{A}_{q\bar{q}}(x,r,\Delta) = 2\pi R_p^2\, e^{-B|t|} N\left(rQ_{\rm sat}(x,|t|),x\right), \tag{2}$$

with the t dependence of the saturation scale being parametrised as

$$Q^2_{\rm sat}\left(x,|t|\right) = Q_0^2(1+c|t|)\,\left(\frac{1}{x}\right)^{\lambda}, \tag{3}$$

in order to interpolate smoothly between the small and intermediate transfer regions. The scaling function N is obtained from the forward saturation model [15].

In the case of nuclear targets, we make use of studies of Ref. [16] where the high energy $l^{\pm}p$, pA and AA collisions have been related through geometric scaling. In that approach, the nuclear saturation scale was assumed to rise with the quotient of the transverse parton densities,

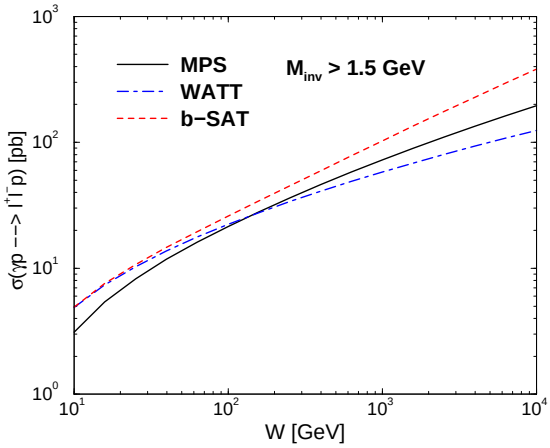


Fig. 1: The integrated cross section ($M_{\ell^+\ell^-} \geq 1.5$ GeV and $|t| \leq 1$ GeV^2) as a function of photon-nucleus centre of mass energy.

$\kappa_A = A\pi R_p^2/(\pi R_A^2)$, to the power $\Delta \approx 1$, that is $Q^2_{\mathrm{sat},A} = \kappa_A^{\Delta}\, Q^2_{\mathrm{sat},p}$ (R_A is the nuclear radius). This assumption successfully describes small-x data for ep and eA scattering using $\Delta = 1.26$ and a same scaling curve for the proton and nucleus [16]. Therefore, we propose the following expression for the elementary dipole amplitude for the nuclear case:

$$\mathcal{A}_{q\bar{q}}(x, r, \Delta; A) = 2\pi R_A^2\, F_A(t)\, N\left(r Q_{\mathrm{sat},A}(x, |t|), x\right), \tag{4}$$

where $F_A(t)$ is the nuclear form factor. It should be stressed that we consider only the coherent nuclear scattering, whereas the incoherent case is neglected.

We investigate the exclusive photoproduction of a heavy timelike photon which decays into a lepton pair, $\gamma p \to \ell^+\ell^- p$. Therefore, for the $\ell^+\ell^-$ invariant mass distribution from the virtual γ^* decay we have (with $Q^2 = M^2_{\ell^+\ell^-}$),

$$\frac{d\sigma}{dM^2_{\ell^+\ell^-}}\left(\gamma p \to \ell^+\ell^- p\right) = \frac{\alpha_{em}}{3\pi M^2_{\ell^+\ell^-}}\,\sigma\left(\gamma p \to \gamma^* p\right). \tag{5}$$

2 Results and Conclusions

In Fig. 1 we show the total cross section, $\sigma(\gamma p \to \ell^+\ell^- p)$, integrated over the dilepton invariant mass $M_{\ell^+\ell^-} \geq 1.5$ GeV. In this plot, we compare the MPS model (solid line) with other implementations of the elementary dipole-nucleon scattering amplitude. For energies $W >> 100$ GeV, a power fit can be performed in the form $\sigma = A\,(W/W_0)^{\alpha}$, with $W_0 = 1$ GeV. Considering the MPS model, one obtains the values $A = 3$ pb and $\alpha = 0.46$. In order to study the sensitivity to the model dependence, we compare the MPS saturation model to two different distinct saturation models. The first one is the recent implementation of the impact parameter Color Glass Condensate model [10] (hereafter WATT, dot-dashed line). The second one is the impact parameter saturation model [8](hereafter b-SAT, long dashed line). In these implementations, the elementary dipole-nucleon scattering amplitude is written in the impact parameter

space. At high energies, a power fit can be also performed for the WATT and b-SAT models. For the WATT impact parameter model, we obtain the parameters $A = 4.3$ pb and $\alpha = 0.37$. In the b-SAT model we have the values $A = 2$ pb and $\alpha = 0.57$. We clearly verify a distinct energy dependence, which depends on the characteristics features of the phenomenological models. The main point is the value of the parameter λ entering at the saturation scale. The WATT model gives the softer energy dependence, which comes from the small value of $\lambda = 0.12$ in the saturation scale, $Q^2_{\rm sat}(x, t = 0) \propto x^{\lambda}$. On the other hand, in the MPS model one has $\lambda = 0.22$ (a factor two larger than in WATT model) and the QCD evolution makes the effective λ value for b-SAT model to be large. The different overall normalization at energies $W \leq 100$ GeV for the MPS model is probably a result of distinct behavior towards low energies.

Concerning the nuclear targets, in Ref. [4] we also compute the integrated cross section per nucleon as a function of energy for $A = 208$ (lead), which is relevant for electromagnetic interactions at AA collisions at the LHC. The nuclear version of MPS model at high energies ($W \geq 100$ GeV) can be parameterized as $\sigma_{\rm MPS}(\gamma A \to \ell^+\ell^- A) = 6.1{\rm pb}\,(W/W_0)^{0.39}$. For the b-SAT model one obtains at high energies $\sigma_{\rm bSAT}(\gamma A \to \ell^+\ell^- A) = 5{\rm pb}\,(W/W_0)^{0.51}$. Accordingly, we verify a larger suppression in the MPS model than in b-SAT, which is directly related to the nuclear saturation scale at each model. Absorption is evident in MPS model, where the effective power on energy has diminished in the nuclear case.

The present calculations are input for the exclusive photoproduction of dileptons in electromagnetic interactions in pp and nucleus-nucleus collisions. Let us concentrate on the pp case, where the processes is characterized by the photon - proton interaction, with the photon stemming from the electromagnetic field of one of the two colliding hadrons. The total cross section for the $p\,p \to p \otimes \ell^+\ell^- \otimes p$ process is obtained by the product of the photon-proton cross section and the photon energy spectrum, $dN/d\omega$, and integration over the photon energy, ω:

$$\sigma\left(pp \to p + \ell^+\ell^- + p\right) = 2\int_0^\infty d\omega \frac{dN_\gamma}{d\omega}\,\sigma\left(\gamma p \to \ell^+\ell^- + p\right) \tag{6}$$

where $\gamma_L = \sqrt{s_{pp}}/2m_p$ is the Lorentz boost of a single beam, $W^2_{\gamma p} \approx 2\omega\sqrt{s_{pp}}$ and $\sqrt{s_{pp}}$ is the centre of mass energy of the hadron-hadron system [1]. The initial factor of 2 in the above equation accounts for the interchange of the photon emitter and the target. This process is characterized by small momentum transfer and energy loss, which implies that the outgoing hadrons should be detected in the forward regions of detectors. The final state is relatively clear, presenting two rapidity gaps and central dilepton production. Therefore, this process has a similar final state as the produced in gamma-gamma scattering. In Table 1, we present an estimative for pp collisions for Tevatron and the LHC energies (integrated over invariant mass $M_{\rm inv} > 1.2$ GeV). For the Tevatron case, we also present the result for the current cut on invariant dilepton mass $3\,{\rm GeV} \leq M_{\ell^+\ell^-} \leq 4\,{\rm GeV}$ which refers to upcoming exclusive dimuon CDF measurements [17]. In order to compare it to the QED case, we quote the value $\sigma(|\eta| < 0.6, 3 < M_{\mu^+\mu^-} < 4\,GeV) = 2.18$ pb from the process $\gamma\gamma \to \mu^+\mu^-$. In the AA the photon flux is enhanced by a factor $\propto Z^2$, then we would expect the cross sections to reach dozens of nanobarns for $PbPb$ collisions at the LHC. The result presented here can be compared to a QCD factorization formalism for exclusive processes involving the GPDs [7]. The authors in Ref [7] have found a strong dependence on the factorization scale. The Compton contribution was estimated to be

$\sqrt{s_{pp}}$	$M_{\ell^+\ell^-} > 1.2$ GeV	3 GeV $\leq M_{\ell^+\ell^-} \leq 4$ GeV
1.96 TeV	7 pb	0.4 pb
14 TeV	25 pb	—

Table 1: Cross section for exclusive dilepton photoproduction at Tevatron and LHC.

1.9 pb at LHC using the cut $2.12 \leq M_{\ell^+\ell^-} \leq 2.35$ GeV and additional cuts on polar and azimuthal angles. Using the same kinematical cut they found a cross section of 2.9 pb for the Bethe-Heitler contribution. We believe that applying similar cuts, our results for the cross section can be compatible with values presented in Ref. [7] for the LHC case.

As a summary, using the color dipole formalism we studied the timelike Compton scattering. Such an approach is robust in describing a wide class of exclusive processes measured at DESY-HERA and at the experiment CLAS (Jeferson Lab.), like meson production, diffractive DIS and DVCS. Our investigation is complementary to conventional partonic description of TCS, which considers quark handbag diagrams (leading order in α_s) and simple models of the relevant GPDs. In particular, the results could be compared to pQCD diagrams involving gluon distributions which are currently unknown. Using current phenomenology for the elementary dipole-hadron scattering, we estimate the order of magnitude of the exclusive photoproduction of lepton pairs. These calculations are input in electromagnetic interactions in pp and AA collisions to measured at the LHC. We found that the exclusive photoproduction of lepton pairs in such reactions should be sizable.

References

[1] K. Hancken et al., Phys. Rept. **458**, 1 (2008).

[2] J. Pinfold, published in DIS 2008, XVI International workshop on Deep Inelastic Scattering and related subjects, 7-11 April, 2008.

[3] N. N. Nikolaev and B. G. Zakharov, Z. Phys. **C49**, 607 (1991); Z. Phys. **C53**, 331 (1992); A. H. Mueller, Nucl. Phys. **B415**, 373 (1994); A. H. Mueller and B. Patel, Nucl. Phys. **B425**, 471 (1994).

[4] M.V.T. Machado, Phys. Rev. D **78**, 034016 (2008).

[5] E.R. Berger, M. Diehl and B. Pire, Eur. Phys. J. C **23**, 675 (2002).

[6] B. Pire, L. Szymanowski and J. Wagner, Nucl. Phys. Proc. Suppl., **179-180**, 232 (2008).

[7] B. Pire, L. Szymanowski and J. Wagner, arXiv:0811.0321 [hep-ph].

[8] H. Kowalski, L. Motyka and G. Watt, *Phys. Rev.* **D74**, 074016 (2006).

[9] C. Marquet, R. Peschanski and G. Soyez, Phys. Rev. D **76**, 034011 (2007).

[10] G. Watt and H. Kowalski, Phys. Rev. D **78**, 014016 (2008).

[11] L. Motyka and G. Watt, Phys. Rev. D **78**, 014023 (2008).

[12] A. G. Shuvaev *et al.*, Phys. Rev. D **60**, 014015 (1999).

[13] A.M. Stasto, K. Golec-Biernat and J. Kwiecinski, *Phys. Rev. Lett.* **86**, 596 (2001).

[14] C. Marquet, R. Peschanski and G. Soyez, *Nucl. Phys.* **A756**, 399 (2005).

[15] E. Iancu, K. Itakura and S. Munier, Phys. Lett. B **590**, 199 (2004).

[16] N. Armesto, C. A. Salgado and U. A. Wiedemann, Phys. Rev. Lett. **94**, 022002 (2005).

[17] M. Albrow, *Central Exclusive Production*, in XXXVIII International Symposium on Multiparticle Dynamics (ISMD2008), Hamburg 15-20 September 2008.

Chapter 5

Working Group
Strategies and Analysis Methods

Convenors:

E.DeWolf (Antwerp)
A.Geiser (DESY)
M.Sjodahl (Manchester)

Colour Reconnections and Top Physics

Daniel Wicke
Bergische Universität Wuppertal
DOI: http://dx.doi.org/10.3204/DESY-PROC-2009-01/42

Abstract
In simulations of hadron collisions the description of multiple parton interactions play an important role. These descriptions cannot be derived from first principles, but are described by models which have a priori unknown parameters. Tevatron data seem to indicate that the description of underlying events requires the presence of some non-trivial colour reconnection effects. Several parameter sets ('tunes') of such models, constrained by fits to Tevatron minimum-bias data, were used to determine the sensitivity of top physics results on the differences of underlying event models. A first attempt to isolate the genuine non-perturbative effects gave an estimate for the uncertainty on the top mass of the order of $\pm 0.5\,\text{GeV}$ from these non-perturbative sources.

1 Introduction

In hadron-hadron collisions in principle more than a single a pair of partons may collide. Collisions beyond the hardest interaction are usually called the underlying event or multiple parton interactions. These additional interactions will add further soft or semi-hard particles to the final state. Because these multiple parton interaction cannot be computed perturbatively event generator use models to incorporate their effects.

Given the size of the proton and the large amount of colour charges present inside a proton it seems be possible that these additional soft or semi-hard interactions modify the colour structure of the hard interaction. LEP studies have shown that mass measurements can be especially sensitive to such colour reconnections. Thus to study the sensitivity of top physics to effects of colour-reconnection and of the underlying event in general as a first step their influence on measurements of the top mass measurements was studied.

The studies summarised in this article are described in detail in [1] and were updated in [2].

2 Colour Reconnection Models

The discussion of colour reconnection in hadron hadron collisions has to start with a dicussion of underlying event models.

Monte Carlo event generators like Pythia 6.4 [3] provide *models* to decribe the effects of the underlying event. Pythia provides two models: the 'old' model [4] treats the underlying event only after initial-state showering of the hard process is complete. It add additional back-to-back parton pairs and feeds these directly into the hadronisation together with the partons from the hard process. The 'new' model [5] interleaves the additional interactions with the initial-state parton shower off the hard process and allows the additional partons to radiate further. Various

options for colour connections and colour reconnections between and inside the multiple parton interaction chains exist.

Like all others these models contain several parameters which are not know a priori and need to be optimised to describe data. Several tunes of Pythia parameters for the old model were obtained by CDF, e.g. Tune A, Tune DW, Tune BW, etc. [6]. A common feature of these tunes is that the parameters describing the probability of non-trivial colour connections between the additional-parton interactions and the hard scattering, `PARP(85)` and `PARP(86)`, are significantly enhanced. This is interpreted as a sign of actual colour reconnections happening in the underlying event.

The models described so far don't contain explicit colour reconnection. Moreover the colour reconnection models studies at LEP [7–10] focused exclusively on WW physics and thus were not directly applicable to hadron collitions. Thus simple models of colour reconnection for more general situation were introduced [11]. These base on an annealing-like algorithm, which minimises the string length and thereby the potential energy of the confinment field. Several variants of the algorithms were implemented in Pythia which vary in the way closed gluon loops are suppressed.

Because the colour reconnection may significanty modify the effects of the underlying event model, the parameters of the colour reconnection model *and* the underlying event model were retuned simultaneously. Tunes for the described colour reconnection models (named S0, S1 and S2) first appeared in Pythia v6.408 and were revised in v6.414 after a bug affecting the p_T ordered shower was fixed [12].

3 Toy Top Mass Measurements

The underlying event and colour reconnection effects may influence the results obtained in measurements of the hard process. At LEP, the W mass was especially sensitive to these effects, thus first the influence of the various models on measurements of the top quark mass at the Tevatron was studied.

Measurements of the top quark [13] consist of three main ingredients: First, a mass estimator based on the reconstructed physics objects, i.e., jets, lepton and missing transverse energy. Such an estimator uses a jet-parton assignment done by either choosing or weighting the various possibilities. Second, current measurements include an overall jet energy scale (JES) correction factor, which reduces the dominating systematic uncertainty by using the well known W mass as an additional constraint. And finally all methods are calibrated to simulation by correcting any offset between the reconstructed top mass and the nominal value of the simulation. It is especially in this last step that the different models may affect the outcome of the procedure.

A simplified toy mass measurement for semileptonic top pair events on generator level was implemented to study the colour reconnection and underlying event effects without dealing with detector simulation and reconstruction effects. This toy mass measurements uses events with exactly four jets from a cone algorithm [14, 15] with $\Delta R = 0.5$, $p_T > 15\,\text{GeV}$. The jet-parton assignment is done by matching the reconstructed jets to the Monte Carlo truth by ΔR keeping only events with a unique assignment. The top mass is computed in each event from the three jets assigned to the hadronically decaying top quark.

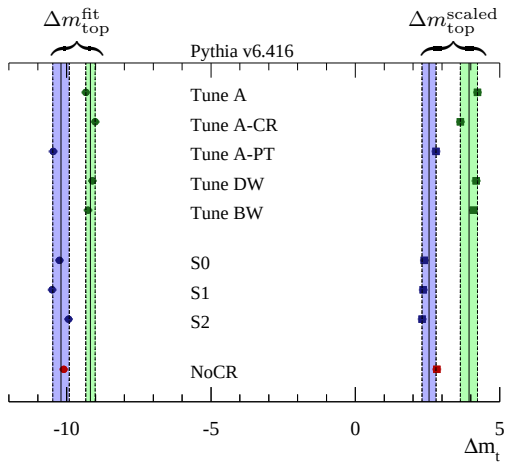


Fig. 1: Comparison of calibration offsets obtained for each model. The column on the left (dots) show the results obtained before JES rescaling, the right column (squares) after rescaling. The statistical precision due to the finite number of generated events is at the level of ± 0.15 GeV.

As mass estimator for the full dataset the peak of the the distribution of reconstructed top mass values is fitted with a Gaussian $m_{\rm top}^{\rm fit}$. At this stage jets aren't corrected for out-of-cone effects so this mass estimator is expected to give results that are lower than the nominal value in the simulation. In analogy to the JES correction factor this can be corrected for by using the W mass information. An event-by-event W mass is reconstructed again by fitting a Gaussian to the distribution of mass values reconstructed from the two jets assigned to the hadronic W decay. A scaled top mass estimator is then constructed as $m_{\rm top}^{\rm scaled} = s_{\rm JES}\, m_{\rm top}^{\rm fit}$ where the scale factor is $s_{\rm JES} = 80.4\,{\rm GeV}/m_W$, with m_W being the W mass obtains from the fit. Thus the simplified top mass measurements provide two results $m_{\rm top}^{\rm fit}$ and $m_{\rm top}^{\rm scaled}$, one before JES correction and one after. For both top mass estimates calibration curves were computed by scanning the nominal top mass and determining the described mass estimator for each of the nominal values. The calibration curves show an excellent linearity. As expected the offset for the un-scaled estimator ($m_{\rm top}^{\rm fit}$) is negative and after scaling the results ($m_{\rm top}^{\rm scaled}$) is closer to the nominal result.

In real top mass measurements such calibration curves are used to correct a possible bias in the mass estimation. Thus comparing the offsets obtained using the various underlying event model tunes yields and estimation of the possible size of the uncertainty due to modelling multiple parton interaction. The offsets evaluated at a nominal mass of $175\,{\rm GeV}$ for the various models are shown in Fig. 1 for both mass estimators. The models exhibit a spread of $\pm 0.8\,{\rm GeV}$ and $\pm 1.0\,{\rm GeV}$ for the $m_{\rm top}^{\rm fit}$ and $m_{\rm top}^{\rm scaled}$ estimators, respectively.

It is observed that the models fall into two classes: Those that utilise the 'old' virtuality-ordered parton shower of Pythia and those that utilise the 'new' p_T-ordered one (highlighted by bands in Fig. 1). The biggest component of the difference is *between* these two classes, indicating a perturbative nature of it. Within each class a spread of less than $\pm 0.5\,{\rm GeV}$ on the top mass remains, which is assigned to the non-perturbative differences between the various models, i.e. to modelling the underlying event and colour reconnection.

The observed model dependence repesents a significant source of uncertainty on the top mass measurement, which has only partially been taken into account by recent top mass results of the Tevatron [13]. It has to be noted, though, that real life measurements may have a different significance to the underlying event than the described toy analysis. Recently, improved tunes of final stated parameter were obtained for Pythia, which might help to reduce the perturbative portion of the observed uncertainty [16, 17].

4 Summary

The description of the underlying event in hadron hadron collisions seems to require colour reconnection, explicit or implicit, to describe Tevatron minimum bias data. A set of new universally applicable models with colour reconnection effects in hadronic final states were tuned to Tevatron data. With these new models and existing older models the influence of changing the underlying event and the colour reconnection model, which includes modifying the parton shower, was studied for a toy mass measurement. Of the spread of results of about $\pm 1.0\,\mathrm{GeV}$ on the reconstructed top mass, about $0.7\,\mathrm{GeV}$ can be attributed to perturbative effects and only less than $0.5\,\mathrm{GeV}$ to non-perturbative sources [1]. These results were obtained with Pythia v6.416 with tunes updated after fixing a bug in the p_T ordered shower.

References

[1] P. Skands and D. Wicke, Eur. Phys. J. **C52**, 133 (2007). hep-ph/0703081.

[2] D. Wicke and P. Z. Skands, Il Nuovo Cimento (2008). arXiv:0807.3248.

[3] T. Sjöstrand, S. Mrenna, and P. Skands, JHEP **05**, 026 (2006). http://projects.hepforge.org/pythia6/, hep-ph/0603175.

[4] T. Sjöstrand and M. van Zijl, Phys. Rev. **D36**, 2019 (1987).

[5] T. Sjöstrand and P. Z. Skands, Eur. Phys. J. **C39**, 129 (2005). hep-ph/0408302.

[6] R. D. Field, *The underlying event in hard scattering processes* (unpublished). ArXiv:hep-ph/0201192, CDF Note 6403; further information available from http://www.phys.ufl.edu/∼rfield/cdf/, 2002.

[7] OPAL Collaboration, G. Abbiendi *et al.*, Phys. Lett. **B453**, 153 (1999). hep-ex/9901019.

[8] OPAL Collaboration, G. Abbiendi *et al.*, Eur. Phys. J. **C45**, 291 (2006). hep-ex/0508062.

[9] ALEPH Collaboration, S. Schael *et al.*, Eur. Phys. J. **C48**, 685 (2006). hep-ex/0604042.

[10] DELPHI Collaboration, J. Abdallah *et al.*, Phys. Lett. **B643**, 147 (2006). hep-ex/0610031.

[11] M. Sandhoff and P. Skands, *Colour annealing: A toy model of colour reconnections* (unpublished). FERMILAB-CONF-05-518-T. In Les Houches 'Physics at TeV Colliders' 2005 SM and Higgs Working Group: Summary report, hep-ph/0604120, 2005.

[12] T. Söstrand, S. Mrenna, and P. Skands, *Pythia 6.416 update notes* (unpublished). http://www.hepforge.org/archive/pythia6/update_notes-6.4.16.txt, 2008.

[13] Tevatron Electroweak Working Group, *A combination of CDF and D0 Results on the Mass of the Top Quark* (unpublished). ArXiv:0803.1683 [hep-ex], 2008.

[14] J. M. Butterworth, J. P. Couchman, B. E. Cox, and B. M. Waugh, *KtJet: A C++ implementation of the $K_\perp$ clustering algorithm* (unpublished). MAN/HEP/2002/02, UCL/HEP 2002-02, October 2002.

[15] W. G. Plano, *Cone jet implementation in the kTjet-package* (unpublished). Private communications.

[16] H. Hoeth, *Tuning and Generator Comparison* (unpublished). Talk given at 1st International Workshop on Multiple Parton Interactions at the LHC, Perugia, October 2008.

[17] P. Skands, *Color Connections, Multijets* (unpublished). Talk given at 1st International Workshop on Multiple Parton Interactions at the LHC, Perugia, October 2008.

Heavy Quark Production at HERA as a Probe of Hard QCD

R. Shehzadi (on behalf of the H1 and ZEUS Collaborations)
Physikalisches Institut, Universität Bonn, Germany

DOI: http://dx.doi.org/10.3204/DESY-PROC-2009-01/105

Abstract

The study of heavy flavor production is a central topic of research at HERA and is an important testing ground for perturbative QCD. A selection of results for charm and beauty production in γp, using different experimental techniques and compared to different theoretical predictions, obtained by the H1 and ZEUS collaborations will be presented.

1 Introduction

Heavy flavor production at HERA is an important tool to investigate our present understanding of the theory of Quantum Chromodynamics (QCD). In $e^{\pm}p$ collisions, the main production mechanism for heavy flavors is the Boson Gluon Fusion (BGF) process. The large mass of the heavy quarks produced in this process provides a hard scale so that calculations in perturbative QCD are expected to be reliable. However, the simultaneous presence of competing hard scales, such as the transverse momentum (p_T) of the heavy quark or the virtuality of the exchanged photon (Q^2) induces additional theoretical uncertainties due to terms in the perturbative expansion which depend logarithmically on the ratio of these scales. Since the perturbative expansion can not be optimized for all scales at once, different calculational approaches have been developed assuming a single hard scale in each. Therefore, comparisons of the measured cross sections with theory predictions are particularly sensitive to the way the perturbative expansion is made.

Different kinematic variables are used to describe the ep interaction at HERA: the photon's virtuality Q^2, the Bjorken scaling variable, x, and the inelasticity, y. Until 1997 HERA ran at a centre-of-mass energy of $\sqrt{s} = 300$ GeV. The proton energy was increased leading to $\sqrt{s} = 320$ GeV for data taken from 1998 onwards. During a shutdown in 2000 and 2001 the accelerator and detectors were upgraded. The period up to 2000 is usually called HERA-I and after 2000 HERA-II. By the end of the running both of the colliding-beam experiments, H1 and ZEUS, had collected about 0.5 fb^{-1} of data.

The kinematic range of the analyzed data can be separated into the following two regimes: photoproduction (γp), where the exchanged photon in the process is almost real, and deep inelastic scattering (DIS), where the exchanged photon is virtual. Experimentally, γp is defined by the scattered electron not being in the acceptance region of the main detectors, corresponding to a cut $Q^2 \lesssim 1$ GeV^2. In the following a small selection of recent measurements of heavy quark production in γp will be presented.

2 Theoretical Models

For heavy flavor photoproduction at HERA, different possible theoretical schemes have been used. These include:

- The leading order (LO) plus parton shower approach, where leading order QCD matrix elements are complemented by parton showers. This approach is implemented in many Monte Carlo (MC) models, e.g. PYTHIA [1], which is based on collinear factorization and DGLAP [2] evolution of parton densities, and CASCADE [3] based on k_T factorization [4] which uses a k_T unintegrated gluon density that is evolved according to CCFM [5] evolution. These MC models are mostly used for acceptance corrections.
- The next-to-leading order (NLO) massive approach [6]. This approach assumes that there is no intrinsic charm or beauty in the proton (or photon). The heavy quarks are only produced dynamically in the hard scattering. This approach is expected to work best when all relevant hard scales e.g. the quark's transverse momentum p_T are of the order of heavy quark mass (m_q). This scheme is also known as fixed order (FO) scheme.
- The NLO massless approach. For $p_T \gg m_q$, large $\log(p_T/m_q)$ terms could in principle spoil the reliability of the predictions. In this case, it might be preferable to switch to massless scheme, in which the m_q is neglected kinematically. The potentially large logarithms can then be resummed to all orders (next-to-leading log (NLL) resummation). Since such an approach is obviously not applicable when $p_T \sim m_q$, schemes have been designed which make a continuous transition between the FO massive and NLL massless scheme. This is often referred to as the GM-VFN (Generalized Mass Variable Flavor Number) scheme [7].

3 Experimental methods

On the experimental side, there are several different methods to tag the heavy quark final state. Different methods often cover different kinematic ranges. The charm-quark events are frequently tagged by the presence of D^* mesons. The measurement of beauty-quark events is difficult due to the fact that beauty production is suppressed with respect to charm production by the large b mass and by its smaller coupling to the photon. Two basic techniques are used to tag beauty events: The measurement of track impact parameters (δ), which enrich beauty production due to the large lifetime of beauty hadrons, and measurements based on semileptonic decays of the b quark. In the latter case, the large momentum of the lepton transverse to the direction of b-initiated jet (p_T^{rel}), due to the large b mass, is used to discriminate against semileptonic charm decays or misidentified light flavor events. Finally, a lepton tag can e.g. be combined with a lifetime tag or with a second lepton tag. The double lepton tag enables one to go to lower transverse momenta. The above mentioned methods have been used by both the H1 and ZEUS collaborations.

4 Charm production

The H1 collaboration has recently released a new measurement of charm photoproduction [8]. This measurement is based on HERA-II data corresponding to an integrated luminosity of 93 pb^{-1} . The charm events are tagged by the presence of a D^* meson decaying in the so-called golden channel $D^{*\pm} \to D^0\pi^\pm$, $D^0 \to K^-\pi^+$. For this, they make use of their new fast track trigger

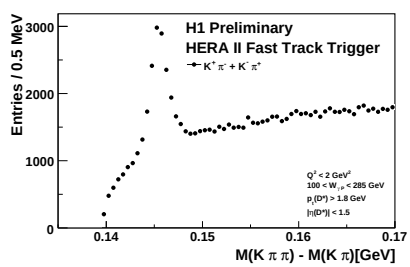


Fig. 1: The distribution of ΔM in γp events

which enables events with D^* candidates to be selected early in the trigger chain and allows to reconstruct their mass. A clear signal is seen as illustrated in Figure 1. The kinematic cuts are also indicated in the figure.
Differential cross sections as a function of $p_T(D^*)$, $\eta(D^*)$ and $W(D^*)$ as well as double differential cross sections in $p_T(D^*)$ and $\eta(D^*)$ have been measured and compared to various QCD models. Differential distributions in $p_T(D^*)$ and $\eta(D^*)$ compared to two models at NLO QCD are shown in Figure 2. The two models are FMNR [6], which is based on the massive scheme

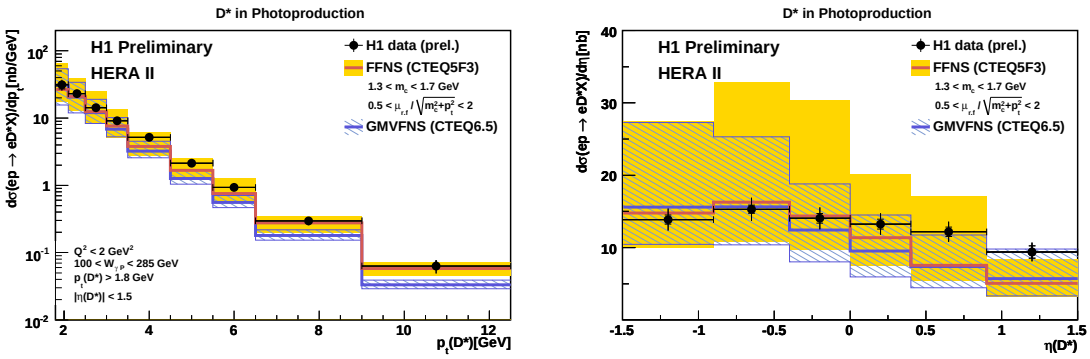


Fig. 2: The H1 measurement of D^* mesons in γp interactions, compared to two QCD models at NLO: the FMNR program in the FFNS (shaded area) and a new calculation in the GM-VFNS (hatched)

and GM-VFNS [9], which uses the combined scheme. Both models show similar behavior. The $p_T(D^*)$ spectrum is well described with a slight deficiency at high p_T in the case of GM-VFNS model. For $\eta(D^*)$ both predictions have a somewhat different shape compared to that of the data and theoretical uncertainties are several times larger than the experimental ones.

5 Beauty production

The H1 and ZEUS collaborations have recently reported new measurements based on lepton tags. The two measurements, one from H1 [10], and one from ZEUS [11] use semileptonic decays to

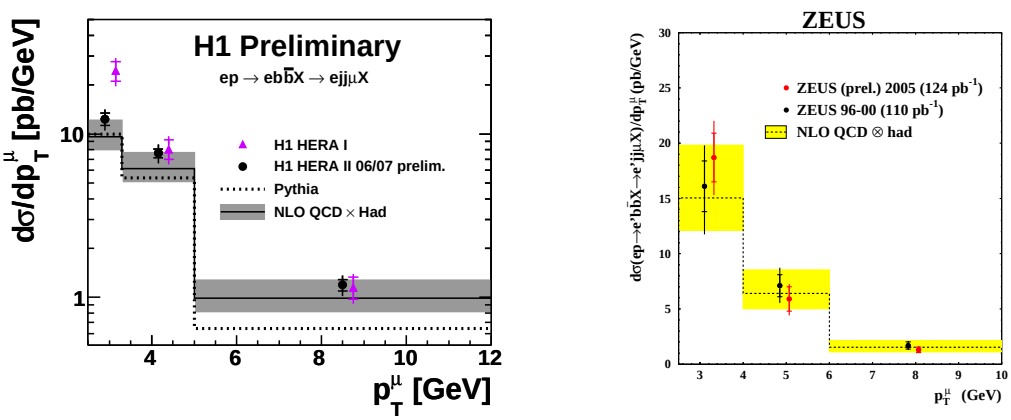


Fig. 3: b-quark production cross-section in γp as a function of the transverse momentum of the muon p_T^{μ}: result from the H1 collaboration (left), result from the ZEUS collaboration (right).

muons to identify heavy quark decays. For this a sample of dijets events requiring at least two jets with $|\eta^{jet1(2)}| < 2.5$ and jet transverse momentum above $p_T^{jet1(2)} > 7(6)$ GeV is used. The fraction of beauty events is then determined from fits to the distributions of p_T^{rel} of the muon with respect to jet axis and the impact parameter δ of the muon track. Both the H1 and ZEUS collaborations use HERA-II data corresponding to integrated luminosities 171pb^{-1} and 124pb^{-1}, respectively. Both measurements cover the range of $0.2 < y < 0.8$, $Q^2 < 1$ GeV^2, muon transverse momentum $p_T^{\mu} > 2.5$ GeV; however the ZEUS data cover a range $-1.6 < \eta^{\mu} < 2.3$ of muon pseudorapidity while the H1 analysis is restricted to $-0.55 < \eta^{\mu} < 1.1$. The cross section in p_T^{μ} for the two analyses is shown in Figure 3. Both analyses show good agreement with perturbative QCD calculations performed with the FMNR program. The excess of data over NLO predictions at low values of jet and muon transverse momentum that was reported in an earlier H1 analysis of HERA-I data [12] is not confirmed by the new H1 analysis.

The ZEUS collaboration has made another measurement based on the identification of both heavy quark decays [13]. This measurement uses HERA-I data corresponding to an integrated luminosity of 114 pb^{-1}. Events with two muons in the final state are selected. Because of the high beauty fraction in such a dimuon sample, jets are not required in the selection. This selection of double tags has several advantages: a larger kinematic range is accessible and the background is reduced substantially. It allows the measurement of $b\bar{b}$ correlations, which probe the next-to-leading order effects. A low p_T threshold for muon identification, $p_T^{\mu} > 1.5$ GeV or even $p_T^{\mu} > 0.75$ GeV for high quality muon candidates and large rapidity coverage makes it possible to measure the total beauty production cross section with relatively small extrapolation. The total cross section for the process $ep \to b\bar{b}X$ at $\sqrt{s} = 318$ GeV has been determined to be $\sigma = 13.9 \pm 1.5(stat.)\ ^{+4.0}_{-4.3}(syst.)$ nb to be compared to the NLO QCD prediction of $\sigma_{tot}^{NLO}(ep \to b\bar{b}X) = 7.5\ ^{+4.5}_{-2.1}$ nb. Within the large uncertainties, in particular of the NLO calculation, the NLO prediction is consistent with the data. Differential cross sections and measurements of $b\bar{b}$ correlations are also obtained and compared to other beauty cross section measurements, MC models and NLO QCD predictions. The distribution of the extracted cross section compared to NLO QCD prediction and leading order MC is shown in Figure 4. Both predictions agree with the data.

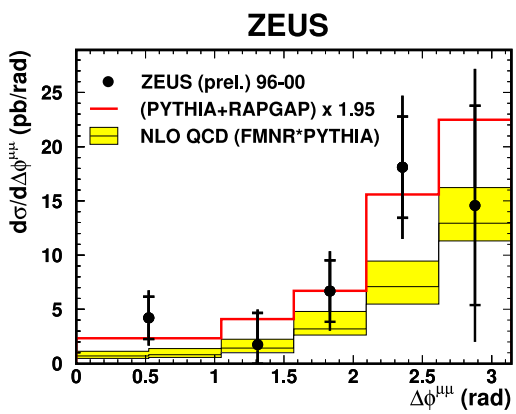


Fig. 4: The dimuon cross-section as a function of the azimuthal angle between the muon in dijet events.

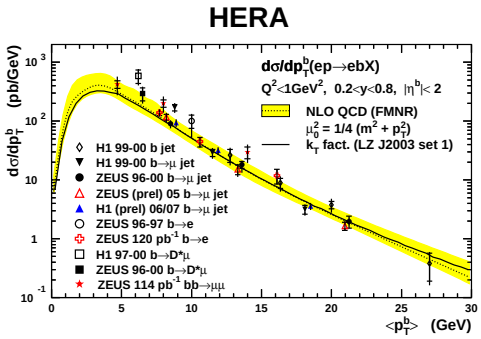


Fig. 5: Cross sections for beauty production in γp at HERA as a function of p_T^b

Figure 5 summarizes all recent HERA measurements of b production in γp as a function of b quark transverse momentum (p_T^b). The different measurements agree well with each other and are in reasonable agreement with the NLO predictions.

6 Conclusion

The study of heavy flavor production in γp at HERA remains a source of interest for testing and understanding the perturbative QCD. Several results based on HERA-II data set are now available. Some of these recent results using different tagging methods were presented. The charm results are in good agreement with NLO QCD. The beauty measurements are also in reasonable agreement with NLO QCD. The uncertainty on experimental results in both beauty and charm production are typically smaller than theoretical uncertainties.

References

[1] T. Sjöstrand *et al.*, Comput. Phys. Commun. **135** (2001) 238

[2] L. N. Lipatov, Sov. J. Nucl. Phys. **20** (1975) 94.

[3] H. Jung and G. P. Salam, Eur. Phys. J. C **19** (2001) 351

[4] S. Catani, M. Ciafaloni, and F. Hautmann, Nucl. Phys. B 366, 135 (1991).

[5] H. Jung, arXiv:hep-ph/9908497

[6] S. Frixione, P. Nason and G. Ridolfi, Nucl. Phys. B **454** (1995) 3.

[7] M. Cacciari, S. Frixione and P. Nason, JHEP **0103** (2001) 006.

[8] H1 Collaboration, *Measurement of D^* meson production in photoproduction*, H1prelim-08-073.

[9] B. A. Kniehl *et al.*, Phys. Rev. D **71** (2005) 014018 arxiv:hep-ph/0410289;
G. Kramer and H. Spiesberger, Eur Phys. J. C **38** (2004) 309 arxiv:hep-ph/0311062.

[10] H1 Collaboration, *A Measurement of beauty photoproduction through decays to muons and jets at HERA-II*, H1prelim-08-071.

[11] ZEUS Collaboration, *Measurement of beauty photoproduction at HERA-II*, ZEUS-prel-07-020.

[12] A. Aktas *et al*. [H1 Collaboration], Eur. Phys. J. C **41** (2005) 453.

[13] S. Chekanov *et al*. [ZEUS Collaboration], *Measurement of beauty production using dimuon events with ZEUS at HERA*, DESY-08-128; arXiv:0811.0894.

What do we learn from forward detectors at LHC ?

Armen Bunyatyan[1,2]
[1] MPI für Kernphysik, Heidelberg, Germany,
[2] Yerevan Physics Institute, Armenia

DOI: http://dx.doi.org/10.3204/DESY-PROC-2009-01/44

Abstract
Small-angle detectors at the LHC give access to a broad physics programme within and beyond the Standard Model. We present here some studies of forward physics processes related to underling event, multi-parton interactions and low-x QCD dynamics.

1 Introduction

The LHC collider will provide the highest energy proton-proton and ion-ion collisions in the lab to date, opening up a phase space for particle production in an unprecedented range spanning $\Delta\eta$ ∼20 units of rapidity. As a general feature, particle production in hadronic collisions is peaked at central rapidities, whereas most of the energy is emitted at very low angles. The ATLAS and CMS detectors not only cover the largest $p_T - \eta$ ranges at mid-rapidity, but they feature extended instrumentation at lager distances far away from the interaction point: ± 11m (ATLAS FCal and CMS HF hadronic calorimeters), ±14 m (ATLAS LUCID and CMS CASTOR sampling calorimeter), ±140 m (Zero-Degree-Calorimeters, ZDCs), and ±240 m (ATLAS Roman Pots). The forward coverage of the CMS interaction region is complemented with the two trackers (T1 and T2 telescopes) and the proton-taggers (Roman Pots) at ±147 and ±220 m of the TOTEM experiment which has common forward physics program with CMS [1]. The rapidity coverage of ATLAS and CMS forward detectors is summarised in Fig.1.

The forward detectors give access to a broad physics program within and beyond the standard model [1, 2]. Here we present studies related to the physics of underlying events and multi-parton interactions and low-x QCD parton dynamics.

2 Underlying Event Studies with CASTOR in the CMS Experiment

Multi-parton interactions (MI) play a significant role in soft and high p_T processes. Especially in case of LHC the understanding of MI is becoming crucial for the high precision measurements. Various Monte Carlo (MC) models have been tuned to describe the Tevatron data [3], exploiting mainly the charged particle multiplicities and particle energy flows in the central η region. The large angular coverage of the LHC detector from the central to the most forward region ($0 < \eta < 6.6$) will allow to study MI over a large rapidity range. Since the multi-parton interactions occur between the remnant partons of the colliding particles, the energy flow in the very forward region is strongly affected and hence are ideal for the MI model tuning. In addition one can study the long range correlations between the activities in central and forward regions.

The long range correlations were investigated [4] with the PYTHIA MC [5], at the level of generated hadrons, using several MI tunes. The charge particle multiplicities in the central rapidity range were calculated for four different energy deposits in the rapidity range $5.2 < \eta < 6.6$,

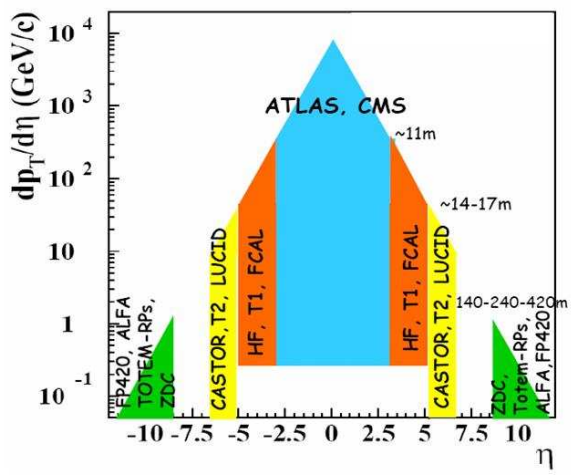


Fig. 1: The rapidity coverage of CMS and ATLAS detectors

which corresponds to the coverage of CMS-CASTOR calorimeter [6, 7]. The distributions for inclusive (minimum bias) QCD processes are shown in the upper part of Fig.2 and for the top production processes in the lower part of the figure. When MI are not generated, the charge particle multiplicities are the same for all energy bins. On the other hand, a clear correlation is seen when MI are included– larger energies in the forward region imply higher charged particle multiplicities and energy flow in the central region. Furthermore, triggering on CASTOR enhances the differences between various MI tunes and thus may contribute to better understanding of multi-parton interaction picture. Comparison of charged particle multiplicities in the inclusive QCD and the top production shows that the top processes not only have higher charged particle multiplicities and energy flow, but also contain more underlying event activity than the inclusive QCD processes. This suggests that a naive approach of subtracting underlying event contribution as determined for inclusive QCD processes from the top events would not work. As already seen from CDF measurements [3] the underlying event properties depend strongly on the collision centrality. The harder the collision is, the more underlying event activity one expects to see. After demanding a hard scale for the inclusive QCD events in form of $E_{\mathrm{T}}^{\mathrm{jet}} > 40$ GeV the differences between underlying event in QCD and in top events almost disappear (Fig.3).

Understanding of underlying event is essential also for the measurements which involve high E_{T} jets in the final state. As the hadronic jets are the results of the parton hadronisation, their measurements give a chance to look inside the dynamics of hard interaction. However, the underlying event produces additional energy in the available phase space which is added by the jet algorithms to the 'true' jet energy, thus spoiling the relation of the jets to the partons. However, it is possible to estimate this 'pedestal' energy from the measurements in the forward calorimeters and subtract it from the reconstructed jet energy [4]. Left side of Figure 4 shows the transverse energy flow around the jet as a function of pseudorapidity for the jets from the PYTHIA MC sample, in five different pseudorapidity bins between -3 and 2.5 and two jet transverse energy ranges. The plot clearly shows the underlying event pedestal, when the MI are simulated, and that the level of pedestal does not depend on the jet pseudorapidity but gets higher for higher jet

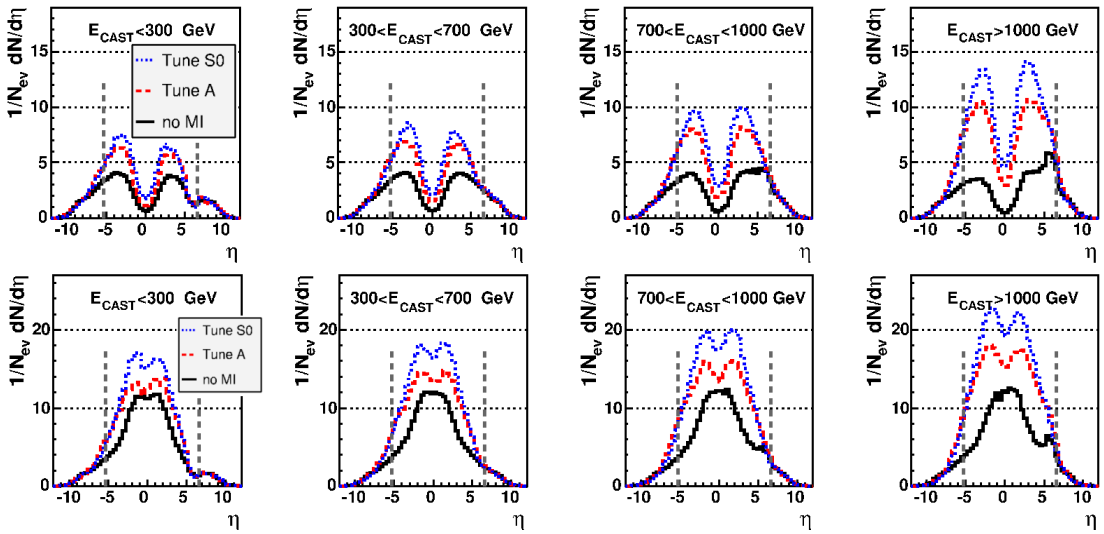


Fig. 2: Charged particle multiplicities as function of η for four different CASTOR energy bins. Shown is PYTHIA MC prediction for inclusive QCD processes (up) and top production (down) processes.

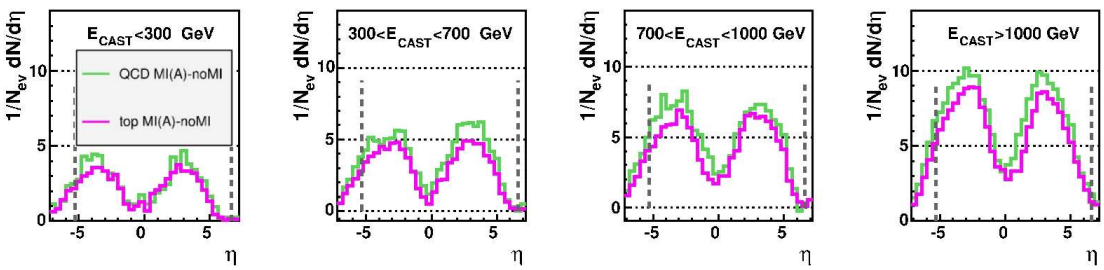


Fig. 3: Charged particle multiplicities due to underlying event activity (MC with MI - MC without MI) as a function of η in top and in inclusive QCD processes after demanding a presence of a hard jet $E_{\mathrm{T}}^{\mathrm{jet}} > 40$ GeV in the central rapidity region $|\eta| < 2.5$. The dashed vertical lines indicate the acceptance of the CMS detector.

energies, i.e. it depends on the hardness of the interaction.

In the right side of Fig.4 the jet profile as a function of pseudorapidity is shown for the PYTHIA simulation with MI. The transverse energy measured in the acceptance range of the CASTOR calorimeter ($5.2 < \eta < 6.6$) is indicated with the dash hatched area. As the underlying event pedestal is rather independent on the position of the jet in the central detector, we attempt to fit the pedestal by a universal function, e.g. $f(\eta) = A/(1 + B \cdot e^{|\eta|-4})$, which also reasonably describes the pedestals for the different MI tunes and for the different cuts on jet transverse energies and pseudorapidities. The two free parameters can be represented by the measured energies in the very forward calorimeters, e.g. CASTOR or HF. An example of the the fit of pedestal by this function is shown in Fig.4 (middle) and the level of pedestal under the jet determined by this method is shown in the right side of Fig.4 as a right hatched histogram. This approach gives reasonable result and can be developed further. In principle, using another Monte

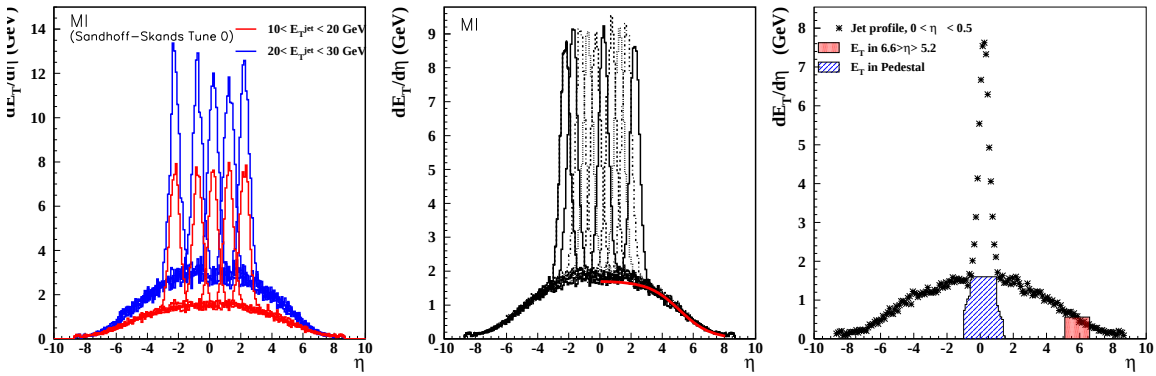


Fig. 4: *(left)* The transverse energy distributions around the jets (jet profile) as a function of pseudorapidity. The different lines represent the different pseudorapidity ranges and the different transverse energy ranges of the jets; *(middle)* The jet profile as a function of pseudorapidity. The different lines correspond to the different ranges of the jet pseudorapidity. The solid line on the right tail of distribution shows the result of the fit of pedestal as described in the text; *(right)* The jet profile as a function of pseudorapidity for the jets with $0 < \eta^{\rm jet} < 0.5$ and $10 < E_{\rm T}^{\rm jet} < 20\ GeV$. The dash hatched histogram is the level of transverse energy in the pseudorapidity range of the CASTOR ($5.2 < \eta < 6.6$). The right hatched histogram below the jet area is the pedestal level determined from the method described in the text.

Carlo or fragmentation models (CASCADE, ARIADNE, etc.) may lead to the different energy distribution of the underlying event, which may require the optimisation of the fitting function.

3 Low-x QCD physics

One of the main HERA observations is that the proton structure function is almost purely gluonic for the low values of the fractional momenta $x = p_{parton}/p_{proton} \lesssim 0.01$. Below $x \simeq 10^{-4}$ the gluon PDF in the proton is however poorly constrained. In this small-x regime one expects non-linear gluon-gluon fusion processes not accounted for in the standard DGLAP/BFKL evolution equations to become important and tame the rise of the parton densities.

Forward instrumentation provides an important lever arm for the measurement of the low-x structure and evolution of the parton densities. Indeed, in a $2 \rightarrow 2$ parton scattering the minimum momentum fraction probed when a particle of momentum p_T is produced at pseudo-rapidity η is $x_{min} \sim p_T \cdot e^{-\eta}/\sqrt{s}$ i.e. x_{min} decreases by a factor of ~ 10 every 2 units of rapidity. The measurement of jets with $p_T \sim 20 - 100$ GeV at forward rapidities ($3 < |\eta| < 6.6$) allows one to probe the PDFs at x values as low as $x \sim 10^{-6}$. In addition to the single inclusive cross sections, the production of events with two similar transverse-momentum jets emitted in each one of the forward/backward directions, the so called "Mueller-Navelet jets", is a particularly sensitive measure of BFKL as well as non-linear parton evolutions. Preliminary CMS analyses indicate that such studies are well feasible measuring jets in each one of the HF calorimeters [8].

4 Forward Jets in the CASTOR calorimeter in the CMS experiment

Events in which an energetic jet is produced in the forward direction close to the proton remnant are sensitive to the higher order processes due to the long rapidity range available for radiation between the jet and the hard scattering vertex. The longitudinal momentum fraction of the proton, x, can be related to the rapidity, y, by approximately $x \sim e^{-y}$, which further suggests that forward physics provides valuable information about low x parton dynamics. The analyses of forward jets at HERA [9, 10] have improved our understanding of higher order processes. Available fixed order calculations (NLO $O(\alpha_s^2)$) as well as the higher order processes approximated by DGLAP parton showers underestimate the HERA data by up to a factor of 2. The data can be described only if the ordering of the transverse momenta of the radiated gluons is broken in the theoretical predictions.

The study is made [11] using the Monte Carlo events generated with the PYTHIA [5] and ARIADNE [12] MC models. PYTHIA is based on LO DGLAP parton showers, which give gluon radiation ordered in transverse momentum with respect to rapidity. In ARIADNE, parton showers are generated by the Color Dipole Model (CDM), resulting in gluon radiation without any ordering in transverse momentum. This corresponds to a BFKL like final state. Events are selected which contain a hadron level jet with a transverse momentum $E_T > 10$ GeV and a pseudorapidity $5.2 < \eta < 6.6$. To suppress events with DGLAP like dynamics, two jets with $E_T > 10$ GeV are required in the central region, $|\eta| < 1.5$. The resulting cross-section is shown in left side of Fig. 5 as a function of the forward jet energy. The CDM model produces more jets at higher energies, while the events with gluon emissions generated according to DGLAP dynamics have a suppressed jet production. At the highest forward jet energies the difference between the models reaches two orders of magnitude.

The feasibility of such measurement with the CASTOR calorimeter at CMS has been studied. Since CASTOR has no segmentation in polar angle it is not possible to define jets according to conventional jet algorithms which use the energy, polar and azimuthal angles of particles. However, a reasonable jet reconstruction is achieved by summing the energy in the most active phi segmenet with the two neighbouring cells. In addition the particle energies were smeared according to resolutions measured in the CASTOR beam test [7] and a noise cut was applied. The predictions from PYTHIA and CDM show that the very high sensitivity to the scheme used for the QCD radiation is still preserved. The response to multiple interactions was studied as well and is shown in right side of Fig. 5. Excluding MI lowers the cross section by roughly an order of magnitude. Except of that, the sensitivity to the different MI tunes and models are fairly small in comparison to the impact of using the CDM. The sensitivity of this measurement to PDF variation was also investigated. The predicted forward jet cross section can not clearly distinguish between the different PDFs.

Thus, the method to measure forward jets in CASTOR in addition to two jets in the central region gives a large sensitity to the dynamics of the parton shower. This is also true if PDF uncertainties and different MI models are taken into account.

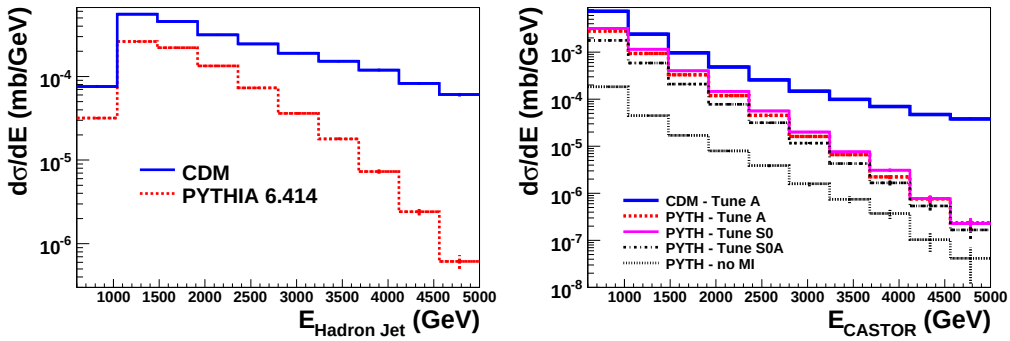


Fig. 5: *(left)* Hadron level cross sections for events with two central jets and a forward jet in the pseudorapidity region of the CASTOR calorimeter. *(right)* Monte Carlo prediction for the 2+forward jet cross section using different MI models and tunes. The predictions are on generator level, but with the forward jet reconstructed as described in the text and forward particle momenta smeared according to CASTOR beam test data.

5 Summary

In conclusion, the studies presented here show that the forward region is very sensitive to the underlying event, multi-parton interactions and low-x QCD dynamics. The measurements in the forward calorimeters, such as CASTOR, can be used to discriminate between the various MI models and to improve the jet reconstruction in the central region. Further possibilities for the improvement of forward particle detection and completing the angular coverage of the detectors have to be investigated [13, 14].

References

[1] *CMS and TOTEM Note on Prospects for Diffractive and Forward Physics 2006; LHCC-G-124*, 2006.

[2] *ATLAS Forward Physics Program, ATL-PHYS-COND-2008-020*, 2008.

[3] CDF Collaboration, D. E. Acosta *et al.*, Phys. Rev. **D70**, 072002 (2004). `hep-ex/0404004`.

[4] Z.Rurikova and A.Bunyatyan, *Underlying Event Studies with CASTOR Calorimeter at CMS.* Presented at 4-th HERA-LHC workshop, CERN, May 2008.

[5] T. Sjostrand, S. Mrenna, and P. Skands, JHEP **05**, 026 (2006). `hep-ph/0603175`.

[6] *CASTOR web page*. $http://cmsdoc.cern.ch/castor$.

[7] X. Aslanoglou et al., Eur. Phys. J. **C52**, 495 (2007). `arXiv:0706.2641`.

[8] D.G. d'Enterria, *Forward Physics at the LHC.* Proceedings of Workshop DIS-2007, Munich 2007; arXiv:0708.0551.

[9] H1 Collaboration, Aktas, A. et al., Eur. Phys. J. **C46**, 27 (2006). `hep-ex/0508055`.

[10] ZEUS Collaboration, Chekanov, S. et al., Phys. Lett. **B632**, 13 (2006). `hep-ex/0502029`.

[11] A.Knutsson, *Forward Jets in the CASTOR calorimeter at CMS.* Presented at 4-th HERA-LHC workshop, CERN, May 2008.

[12] L. Lonnblad, Comput. Phys. Commun. **71**, 15 (1992).

[13] V.Andreev, A.Bunyatyan, H.Jung, M.Kapishin, L.Lytkin, *Proposal to Upgrade the Very Forward Region at CMS.* Proceedings of HERA-LHC Workshop, CERN-2005-014, DESY-PROC-2005-001.

[14] A.Bunyatyan et al., *Calorimetric Coverage at Large Rapidities in CMS.* Presented at 3-d HERA-LHC workshop, DESY, March 2007.

Recent L3 Results (and Questions) on BEC at LEP

W. J. Metzger
Radboud University, Nijmegen, The Netherlands

DOI: http://dx.doi.org/10.3204/DESY-PROC-2009-01/45

Abstract
Results of two recent studies of Bose-Einstein correlations (BEC) in hadronic Z decays are reported. The first finds that a good description of the two-pion correlation function is achieved using a Lévy stable distribution in conjunction with a hadronization model having highly correlated configuration and momentum space, the τ-model. Using the results of this parametrization, the space-time source function is reconstructed. The second investigates the question of the existence of inter-string BEC, unfortunately without clear conclusions.

1 Introduction

We study BEC in hadronic Z decay using data collected by the L3 detector at an $\mathrm{e^+e^-}$ center-of-mass energy of $\sqrt{s} \simeq 91.2$ GeV. Approximately 36 million like-sign pairs of well-measured charged tracks from about 0.8 million hadronic Z decays are used [1]. Events are classified as two- or three-jet events using calorimeter clusters with the Durham jet algorithm. To determine the thrust axis of the event we also use calorimeter clusters.

The two-particle correlation function of two particles with four-momenta p_1 and p_2 is given by the ratio of the two-particle number density, $\rho_2(p_1, p_2)$, to the product of the two single-particle densities, $\rho_1(p_1)\rho_1(p_2)$. Since we are interested only in the correlation, R_2, due to Bose-Einstein interference, the product of single-particle densities is replaced by $\rho_0(p_1, p_2)$, the two-particle density that would occur in the absence of BEC: $R_2(p_1, p_2) = \frac{\rho_2(p_1,p_2)}{\rho_0(p_1,p_2)}$. An event mixing technique is used to construct ρ_0.

Since the mass of the identical particles of the pair is fixed, R_2 is defined in six-dimensional momentum space, which is often reduced to a single dimension, the four-momentum difference $Q = \sqrt{-(p_1 - p_2)^2}$. But there is no reason to expect the hadron source to be spherically symmetric in jet fragmentation. In fact, the source is found to be elongated along the jet axis [2], but only by about 25%, which suggests that a parametrization in terms of the single variable Q, may be a good approximation. This is confirmed by studies of various decompositions of Q [1, 3].

2 Parametrizations of BEC

With a few assumptions [4], R_2 is related to the Fourier transform, $\tilde{f}(Q)$, of the (configuration space) density distribution of the source, $f(x)$:

$$R_2(p_1, p_2) = \gamma \left[1 + \lambda |\tilde{f}(Q)|^2\right] (1 + \delta Q) \ . \tag{1}$$

The parameter γ and the $(1 + \delta Q)$ term are introduced to parametrize possible long-range correlations not adequately accounted for in ρ_0, and λ to account for several factors, such as lack of complete incoherence of particle production and presence of long-lived resonance decays.

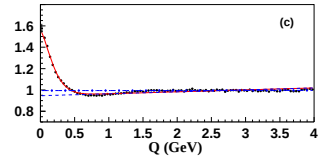


Fig. 1: The Bose-Einstein correlation function R_2 for two-jet events. The curve corresponds to a fit of the Lévy parametrization (2). The dashed line represents the long-range part of the fit, *i.e.*, $\gamma(1+\delta Q)$. The dot-dashed line represents a linear fit in the region $Q > 1.5\,\mathrm{GeV}$.

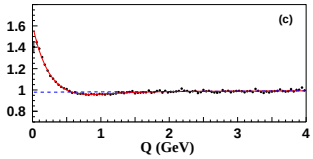


Fig. 2: The Bose-Einstein correlation function R_2 for two-jet events. The curve corresponds to the fit of the one-sided Lévy parametrization, (3), as described in the text. The dashed line represents the long-range part of the fit, *i.e.*, $\gamma(1+\delta Q)$.

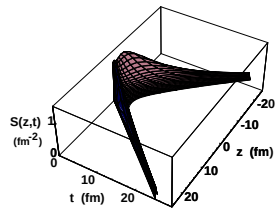


Fig. 3: The temporal-longitudinal part of the source function normalized to the average number of pions per event.

2.1 Static parametrizations

A model-independent way to study deviations from the Gaussian is to use [5] the Edgeworth expansion about a Gaussian. Another way is to replace it in configuration space by a symmetric Lévy distribution. These parametrizations lead to

$$R_2(Q) = \gamma\left(1+\lambda\exp\left(-(RQ)^\alpha\right)\left[1+\frac{\kappa}{3!}H_3(RQ)\right]\right)(1+\delta Q)\ , \qquad (2)$$

where $\alpha = 2$ for the Gaussian and Edgeworth parametrizations; $0 < \alpha \leq 2$ for the Lévy parametrization; and $\kappa = 0$ except in the Edgeworth case where κ is the third-order cumulant moment and $H_3(RQ) \equiv (\sqrt{2}RQ)^3 - 3\sqrt{2}RQ$ is the third-order Hermite polynomial.

The Edgeworth and Lévy parametrizations indeed fit the low-Q peak much better than the purely Gaussian parametrizations, yielding, respectively, $\kappa = 0.71 \pm 0.06$ and $\alpha = 1.34 \pm 0.04$. However, the χ^2 are still poor. Both the symmetric Lévy (Fig. 1) and the Edgeworth parametrizations do a fair job of describing the region $Q < 0.6\,\mathrm{GeV}$, but fail at higher Q, particularly the region 0.6–1.5 GeV where R_2 dips below unity, indicative of an anti-correlation. This is clearly seen in Fig. 1 by comparing the data in this region to an extrapolation of a linear fit, (2) with $\lambda = 0$, in the region $Q \geq 1.5\,\mathrm{GeV}$. The inability to describe this dip in R_2 is the primary reason for the failure of both parametrizations.

2.2 Time dependence of the source

The parametrizations discussed so far all assume a static source. The parameter R, representing the size of the source as seen in the rest frame of the pion pair, is a constant. It has, however, been observed that R depends on the transverse mass, $m_\mathrm{t} = \sqrt{m^2 + p_\mathrm{t}^2}$, of the pions [6].

In the previous section we have seen that BEC depend, at least approximately, only on Q and not on its components separately. Further, we have seen that R_2 in the region 0.6–1.5 GeV dips below its values at higher Q. A model which predicts such Q-dependence as well as an m_t-dependence is the τ-model [7], in which it is assumed that the average production point in the overall center-of-mass system, $\overline{x} = (\overline{t}, \overline{r}_x, \overline{r}_y, \overline{r}_z)$, of particles with a given four-momentum k is given by $\overline{x}^\mu(k^\mu) = a\tau k^\mu$. In the case of two-jet events, $a = 1/m_\mathrm{t}$, where m_t is the transverse mass and $\tau = \sqrt{\overline{t}^2 - \overline{r}_z^2}$ is the longitudinal proper time. For isotropically distributed particle

production, τ is, instead, the proper time, and the transverse mass is replaced by the mass, while for the case of three-jet events the relation is more complicated. The second assumption is that the distribution of $x^\mu(k^\mu)$ about its average, $\delta_\Delta(x^\mu(k^\mu) - \overline{x}^\mu(k^\mu))$, is narrower than the proper-time distribution. Then R_2 is found [8] to depend only on Q, the values of a of the two pions, and $\widetilde{H}$, the Fourier transform of the distribution of τ, $H(\tau)$. Since there is no particle production before the onset of the collision, $H(\tau)$ should be a one-sided distribution. We choose a one-sided Lévy distribution, which is characterized by three parameters: the index of stability α, the proper time of the start of particle emission τ_0, and $\Delta\tau$, which is a measure of the width of $H(\tau)$. Replacing the individual values of a of the two pions by their average results then (suppressing the normalization and long-range correlations) in [8]

$$R_2(Q,\bar{a}) = 1 + \cos\left[\bar{a}\tau_0 Q^2 + \tan\left(\frac{\alpha\pi}{2}\right)\left(\frac{\bar{a}\Delta\tau Q^2}{2}\right)^\alpha\right]\exp\left[-\left(\frac{\bar{a}\Delta\tau Q^2}{2}\right)^\alpha\right] . \quad (3)$$

Before proceeding to fits of (3), we first consider a simplification obtained by assuming an average $\bar{a}$-dependence, which is implemented in an approximate way by defining an effective radius, $R = \sqrt{\bar{a}\Delta\tau/2}$. This results in

$$R_2(Q) = \gamma\left[1 + \lambda\cos\left[\bar{a}\tau_0 Q^2 + (R_\mathrm{a}Q)^{2\alpha}\right]\exp\left(-(RQ)^{2\alpha}\right)\right](1+\delta Q) , \quad (4)$$

where R_a is related to R by

$$R_\mathrm{a}^{2\alpha} = \tan\left(\frac{\alpha\pi}{2}\right)R^{2\alpha} . \quad (5)$$

For two-jet events (Durham, $y_\mathrm{cut} = 0.006$) a good fit (χ^2/dof = 97/95), shown in Fig. 2, is achieved with the additonal assumption $\tau_0 = 0$. However, for three-jet events it is necessary to relax (5), *i.e.*, regard R_a as a free parameter, while keeping $\tau_0 = 0$ (χ^2/dof = 102/94). Alternatively, (5) can be kept but $\bar{a}\tau_0$ made a free parameter, although the description is somewhat worse (χ^2/dof = 127/94). The fits describe well the dip in the 0.6–1.5 GeV region, as well as the low-Q peak. We speculate that the need for an additional free parameter for three-jet events could be that the replacement of the individual values of a by their average is less valid than for two-jet events or that the onset of particle production might be somewhat later for three-jet events than for two-jet events. Whatever the reason, we now turn our attention exclusively to two-jet events

Fits of (3) to the two-jet data are performed in several m_t intervals. The quality of the fits is acceptable and the fitted values of the parameters, α, τ_0 and $\Delta\tau$, are stable and within errors independent of m_t, as expected in the τ-model. Their values (weighted averages of the values found in the four m_t intervals) are $\tau_0 = 0 \pm 0.01$ fm, $\alpha = 0.43 \pm 0.03$ and $\Delta\tau = 1.8 \pm 0.4$ fm. Using these values we reconstruct the space-time picture of the emitting process for two-jet events.

Given the symmetry of two-jet events, the emission function (in cylindrical coordinates) in the τ-model is [8]

$$S_\mathrm{x}(r,z,t) = H(\tau)P(r,\eta) = H(\tau)\left(\frac{m_\mathrm{t}}{\tau}\right)^3\rho_{\mathrm{p_t}}(rm_\mathrm{t}/\tau)\rho_\mathrm{y}(\eta) , \quad (6)$$

where η is the space-time rapidity, y the rapidity, $p_{\rm t}$ the transverse momentum, and $\rho_{\rm p_t}$ and $\rho_{\rm y}$ are the inclusive single particle $p_{\rm t}$ and y distributions and where we have assumed that $P(r,\eta)$ can be factorized.

Using $H(\tau)$ as obtained from the BEC fits of (3) together with the inclusive rapidity and $p_{\rm t}$ distributions [1], the full emission function is reconstructed. Its integral over the transverse distribution (Fig. 3.) exhibits a "boomerang" shape with a maximum at low t and z and tails extending to very large values of t and z, a feature also observed in hadron-hadron [9] and heavy ion collisions [10]. The transverse part, obtained by integrating over z and azimuthal angle, is shown in Fig. 4 for various proper times. Particle production starts immediately, increases rapidly and decreases slowly forming an expanding ring-like structure.

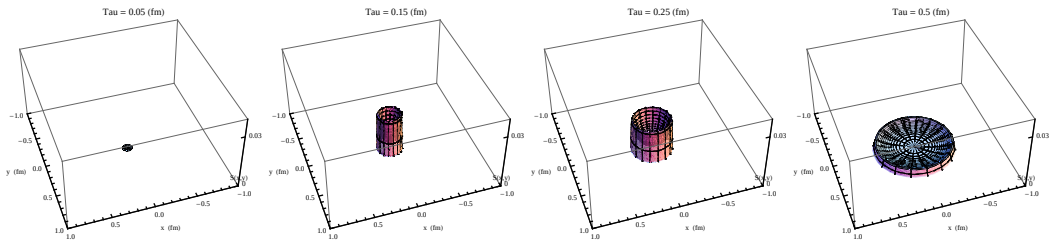


Fig. 4: The transverse source function normalized to the average number of pions per event for various proper times.

3 Inter-string BEC

The question of the existence of inter-string BEC rose to prominence during the measurement at LEP of the mass of the W boson. Uncertainty as to its existence and how to model it was one of the largest, along with the question of color reconnection, contributions to the systematic uncertainty on the mass measured in the channel $\rm e^+e^-\!\!\rightarrow W^+W^-\!\!\rightarrow q\bar{q}q\bar{q}$. No evidence of inter-string BEC was found [11], but the significance of the result was limited by poor statistics. Here we examine another channel involving two strings: $\rm e^+e^-\!\!\rightarrow q g\bar{q}$ where the gluon is connected to the quark by one string and to the anti-quark by another. This channel has been studied briefly in DELPHI data [12], with no definite conclusion. Here we present new results with L3 data [13].

The influence of inter-string BEC on R_2 depends on the amount of 'overlap', both in momentum- and configuration-space. Full momentum-overlap means that the distribution of $\vec{p}$ for pions from string 1 is the same as that for pions from string 2. If there is no overlap in momentum space, inter-string BEC can not take place, and the BEC parameters for two strings (λ_2 and r_2) will be the same as those for one string (λ_1 and r_1). If there is full overlap in momentum space, the expectations are:

	no spatial overlap	full spatial overlap
Inter-string BEC	$\lambda_2 = \lambda_1 \quad r_2 > r_1$	$\lambda_2 = \lambda_1 \quad r_2 = r_1$ (HBT) $\quad r_2 > r_1$ (Lund)
No inter-string BEC	$\lambda_2 < \lambda_1 \quad r_2 = r_1$	$\lambda_2 < \lambda_1 \quad r_2 = r_1$

where the expectation for r in the case of full spatial overlap and inter-string BEC depends on whether r is measured along the color field (Lund) or directly (HBT).

A comparison of BEC in 2-jet (1-string) and 3-jet (2-string) events finds very weak dependence of λ and r on $y_{\rm cut}$. The value of λ_1 is somewhat larger than λ_2, which might suggest an absence of inter-string BEC. However, r_2 is somewhat larger than r_1, suggesting the opposite.

Samples of single jets are defined based on jet configuration and on b-tagging. The gluon content of the various samples varies from zero to 75%. There is no evidence for a dependence of λ or r on the gluon fraction, suggesting the presence of inter-string BEC *à la* HBT.

The degree of overlap should be greatest in the tip of the gluon jet. Therefore, BEC are measured in various intervals of $x = E/E_{\rm jet}$ and of rapidity with respect to the jet direction. The value of λ is found to decrease with increasing x or rapidity, but this occurs in quark jets as well as in gluon jets suggesting that it is not an inter-string effect. The value of r does not decrease with increasing x or rapidity in contradiction to the expectation of inter-string BEC *à la* HBT.

The results are thus inconclusive. Inter-string BEC remains an open question.

References

[1] T. Novák, *Bose-Einstein Correlations in e^+e^- Annihilation*. Ph.D. Thesis, Radboud Univ. Nijmegen, 2008.

[2] L3 Collaboration, M. Acciarri *et al.*, Phys. Lett. **B458**, 517 (1999);
OPAL Collaboration, G. Abbiendi *et al.*, Eur. Phys. J. **C16**, 423 (2000);
DELPHI Collaboration, P. Abreu *et al.*, Phys. Lett. **B471**, 460 (2000);
ALEPH Collaboration, A. Heister *et al.*, Eur. Phys. J. **C36**, 147 (2004).

[3] TASSO Collaboration, M. Althoff *et al.*, Z. Phys. **C30**, 355 (1986).

[4] G. Goldhaber, S. Goldhaber, W. Lee, and A. Pais, Phys. Rev. **120**, 300 (1960);
D. H. Boal, C.-K. Gelbke, and B. K. Jennings, Rev. Mod. Phys. **62**, 553 (1990);
T. Csörgő, Heavy Ion Physics **15**, 1 (2002).

[5] T. Csörgő and S. Hegyi, in *Proc. XXVIIIth Rencontres de Moriond*, eds. E. Augé and J. T. T. Vân, p. 635. Editions Frontières, Gif-sur-Yvette, France, 1993;
T. Csörgő, in *Proc. Cracow Workshop on Multiparticle Production*, eds. A. Białas *et al.*, p. 175. World Scientific, Singapore, 1994.

[6] B. Lörstad and O. Smirnova, *Transverse mass dependence of Bose-Einstein correlation radii in* $\rm e^+e^-$ *annihilation at LEP energies*, in *Proc. 7*$^{\rm th}$ *Int. Workshop on Multiparticle Production "Correlations and Fluctuations"*, eds. R. Hwa *et al.*, p. 42. World Scientific, Singapore, 1997;
J. van Dalen, *A two-dimensional study of Bose-Einstein correlations in Z decays at LEP*, in *Proc. 8*$^{\rm th}$ *Int. Workshop on Multiparticle Production "Correlations and Fluctuations '98: From QCD to Particle Interferometry"*, eds. T. Csörgő *et al.*, p. 37. World Scientific, Singapore, 1999;
OPAL Collaboration, G. Abbiendi *et al.*, Eur. Phys. J. **C52**, 787 (2007).

[7] T. Csörgő and J. Zimányi, Nucl. Phys. **A517**, 588 (1990).

[8] T. Csörgő, W. Kittel, W. Metzger, and T. Novák, Phys. Lett. **B663**, 214 (2008).

[9] NA22 Collaboration, N. Agababyan *et al.*, Phys. Lett. **B422**, 359 (1998).

[10] A. Ster, T. Csörgő, and B. Lörstad, Nucl. Phys. **A661**, 419 (1999).

[11] LEP Electroweak Working Group, *A Combination of Preliminary Electroweak Measurements and Constraints on the Standard Model*, Technical Report CERN-PH-EP/2005-051, `hep-ex/0511027`, 2005.

[12] N. van Remortel, *Bose-Einstein Correlations in W pair production and multi-jet Z^0 decays at LEP*. Ph.D. Thesis, Univ. Antwerpen, 2003.

[13] Q. Wang, *Inter-string Bose-Einstein Correlations in Hadronic Z Decays using the L3 Detector at LEP*. Ph.D. Thesis, Radboud Univ. Nijmegen, 2008.

Bose-Einstein or HBT correlations in high energy reactions

T. Csörgő *
MTA KFKI RMKI, H-1525 Budapest 114, P.O.Box 49, Hungary
DOI: http://dx.doi.org/10.3204/DESY-PROC-2009-01/46

Abstract
Concepts of thermalization and hydrodynamical behavior are applied from time to time to $e^+ + e^-$, hadron+hadron and heavy ion collisions. These applications are scrutinized paying attention to particle multiplicities, spectra, and Bose-Einstein correlations in particular. Can hydrodynamics describe these data?

1 Introduction

In 2008, the speakers of the International Symposium on Multiparticle Dynamics were given a quiz of 18 questions, that were compiled by Hannes Jung and Gösta Gustafson, the Chair and the Co-Chair of this meeting [1]. My goal is to discuss three of these problems:

1. Can thermal & hydrodynamical models describe e^++e^-, h+p and A+B reactions? [1]
2. What heavy ion physics can learn from e^++e^-, h^-+p and p+p collisions?
3. How can correlations be used to determine the size of the interaction region and the characteristics of phase transitions?

These questions are related to Bose-Einstein correlations, that appear due to the symmetrization of hadronic final states for the interchange of identical bosons, and are also known by other names, for example Hanbury Brown – Twiss or HBT correlations in heavy ion collisions, intensity interferometry, or intensity correlations [2]. These correlations are also tools of femtoscopy, because they are used to measure length scales on the femtometer scale [3–5].

2 The shortest film ever made: e^+ e^- collisions at LEP

In e^+ e^- collisions, Bose-Einstein correlations were used to record the fastest film ever made: the formation of a ring-like, *non-thermal* source in the transverse plane of jet production, a process that ends in less than 10^{-23} seconds [6, 7]. Can *thermal* models describe multiplicities, spectra and correlations in these collisions?

A number of recent papers consider the possibility of thermal particle production in e^+ e^- reactions. Two recent, interesting examples are refs. [8] and [9], that present thermal model fits to these data with similar level of statistical significance but with very different physics conclusions. A model cannot be excluded with the help of mathematical statistics if its confidence level is CL$\geq 0.1\%$, thus the probability that the model describes the data is at least one in thousand.

Fig. 1 of ref. [8] is a very beautiful plot indicating intriguing similarities between particle abundances in e^+ e^- at $\sqrt{s_{NN}}$ = 91 GeV and thermal model calculations. The fit quality is

* e-mail: csorgo@rmki.kfki.hu
[1] Instead of the originally given e^-+p problem, let me discuss soft hadron-proton collisions, for clarity.

characterized by a χ^2/NDF = 631/30. The corresponding confidence level is CL = 1.1 10^{-111} %. This confidence level is an extremely small positive number and so the probability that the thermal particle production describes this data set is practically zero [8] . These authors also observe and point out correctly that the statistical or thermodynamical description of these data fails completely at the high level of present experimental precision. Approximate qualitative agreement between thermal particle production and data can only be obtained if the relative errors on these data are magnified to about 10 % [8]. Their conclusion can be contrasted to other manuscripts, that claim that a thermodynamical or statistical description of particle multiplicities in e^+ e^- reactions is possible. For example, the same data set was analyzed in ref. [9] , using a slightly different thermal model description and the quality of their fit is given in their Table V as χ^2/NDF = 215./27 . The corresponding confidence level is CL = 3.4 10^{-29} % hence the probability that this thermal model describes particle abundances in electron-positron annihilation is practically zero. When the analysis is restricted to include only those 15 resonances in the fitting, whose width is less than 10 MeV, the same thermal model description yields χ^2/NDF = 39./12 . The confidence level of this fit is still CL = 1.1 10^{-2} % , which is many orders of magnitude improvement, but still an order of magnitude less than the conventional threshold of acceptance, CL = 0.1 %. Thus thermal particle production models do not describe the multiplicities of elementary particles of e^+ e^- at $\sqrt{s_{NN}}$ = 91 GeV in an acceptable manner.

Two important and well known features of hadronic spectra also disagree with a thermal, statistical picture of particle production. The observation of jets (2 and 3 jet events at this energies) can be contrasted to the lack of preferred direction in the initial conditions and in a thermal picture of particle production. Perhaps the thermal picture can be limited to the transverse direction? The power-law tail the transverse momentum spectra, which can be explained in terms of perturbative QCD processes and jets decaying to jets to jets and in particular the correlations among these jets are inconsistent with a thermal and/or a hydrodynamical interpretation, that lead typically to exponential spectra. Furthermore, generalized thermal models that describe the spectra cannot naturally interpret the correlation structures observed in two and three jet events which are basically energy momentum conservation laws and have a trivial interpretation in partonic picture, the emission of quark and gluon jets in perturbative QCD.

Bose-Einstein correlations are more subtle features of two-particle distributions. They carry information on the space-time structure and on the chaotic or coherent nature of particle emitting sources. Recently measured Bose-Einstein correlations disagree qualitatively with the hypothesis that the produced particles are emitted from a thermal or hydrodynamical source in $e^+ + e^-$ reactions, because in thermal models the two-particle Bose-Einstein correlation function is always given by a 1 + positive definite function, and this constraint is violated by a recent analysis of L3 data [7,10].With other words, there is no region of two-particle relative momentum space, where a chaotic (or thermal) picture of particle production would lead to anti-correlations. However, recently analyses L3 data as detailed in ref. [7, 10] indicate very clearly the existence of a region of anti-correlation: if the correlation functions are measured as a function of the Lorentz invariant relative momentum variable $Q = \sqrt{-(k_1 - k_2)^2}$, where k_i stands for the four-momentum of particle i, a dip is found experimentally in the region of 0.6 GeV $< Q <$ 1.5 GeV, as indicated in Fig. 1. In this kinematic range the errors are small. This feature is shown in greater details in Fig 1. L3 data from ref. [7] are compared to a Gaussian fit, $C(Q) =$

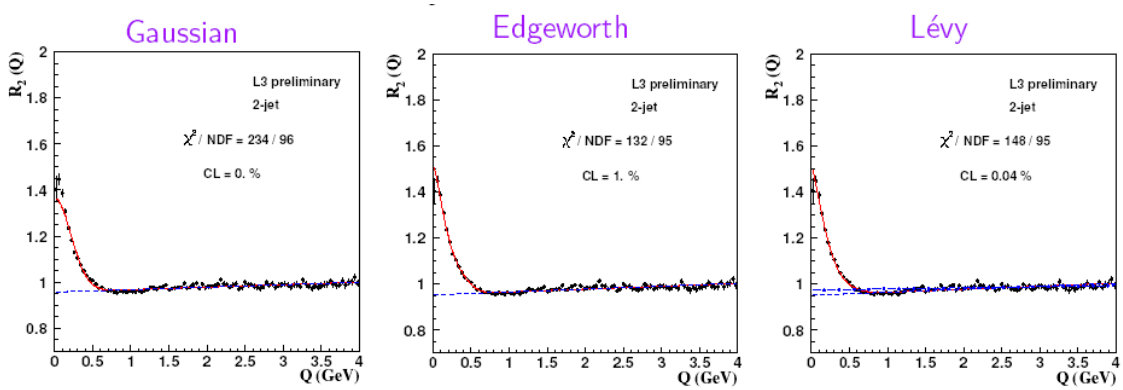


Fig. 1: Comparison of Gaussian (left), Edgeworth (middle) and Lévy fits to L3 Bose-Einstein correlation functions. The 1+ positive definite forms, Gaussian and Lévy do not have a statistically acceptable level, CL $< 0.1\%$. The Edgeworth expansion has an acceptable CL = 1 % and describes the dip using a 1+ non-positive definite expression.

$1 + \lambda \exp(-Q^2R^2)$, $\chi^2/NDF = 234./96$ and the corresponding confidence level is practically zero. A generalization of the Gaussians is given by the symmetric Lévy form $C(Q) = 1 + \lambda \exp(-Q^\alpha R^\alpha)$, $\chi^2/NDF = 148./95$, CL = 0.04 %. This is only a factor of 2.5 below the conventional domain of acceptable results, but the chance that this form represents the data is only 4 in 10000. This form however is 1 + a positive definite function. The right panel also indicates a linear fit to the long range, $Q > 1.5$ GeV correlations, shown with a dot-dashed line. It describes the data in the fitted $Q > 1.5$ GeV region, and it clearly cuts into the "dip" region of the data, located at $0.6 < Q < 1.5$ GeV . When a Lévy fit form is enforced, these long range correlations get distorted, pushed below the dip region by the fit, as indicated by the dashed line in the right panel, and the overall fit quality is decreased below the limit of acceptability, CL < 0.1 %. The best fit is achieved using an Edgeworth expansion, $C(Q) = 1+\lambda \exp(-Q^2R^2)[1+\kappa_3 H_3(QR)]$, where $H_3(x)$ is the third order Hermite polynomial, see ref. [7] for details. This Edgeworth fit has a statistically acceptable CL = 1 % and describes the dip using 1 + a non-positive definite expression, in a model and interpretation independent manner.

The τ-model of ref. [11] also predicted the existence of such anti-correlated regions, based on the assumption that $e^+ + e^-$ annihilations indeed correspond to point-like collisions hence the produced particles with a given momentum k^μ appear in a direction parallel to their momentum, $x^\mu \propto k^\mu$, however with a broad proper-time distribution $H(\tau)$. This model leads to simple fitting forms, that improve the description of the data as compared to the model-independent Edgeworth expansion method, CL is increased from 1 % to 40 % , and when the fit parameters are required to satisfy the model constraints, CL is slightly increased to 42 % , see ref. [7] for details. The parameters of the proper-time distribution are determined from detailed fits to the L3 Bose-Einstein correlation functions. This way the proper-time evolution of particle production is reconstructed in these reactions, and the following points can be made: in 2-jet events, particle emission starts just after the collision, so that the most probable value for τ is 0.3 fm/c, but this one-sided proper-time distribution has a power-law tail, corresponding to a one-sided Lévy distribution with an index of stability of $\alpha = 0.42 \pm 0.01$. Using a recently developed method based on the τ-model [12], even a movie of the space-time evolution of particle emission can be

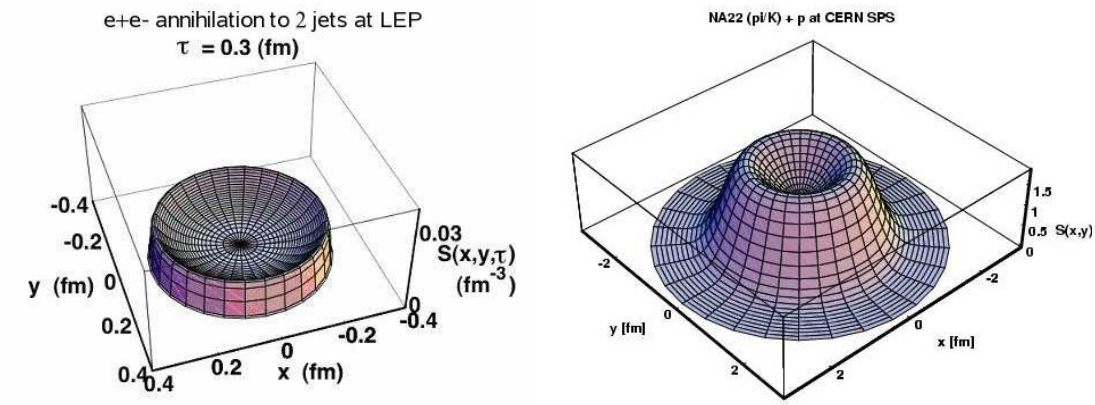


Fig. 2: Left panel: A snapshot picture from the reconstructed video of jet formation in the transverse plane of 2-jet events in $e^+ + e^-$ annihilation at LEP at $\tau = 0.3$ fm/c. A non-thermal, expanding ring is observed, the amplitude of the ring diminishes very quickly, while its radius grows nearly with the speed of light. Right panel: The reconstructed transverse part of the particle emission function in h+p reactions at CERN SPS as inferred from Bose-Einstein correlations and single particle spectra as measured by the NA22 collaboration, describing a tiny ring of fire.

reconstructed. This movie – the shortest film ever recorded – practically ends in about 0.3 fm/c.

3 The smallest ring of fire: h+ p and p+p collisions

In hadron-proton collisions, Bose-Einstein correlations have been used to make a snapshot picture of the smallest ring of fire, ever detected: the diameter is less than 1 fm or 10^{-15} m, but the source seems to be thermal. The ring formation here is a hydrodynamical effect, the temperature drops from $T \approx 140$ MeV in the center to nearly zero within about 1 fm radial distance, hence a strong pressure gradient builds up. However, the experimentally seen transverse flow is too week to move the matter away from the surface, hence a pile-up at the surface, a fire-ring is found [2, 13]. A similarly hydrodynamical ring of fire formation due to large temperature gradients and small transverse flows can be inferred from a simultaneous analysis of single particle spectra of pions, kaons, protons and STAR preliminary Bose-Einstein or HBT correlation radii of pion pairs in $\sqrt{s_{NN}} = 200$ GeV p+p collisions at RHIC [14].

4 The hottest and most perfect fluid: $Au + Au$ collisions at RHIC

In Au+Au collisions at $\sqrt{s_{NN}} = 200$ GeV at the RHIC accelerator at BNL, Bose-Einstein correlation measurements also yield snapshot pictures of the hottest and most perfect fluid, ever made in a laboratory experiment.

The following milestones lead to this important discovery: PHENIX was the first to observe a *new phenomena* in 0-10 % central Au+Au collisions at $\sqrt{s_{NN}} = 130$ GeV at RHIC: the suppression of particle production with high transverse momentum, the first RHIC discovery that made it to the cover page of The Physical Review Letters in January 2002. However, it was not clear initially if this effect is due to the nuclear modification of the structure functions (initial

conditions) at such a high energies, or if this is indeed a hadronic final state effect. As a control, $d+Au$ measurement was performed and all the four RHIC collaborations: BRAHMS, PHENIX, PHOBOS and STAR reported the absence of suppression in these reactions. This discovery implied that the suppression in Au+Au reaction is a final state effect, due to the formation of *a new form of matter*, that also made its way to the cover page of the Physical Review Letters in August 2003. The third milestone was the publication of the so called "White Papers" or review papers by all the four RHIC experiments. After several year's worth of high energy collisions, and from a detailed analysis of the elliptic flow data, a consensus interpretation emerged that the fireball made in Au+Au collisions at RHIC behaves like a liquid of strongly interacting constituents, also known as "the perfect fluid". This discovery became also known as the Top Physics Story for 2005 by the American Institute of Physics. This discovery has been considerably sharpened when STAR and PHENIX pointed out that the observed elliptic flow patterns scale with the number of constituent quarks and strange and even charm quarks participate in the flow. Although the theoretical interpretation of this effect is still open for discussions in particular because the unsolved problem of quark confinement in QCD prevents the application of first principle QCD calculations for this phenomena, in my opinion the experimental evidence is very clear, it is irrefutable that quark degrees of freedom are active and the perfect fluid seen in Au+Au collisions is a fluid of quarks [16]. (The role of gluons is less clear and less directly measurable from the experimental point of view.) The fifth milestone was the quantification, how perfect is the perfect fluid at RHIC? Answers were obtained by measuring the so called kinematic viscosity η/s, which is the ratio of the shear viscosity to the entropy density. Two theoretical analyses were published in 2007 based on elliptic flow patters, a third measurement was based on the transverse momentum correlations, while PHENIX studied the energy loss and flow of heavy (charmed) quarks and based on a charm diffusion picture, found that $\eta/s = (1.3-2.0)\frac{1}{4\pi}$ [16]. Even more recently, PHENIX was able to put a lower limit on the initial temperature of the fireball at RHIC from the analysis of direct photon data [17], $T_i > 220$MeV. These numbers can be compared to similar characteristics of other known fluids, like water, liquid nitrogen or helium, see Fig. 3, based on refs. [18, 19].

Note that ^{4}He becomes superfluid at extremely low temperatures and its kinematic viscosity η/s reaches a minimum at the onset of superfluidity, so for superfluid ^{4}He $\eta/s \geq 10\frac{1}{4\pi}$. The matter created in Au+Au collisions at RHIC has temperatures larger than 2 Terakelvin, nevertheless its kinematic viscosity is the lowest value ever produced in laboratory: it is at least a factor of 4 smaller than that of superfluid ^{4}He. We may thus refer this property of the matter created in Au+Au collisions at RHIC as *high temperature superfluidity* [20]: the matter created in Au+Au collisions at RHIC is the most perfect fluid ever made by humans.

We gain information on the type of transition from hadronic matter to quark matter with the help of the Bose-Einstein correlations. By now, circumstantial evidence is obtained that this transition is either a cross-over or, a non-equilibrium transition. This consensus opinion is based on important and highly selective constraints given by Bose-Einstein correlations and particle interferometry data in Au+Au collisions at RHIC [5].

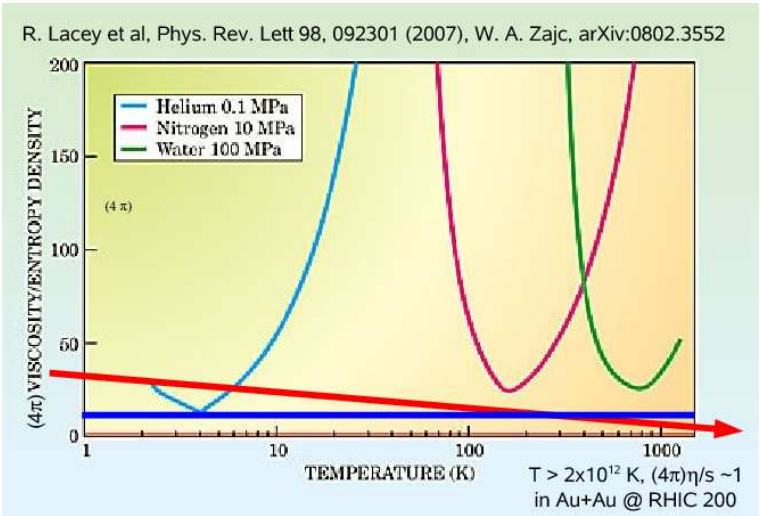


Fig. 3: Comparison of the properties of the perfect fluid created in $\sqrt{s_{NN}} = 200$ GeV Au+Au collisions with less extraordinary materials like water, nitrogen or helium.

5 Conclusions

After having discussed e^+ e^-, hadron-proton and heavy ion reactions one after the other, and based on the presented evidence let me attempt to give answers to the questions discussed in the Introduction, keeping in mind that these answers were worked out predominantly from the point of view of Bose-Einstein correlations and their models in these reactions.

Can thermal & hydrodynamical models describe e^++e^-, h+p and A+B reactions? It seems that thermal models cannot interpret particle multiplicities, spectra and Bose-Einstein correlations in e^+ + e^- reactions at the present level of experimental precision, and using the conventional threshold for acceptable confidence levels (99.9 % $\geq$ CL $\geq$ 0.1 %). However, hydrodynamical and thermal models are remarkably successful in describing soft ($p_t < 1.5$ GeV) hadron-proton, proton-proton and heavy ion reactions. At higher values of the transverse momenta, jet physics and interaction of jets and the hydrodynamical medium opens up new research directions at the intersection of particle and nuclear physics.

What heavy ion physics can learn from e^++e^-, h^-+p and p+p collisions? One lesson that I presented was to take statistical analysis and confidence level determinations seriously. Based on detailed and precision analysis of Bose-Einstein correlations in two-jet events and a simultaneous analysis of single particle spectra, the time evolution, a movie or a video like film of particle emission has been already reconstructed in e^+ e^- reactions at LEP. In heavy ion physics, only snapshot like pictures can be reconstructed at present. Further developments of the femtoscopic tools are needed to allow for a video like reconstruction of the time evolution of particle emission in heavy ion reactions. Based on Bose-Einstein data in e^+ + e^- reactions, it seems that the most probable value of the proper-time parameter of particle production is $\tau = 0.3$ fm/c, a surprisingly short value. It would be interesting to consider the phenomenological consequences of this number in heavy ion reactions, and if possible, to extract similar numbers

for jets that are produced in a nuclear medium.

How can correlations be used to determine the size of the interaction region and the characteristics of phase transitions? Of course a complete answer to this question goes well beyond the scope of this conference contribution. Let me just emphasize here, that correlations are routinely used to take a snapshot picture of the interaction region [2–5]. The resolution of these snapshot pictures has been increased recently and more detailed information about structures (like a ring of fire) or heavy tails (non-Gaussian behavior) are seen in all kind of reactions [5]. Recent progress even allowed for the determination of the time evolution of the region of particle production in $e^+ e^-$ reactions, based on a non-thermal description. Similar techniques are not yet developed for soft hadron-proton, proton-proton and heavy ion collisions, where the thermodynamical and hydrodynamical models can readily be applied. However, in heavy ion reactions matter formation and also a transition to a perfect fluid of quarks has been experimentally proven (although with open theoretical issues). Bose-Einstein correlations have been proven to constrain models in an extremely efficient manner. At present, models with a strong first order QCD phase transition or with a second order phase transition point disagree with Bose-Einstein correlation data in heavy ion collisions at RHIC, however, models with a cross-over transition or with non-equilibrium rehadronization scenario cannot be excluded at present [5, 21].

Acknowledgments: It is my pleasure to thank the Organizers for a most professionally organized conference. This research was supported by the OTKA grants NK73143, T49466 as well as by a Senior Scholarship Award of the Hungarian-American Enterprise Scholarship Fund.

References

[1] Topics and Questions defined by H. Jung and G. Gustafson for ISMD 2008: `http://ismd08.desy.de/e60/` .

[2] T. Csörgő, Heavy Ion Phys. **15** (2002) 1 [arXiv:hep-ph/0001233] .

[3] R. Lednicky, arXiv:nucl-th/0212089 .

[4] M. A. Lisa, S. Pratt, R. Soltz and U. Wiedemann, Ann. Rev. Nucl. Part. Sci. **55** (2005) 357 [arXiv:nucl-ex/0505014] .

[5] S. Bekele *et al.*, arXiv:0706.0537 [nucl-ex] .

[6] T. Novák [L3 Collaboration], Acta Phys. Hung. A **27** (2006) 479 .

[7] T. Novák, PhD Thesis, University of Nijmegen, 2008, `http://webdoc.ubn.ru.nl/mono/n/novak_t/bosecoine.pdf` .

[8] A. Andronic, F. Beutler, P. Braun-Munzinger, K. Redlich and J. Stachel, arXiv:0804.4132 [hep-ph] .

[9] F. Becattini, P. Castorina, J. Manninen and H. Satz, arXiv:0805.0964 [hep-ph] .

[10] W. Metzger [L3 Collaboration], Talk presented at ISMD 2008 .

[11] T. Csörgő and J. Zimanyi, Nucl. Phys. A **517** (1990) 588 .

[12] T. Csörgő, W. Kittel, W. J. Metzger and T. Novák, Phys. Lett. B **663**, 214 (2008) [arXiv:0803.3528 [hep-ph]]. .

[13] N. M. Agababyan et al, NA22/EHS Collaboration, Phys. Lett. B **422** (1998) 395 .

[14] T. Csörgő, M. Csanád, B. Lörstad and A. Ster, Acta Phys. Hung. A **24** (2005) 139 [arXiv:hep-ph/0406042]. .

[15] A. Adare *et al.* [PHENIX Collaboration], Phys. Rev. Lett. **98** (2007) 162301 [arXiv:nucl-ex/0608033]. .

[16] A. Adare *et al.* [PHENIX Collaboration], Phys. Rev. Lett. **98** (2007) 172301 [arXiv:nucl-ex/0611018]. .

[17] A. Adare *et al.* [PHENIX Collaboration], arXiv:0804.4168 [nucl-ex]. .

[18] R. A. Lacey *et al.*, Phys. Rev. Lett. **98** (2007) 092301 [arXiv:nucl-ex/0609025]. .

[19] W. A. Zajc, Nucl. Phys. A **805** (2008) 283 [arXiv:0802.3552 [nucl-ex]]. .

[20] T. Csörgő, M. I. Nagy and M. Csanád, J. Phys. G **35**, 104128 (2008) [arXiv:0805.1562 [nucl-th]]. .

[21] T. Csörgő and S. S. Padula, Braz. J. Phys. **37** (2007) 949 [arXiv:0706.4325 [nucl-th]]. .

QCD and Monte Carlo generators

Zoltán Nagy
DESY, Notkestrasse 85, 22607 Hamburg, Germany E-mail: Zoltan.Nagy@desy.de
DOI: http://dx.doi.org/10.3204/DESY-PROC-2009-01/47

Abstract
In this talk I gave a brief summary of leading order, next-to-leading order and shower calculations. I discussed the main ideas and approximations of the shower algorithms and the related matching schemes. I tried to focus on QCD issues and open questions instead of making a inventory of the existing programs.

1 Fix order calculations

1.1 Born level calculations

The simplest calculation what one can do is the Born level fix order calculation. This calculation involves the phase space integral of the tree level matrix element square and the jet measurement function. The structure of the cross section is

$$\sigma[F_J] = \int_m d\Gamma^{(m)}(\{p\}_m)|\mathcal{M}(\{p\}_m)|^2 F_J(\{p\}_m) \ , \tag{1}$$

where $d\Gamma^{(m)}(\{p\}_m)$ is the phase space integral measure, $\mathcal{M}(\{p\}_m)$ represents the m-paraton tree level matrix element and $F_J(\{p\}_m)$ is the jet measurement function that defines the physical observable.

This calculation is relatively simple. The integral is free from the infrared and ultraviolet singularities. The matrix element is basically a complicated expression but it can be generated in a automated way. Several implementations can be found in the literature, ALPGEN, GRACE, HELAC, MADGRAPH and SHERPA [1].

We can say that the tree level cross sections can predict the shape of the cross sections but in general they have several defects: i) Since it is the leading order term in the strong coupling expansion the result strongly depends on the unphysical renormalization and factorization scheme. ii) The exclusive physical quantities suffer on large logarithms. In the phase space regions where these logarithms are dominant the predictions are unreliable. iii) In the Born level calculations every jet is represented by a single parton, thus we don't have any information about the jet inner structure. iv) On the other hand in a real measurement, in the detector we can see hadrons and every jet consists many of them. We are not able to consider hadroniziation effects in the Born level calculations.

1.2 Next-to-leading order calculations

We can increase the precision of our theory (QCD) prediction by calculating the next term in the perturbative expansion, the next-to-leading order correction (NLO). However this is just one order higher to the Born cross section but the complexity of the calculations increases enormously. We have to face to algebraic and analytic complexity.

The naive structure of the NLO calculation is

$$\sigma_{\rm NLO} = \int_N d\sigma^B + \int_{N+1} d\sigma^R + \int_N d\sigma^V \quad . \tag{2}$$

Here σ^B, σ^R and σ^V correspond to the Born, real and virtual contributions, respectively. This expression is well defined only in $d = 4 - 2\epsilon$ dimension because both the real and virtual terms are singular separately in $d = 4$ dimension, but their sum is finite. Thus we cannot calculate them separately, first we have to regularize this integral. In the real part the singularities comes from the phase space integral from the regions where a gluon becomes soft or two partons become collinear and the integral over these degenerated phase space regions leads to contributions those are proportional to $1/\epsilon$ and $1/\epsilon^2$. The infrared singularity structure of the virtual contributions is exactly the same but with opposite sign, thus they cancel each other. To achieve this cancellation we have to reorganize our calculation in such a way that can be carried out in $d = 4$ dimension

$$\sigma_{\rm NLO} = \int_N d\sigma^B + \int_{N+1} \left[d\sigma^R - d\sigma^A\right]_{\epsilon=0} + \int_N \left[d\sigma^V + \int_1 d\sigma^A\right]_{\epsilon=0} \quad . \tag{3}$$

Here we subtracted the approximated version of real contribution and added it back in different form. In the second term $d\sigma^A$ cancels the singularities of $d\sigma^R$ and it is safe to perform the integral in $d = 4$ dimension while in the third term the explicit singularities of $d\sigma^V$ are cancelled by $\int_1 d\sigma^A$, where we performed the integral over the unresolved phase space analytically. It is important that the approximated real contribution has universal structure. This term is based on the soft and collinear factorization property of the QCD matrix elements. A general subtraction scheme was defined by Catani and Seymour [2] and the extenion of this method for massive fermions is also available [3].

The NLO calculation can be carried out but it hasn't been automated like the Born level calculations. The most complicated processes what we can calculate are $2 \to 3$ type [4]. To go beyond this limit we have to find an efficient way to compute the virtual correction. Recently we have had some very promising developement on this area [5].

With the NLO corrections we can significantly reduce the dependence on the renormalization and factorization scales but in some cases it is not enough and the NNLO is also required. In these calculations one of the jet is represented by two partons. This can give some minimal information about the inner jet structure but is still very poor. The exclusive quantities still suffer on large logarithms and we are still not able to consider hadronization effects.

1.3 Next-to-next-to-leading order calculation

For some processes and/or jet observables it is important to know the cross sections at next-to-next-to-leading order level. In this cases the NLO K-factor usually large even larger than 2 which means that the NLO correction doesn't reduce the scale dependences. Recently some simple but important processes have been calculated using sector decomposition method [6] and there are some ongoing developments on defining a general scheme for NNLO calculations [7].

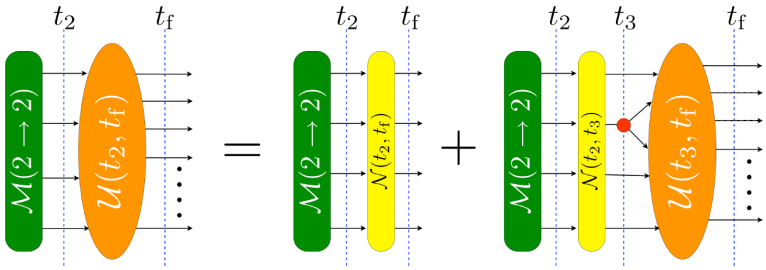


Fig. 1: Evolution equation. The shower (*orange rectangle*) starts from the hard matrix elements (*green rounded rectangle*) and the partons are evolved to the final scale without splitting (*yellow rounded rectengle*) or with splitting at an intermediate time (*red circle*) and evolved to the finial scale with possible splittings.

2 Leading order parton shower

The fixed order calculations are systematically defined order by order and usually give good description of the data over the phase space where the large p_T event are the dominant. In any order we still have to deal with the presence of the large logarithms and we cannot consider hadronization effect.

There is an other way to calculate crass section in the perturbative framework, the parton shower calculations. Consider the parton shower picture of hadron-hadron scattering in which there is some sort of hard event, say jet production. The parton shower description starts form hard scattering and proceeds forward to the softer scattering. In the final state the shower proceed forward in real time but for initial state parton the sowers proceeds backward in real time.

2.1 Shower evolution

The parton shower evolution can be represented by an evolution equation and it is the solution of the following integral equation

$$\mathcal{U}(t_f,t_2)\big|\mathcal{M}_2\big) = \mathcal{N}(t_f,t_2)\big|\mathcal{M}_2\big) + \int_{t_2}^{t_f} dt_3\, \mathcal{U}(t_f,t_3)\mathcal{H}(t_3)\mathcal{N}(t_3,t_2)\big|\mathcal{M}_2\big) \quad . \tag{4}$$

The shower evolution starts form the hard scattering and it is represented by the function $\big|\mathcal{M}_2\big)$ that is a probability of a given partonic state in shower time t_2. Then $\mathcal{U}(t_f,t_2)$ is the probability function of having a particular partonic state in a later evolution time t_f. The evolution operator is sum of two terms. The first term in Eq. (4) represents parton evolution without splitting. The non splitting operator $\mathcal{N}(t_f,t_2)$ that inserts Sudakov factors giving the probability that nothing happens between time t_2 and t_f. The Sudakov is the exponentiated inclusive (summed over spin and color and integrated over the momenta of unresolved partons) splitting kernel. The second term in Eq. (4) represent the splitting. The partonic state is evolved without splitting to an intermediate time t_3 and splitting happens given by the splitting operator $\mathcal{H}(t_3)$ and the system is evolved with possible splitting from t_3 to t_f. The splitting operator is based on the universal soft and collinear factorization property of the QCD matrix element. This evolution equation is depicted in Figure 1.

2.2 Splitting operator

The splitting operator of the leading order (LO) shower is derived from the factorization property of the QCD matrix elements in the soft and collinear limits. This factorization property is universal. When two partons become collinear or a gluon soft the QCD matrix element becomes singular in these phase space regions. The matrix element factorize to a product of a singular factor and the hard matrix element. This singular factor help us to construct the splitting operator of the shower algorithm.

$$\overline{\mathcal{H}}(t) = \sum_{l=1}^{m} \sum_{\substack{k=1 \\ k\neq l}}^{m} \boldsymbol{T}_l \cdot \boldsymbol{T}_k \, V_{lm+1}(\hat{p}_l, \hat{p}_{m+1}) \left[V_{km+1}(\hat{p}_k, \hat{p}_{m+1}) - V_{lm+1}(\hat{p}_l, \hat{p}_{m+1}) \right]^* \quad . \tag{5}$$

The first term is singular only in the soft limit while the second term is singular both in the soft and collinear limit. The soft term has non-tivial color structure because of the soft gluon makes color connections all the possible way between the hard partons. The collinear contribution (second term) is simple in the color space but it introduce correlations in the spin space. Note, if we want to consider spin and color correlations properly in the parton shower we *cannot* avoid negative weights. So far there is only one algorithm has been defined along this ideas [8] but it hasn't been implemented yet.

From the point of the implementation, the color and correlations make some complications but one can impose some further approximations to simplify it. HERWING [9] and OLD PYTHIA [10] implement direct angular ordering [11] to simplify the splitting operator. One can show that the expression under the square brackets vanishes in large angle limit when $\vartheta_{lk} \ll \vartheta_{lm+1},\ \vartheta_{km+1}$ (The ϑ_{ij} denotes the angle between momenta p_i and p_j.). This effect is know as *color coherence*.

The other way to simplify the color structure is to expand the splitting kernel in powers of $1/N_c^2$, where N_c is the number of the color states in fundamental representation. Keeping only the leading color contributions the color connection operator $\boldsymbol{T}_l \cdot \boldsymbol{T}_k$ becomes diagonal and the shower can be implemented as a Markovian process. The ARIADNE [12], VINCIA [13], NEW PYTHIA [10] and the Catani-Seymour dipole shower implementations [14] are based on the leading color approximation.

The parton shower algorithms have been derived from perturbative QCD but we cannot consider them as theory predictions because they use rather nonsystematic approximations. The original idea was to consider and simulate higher order matrix element by using only soft and collinear factorization of the QCD matrix elements. This is a systematical approximation since the factorization properties of the matrix elements are held all order. At the end of this section it is worthwhile to highlight the addition approximations and the limitation of the available parton shower implementations:

1. The current parton shower programs are still leading order calculations even though they consider higher order contributions.
2. The phase space is usually treated approximately. The angular ordered showers don't cover the phase space properly ("dead cone").
3. The direct angular ordering or the leading color approximation neglect the color correlations. The color interferences could be significant in the case of non-global observables [15]. Usually the spin correlations are also neglected.

4. They are not defined systematically. The direct angular ordering is not defined or hard to define at higher order. Even the kinematics of the dipole shower model is inconsistent with the higher order.
5. The only exact matrix element in the calculations is $2 \to 2$ like. If we want to calculate say $3, 4, 5, ...$-jet cross section we should use $2 \to 3, 4, 5, ...$ LO or NLO matrix elements. In the next section I discuss the matching of shower to exact matrix elements.
6. More questions on perturbative and non-perturbative effects: Does the shower resums the leading and the next-to-leading logarithms properly? What is underlying event? How can we model it? How to consider quantum interferences in hadronization models?

3 Matching parton showers to fix order calculations

3.1 Born level matching

The standard shower has a deficiency, which is illustrated in Figure 2. The left-hand picture depicts a term contributing to the standard shower. In this term, there are Sudakov factors and $1 \to 2$ parton splitting functions. If we omit the Sudakov factors, we have the $1 \to 2$ parton splittings as depicted in the middle picture. These splittings are approximations based on the splitting angles being small or one of the daughter partons having small momentum. Thus the shower splitting probability with two splittings approximates the exact squared matrix element for $2 \to 4$ scattering. The approximation is good in parts of the final state phase space, but not in all of it. Thus one might want to replace the approximate squared matrix element of the middle picture with the exact squared matrix element of the right-hand picture. However, if we use the exact squared matrix element, we lack the Sudakov factors.

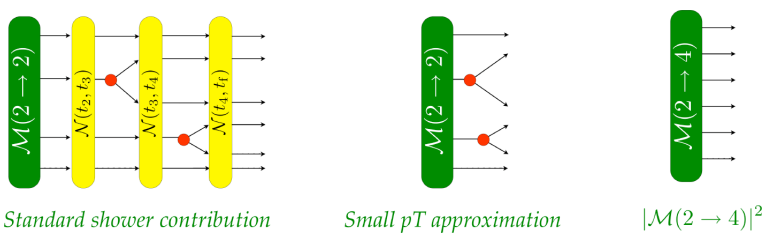


Fig. 2: The left-hand picture is the $2 \to 4$ cross section in shower approximation. The center picture is the shower approximation omitting the Sudakov factors. The right hand picture is the exact tree level $2 \to 4$ cross section. The cross section based on splitting functions (middle picture) is a collinear/soft approximation to this.

One can improve the approximation as illustrated in Figure 3. We reweight the exact squared matrix element by the ratio of the shower approximation with Sudakov factors to the shower approximation without Sudakov factors. The idea is to insert the Sudakov factors into the exact squared matrix element. This is the essential idea in the paper of Catani, Krauss, Kuhn, and Webber [16]. They use the k_T jet algorithm to define the ratio needed to calculate the Sudakov reweighting factor.

There is another way to improve shower. First we generate the event according to the shower and then rewieght it by the ratio of the exact and approximated matrix element. The

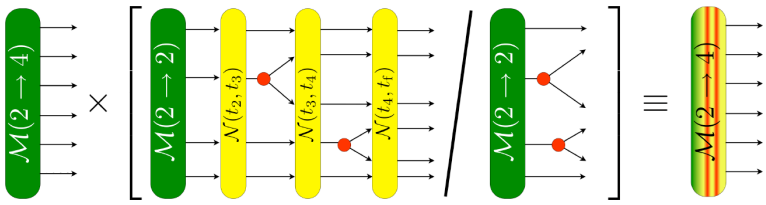


Fig. 3: An improved version of the $2 \to 4$ cross section. First we generate the 4-parton configuration according to the exact matrix element and take the shower approximation (with sudakov factors), divide by the approximate collinear squared matrix element, and multiply by the exact tree level squared matrix element. The graphical symbol on the right hand side represents this Sudakov reweighted cross section.

approximated matrix element is calculated over a unique emission history that is determined by a jet algorithm. The original MLM algorithm [17] uses the cone algorithm. The advantage of this method over the CKKW method is that the algorithm use the native Sudakov factors of the underlying parton shower.

There is a further step in implementing this idea. CKKW divide the shower evolution into two stages, $0 < t < t_{\rm ini}$ and $t_{\rm ini} < t < t_{\rm f}$, where $t_{\rm ini}$ is a parameter that represents a moderate P_T scale and $t_{\rm f}$ represents the very small P_T scale at which showers stop and hadronization is simulated. With this division, the Sudakov reweighting can be performed for the part of the shower at scale harder than $t_{\rm ini}$, as depicted in Figure 4. Evolution from $t_{\rm ini}$ to $t_{\rm f}$ is done via the ordinary shower algorithm.

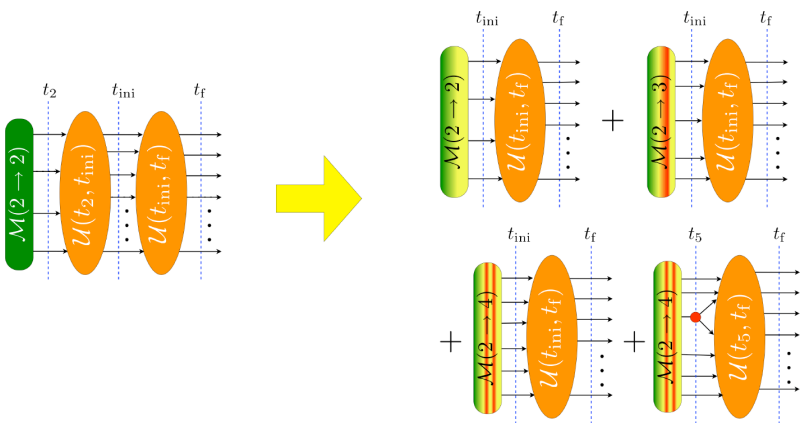


Fig. 4: Shower with CKKW jet number matching. The calculation for n jets at scale $t_{\rm ini}$ is based on the Sudakov reweighted tree level cross section for the production of n partons.

This method can be extended for NLO level matrix elements as it was shown for electron-positron annihilation in Ref. [18]. The required NLO adjustments are a little complicated, so I do not discuss them here.

3.2 Next-to-leading order matching

Matching parton shower with NLO fix order calculation is a very active field of parton shower developments. There are two basic approaches. First one is the MC@NLO project [19]. The main idea here is to avoid the double counting by introducing extra counterterm which is extracted out from the underlying shower algorithm. This method has been applied for several $2 \to 0 + X$ where no colored object in the final state and some $2 \to 1 + X$, $2 \to 2 + X$ processes, where the QCD particles in the final state are heavy [19].

The other approach was originally proposed by Krämer and Soper [20] and they implemented it for $e^+e^- \to$ 3-jets. The idea is to include the first step of the shower in the NLO calculation and then start the parton shower from this configuration. Based on this concept some matching algorithm have been proposed but they have been implemented for some processes [14, 18, 21]. In the following I discuss in detail only the MC@NLO approach because only this scheme has been implemented for LHC processes so far.

Let us start with the NLO cross section. After applying a subtraction scheme to remove the infrared singularities, we have

$$\sigma_{\rm NLO} = \int_m \left[d\sigma^B + d\sigma^V + d\sigma^C + \int_1 d\sigma^A\right] F_{\rm J}^{(m)} + \int_{m+1} \left[d\sigma^{\rm R} F_{\rm J}^{(m+1)} - d\sigma^{\rm A} F_{\rm J}^{(m)}\right] \quad , \quad (6)$$

where $d\sigma^B$, $d\sigma^{\rm R}$, $d\sigma^V$, $d\sigma^C$ and $d\sigma^A$ are the Born, real, virtual contributions, collinear counterterm and subtraction term of the NLO scheme, respectively. The physical quantity is defined by the functions $F_{\rm J}^{(m)}$ and $F_{\rm J}^{(m+1)}$.

The naive way to add parton shower corrections is to replace the jet functions with the shower interface function. This approach is not good because it leads to double counting. It is easy to see, the shower that starts from the Born term generates higher order contributions those are already considered by NLO terms.

To avoid double counting Frixione and Webber [19] organized the calculation in the following way:

$$\begin{aligned}\sigma_{\rm MC} = & \int_m \left[d\sigma^B + d\sigma^V + d\sigma^C + \int_1 d\sigma^A\right] I_{\rm MC}^{(2\to m)} \\ & + \int_{m+1} \left[d\sigma_{m+1}^{\rm R} - d\sigma_{m+1}^{\rm MC}\right] I_{\rm MC}^{(2\to m+1)} + \int_{m+1} \left[d\sigma_{m+1}^{\rm MC} - d\sigma_{m+1}^{\rm A}\right] I_{\rm MC}^{(2\to m)} \quad .\end{aligned} \quad (7)$$

Here the contribution $d\sigma_{m+1}^{\rm MC}$ is extracted from the underlying parton shower algorithm. The functions $I_{\rm MC}^{(2\to m)}$ and $I_{\rm MC}^{(2\to m+1)}$ are the interface functions to the shower. We have different choices for the m and $m+1$ parton interface functions, thus we have

$$I_{\rm MC}^{(2\to m)} \sim \mathcal{U}(t_{\rm f}, t_m) \qquad \text{and} \qquad I_{\rm MC}^{(2\to m+1)} \sim \mathcal{U}(t_{\rm f}, t_{m+1})\mathcal{N}(t_{m+1}, t_m) \quad . \quad (8)$$

In the m-parton case we simply start the shower from the m-parton configuration while in the $m+1$ parton case first we insert some Sudakov factor representing the probability of nothing happens between the m-parton and $m+1$ parton states and starts the shower from the $m+1$ parton configuration.

There are some limitation of the MC@NLO approach: i) It is worked out for HERWIG. One has to redo the Monte Carlo subtraction scheme if we want to match say PYTHIA to NLO computations. ii) Matching procedure is defined only for simple processes like $2 \to 0 + X, 1 + X, 2$. iii) The double counting problem is not fully solved but it is probably numerically invisible because of the strong Sudakov suppression. The problem related to the soft singularities but it appears only in the $2 \to 2$ or more complicated processes where the color structure is not trivial.

4 Conclusions

Parton shower event generators have proved to be an essential tool for particle physics. These computer programs perform calculations of cross sections according to an approximation to the standard model or some of its possible extensions. Because of the great success of these programs, it is worthwhile to investigate possible improvements.

In a typical parton shower event generator, the physics is modeled as a process in classical statistical mechanics. Some number of partons are produced in a hard interaction. Then each parton has a chance to split into two partons, with the probability to split determined from an approximation to the theory. Parton splitting continues in this probabilistic style until a complete parton shower has developed.

The underlying approximation is the factorization of amplitudes in the soft or collinear limits. However, further approximations are usually added: i) The interference between a diagram in which a soft gluon is emitted from one hard parton and a diagram in which the same soft gluon is emitted from another hard parton is treated in an approximate way, with the "angular ordering" approximation. ii) Color is treated in an approximate way, valid when $1/N_c^2 \to 0$ where $N_c = 3$ is the number of colors. iii) Parton spin is treated in an approximate way. According to the full quantum amplitudes, when a parton splits, the angular distribution of the daughter partons depends on the mother parton spin and even on the interference between different mother-parton spin states. This dependence is typically ignored. With the use of these further approximations, one can get to a formalism in which the shower develops according to classical statistical mechanics with a certain evolution operator.

I think the way to improve the parton showers is to formulate it based on the factorization of amplitudes in the soft or collinear limits in which one does not make the additional approximations enumerated above. For this, one would have to use quantum statistical mechanics instead of classical statistical mechanics.

On the other hand the parton shower algorithm should cooperate with exact LO and NLO matrix elements. Currently we have some very promising tools such as CKKW, MLM and MC@NLO matching schemes. The CKKW and MLM matching procedures patch the "hole" between the Born level fix order and the shower calculations while the MC@NLO and other NLO matching schemes do the same between the shower and fix order NLO calculations. If we want more precise tools we need more advanced framework. We need a general LO shower framework that naturally includes the LO and NLO calculation. Or phrase it differently, we should reformulate the LO and NLO calculation to make the shower part of them.

5 Acknowledgment

I am greatful to the organizers of the ISMD2008 workshop for their invitation as well as for providing a pleasant atmosphere during the meeting. This work was supported by the Hungarian Scientific Research Fund grants OTKA T-60432.

References

[1] M. L. Mangano, M. Moretti, F. Piccinini, R. Pittau and A. D. Polosa, JHEP **0307** (2003) 001 [arXiv:hep-ph/0206293]; G. Belanger, F. Boudjema, J. Fujimoto, T. Ishikawa, T. Kaneko, K. Kato and Y. Shimizu, Phys. Rept. **430** (2006) 117 [arXiv:hep-ph/0308080]; A. Kanaki and C. G. Papadopoulos, Comput. Phys. Commun. **132** (2000) 306 [arXiv:hep-ph/0002082]; F. Maltoni and T. Stelzer, JHEP **0302** (2003) 027 [arXiv:hep-ph/0208156]; T. Gleisberg, S. Hoche, F. Krauss, A. Schalicke, S. Schumann and J. C. Winter, JHEP **0402** (2004) 056 [arXiv:hep-ph/0311263].

[2] S. Catani and M. H. Seymour, Nucl. Phys. B **485** (1997) 291 [Erratum-ibid. B **510** (1998) 503] [arXiv:hep-ph/9605323].

[3] S. Catani, S. Dittmaier, M. H. Seymour and Z. Trocsanyi, Nucl. Phys. B **627** (2002) 189 [arXiv:hep-ph/0201036].

[4] Z. Nagy, Phys. Rev. D **68** (2003) 094002 [arXiv:hep-ph/0307268]; Z. Nagy and Z. Trocsanyi, Phys. Lett. B **634** (2006) 498 [arXiv:hep-ph/0511328]; J. M. Campbell, R. Keith Ellis and G. Zanderighi, JHEP **0610** (2006) 028 [arXiv:hep-ph/0608194]; J. Campbell, R. K. Ellis and D. L. Rainwater, Phys. Rev. D **68** (2003) 094021 [arXiv:hep-ph/0308195].

[5] G. Ossola, C. G. Papadopoulos and R. Pittau, Nucl. Phys. B **763** (2007) 147 [arXiv:hep-ph/0609007]; T. Binoth, J. P. Guillet and G. Heinrich, JHEP **0702** (2007) 013 [arXiv:hep-ph/0609054]; Z. Nagy and D. E. Soper, JHEP **0309** (2003) 055 [arXiv:hep-ph/0308127]; C. F. Berger, Z. Bern, L. J. Dixon, D. Forde and D. A. Kosower, Phys. Rev. D **74** (2006) 036009 [arXiv:hep-ph/0604195]; Z. Bern, L. J. Dixon and D. A. Kosower, Phys. Rev. D **71** (2005) 105013 [arXiv:hep-th/0501240]; C. Anastasiou, R. Britto, B. Feng, Z. Kunszt and P. Mastrolia, JHEP **0703** (2007) 111 [arXiv:hep-ph/0612277]; R. Britto, B. Feng and P. Mastrolia, Phys. Rev. D **73** (2006) 105004 [arXiv:hep-ph/0602178]; T. Binoth, G. Heinrich, T. Gehrmann and P. Mastrolia, Phys. Lett. B **649** (2007) 422 [arXiv:hep-ph/0703311];W. T. Giele, Z. Kunszt and K. Melnikov, JHEP **0804** (2008) 049 [arXiv:0801.2237 [hep-ph]]

[6] G. Heinrich, Nucl. Phys. Proc. Suppl. **116** (2003) 368 [arXiv:hep-ph/0211144]; T. Binoth and G. Heinrich, Nucl. Phys. B **693** (2004) 134 [arXiv:hep-ph/0402265]; C. Anastasiou, K. Melnikov and F. Petriello, Phys. Rev. Lett. **93** (2004) 262002 [arXiv:hep-ph/0409088].

[7] A. Gehrmann-De Ridder, T. Gehrmann, E. W. N. Glover and G. Heinrich, Nucl. Phys. Proc. Suppl. **160** (2006) 190 [arXiv:hep-ph/0607042]; A. Gehrmann-De Ridder, T. Gehrmann and E. W. N. Glover, JHEP **0509** (2005) 056 [arXiv:hep-ph/0505111]; G. Somogyi, Z. Trocsanyi and V. Del Duca, JHEP **0701** (2007) 070 [arXiv:hep-ph/0609042]; G. Somogyi and Z. Trocsanyi, JHEP **0701** (2007) 052 [arXiv:hep-ph/0609043]; S. Catani and M. Grazzini, arXiv:hep-ph/0703012; S. Weinzierl, Phys. Rev. D **74** (2006) 014020 [arXiv:hep-ph/0606008]; A. Gehrmann-De Ridder, T. Gehrmann, E. W. N. Glover and G. Heinrich, Phys. Rev. Lett. **100** (2008) 172001 [arXiv:0802.0813 [hep-ph]].

[8] Z. Nagy and D. E. Soper, JHEP **0709** (2007) 114 [arXiv:0706.0017 [hep-ph]]; JHEP **0803** (2008) 030 [arXiv:0801.1917 [hep-ph]]; JHEP **0807** (2008) 025 [arXiv:0805.0216 [hep-ph]].

[9] G. Marchesini, B. R. Webber, G. Abbiendi, I. G. Knowles, M. H. Seymour and L. Stanco, Comput. Phys. Commun. **67** (1992) 465 ; S. Gieseke *et al.*, [arXiv:hep-ph/0609306].

[10] T. Sjöstrand, Comput. Phys. Commun. **82** (1994) 74; T. Sjöstrand, S. Mrenna and P. Skands, JHEP **0605** (2006) 026 [arXiv:hep-ph/0603175].

[11] G. Marchesini and B. R. Webber, Nucl. Phys. B **238** (1984) 1; R. K. Ellis, G. Marchesini and B. R. Webber, Nucl. Phys. B **286** (1987) 643 [Erratum-ibid. B **294** (1987) 1180].

[12] L. Lönnblad, Comput. Phys. Commun. **71** (1992) 15.

[13] W. T. Giele, D. A. Kosower and P. Z. Skands, Phys. Rev. D **78** (2008) 014026 [arXiv:0707.3652 [hep-ph]].

[14] Z. Nagy and D. E. Soper, arXiv:hep-ph/0601021; M. Dinsdale, M. Ternick and S. Weinzierl, Phys. Rev. D **76** (2007) 094003 [arXiv:0709.1026 [hep-ph]];S. Schumann and F. Krauss, JHEP **0803** (2008) 038

[15] J. R. Forshaw, A. Kyrieleis and M. H. Seymour, JHEP **0608** (2006) 059 [arXiv:hep-ph/0604094]; M. Dasgupta and G. P. Salam, Phys. Lett. B **512** (2001) 323 [arXiv:hep-ph/0104277].

[16] S. Catani, F. Krauss, R. Kuhn and B. R. Webber, JHEP **0111** (2001) 063 [arXiv:hep-ph/0109231]; L. Lönnblad, JHEP **0205** (2002) 046 [arXiv:hep-ph/0112284]; N. Lavesson and L. Lönnblad, JHEP **0507** (2005) 054 [arXiv:hep-ph/0503293];

[17] M. L. Mangano, M. Moretti, F. Piccinini and M. Treccani, JHEP **0701** (2007) 013 [arXiv:hep-ph/0611129].

[18] Z. Nagy and D. E. Soper, JHEP **0510** (2005) 024 [arXiv:hep-ph/0503053].

[19] S. Frixione and B. R. Webber, JHEP **0206** (2002) 029 [arXiv:hep-ph/0204244]; S. Frixione, P. Nason and B. R. Webber, JHEP **0308** (2003) 007 [arXiv:hep-ph/0305252]; S. Frixione and B. R. Webber, arXiv:hep-ph/0612272.

[20] M. Krämer and D. E. Soper, Phys. Rev. D **69** (2004) 054019 [arXiv:hep-ph/0306222]; D. E. Soper, Phys. Rev. D **69** (2004) 054020 [arXiv:hep-ph/0306268]; M. Krämer, S. Mrenna and D. E. Soper, Phys. Rev. D **73** (2006) 014022 [arXiv:hep-ph/0509127].

[21] P. Nason, JHEP **0411** (2004) 040 [arXiv:hep-ph/0409146]; S. Alioli, P. Nason, C. Oleari and E. Re, arXiv:0812.0578 [hep-ph]

On factorization scheme suitable for NLO Monte Carlo event generators

Karel Kolar
Institute of Physics, Academy of Sciences of the Czech Republic, Prague
DOI: http://dx.doi.org/10.3204/DESY-PROC-2009-01/48

Abstract
The choice of a factorization scheme suitable for Monte Carlo simulations of NLO initial state parton showers is discussed in this contribution.

1 Introduction

Generating initial state parton showers (IPS) in hadronic collisions at the NLO accuracy is a task for which no satisfactory solution has so far been found. An attempt at solving this problem which is presented in this contribution is based on an exploitation of the freedom in the choice of the factorization scheme.

As a simple illustration, consider a non–singlet nucleon structure function $F_{\rm NS}\big(x,Q^2\big)$. Its Mellin moments are given as the product

$$F_{\rm NS}\big(n,Q^2\big) = C_{\rm NS}\left(n,\frac{Q}{M},{\rm FS}\right) q_{\rm NS}(n,M,{\rm FS})\,, \tag{1}$$

where $C_{\rm NS}(n,Q/M,{\rm FS})$ stands for Mellin moments of the corresponding coefficient function and $q_{\rm NS}(n,M,{\rm FS})$ represents Mellin moments of the relevant non–singlet parton distribution function. Both $C_{\rm NS}(n,Q/M,{\rm FS})$ and $q_{\rm NS}(n,M,{\rm FS})$ depend on a particular factorization scheme FS and on a factorization scale M, however, their product (1) is independent of both of them. The coefficient function $C_{\rm NS}(n,Q/M,{\rm FS})$ is calculable within the framework of perturbative QCD and can thus be expanded in powers of the QCD coupling $a\equiv\alpha_{\rm s}/\pi$

$$C_{\rm NS}\left(n,\frac{Q}{M},{\rm FS}\right) = \sum_{k=0}^{\infty} a^k(\mu,{\rm RS})\, C_{\rm NS}^{(k)}\left(n,\frac{Q}{M},{\rm FS},\mu,{\rm RS}\right). \tag{2}$$

Although both the coupling $a(\mu,{\rm RS})$ and the coefficients $C_{\rm NS}^{(k)}(n,Q/M,{\rm FS},\mu,{\rm RS})$ depend on a particular renormalization scheme RS and on a renormalization scale μ, which is in principle different from M, the series, if summed to all orders, is independent of both the RS and μ. The non–singlet parton distribution function $q_{\rm NS}(n,M,{\rm FS})$ satisfies the evolution equation[1]

$$\frac{{\rm d}q_{\rm NS}(n,M,{\rm FS})}{{\rm d}\ln M} = a(M)\, P_{\rm NS}(n,M,{\rm FS})\, q_{\rm NS}(n,M,{\rm FS})\,, \tag{3}$$

[1] From the relations (3) and (4), we see that the non–singlet distribution function $q_{\rm NS}(n,M,{\rm FS})$ also depends on the renormalization scheme in which the renormalized coupling $a(M)$ is defined. This scheme can in principle be different from that used for the expansion of the coefficient function $C_{\rm NS}(n,Q/M,{\rm FS})$, but usually these schemes are chosen to be identical.

where the non–singlet splitting function $P_{\rm NS}(n,M,{\rm FS})$ can be expanded in powers of $a(M)$

$$P_{\rm NS}(n,M,{\rm FS}) = \sum_{k=0}^{\infty} a^k(M)\, P_{\rm NS}^{(k)}(n,{\rm FS})\,. \tag{4}$$

In the next–to–leading order approximation, we retain only the first two terms in the expansions (2) and (4):

$$C_{\rm NS}\left(n,\frac{Q}{M},{\rm FS}\right) \;=\; C_{\rm NS}^{(0)}(n) + a(\mu)\, C_{\rm NS}^{(1)}\left(n,\frac{Q}{M},{\rm FS}\right), \tag{5}$$

$$P_{\rm NS}(n,M,{\rm FS}) \;=\; P_{\rm NS}^{(0)}(n) + a(M)\, P_{\rm NS}^{(1)}(n,{\rm FS}) \tag{6}$$

and the NLO coupling $a(\mu)$ obeys the differential equation

$$\frac{{\rm d}a(\mu)}{{\rm d}\ln\mu} = -ba^2(\mu)\Big(1+ca(\mu)\Big). \tag{7}$$

The LO terms $C_{\rm NS}^{(0)}(n)$ and $P_{\rm NS}^{(0)}(n)$ are universal — independent of any unphysical quantities such as renormalization and factorization scales and schemes. The NLO contributions $C_{\rm NS}^{(1)}(n,Q/M,{\rm FS})$ and $P_{\rm NS}^{(1)}(n,{\rm FS})$ satisfy the following condition

$$C_{\rm NS}^{(1)}\left(n,\frac{Q}{M},{\rm FS}\right) = C_{\rm NS}^{(0)}(n)\left[\kappa(n) + P_{\rm NS}^{(0)}(n)\ln\frac{Q}{M} + \frac{1}{b}P_{\rm NS}^{(1)}(n,{\rm FS})\right], \tag{8}$$

where $\kappa(n)$ is a scale and scheme factorization invariant. The ambiguity related to the factorization procedure is already at the NLO large, because the splitting function $P_{\rm NS}^{(1)}(x,{\rm FS})$ is completely arbitrary function — for any function $f(x)$, there always exists such a factorization scheme FS in which $P_{\rm NS}^{(1)}(x,{\rm FS}) = f(x)$. There are two prominent choices of the splitting function $P_{\rm NS}^{(1)}(n,{\rm FS})$, which are in some sense opposite to each other. In the first one, the splitting function $P_{\rm NS}^{(1)}(n,{\rm FS})$ is set equal to zero. For this choice, which will be called the ZERO factorization scheme, the evolution of the distribution function $q_{\rm NS}(n,M,{\rm FS})$ is formally identical to the LO one and all NLO corrections are thus contained in the NLO coefficient function $C_{\rm NS}^{(1)}(n,Q/M,{\rm FS})$. The latter choice consists in selecting the splitting function $P_{\rm NS}^{(1)}(n,{\rm FS})$ in such a way that the NLO coefficient function $C_{\rm NS}^{(1)}(n,Q/M,{\rm FS})$ vanishes for $M=Q$ (see the equation (8)). In this case, the relation between the structure function $F_{\rm NS}\big(x,Q^2\big)$ and the distribution function $q_{\rm NS}(n,M,{\rm FS})$ has the same form as in the LO and all NLO corrections are included in the evolution of the distribution function $q_{\rm NS}(n,M,{\rm FS})$. This type of choice is the essence of the so called DIS factorization scheme introduced in [1], which is widely used in phenomenology. The factorization scheme dependence of NLO theoretical predictions for physical quantities is studied, for instance, in [2], where only factorization schemes interpolating between the DIS and $\overline{\rm MS}$ factorization schemes are considered.

The factorization scheme specifies the way in which the so called collinear singularities, which are contained in cross–sections at parton level, are absorbed into the dressed parton distribution functions. Within the framework of dimensional regularization, the relation between the

dressed and bare distribution functions is given in the general case by the formula

$$D_i(x,M,\mathrm{FS}) = \sum_j \int_x^1 \frac{\mathrm{d}y}{y} D_j^{(0)}\!\left(\frac{x}{y}\right)\left[\delta_{ij}\delta(1-y) + a(M)\left(\frac{1}{\epsilon}A_{ij}^{(11)}(y) + A_{ij}^{(10)}(y)\right) + \right.$$
$$\left. + a^2(M)\left(\frac{1}{\epsilon^2}A_{ij}^{(22)}(y) + \frac{1}{\epsilon}A_{ij}^{(21)}(y) + A_{ij}^{(20)}(y)\right) + \cdots\right]. \quad (9)$$

The matrices $A_{ij}^{(k0)}(x)$ can be chosen arbitrarily and their choice fully specifies the factorization scheme. The factorization scheme can also be specified by higher order splitting functions $P_{ij}^{(k)}(x,\mathrm{FS})$, $k \geq 1$, which we can choose at will. The most widely used factorization scheme is the so called $\overline{\mathrm{MS}}$ factorization scheme, which is defined by setting the matrices $A_{ij}^{(k0)}(x)$ equal to zero[2] and is thus convenient for theoretical calculations.

At present time many QCD cross–sections at parton level are known at the NLO accuracy. However, the algorithms that are used for their incorporation in Monte Carlo event generators attach to them the IPS only at the LO accuracy because generating IPS at the NLO accuracy is very complicated in the standard $\overline{\mathrm{MS}}$ factorization scheme. The reasons for that are basically two: The NLO splitting functions no longer correspond to basic QCD vertices and the splitting functions at the NLO approximation are negative for some x, which prevents us from using straightforward probabilistic interpretation. Because the IPS induce the scale dependence of parton distribution functions, it is inconsistent to attach the LO IPS to NLO QCD cross–sections, which include NLO parton distribution functions. This deficiency could be removed by choosing the ZERO factorization scheme, in which the NLO IPS are formally identical to the LO ones and all NLO corrections are thus put into hard scattering cross–sections. The main advantage of this approach is the fact that the existing algorithms for parton showering and for attaching parton showers to NLO cross–sections need not be changed. The only step necessary to do is transforming parton level cross–sections from the standard $\overline{\mathrm{MS}}$ factorization scheme to the ZERO factorization scheme and determining parton distribution functions in the ZERO scheme.

2 The transformation of hard scattering cross–sections

In the case of a hadron collision, a cross–section $\sigma(P)$ (in general differential) depending on observables P is given by the formula

$$\sigma(P) = \sum_{ij} \int_0^1 \int_0^1 \mathrm{d}x_1\,\mathrm{d}x_2\, D_{i/A}(x_1,M,\mathrm{FS})\, D_{j/B}(x_2,M,\mathrm{FS})\, \sigma_{ij}(x_1,x_2;P;M,\mathrm{FS}), \quad (10)$$

where $D_{i/A}(x,M,\mathrm{FS})$ and $D_{i/B}(x,M,\mathrm{FS})$ are the parton distribution functions of the colliding hadrons. The partonic cross–section $\sigma_{ij}(x_1,x_2;P;M,\mathrm{FS})$ can be expanded in powers of the QCD coupling $a(\mu)$:

$$\sigma_{ij}(x_1,x_2;P;M,\mathrm{FS}) = \sigma_{ij}^{(0)}(x_1,x_2;P) + a(\mu)\,\sigma_{ij}^{(1)}(x_1,x_2;P;M,\mathrm{FS}) + \mathcal{O}\big(a^2(\mu)\big). \quad (11)$$

[2] with the renormalized coupling $a(M)$ defined in the $\overline{\mathrm{MS}}$ renormalization scheme

The LO cross–section $\sigma_{ij}^{(0)}(x_1, x_2; P)$ is independent of the factorization scale and scheme. The dependence of the NLO cross–section $\sigma_{ij}^{(1)}(x_1, x_2; P; M, \mathrm{FS})$ on the factorization scale and scheme is determined by the formula

$$\sigma_{ij}^{(1)}(x_1, x_2; P; M, \mathrm{FS}) = \sigma_{ij}^{(1)}(x_1, x_2; P; M_0, \overline{\mathrm{MS}}) + \sum_k \int_0^1 \mathrm{d}y \Big[\sigma_{ik}^{(0)}(x_1, yx_2; P) \times \tag{12}$$

$$\times \left(P_{kj}^{(0)}(y) \ln \frac{M_0}{M} + T_{kj}^{(1)}(y, \mathrm{FS}) \right) + \sigma_{kj}^{(0)}(yx_1, x_2; P) \left(P_{ki}^{(0)}(y) \ln \frac{M_0}{M} + T_{ki}^{(1)}(y, \mathrm{FS}) \right) \Big].$$

What we need for the conversion to the factorization scheme FS is the knowledge of the corresponding matrix function $T_{ij}^{(1)}(x, \mathrm{FS})$ [3], which is process independent. In the space of Mellin moments, the matrix $T_{ij}^{(1)}(n, \mathrm{FS})$ satisfies the following matrix equation:

$$\Big[\mathbf{T}^{(1)}(n, \mathrm{FS}), \mathbf{P}^{(0)}(n) \Big] - b\mathbf{T}^{(1)}(n, \mathrm{FS}) = \mathbf{P}^{(1)}(n, \overline{\mathrm{MS}}) - \mathbf{P}^{(1)}(n, \mathrm{FS}) \,. \tag{13}$$

3 The ZERO factorization scheme

The solution of the preceding equation (13) for the ZERO factorization scheme reads

$$\begin{aligned}
&T_{q_iq_j}^{(1)}(n) = T_{\bar{q}_i\bar{q}_j}^{(1)}(n) = T_3^{(1)}(n) - \tfrac{1}{b} P_{q_iq_j}^{(1)}(n, \overline{\mathrm{MS}}), \qquad T_{q_iG}^{(1)}(n) = T_{\bar{q}_iG}^{(1)}(n) = T_1^{(1)}(n), \\
&T_{q_i\bar{q}_j}^{(1)}(n) = T_{q_i\bar{q}_j}^{(1)}(n) = T_3^{(1)}(n) - \tfrac{1}{b} P_{q_i\bar{q}_j}^{(1)}(n, \overline{\mathrm{MS}}), \qquad T_{Gq_i}^{(1)}(n) = T_{G\bar{q}_i}^{(1)}(n) = T_2^{(1)}(n), \\
&T_{GG}^{(1)}(n) = -\tfrac{1}{b} P_{GG}^{(1)}(n, \overline{\mathrm{MS}}) - 2n_{\mathrm{f}} T_3^{(1)}(n),
\end{aligned} \tag{14}$$

where the unknown functions $T_i^{(1)}(n)$ can be expressed in terms of the Mellin moments of the LO and NLO splitting functions. The Mellin inversion of $T_i^{(1)}(n)$ has to be calculated numerically. This was performed for three and four effectively massless flavours. The obtained results are very surprising because for $x \lesssim 0.1$

$$T_i^{(1)}(x) \approx C_i x^{-\xi} \quad \text{with} \;\; \xi(n_{\mathrm{f}} = 3) \doteq 4.63 \;\; \text{and} \;\; \xi(n_{\mathrm{f}} = 4) \doteq 3.85 \tag{15}$$

and the coefficients C_i are so large that the functions $T_i^{(1)}(x)$ strongly dominate over the NLO splitting functions $P_{kl}^{(1)}(x, \overline{\mathrm{MS}})$ in this region ($x \lesssim 0.1$). So the question of applicability of the ZERO factorization scheme arises.

The parton distribution functions in the ZERO factorization scheme are plotted for $x \in (10^{-3}, 10^{-1})$ in Figure 1. In this region they behave like $x^{-\xi}$ with ξ close to that in the relation (15). The ZERO factorization scheme can thus provide reasonable predictions only if large cancellation between positive and negative values occurs in expressions for physical quantities. Hence, within the framework of numerical computations, the ZERO factorization scheme can only be used in kinematic regions where $x \gtrsim 0.1$. The only exception is its application in the non–singlet case, where the functions $T_i^{(1)}(x)$ do not appear and no problems with large numbers occur.

[3] $T_{ij}^{(1)}(x, \mathrm{FS}) = -A_{ij}^{(10)}(x, \mathrm{FS})$, where the matrix $A_{ij}^{(10)}(x, \mathrm{FS})$ is defined in the relation (9).

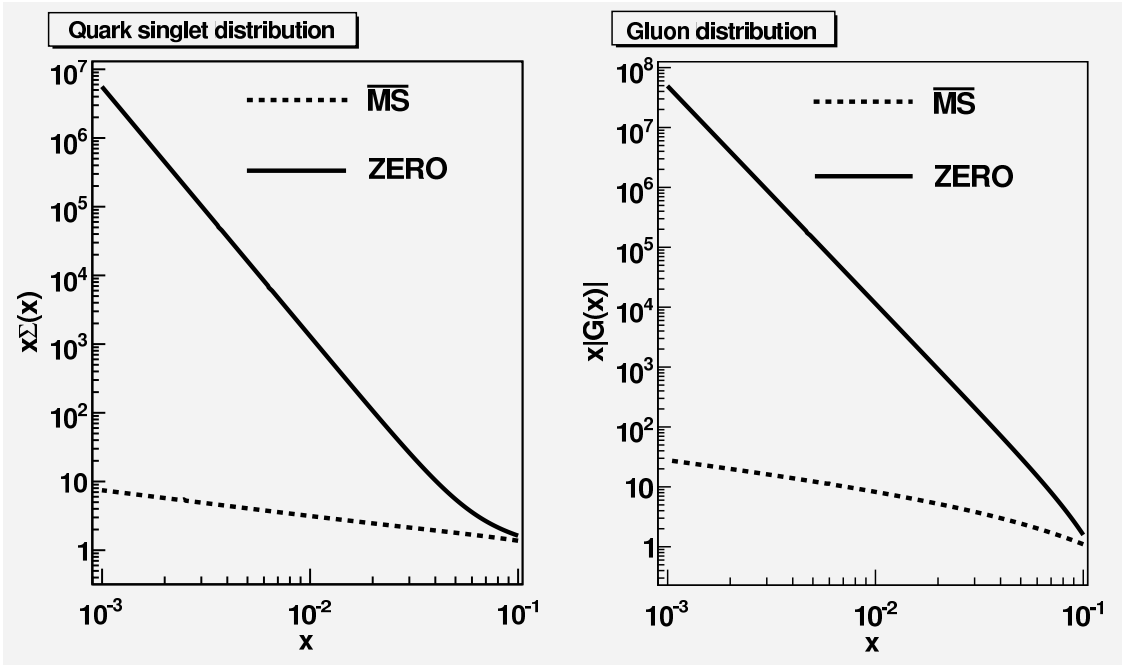


Fig. 1: Comparison of the ZERO and $\overline{\rm MS}$ parton distributions at $M = 50\,{\rm GeV}$. The $\overline{\rm MS}$ distributions were obtained by evolving the starting distributions of the MRST98 set [3] with the fixed number of active flavours $n_{\rm f} = 3$ (only light flavours are taken into account). The ZERO distributions were calculated from the $\overline{\rm MS}$ ones by using a numerical transformation method based on Mellin moments. Note that the gluon distributions are plotted in their absolute value because the ZERO gluon distribution is negative in the displayed region. The zero point where the ZERO gluon distribution changes the sign is close to $x = 0.1$.

4 Summary and conclusion

The ZERO factorization scheme is optimal for Monte Carlo simulations of NLO initial state parton showers. However, because of the problems with large numbers, this scheme has too little range of applicability in numerical calculations. The ZERO factorization scheme should thus be replaced by some "almost ZERO" factorization scheme which is sufficiently close to the ZERO factorization scheme and is free of problems with large numbers. Searching for such a factorization scheme has already been started.

Acknowledgments. The author would like to thank J. Chýla for careful reading of this contribution and valuable suggestions. This work was supported by the projects LC527 of Ministry of Education and AVOZ10100502 of the Academy of Sciences of the Czech Republic.

References

[1] G. Altarelli, R.K. Ellis and G. Martinelli, Nucl. Phys. **B143**, 521 (1978).

[2] P. Anandam and D.E. Soper, Phys. Rev. **D61**, 094003 (2000).

[3] A.D. Martin, R.G. Roberts, W.J. Stirling and R.S. Thorne, Eur. Phys. J. **C4**, 463 (1998).

Review on recent developements in jet finding

Juan Rojo
LPTHE, UPMC – Paris 6 and Paris-Diderot – Paris 7, CNRS UMR 7589, Paris (France)
INFN, Sezione di Milano, Via Celoria 16, I - 20133, Milano (Italy)
DOI: http://dx.doi.org/10.3204/DESY-PROC-2009-01/49

Abstract
We review recent developements related to jet clustering algorithms and jet finding. These include fast implementations of sequential recombination algorithms, new IRC safe algorithms, quantitative determination of jet areas and quality measures for jet finding, among many others. We also briefly discuss the status of jet finding in heavy ion collisions, where full QCD jets have been measured for the first time at RHIC.

Recent developements in jet algorithms With the upcoming start-up of the LHC, jet finding techniques have received considerable attention. In this brief review, we outline some of the most important developements in jet algorithms and related subjects in the recent years. Much more detailed reviews can be found in [1, 2].

An important developement has been the fast implementation of the k_T [3] and Cambridge/Aachen [4, 5] jet algorithms. Prior to 2005, existing implementations scaled as N^3, with N the number of particles to be clustered, thus making it unpractical for high multiplicity collisions like pp at the LHC and even more in Heavy Ions Collisions (HIC). Thanks to computational geometry methods, the performance of these algorithms was made to scale as $N \ln N$ [6]. These fast implementations are available through the `FastJet` package [7], together with area-based subtraction methods and plugins to external jet finders (see below).

Another important achievement has been the formulation of a practical (scaling as $N^2 \ln N$) infrared and collinear (IRC) safe cone algorithm, SISCone [8]. Unlike all other commonly used cone algorithms, SISCone is IRC safe to all orders in perturbation theory by construction. This property allows one to compare any perturbative computation with experimental data, which for IRC unsafe algorithms is impossible beyond some fixed order, indicated in Fig. 2. As discussed in [8], the phenomenological implications of SISCone when compared with the (IRC unsafe) commonly used MidPoint cone algorithm range from few percent differences in the inclusive jet spectrum, somewhat larger in the presence of realistic Underlying Event (UE), up to 50% differences for more exclusive observables, like the tails of jet-mass spectra in multi-jet events.

There has been historically some confusion about the concept of the *size* of a jet, specially since the naive jet area is ambiguous beyond LO. The situation was recently clarified by the introduction of quantitative definitions of jet areas based on the *catchment* properties of hard jets with respect to very soft particles, called *ghosts* in [9]. Examples of jet areas defined with such a technique are shown in Fig. 1. On top of their theoretical importance, jet areas have important applications related to the subtraction of soft backgrounds coming from the UE or from Pile-Up (PU), both in pp and in AA collisions, as discussed in [10].

Another recently developed IRC safe jet algorithm is the anti-k_t algorithm [11]. This algorithm is related to k_T and Cam/Aa by its distance measure, $d_{ij} \equiv \min(k_{ti}^{2p}, k_{tj}^{2p})\Delta R_{ij}^2/R^2$, with $p = -1$ ($p = 1$ corresponds to k_T and $p = 0$ to Cam/Aa). The anti-k_T algorithm has the property of being soft-resilient, that is, due to its distance soft particles are always clustered with hard particles first. This property leads to rather regular jet areas, which become perfectly circular in the limit in which all hard particles are separated in the (y, ϕ) plane by at least a distance R, as can be seen in Fig. 1. Another important advantage of the anti-k_t algorithm is that it has a very small back-reaction [9], that is, the presence of a soft background has reduced effects on which hard particles are clustered into a given jet.

The recent progress in jet algorithms can be summarized in Fig. 2. Each IRC unsafe cone jet algorithm can now be replaced by the corresponding IRC safe one, with a similar physics performance, shown in the last column of Fig. 2. SISCone is the natural IRC safe replacement for MidPoint-type iterative cone algorithms with split-merge (IC-SM), while anti-k_T is so for iterative cone algorithms of the progressive removal (IC-PR) type [1].

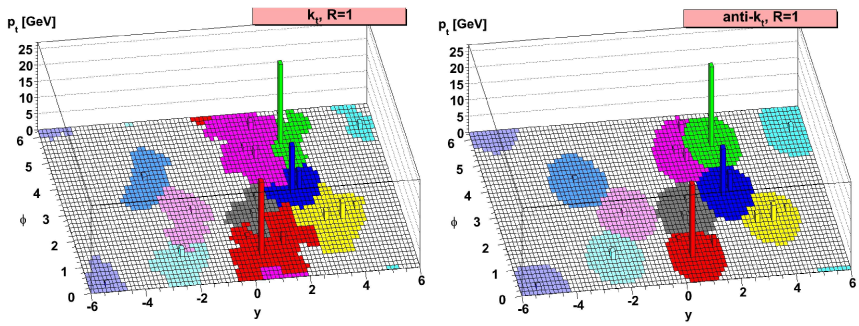


Fig. 1: Jet areas for the k_t (left) and anti-k_t (right) algorithms for $R = 1$.

This brief review is unable to cover many other interesting developements related to jets and jet finding in the recent years. Some of those not discussed here include the use of jet substructure as a useful technique to improve signal significance in various channels at the LHC (see for example [12–14]), analytical studies of the interplay between perturbative and non-perturbative effects in jet finding [15], the infrared safe definition of jet flavour and its application to precision predictions for $b-$jets at hadron colliders [16, 17] or the impact of jet measurements, both at the Tevatron and at HERA, in global analysis of PDFs [18, 19].

Performance of jet algorithms at LHC A recurring question in jet studies is "what is the best jet definition for a given specific analysis"? Most existing techniques either use as a reference unphysical Monte Carlo partons (an ambiguous concept beyond LO) and/or assume some shape for the measured kinematical distributions. To overcome these disadvantages, a new strategy to quantify the performance of jet definitions in kinematic reconstruction tasks has been recently introduced [20], which is designed to make use exclusively of physical observables.

In Ref. [20] two quality measures respecting the above requirements are proposed, and applied to the kinematic reconstruction of invariant mass distributions in dijet events for a wide

Algorithm	Type	IRC status	Evolution
exclusive k_t	$SR_{p=1}$	OK	$N^3 \to N \ln N$
inclusive k_t	$SR_{p=1}$	OK	$N^3 \to N \ln N$
Cambridge/Aachen	$SR_{p=0}$	OK	$N^3 \to N \ln N$
Run II Seedless cone	SC-SM	OK	$\to$ SISCone
CDF JetClu	IC_r-SM	IR_{2+1}	[$\to$ SISCone]
CDF MidPoint cone	IC_{mp}-SM	IR_{3+1}	$\to$ SISCone
CDF MidPoint searchcone	$IC_{se,mp}$-SM	IR_{2+1}	[$\to$ SISCone]
D0 Run II cone	IC_{mp}-SM	IR_{3+1}	$\to$ SISCone [with p_t cut?]
ATLAS Cone	IC-SM	IR_{2+1}	$\to$ SISCone
PxCone	IC_{mp}-SD	IR_{3+1}	[little used]
CMS Iterative Cone	IC-PR	$Coll_{3+1}$	$\to$ anti-k_t
PyCell/CellJet (from Pythia)	FC-PR	$Coll_{3+1}$	$\to$ anti-k_t
GetJet (from ISAJET)	FC-PR	$Coll_{3+1}$	$\to$ anti-k_t

SR = seq.rec.; IC = it.cone; FC = fixed cone;
SM = split–merge; SD = split–drop; PR = progressive removal

Fig. 2: Summary of the progress in jet algorithms since 2005.

range of energies. These quality measures can in turn be mapped into an effective luminosity ratio, defined as

$$\rho_{\mathcal{L}}(\mathrm{JD}_2/\mathrm{JD}_1) \equiv \frac{\mathcal{L}(\text{needed with JD}_2)}{\mathcal{L}(\text{needed with JD}_1)} = \left[\frac{\Sigma\,(\mathrm{JD}_1)}{\Sigma\,(\mathrm{JD}_2)}\right]^2 . \tag{1}$$

Given a certain signal significance Σ with jet definition JD_2, $\rho_{\mathcal{L}}(\mathrm{JD}_2/\mathrm{JD}_1)$ indicates the factor more luminosity needed to obtain the same significance as with jet definition JD_1.

The results of [20] over a large range of jet definitions,[1] summarized in Fig. 3, indicate that for gluon jets, and in general for TeV scales, there are significant benefits from using larger radii that those commonly used, up to $R \gtrsim 1$. In general, SISCone and C/A-filt (Cam/Aa supplemented with a filtering procedure [12]) show the best performance. These conclusions are robust in the presence of high-luminosity PU, when subtracted with the jet area technique [10].

Jet finding in AA collisions at RHIC and LHC While QCD jets are ubiquitous in pp collisions, until this year no real jet reconstruction had been obtained in the much more challenging environment of HIC. Indeed, usually in HIC one refers to the leading particle of the event as a *jet*. However, reconstructing full QCD jets provides a much more precise window to the properties of the hot and dense medium created in the collision than just leading particles.

The difficulty in reconstructing jets in HIC stems from the huge backgrounds, which need to be subtracted in order to compare with baseline results. There are various techniques to subtract such large backgrounds. In [10] it was shown how the `FastJet` jet area method could efficiently subtract such backgrounds in HIC at the LHC with a good accuracy (see Fig. 4).

A major breakthrough in jet finding was the recent first measurement of QCD jets in HIC by the STAR collaboration at RHIC [22]. In Fig. 4 we show their measurement with the k_T

[1] There results can also be accessed through an interactive web tool [21] which allows the user to compare the jet finding quality for a wide range of parameters (jet algorithm, R, value of PU, ...).

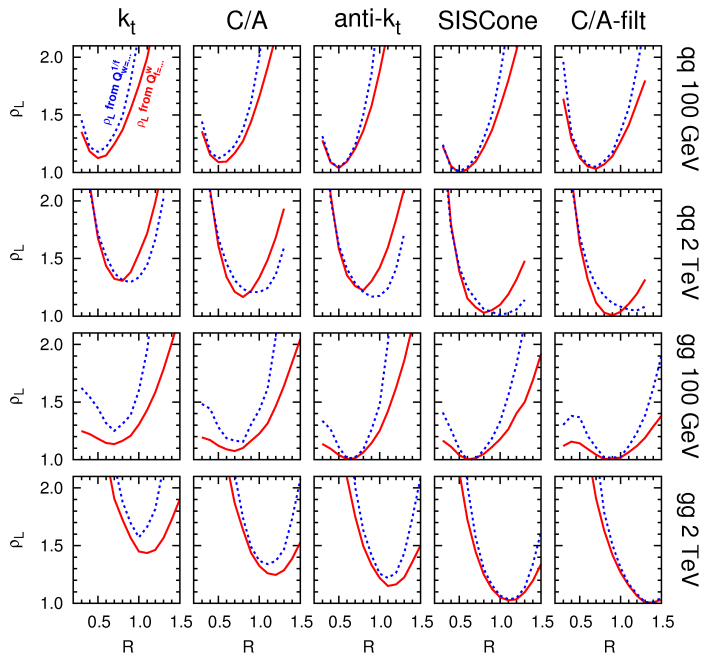


Fig. 3:
The effective luminosity ratio, Eq. 1, for quark and gluon jets at 100 GeV and 2 TeV [20].

algorithm. These results should have important consequences for understanding the medium properties in HIC.

It would be important, after these initial measurements, to improve the control on the accuracy of the subtraction procedure, as well as to understand the differences between the performances of different jet algorithms. Ongoing studies [23] suggest that one of the important sources of systematic error in the HIC jet reconstruction is back-reaction [9], therefore anti-k_t is potentially interesting in this situation due to its small back-reaction [11]. Ref. [23] also investigates how the use of local ranges for the determination of the background level ρ might help reducing the effects of point-to-point background fluctuations. However, more work is still required in order to determine the optimal settings for jet finding in HIC.

Outlook Jet finding has seen a large number of important developements in the recent years, However, there is still room for more progress, which should be driven by the actual requirements of LHC data analysis. Jet finding will also be essential to exploit the heavy-ion program at the LHC as proved by the latest RHIC jet measurements.

Acknowledgments This work has been supported by the grant ANR-05-JCJC-0046-01 (France). The author wants to acknowledge M. Cacciari, G. Salam and G. Soyez for help and material while preparing this review.

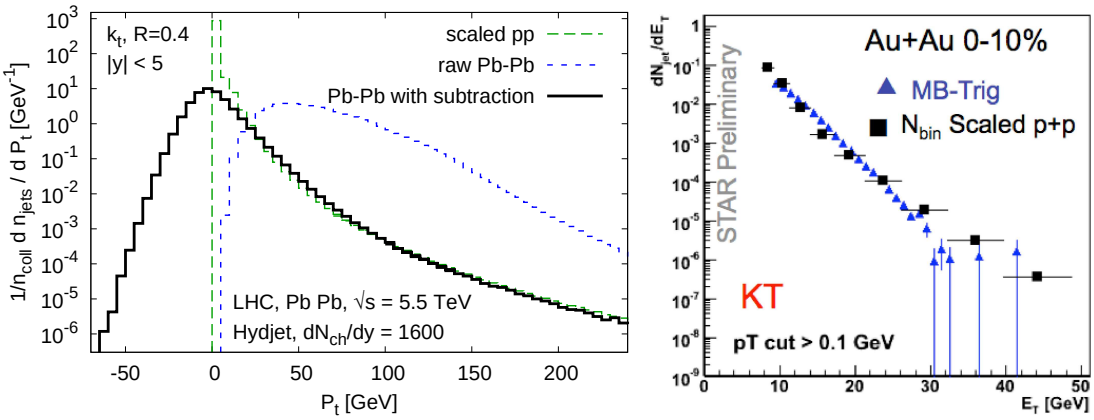


Fig. 4:
Left: the simulated inclusive jet spectrum at the LHC with the k_T algorithm, including subtraction, from [10]. Right: the inclusive jet spectrum measured with k_T by STAR at RHIC, from [22].

References

[1] C. Buttar *et al.* (2008). 0803.0678 [hep-ph].

[2] S. D. Ellis, J. Huston, K. Hatakeyama, P. Loch, and M. Tonnesmann, Prog. Part. Nucl. Phys. **60**, 484 (2008). 0712.2447.

[3] S. Catani, Y. L. Dokshitzer, M. H. Seymour, and B. R. Webber, Nucl. Phys. **B406**, 187 (1993).

[4] S. Catani, Y. L. Dokshitzer, M. Olsson, G. Turnock, and B. R. Webber, Phys. Lett. **B269**, 432 (1991).

[5] M. Wobisch and T. Wengler (1998). hep-ph/9907280.

[6] M. Cacciari and G. P. Salam, Phys. Lett. **B641**, 57 (2006). hep-ph/0512210.

[7] M. Cacciari, G. P. Salam, and G. Soyez (2005-2008). http://www.lpthe.jussieu.fr/∼salam/fastjet.

[8] G. P. Salam and G. Soyez, JHEP **05**, 086 (2007). 0704.0292 [hep-ph].

[9] M. Cacciari, G. P. Salam, and G. Soyez, JHEP **04**, 005 (2008). 0802.1188.

[10] M. Cacciari and G. P. Salam, Phys. Lett. **B659**, 119 (2008). 0707.1378.

[11] M. Cacciari, G. P. Salam, and G. Soyez, JHEP **04**, 063 (2008). 0802.1189.

[12] J. M. Butterworth, A. R. Davison, M. Rubin, and G. P. Salam, Phys. Rev. Lett. **100**, 242001 (2008). 0802.2470.

[13] D. E. Kaplan, K. Rehermann, M. D. Schwartz, and B. Tweedie, Phys. Rev. Lett. **101**, 142001 (2008). 0806.0848.

[14] J. Thaler and L.-T. Wang, JHEP **07**, 092 (2008). 0806.0023.

[15] M. Dasgupta, L. Magnea, and G. P. Salam, JHEP **02**, 055 (2008). 0712.3014.

[16] A. Banfi, G. P. Salam, and G. Zanderighi, Eur. Phys. J. **C47**, 113 (2006). hep-ph/0601139.

[17] A. Banfi, G. P. Salam, and G. Zanderighi, JHEP **07**, 026 (2007). 0704.2999.

[18] NNPDF Collaboration, R. D. Ball *et al.* (2008). 0808.1231.

[19] P. M. Nadolsky *et al.*, Phys. Rev. **D78**, 013004 (2008). 0802.0007.

[20] M. Cacciari, J. Rojo, G. P. Salam, and G. Soyez (2008). 0810.1304.

[21] M. Cacciari, J. Rojo, G. P. Salam, and G. Soyez (2008), http://quality.fastjet.fr/.

[22] STAR Collaboration, S. Salur (2008). 0809.1609.

[23] M. Cacciari, J. Rojo, G. P. Salam, and G. Soyez , in preparation.

Multi-particle production and TMD distributions

F. Hautmann
Theoretical Physics Department, University of Oxford, Oxford OX1 3NP
DOI: http://dx.doi.org/10.3204/DESY-PROC-2009-01/51

Abstract
We present a brief discussion on the application of transverse-momentum dependent (TMD) parton distributions to jet physics and parton showers.

1 Introduction

The interpretation of experimental data for multi-particle final states at the Large Hadron Collider will rely both on perturbative calculations for multi-leg scattering amplitudes and on realistic event simulation by parton-shower Monte Carlo generators.

Owing to the complex kinematics involving multiple hard scales and the large phase space opening up at very high energies, high-multiplicity events are potentially sensitive to effects of QCD initial-state radiation that depend on the finite transverse-momentum tail of partonic matrix elements and distributions. These effects are not included in the branching algorithms of standard shower Monte Carlo event generators, based on collinear jet evolution. On the other hand, they are taken into account only partially in perturbative fixed-order calculations, order-by-order through higher-loop contributions. Such effects are present to all orders in α_s and can become logarithmically enhanced at high energy.

The phenomenological significance of finite-$k_\perp$ corrections to parton showers is largely associated with effects of coherence of multiple gluon emission for small parton momentum fractions. This report discusses results of implementing these effects in Monte Carlo calculations by using coherent-branching methods based on transverse momentum dependent (TMD) distributions and matrix elements.

2 Parton showers and color coherence effects

The approach of standard parton-shower event generators, such as HERWIG and PYTHIA, relies on the dominance of collinear gluon emission. The evolution of jets developing from the hard event (both "forwards" and "backwards") is described in the first approximation through radiation of gluons predominantly at small angle from highly energetic partonic lines.

Besides collinear, incoherent emission the approach of these generators also incorporates coherent soft-gluon emission from partonic lines carrying longitudinal momentum fraction x of order 1. The phenomenological relevance of these contributions has been emphasized by extensive collider data studies [1]. An example [1] based on recent Tevatron data for $p\bar{p}$ jet fragmentation is shown in Fig. 1. This illustrates the comparison of theory predictions with and without color coherence effects with di-jet Tevatron data and with earlier e^+e^- and e^+p data.

However at the LHC, due to the phase space opening up for large center-of-mass energies, jet production enters a new regime with a great many events characterized by multiple hard

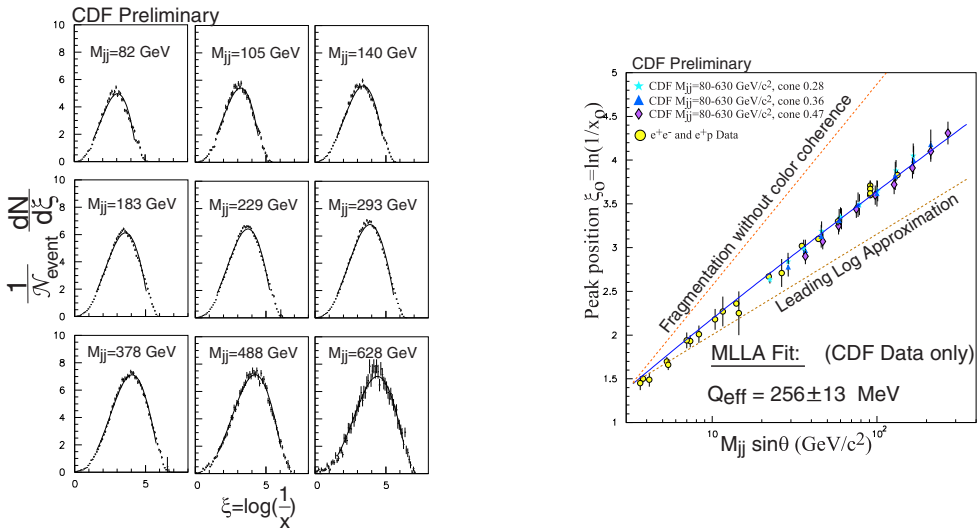


Fig. 1: Comparison [1] of predictions including soft-gluon coherence with jet fragmentation data at the Tevatron.

scales, in which (a) effects of emissions that are not collinearly ordered become increasingly non-negligible, and (b) coherence effects set in from space-like partons carrying momentum fractions $x \ll 1$. These effects are not included in standard shower Monte Carlo generators.

The theoretical framework to take account of non-collinear emission and coherence in the space-like branching requires the introduction of partonic distributions unintegrated not only in the longitudinal momenta but also in the transverse momenta [2–4]. The corrections to collinear ordering correspond to higher-order radiative terms [5, 6] in the associated jet distributions that are logarithmically enhanced in the ratio $\sqrt{s}/E_T$ of the total energy $\sqrt{s}$ to the jet transverse energy. We next turn to these corrections and discuss their role in a few examples.

3 TMD distributions

The investigation of how to define transverse-momentum dependent (TMD), or unintegrated, parton distribution functions (Fig. 2) has been the subject of much activity in the last few years. See for instance reviews and references in [2–4]. In the general case, to characterize such distributions gauge-invariantly over the whole phase space is a difficult question, and a number of open issues remain. In the case of small x, TMD distributions can be introduced in a gauge-invariant manner using high-energy factorization [5].

This result was used early on both for Monte-Carlo simulations [6] of $\mathrm{x} \to 0$ parton showers and for numerical resummation programs [7] for $\ln$ x corrections to QCD evolution equations [8]. For structure function's evolution, methods are being developed [9] to match the $\mathrm{k}_\perp$-dependent, small-x dynamics with perturbative collinear dynamics. For the full simulation of exclusive components of hadronic final states, on the other hand, such matching is more complex, and will be critical for turning present event generators based on unintegrated pdf's into

general-purpose Monte-Carlo tools [4, 10].

Observe that unintegrated pdf's may also provide a more natural framework to discuss the $k_\perp$ distribution of the soft underlying event [11] (minijets, soft hadrons), multiple interactions, and possibly the approach to the saturation regime [12, 13].

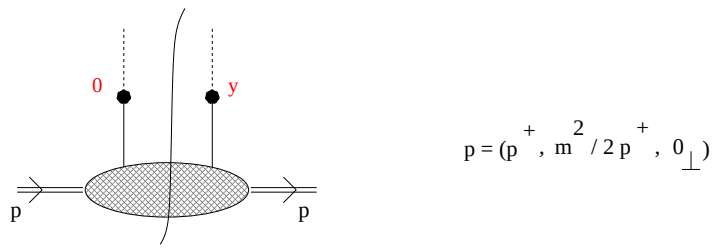


Fig. 2: Correlation function measuring the parton distribution in the target of momentum p. For TMD distributions the distance y between the two parton fields has nonzero transverse component.

It is worth noting that a physical picture of non-collinear gluon radiation that is complementary to that of TMD distributions is based on showers of color dipoles [14] and is also being applied to the initial-state jet [15]. See [16] for a study of critical issues in the relation of this approach with the parton formulation. Either at parton or dipole level, open questions involve methods for properly combining contributions from infrared regions with high-energy subgraphs. To this end we expect systematic subtraction techniques such as those in [17] to be helpful.

In the next section we give examples of Monte Carlo results implementing unintegrated distributions and applications to jet phenomenology.

4 Angular correlations in multi-jet production

The effects of coherent space-like branching based on TMD distributions are investigated in [18] for angular and momentum correlations in multi-jet final states. For a multi-jet event, consider for instance the distribution in the azimuthal angle $\Delta\phi$ between the two hardest jets. At the LHC such measurements may become accessible relatively early and be used to probe the description of complex hadronic final states by QCD and Monte Carlo generators. Experimental data on $\Delta\phi$ correlations are available from the Tevatron [19] (Fig. 3) and from Hera [20] (Fig. 4). The Tevatron measurements are dominated [18] by leading-order QCD processes, with higher radiative orders providing small corrections, and they are reasonably well described both by collinear showers (HERWIG and the new tuning of PYTHIA [19, 21]) and by fixed-order NLO calculations. The Hera $\Delta\phi$ measurements, on the other hand, are much more sensitive to higher orders in the dynamics of color emission and present a more complex case, likely to be closer to the situation at the LHC.

In particular, it is noted in [18, 22] that di-jet $\Delta\phi$ correlations [20] are affected by sizeable sub-leading corrections, resulting in large theoretical uncertainties at NLO. Analogous effects are

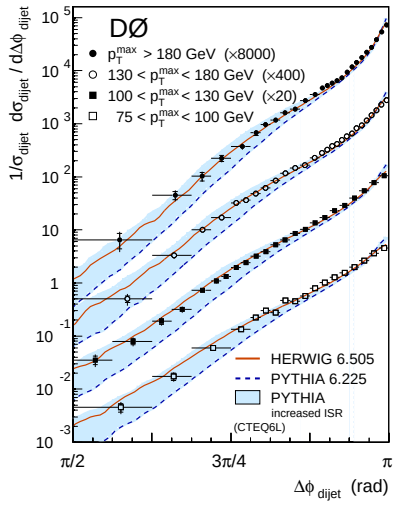


Fig. 3: Dijet azimuthal correlations measured by D0 along with the HERWIG and PYTHIA results [19].

observed in the three-jet cross section [20] particularly for the small-$\Delta\phi$ and small-x bins. The large corrections arise from regions with three well-separated hard jets in which the parton lines in the initial state decay chain are not ordered in transverse momentum. These corrections can be treated and summed to all orders, including coherence effects, by parton branching [18], using matrix elements and distributions at fixed transverse momentum $k_\perp$ according to the factorization [5]. Fig. 4 compares $k_\perp$-shower (CASCADE) and collinear-shower (HERWIG) results with the measurements [20] for the jet distributions in the azimuthal separation $\Delta\phi$ (left hand side) and in the transverse momentum imbalance $\Delta p_T^{1,2}/(2E_T^1)$ (right hand side) between the highest E_T jets.

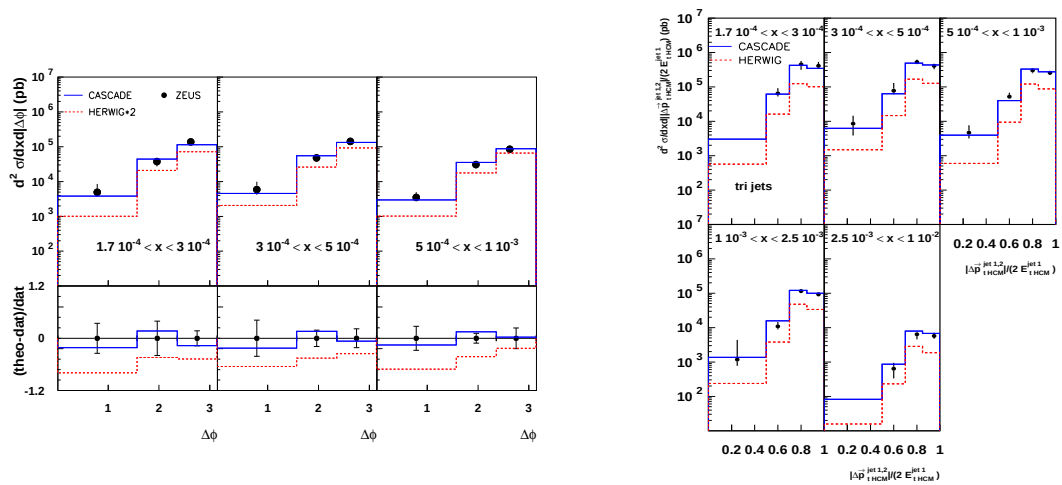


Fig. 4: (left) Angular correlations and (right) momentum correlations [18] in three-jet final states measured by [20], compared with k-shower (CASCADE) and collinear-shower (HERWIG) Monte Carlo results.

The shape of the distributions is described reasonably well by the $k_\perp$-shower, while HER-

WIG is not sufficient to describe the measurements at small $\Delta\phi$ and small Δp_T. In particular, in the plot on the left in Fig. 4 we multiply the HERWIG result by a constant factor equal to 2, which is the K-factor needed to get the normalization approximately correct in the two-jet region [18]. Still we see a noticeable difference in the shape for the three-jet cross section.

We observe that the interpretation of the jet correlation data in terms of corrections to collinear ordering is consistent with the finding [20] that while inclusive jet rates are reliably predicted by NLO fixed-order results, NLO predictions are affected by large corrections to di-jet azimuthal distributions (going from $\mathcal{O}(\alpha_s^2)$ to $\mathcal{O}(\alpha_s^3)$) in the small-$\Delta\phi$ and small-x region, and begin to fall below the data for three-jet distributions in the smallest $\Delta\phi$ bins.

The coherence effects that we have encoded in the unintegrated pdf's and matrix elements show up in the region of small $\Delta\phi$. At large $\Delta\phi$, on the other hand, the physical picture may be affected by further dynamical features. The physics of non-abelian Coulomb phase [23] can lead to quantitative effects, possibly giving rise to high-order logarithms by Coulomb/radiative mixing terms [24]. Also, contributions from endpoint singularities [10, 25, 26] affect the large-x behavior at fixed $k_\perp$. More investigations in these areas are warranted.

5 Further applications

Besides jet final states, the corrections to collinear-ordered showers that we are discussing also affect heavy mass production, including final states with heavy bosons and heavy flavor.

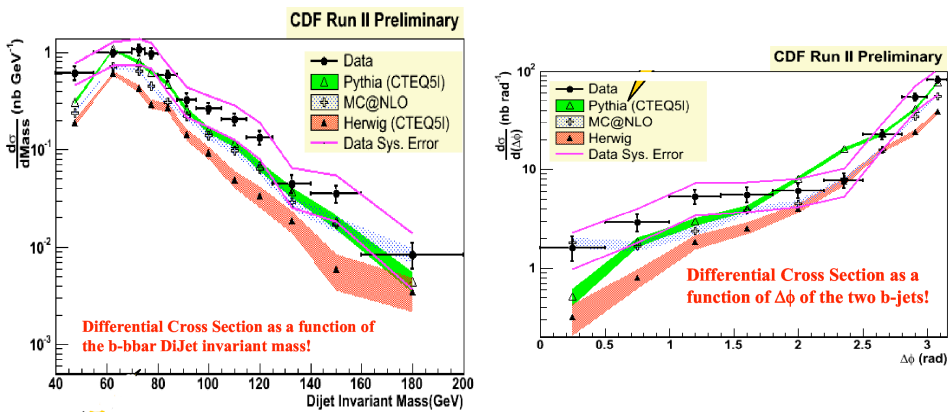


Fig. 5: Distributions in di-jet invariant mass and azimuthal separation for b-jet production at the Tevatron [1].

An example is provided by bottom-quark production. Going from the Tevatron to the LHC [27] implies a sharp increase in the relative fraction of events dominated by the $g \to b\,\bar{b}$ subprocess coupling to the spacelike jet. This is bound to affect the reliability of shower calculations based on collinear ordering (as well as the stability of NLO perturbative predictions), as these do not properly account for contributions of $b\,\bar{b}$ in association with two hard jets, with p_t of the heavy quark pair large compared to the bottom-quark mass but small compared to the transverse momenta of the individual associated jets. These kinematic regions are the analogue of the regions unordered in $k_\perp$ considered earlier for jet correlations. The contribution of unordered configurations coupling to $g \to b\,\bar{b}$ will reduce the numerical stability of collinear-based predictions (NLO, or parton-shower, or their combination [28]) with respect to renormaliza-

tion/factorization scale variation in the case of LHC. On the other hand, these are precisely the configurations that the $k_\perp$ Monte Carlo shower is designed to treat.

Distributions of b-jets in invariant mass and azimuthal separation are being studied at the Tevatron. Collinear-shower descriptions of the data in Fig. 5 [1] do not appear to be fully satisfactory especially at small $\Delta\phi$. Phenomenological studies including $k_\perp$-showers would be interesting. As noted earlier, this may also affect the underlying event description.

Even more complex multi-scale effects than those discussed so far are expected [29] in the associated production of bottom quark pairs and W/Z bosons [30], and possibly in final states with Higgs bosons [31] especially for measurements of the less inclusive distributions and correlations. Vector boson production probes quark-initiated channels [32, 33] and is relevant for early phenomenology at the LHC, as the possible broadening of W and Z p_T distributions [34] affects the use of these processes as luminosity monitor [35].

The use of forward detectors at the LHC will allow one to measure correlations between hard events across large rapidity intervals. Such rapidity correlations are sensitive to coherent multi-gluon states emitted without any strong ordering in transverse momenta. An example of these effects is investigated in the study in progress [36] for high-p_T jets in the LHC forward region.

References

[1] B. R. Webber, CERN Academic Training Lectures (2008).

[2] J. C. Collins (2001). hep-ph/0106126.

[3] T. C. Rogers (2007). arXiv:0712.1195 [hep-ph].

[4] F. Hautmann and H. Jung, Nucl. Phys. Proc. Suppl. **184**, 64 (2008). arXiv:0712.0568 [hep-ph];
F. Hautmann and H. Jung, AIP Conf. Proc. **1056**, 79 (2008). arXiv:0808.0873 [hep-ph].

[5] S. Catani, M. Ciafaloni, and F. Hautmann, Phys. Lett. **B242**, 97 (1990);
S. Catani, M. Ciafaloni, and F. Hautmann, Nucl. Phys. **B366**, 135 (1991);
S. Catani, M. Ciafaloni, and F. Hautmann, Phys. Lett. **B307**, 147 (1993).

[6] G. Marchesini and B. R. Webber, Nucl. Phys. **B386**, 215 (1992).

[7] R. K. Ellis, F. Hautmann, and B. R. Webber, Phys. Lett. **B348**, 582 (1995). hep-ph/9501307.

[8] L. N. Lipatov, Phys. Rept. **286**, 131 (1997). hep-ph/9610276.

[9] G. Altarelli, R. D. Ball, and S. Forte, PoS **RADCOR2007**, 028 (2007). arXiv:0802.0968 [hep-ph];
M. Ciafaloni, PoS **RADCOR2007**, 029 (2007).

[10] F. Hautmann, Phys. Lett. **B655**, 26 (2007). hep-ph/0702196;
F. Hautmann (2007). arXiv:0708.1319 [hep-ph].

[11] G. Gustafson (2007). arXiv:0712.1941 [hep-ph].

[12] L. Motyka, K. Golec-Biernat, and G. Watt (2008). arXiv:0809.4191 [hep-ph].

[13] K. Kutak and H. Jung (2008). arXiv:0812.4082 [hep-ph].

[14] G. Gustafson, Phys. Lett. **B175**, 453 (1986).

[15] L. Lonnblad and M. Sjodahl, JHEP **05**, 038 (2005). hep-ph/0412111;
L. Lonnblad and M. Sjodahl, JHEP **02**, 042 (2004). hep-ph/0311252;
G. Gustafson, L. Lonnblad, and G. Miu, JHEP **09**, 005 (2002). hep-ph/0206195.

[16] Y. L. Dokshitzer and G. Marchesini (2008). arXiv:0809.1749 [hep-ph].

[17] J. C. Collins and F. Hautmann, JHEP **03**, 016 (2001). hep-ph/0009286;
J. C. Collins and F. Hautmann, Phys. Lett. **B472**, 129 (2000). hep-ph/9908467;
F. Hautmann, Nucl. Phys. **B604**, 391 (2001). hep-ph/0102336;
F. Hautmann (1997). hep-ph/9708496.

[18] F. Hautmann and H. Jung, JHEP **10**, 113 (2008). arXiv:0805.1049 [hep-ph].

[19] D0 Collaboration, V. Abazov *et al.*, Phys. Rev. Lett. **94**, 221801 (2005). hep-ex/0409040.

[20] ZEUS Collaboration, S. Chekanov *et al.*, Nucl. Phys. **B786**, 152 (2007). arXiv:0705.1931 [hep-ex].

[21] TeV4LHC QCD Working Group Collaboration, M. Albrow *et al.* (2006). hep-ph/0610012.

[22] F. Hautmann and H. Jung (2008). arXiv:0804.1746 [hep-ph].

[23] S. M. Aybat and G. Sterman (2008). arXiv:0811.0246 [hep-ph].

[24] J. R. Forshaw, A. Kyrieleis, and M. H. Seymour, JHEP **09**, 128 (2008). arXiv:0808.1269 [hep-ph];
M. H. Seymour (2007). arXiv:0710.2733 [hep-ph].

[25] J. C. Collins, in Perturbative QCD (ed. A. Mueller), p. 573 (1989).

[26] I. O. Cherednikov and N. G. Stefanis, Nucl. Phys. **B802**, 146 (2008). arXiv:0802.2821 [hep-ph];
I. O. Cherednikov and N. G. Stefanis (2007). arXiv:0711.1278 [hep-ph].

[27] J. Baines *et al.*, Heavy Quark Working Group: summary report (2006). hep-ph/0601164.

[28] S. Frixione, P. Nason, and B. R. Webber, JHEP **08**, 007 (2003). hep-ph/0305252.

[29] J. Bartels *et al.*, Hera-LHC Workshop Proceedings (2008);
M. Deak and F. Schwennsen, JHEP **09**, 035 (2008). arXiv:0805.3763 [hep-ph];
S. P. Baranov, A. V. Lipatov, and N. P. Zotov, Phys. Rev. **D78**, 014025 (2008). arXiv:0805.4821 [hep-ph].

[30] M. L. Mangano, Nucl. Phys. **B405**, 536 (1993).

[31] H. Jung, Mod. Phys. Lett. **A19**, 1 (2004). hep-ph/0311249;
A. Kulesza, G. Sterman, and W. Vogelsang, Phys. Rev. **D69**, 014012 (2004). hep-ph/0309264;
F. Hautmann, Phys. Lett. **B535**, 159 (2002). hep-ph/0203140.

[32] S. Marzani and R. D. Ball (2008). arXiv:0812.3602 [hep-ph].

[33] S. Catani and F. Hautmann, Nucl. Phys. **B427**, 475 (1994). hep-ph/9405388;
S. Catani and F. Hautmann, Phys. Lett. **B315**, 157 (1993).

[34] S. Berge, P. M. Nadolsky, F. I. Olness, and C. P. Yuan, AIP Conf. Proc. **792**, 722 (2005). hep-ph/0508215.

[35] A. M. Cooper-Sarkar (2007). arXiv:0707.1593 [hep-ph].

[36] M. Deak *et al.*, in progress (2008).

Bose-Einstein study of position-momentum correlations of charged pions in hadronic Z^0 decays

C. Ciocca, on behalf the OPAL Collaboration
Bologna University and INFN
DOI: http://dx.doi.org/10.3204/DESY-PROC-2009-01/76

Abstract
Bose-Einstein correlations in pairs of identically charged pions produced in e^+e^- annihilations at Z^0 peak are studied for the first time assuming a dynamic emitting source. The correlation functions are analyzed in intervals of average pair transverse momentum and pair rapidity, to investigate correlations between pion production points and momenta. The Yano-Koonin and Bertsch-Pratt parameterizations are used to estimate the source parameters and the velocity of source elements with respect to the centre-of-mass frame. The source rapidity scales with pair rapidity, and both longitudinal and transverse dimensions decrease for increasing average pair transverse momenta, in agreement with an expanding source.

1 Using BEC to obtain informations on particle source created in interactions

The space-time structure and evolution of a source emitting particles can be probed using intensity interferometry. Bose-Einstein correlations (BEC) in pairs of identical bosons have been analysed extensively for different energies and initial states, evolving from studies with one-dimensional correlation function and static source hypothesis to dynamic source and multi-dimensional refined investigations.

In the case of a dynamic source, the expansion leads to correlations between particle emission points and 4-momenta (position-momentum correlations). The correlation function depends on both the relative 4-momentum q and the average 4-momentum K of the pair: $C(p_1, p_2) = C(q, K)$ where $q = (p_1 - p_2)$ and $K = (p_1 + p_2)/2$. The measured radii correspond to regions of homogeneity in K (effective source elements) from which pions are emitted with momenta similar enough to interfere and contribute to the correlation function.

2 Analysis procedure and correlation functions

Bose-Einstein correlation are analyzed to investigate dynamical features of the pion emitting source created after e^+e^- annihilation at centre-of-mass energy of about 91 GeV. Results are based on the high statistics data obtained with the OPAL detector at LEP. All details of the analysis can be found in [1]. Three-dimensional correlations are measured as functions of two different sets of components of the pair 4-momentum difference q, in two suitable frames, to be fitted by two parametrizations of interest. The first set, $(Q_\ell, Q_{\mathrm{t_{side}}}, Q_{\mathrm{t_{out}}})$, is evaluated in the Longitudinally CoMoving System (LCMS) [2] and the second set, $(q_\mathrm{t}, q_\ell, q_0)$, in the center-of-mass frame (CMS). Experimentally, the correlation functions C are defined, in a small phase space volume

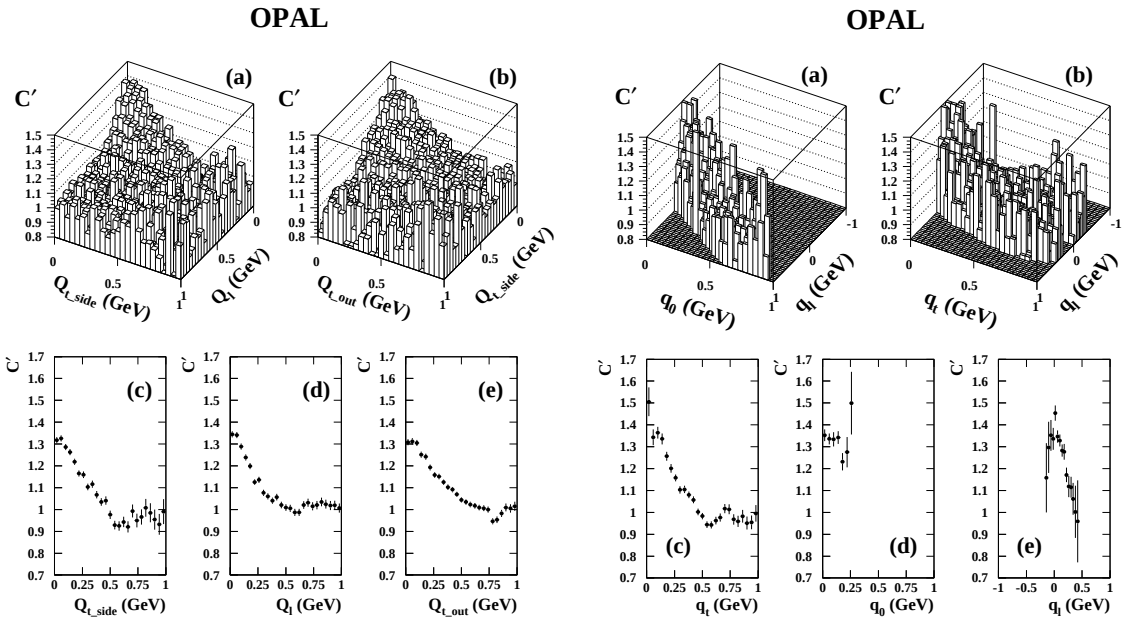


Fig. 1: Projections of correlation functions $C'(Q_\ell, Q_{\mathrm{t_{side}}}, Q_{\mathrm{t_{out}}})$ (left) and $C'(q_\mathrm{t}, q_\ell, q_0)$ (right) in bin $0.8 \leq |Y| < 1.6$ and 0.3 GeV $\leq k_\mathrm{t} <$ 0.4 GeV, obtained for low values ($<$ 0.2 GeV) of the remaining variables.

around each triplet of variables, as number of like-charge pairs divided by number of unlike-charge pairs. To reduce distorsions due to long-range correlations and pions from resonance decays, the double ratio C' of C in data and in a sample of Monte Carlo events without BEC, $C' = C^{\mathrm{DATA}}/C^{\mathrm{MC}}$, is introduced. The dependence of $C'(Q_\ell, Q_{\mathrm{t_{side}}}, Q_{\mathrm{t_{out}}})$ and $C'(q_\mathrm{t}, q_\ell, q_0)$ on K is analyzed by selecting pions in intervals of two components of K, the pair rapidity and the pair average transverse momentum with respect to the event thrust direction:

$$|Y| = \frac{1}{2}\ln\left[\frac{(E_1+E_2)+(p_{\ell,1}+p_{\ell,2})}{(E_1+E_2)-(p_{\ell,1}+p_{\ell,2})}\right] \qquad k_\mathrm{t} = \frac{1}{2}\left|(\vec{p}_{\mathrm{t},1}+\vec{p}_{\mathrm{t},2})\right| \tag{1}$$

Two-dimensional and one-dimensional projections of the correlation functions are shown in Fig.1, where cuts ($<$ 0.2 GeV) are applied on other variables. Central bin corresponding to pair rapidities and transverse momenta in the intervals $0.8 \leq |Y| < 1.6$ and 0.3 GeV $\leq k_\mathrm{t} < 0.4$ GeV is chosen. BEC enhancements are visible in data at low Q_ℓ, $Q_{\mathrm{t_{side}}}$ and $Q_{\mathrm{t_{out}}}$ as q_ℓ and q_t. The range available to the variable q_0 instead is quite restricted, and no BEC peak can be observed. The condition: $[(q_\mathrm{t}^2 + q_\ell^2) - q_0^2]$ invariant > 0, and the bound on pair rapidity constrain the correlation function to be different from zero only in a limited region of (q_ℓ, q_0) plane.

3 Results from BP and YK parametrizations

Two parameterizations are used to extract source dimensions. The Bertsch-Pratt (BP) [3]

$C'(Q_\ell, Q_{\mathrm{t_{side}}}, Q_{\mathrm{t_{out}}}) =$

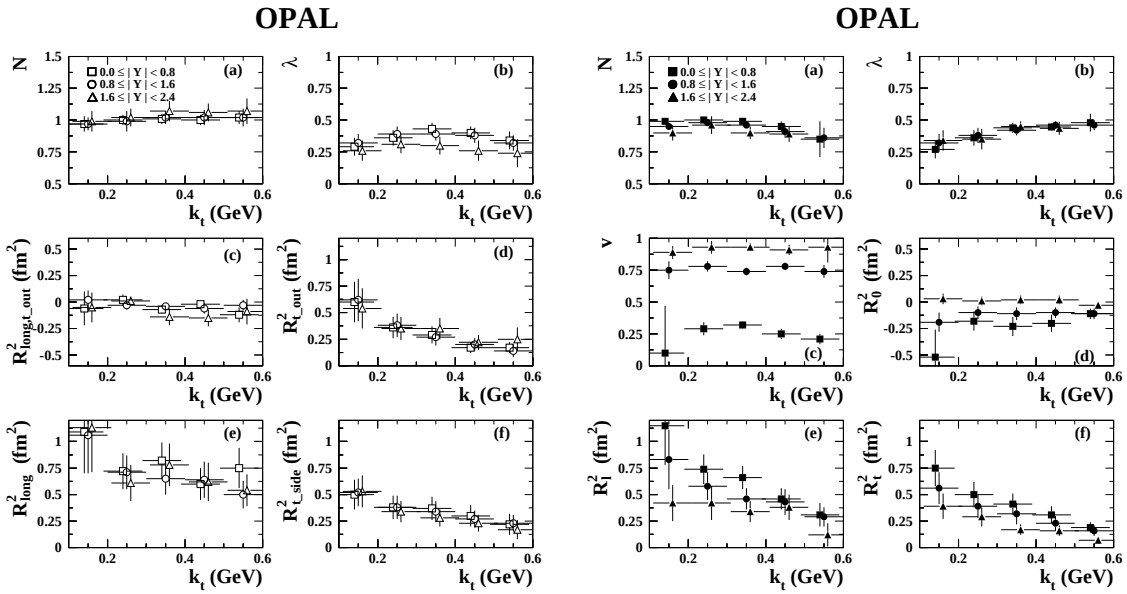


Fig. 2: Best-fit parameters of Bertsch-Pratt parameterization to correlation function $C'(Q_\ell, Q_{\mathrm{t_{side}}}, Q_{\mathrm{t_{out}}})$ (left) and of Yano-Koonin to $C'(q_\mathrm{t}, q_\ell, q_0)$ (right), as a function of k_t, for different intervals of rapidity $|Y|$. Horizontal bars represent bin widths and vertical bars include statistical and systematic errors, added in quadrature.

$$N[1+\lambda \mathrm{e}^{-(Q_\ell^2 R_{\mathrm{long}}^2 + Q_{\mathrm{t_{side}}}^2 R_{\mathrm{t_{side}}}^2 + Q_{\mathrm{t_{out}}}^2 R_{\mathrm{t_{out}}}^2 + 2Q_\ell Q_{\mathrm{t_{out}}} R_{\mathrm{long,t_{out}}}^2)}]F(Q_\ell, Q_{\mathrm{t_{side}}}, Q_{\mathrm{t_{out}}}) \qquad (2)$$

and Yano-Koonin (YK) [4]

$$C'(q_\mathrm{t}, q_\ell, q_0) = N\{1+\lambda \mathrm{e}^{-[q_\mathrm{t}^2 R_\mathrm{t}^2 + \gamma^2 (q_\ell - v q_0)^2 R_\ell^2 + \gamma^2 (q_0 - v q_\ell)^2 R_0^2]}\}F(q_\mathrm{t}, q_\ell, q_0) \qquad (3)$$

In both parameterizations, N is a normalization factor and λ measures the degree of incoherence (related to fraction of pairs that interfere). The functions $F(Q_\ell, Q_{\mathrm{t_{side}}}, Q_{\mathrm{t_{out}}}) = (1 + \epsilon_{\mathrm{long}} Q_\ell + \epsilon_{\mathrm{t_{side}}} Q_{\mathrm{t_{side}}} + \epsilon_{\mathrm{t_{out}}} Q_{\mathrm{t_{out}}})$ and $F(q_\mathrm{t}, q_\ell, q_0) = (1 + \delta_\mathrm{t} q_\mathrm{t} + \delta_\ell q_\ell + \delta_0 q_0)$, where ϵ_i and δ_i are free parameters, take into account residual long-range correlations, due to energy and charge conservation. In Eq.2, $R_{\mathrm{t_{side}}}$ and R_{long} are transverse and longitudinal radii in LCMS, $R_{\mathrm{t_{out}}}$ and the cross-term $R_{\mathrm{long,t_{out}}}$ are a combination of both spatial and temporal extentions of the source. The difference $R^2_{\mathrm{t_{out}}} - R^2_{\mathrm{t_{side}}}$ is proportional to the duration of particle emission process. In Eq.3, where $\gamma = 1/\sqrt{1-v^2}$ and $c = 1$, v is the longitudinal velocity of the source element in CMS frame, R_0 measure the duration of particle emission process, R_t and R_ℓ are transverse and longitudinal radii.

Best-fit parameters of BP and YK parametrizations to $C'(Q_\ell, Q_{\mathrm{t_{side}}}, Q_{\mathrm{t_{out}}})$ and $C'(q_\mathrm{t}, q_\ell, q_0)$ in the different $|Y|$ and k_t intervals are shown in Fig.2. BP parameters show a minor dependence on rapidity while depend on k_t. $R^2_{\mathrm{t_{side}}}$, $R^2_{\mathrm{t_{out}}}$ and, less markedly, R^2_{long} decrease with increasing k_t. The presence of correlations between particle production points and momenta indicates that source expands during emission process. R^2_{long} is larger than $R^2_{\mathrm{t_{side}}}$, in agreement with a source elongated in the direction of the event thrust axis [5]. The cross-term parameter $R^2_{\mathrm{long,t_{out}}}$ is compatible with zero, apart from a few bins at the highest rapidity interval. The difference

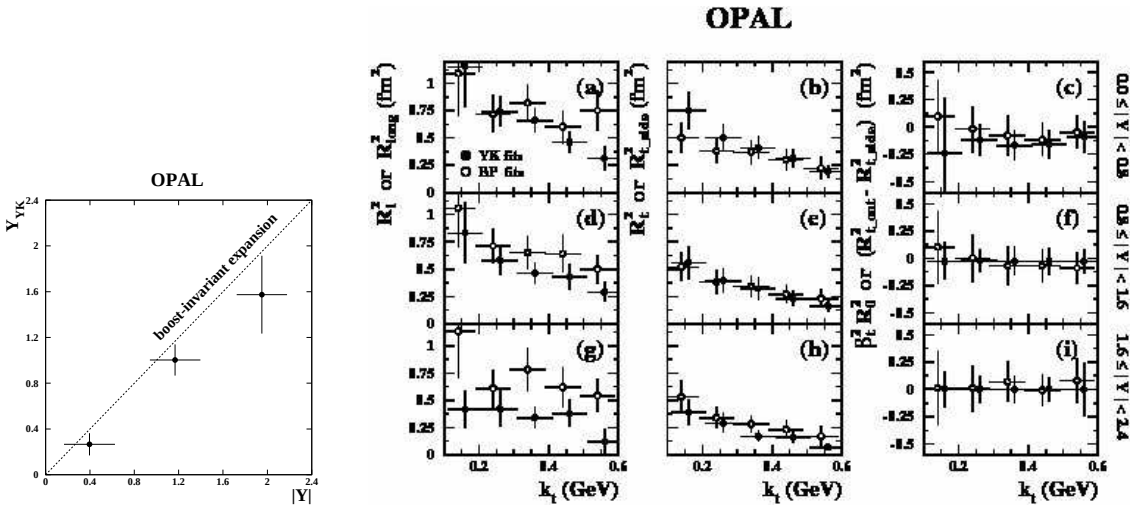


Fig. 3: Left: Yano-Koonin rapidity $Y_{\rm YK}$ as a function of pair rapidity $|Y|$. Right: BP parameters (open dots) compared with YK parameters (full dots): longitudinal radius, transverse radius and duration of emission process. Errors include statistical and systematic uncertainties, added in quadrature.

$R^2_{\rm t_{out}} - R^2_{\rm t_{side}}$ for $|Y| < 1.6$ is positive at low $k_{\rm t}$, then decreases and becomes negative for $k_{\rm t} \geq 0.3$ GeV, while in the interval $1.6 \leq |Y| < 2.4$ is compatible with zero for all $k_{\rm t}$. As a consequence, it is not possible to estimate the particle emission duration from $R^2_{\rm t_{out}} - R^2_{\rm t_{side}}$. YK parameters show dependence on both Y and $k_{\rm t}$. Both $R^2_{\rm t}$ and R^2_{ℓ} decrease with increasing $k_{\rm t}$ and $|Y|$ and R^2_{ℓ} are larger than $R^2_{\rm t}$. This agrees again with an expanding, longitudinally elongated source. R^2_0 is compatible with zero at high rapidities, and assumes negative values for $|Y| < 1.6$. This excludes an interpretation in terms of duration of particle emission process. Difficulties in achieving reliable results for R^2_0 parameter in YK fits are reported in literature [6], due to the limited phase-space available in $\gamma^2(q_0 - vq_\ell)^2$. The source velocity v does not depend on $k_{\rm t}$, but it is strongly correlated with pair rapidity. The dependence of v on $|Y|$ is presented in terms of Yano-Koonin rapidity

$$Y_{\rm YK} = \frac{1}{2} \ln \left(\frac{1+v}{1-v} \right) \tag{4}$$

as a function of pair rapidity $|Y|$, in Fig.3 (left). $Y_{\rm YK}$ measures the rapidity of the source element with respect to the centre-of-mass frame: a static source would correspond to $Y_{\rm YK} \approx 0$ for any $|Y|$ while for a boost-invariant expanding source the strict correlation $Y_{\rm YK} = |Y|$ is expected. A clear positive correlation between $Y_{\rm YK}$ and $|Y|$ is observed, even if $Y_{\rm YK} < |Y|$ at the largest pair rapidities, in agreement with a source which is emitting in a nearly boost-invariant way.

4 Comparison between BP and YK parameters

The following relations should hold between BP and YK parameters measured in LCMS and CMS frames, respectively [7]:

$$R^2_{\mathrm{t_{side}}} = R^2_{\mathrm{t}} \quad (5)$$

$$R^2_{\mathrm{long}} = \gamma^2_{\mathrm{LCMS}}(R^2_\ell + \beta^2_{\mathrm{LCMS}} R^2_0) = R^2_\ell \quad (6)$$

$$R^2_{\mathrm{t_{out}}} - R^2_{\mathrm{t_{side}}} = \beta^2_{\mathrm{t}}\gamma^2_{\mathrm{LCMS}}(R^2_0 + \beta^2_{\mathrm{LCMS}} R^2_\ell) = \beta^2_{\mathrm{t}} R^2_0 \quad (7)$$

where β_{LCMS} is the velocity of the source element measured in LCMS, $\gamma_{\mathrm{LCMS}} = 1/\sqrt{1-\beta^2_{\mathrm{LCMS}}}$ and $\beta^2_{\mathrm{t}} = \left\langle \frac{2k_{\mathrm{t}}}{E_1+E_2} \right\rangle^2$, where brackets stand for the average over all pairs in given $|Y|$ and k_{t} interval. For a boost-invariant source, $\beta_{\mathrm{LCMS}} = 0$. In Fig.3 (right), the BP parameters R^2_{long}, $R^2_{\mathrm{t_{side}}}$ and $R^2_{\mathrm{t_{out}}} - R^2_{\mathrm{t_{side}}}$ are compared with the YK parameters R^2_ℓ, R^2_{t} and $\beta^2_{\mathrm{t}}\mathrm{R}^2_0$. R^2_{long} is systematically larger than R^2_ℓ in all rapidity intervals in agreement with a source whose expansion is not exactly boost-invariant. $R^2_{\mathrm{t_{side}}} = R^2_{\mathrm{t}}$ within errors, with possible deviations at low k_{t}. The negative values of R^2_0 and $R^2_{\mathrm{t_{out}}} - R^2_{\mathrm{t_{side}}}$ appearing in the two first rapidity intervals prevent an interpretation in terms of the duration of particle emission process.

5 Conclusion and discussion

An analysis of BEC in $\mathrm{e^+e^-}$ annihilation events at $\mathrm{Z^0}$ peak performed in bins of average 4-momentum of the pair, K, is presented for the first time and dynamic features of the pion emitting source are investigated. Transverse and longitudinal radii decrease for increasing k_{t}, indicating the presence of correlations between particle production points and momenta. The Yano-Koonin rapidity scales approximately with pair rapidity, in agreement with a nearly boost-invariant expansion of the source. Limitations in the available phase space did not allow measurement of the duration of particle emission process.

Similar results are observed in more complex systems from pp and heavy-ion collisions. Negative values of R^2_0 are suggested as indicators for source opacity, i.e. surface dominated emission [8]. A similar dependence of $R^2_{\mathrm{t_{out}}} - R^2_{\mathrm{t_{side}}}$ on k_{t} is reported in heavy-ion collision experiments [9] [see Florkowski in these proceedings]. The τ model, based on Bjorken-Gottfried condition [10] predict expansion ring in transverse direction [see Csörgő and Metzger in these proceedings].

References

[1] OPAL Collaboration, G. Abbiendi *et al.,* Eur. Phys. J. **C52**, 787 (2007).

[2] T. Csörgő and S. Pratt, Proc. Workshop on Relativistic Heavy Ion Physics at Present and Future Accelerators, eds. T. Csörgő and others, Budapest **KFKI**, 75 (1991).

[3] S. Pratt, Phys. Rev. **D33**, 1314 (1986).

[4] F. Yano and S. Koonin, Phys. Lett. **B78**, 556 (1978).

[5] OPAL Collaboration, G. Abbiendi *et al.,* Eur. Phys. J. **C16**, 423 (2000).

[6] B. Tomášik and U. Heinz, Acta Physica Slovaca **49**, 251 (1999).

[7] U. Heinz, Nucl. Phys. **A610**, 264 (1996).

[8] H. Heiselberg and A. P. Vischer, Eur. Phys. J. **C1**, 593 (1998).

[9] STAR Collaboration, C. Adler *et al.,* Phys. Rev. Lett. **87**, 082301 (2001).

[10] A. Bialas *et al.,* Phys. Rev. **D62**, 114007 (2000).

Squeezed correlations among particle-antiparticle pairs

Sandra S. Padula[1]†, *Danuce M. Dudek*[1], *Otávio Socolowski Jr.*[2]
[1]IFT-UNESP, Rua Pamplona, 145, 01405-900 São Paulo, SP, Brazil,
[2]IMEF - FURG - Caixa Postal 474, 9620-900, Rio Grande, RS, Brazil

DOI: http://dx.doi.org/10.3204/DESY-PROC-2009-01/77

Abstract

The hadronic correlation among particle-antiparticle pairs was highlighted in the late 1990's, culminating with the demonstration that it should exist if the masses of the hadrons were modified in the hot and dense medium formed in high energy heavy ion collisions. They were called Back-to-Back Correlations (BBC) of particle-antiparticle pairs, also known as squeezed correlations. However, even though they are well-established theoretically, such hadronic correlations have not yet been experimentally discovered. Expecting to compel the experimentalists to search for this effect, we suggest here a clear way to look for the BBC signal, by constructing the squeezed correlation function of $\phi\phi$ and K^+K^- pairs at RHIC energies, plotted in terms of the average momentum of the pair, $\mathbf{K_{12}}=\frac{\mathbf{1}}{\mathbf{2}}(\mathbf{k_1}+\mathbf{k_2})$, inspired by procedures adopted in Hanbury-Brown & Twiss (HBT) correlations.

1 Basic Formalism

Back-to-Back Correlations (BBC) of particle-antiparticle pairs, also called hadronic squeezed correlations, were predicted to exist if their masses were modified in the hot and dense medium formed in high energy heavy ion collisions. The formalism corresponding to the bosonic case was developed in Ref. [1]. Shortly after that, similar correlations were shown to exist among fermion-antifermion pairs with in-medium modified masses [2], and they were treated by an analogous formalisms. However, in contrast to what is observed in quantum statistical correlations of identical hadrons (the HBT effect), where bosons with similar momenta have positive correlations, while fermions with similar momenta are anti-correlated, the fermionic (fBBC) and the bosonic (bBBC) Back-to-Back Correlations are both positive correlations with unlimited intensity. The similarities of the fBBC and the bBBC curves were illustrated in Fig. 1 of Ref. [2], where squeezed correlations of two ϕ-mesons and of $\bar{p}p$ were chosen as illustration. In what follows, we will focus our discussion in the bosonic case, illustrating the effect by considering $\phi\phi$ pairs, and also introducing some results on K^+K^- pairs.

In the case of ϕ-mesons (which are their own antiparticles) with in-medium modified masses, the joint probability for observing two such particles, i.e., the two-particle distribution, is written as $N_2(\mathbf{k}_1,\mathbf{k}_2)=\omega_{\mathbf{k}_1}\omega_{\mathbf{k}_2}\left[\langle a^\dagger_{\mathbf{k}_1}a_{\mathbf{k}_1}\rangle\langle a^\dagger_{\mathbf{k}_2}a_{\mathbf{k}_2}\rangle+\langle a^\dagger_{\mathbf{k}_1}a_{\mathbf{k}_2}\rangle\langle a^\dagger_{\mathbf{k}_2}a_{\mathbf{k}_1}\rangle+\langle a^\dagger_{\mathbf{k}_1}a^\dagger_{\mathbf{k}_2}\rangle\langle a_{\mathbf{k}_2}a_{\mathbf{k}_1}\rangle\right]$, after applying a generalization of Wick's theorem for locally equilibrated systems. The first term corresponds to the product of the spectra of the two ϕ's, $N_1(\mathbf{k}_i)=\omega_{\mathbf{k}_i}\frac{d^3N}{d\mathbf{k}_i}=\omega_{\mathbf{k}_i}\langle a^\dagger_{\mathbf{k}_i}a_{\mathbf{k}_i}\rangle$, being $a^\dagger_{\mathbf{k}}$ and $a_{\mathbf{k}}$ the free-particle creation and annihilation operators of the scalar quanta, and $\langle\ldots\rangle$

† speaker

means thermal averages. The second term contains the identical particle contribution which, together with the first term, gives rise to the femtoscopic (or Hanbury-Brown & Twiss) effect, and is represented by the square modulus of the so-called chaotic amplitude, $G_c(\mathbf{k}_1,\mathbf{k}_2) = \sqrt{\omega_{\mathbf{k}_1}\omega_{\mathbf{k}_2}}\,\langle a^\dagger_{\mathbf{k}_1} a_{\mathbf{k}_2}\rangle$. The third term, when written as the square modulus of the squeezed amplitude, $G_s(\mathbf{k}_1,\mathbf{k}_2) = \sqrt{\omega_{\mathbf{k}_1}\omega_{\mathbf{k}_2}}\,\langle a_{\mathbf{k}_1} a_{\mathbf{k}_2}\rangle$, is identically zero in the absence of in-medium mass-shift. However, if the masses of the particles are modified, it gives rise to the squeezed correlation function, together with the first term. In summary, in terms of these amplitudes, the $\phi\phi$ correlation function can be written as

$$C_2(\mathbf{k}_1,\mathbf{k}_2) = 1 + \frac{|G_c(\mathbf{k}_1,\mathbf{k}_2)|^2}{G_c(\mathbf{k}_1,\mathbf{k}_1)G_c(\mathbf{k}_2,\mathbf{k}_2)} + \frac{|G_s(\mathbf{k}_1,\mathbf{k}_2)|^2}{G_c(\mathbf{k}_1,\mathbf{k}_1)G_c(\mathbf{k}_2,\mathbf{k}_2)}, \qquad (1)$$

the first two terms corresponding to the identical particle (HBT) correlation, whereas the first and the last terms represent the correlation function between the particle and its antiparticle, i.e., the squeezed part. In the case of charged mesons, as in the K^+K^-, only the first and the last terms contribute to the squeezed correlation, if their masses change.

In the definition of the amplitudes $G_c(\mathbf{k}_i,\mathbf{k}_j)$ and $G_s(\mathbf{k}_i,\mathbf{k}_j)$, the annihilation (creation) operator of the asymptotic, observed bosons with momentum $k^\mu=(\omega_k,\mathbf{k})$, i.e., a ($a^\dagger$), is related to the in-medium annihilation (creation) operator b ($b^\dagger$), corresponding to thermalized quasi-particles, by the Bogoliubov-Valatin transformation,

$$a_k = c_k b_k + s^*_{-k} b^\dagger_{-k} \;\;;\;\; a^\dagger_k = c^*_k b^\dagger_k + s_{-k} b_{-k} \;\;;\;\; f_{i,j}(x) = \frac{1}{2}\log\left[\frac{K^\mu_{i,j}(x)\,u_\mu(x)}{K^{*\nu}_{i,j}(x)\,u_\nu(x)}\right]. \qquad (2)$$

In Eq. (2), $c_k \equiv \cosh(f_k)$, $s_k \equiv \sinh(f_k)$. The argument, f_k, is called *squeezing parameter*, since the transformation in Eq. (2) is equivalent to a squeezing operation. The in-medium modified mass, m_*, is related to the asymptotic mass, m, by $m^2_*(|\mathbf{k}|) = m^2 - \delta M^2(|\mathbf{k}|)$. Although in the general case m_* could be momentum-dependent, it is here assumed to be a constant mass-shift. For a hydrodynamical ensemble, both the chaotic and the squeezed amplitudes, G_c and G_s, respectively, can be written in a special form derived in [3], and developed in [1, 4].

2 Results

The formulation for both bosons and fermions was initially derived for a static, infinite medium [1, 2]. More recently, it was shown [4] in the bosonic case that, even for finite-size systems expanding with moderate flow, the squeezed correlation may survive with sizable strength to be observed experimentally. Similar behavior is expected in the fermionic case. In that analysis, a non-relativistic treatment with flow-independent squeezing parameter was adopted for the sake of simplicity, which allowed for obtaining analytical results. The detailed discussion is in Ref. [4], where the maximum value of $C_s(\mathbf{k},-\mathbf{k})$, was studied as a function of the modified mass, m_*, considering pairs with exact back-to-back momenta, $\mathbf{k}_1{=}{-}\mathbf{k}_2{=}\mathbf{k}$. This type of analysis represents an analogous procedure as to studying only the intercept parameter of the HBT correlation function. This is illustrated in Fig. 1(a), which shows the variation of the maximum of the squeezed correlation in the absence of flow, in three parts. The top and middle plots are results of a recent simulation, where the momenta of each particle in the pair is generated, the squeezed

correlation is then estimated and the bins are filled. The bottom plot is obtained by attributing precise values to the variables, then calculating $C_s(m_*, q_{12})$. This shows that the simulation is indeed reproducing the calculation, for small bin sizes. We can also see from Fig. 1(a) that the simulation shows practically no sensitivity to the cuts introduced in the momentum generation, in order to mimic the experimental cuts in p_T, η, azimuthal angle, etc [5]. Although this study illustrated many points of theoretical interest, it was not helpful for motivating the experimental search of the BBC's, since the modified mass is not accessible to direct measurement.

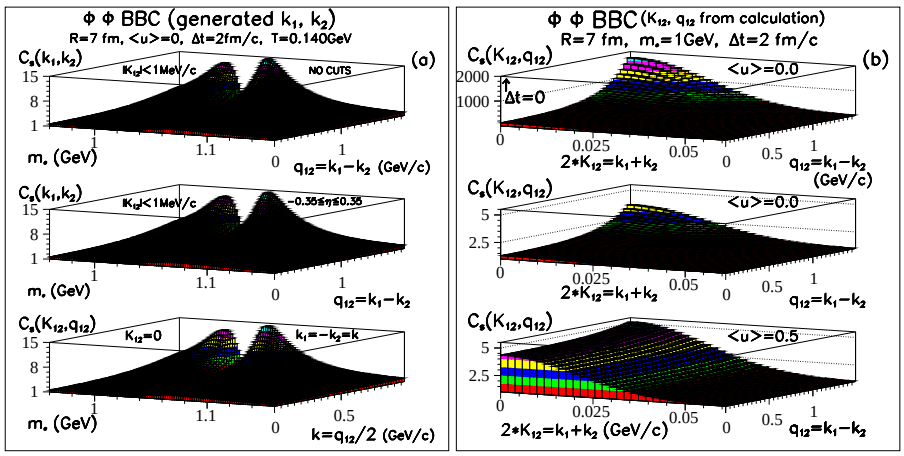


Fig. 1: Part (a) shows the squeezed-pair correlation as a function of the in-medium mass, m_*, and of the back-to-back momentum of each particle, for a static medium ($\langle u \rangle = 0$)). In (b) the effects of finite emission time ($\Delta t = 2$fm/c) and of radial flow ($\langle u \rangle = 0.5$) are shown, for fixed $m_* = 1$GeV .

A more realistic analysis would involve combinations of the momenta of the particles, in terms of which the BBC could be searched for, even though we would have to make a more precise hypothesis concerning the mass-shift. For the sake of simplicity and for illustrating the procedure, we will assume here a constant value for m_*. Within the non-relativistic approach of [4], we suggest to combine the particle-antiparticle momenta, $(\mathbf{k}_1, \mathbf{k}_2)$, into the pair average momentum, $\mathbf{K} = \frac{1}{2}(\mathbf{k}_1 + \mathbf{k}_2)$, and analyze the squeezed correlation function in terms of $|\mathbf{K}|$, similarly to what is done in HBT interferometry. The maximum of the BBC effect is reached when $\mathbf{k}_1 = -\mathbf{k}_2 = \mathbf{k}$, corresponding to $|\mathbf{K}| = 0$. Therefore, the squeezed correlation should be investigated as $C_s(\mathbf{k}_1, \mathbf{k}_2) = C_s(\mathbf{K}, \mathbf{q})$, around the zero of the average momentum. For simplicity, we analyze here the behavior of the correlation function, detailed in [4], by attributing values to $|\mathbf{K}|$ and $|\mathbf{q}|$, as shown in Fig. 1(b), where the in-medium mass of the ϕ's was fixed to $m_* = 1.0$ GeV. In the top and middle plots, a static system ($\langle u \rangle = 0$) was considered. By comparing these two plots, we can see the dramatic rôle played by the finite emission times, which reduces the BBC signal by more than two orders of magnitude. This was obtained when considering an exponential emission, leading to a Lorentzian factor $F(\Delta t) = [1 + (\omega_1 + \omega_2)^2 \Delta t^2]^{-1}$, with $\Delta t = 2$ fm/c, multiplying the second and the third terms in Eq. (1). From Fig. 1(b) we also see that, in the absence of flow, the squeezed correlation intensity grows faster for higher values $|\mathbf{q}|$ than the corresponding case in the presence of flow. However, in this last one it is stronger even for

smaller values of $|\mathbf{q}|$, showing that the presence of flow could help to enhance the signal.

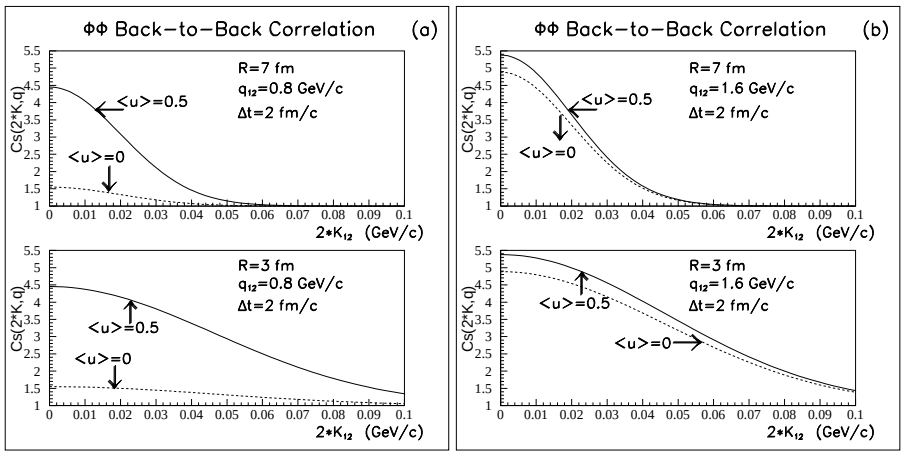


Fig. 2: The response of the BBC function to system sizes with $R = 7$ fm (top plots) and $R = 3$ fm (bottom plots) is shown, for $\Delta t = 2$ fm/c. In (a), the relative momentum was fixed to $q_{12} = 0.8$ GeV/c. In part (b), $q_{12} = 1.6$ GeV/c.

The sensitivity of the squeezed-pair correlation to the size of the region where the mass-change occurs is shown in Fig. 2, for two values of the system radii, $R = 7$ fm and $R = 3$ fm, fixing the relative momentum of the pair to (a) $q_{12} = 0.80$ GeV/c and (b) $q_{12} = 1.6$ GeV/c. The plots were obtained by attributing values to K_{12} and q_{12}. We can see that the size of the squeezing region is reflected in the inverse width of the curves plotted as function of $2|\mathbf{K}|$.

The investigation of the squeezed correlation in terms of $2\mathbf{K}$ is applicable when treating non-relativistic flow. In the case of a fully relativistic study, a four-momentum variable can be constructed, as $Q_{back} = (\omega_1 - \omega_2, \mathbf{k}_1 + \mathbf{k}_2) = (q^0, 2\mathbf{K})$, as introduced in Ref. [6]. Moreover, it would be preferable to redefine this variable as $Q^2_{bbc} = -(Q_{back})^2 = 4(\omega_1\omega_2 - K^\mu K_\mu)$, because its non-relativistic limit recovers $Q^2_{bbc} \to (2\mathbf{K})^2$.

The above analysis could also be applied to other particles that are not their own antiparticles. For showing it, we investigate the case of K^+K^- squeezed correlations, as illustrated in Fig. 3, for an expanding system with radial flow parameter $\langle u \rangle = 0.5$. In part (a), the squeezed correlation is shown as a function of the in-medium mass, m_*, also varying the back-to-back momentum of particle and antiparticle. In part (b), the squeezed correlation is plotted as a function of (K_{12},q_{12}), fixing the kaon in-medium modified mass to $m_* = 650$ MeV. These plots do not come from simulation, but were obtained by attributing values to the plotting variables.

3 Conclusions

We discussed here some of the main results on the squeezed correlations, within an a non-relativistic approach developed earlier. We suggest an effective way to search for it in heavy ion collisions at RHIC, emphasizing the need for experimentally observe this signal. This should be done by plotting the hadronic squeezed correlations in terms of the average momentum of the pair, $(2\mathbf{K})^2$, which is the non-relativistic limit of the four-vector $Q^2_{bbc} = 4(\omega_1\omega_2 - K^\mu K_\mu)$. We

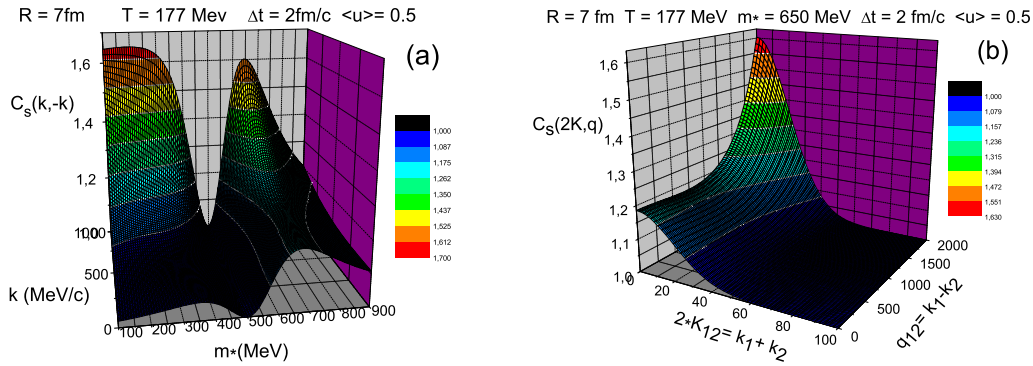


Fig. 3: Part (a) shows the squeezed correlation as a function of possible in-medium mass of the kaons, m_*, and of the momentum of each particle in the pair, $|\mathbf{k}|$. In part (b), it is plotted as a function of K_{12} and q_{12}, considering $m_* = 650$ MeV, which corresponds to roughly the highest value of the correlation in part (a).

showed some results that would be expected in the case of $\phi\phi$ back-to-back correlations, as well in the case of the K^+K^- pairs. We also illustrated the effects of finite system sizes, finite times and flow. We could see that finite emission times reduce the signal substantially, and that, in the presence of flow, the signal is stronger over the momentum regions in the plots, i.e., roughly for $0 \leq |\mathbf{K}_{12}| \leq 60$ MeV/c and $|\mathbf{q}_{12}| \leq 2000$ MeV/c, suggesting that flow may enhance the chances of observing the BBC signal. We also saw that the correlation function reflects the size of the region where the squeezing occurred. Finally, we should emphasize that the absence of squeezing, i.e., if there is no in-medium mass modification, the squeezed correlation functions would be unity for all values of $2|\mathbf{K}_{12}|$ and $|\mathbf{q}_{12}|$.

3.1 Acknowledgments

SSP is very grateful to the Organizing Committee of the ISMD 2008, and specially to Hannes Jung, for the kind support to attend the symposium, thus making her participation possible. DMD thanks CAPES and FAPESP for the financial support.

References

[1] M. Asakawa, T. Csörgő and M. Gyulassy, Phys. Rev. Lett. **83**, 4013 (1999).

[2] P. K. Panda, T. Csörgő, Y. Hama, G. Krein and Sandra S. Padula, Phys. Lett. **B512**, 49 (2001).

[3] A. Makhlin and Yu. Sinyukov, Sov. J. Nucl. Phys. **46**, 354 (1987); Yu. Sinyukov, Nucl. Phys. **A566**, 589c (1994).

[4] Sandra S. Padula, Y. Hama, G. Krein, P. K. Panda, and T. Csörgő, Phys. Rev. **C73**, 044906 (2006).

[5] S. S. Adler et al., PHENIX Collaboration, Phys. Rev. **C72**, 014903 (2005).

[6] Sandra S. Padula, O. Socolowski Jr., T. Csörgő, and M. Nargy, J. Phys. **G35**: Nucl. Part. Phys., 104141 (2008).

An approach to QCD phase transitions via multiplicity fluctuations and correlations

Kensuke Homma from RHIC-PHENIX
Physical Science, Graduate School of Science, Hiroshima University, Higashi-hiroshima 739-8526, Japan

Abstract
We focus on a strategy to probe the QCD phase transition via multiplicity fluctuations and correlations. Based on the strategy, a susceptibility has been measured by the PHENIX collaboration at RHIC. As a qualitative comparison of the susceptibility with correlation amplitudes and widths in the longitudinal direction presented by STAR collaboration at RHIC, we found a similar trend which indicates rapid transitions in the susceptibility as a function of collision centrality.

1 Why do we search for QCD phase transition

The central paradigm of modern physics is that phase transitions via spontaneous symmetry breaking are sources of matter creations. The prominent example is the 1st order phase transition at the inflational expansion followed by the GUT phase transition. The latent heat of the transition is the source of big-bang. Then the EW phase transition follows. If the transition is 1st order, we can produce the baryogenesis at the transition, which is unfortunately unreachable by the current experimental technology. Then we expect quark-gluon to hadron phase transition. It should be stressed that this QCD related phase transition is unique one which would be directly testable by the present laboratory experiments. Therefore it is crucial to understand nature of the transition quantitatively by substantiating that the QCD phase transition surely takes place.

The conjectured QCD phase diagram is discussed on temperature T vs. baryo-chemical potential μ_B plane, where the lattice gauge theory predicts that the chiral transition at finite T and $\mu_B = 0$ is smooth crossover with finite quark masses, while there are only model calculations which suggest the transition is 1st order in $T \sim 0$ and μ_B [1]. As the logical connection, we can expect QCD Critical Point (QCP) at the end of the 1st order transition line which crosses with the crossover line. However, on the location of QCP, the theoretical agreements are rather poor [1] at present. In addition, we need to understand the phase transition on the deconfinement as well. The relation between chiral and deconfinement phase transition is not understood even at the qualitative level.

As good scientific subjects in a strict sense, let us bring two clear cases as follows. The first case is that if we find an octopus on Mars, we can refute a hypothesis that there is no creature on Mars. The second case is that if we can not find Higgs below 1TeV, we can refute the Higgs sector of the standard model. How about QCP? Unfortunately, even if we can not find QCP, we can not refute QCD at finite T and finite μ_B. Then, what can we refute? Is this a scientific question to be seriously asked? Actually the worthiness of the QCP search is similar to the first case. If we find a critical point, we can refute the empty diagram at the QCD scale and it eventually supports

the central idea that phase transitions can be actually sources of matter creations in the testable unique place. Therefore this subject has an impact even beyond the QCD scale.

What Relativistic Heavy Ion Collider (RHIC) at Brookhaven National Laboratory achieved so far is the formation of dense medium and the observation of bulk flows with the partonic degrees of freedom [2]. In addition, the PHENIX collaboration at RHIC has provided estimates on the initial temperature by directly measuring low p_T photons via di-electron channel [3], which suggests the conservative initial temperature is well above critical temperature T_c of $\sim$ 170MeV which is the prediction by the QCD lattice simulation. This guarantees that we can surely put collision system well above T_c on the phase diagram at the initial stage of the system evolution.

2 Strategy

For instance, in the Ising model, spatial sizes of spin correlation patterns become smaller and smaller as temperature goes up. However, on top of T_c, we can see various sizes of correlated areas. To identify $T = T_c$, we can introduce a scale transformation or change the resolution to the system. In $T > T_c$ or $T < T_c$, the system maintains a typical correlation length scale. However, on top of T_c, we see the disappearance of those typical lengths, that is, the appearance of a mixture of many length scales. This is so called fractal nature, because even if we change the resolution, we would meet the same situation where we can not find a typical length scale. This nature can be a general indication of $T = T_c$.

Let us apply this picture to the expanding medium in QCD matter produced at RHIC. In the initial stage of the collisions, we expect some external field h along longitudinal direction. We do not argue what actually causes the field in concrete here. Whatever it is, a dilatation wave due to initially embedded fluctuations would have very short wave length in the confined medium just after the collision and the wave number would evolve as system expands. If there is a phase transition, as the temperature approaches to T_c, new wave numbers would appear and on top of T_c, various wave numbers from short to long lengths would appear in the system. However, if the background fluid medium is rapidly diluted, at some moment, the growth of the wave numbers would freeze. Since we expect a rapid expansion in the high energy heavy ion collisions [4], we focus on the density-density correlation in the longitudinal space z. In this picture, the longitudinal field density fluctuations from the mean density as a function of z,

$$\phi(z) = \rho(z) - < \rho > \tag{1}$$

is a natural order parameter.

Longitudinal space coordinate z can be transformed into rapidity coordinate y in each proper frame of sub element characterized by a formation time τ where dominant density fluctuations are simultaneously embedded. In such a scenario, z can be directly related with y via $dz = \tau \cos(y) dy$ and the free energy as a function of temperature T and an order parameter ϕ can be expressed as

$$F(T,\phi) = \int_{\delta y} dy \int_{S_\perp} d^2x_\perp \left\{ \frac{1}{2\tau^2 \cosh(y)} \left(\frac{\partial \phi}{\partial y} \right)^2 + \cosh(y) \left(\frac{1}{2} (\nabla_\perp \phi)^2 + U(\phi) \right) \right\} \tag{2}$$

where the approximation of $\cosh(y) \sim 1$ and $\eta \sim y$ is valid in a narrow mid-rapidity region in high energy heavy ion collisions, $U(\phi)$ is an arbitrary potential term and degrees of freedom in the transverse plane will be integrated out in the following discussion. Since most of experimentally accessible phase spaces are relatively far from the phase boundary or critical end-point, it is natural to use the polynomial expansion(Ginzburg-Landau) for the potential term as long as order parameter ϕ is very small, which is a valid assumption when the system evolves from the higher temperature side as in top energy at RHIC. As the potential term, we assume up to only second order term in ϕ as an approximation when the system is very far from a critical temperature T_c. In such a case, we expect correlations between fluctuations in densities at different points which lead to a two-point correlation function with the form of $\alpha e^{-z/\xi} + \beta$, where z is the one-dimensional distance, α is the strength of the correlation, β is a constant to absorb the degrees of freedom in the transverse plane and the experimental bias such as centrality definitions and $\xi \propto (T - T_c)^{-1/2}$ is the spatial correlation length. A large increase of ξ near T_c can be a good indicator for $T \sim T_c$. In addition to ξ, the product $\alpha\xi$ can also be a good indicator of a phase transition which behaves as $(1 - T_c/T)^{-1}$. In the GL framework, this quantity is related to the susceptibility $\chi_k = \partial\phi_k/\partial h$ with respect to the external field h in the long wavelength limit $k = 0$ where k is a wave number of a dilatation wave. The details of the derivation of the relations can be found in [5] and the appendix of [6]. More strong indication of $T = T_c$ is the transition of the functional form of the two point correlation function from the exponential to the power law form due to higher order terms in GL free energy, since the order parameter becomes large at $T = T_c$ and we can not neglect higher order terms, or can not introduce polynomial expansion any more. Therefore, the strategy to search for $T = T_c$ would be two folds:

1. Search for increase of correlation length and susceptibility determined by exponential form in $T > Tc$.
2. Search for transition of two point correlations from the exponential to the power law form which needs higher order terms in the free energy density. This would be a stronger indication of $T = T_c$.

3 Data analysis

As a density measurement, we can use the non identified inclusive charged particle multiplicity distributions measured in magnetic field off condition to enhance soft pions which are relevant for discussion on the phase transition. The two point density correlation can be extracted from the differential analysis on multiplicity as a function of pseudorapidity window size $\delta\eta$.

Negative Binomial Distributions (NBD) are fit to the measured multiplicity distributions, and the NBD parameters μ (mean) and k^{-1} (deviation from a Poissonian width) are determined. The product of the correlation strength α and the correlation length ξ is extracted from a known relation between the product of $\alpha\xi$ and the NBD k parameter as a function of $\delta\eta$. The relation between the NBD k parameter and the pseudorapidity window size $\delta\eta$ is known as [5, 6]

$$k^{-1}(\delta\eta) = \frac{2\alpha\xi^2(\delta\eta/\xi - 1 + e^{-\delta\eta/\xi})}{\delta\eta^2} + \beta. \tag{3}$$

Although we have presented the preliminary results in [5] on α and ξ separately, we found strong correlations between the two parameters. This was due to the smallness of ξ in heavy ion col-

lisions. In the limit of $\xi \ll \delta\eta$, which we believe holds in this measurement, Eq. (3) can be approximated as

$$k(\delta\eta) = \frac{1}{2\alpha\xi/\delta\eta + \beta} \quad (\xi \ll \delta\eta), \tag{4}$$

where experimentally we can not resolve α and ξ separately, but the product $\alpha\xi$ can be directly determined.

Once α, ξ and μ are obtained from the NBD fits, one can measure the product of the susceptibility and the corresponding temperature by the following relation:

$$\chi_{k=0}T \propto \mu^2\xi\alpha. \tag{5}$$

Experimentally it is enough to see how the $\chi_{k=0}T$ behaves as a function of a quantity which reflects T. We expect a monotonic correspondence between initial temperature and collision energy and/or centrality based on the Bjorken picture [7]. Therefore either the number of participant nucleons N_{part} or total multiplicity or Bjorken energy density is expected to scale initial temperatures monotonically. Thus the critical behavior of $\chi_{k=0}T$ near T_c can be observed as a non-monotonic increase as a function of these parameters.

4 Results and comparison with STAR data

Top two figures in Fig.1 show the comparison of $\chi_{k=0}T \propto \mu^2\alpha\xi$ vs. normalized charged particle multiplicity to that of top 5% centrality in Au+Au at $\sqrt{s_{NN}} = 200$ GeV with Cu+Cu collisions at the same collision energy and Au+Au collisions at $\sqrt{s_{NN}} = 62.4$ GeV from the PHENIX collaboration. Bottom two figures in Fig.1 have been presented by the STAR collaboration at Quark Matter 2008 [8] where amplitudes and widths of two particle correlation function in the pseudorapidity direction as a function of Bjorken energy density with the formation time of 1 fm/c are shown in in Au+Au at $\sqrt{s_{NN}}$ =200 and 62.4 GeV. We need to take a product between the amplitudes and the widths to compare them with the susceptibility we introduced here. Both PHENIX and STAR data show qualitatively similar trends in the equivalent quantity which indicate a rapid transition from $N_{part} \sim 60$ in Au+Au at $\sqrt{s_{NN}} = 200$ GeV. This might suggest that the system reaches $T \sim T_c$ or a phenomenological threshold effect which is not necessarily relevant for the QCD phase transition. However, it should be noted that the pseudorapidity window size around $\eta = 0$ is very different between STAR and PHENIX. In addition, two particle correlation functional form at $\eta \sim 0$ seems to be biased by the linear subtraction process of many known two particle correlation functional forms in the STAR case, while PHENIX can not exclude HBT effects completely at short distance in the analysis based on the integrated two point correlation function.

5 Summary

RHIC created strongly coupled high temperature and opaque state with partonic d.o.f. This is the very beginning of the scientific program on quantitative understanding of the QCD phase structure. The correlation functional form derived from GL free energy density up to 2nd order term in the high temperature limit (exponential form) is consistent with what was observed in

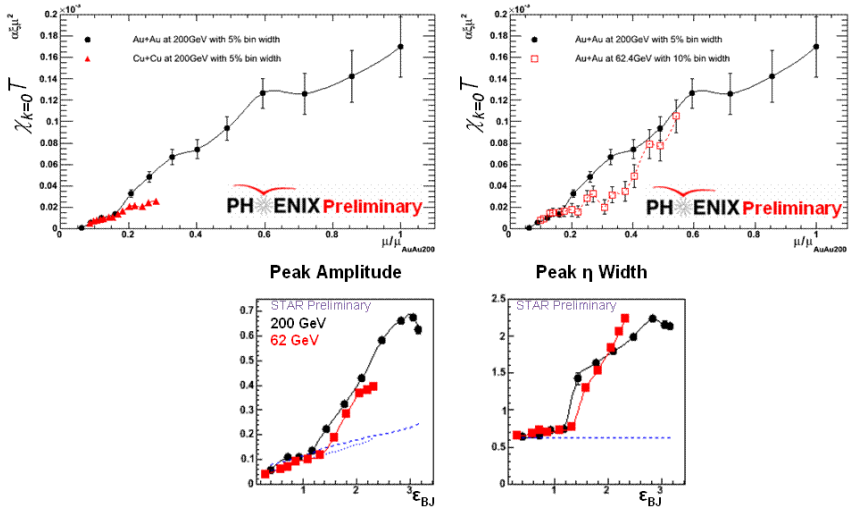


Fig. 1: Top two figures from PHENIX: comparison of $\chi_{k=0}T \propto \mu^2\alpha\xi$ vs. normalized charged particle multiplicity to that of top 5% centrality in Au+Au at $\sqrt{s_{NN}} = 200$ GeV(black circle) with Cu+Cu collisions(red triangle) at the same collision energy and Au+Au collisions at $\sqrt{s_{NN}} = 62.4$ GeV(red square). Bottom two figures from STAR: correlation amplitudes (left) and correlation widths(right) of two particle correlation functions in η direction as a function of Bjorken energy density in Au+Au at $\sqrt{s_{NN}} = 200$(black circle) and 62.4 GeV(red square). The product between the amplitudes and the widths in the STAR data is qualitatively equivalent to $\chi_{k=0}T$ in the PHENIX data.

NBD k vs. $\delta\eta$ in three collision systems. However, transitions from the exponential to the power law functional form were not obviously seen. Centrality dependence of the product between susceptibility and temperature is qualitatively consistent with what STAR observed as amplitudes and widths of the longitudinal two particle correlations with low p_T particles. Both indicate rapid transition as a function of collision centrality. This might suggest that either the system reaches $T \sim T_c$ or a phenomenological threshold effect like creation of a thermalized system. Further investigations would unveil the nature of the transition.

References

[1] M. A. Stephanov, Prog. Theor. Phys. Suppl. **153**, 139 (2004); Int. J. Mod. Phys. A **20**, 4387 (2005).

[2] K. Adcox *et al.* [PHENIX Collaboration], Nucl. Phys. A **757**, 184 (2005) [arXiv:nucl-ex/0410003].

[3] A. Adare *et al.* [PHENIX Collaboration], arXiv:0804.4168 [nucl-ex].

[4] N. Sasaki *et al.*, Europhys. Lett. **54**, 38-44 (2001).

[5] K. Homma [PHENIX Collaboration], PoS C **POD2006**, 007 (2006) [arXiv:nucl-ex/0703046].

[6] S. S. Adler *et al.* [PHENIX Collaboration], Phys. Rev. C **76**, 034903 (2007) [arXiv:0704.2894 [nucl-ex]].

[7] J. D. Bjorken, Phys. Rev. D **271401983.**

[8] M. Daugherity [STAR Collaboration], J. Phys. G **35**, 104090 (2008) [arXiv:0806.2121 [nucl-ex]].

Antibaryon to Baryon Production Ratios in Pb-Pb and p-p collision at LHC energies of the DPMJET-III Monte Carlo

F.W.Bopp[1]†, *J.Ranft*[1], *R.Engel*[2], *S.Roesler*[3]
[1]Siegen University, Siegen, Germany,
[2]Forschungszentrum Karlsruhe, Karlsruhe, Germany,
[3]CERN, Geneva, Switzerland

DOI: http://dx.doi.org/10.3204/DESY-PROC-2009-01/79

Abstract
A sizable component of stopped baryons is predicted for pp and $PbPb$ collisions at LHC. Based on an analysis of RHIC data within the framework of our multi-chain Monte Carlo DPMJET-III the LHC predictions for pp and $PbPb$ are presented.

1 Introduction

DPMJET is a Monte Carlo program for the scattering of hadrons or nuclei. It utilizes PHOJET for the scattering of individual hadrons and parts of PYTHIA for the decay of partonic strings. The present version is DPMJET III. For the most recent general LHC predictions we refer to Ranft's CERN talk [1,2]. Here the focus is on a particular aspect and baryon stopping is addressed [3,4].

There are different components to baryon stopping. Most interesting we consider *the component without leading quarks.* The actual baryon transport is here just an effect of the orientation of the color-compensation during the soft hadronisation.

Baryon stopping is not new. The phenomenology was developed 30 years ago [5] in "*Dual*" models in a "*Topological*" framework [6]. Critical are various baryonium Regge intercepts

$$\alpha^0_{Barionium},\ \alpha^1_{Barionium},\ \text{or}\quad \alpha^2_{Barionium}$$

of processes in which the exchanged baryonia respectively contain 0, 1 or 2 quark pairs transporting 0, 1 or 2 valence quarks. The idea is that $\alpha^2_{Barionium}$ is dominant in the leading region. As it has a low intercept it will not reach very far and the next baryonium will take over in a more central region. Eventually a flattish $\alpha^0_{Barionium}$contribution will survive. The intercepts were estimated using the energy dependence of annihilation cross sections [5] and the inclusive baryonic charge distributions [7]. Some ambiguity remains for the intercept of the long range component and a confirmation of the flattish distribution indicated by HERA and RHIC data at LHC would be useful.

Today such baryon processes are still of fundamental interest. Many people are convinced that under specified conditions very high energy hadronic scattering can be understood with BFKL Pomeron exchanges described by ladders of dispersion graphs. In these graphs soft effects are thought to be contained in effective gluon exchanges calculated in a self-consistent way. In

† speaker

principle these soft effects include the color compensating mechanism usually modeled as two strings neutralizing triplet colors.

In string phenomenology it is assumed that these predictions somehow apply to minimum bias physics. The idea is that BFKL QCD results extrapolate smoothly into the minimum bias region where a suitable truncation has to be modeled.

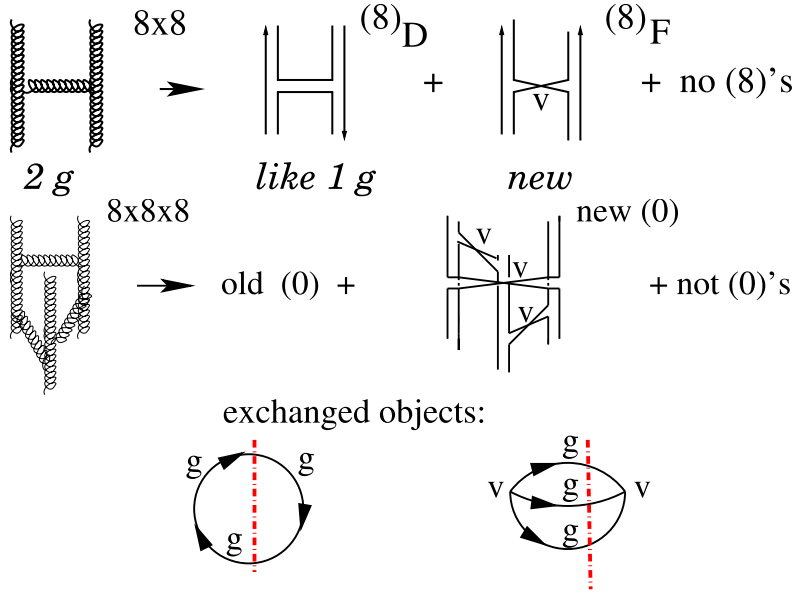


Fig. 1: Structure of Odderon

At some level an untruncated soft or collinear QCD calculation would operate in phantasy space as the end entropy can never be exceeded. In hadronic string models the scattering is assumed to end with the production of independently decaying strings. Such a few string state contains comparatively low entropy. In this way the required truncation is taken to be sufficiently servere to allow for no really separate non perturbative contribution as the effective radius of convergence is not crossed.

In this way semihard calculations offer a stringent guidance for modeling the non-perturbative region. With few added assumptions the very successful Dual-Parton / Quark-Gluon-String model [8] description of all relevant data is obtained.

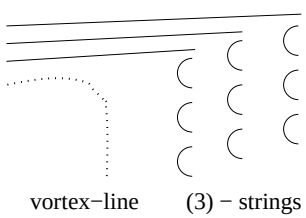


Fig. 2: Proton contribution

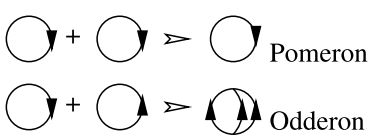


Fig. 3: Fusion contribution

However, there is a problem. Beside the Pomeron semihard theory predicts *a three gluon Odderon exchange* [9, 10]. It is a necessary ingredient of the approach. In comparison to the Pomeron it has to have a similar but somewhat lower intercept. Parameterizations of available cross sections require a small coupling to nucleons.

In Fig. 1 we consider the Odderon to the leading $1/N_c$ order. Two gluons can couple into an octet with even or odd C parity (line 1). With a third gluon they can then couple to an even or odd C parity singlet (line 2). The exchanged topological object is a cylinder or a baryonium (line 3). In inelastic collisions this object can be cut in the way indicated by the dashed line through the reggeized gluons.

The central observation is that a vortex line can remain on each side. In inelastic exchanges Odderons can contribute to baryonic charge exchange with three strings as shown in Fig. 2 .

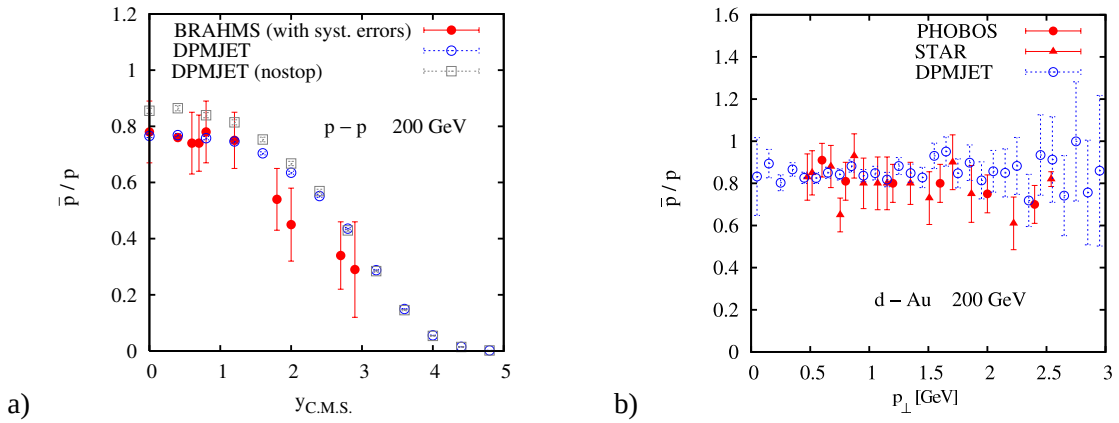


Fig. 5: RHIC data compared with the DPMJET results

That the Odderon has to be attached exactly to the vortex line might explain why the Odderon coupling to the proton is considerable smaller than the Pomeron coupling. Guided by Kwiecinski's and Balitskij's, Kovchegov's calculations for semihard processes *strings can fuse*. Topologically there are two posibilities (Fig. 3). The fusion probability should here be mainly determined by geometry. There should be plenty of Odderons in Pomeron fusion processes.

2 Comparing with RHIC and Tevetron Results

The first experimental indication for a flat component came from preliminary H1 data at HERA [11]. As RHIC runs pp or *heavy ions* instead of $p\bar{p}$ the central asymmetry allows to address the asymmetry better than the SPS or Tevatron collider and the data seem to require a rather flat contribution [12].

In the Dual-Parton-Model generator, DPMJET III [13], there are several components affecting the position of the net baryon charge. The transport mechanisms from these contributions are not sufficient. To obtain the needed long range baryon transport we introduced a new string interaction reshuffling the initial strings configuration in a certain way indicated in Fig. 4. It effectively introduces a baryonium exchange at the top with an intercept of $\alpha^0_{Barionium} = 0.5$.

A good fit is obtained for the BRAHMS data on the ratio $\bar{p}/p$ as function of y_{cm} (Fig. 5a) [14]. However, for nucleons at this energy the contribution comes mainly from non flipping effects. The empty squares show the result without flipping,

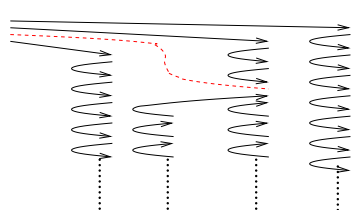


Fig. 4: The flipped configuration

This changes for nuclei where multiple Pomeron exchanges appear as required by Glauber theory. For nuclear scattering fusion of complete strings which are geometrically close (< 0.75fm) is needed to reduce the spectral density. It also can lead to effective quarkless baryonium exchanges.

Fig. 5b shows agreement with PHOBOS and STAR [15, 16] collaborations data. No $p_\perp$ dependence is visible in the considered soft range. The same applies to the centrality dependence.

For strange baryons good agreement is obtained with the net Λ's distribution compared with data from the STAR collaboration. For the Ξ asymmetry - which is also available - a possibly observed backward peak is not reproduced. The Ω-asymmetry measured by the E791 collaboration [17] in πp scattering is shown in Fig. 6 . The inclusion of the baryonium production (Fig. 6 insert) moves the result from the crosses to the squares to reproduce the filled square data.

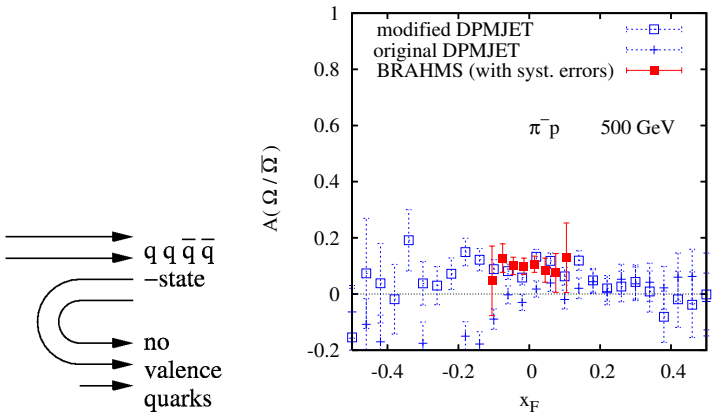


Fig. 6: Net Ω distribution and Tevatron data where the asymmetry

$$A(\Omega/\bar{\Omega}) = (N_\Omega - N_{\bar{\Omega}})/(N_\Omega + N_{\bar{\Omega}})$$

3 Prediction for LHC Data

Turning to LHC the DPMJET III prediction for the pseudo rapidity of p, $\bar{p}$, and $p - \bar{p}$ and the asymmetry are shown in Fig.7 . The new baryon stopping process is now stronger than before as the Pomeron number increased with energy. With the effective intercept of 0.5 the present implementation of the baryon stopping is a rather conservative estimate. For an intercept of 1.0 the value at $\eta = 0$ would roughly correspond to the present value of $\eta = 4$

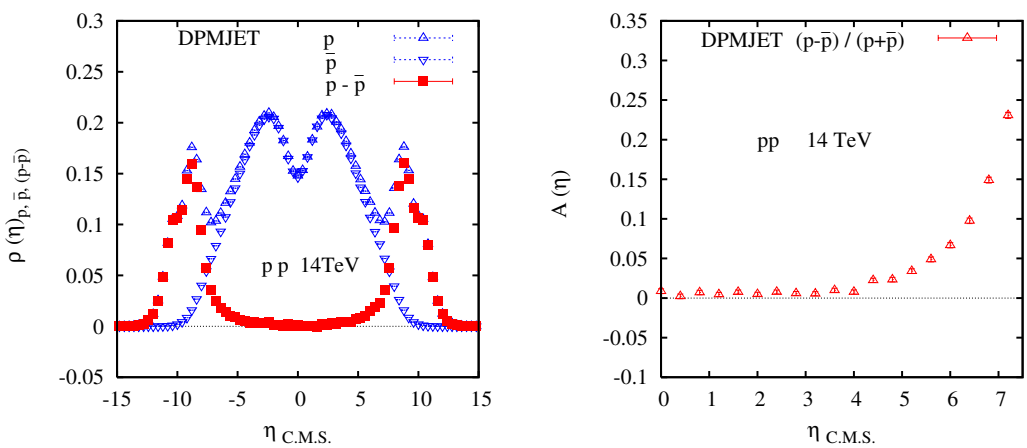
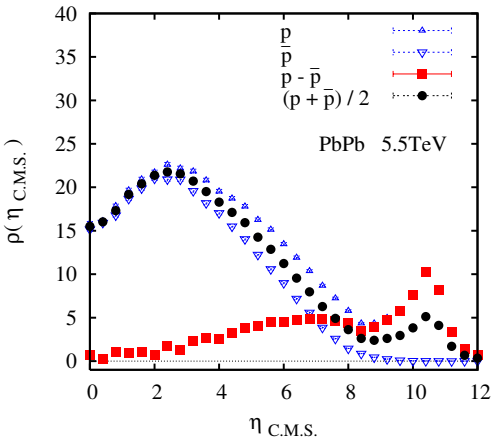
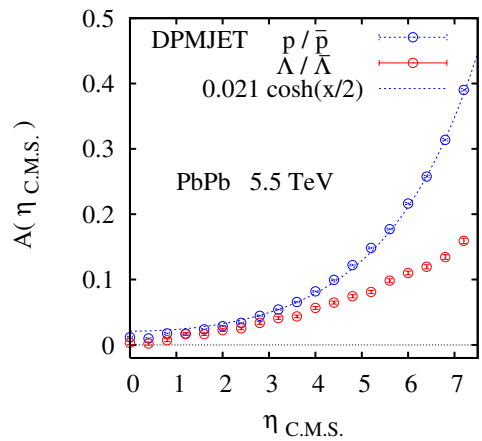


Fig. 7: $pp-$LHC predictions for p and $\bar{p}$

For heavy ion collisions the baryon stopping gets even stronger. The pseudorapidity proton distributions in $PbPb$ scattering are given in Fig. 8.



8)



9)

Fig. 8: $PbPb-$LHC predictions for p and $\bar{p}$

Fig. 9: $PbPb-$central LHC predictions for the p resp. Λ asymmetry

Especially interesting are the most central 10% of the events. The DPMJET III prediction for the proton and Λ asymmetries in such events is shown in Fig 9. There is some uncertainty in this prediction as the model in its present form does not reproduce the full elliptic flow. Hopefully the net baryon distribution is not affected by missing a non-initial state effect. The line drawn corresponds to an $\alpha^0_{Barionium} = 0.5$ with an arbitrary normalization. It is a safe, quite conservative estimate and it could be considerably flatter.

To conclude there is a strong evidence for a significant baryon stopping component. There is still some uncertainty how high the intercept has to be and LHC measurements will be useful.

References

[1] F. W. Bopp, R. Engel, J. Ranft, and S. Roesler (2007). `0706.3875`.

[2] E. . Armesto, N. *et al.*, J. Phys. **G35**, 054001 (2008). `0711.0974`.

[3] F. W. Bopp, R. Engel, J. Ranft, and S. Roesler (2007). `0706.3870`.

[4] F. W. Bopp, J. Ranft, R. Engel, and S. Roesler, Phys. Rev. **C77**, 014904 (2008). `hep-ph/0505035`.

[5] G. C. Rossi and G. Veneziano, Nucl. Phys. **B123**, 507 (1977).

[6] G. F. Chew and C. Rosenzweig, Phys. Rept. **41**, 263 (1978).

[7] P. Aurenche and F. W. Bopp, Nucl. Phys. **B119**, 157 (1977).

[8] A. Capella, U. Sukhatme, C.-I. Tan, and J. Tran Thanh Van, Phys. Rept. **236**, 225 (1994).

[9] J. Bartels, L. N. Lipatov, and G. P. Vacca, Phys. Lett. **B477**, 178 (2000). `hep-ph/9912423`.

[10] Y. Hatta, E. Iancu, K. Itakura, and L. McLerran, Nucl. Phys. **A760**, 172 (2005). `hep-ph/0501171`.

[11] H1 and ZEUS Collaboration, L. Shcheglova. Prepared for 30th International Symposium on Multiparticle Dynamics (ISMD 2000), Tihany, Lake Balaton, Hungary, 9-15 Oct 2000.

[12] F. Bopp and M. Shabelski, Eur. Phys. J. **A28**, 237 (2006). `hep-ph/0603193`.

[13] S. Roesler, R. Engel, and J. Ranft (2000). `hep-ph/0012252`.

[14] BRAHMS Collaboration, I. G. Bearden *et al.*, Phys. Lett. **B607**, 42 (2005). `nucl-ex/0409002`.

[15] PHOBOS Collaboration, P. Steinberg *et al.*, J. Phys. G **30**, S683 (2004).

[16] STAR Collaboration, J. Adams *et al.*, Phys. Lett. **B637**, 161 (2006). `nucl-ex/0601033`.

[17] E791 Collaboration, E. M. Aitala *et al.*, Phys. Lett. **B496**, 9 (2000). `hep-ex/0009016`.

Chapter 6

Working Group New Physics

Convenors:

G. Weiglein (Durham)
A. DeRoeck (CERN)

New Signals and Challenges for the LHC

Matthew Strassler
Rutgers University

Abstract
Models with hidden sectors, including many non-minimal versions of well-known models, can pose substantial challenges for the LHC experiments. This is illustrated using the hidden valley scenario.

1 Introduction and Motivation

Hundreds of theoretical and experimental studies have been done in preparation for the advent of the Large Hadron Collider (LHC). But these studies are hardly comprehesive; most involve explorations of "minimal" theories, which aim to address a problem in particle physics and contain the minimal structure required for that purpose. For example, most supersymmetric studies are of the Minimal Supersymmetric Standard Model (MSSM). But is the MSSM well-motivated?

On the one hand, supersymmetry (SUSY) is clearly well-motivated. It is our best candidate for solving the hierarchy problem without introducing FCNCs or large corrections to precision electroweak observables. Moreover, it appears naturally in our best current theory of quantum gravity: string theory. On the other hand, *the word "minimal" is not so obviously well-motivated.* Minimalism does not solve any problem in particle physics; it is motivated by aesthetic criteria: elegance, simplicity, etc. One might view such criteria as good motivation if experience suggested that nature always was elegant and simple. But is the Standard Model "minimal"? The muon, the third generation, CP violation and neutral currents have all been viewed, at various times, as unmotivated and unnecessary complications that nature is unlikely to present. Moreover, minimalism is quite difficult to obtain in string theory. Attempts to find the SM within string theory bring along extra gauge factors and matter, some of which are coupled to the SM more strongly than gravitationally.

Why do theorists dislike non-minimal models? A more complicated Lagrangian has more parameters, and therefore fewer precise predictions and more ambiguity about the details of the spectrum, decays, etc., as well as fewer constraints from existing data. But for these features to generate a dislike is a bias — a *cultural* bias, one which nature may not share. The problem is that it is dangerous to disregard non-minimal models: they can have wildly different LHC phenomenology from the corresponding minimal models, and often generate surprising and difficult signatures for the LHC experiments.

1.1 Sensitivity of the Higgs boson

The decay modes of Higgs bosons are easily altered by new interactions. This is especially true of light SM Higgs bosons, or CP-odd Higgs bosons in two-Higgs-doublet models, which are narrow, as they decay through a small coupling (mainly to b quarks.)

As a simple exercise to illustrate the point, let us add one new real scalar S to the SM. Depending on the couplings of S to itself and to the Higgs boson H, one may obtain

- An invisible higgs;
- Two scalars, h decaying to $b\bar{b}$ and H decaying to WW and ZZ;
- Two scalars, h decaying to $\tau^+\tau^-$, and H decaying to hh;
- A Higgs decaying to two long-lived particles, which decay in flight to $b\bar{b}$ or $\tau^+\tau^-$.

Any of these final states poses challenges for reconstruction and experimental analysis at the LHC detectors, and the last even challenges the trigger system.

Some recent investigations of this possibility have focused on the Next-to-Minimal Supersymmetric Standard Model (NMSSM) [1], and have pointed out that the LEP experiments might have missed $h \to aa \to (\tau^+\tau^-)(\tau^+\tau^-)$, where a is a pseudoscalar. Other possible final states include $h \to b\bar{b}b\bar{b}$. These final states would pose a significant challenge for the LHC. In fact, as they pointed out, a search for the a at B factories may be the best approach. Higher multiplicity decays, such as Higgs to 6 or 8 b's or τs, arise in non-minimal SUSY [2] and in wide classes of models within the Hidden Valley Scenario [3–5]. Decays to two new spin-one particles, giving occasional 4-lepton final states, can arise in many models with hidden sectors [3, 6, 7]. Decays to two (or more) long-lived neutral objects, giving 2 or more displaced vertices, arise in Hidden Valleys and other related models [4], and in R-parity Violating SUSY [8].

This diversity of possibilities arises from the ease with which the Higgs can couple to hidden sectors, through a renormalizable coupling $(HH^*)\mathcal{O} \to \langle v \rangle h\mathcal{O}$, where $\mathcal{O}$ is a composite operator built from fields in a new sector.

1.2 Hidden Valleys

But access to hidden sectors, as Zurek and I emphasized [3–6] can occur through many channels. Rare decays of the W and Z, and decays of Z' bosons, new neutrinos, the lightest supersymmetric particle "LSP" (or the lightest Kaluza-Klein particle or T-parity-odd particle [LKP/LTP]), certain KK resonances, black holes, etc., all can serve to open a door to a new sector of particles and forces. These decays (whose branching fractions can sometimes reach 100 %) often exhibit unusual features, such as:

- High multiplicity final states (often mostly jets, sometimes with no leptons or photons; often highly variable in multiplicity; often with unusual clustering; generally non-thermal and often with small cross-sections, unlike black holes)
- Multiple long-lived particles in the final state (with lifetimes often in the psec to μsec range which produce observably-displaced vertices)
- Possible new light neutral particles (with masses essentially unconstrained, as LEP puts very few constraints on electroweak- and color-singlet particles.)

While some of these phenomena have appeared before in the literature, typically in corners of parameter space of minimal or nearly-minimal models, very few have they been studied by the experimental groups. And in models with hidden sectors, they are commonplace!

In the Hidden Valley (HV) scenario [3], a hidden sector interacts with the SM at the TeV scale, as illustrated in Fig. 1. The scenario covers a very wide variety of models. A typical model has a valley-sector, or "v-sector", containing a new gauge group and matter; this is represented by the "valley" on the right, with the standard model sector on the left. One or more particles serves to connect the two sectors, and is represented by the mountain between the two valleys.

HV models often produce high-multiplicity events because of the effects shown in the figure: first, v-particles are produced; then valley dynamics, which might include v-cascade decays, v-parton showers, v-hadronization, etc., can increase the number of v-particles; and finally, if the v-sector dynamics prevents some v-particles from decaying within the v-sector, these v-particles may decay to the SM sector. Each step increases the number of particles.

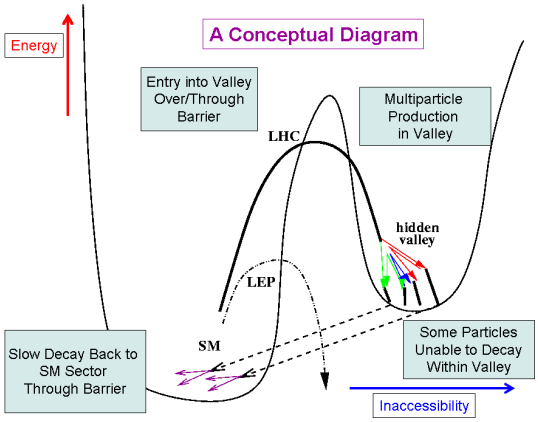


Fig. 1: Conceptual diagram of a Hidden Valley.

High multiplicity events may confuse standard reconstruction algorithms, defy typical search strategies, etc. Backgrounds to such events are hard to calculate or measure. In events with many quarks, jets from jet algorithms will not match to short-distance quarks. Highly-boosted v-particles, which are common, can have daughters that merge into a single jet, or which violate standard isolation criteria for taus, leptons and photons. Soft quarks are also common, and these, rather than producing jets, may be confused with an active underlying event or with effects of pileup.

Meanwhile, v-particle decays to the SM are often slow because they are mediated by a product of a standard model operator times a v-sector operator: $\mathcal{O}_{SM} \times \mathcal{O}_v$. If the total dimension of the product > 4, decay rates are suppressed. For example, a v-particle of mass m with a decay through a dimension 7 operator has a decay width proportional to $(m/\mathrm{TeV})^6$.

Long-lived particles can pose substantial challenges for detectors. Though they have no SM background, they typically have detector backgrounds arising from "secondary" interactions: collisions of high-momentum hadrons with detector material. Moreover, no trigger pathway is aimed at such particles, and existing triggers can have poor efficiency, especially for low-energy displaced jets. Also, reconstruction software can be confused by the unusual tracking environment. CDF and D0 analyses searching for Higgs decays to two long-lived particles have taken 2 years. In fact, as we pointed out, LHCb, designed to find B mesons, could actually beat ATLAS and CMS to a discovery of new long-lived particles [4, 8].

Example: A Higgsed Hidden Valley: As illustration, consider a theory with v-gauge group G, broken completely so that the v-gauge bosons Y get mass $g\langle X\rangle$, where X is a v-Higgs boson of mass m_X. Through loop effects, the Y bosons can mix with the standard model Z, typically with a tiny mixing angle. Just as in the SM, $X \to YY$ is allowed if $m_X > 2m_Y$. The presence of an X^2H^2 term allows mixing of X and H and a coupling $H \to XX$. Putting these together, a number of processes, if kinematically allowed, are predicted, including

- $H \to X^* \to YY \to Z^*Z^* \to$ 2 pairs of SM fermions
- $H \to XX \to YYYY \to Z^*Z^*Z^*Z^* \to$ 4 pairs of SM fermions

(where Z^* is an off-shell Z). One can uncover this hidden sector through Higgs boson decays, with the light neutral Y resonance(s) appearing first in dilepton pairs, then the X and H resonances in Y resonance pairs. If the Y is long-lived, it might first be discovered through its decay

by a displaced vertex.

Example: A Confining Hidden Valley: Here is another example. A heavy resonance, such as a Z' or heavy Higgs, can decay into a hidden valley. In Fig. 2 is shown a process in which a quark-antiquark pair make a Z' boson, which then decays to v-quarks which are charged under the v-group G. In a QCD-like v-sector, the v-quarks undergo a v-parton shower and form v-jets of v-hadrons. Some of these v-hadrons can decay back to standard model particles, making a complex, high-multiplicity final state. Depending on parameters, the decays of the v-hadrons may be prompt or displaced. The resulting final states can look like Fig. 3.

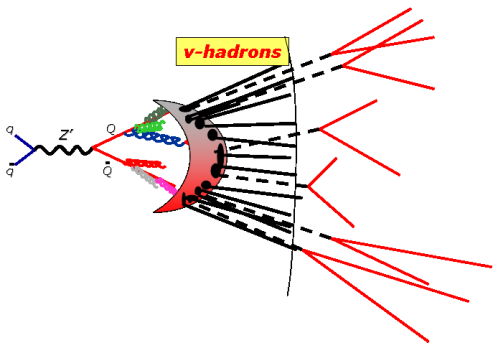


Fig. 2: Decay of a Z' into v-quarks Q, leading to v-jets of v-hadrons, some of which decay to SM particles.

So far I have assumed QCD-like confinement here. But nonperturbative phenomena in other theories are very different from QCD. For example, v-jets may be very different from QCD jets. In these cases, the resulting signatures cannot be reliably predicted. (There is one exception: a v-sector with a large 't Hooft coupling and an AdS/CFT dual description is known to have no jets at all, and to produce spherical events with many soft particles [6, 9].) At the LHC, a model of a phenomenon is often needed in order to find it; otherwise, it is hard to determine backgrounds, trigger efficiencies, and so forth. Thus the unknown dynamics of a hidden valley could obscure it at the LHC if we are not sufficiently thoughtful in advance. What range of analysis methods should be used to look for hidden valleys? At the moment there is no satisfactory answer, and more study is clearly needed.

Models with quirks: The coupling of the SM to a v-sector can come through a loop effect. Consider a confining hidden valley with v-group G, no light v-quarks, and a confinement scale Λ. In addition the model has massive particles ($m \gg 100$ GeV) charged under both the SM and the v-group. These particles are sometimes called "quirks" [10]. Flux tubes in the group G are stable, so quirks are eternally bound. Quirks are created in pairs in an excited state; they oscillate, gradually decay to their ground state, and finally annihilate to v-gluons or to SM gauge bosons. In the former case, the v-gluons form v-glueballs, which in turn decay slowly to SM gauge bosons through interactions induced by quirk loops. Remarkable unstudied phenomena can result, depending on the scale Λ.

- Two heavy charged/colored objects bound together by a macroscopically long, microscopically thick string;
- A mesoscopic dipole state;
- Relaxation to the ground state via emission of many soft pions or photons.

I'd like to say a couple of words about the last case [11]. Colored quirks with mass of 1 TeV will typically be produced ~ 300 GeV above threshold. Annihilation may sometimes occur only after relaxation to the ground state; if so, where does the 300 GeV of kinetic energy go? Kang and Luty showed that for a wide range of Λ, the answer is: "soft pions". While many of the resulting 100–200 soft charged pions do not reach the calorimeter, their tracks from the primary

vertex are notable. In events where the quirk annihilation products are visible (for example, if the quirks annihilate to two TeV-scale jets, leptons or photons) a large number of tracks from the primary vertex should also appear, distributed in a spherical or oblong shape in the quirk rest frame, rather than cylindrically distributed in the lab frame, as for a typical underlying event.

The v-gluons to which quirks sometimes annihilate may give a strong HV signature. Since there are no light v-quarks, the v-gluons form v-glueballs. From lattice simulations we know there are many stable v-glueballs: 0^{++}, 0^{-+}, 2^{++}, 2^{-+}, 1^{+-}, etc. Via loops of quirks, the v-glueballs will decay to two SM gauge bosons (gluons, Ws, Zs, photons) or to a photon/Z plus another v-glueball [12]. The resulting final states have mostly jets, with occasional photons. One may trigger on and select events with 1 or more hard photon, and then detect the resonances from v-glueball decays to photon pairs, and/or the displaced jet-pairs from any long-lived v-glueballs.

In summary, non-minimal models are motivated by string theory and disfavored only by aesthetic criteria. They can drastically alter the phenomenology of common models, such as the SM itself, SUSY, Extra Dimensions, etc. In the Hidden Valley scenario and beyond, little-studied high-multiplicity final states, with new light and often long-lived neutral particles, can result. High-multiplicity challenges jet reconstruction and event interpretation; long lifetimes can be problematic for experimental analysis, reconstruction, and even the trigger. Quirks often arise in Hidden Valley models. In addition to the typical HV signatures (resonant v-glueball decays, possibly displaced), they can give a novel signature that hides in the underlying event.

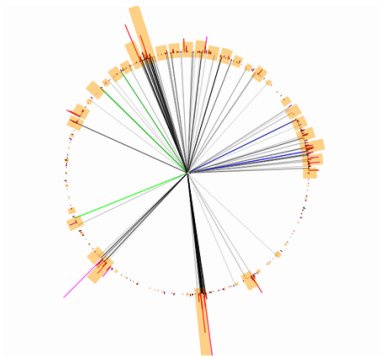


Fig. 3: Event display of a high-multiplicity state arising from the process in Fig. 2, in a model where the v-hadrons decay mainly to $b\bar{b}$ pairs.

References

[1] R. Dermisek and J. F. Gunion, Phys. Rev. Lett. **95**, 041801 (2005). hep-ph/0502105;
U. Ellwanger, J. F. Gunion, and C. Hugonie, JHEP **07**, 041 (2005). hep-ph/0503203;
R. Dermisek and J. F. Gunion, Phys. Rev. **D73**, 111701 (2006). hep-ph/0510322.

[2] S. Chang, P. J. Fox, and N. Weiner, JHEP **08**, 068 (2006). hep-ph/0511250.

[3] M. J. Strassler and K. M. Zurek, Phys. Lett. **B651**, 374 (2007). hep-ph/0604261.

[4] M. J. Strassler and K. M. Zurek, Phys. Lett. **B661**, 263 (2008). hep-ph/0605193.

[5] M. J. Strassler (2006). hep-ph/0607160.

[6] M. J. Strassler (2008). 0801.0629.

[7] S. Gopalakrishna, S. Jung, and J. D. Wells, Phys. Rev. **D78**, 055002 (2008). 0801.3456.

[8] L. M. Carpenter, D. E. Kaplan, and E.-J. Rhee, Phys. Rev. Lett. **99**, 211801 (2007). hep-ph/0607204.

[9] D. M. Hofman and J. Maldacena, JHEP **05**, 012 (2008). 0803.1467;
Y. Hatta, E. Iancu, and A. H. Mueller, JHEP **05**, 037 (2008). 0803.2481.

[10] J. Kang, M. A. Luty, and S. Nasri, JHEP **09**, 086 (2008). hep-ph/0611322.

[11] J. Kang and M. A. Luty (2008). 0805.4642.

[12] J. Juknevich, D. Melnikov, and M. J. Strassler, in preparation.

New physics search in the LHCb era

Tobias Hurth
CERN, Theory Group, CH-1211 Geneva 23, Switzerland
SLAC, Stanford University, Stanford, CA 94309, USA

DOI: http://dx.doi.org/10.3204/DESY-PROC-2009-01/85

Abstract
We present theoretical and experimental preparations for an indirect search for new physics (NP) using the rare decay $\overline{B}_d \to \overline{K}^{*0}\mu^+\mu^-$. We design new observables with very small theoretical uncertainties and good experimental resolution.

1 Introduction

At the start of the LHC we are confronted with the experimental fact that all data on flavour observables from Babar, Belle, CLEO and also from D0 and CDF are consistent with the Standard Model (SM) predictions [1]. This implies that generic new physics (NP) contributions in $K - \bar{K}$ mixing for example guide us to a new-physics scale of $10^3 - 10^4$ TeV depending if the new contributions enter at loop- or tree-level. This is in strong contrast to the working hypothesis of the LHC that there is NP "around the corner" at 1 TeV in order to stabilise the Higgs boson mass. Therefore, any NP at the 1 TeV scale has to have a non-generic flavour structure and we have to understand why new flavour-changing neutral currents (FCNC) are suppressed. Rare decays and CP violating observables allow an analysis of this flavour problem.

The crucial problem in the new physics search within flavour physics is the optimal separation of NP effects from hadronic uncertainties. It is well known that inclusive decay modes are dominated by partonic contributions; non-perturbative corrections are in general rather small [2, 3]. Also ratios of exclusive decay modes such as asymmetries are well suited for the new-physics search. Here large parts of the hadronic uncertainties partially cancel out; for example, there are CP asymmetries that are governed by one weak phase only; thus the hadronic matrix elements cancel out completely. It is the latter opportunity which represents the general strategy followed by LHC*b* for the construction of theoretically clean observables.

In this letter we briefly discuss the theoretical and experimental preparations for an indirect NP search using the rare decay $\overline{B}_d \to \overline{K}^{*0}\mu^+\mu^-$ based on the QCDf/SCET approach [4]. QCD corrections are included at the next-to-leading order level and also the impact of the unknown Λ/m_b corrections is made explicit.

The exclusive decay $\overline{B}_d \to \overline{K}^{*0}\mu^+\mu^-$ was first observed at Belle [5]. It offers a rich phenomenology of various kinematic distributions beyond the measurement of the branching ratio. We note that some experimental analyses of those angular distributions are already presented by the B factories [6, 7, 9, 10]. Those experimental results already have a significant impact on the model-independent constraints within the minimal flavour violation approach [8].

Large increase in statistics at LHC*b* [11–13] for $\overline{B}_d \to \overline{K}^{*0}\mu^+\mu^-$ will make much higher precision measurements possible. There are also great opportunities at the future (Super-)B

factories in this respect [14–17].

Previously proposed angular distributions and CP violating observables in $\overline{B}_d \to \overline{K}^{*0}\mu^+\mu^-$ are reviewed in Ref. [23], and more recently QCDf analyses of such angular distributions [24,25] and CP violating observables [26], based on the NLO results in Ref. [27], were presented.

2 QCD factorization, SCET

Regarding the hadronic matrix elements of exclusive modes, the method of QCD-improved factorization (QCDf) has been systemized for non-leptonic decays in the heavy-quark limit. This method allows for a perturbative calculation of QCD corrections to naive factorization and is the basis for the up-to-date predictions for exclusive rare B decays in general [18].

A quantum field theoretical framework was proposed – known under the name of soft-collinear effective field theory (SCET) – which allows for a deeper understanding of the QCDf approach [19, 20]. In contrast to the heavy-quark effective theory (HQET), SCET does not correspond to a local operator expansion. HQET is only applicable to B decays, when the energy transfer to light hadrons is small, for example to $B \to D$ transitions at small recoil to the D meson. HQET is not applicable, when some of the outgoing, light particles have momenta of order m_b; then one faces a multi scale problem that can be tackled within SCET.

There are three scales: a) $\Lambda = \text{few} \times \Lambda_{\rm QCD}$ the *soft* scale set by the typical energies and momenta of the light degrees of freedom in the hadronic bound states; b) m_b the *hard* scale set by the heavy-b-quark mass and also by the energy of the final-state hadron in the B-meson rest frame; and c) the hard-collinear scale $\mu_{\rm hc} = \sqrt{m_b \Lambda}$ appears through interactions between soft and energetic modes in the initial and final states. The dynamics of hard and hard-collinear modes can be described perturbatively in the heavy-quark limit $m_b \to \infty$. Thus, SCET describes B decays to light hadrons with energies much larger than their masses, assuming that their constituents have momenta collinear to the hadron momentum.

However, we emphasize that within the QCDf/SCET approach, a general, quantitative method to estimate the important Λ/m_b corrections to the heavy-quark limit is missing which has important phenomenological consequences.

A careful choice of observables needs to be made to take full advantage of the exclusive decay $\overline{B}_d \to \overline{K}^{*0}\mu^+\mu^-$, as only in certain ratios such as CP and forward-backward asymmetries, the hadronic uncertainties cancel out making such ratios the only observables that are highly sensitive to NP.

Within the QCDf/SCET approach one finds crucial form factor relations [21] which simplify the theoretical structure of various kinematical distributions such that, at least at the leading order (LO) level any hadronic uncertainties cancel out. A well-known example of this is the zero-crossing of the forward-backward asymmetry. In [4] new observables of this kind in the $\overline{B}_d \to \overline{K}^{*0}\mu^+\mu^-$ decay were proposed which have very small theoretical uncertainties and good experimental resolution. The only difference to the forward-backward asymmetry is that within these new observables the hadronic form factors cancel out for *all* values of the dilepton mass.

3 Theoretical preliminaries

The decay $\overline{B}_d \to \overline{K}^{*0}\ell^+\ell^-$ with $\overline{K}^{*0} \to K^-\pi^+$ on the mass shell is completely described by four independent kinematic variables, the lepton-pair invariant mass squared, q^2, and the three angles θ_l, θ_K, ϕ. Summing over the spins of the final particles, the differential decay distribution of $\overline{B}_d \to \overline{K}^{*0}\ell^+\ell^-$ can be written as [28–31]:

$$\frac{d^4\Gamma_{\overline{B}_d}}{dq^2\, d\theta_l\, d\theta_K\, d\phi} = \frac{9}{32\pi} I(q^2, \theta_l, \theta_K, \phi) \sin\theta_l \sin\theta_K$$

with

$$\begin{aligned} I &= I_1 + I_2\cos 2\theta_l + I_3 \sin^2\theta_l \cos 2\phi + I_4 \sin 2\theta_l \cos\phi + I_5 \sin\theta_l \cos\phi \\ &\quad + I_6 \cos\theta_l + I_7 \sin\theta_l \sin\phi + I_8 \sin 2\theta_l \sin\phi + I_9 \sin^2\theta_l \sin 2\phi. \end{aligned}$$

The I_i depend on products of the seven complex K^* spin amplitudes, $A_{\perp L/R}$, $A_{\parallel L/R}$, $A_{0L/R}$, A_t with each of these a function of q^2; the explicit formulae are given in the appendix. A_t is related to the time-like component of the virtual K^*, which does not contribute in the case of massless leptons and can be neglected if the lepton mass is small in comparison to the mass of the lepton pair. We will consider this case in our present analysis.

The six complex K^* spin amplitudes of the massless case are related to the well-known helicity amplitudes (used for example in [29, 30, 32]):

$$A_{\perp,\parallel} = (H_{+1} \mp H_{-1})/\sqrt{2}, \quad A_0 = H_0. \tag{1}$$

The crucial theoretical input we use in our analysis is the observation that in the limit where the initial hadron is heavy and the final meson has a large energy [21] the hadronic form factors can be expanded in the small ratios $\Lambda_{\rm QCD}/m_b$ and $\Lambda_{\rm QCD}/E$, where E is the energy of the light meson. Neglecting corrections of order $1/m_b$ and α_s, the seven a priori independent $B \to K^*$ form factors reduce to two universal form factors $\xi_\perp$ and $\xi_\parallel$ [21, 22] and one finds that the spin amplitudes at leading order in $1/m_b$ and α_s have a very simple form:

$$\begin{aligned} A_{\perp L,R} &= \sqrt{2} N m_B (1-\hat{s}) \times \left[(\mathcal{C}_9^{(\rm eff)} \mp \mathcal{C}_{10}) + \frac{2\hat{m}_b}{\hat{s}} (\mathcal{C}_7^{(\rm eff)} + \mathcal{C}_7^{\prime(\rm eff)}) \right] \xi_\perp(E_{K^*}), \\ A_{\parallel L,R} &= -\sqrt{2} N m_B (1-\hat{s}) \times \left[(\mathcal{C}_9^{(\rm eff)} \mp \mathcal{C}_{10}) + \frac{2\hat{m}_b}{\hat{s}} (\mathcal{C}_7^{(\rm eff)} - \mathcal{C}_7^{\prime(\rm eff)}) \right] \xi_\perp(E_{K^*}), \\ A_{0L,R} &= -\frac{N m_B}{2\hat{m}_{K^*}\sqrt{\hat{s}}} (1-\hat{s})^2 \left[(\mathcal{C}_9^{(\rm eff)} \mp \mathcal{C}_{10}) + 2\hat{m}_b (\mathcal{C}_7^{(\rm eff)} - \mathcal{C}_7^{\prime(\rm eff)}) \right] \xi_\parallel(E_{K^*}), \end{aligned} \tag{2}$$

with $\hat{s} = q^2/m_B^2$, $\hat{m}_i = m_i/m_B$. Here we neglected terms of $O(\hat{m}_{K^*}^2)$. It is important to mention that the theoretical simplifications are restricted to the kinematic region in which the energy of the K^* is of the order of the heavy quark mass, i.e. $q^2 \ll m_B^2$. Moreover, the influences of very light resonances below 1 GeV question the QCD factorization results in that region. Thus, we will confine our analysis of all observables to the dilepton mass in the range $1\mathrm{GeV}^2 \le q^2 \le 6\mathrm{GeV}^2$.

4 Construction of theoretically clean observables

By inspection one finds that the distribution functions I_i in the differential decay distribution (see Eq. (10)) are *invariant* under three symmetry transformations which are given explicitly in the appendix (see Eqs. (11-13)). This implies that only 9 of the 12 K^* spin amplitudes are *independent* and that they can be fixed by an full angular fit to the 9 independent coefficients of the differential decay distribution. Another direct consequence is that any observable based on the differential decay distribution has also to be invariant under the same symmetry transformations.

Besides this mandatory criterium there are further criteria required for an interesting observable. [**Simplicity:**] A simple functional dependence on the 9 independent measurable distribution functions; at best it should depend only from one or two in the numerator and denominator of an asymmetry. [**Cleanliness:**] At leading order in Λ/m_b and in α_s the observable should be independent of any form factor, at best for all q^2. Also the influence of symmetry-breaking corrections at order α_s and at order Λ/m_b should be minimal. [**Sensitivity:**] The sensitivity to the $\mathcal{C}_7^{\prime(\mathrm{eff})}$ Wilson coefficient representing NP with another chirality than in the SM should be maximal. [**Precision:**] The experimental precision obtainable should be good enough to distinguish different NP models.

In the limit where the $\overline{K}^{*0}$ meson has a large energy, only two independent form factors occur in $A_{0L/R}$ and in $A_{\perp L/R}$ and $A_{\parallel L/R}$. Clearly, any ratio of two of the nine measurable distribution functions proportional to the same form factor fulfil the criterium of symmetry, simplicity, and theoretical cleanliness up to Λ/m_b and α_s corrections. However, the third criterium, a sensitivity to a special kind of NP and the subsequent requirement of experimental precision, singles out particular combinations. In [4] we focused on new right-handed currents. Other NP sensitivities may single out other observables as will be analysed in a forthcoming paper [33].

5 Results

The first surprising result is that the previously proposed quantity $A_T^{(1)}$ [29],

$$A_T^{(1)} = \frac{\Gamma_- - \Gamma_+}{\Gamma_- + \Gamma_+} = \frac{-2\Re(A_\parallel A_\perp^*)}{|A_\perp|^2 + |A_\parallel|^2} \,. \tag{3}$$

with $\Gamma_\pm = |H_{\pm 1}^L|^2 + |H_{\pm 1}^R|^2$ does not fulfil the most important criterium of symmetry while it has very attractive new physics sensitivity [24, 25]. Therefore, it is not possible to extract $A_T^{(1)}$ from the full angular distribution which is constructed after summing over the spins of the final particles. Because it seems practically not possible to measure the helicity of the final states on a *event-by-event* basis, $A_T^{(1)}$ cannot be measured at either LHC*b* or at a Super-B factory with electrons or muons in the final state.

One finds that the well-known quantities, the forward-backward asymmetry A_{FB} and the longitudinal K^* polarization F_L fulfill the symmetry but they include larger theoretical uncertainties due to the fact that the form factors do not cancel at leading order level for all dilepton masses. Moreover, the sensitivity to right-handed currents is marginal as it is shown below,

$$A_{\mathrm{FB}} = \frac{3}{2} \frac{\Re(A_{\parallel L} A_{\perp L}^*) - \Re(A_{\parallel R} A_{\perp R}^*)}{|A_0|^2 + |A_\parallel|^2 + |A_\perp|^2} \tag{4}$$

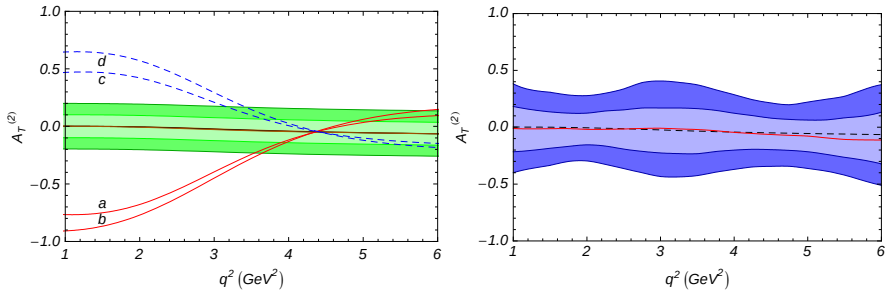


Fig. 1: For $A_T^{(2)}$, theoretical errors (top), experimental errors (bottom) as a function of the squared dimuon mass, see text for details.

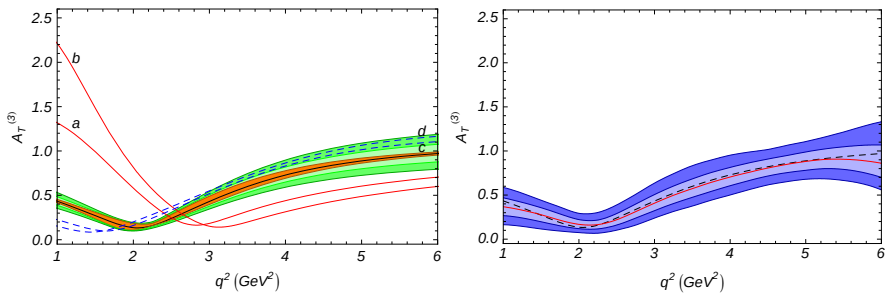


Fig. 2: $A_T^{(3)}$, as in Fig.1.

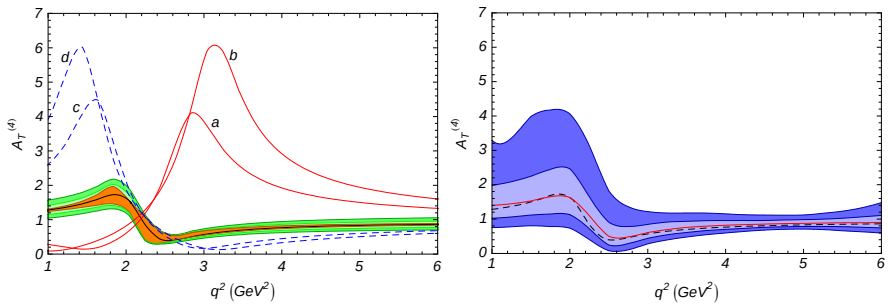


Fig. 3: $A_T^{(4)}$, as in Fig.1.

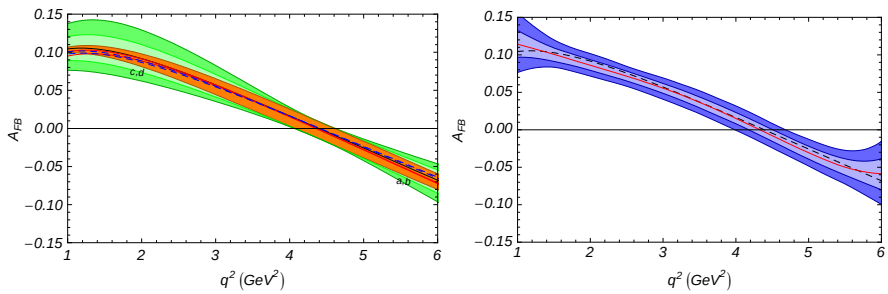


Fig. 4: A_{FB}, as in Fig.1.

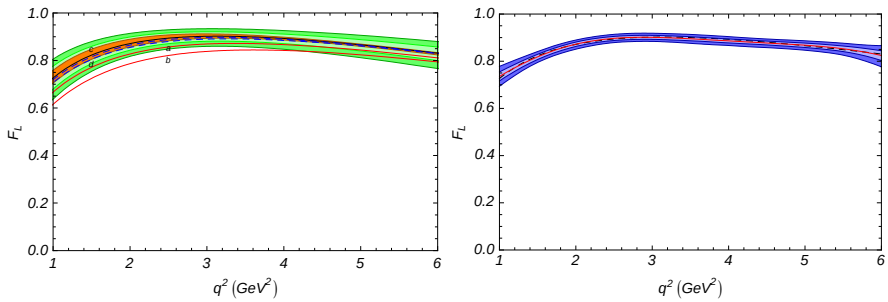


Fig. 5: F_L, as in Fig.1.

where for $i, j = 0, \|, \perp$

$$A_i A_j^* \equiv A_{iL}(q^2) A_{jL}^*(q^2) + A_{iR}(q^2) A_{jR}^*(q^2),$$

$$F_L(q^2) = \frac{|A_0|^2}{|A_0|^2 + |A_\||^2 + |A_\perp|^2}. \tag{5}$$

In contrast, the following three observables,

$$A_T^{(2)} = \frac{|A_\perp|^2 - |A_\||^2}{|A_\perp|^2 + |A_\||^2}, \quad A_T^{(3)} = \frac{|A_{0L} A_{\|L}^* + A_{0R}^* A_{\|R}|}{\sqrt{|A_0|^2 |A_\perp|^2}}\,, \tag{6}$$

$$A_T^{(4)} = \frac{|A_{0L} A_{\perp L}^* - A_{0R}^* A_{\perp R}|}{|A_{0L}^* A_{\|L} + A_{0R} A_{\|R}^*|}\,, \tag{7}$$

are theoretically clean for *all* dilepton masses and also show a very high sensitivity to right-handed currents.

In the following figures the results on the observables, F_L, A_{FB}, $A_T^{(2)}$, $A_T^{(3)}$, and $A_T^{(4)}$ are illustrated: For all the observables the theoretical sensitivity is plotted on the top of each figure. The thin dark line is the central NLO result for the SM and the narrow inner dark (orange) band that surrounds it corresponds to the NLO SM uncertainties due to both input parameters and perturbative scale dependence. Light grey (green) bands are the estimated $\Lambda/m_b \pm 5\%$ corrections for each spin amplitude while darker grey (green) ones are the more conservative $\Lambda/m_b \pm 10\%$ corrections. The curves labelled (a)–(d) correspond to four different benchmark points in the MSSM for righthanded currents (for more details see [4]). The experimental sensitivity for a dataset corresponding to 10 fb^{-1} of LHC*b* data is given in each figure on the bottom, assuming the SM. Here the solid (red) line shows the median extracted from the fit to the ensemble of data and the dashed (black) line shows the theoretical input distribution. The inner and outer bands correspond to 1σ and 2σ experimental errors.

The observables $A_T^{(3)}$ and $A_T^{(4)}$ offer sensitivity to the longitudinal spin amplitude $A_{0L,R}$ in a controlled way compared to the old observable F_L: the dependence on both the parallel and perpendicular soft form factors $\xi_\|(0)$ and $\xi_\perp(0)$ cancels at LO. A residual of this dependence may appear at NLO, but as shown in Figs. 2 and 3, it is basically negligible. It is also remarkable that for $A_T^{(3)}$ and $A_T^{(4)}$ at low q^2 the impact of this uncertainty is less important than the

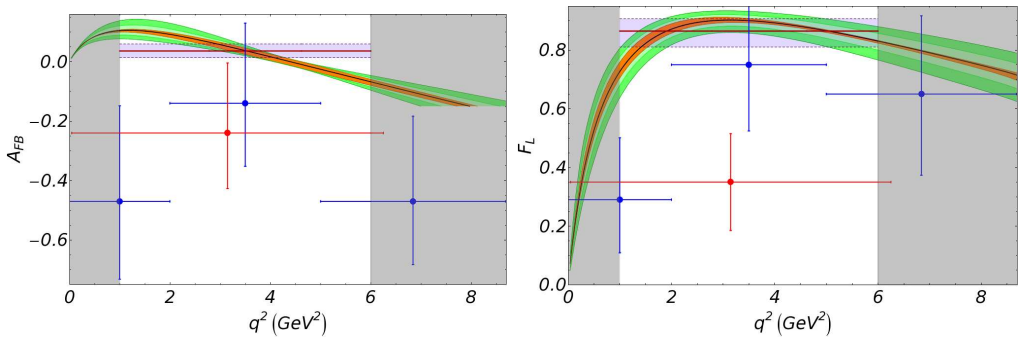


Fig. 6: Belle (black/blue) and BaBar (grey/red) data points on F_L and on A_{FB} with SM predictions and weighted SM averages over the bin $q^2 \in [1\,\mathrm{GeV}^2, 6\,\mathrm{GeV}^2]$

uncertainties due to input parameters and scale dependence. The observables $A_T^{(3)}$ and $A_T^{(4)}$ also present a different sensitivity to $\mathcal{C}_7'$ via their dependence on $A_{0L,R}$ compared with $A_T^{(2)}$. This may allow for a particularly interesting cross check of the sensitivity to this chirality flipped operator $\mathcal{O}_7'$; for instance, new contributions coming from tensor scalars and pseudo-scalars will behave differently among the set of observables.

Another remarkable point that becomes clear when comparing the set of clean observables $A_T^{(2)}$, $A_T^{(3)}$ and $A_T^{(4)}$ versus the old observables F_L and A_{FB} concerns the potential discovery of NP, in particular of new right-handed currents. There are large deviations from the SM curve from the ones of the four supersymmetric benchmark points. A large deviation from the SM for $A_T^{(2)}$, $A_T^{(3)}$ or $A_T^{(4)}$ can thus show the presence of right-handed currents in a way that is not possible with F_L or A_{FB}. In the latter cases the deviations from the SM prediction of the same four representative curves are marginal.

In the experimental plots we find a good agreement between the central values extracted from the fits and the theoretical input. Any deviations seen are small compared to the statistical uncertainties. The experimental resolution for F_L is very good but with the small deviations from the SM expected this is not helpful in the discovery of new right-handed currents. Comparing the theoretical and experimental figures for the other observables it can be seen that in particular $A_T^{(3)}$ show great promise to distinguish between NP models.

Finally, let us mention that the old observables F_L and A_{FB} are already accessible to the BaBar [10, 34] and Belle [35] experiments. The first measurements are shown in Fig. 6 with the SM predictions and the weighted SM averages over the bin $q^2 \in [1\,\mathrm{GeV}^2, 6\,\mathrm{GeV}^2]$. All the present data is compatible with the SM predictions. For example, the first measurement of the Babar collaboration on F_L in the low-q^2 region is given as an average over the bin $q^2 \in [4m_\mu^2, 6.25\,\mathrm{GeV}^2]$:

$$F_L([4m_\mu^2, 6.25\,\mathrm{GeV}^2]) = 0.35 \pm 0.16 \pm 0.04; \tag{8}$$

while the theoretical average, weighted over the rate, using the bin, $q^2 \in [1\,\mathrm{GeV}^2, 6\,\mathrm{GeV}^2]$, based on our results is given by:

$$F_L([1\,\mathrm{GeV}^2, 6\,\mathrm{GeV}^2]) = 0.86^{+0.04}_{-0.05}. \tag{9}$$

Here, one should keep in mind that the spectrum below $1\,\mathrm{GeV}^2$ is theoretically problematic due to the influence of very light resonances; moreover the rate and also the polarisation F_L are changing dramatically around $1\,\mathrm{GeV}^2$. Therefore, we strongly recommend to use the standard bin from $1\,\mathrm{GeV}^2$ to $6\,\mathrm{GeV}^2$ in all future measurements.

6 Summary

The full angular analysis of the decay $\overline{B}_d \to \overline{K}^{*0}\mu^+\mu^-$ at the LHC*b* experiment offers great opportunities for the new physics search. New observables can be designed to be sensitive to a specific kind of NP operator within the model-independent analysis using the effective field theory approach. The new observables $A_T^{(2)}$, $A_T^{(3)}$ and $A_T^{(4)}$ are shown to be highly sensitive to right handed currents. Clearly, theoretical progress on the Λ/m_b corrections would enhance their sensitivity significantly and would be highly desirable in view of a possible upgrade of the LHC*b* experiment. Moreover, we have shown that the previously discussed angular distribution $A_T^{(1)}$ cannot be measured at either LHC*b* or at a Super-B factory.

Acknowledgement

Support of the Eupopean network Heptools is acknowledged.

Appendix

We add here the explicit formula for the distribution functions and their symmetries:

In the massless limit, the distribution functions I_i depend on products of the six complex K^* spin amplitudes, $A_{\perp L/R}$, $A_{\parallel L/R}$, $A_{0L/R}$:

$$
\begin{aligned}
I_1 &= \frac{3}{4}\left(|A_{\perp L}|^2 + |A_{\parallel L}|^2 + (L \to R)\right)\sin^2\theta_K + + \left(|A_{0L}|^2 + |A_{0R}|^2\right)\cos^2\theta_K \\
&\equiv a\sin^2\theta_K + b\cos^2\theta_K, \\
I_2 &= \frac{1}{4}(|A_{\perp L}|^2 + |A_{\parallel L}|^2)\sin^2\theta_K + -|A_{0L}|^2\cos^2\theta_K + (L \to R) \\
&\equiv c\sin^2\theta_K + d\cos^2\theta_K, \\
I_3 &= \frac{1}{2}\Big[(|A_{\perp L}|^2 - |A_{\parallel L}|^2)\sin^2\theta_K + (L \to R)\Big] \equiv e\sin^2\theta_K, \\
I_4 &= \frac{1}{\sqrt{2}}\Big[\Re(A_{0L}A_{\parallel L}^*)\sin 2\theta_K + (L \to R)\Big] \equiv f\sin 2\theta_K, \\
I_5 &= \sqrt{2}\Big[\Re(A_{0L}A_{\perp L}^*)\sin 2\theta_K - (L \to R)\Big] \equiv g\sin 2\theta_K, \\
I_6 &= 2\Big[\Re(A_{\parallel L}A_{\perp L}^*)\sin^2\theta_K - (L \to R)\Big] \equiv h\sin^2\theta_K, \\
I_7 &= \sqrt{2}\Big[\Im(A_{0L}A_{\parallel L}^*)\sin 2\theta_K - (L \to R)\Big] \equiv j\sin 2\theta_K, \\
I_8 &= \frac{1}{\sqrt{2}}\Big[\Im(A_{0L}A_{\perp L}^*)\sin 2\theta_K + (L \to R)\Big] \equiv k\sin 2\theta_K,
\end{aligned}
$$

$$I_9 \;=\; \Big[\Im(A^*_{\|L}A_{\perp L})\sin^2\theta_K + (L\to R)\Big] \equiv m\sin^2\theta_K. \tag{10}$$

Taking into account $a = 3c$ and $b = -d$, we are left with 9 independent parameters which can be fixed experimentally in a full angular fit.

The distribution functions are *invariant* under the following three independent symmetry transformations of the spin amplitudes as one easily verifies, using the explicit formulae given above: (1) a global phase transformation of the L-amplitudes

$$A^{'}_{\perp L} = e^{i\phi_L}A_{\perp L},\;\; A^{'}_{\|L} = e^{i\phi_L}A_{\|L},\;\; A^{'}_{0L} = e^{i\phi_L}A_{0L}; \tag{11}$$

(2) a global transformation of the R-amplitudes

$$A^{'}_{\perp R} = e^{i\phi_R}A_{\perp R},\;\; A^{'}_{\|R} = e^{i\phi_R}A_{\|R},\;\; A^{'}_{0R} = e^{i\phi_R}A_{0R}; \tag{12}$$

and (3) a continuous $L \leftrightarrow R$ rotation

$$\begin{aligned}
A^{'}_{\perp L} &= +\cos\theta A_{\perp L} + \sin\theta A^*_{\perp R},\; A^{'}_{\perp R} = -\sin\theta A^*_{\perp L} + \cos\theta A_{\perp R}\\
A^{'}_{0L} &= +\cos\theta A_{0L} - \sin\theta A^*_{0R},\;\; A^{'}_{0R} = +\sin\theta A^*_{0L} + \cos\theta A_{0R}\\
A^{'}_{\|L} &= +\cos\theta A_{\|L} - \sin\theta A^*_{\|R},\;\; A^{'}_{\|R} = +\sin\theta A^*_{\|L} + \cos\theta A_{\|R}.
\end{aligned} \tag{13}$$

References

[1] M. Artuso *et al.*, arXiv:0801.1833 [hep-ph].

[2] T. Hurth, Rev. Mod. Phys. **75** (2003) 1159 [arXiv:hep-ph/0212304].

[3] T. Hurth, Int. J. Mod. Phys. A **22** (2007) 1781 [arXiv:hep-ph/0703226].

[4] U. Egede, T. Hurth, J. Matias, M. Ramon and W. Reece, arXiv:0807.2589 [hep-ph].

[5] A. Ishikawa *et al.* [Belle Collaboration], Phys. Rev. Lett. **91** (2003) 261601 [arXiv:hep-ex/0308044].

[6] B. Aubert *et al.* [BABAR Collaboration], Phys. Rev. Lett. **91** (2003) 221802 [arXiv:hep-ex/0308042].

[7] A. Ishikawa *et al.*, Phys. Rev. Lett. **96** (2006) 251801 [arXiv:hep-ex/0603018].

[8] T. Hurth, G. Isidori, J. F. Kamenik and F. Mescia, arXiv:0807.5039 [hep-ph].

[9] B. Aubert *et al.* [BABAR Collaboration], Phys. Rev. D **73** (2006) 092001 [arXiv:hep-ex/0604007].

[10] B. Aubert *et al.* [BABAR Collaboration], arXiv:0804.4412 [hep-ex].

[11] J. Dickens, V. Gibson, C. Lazzeroni and M. Patel, CERN-LHCB-2007-038.

[12] J. Dickens, V. Gibson, C. Lazzeroni and M. Patel, CERN-LHCB-2007-039.

[13] U. Egede, CERN-LHCB-2007-057.

[14] T. Browder, M. Ciuchini, T. Gershon, M. Hazumi, T. Hurth, Y. Okada and A. Stocchi, JHEP **0802** (2008) 110 [arXiv:0710.3799 [hep-ph]].

[15] M. Bona *et al.*, arXiv:0709.0451 [hep-ex].

[16] J. L. . Hewett *et al.*, arXiv:hep-ph/0503261.

[17] A. G. Akeroyd *et al.* [SuperKEKB Physics Working Group], arXiv:hep-ex/0406071.

[18] M. Beneke, G. Buchalla, M. Neubert and C. T. Sachrajda, Phys. Rev. Lett. **83** (1999) 1914.

[19] C. W. Bauer, S. Fleming, D. Pirjol and I. W. Stewart, Phys. Rev. D **63** (2001) 114020 [arXiv:hep-ph/0011336].

[20] M. Beneke, A. P. Chapovsky, M. Diehl and T. Feldmann, Nucl. Phys. B **643** (2002) 431 [arXiv:hep-ph/0206152].

[21] J. Charles, A. Le Yaouanc, L. Oliver, O. Pène, and J.-C. Raynal, Phys. Rev. D **60**, 014001 (1999); Phys. Lett. B **451**, 187 (1999). See also M. J. Dugan and B. Grinstein, *ibid.* **255**, 583 (1991).

[22] M. Beneke and T. Feldmann, Nucl. Phys. B **592** (2001) 3 [hep-ph/0008255].

[23] F. Krüger, Chapter 2.17 of Ref. [16].

[24] F. Kruger and J. Matias, Phys. Rev. D **71**, 094009 (2005);

[25] E. Lunghi and J. Matias, JHEP **0704** (2007) 058 [arXiv:hep-ph/0612166].

[26] C. Bobeth, G. Hiller and G. Piranishvili, arXiv:0805.2525 [hep-ph].

[27] M. Beneke, T. Feldmann and D. Seidel, Nucl. Phys. B **612** (2001) 25 [arXiv:hep-ph/0106067]; Eur. Phys. J. C **41** (2005) 173 [arXiv:hep-ph/0412400].

[28] F. Krüger, L. M. Sehgal, N. Sinha, and R. Sinha, Phys. Rev. D **61**, 114028 (2000); **63**, 019901(E) (2001).

[29] D. Melikhov, N. Nikitin, and S. Simula, Phys. Lett. B **442**, 381 (1998).

[30] C. S. Kim, Y. G. Kim, C.-D. Lü, and T. Morozumi, Phys. Rev. D **62**, 034013 (2000).

[31] A. Faessler, T. Gutsche, M. A. Ivanov, J. G. Körner, and V. E. Lyubovitskij, EPJdirect **C4**, 18 (2002).

[32] A. Ali and A. S. Safir, Eur. Phys. J. C **25**, 583 (2002).

[33] U. Egede,T. Hurth,J. Matias,M. Ramon and W. Reece, in preparation.

[34] Talk by K.Flood (BaBar collaboration) at ICHEP2008, see http://ichep08.com/ .

[35] Talk by J.-T.Wei (Belle collaboration) at ICHEP2008, see http://ichep08.com/ .

Searches for Physics beyond the Standard Model

Arnd Meyer (meyera@physik.rwth-aachen.de)
III. Phys. Inst. A, RWTH Aachen University, 52074 Aachen, Germany
DOI: http://dx.doi.org/10.3204/DESY-PROC-2009-01/63

Abstract
Recent results on searches for new physics from Run II of the Tevatron are reported. The D0 and CDF experiments have already collected more than 4 fb^{-1} of integrated luminosity each, allowing for a large number of new phenomena searches in many different final states. No deviations from the standard model expectations are found, and the presented limits on new physics are in many cases the world's best.

A large number of solutions has been proposed for all of the deficits of the standard model (SM) that we know about since many years – be it the non-unification of couplings at a high scale, the quadratic divergences in the loop corrections to the Higgs boson mass, or the lack of a decent dark matter candidate. The most popular models of new physics involve supersymmetry. However, supersymmetry doesn't explain the number of fermion generations, or their mass spectrum and charges. In this talk, a few selected recent results from the D0 and CDF experiments of searches for manifestations of new physics are reported. Details for all Tevatron results can be found at [1].

1 Lepton compositeness

Both CDF and D0 have searched for excited electrons and muons as signs of lepton compositeness. Recently, an analysis of excited electron production has been published [2]. D0 searched for associated production of an electron and an excited electron, with the latter decaying to an electron and a photon. The production is approximated as a contact interaction, while the decay is assumed to proceed either exclusively through a gauge interaction, or a combination of gauge and contact interactions, with the relative fraction of the two depending on the mass of the excited electron and the compositeness scale Λ. The D0 result, based on 1.0 fb^{-1} of data, is shown in Fig. 1, excluding $m_{e^*} < 756$ GeV for $\Lambda = 1$ TeV at 95% C.L.; depending on the value of Λ and the assumed branching fractions, masses up to about 1 TeV are excluded.

2 Supersymmetry

In minimal supergravity, the two most interesting final states are firstly multiple jets and missing E_T, the generic signal of squark and gluino production, and secondly the trilepton signature, due to chargino and neutralino production. In the D0 analysis [3], based on 2.1 fb^{-1}, the observed event numbers in three dedicated analyses (2, 3, 4 jets plus $\not\!\!E_T$) are converted into an exclusion domain in the plane of the squark and gluino masses (Fig. 2 left). Squark masses below 379 GeV and gluino masses below 308 GeV are excluded, while the lower limit for equal squark and gluino masses is 390 GeV. Both in this result and in the CDF trilepton analysis [4], results are also presented in the $(m_0, m_{1/2})$ plane, as shown in Fig. 2 (right) for the trilepton analysis.

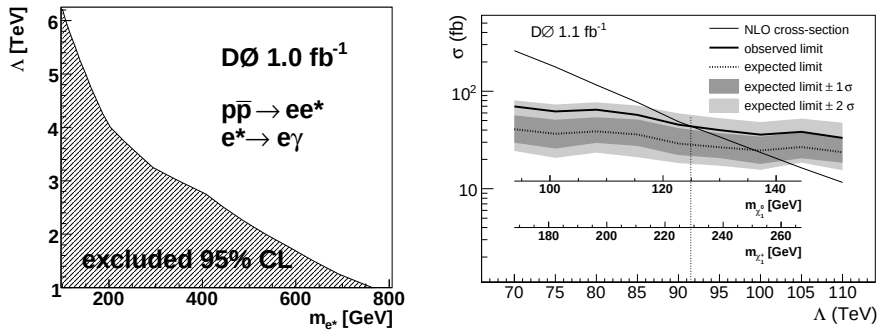


Fig. 1: (Left) Exclusion region in the search for excited electrons produced in contact interactions in the decay mode $e^* \to e\gamma$. (Right) Cross section limits and theoretical predictions in a model of gauge-mediated SUSY breaking.

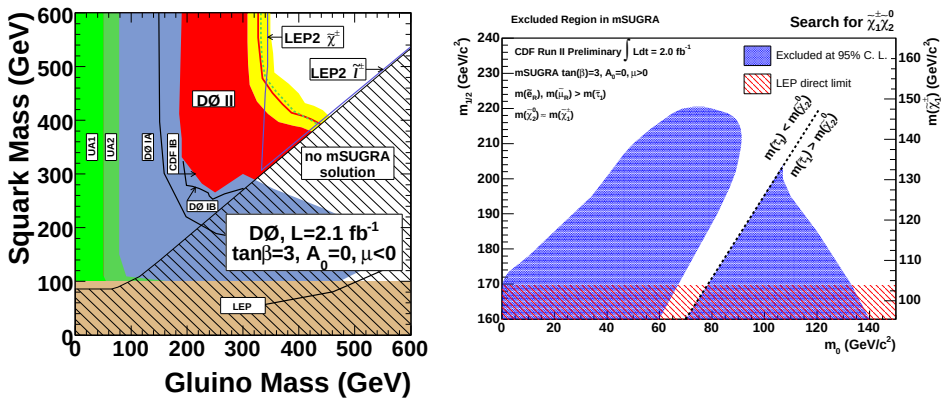


Fig. 2: (Left) Region in the plane of gluino and squark masses excluded by searches for supersymmetry in the jets plus $\not\!\!E_T$ channel. (Right) Region in the $(m_0, m_{1/2})$ plane excluded by searches in the trilepton channel.

Alternative SUSY scenarios include models with gauge-mediated SUSY breaking, where the gravitino is the lightest SUSY particle. The phenomenology depends on the next-to-lightest SUSY particle (stau or neutralino), and its lifetime. If the neutralino promptly decays to a gravitino and photon, the characteristic signature is $\gamma\gamma + \not\!\!E_T$. The latest result in this channel from D0 [5] is shown in Fig. 1 (right), excluding a lightest chargino with masses below 229 GeV.

3 Large extra dimensions

Models postulating the existence of extra spatial dimensions have been proposed to solve the hierarchy problem posed by the large difference between the Planck scale $M_{pl} \simeq 10^{16}$ TeV, at which gravity is expected to become strong, and the scale of electroweak symmetry breaking, $\simeq 1$ TeV. In the large extra dimensions model of Arkani-Hamed, Dimopoulos and Dvali, it is possible to produce gravitons which immediately disappear into bulk space, leading to an excess of events with a high transverse energy photon or jet and large missing transverse energy. A recent compilation by CDF [6] of their results in these two signatures is shown in Fig. 3 (left); the combined limits on the fundamental Planck scale range between $M_D > 1400$ GeV and $M_D > 940$ GeV at 95% C.L. for numbers of extra dimensions from 2 to 6.

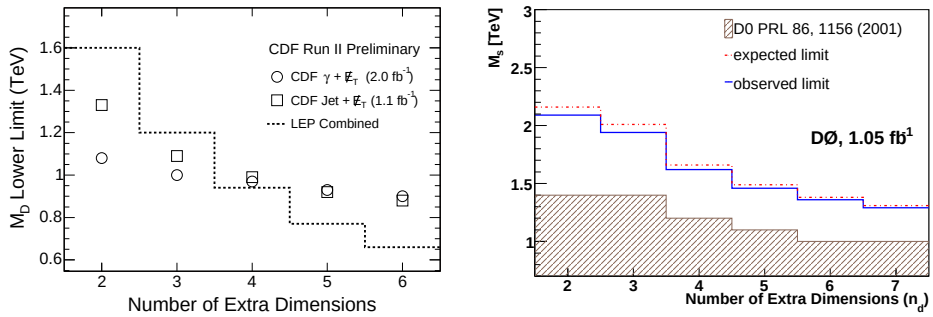


Fig. 3: (Left) Limits on the fundamental Planck scale M_D as a function of the number of extra dimensions in the single photon and single jet channels. (Right) Limits on the effective Planck scale M_s as a function of the number of extra dimensions obtained in the $ee/\gamma\gamma$ channel.

The virtual exchange of KK gravitons would modify the cross sections for SM processes like the production of fermion or boson pairs. The sensitivity is expressed in terms of the scale M_s, which is expected to be close to M_D. In a recent analysis [7] based on an integrated luminosity of 1.05 fb^{-1}, D0 has investigated the high mass e^+e^- and $\gamma\gamma$ mass spectrum, and has found no indications for large extra dimensions. Limits on M_s are set as shown in Fig. 3 (right), for example $M_s > 1.62$ TeV for $n_d = 4$ at 95% C.L.

4 Randall-Sundrum gravitons

In the model by Randall and Sundrum, gravity is located on a $(3+1)$-dimensional brane that is separated from the SM brane in a fifth dimension with warped metric. The gravitons appear as towers of KK excitations with masses and widths determined by model parameters. These parameters can be expressed in terms of the mass of the first excited mode of the graviton, M_1, and the dimensionless coupling to the standard model fields, $k\sqrt{8\pi}/M_{pl}$. If it is light enough, the first excited graviton mode could be resonantly produced at the Tevatron. D0 has published [8] new results in the search for Randall-Sundrum gravitons based on 1 fb^{-1}of data. The invariant mass spectrum in the e^+e^- and $\gamma\gamma$ final states has been used. General agreement between data and the background expectation is observed. Using a sliding mass window technique, upper cross section limits are derived, which are then translated into lower mass limits for the lowest excited mode of RS gravitons (Fig. 4 left). For a coupling parameter $k\sqrt{8\pi}/M_{pl} = 0.1$ (0.01), masses $M_1 < 900$ (300) GeV are excluded at 95% C.L.

The CDF dielectron spectrum [9] obtained in a data sample corresponding to 2.5 fb^{-1} is shown in Fig. 4 (right). An excess of data over background with a significance of 2.5σ after accounting for the 'trials factor' is found for an e^+e^- mass window at 240 GeV. In this analysis, RS gravitons with a mass $M_1 < 848$ GeV are excluded at 95% C.L. for $k\sqrt{8\pi}/M_{pl} = 0.1$.

5 New heavy gauge bosons

A possible way of resolving the inherent problems of the standard model is by extending the gauge sector of the theory. In the search for singly charged gauge bosons, D0 looked for a SM-like W' decaying to an electron and a neutrino [10]. The limit, obtained from a study of the

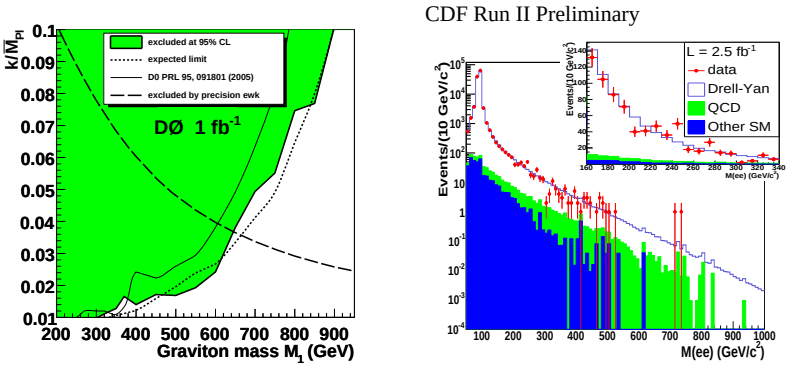


Fig. 4: (Left) Excluded region in the plane of $k\sqrt{8\pi}/M_{pl}$ and graviton mass. (Right) Invariant dielectron mass distribution. The inset shows the region around 240 GeV on a linear scale.

transverse mass spectrum in 1 fb^{-1} of data, requires $m(W') > 1.0$ TeV at 95% C.L. (Fig. 5 left). As an example of a search for a Z' decaying into charged leptons, Fig. 5 (right) shows the (inverse) invariant mass distribution CDF obtained in 2.3 fb^{-1} of dimuon data [11]. No significant excess above the standard model expectation is observed. For a SM-like Z', masses below 1.03 TeV are excluded at 95% C.L.

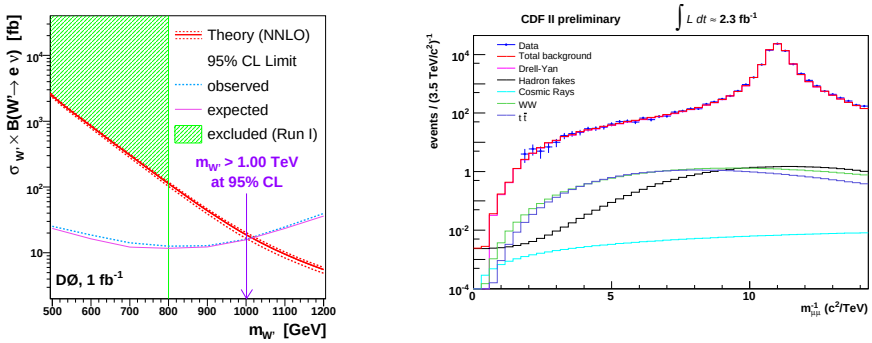


Fig. 5: (Left) Cross section upper limits for the production of a SM-like W'. (Right) Dimuon inverse invariant mass distribution used for resonance searches.

6 Leptoquarks

Leptoquarks (LQ) are a natural consequence of the unification of quarks and leptons into a single multiplet, and as such are expected to be gauge bosons as well. In some models they can be relatively light and accessible at colliders. Experimentally, it is customary to consider one LQ per generation. These are assumed to be very short-lived and decay to a quark and a lepton. The branching fraction to a charged lepton and a quark is then denoted as β. At hadron colliders, leptoquarks can be pair-produced through the strong interaction. Both experiments have searched for leptoquarks of all three generations in different decay modes. A typical result is the recent update [12] in the channel $e^+e^-q\bar{q}$, sensitive for first generation LQ with large β. A lower limit of 299 GeV at 95% C.L. on the mass of a scalar LQ with $\beta = 1$ is set (see Fig. 6 left).

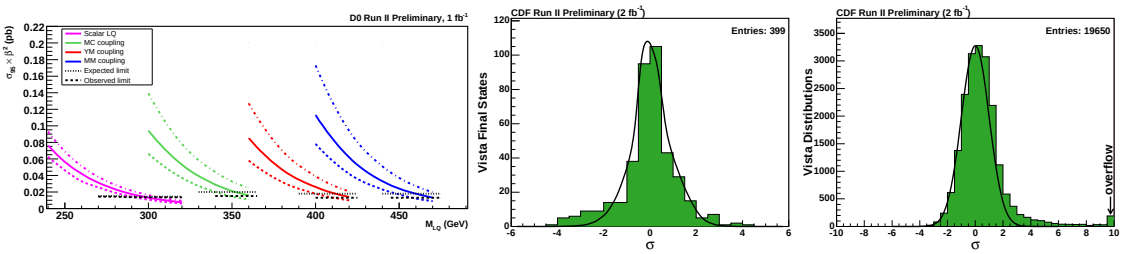


Fig. 6: (Left) Cross sections and limits as a function of the scalar and vector LQ mass (for three different coupling scenarios). The LO (vector LQ) or NLO (scalar) theoretical cross sections are drawn for different values of the renormalization scale. (Middle and Right) Overview of agreement between data and SM expectation in standard deviations for final states (middle) and kinematic distributions (right) in the model independent search.

7 Global search

The CDF collaboration has recently updated a model independent search for deviations from the SM with an integrated luminosity of 2 fb^{-1} [13]. Events are categorized in terms of their content in high p_T objects: electrons, muons, taus, photons, jets, b jets, and neutrinos ($\not\!\!E_T$). After applying several correction factors, the 399 final states are compared in terms of their normalization with the expectations from all SM processes. In a second step, a total of 19650 kinematic distributions are scrutinized. After accounting for the trial factors, remaining significant deviations (see Fig. 6) are interpreted as being due to the inadequate modeling of soft QCD effects.

8 Summary

D0 and CDF have searched for a wide variety of new phenomena beyond the SM. No signs for new physics have been found using an integrated luminosity of $1-3$ fb^{-1}. With more than 4 fb^{-1} recorded by each experiment, updates will remain interesting until the LHC delivers results.

References

[1] Details at `http://www-d0.fnal.gov/Run2Physics/WWW/results/np.htm` and `http://www-cdf.fnal.gov/physics/exotic/exotic.html`.

[2] V. M. Abazov *et al.* (D0 Collaboration), Phys. Rev. D **77**, 091102 (2008).

[3] V. M. Abazov *et al.* (D0 Collaboration), Phys. Lett. **B 660**, 449 (2008).

[4] T. Aaltonen *et al.* (CDF Collaboration), arXiv:0808.2446 [hep-ex].

[5] V. M. Abazov *et al.* (D0 Collaboration), Phys. Lett. **B 659**, 856 (2008).

[6] T. Aaltonen *et al.* (CDF Collaboration), arXiv:0807.3132 [hep-ex].

[7] V. M. Abazov *et al.* (D0 Collaboration), arXiv:0809.2813 [hep-ex].

[8] V. M. Abazov *et al.* (D0 Collaboration), Phys. Rev. Lett. **100**, 091802 (2008).

[9] T. Aaltonen *et al.* (CDF Collaboration), arXiv:0810.2059 [hep-ex].

[10] V. M. Abazov *et al.* (D0 Collaboration), Phys. Rev. Lett. **100**, 031804 (2008).

[11] T. Aaltonen *et al.* (CDF Collaboration), arXiv:0811.0053 [hep-ex].

[12] D0 Collaboration, D0 Note 5644-CONF, http://www-d0.fnal.gov/Run2Physics/WWW/results/prelim/NP/N62.

[13] T. Aaltonen *et al.* (CDF Collaboration), arXiv:0809.3781 [hep-ex].

Discovery potential at the LHC: channels relevant for SM Higgs

I. Tsukerman on behalf of ATLAS and CMS collaborations
ITEP, Moscow, Russia

DOI: http://dx.doi.org/10.3204/DESY-PROC-2009-01/64

Abstract
The discovery potential of Standard Model Higgs searches at the LHC at 14 TeV center-of-mass energy is reviewed. Decay channels such as $H \to \gamma\gamma$, $H \to ZZ^\star \to 4\ell$, $H \to WW^\star$ and $H \to \tau\tau$ are considered. Results are based on the most recent full GEANT-based simulations performed by the ATLAS and CMS experiments.

1 Introduction

The primary objective of the Large Hadron Collider (LHC) at CERN is to study the origin of electroweak symmetry breaking. Within the Standard Model (SM), the Higgs mechanism [1] is invoked to explain this breaking and the Higgs boson remains the only particle that has not been discovered so far. The direct search at the e^+e^- collider LEP has led to a lower bound on its mass of 114.4 GeV at 95% C.L. [2]. In addition, high precision electroweak data constrain the mass of the Higgs boson via their sensitivity to loop corrections. The upper limit is $m(H) \leq 185$ GeV at 95% C.L. provided the LEP result is also used in the determination of this limit [3]. At last, combined preliminary results from the Tevatron experiments CDF and D0 based on 3 fb^{-1} accumulated data at 1.8 TeV lead to a 95% C.L. exclusion of a Higgs boson with $m(H)$=170 GeV [4]. Both ATLAS and CMS experiments at the LHC, scheduled for proton-proton collision data taking in summer 2009, have been designed to search for the Higgs boson over a wide mass range [5]. In these proceedings the sensitivity for each experiment to discover or exclude the SM Higgs boson as well as recent developments that have enhanced this sensitivity are summarized.

2 SM Higgs production at the LHC

Theoretical predictions for NLO SM Higgs production cross-sections at 14 TeV energy as a function of $m(H)$ [6] are shown in Fig.1 (left). The dominant production mechanism, which proceeds via a top-quark loop, is gluon-gluon fusion ($gg \to H$). It gives rise to 20–40 pb SM Higgs cross section in the mass range between 114 and 185 GeV. The vector-boson fusion (VBF) process ($qq \to qqH$) has a factor of eight smaller cross section. However, in this case, the Higgs boson is accompanied by two energetic jets going mainly into the forward directions. Usually they have large pseudorapidity gap in-between. In addition, there is no colour flow between these *tagging* jets which allows for use of *a central jet veto* to reduce backgrounds. $q\bar{q} \to HW$, $q\bar{q} \to HZ$ and $gg, q\bar{q} \to t\bar{t}H$ processes have smaller cross sections.

3 SM Higgs discovery final states

The SM Higgs boson is predicted to have many decay channels with branching ratios which strongly depend on its mass (Fig.1 (right)). The evaluation of the search sensitivity of the various channels should take into account the cross-sections of the relevant backgrounds.

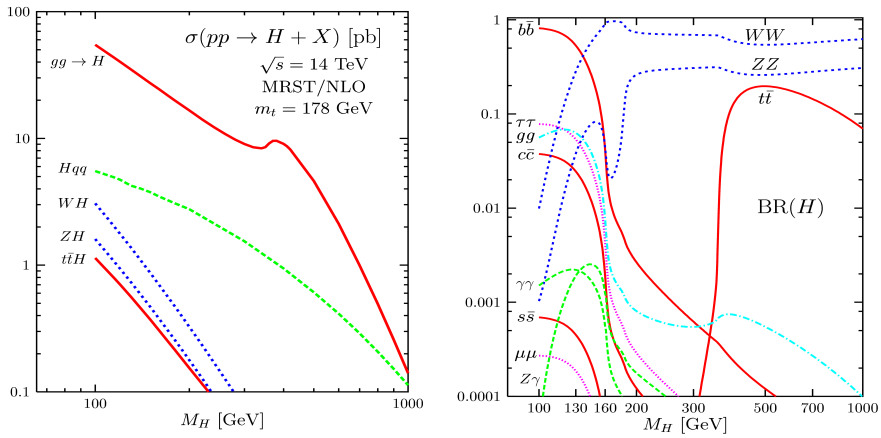


Fig. 1: Left: Theoretical predictions for SM Higgs boson production cross sections at LHC energies. Right: Theoretical predictions for SM Higgs boson decay branching ratios.

At low Higgs mass the dominant decay mode is through $b\bar{b}$. However, due to the enormous QCD backgrounds this channel is not good for the SM Higgs discovery. The $\gamma\gamma$ final state, which appears when the Higgs decays via bottom, top and W-loops, has a small branching fraction. However, excellent diphoton invariant-mass resolution and γ/jet separation can make this mode one of the best discovery channels. $H \to \tau\tau$ has a sizeable rate and should be visible with good purity via the VBF Higgs production mode.

If the Higgs mass is larger, the $H \to WW^\star$ final states are powerful as well as the mode $H \to ZZ^\star \to 4\ell$. In the last case, the resulting branching ratio is small but the signal is easy to trigger on and allows for full reconstruction of the Higgs mass.

Both ATLAS and CMS Collaborations have performed extensive GEANT-based Monte Carlo [7] studies with full simulation and reconstruction to determine the experimental viability of many Higgs decay channels. Results of the recent studies [8] for the most attractive signatures, namely $H \to \gamma\gamma$, $H \to ZZ^\star \to 4\ell$, $H \to WW^\star$ and VBF $H \to \tau\tau$ are summarized below.[1]

3.1 $H \to \gamma\gamma$

Despite a only 0.2% branching ratio in the Higgs mass region 120–140 GeV, $H \to \gamma\gamma$ remains a promising channel as the signal signature is very clean. Irreducible backgrounds come from continuum production of diphotons, $q\bar{q}, gg \to \gamma\gamma$. Reducible backgrounds are mostly due to γ-jet and jet-jet events, where one or more jets are misidentified as photons. Studies performed by both the ATLAS and CMS experiments consider the signal and backgrounds at NLO level. Thanks to a very good electromagnetic energy resolution, with a simple cut-based analysis for an integrated luminosity of 30 fb^{-1} one can obtain a significance above 5σ in the CMS experiment for the mass range 115–140 GeV (Fig.2 (top left)). Having a worse energy resolution, ATLAS nevertheless can reach almost the same significance as the high-granularity electromagnetic calorimeter with longitudinal samplings is capable of determining the primary vertex with

[1] Another summaries of SM Higgs searches were presented at this year conferences, see, e.g. Ref. [9].

great precision. Both experiments have looked beyond a simple cut-based analysis and enhanced the signal significance by 30–50% (Fig.2 (top left)).

3.2 $H \to ZZ^\star \to 4\ell$

The "golden" channels (4μ, $2e2\mu$ and $4e$ final states of $ZZ^\star$ decays) are expected to be good for discovery in a wide mass range (except $m(H)$ $\leq$130 GeV and $m(H) \approx 2m_W$). The dominant background is the $ZZ^\star$-continuum with smaller contributions from $Zb\bar{b}$ and $t\bar{t}$ processes. Through the use of impact parameter and lepton isolation requirements the latter two (which are important only at low $m(H)$) can be significantly reduced. Simulations of the signal and the $q\bar{q} \to ZZ^\star$ backgrounds were made up to the NLO level. An additional 20–30% contribution from the $gg \to ZZ^\star$ process was also taken into account. A 5σ discovery in $H \to ZZ^\star \to 4\ell$ mode is possible in much of the allowed $m(H)$ space with less than 30 fb^{-1} of integrated LHC luminosity (Fig.2 (top right)).

3.3 $H \to WW^\star$

$H \to WW^\star$ is the main search channel in the Higgs mass range $2m_W \leq m(H) \leq 2m(Z)$ due to a very large $H \to WW$ branching ratio (Fig.1 (left)). This mode is also good at lower masses (down to $m(H) \approx$ 130 GeV) and at high $m(H)$. Two different final states are considered: $\ell\nu\ell\nu$ and $\ell\nu qq$. Unlike the $H \to ZZ \to 4\ell$ and $H \to \gamma\gamma$ channels, full mass reconstruction is not possible therefore an accurate background estimate is critical. The dominant background for this analysis is $q\bar{q}, gg \to WW^\star$-production in the case of H + 0 jets signal. This background can be suppressed by exploiting the spin correlation between the two final state leptons. For H + 2 jets, where the contribution from $qq \to qqH$ process is the most important, $t\bar{t}$-production is the main background which can be reduced by the *forward jet tagging* and *central jet veto* requirements. NLO-level studies (with systematics included) have shown that less than 2 fb^{-1} integrated luminosity would be sufficient for a 5σ discovery of the SM Higgs with $m(H)$ =160–170 GeV. Let us note that using the VBF $H \to WW^\star \to e\nu\mu\nu$ mode alone, ATLAS is able to observe this particle with 10 fb^{-1} of integrated luminosity provided 150 GeV $\leq m(H) \leq$ 180 GeV (Fig.2 (bottom left)).

3.4 **VBF** $H \to \tau\tau$

In gluon-fusion production mode the $H \to \tau\tau$ channel is not promising due to large backgrounds. However, one can consider the $qq \to qqH$ process which helps to reduce contributions coming mainly from the $Z/\gamma^\star \to \tau\tau$ + jets and $t\bar{t}$ processes. Data-driven methods for understanding the dominant backgrounds have been investigated. Three final states of τ decays are considered: lepton-lepton, lepton-hadron and also hadron-hadron. Despite the presence of neutrinos, mass reconstruction can be done via the collinear approximation where τ decay daughters are assumed to go in the same directions as their parents. The resolution on the reconstructed mass ($\sim$ 10 GeV) is mainly affected by the missing transverse energy resolution. Simulations performed by ATLAS and CMS have shown that the combination of the lepton-lepton and lepton-hadron channels should allow for a 5σ measurement with 30 fb^{-1} LHC luminosity in the range 115 GeV $\leq m(H) \leq$ 125 GeV (Fig.2 (bottom right)).

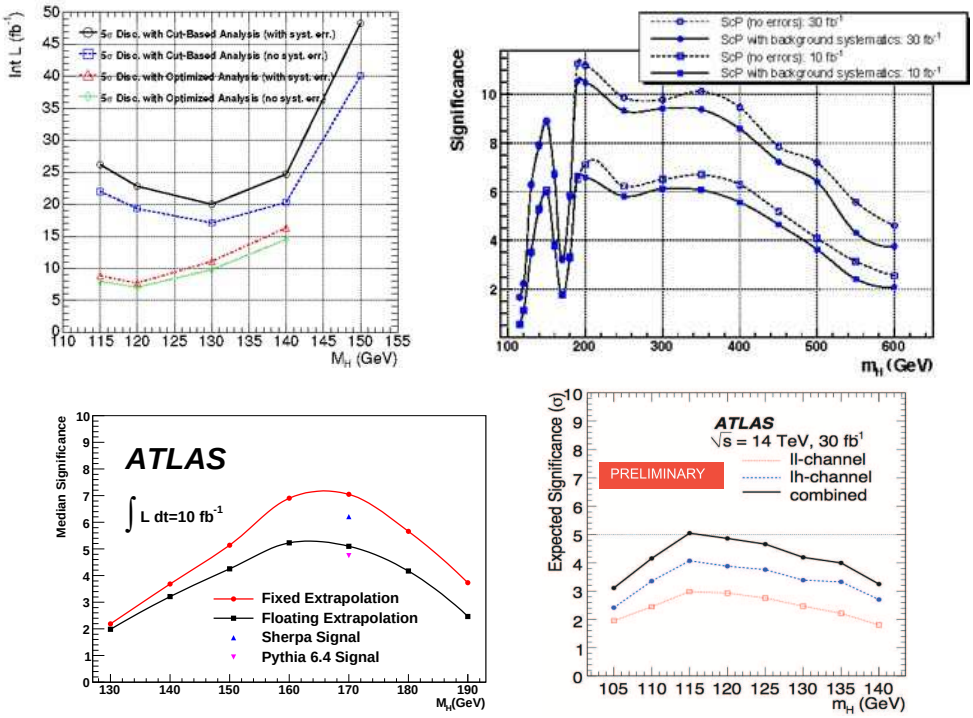


Fig. 2: SM Higgs discovery potential for specific decay modes. Top left: CMS, $H \to \gamma\gamma$. Top right: CMS, $H \to ZZ^\star \to 4\ell$. Bottom left: ATLAS, VBF $H \to WW^\star \to e\nu\mu\nu$. Bottom right: ATLAS, VBF $H \to \tau\tau$.

4 Summary of SM Higgs discovery potential

Figure 3 (left) shows integrated luminosity needed for the 5σ discovery of the inclusive Higgs boson production with the decay modes $H \to \gamma\gamma$, $H \to ZZ^\star \to 4\ell$ and $H \to WW^\star \to \ell\nu\ell\nu$ in the CMS experiment. In the most complicated region below $m(H)$ =130 GeV, less than 10 fb^{-1} would be sufficient while in the range 155 GeV$\leq m(H) \leq$400 GeV only 3 fb^{-1} are required. The signal significance as a function of the Higgs boson mass for 30 fb^{-1} of integrated LHC luminosity for the different Higgs boson production and decay channels is shown in Fig.3 (right). Here $H \to \tau\tau \to \ell\nu j\nu$ and $H \to WW^\star \to \ell\nu jj$ final states are also included. For $m(H)$ between 115 and 500 GeV 10σ discovery can be reached.

In summary, one can conclude that with integrated LHC luminosity of $\sim$5 fb^{-1} it is possible to discover SM Higgs boson provided its mass is above the 114 GeV limit obtained by LEP [10]. It is sufficient to accumulate 1 fb^{-1} for a 95% C.L. exclusion in the full allowed mass range.[2]

5 Acknowledgments

The author would like to thank the ATLAS and CMS Collaborations, in particular, M. Duehrssen, L. Fayard, R. Goncalo, K. Jakobs, V. Khovanskiy, B. Mellado, B. Murray, A. Nikitenko, A. Nisati, W. Quayle, T. Vickey and B. Wosiek.

[2]These statements are based on older simulations [11]. However one would not expect major changes when new results will be included.

References

[1] F. Englert and R. Brout, Phys. Rev. Lett. **13**, 321 (1964);
P. W. Higgs, Phys. Lett. **12**, 132 (1964);
P. W. Higgs, Phys. Rev. Lett. **13**, 508 (1964).

[2] LEP Higgs Working Group Collaboration, R. Barate *et al.*, Phys. Lett. **B565**, 61 (2003).

[3] The LEP Electroweak Working Group, http://lepewwg.web.cern.ch/LEPEWWG (July 2008).

[4] G. Bernardi *et al.* Tevatron New Phenomena Higgs Working Group, http://arxiv.org/pdf/0808.0534.

[5] ATLAS Collaboration, G. Aad *et al.*, JINST **3**, S08003 (2008);
CMS Collaboration, R. Adolphi *et al.*, JINST **3**, S08004 (2008).

[6] A. Djouadi, Phys. Rept. **457**, 1 (2008).

[7] S. Agostinelli *et al.*, Nucl. Inst. Meth. **A506**, 250 (2003).

[8] ATLAS Collaboration. CERN-OPEN-2008-020, Geneva (2008), to appear;
CMS Collaboration, G. L. Bayatian *et al.*, J. Phys. **G34**, 995 (2007). CMS technical design report, volume II: Physics performance.

[9] R. Goncalo, Proc. of the 34th Int. Conf. on High Energy Physics, Philadelphia, USA, 2008;
T. Vickey, Proc. of the XLIIIrd Rencontres de Moriond, La Thuile, Italy (2008);
A.Nisati, "Anticipating Physics at the LHC" Workshop, Kavli Inst. for Theor. Phys., Santa Barbara, USA, June 2, 2008.

[10] J.J. Blaising et al, Potential LHC contributions to Europe's future strategy at the high-energy frontier. http://council-strategygroup.web.cern.ch/council-strategygroup/BB2/contributions/Blaising2.pdf, 2006.

[11] ATLAS detector and physics performance. Technical design report. Vol. 2, CERN-LHCC-99-15 (1999);
S. Asai *et al.*, Eur. Phys. J. **C32S2**, 19 (2004);
CMS, the Compact Muon Solenoid: Technical proposal, CERN-LHCC-94-38 (1994).

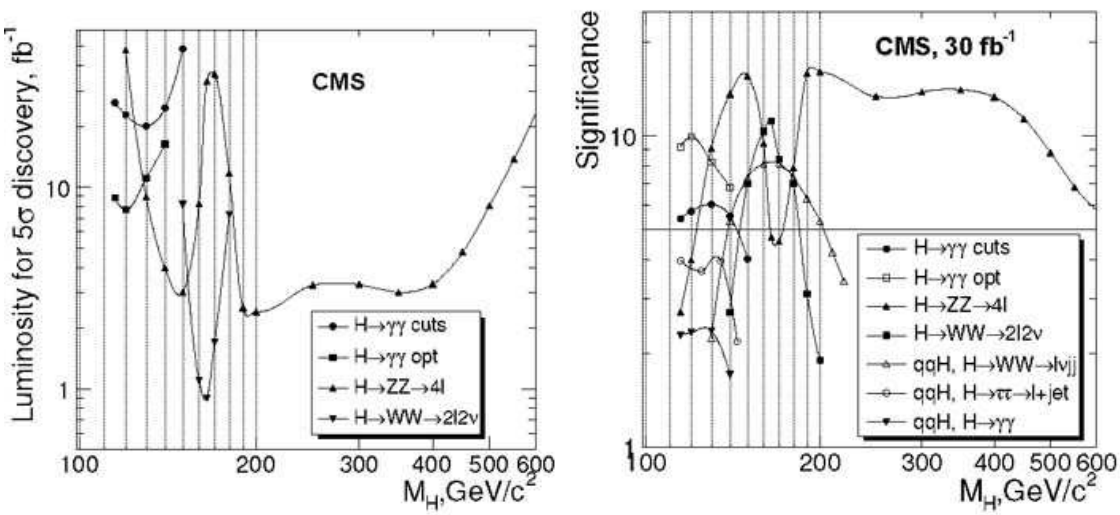


Fig. 3: Left: Integrated luminosity needed for 5σ discovery of the inclusive Higgs boson production pp$\rightarrow$ H + X with the Higgs boson decay modes $H \rightarrow \gamma\gamma$, $H \rightarrow ZZ^{\star} \rightarrow 4\ell$ and $H \rightarrow WW^{\star} \rightarrow \ell\nu\ell\nu$ in the CMS experiment. Right: The signal significance as a function of the Higgs boson mass for 30 fb^{-1} of the integrated luminosity for the different Higgs boson production and decay channels in the CMS experiment.

Central Exclusive Production of BSM Higgs bosons at the LHC

S. Heinemeyer[1], *V.A. Khoze*[2†], *M.G. Ryskin*[3], *M. Taševský*[4] *and G. Weiglein*[2]
[1]Instituto de Fisica de Cantabria (CSIC-UC), Santander, Spain,
[2]IPPP, Department of Physics, Durham University, Durham DH1 3LE, U.K.,
[3]Petersburg Nuclear Physics Institute, Gatchina, St. Petersburg, 188300, Russia,
[4]Institute of Physics of the ASCR, Na Slovance 2, 18221 Prague 8, Czech Republic
DOI: http://dx.doi.org/10.3204/DESY-PROC-2009-01/60

Abstract
The prospects for central exclusive diffractive (CED) production of MSSM Higgs bosons at the LHC are reviewed. These processes can provide important information on the $\mathcal{CP}$-even Higgs bosons, allowing to probe interesting regions of the m_A–$\tan\beta$ parameter plane. The sensitivity of the searches in the forward proton mode for the Higgs bosons in the so-called CDM-benchmark scenarios and the effects of fourth-generation models on the CED Higgs production are briefly discussed.

1 Introduction

The physics potential of forward proton tagging at the LHC has attracted much attention in the last years, see for instance [1–5]. The combined detection of both outgoing protons and the centrally produced system gives access to a unique rich programme of studies of QCD, electroweak and BSM physics. Importantly, these measurements will provide valuable information on the Higgs sector of MSSM and other popular BSM scenarios, see [6–9].

As it is well known, many models of new physics require an extended Higgs sector. The most popular extension of the SM is the MSSM, where the Higgs sector consists of five physical states. At lowest order the MSSM Higgs sector is $\mathcal{CP}$-conserving, containing two $\mathcal{CP}$-even bosons, h and H, a $\mathcal{CP}$-odd boson, A, and the charged bosons $H^\pm$. It can be specified in terms of the gauge couplings, the ratio of the two vacuum expectation values, $\tan\beta \equiv v_2/v_1$, and the mass of the A boson, m_A. The Higgs phenomenology in the MSSM is strongly affected by higher-order corrections (see [10] for reviews). Proving that a detected new state is, indeed, a Higgs boson and distinguishing the Higgs boson(s) of the SM or the MSSM from the states of other theories will be far from trivial. In particular, it will be of utmost importance to determine the spin and $\mathcal{CP}$ properties of a new state and to measure precisely its mass, width and couplings.

Forward proton detectors installed at 220 m and 420 m around ATLAS and / or CMS (see [4, 5, 11]) will provide a rich complementary physics potential to the "conventional" LHC Higgs production channels. The CED processes are of the form $pp \to p \oplus H \oplus p$, where the $\oplus$ signs denote large rapidity gaps on either side of the centrally produced state. If the outgoing protons remain intact and scatter through small angles then, to a very good approximation, the primary di-gluon system obeys a $J_z = 0$, $\mathcal{CP}$-even selection rule [12]. Here J_z is the projection

[†] speaker

of the total angular momentum along the proton beam. This permits a clean determination of the quantum numbers of the observed resonance which will be dominantly produced in a 0^+ state. Furthermore, because the process is exclusive, the proton energy losses are directly related to the central mass, allowing a potentially excellent mass resolution, irrespective of the decay channel. The CED processes allow in principle all the main Higgs decay modes, $b\bar{b}$, WW and $\tau\tau$, to be observed in the same production channel. In particular, a unique possibility opens up to study the Higgs Yukawa coupling to bottom quarks, which, as it is well known, may be difficult to access in other search channels at the LHC. Within the MSSM, CED production is even more appealing than in the SM. The coupling of the lightest MSSM Higgs boson to $b\bar{b}$ and $\tau\tau$ can be strongly enhanced for large values of $\tan\beta$ and relatively small m_A. On the other hand, for larger values of m_A the branching ratio $\mathrm{BR}(H \to b\bar{b})$ is much larger than for a SM Higgs of the same mass. As a consequence, CED $H \to b\bar{b}$ production can be studied in the MSSM up to much higher masses than in the SM case.

Here we briefly review the analysis of [7] where a detailed study of the CED MSSM Higgs production was performed (see also Refs. [6, 8, 13] for other MSSM studies). This is updated by taking into account recent theoretical developments in background evaluation [14] and using an improved version [15] of the code `FeynHiggs` [16] employed for the cross section and decay width calculations. These improvements are applied for the CED production of MSSM Higgs bosons [7] in the benchmark scenarios of [17], the so-called CDM-benchmark scenarios, and in a fourth-generation model.

2 Signal and background rates and experimental aspects

The Higgs signal and background cross sections can be approximated by the simple formulae given in [6, 7]. For CED production of the MSSM h, H-bosons the cross section σ^{excl} is

$$\sigma^{\mathrm{excl}}\,\mathrm{BR}^{\mathrm{MSSM}} = 3\,\mathrm{fb}\left(\frac{136}{16+M}\right)^{3.3}\left(\frac{120}{M}\right)^{3}\frac{\Gamma(h/H\to gg)}{0.25\ \mathrm{MeV}}\,\mathrm{BR}^{\mathrm{MSSM}}, \tag{1}$$

where the gluonic width $\Gamma(h/H \to gg)$ and the branching ratios for the various MSSM channels, $\mathrm{BR}^{\mathrm{MSSM}}$, are calculated with `FeynHiggs2.6.2` [15]. The mass M (in GeV) denotes either M_h or M_H. The normalisation is fixed at $M = 120$ GeV, where $\sigma^{\mathrm{excl}} = 3$ fb for $\Gamma(H^{\mathrm{SM}} \to gg) = 0.25$ MeV. In Ref. [6, 7] the uncertainty in the prediction for the CED cross sections was estimated to be below a factor of ~ 2.5. According to [2, 7, 14, 18], the overall background to the 0^+ Higgs signal in the $b\bar{b}$ mode can be approximated by

$$\frac{\mathrm{d}\sigma^{B}}{\mathrm{d}M} \approx 0.5\,\mathrm{fb/GeV}\left[A\left(\frac{120}{M}\right)^{6} + \frac{1}{2}C\left(\frac{120}{M}\right)^{8}\right] \tag{2}$$

with $A = 0.92$ and $C = C_{\mathrm{NLO}} = 0.48 - 0.12 \times (\ln(M/120))$. This expression holds for a mass window $\Delta M = 4 - 5$ GeV and summarises several types of backgrounds: the prolific $gg^{PP} \to gg$ subprocess can mimic $b\bar{b}$ production due to the misidentification of the gluons as b jets; an admixture of $|J_z| = 2$ production; the radiative $gg^{PP} \to b\bar{b}g$ background; due to the non-zero b-quark mass there is also a contribution to the $J_z = 0$ cross section of order m_b^2/E_T^2. The first term in the square brackets corresponds to the first three background sources [7], evaluated

for $P_{g/b} = 1.3\%$, where $P_{g/b}$ is the probability to misidentify a gluon as a b-jet for a b-tagging efficiency of 60% [1]. The second term describes the background associated with bottom-mass terms in the Born amplitude, where one-loop corrections [14] are accounted for in $C_{\rm NLO}$. The NLO correction suppresses this contribution by a factor of about 2, or more for larger masses.

The main experimental challenge of running at high luminosity, $10^{34}\,\mathrm{cm}^{-2}\,\mathrm{s}^{-1}$, is the effect of pile-up, which can generate fake signal events within the acceptances of the proton detectors as a result of the coincidence of two or more separate interactions in the same bunch crossing, see [4,7,8,11] for details. Fortunately, as established in [8], the pile-up can be brought under control by using time-of-flight vertexing and cuts on the number of charged tracks. Also in the analysis of [7] the event selections and cuts were imposed such as to maximally reduce the pile-up background. Based on the anticipated improvements for a reduction of the overlap backgrounds down to a tolerable level, in the numerical studies in [7, 11] and in the new results below the pile-up effects were assumed to be overcome.

At nominal LHC optics, proton taggers positioned at a distance ± 420 m from the interaction points of ATLAS and CMS will allow a coverage of the proton fractional momentum loss ξ in the range 0.002–0.02, with an acceptance of around 30% for a centrally produced system with a mass around $120\ \mathrm{GeV}$. A combination with the foreseen proton detectors at ± 220 m [19] would enlarge the ξ range up to 0.2. This would be especially beneficial because of the increasing acceptance for higher masses [7]. The main selection criteria for $h, H \to b\bar{b}$ are either two b-tagged jets or two jets with at least one b-hadron decaying into a muon. Details on the corresponding selection cuts and triggers for WW and $\tau\tau$ channels can be found in [7, 11, 20]. Following [7] we consider four luminosity scenarios: "60 fb^{-1}" and "600 fb^{-1}" refer to running at low and high instantaneous luminosity, respectively, using conservative assumptions for the signal rates and the experimental sensitivities; possible improvements of both theory and experiment could allow for the scenarios where the event rates are higher by a factor of 2, denoted as "60 fb^{-1} eff$\times$2" and "600 fb^{-1} eff$\times$2".

3 Prospective sensitivities for CED production of the $\mathcal{CP}$-even Higgs bosons

Below we extend the analysis of the CED production of $H \to b\bar{b}$ and $H \to \tau\tau$ carried out in [7] and consider the benchmark scenarios of [17]. The improvements consist of the incorporation of the one-loop corrections to the mass-suppressed background [14] and in employing an updated version of `FeynHiggs` [15, 16] for the cross section and decay width calculations. Furthermore we now also display the limits in the m_A–$\tan\beta$ planes obtained from Higgs-boson searches at the Tevatron. For the latter we employed a preliminary version of the new code `HiggsBounds`, see [21] (where also the list of CDF and D0 references for the incorporated exclusion limits can be found).

The two plots in Fig. 1 exemplify our new results for the case of the $M_h^{\rm max}$ scenario [17]. They display the contours of 3σ statistical significance for the $h \to b\bar{b}$ and $H \to b\bar{b}$ channels. The left-hand plot shows that while the allowed region at high $\tan\beta$ and low m_A can be probed also with lower integrated luminosity, in the "600 fb^{-1} eff$\times$2" scenario the coverage at the 3σ level extends over nearly the whole m_A–$\tan\beta$ plane, with the exception of a window around

[1] Further improvements in the experimental analysis could allow to reduce $P_{g/b}$.

$m_A \approx 130 - 140$ GeV (which widens up for small values of $\tan\beta$). The coverage includes the case of a light SM-like Higgs, which corresponds to the region of large m_A. It should be kept in mind that besides giving an access to the bottom Yukawa coupling, which is a crucial input for determining all other Higgs couplings [22], the forward proton mode would provide valuable information on the Higgs $\mathcal{CP}$ quantum numbers and allow a precise Higgs mass measurement and maybe even a direct determination of its width.

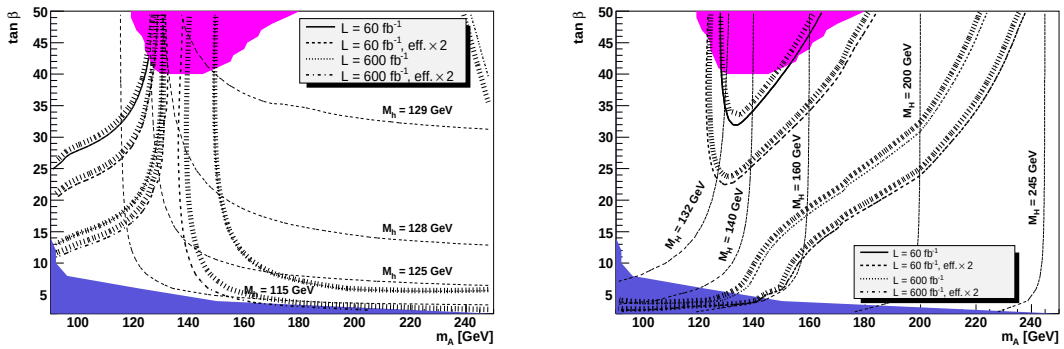


Fig. 1: Contours of 3σ statistical significance for the $h \to b\bar{b}$ channel (left) and for the $H \to b\bar{b}$ channel (right) in the $M_h^{\rm max}$ benchmark scenario with $\mu = +200$ GeV. The results were calculated using Eqs. (1) and (2) for $A = 0.92$ and $C = C_{\rm NLO}$ for effective luminosities of "60 fb^{-1}", "60 fb^{-1} eff$\times$2", "600 fb^{-1}" and "600 fb^{-1} eff$\times$2". The values of M_h and M_H are shown by the contour lines. The medium dark shaded (blue) regions correspond to the LEP exclusion bounds, while the Tevatron limits are shown by the dark shaded (purple) regions.

The properties of the heavier boson H differ very significantly from the ones of a SM Higgs with the same mass in the region where $M_H \gtrsim 150$ GeV. While for a SM Higgs the BR$(H \to b\bar{b})$ is strongly suppressed, the decay into bottom quarks is the dominant mode for the MSSM Higgs boson H. The 3σ significance contours in the m_A–$\tan\beta$ plane are displayed in the right-hand plot of Fig. 1. While the area covered in the "60 fb^{-1}" scenario is to a large extent already ruled out by Tevatron Higgs searches [21], in the "600 fb^{-1} eff$\times$2" scenario the reach for the heavier Higgs goes beyond $M_H \approx 235$ GeV in the large $\tan\beta$ region. At the 5σ level, which is not shown here, the reach extends up to $M_H \approx 200$ GeV. Thus, CED production of the H with the subsequent decay to $b\bar{b}$ provides a unique opportunity for accessing its bottom Yukawa coupling in a mass range where for a SM Higgs boson the $b\bar{b}$ decay rate would be negligibly small. In the "600 fb^{-1} eff$\times$2" scenario the discovery of a heavy $\mathcal{CP}$-even Higgs with $M_H \approx 140$ GeV will be possible for all allowed values of $\tan\beta$.

In [23] four new MSSM benchmark scenarios were discussed in which the abundance of the lightest SUSY particle, the lightest neutralino, in the early universe is compatible within the m_A–$\tan\beta$ plane with the cold dark matter (CDM) constraints as measured by WMAP. The parameters chosen for the benchmark planes are also in agreement with electroweak precision and B-physics constraints, see [23] for further details. We studied the prospects of CED Higgs production for the $b\bar{b}$ and $\tau\tau$ channels within these so-called CDM benchmark scenarios. The detailed results will be published elsewhere [24].

Here we show two plots in Fig. 2, exemplifying our new results in one of the benchmark

planes (called **P3**). They display the 3σ statistical significances for the $h \to b\bar{b}$ and $H \to b\bar{b}$ processes calculated in the same way as in the analysis presented in Fig. 1. The results for the $h \to b\bar{b}$ channel, shown in the left plot of Fig. 2, are very similar to the $M_h^{\rm max}$ scenario. In the highest luminosity scenario, "600 fb^{-1} eff$\times$2" the $h \to b\bar{b}$ channel covers nearly the whole m_A–$\tan\beta$ plane, leaving only a small funnel around $m_A \approx 125$ GeV uncovered. The reach for the $H \to b\bar{b}$ channel, shown in the right plot of Fig. 2, is slightly better than in the $M_h^{\rm max}$ scenario. The area covered in the lowest luminosity scenario, "60 fb^{-1}", goes down to $\tan\beta = 25$, so that a larger fraction of the parameter space covered at this luminosity is unexcluded by the present Tevatron Higgs searches. The reach at $\tan\beta = 50$ in the "600 fb^{-1} eff$\times$2" scenario goes somewhat beyond $M_H = 240$ GeV at the 3σ level.

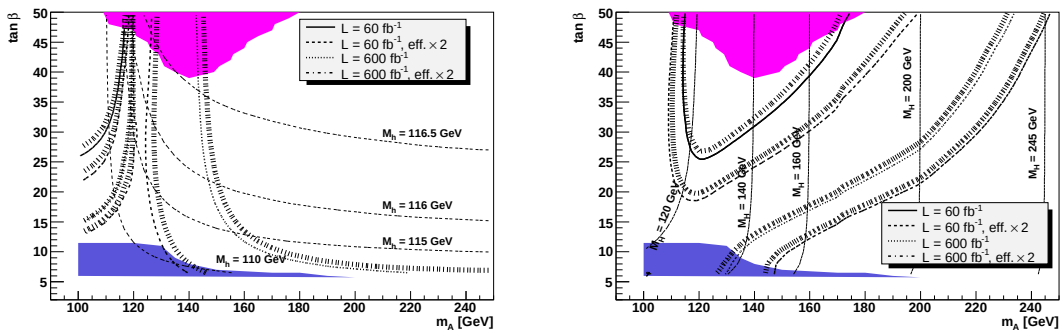


Fig. 2: Contours of 3σ statistical significances for the $h \to b\bar{b}$ channel (left) and for the $H \to b\bar{b}$ channel (right) within the CDM benchmark scenario **P3**. The results are calculated using the same procedure as in Fig. 1.

Finally, we also studied the implications of a fourth generation of chiral matter on the CED Higgs production. The interest in this simple kind of new physics has recently been renewed, see for example [25]. Within the four-generation scenario the Higgs boson phenomenology, including the search strategies, is strongly affected. In particular, the contribution of the fourth-generation quarks gives rise to an enhancement of the gluonic partial width, $\Gamma(H \to gg)$, by about a factor of 9 compared to the SM case. As a consequence, the branching ratios of a light Higgs boson into other final states, such as BR$(H \to \gamma\gamma)$, are significantly suppressed. The CED production rate, on the other hand, benefits from the enhancement of the gluonic partial width. The current Tevatron data together with LEP limits rule out a Higgs boson in a fourth generation model below about 210 GeV, apart from a low mass window between 115–130 GeV. The CED mechanism offers good prospects to cover this low-mass region with the rate of the signal $b\bar{b}$ events exceeding the SM rate by a factor of about 5–6. For higher Higgs masses above 210 GeV the rate of the $H \to WW$ and $H \to ZZ$ events is roughly enhanced by a factor of 9 compared to the SM case. Recall that in this larger mass region the acceptances of the forward proton detectors (if installed both at ± 420 m and ± 220 m from the interaction points) and experimental selection efficiencies are substantially higher that in the low mass region [7,20]. In the mass range 200–250 GeV the channel $H \to ZZ$ is especially beneficial, since the only physical background which arises in the semileptonic channel and is caused by the Z-strahlung process $pp \to p + Zjj + p$ can be strongly reduced [18]. For illustration we give an estimate of the expected number of signal events for the CED Higgs production in a four-generation case

with an integrated luminosity of 60 fb^{-1}. With the proton tagger acceptances and event selection efficiencies given in [7, 20] we can expect about 25 $H \to b\bar{b}$ events at $M_H = 120$ GeV and about 45 WW events (when at least one W decays leptonically). In both cases the evaluated signal-to-background ratio S/B is greater than 5.

Acknowledgements

We are grateful to W.J. Stirling for collaboration in the early stages of this work, and we thank O. Brein, A. De Roeck, J. Ellis, A. Martin and T. Tait for useful discussions. This work was supported in part by the European Community's Marie-Curie Research Training Network under contract MRTN-CT-2006-035505 'Tools and Precision Calculations for Physics Discoveries at Colliders' (HEPTOOLS) and MRTN-CT-2006-035657 'Understanding the Electroweak Symmetry Breaking and the Origin of Mass using the First Data of ATLAS' (ARTEMIS).

References

[1] V.A. Khoze, A.D. Martin and M.G. Ryskin, *Eur. Phys. J.* **C 23**, 311 (2002).

[2] A. De Roeck *et al.*, *Eur. Phys. J.* **C 25**, 391 (2002).

[3] J. Forshaw and A. Pilkington, *In *Hamburg 2007, Blois07, Forward physics and QCD* 130-136.*

[4] M. G. Albrow *et al.* [FP420 R and D Collaboration], arXiv:0806.0302 [hep-ex].

[5] P. J. Bussey, arXiv:0809.1335 [hep-ex].

[6] A.B. Kaidalov *et al.*, *Eur. Phys. J.* **C 33**, 261 (2004).

[7] S. Heinemeyer *et al.*, *Eur. Phys. J.* **C 53**, 231 (2008) [arXiv:0708.3052 [hep-ph]].

[8] B. Cox, F. Loebinger and A. Pilkington, *JHEP* **0710**, 090 (2007) [arXiv:0709.3035 [hep-ph]].

[9] J. R. Forshaw *et al.*, *JHEP* **0804**, 090 (2008) [arXiv:0712.3510 [hep-ph]].

[10] S. Heinemeyer, *Int. J. Mod. Phys.* **A 21** 2659 (2006); A. Djouadi, *Phys. Rept.* **459** (2008) 1.

[11] CERN/LHCC 2006-039/G-124, CMS Note 2007/002, TOTEM Note 06-5.

[12] V.A. Khoze, A.D. Martin and M. Ryskin, *Eur. Phys. J.* **C 19** 477 (2001) [Errat.-ibid. **C 20** 599 (2001)],

[13] V.A. Khoze, A.D. Martin, M. Ryskin, *Eur. Phys. J.* **C 34** 327 (2004); J. Ellis, J. Lee, A. Pilaftsis, *Phys. Rev.* **D 70** 075010 (2004); *Phys. Rev.* **D 71** 075007 (2005); M. Boonekamp et al., *Phys. Rev.* **D 73** 115011 (2006).

[14] A. G. Shuvaev *et al.*, Eur. Phys. J. C **56**, 467 (2008).

[15] See: `www.feynhiggs.de`.

[16] S. Heinemeyer, W. Hollik and G. Weiglein, *Comp. Phys. Commun.* **124** (2000) 76; *Eur. Phys. J.* **C 9** (1999) 343; G. Degrassi *et al.*, *Eur. Phys. J.* **C 28** (2003) 133; M. Frank *et al.*, *JHEP* **0702** (2007) 047.

[17] M. Carena *et al.*, *Eur. Phys. J.* **C 26** 601 (2003); *Eur. Phys. J.* **C 45** 797 (2006).

[18] V.A. Khoze, M. Ryskin and W.J. Stirling, *Eur. Phys. J.* **C 48** 797 (2006).

[19] V. Berardi et al. [TOTEM Collab.], TDR, CERN-LHCC-2004-002, TOTEM-TDR-001, January 2004; RP220 project at ATLAS, see: `cern.ch/project-rp220`.

[20] B. E. Cox *et al.*, *Eur. Phys. J.* **C 45** (2006) 401

[21] P. Bechtle *et al.*, see `www.ippp.dur.ac.uk/HiggsBounds`.

[22] M. Dührssen et al., *Phys. Rev.* **D 70** (2004) 113009.

[23] J. Ellis *et al.*, *JHEP* **0710** (2007) 092; J. Ellis *et al.*, *JHEP* **0708**, 083 (2007).

[24] S. Heinemeyer *et al.*, to be published.

[25] G. D. Kribs *et al. Phys. Rev.* **D 76**, 075016 (2007)

[26] V. A. Khoze, M. G. Ryskin and W. J. Stirling, *Eur. Phys. J.* **C 44**, 227 (2005)

A bottom-up strategy for reconstructing the underlying MSSM parameters at the LHC

J.-L. Kneur
Lab. Physique Thorique et Astroparticules, UMR5207 CNRS, Univ. Montpellier 2, France
DOI: http://dx.doi.org/10.3204/DESY-PROC-2009-01/84

Abstract
We illustrate a particular "bottom-up" reconstruction of MSSM parameters at the LHC for both general and constrained MSSM, starting from a limited set of particle mass measurements, using gluino/squark cascade decays and the lightest Higgs boson mass. Our method gives complementary information to more standard "top-down" reconstruction approaches and is not restricted to the LHC data properties.

1 Introduction

If new physics is seen at LHC a very first non trivial issue will be to distinguish supersymmetry from other beyond standard model (BSM) scenarios, like extra dimensions, little Higgs models etc. If evidence for low energy supersymmetry is found, the next crucial step would be to measure Minimal Supersymmetric Standard Model (MSSM) [1] basic parameters accurately enough to extract precisely the underlying SUSY-breaking mechanism. This may not be easy if only a limited part of the predicted MSSM sparticles will be discovered and some of their properties measured with the prospected LHC accuracies. Most reasonable scenarios assume that the lightest Higgs scalar h could be discovered, and some of the squarks and the gluino are copiously produced (if not too heavy) at the LHC due to their strong interactions. In addition some of the neutralinos, including the lightest supersymmetric sparticle (LSP), could be identified and have their masses extracted indirectly from detailed study of squark and gluino cascade decays (see e.g. [2]). Various analysis have been conducted [3, 4] to reconstruct the basic MSSM parameter space from the above assumed experimental measurements. A largely illustrated strategy, in a so-called "top-down" approach, is to start from a given supersymmetry-breaking model at very high grand unification (GUT) scale, predicting for given input parameter values of the superpartner spectrum at experimentally accessible energy scales, and next fitting this spectrum (with other observables like cross-sections etc) to the data to extract constraints on the model parameters (see e.g. [5] for recent elaborated fitting techniques). There is however a lively debate now on what will be the most efficient approaches, either the above "top-down", or some alternative bottom-up reconstruction methods; or more "blind" analysis, etc. Among other things there has been some concern raised about the "LHC inverse problem" i.e. the possible occurence of discrete ambiguities (potentially many) in reconstructing basic MSSM parameters [6].

Our aim here is to illustrate a recent alternative bottom-up reconstruction strategy [7], based on a rather "minimal" set of identified sparticles, within different scenarios (e.g. with GUT scale universality assumptions or not). Our approach is based on inverse mapping relations between measured masses and basic parameters. This has been investigated in the past [8, 9] but mainly at tree-level approximation and in the context of the ILC. One of the novelty here is

to incorporate radiative corrections into our framework at realistic level, and very similarly to the way in which radiative corrections are included in more conventional top-down calculations. This allows to keep most advantages of the bottom-up approach. Our analysis is far from being fully realistic concerning the LHC data simulations, not using sophisticated Monte Carlo tools that are ultimately necessary. But the accent is on considering as much as possible realistic and minimal LHC sparticle identifications, using a limited set of sparticle mass measurements.

2 Experimental assumptions and strategy

At the LHC, one expects to determine quite accurately some sparticle masses (see Table 1 for the SPS1a benchmark study) from "kinematical endpoints" analysis of (2-body) cascade decays:

$$\tilde{g} \to \tilde{q}_L q \to \chi_2^0 q_f q \to \tilde{l}_R l q_f q \to \chi_1^0 l_f l q_f q \tag{1}$$

We assume in our analysis that the lightest Higgs mass m_h will be also measured with good accuracy, mainly through its $\gamma\gamma$ decay mode.

scenarios (+th assumptions)	measured mass	expected LHC accuracy (GeV)	decay or process
(minimal):	$m_{\tilde{g}}$,	7.2	$\tilde{g}$ cascade decay
S_1(MSSM),	$m_{\tilde{N}_1}$,	3.7	" "
S_2(universality)	$m_{\tilde{N}_2}$.	3.6	" "
S_4,	$m_{\tilde{q}_L}$,	3.7	" "
S_4' (universality)	$m_{\tilde{l}_R}$	6.0	" "
$S_3 = S_1$ +:	$m_{\tilde{N}_4}$	5.1	$\tilde{q}_L \to \tilde{\chi}_4^0 +$ .. cascade
S_5,	$m_{\tilde{b}_1}$,	7.5	$\tilde{g}$ cascade decay
S_5' (universality)	$m_{\tilde{b}_2}$	7.9	" "
$S_6 = S_2 + S_4' + S_5'$ +:	m_h	0.25 (exp)–2 (th)	$h \to \gamma\gamma$ (mainly)

Table 1: Different scenarios S_i on the amount of sparticle mass measurements at the LHC from gluino cascade and other decays with different theoretical assumptions (see ref. [7] for more details). Mass accuracies correspond to SPS1a benchmark studies, combined from refs. [2, 3].

3 Analytic inverse mapping from masses to basic parameters

In the unconstrained MSSM there are three naturally separated sectors (at tree level):
- the gauginos/Higgsinos sector involving the basic MSSM parameters M_1, M_2, μ, and $\tan\beta$;
- the squarks/slepton sector involving μ, $\tan\beta$, and soft scalar terms $\tilde{m}_{q_L}$, $\tilde{m}_{q_R}$, $\tilde{m}_{e_L}$,...;
- the Higgs sector involving μ, $\tan\beta$, M_{H_u}, M_{H_d}, M_A.

In each sector one can derive simple analytic inversions (at tree-level), i.e. linear or quadratic equations [7] that express basic MSSM parameters as function of sparticle masses. Our precise strategy evidently depends on the available input masses (as it is also the case in a top-down approach). We proceed step by step in the three sectors rather than doing "all at once" fits.

3.1 Incorporating radiative corrections

Radiative corrections (RC) to sparticle masses evidently spoil the above simple inverse mapping picture, by introducing highly non-linear dependence on all parameters, so that "brute force" inversion is untractable. However to very good approximation, RC keep a tree-level form, e.g. in ino sector: $\mu \to \mu + \Delta\mu$, $M_1 \to M_1 + \Delta M_1$,.. (where $\Delta\mu$, ΔM_1, ΔM_2 depend on other sector: squarks, sleptons, etc), such that it preserves analytic inversion. Moreover the leading RC for $\tilde{g}$ involve $\tilde{q}$ of cascade (and reciprocally), thus depending on already known parameters. Once some of the MSSM parameters are determined, one can eventually assume universality (SUGRA) relations *within* loops as a reasonable approximation in many cases. In our analysis we solve the analytical (tree-level) inversion equations for various input/output choices, after incorporating leading RC relating pole to running masses in the above manner. We then vary mass input within errors (with uniform "flat prior" or Gaussian distributions) to determine constraints on output basic MSSM parameters within different asumptions on e.g. soft term universality at high scale.

3.2 Gaugino/Higgsino sector from Neutralino masses

Brute inversion of the neutralino mass matrix would be cumbersome and need all four neutralino mass input. More interestingly, one can extract two relations [7,8] involving only the two relevant neutralino mass input, to be used differently depending on input/output choice:

$$P_{12}^2 + (\mu^2 + m_Z^2 - M_1 M_2 + (M_1 + M_2) S_{12} - S_{12}^2) P_{12} + \mu m_Z^2 M_{12} \sin 2\beta - \mu^2 M_1 M_2 = 0 \quad (2)$$

$$\begin{aligned}(M_1 + M_2 - S_{ij}) P_{12}^2 + (\mu^2 (M_1 + M_2) + m_Z^2 M_{12} - \mu \sin 2\beta)) P_{12} \\ + \mu (m_Z^2 M_{12} \sin 2\beta - \mu M_1 M_2) S_{12} = 0 \end{aligned} \quad (3)$$

with $M_{12} \equiv c_W^2 M_1 + s_W^2 M_2$, $S_{12} \equiv \tilde{m}_{N_1} + \tilde{m}_{N_2}$, $P_{12} \equiv \tilde{m}_{N_1} \tilde{m}_{N_2}$. In unconstrained MSSM this determines M_1, M_2 for given μ, $\tan\beta$ $m_{\tilde{N}_1}, m_{\tilde{N}_2}$ input [7], up to a possible twofold ambiguity, $M_1 < M_2$ or $M_1 > M_2$, due to the use of only mass input. If a third neutralino mass $m_{\tilde{N}_4}$ can be measured, it gives a simple analytic determination of μ independently of $\tan\beta$, again with discrete ambiguities on the $M_1, M_2, |\mu|$ relative ordering in unconstrained MSSM. Resulting bounds on $M_1, M_2, |\mu|$ for input accuracies of Table 1 are illustrated in Table 2. In addition one can check specific SUSY-breaking models by comparing these bounds with the M_1, M_2 determination from M_3, e.g. from mSUGRA GUT universality or different M_i relations in other models. Alternatively for any M_i relations assumed, one can determine μ and $\tan\beta$ from the very same Eqs. (2),(3): the corresponding constraints for universal $M_i(Q_{GUT})$ are given in Table 2.

4 Squark, slepton parameter (first two generations)

From the expression of sfermion masses in unconstrained MSSM, e.g for $\tilde{u}_1, \tilde{e}_2$:

$$\begin{aligned} m_{\tilde{u}_1}^2 &= m_{\tilde{u}_L}^2 + (\frac{1}{2} - \frac{2}{3} s_W^2) m_Z^2 \cos 2\beta \\ m_{\tilde{e}_2}^2 &= m_{\tilde{e}_R}^2 - s_W^2 m_Z^2 \cos 2\beta \end{aligned} \quad (4)$$

we can take linear combinations to eliminate the $\tan\beta$ dependence, obtaining in this way constraints on the relevant soft scalar terms independently of $\tan\beta$. Moreover the RG evolution in

this sector only depends (at one-loop) on gaugino M_i and gauge couplings, so that to good approximation and without further assumptions than the available input from (1) we can determine $m_0^{q,l}$ at GUT scale (upon assuming now squark-slepton universality):

$$86 \text{ GeV} \lesssim m_0^{q,l} \lesssim 112 \text{ GeV} \tag{5}$$

5 Third generation squark and Higgs sectors with universality assumptions

We can determine the sbottom parameters m_{Q3_L}, m_{b_R} with quite good accuracy both from sbottom masses and/or from (5) if assuming scalar universality (see Table 2). For the Higgs parameters reconstruction, in unconstrained MSSM the prospects at LHC are not optimistic if assuming solely the input from Table 1. In contrast universality assumptions relate $m_0^{q,l}$ to scalar terms m_{H_d}, m_{H_u}, thus predicting m_A value:

$$\bar{m}_A^2(m_0) = m_{H_d}^2 + m_{H_u}^2 + 2\mu^2 = \frac{\bar{m}_h^2(m_Z^2 - \bar{m}_h^2)}{m_Z^2 \cos^2 2\beta - \bar{m}_h^2} + RC(m_t, X_t, \cdots) \tag{6}$$

where the second equality is a naive (tree-level) relation defining m_A from m_h: this is clearly unrealistic since very important RC enter this relation, sketchily denoted here as $RC(m_t, X_t, \cdots)$. Those RC involve essentially running-to-pole m_h, m_A mass corrections and as is well-known depend strongly on the top mass and stop parameters (with $X_t \equiv A_t - \mu/\tan\beta$), among other MSSM parameters. The naive Eq. (6) nevertheless defines our strategy: For m_h accuracy from Table 1 and m_A determined from squark/slepton with universality assumptions, Eq. (5), we can put some constraints on e.g. $RC(m_t, X_t)$ and/or $\tan\beta$. For the Higgs sector RC we use actually (elaborated) approximations of one- and two-loop expressions [10] which differ from the full one-loop + leading two-loop results [11] by 1-2 GeV, i.e. of the order of theoretical uncertainties.

Finally, once the parameters are determined at low scale, we evolve them to GUT scale with bottom-up renormalization group evolution (RGE)[1], studying error propagation from low to high energy, which can be important for some parameters notably in the scalar sector.

6 Conclusion

We presented a quite simple-minded bottom-up approach essentially based on analytic inverse mapping from sparticle masses to basic MSSM parameters. It incorporates radiative corrections at realistic level but is certainly not yet very elaborated as compared to the state-of-the art in more standard top-down simulation tools. From assumptions in Table 1, not surprisingly the constraints (summarized in Table 2) are quite good for the gaugino/Higgsino and squark/slepton soft terms, even for unconstrained MSSM, while the determination of other parameters like $\tan\beta$ notably is much less accurate. Those results compare reasonably well with more standard top-down fitting results [5], but this bottom-up approach also provides complementary information with a clear handle e.g on discrete reconstruction amibiguities, or other possible obstacles. This could hopefully suggest new strategies, helping to distinguish from other BSM scenarios since it exhibits theoretical constraints (e.g. correlations) specific to MSSM and not automatically foreseen by "global" fit approaches.

[1] An appropriate bottom-up RGE option is publically available for the SuSpect [12] code versions ≥ 2.40.

Table 2: Combined constraints on some MSSM basic parameters from bottom-up reconstruction. * indicates discrete reconstruction amibiguities.

Assumptions	Parameter	Constraint (GeV)	SPS1a
gen. MSSM,	$M_1(Q_{EWSB})^\star$	$\sim$95–115	101.5
$m_{\tilde{g}}, m_{\tilde{N}_1}, m_{\tilde{N}_2}$.	$M_2(Q_{EWSB})^\star$	$\sim$175–220	191.6
	$M_3(Q_{EWSB})$	$\sim$580–595	586.6
	$\mu(Q_{EWSB})$	$\sim$280–750	357
+ m_{N_4}	$\mu(Q_{EWSB})^\star$	$\sim$350–372	357
$\tilde{q}, \tilde{l}$-universality	$m_0^{q,l}(Q_{GUT})$	$\sim$90–112	100
M_i-universality	$M_i(Q_{GUT})$	$\sim$ 245–255	250
$\tilde{b}_1, \tilde{b}_2$ +universality	$\tan\beta(Q_{EWSB})$	$\sim$3–28	9.74
	$m_{Q3_L}(Q_{EWSB})$	$\sim$490–506	497
	$m_{b_R}(Q_{EWSB})$	$\sim$512–530	522
mSUGRA	m_0	$\sim$90-112	100
	$m_{1/2}$	$\sim$245–255	250
	$-A_0$	$\sim$ -100-350	100
	$\tan\beta(m_Z)$	$\sim$ 5.5–28	10

Whatever the approach, the parameter determination will be clearly improved if using the most sophisticated analysis, both experimental and theoretical. This probably involves new developments in calculating parameter-to-mass relations (as well as all possible signals) at higher order accuracy, using new observables, but also exploiting all possible low energy constraints and the crucial interplay with dark matter observables.

References

[1] For MSSM reviews see e.g. H. P. Nilles, Phys. Rept. **110**, 1 (1984); R. Barbieri, Riv. Nuovo Cim. **11N4**, 1 (1988); R. Arnowitt and Pran Nath, Report CTP-TAMU-52-93; M. Drees and S.P. Martin, hep-ph/9504324; J. Bagger, Lectures at TASI-95, hep-ph/9604232; S.P. Martin, hep-ph/9709356; S. Dawson, hep-ph/9712464.

[2] B.K. Gjelsten, D.J. Miller and P. Osland, JHEP 0506 (2005) 015.

[3] G. Weiglein et al, Phys. Rept. 426 (2006) 47.

[4] J.A. Aguilar-Saavedra et al, Eur. Phys. J. C46 (2006) 43.

[5] R. Lafaye, T. Plehn, M. Rauch and D. Zerwas, Eur.Phys.J. C54(2008) 617.

[6] N. Arkani-Hamed, G.L. Kane, J. Thaler and L.-T. Wang, JHEP 0608 (2006) 070.

[7] J.-L. Kneur and N. Sahoury, arXiv:0808.0144.

[8] J.-L. Kneur and G. Moultaka, Phys. Rev. D59 (1999) 015005; J.-L. Kneur and G. Moultaka, Phys. Rev. D 61 (2000) 095003.

[9] S.Y Choi et al, Eur. Phys. J. C14 (2000) 535; S.Y. Choi et al, Eur. Phys. J. C22 (2001) 563; G. Moortgat-Pick et al, Phys. Rept. 460 (2008) 131;

[10] S. Heinemeyer, W. Hollik and G. Weiglein, Phys.Lett. B455 (1999) 179; ibid, hep-ph/0002213.

[11] see e.g. S. Heinemeyer, Eur. Phys. Jour. C22 (2001) 521.

[12] A. Djouadi, J-L. Kneur and G. Moultaka, "SuSpect", Comput. Phys. Commun. 176 (2007) 426.

Supersymmetry and other beyond the Standard Model physics: Prospects for determining mass, spin and CP properties

Wolfgang Ehrenfeld for the ATLAS Collaboration
Deutsches Elektronen Synchrotron, Notkestrasse 85, 22603 Hamburg, Germany
DOI: http://dx.doi.org/10.3204/DESY-PROC-2009-01/61

Abstract
The prospects of measuring masses, spin and CP properties within Supersymmetry and other beyond the Standard Model extensions at the LHC are reviewed. Emphasis is put on models with missing transverse energy due to undetected particles, as in Supersymmetry or Universal Extra Dimensions.

1 Introduction

It is widely expected that the Large Hadron Collider (LHC), which started very successfully on the 10th September 2008 with single beam injection, will uncover physics beyond the present Standard Model (SM) of particle physics. Supersymmetry (SUSY) is one of the most promising candidates for new physics. Among its virtues are the potential to overcome the hierarchy problem, to provide a dark matter candidate and make a unification of gauge coupling constants at a high energy scale possible. If the SUSY mass scale is in the sub-TeV range, already first LHC data will likely be sufficient to claim a discovery of new physics although new physics do not strictly mean SUSY as other new physics scenarios can have similar features and properties. In order to distinguish different scenarios of new physics and to determine the full set of model parameters within one scenario as many measurements of the new observed phenomena as possible are needed. This includes the precise measurement of masses, spins and CP properties of the newly observed particles.

Both multi-purpose experiments at the LHC, ATLAS [1] and CMS [2], are designed for these measurements. They will be able to pin down the exact model of new physics, e. g. to distinguish SUSY from Universal Extra Dimensions (UED).

2 Supersymmetry

In the following we assume R-parity conservation. As a consequence sparticles can only be produced in pairs and the lightest SUSY particle (LSP) is stable, which usually escapes detection in high-energy physics detectors. At LHC energies mostly pairs of squarks or gluinos are produced in proton-proton collisions, which then subsequently decay via long cascades into the LSP. Typical event topologies at the LHC are multi jet events with zero or more leptons and missing transverse energy due to the two LSPs. In the case of ATLAS these events will be triggered using a combined jet and missing E_T trigger. The selection is mainly based on four jets ($p_T^{j_1} > 100\,\mathrm{GeV}$, $p_T^{j_2,j_3,j_4} > 50\,\mathrm{GeV}$) and missing E_T ($E_T^{\mathrm{mis}} > 100\,\mathrm{GeV}, 0.2 m_{\mathrm{eff}}$). The effective mass, m_{eff}, is the scalar sum of missing E_T and the transverse momentum of the four leading jets. For further details see [3]. With this kind of selection minimal Supergravity (mSUGRA) models up to $m_{1/2} \sim 0.7\,\mathrm{TeV}$ or $m_0 \sim 3\,\mathrm{TeV}$ can be discovered with a luminosity of $1\,\mathrm{fb}^{-1}$.

2.1 Mass Measurements

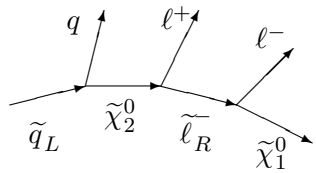


Fig. 1: Prime example of a SUSY decay chain for SUSY mass reconstruction. The first lepton in the decay chain is called the *near* lepton while the other is called the *far* lepton.

After the discovery of new physics beyond the SM as many measurements of the production process and particle properties are needed to pin-down the exact model of new physics. For example the masses of the new particles can be used to distinguish between different SUSY models. Due to the two escaping LSPs in every SUSY event, no mass peaks can be reconstructed and masses must be measured by other means. In mSUGRA models the main source of mass information is provided by $\widetilde{\chi}_2^0$ decays, such as $\widetilde{\chi}_2^0 \to \widetilde{\ell}^{\pm}\ell^{\mp} \to \widetilde{\chi}_1^0\ell^+\ell^-$ (see Fig. 1). First we consider the invariant mass spectrum of the two leptons $m_{\ell\ell}$ from the decay chain in Fig. 1. Due to the scalar nature of the slepton, the invariant mass exhibits a triangular shape with a sharp drop-off at a maximal value $m_{\ell\ell}^{\max}$. The position of this endpoint depends on the masses of the involved sparticles:

$$m_{\ell\ell}^{\max} = m_{\widetilde{\chi}_2^0}\sqrt{1-\left(\frac{m_{\widetilde{\ell}_R}}{m_{\widetilde{\chi}_2^0}}\right)^2}\sqrt{1-\left(\frac{m_{\widetilde{\chi}_1^0}}{m_{\widetilde{\ell}_R}}\right)^2}. \quad (1)$$

Combinatorial background from SM and other SUSY processes is subtracted using the flavor-subtraction method. The endpoint is measured from the di-lepton (electron and muon) mass distribution $N(\mathrm{e}^-\mathrm{e}^+)/\beta + \beta N(\mu^-\mu^+) - N(\mathrm{e}^{\pm}\mu^{\mp})$, where N is the number of selected events and β is the ratio of the electron and muon reconstruction efficiency ($\beta \simeq 0.86$) [3]. Figure 2 shows the mass distribution for different mSUGRA benchmark points[1]. The SU3 point is an example of a simple two-body decay (Fig. 2(b)), SU4 illustrates a more complex three-body decay (Fig. 2(c)) and SU1 two two-body decays (Fig. 2(a)). In all cases the $m_{\ell\ell}$ endpoint can be measured without a bias although the needed luminosity is quite different. Further, the fit function to extract the endpoint(s) needs to be adjusted to the underlying mass spectrum. The expected sensitivity is summarized in Tab. 1 including the assumed luminosity. A similar analysis can be performed if we replace electrons and muons by taus. Due to the additional neutrinos from the tau decay, the visible di-tau mass distribution is not triangular any more (see Fig. 2(d)). This complicates measuring the endpoint of the spectrum. A solution to this problem is to fit a suitable function to the trailing edge of the visible di-tau mass spectrum and use the inflection point as an endpoint sensitive observable, which can be related to the true endpoint using a simple MC based calibration procedure. Figure 2(d) shows the charge subtracted visible di-tau mass distribution $N(\tau^-\tau^+) - N(\tau^{\pm}\tau^{\pm})$ which is used to suppress background from fake taus and combinatorial background. The expected sensitivity is listed in Tab. 1. Please note that the third error is due to the SUSY-model dependent polarization of the two taus. On the other hand this influence of the tau polarization on the di-tau mass distribution can be used to measure the tau polarization from the mass distribution and distinguish different SUSY models from each other.

By including the jet produced in association with the $\widetilde{\chi}_2^0$ in the $\widetilde{q}_L$ decay (see Fig. 1), several other endpoints of measurable mass combinations are possible: $m_{q\ell(\mathrm{low})}^{\max}$, $m_{q\ell(\mathrm{high})}^{\max}$, $m_{q\ell\ell}^{\min}$, $m_{q\ell\ell}^{\max}$. The label min/max denotes the upper/lower endpoint of the spectrum. In the case of $m_{q\ell}^{\max}$ the near and the far lepton can not be distinguished in most of the SUSY models and instead the

[1] Within ATLAS the mSUGRA benchmark points are called SU*X*. SU1: $m_0 = 70\,\mathrm{GeV}, m_{1/2} = 350\,\mathrm{GeV}, A_0 = 0, \tan\beta = 10, \mu > 0$ SU3: $m_0 = 100\,\mathrm{GeV}, m_{1/2} = 300\,\mathrm{GeV}, A_0 = -300, \tan\beta = 6, \mu > 0$ SU4: $m_0 = 200\,\mathrm{GeV}, m_{1/2} = 160\,\mathrm{GeV}, A_0 = -400, \tan\beta = 10, \mu > 0$

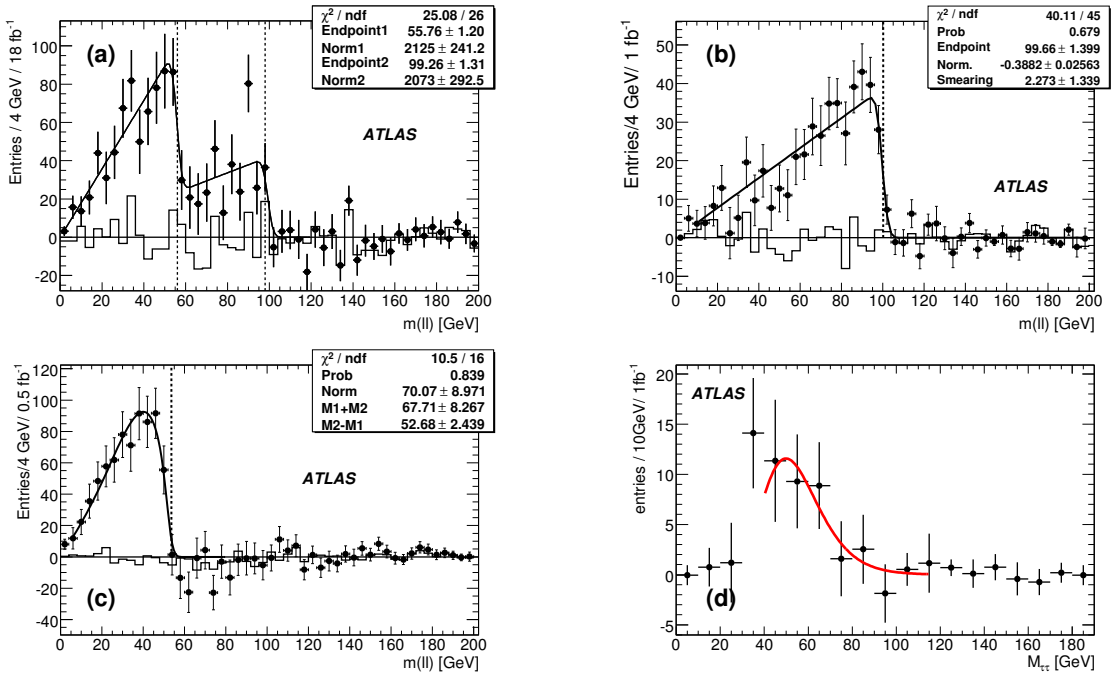


Fig. 2: Flavour subtracted di-lepton mass spectrum for different mSUGRA benchmark points: (a) SU1($\ell = e, \mu$), (b) SU3($\ell = e, \mu$), (c) SU4($\ell = e, \mu$), (d) SU3($\ell = \tau$).

minimum/maximum of the mass $m_{q\ell^{\pm}}$ is used. As in the di-lepton case a suitable fit function for each observable is needed. The expected sensitivity to the different mass combinations for the SU3 model are summarized in Tab. 1.

These five mass combinations can be used to extract the underlying high mass model parameters using fitting programs like Fittino [4] or SFitter [5].

2.2 Spin Measurements

Measuring the number of new particles and their masses will give us enough information to extract model parameters for a certain extension of the SM. However, the mass information will not always be enough to distinguish different scenarios of new physics. For example, UED with Kaluza-Klein (KK) parity can be tuned in such a way that it reproduces the mass spectrum of certain SUSY models. However, the spin of the new particles is different and can be used to discriminate between these models.

The standard SUSY decay chain (see Fig. 1) can also be used to measure the spin of $\widetilde{\chi}_2^0$ [6]. A charge asymmetry A is expected in the invariant masses $m_{q\ell^{\mathrm{near}(\pm)}}$ formed by the quark and the near lepton. It is defined as $A = (s^+ - s^-)/(s^+ + s^-)$, where $s^{\pm} = d\sigma/dm_{q\ell^{\mathrm{near}(\pm)}}$. In most of the cases it is experimentally not possible to distinguish between near and far lepton and hence only $m_{q\ell^{\pm}}$ can be measured, diluting A. Further, the asymmetry from the corresponding $m_{\overline{q}\ell^{\mp}}$ charge distribution is the same as the asymmetry for $m_{q\ell^{\pm}}$, but with opposite sign. Usually it is not possible to distinguish q jets from $\overline{q}$ jets at the LHC. On the other side more squarks than anti-squarks will be produced. The expected asymmetry A for SU3 is shown in Fig. 3 for a

observable	benchmark point	true mass [GeV]	expected mass [GeV]	luminosity [fb^{-1}]
$m_{\ell\ell}$	SU1	56.1	$55.8 \pm 1.2 \pm 0.2$	18
$m_{\ell\ell}$	SU1	97.9	$99.3 \pm 1.3 \pm 0.3$	18
$m_{\ell\ell}$	SU3	100.2	$99.7 \pm 1.4 \pm 0.3$	1.0
$m_{\tau\tau}$	SU3	98	$102 \pm 17 \pm 5.5 \pm 7$	1.0
$m_{\ell\ell}$	SU4	53.6	$52.7 \pm 2.4 \pm 0.2$	0.5
$m^{\max}_{q\ell(\mathrm{low})}$	SU3	325	$333 \pm 6 \pm 6 \pm 8$	1.0
$m^{\max}_{q\ell(\mathrm{high})}$	SU3	418	$445 \pm 11 \pm 11 \pm 11$	1.0
$m^{\min}_{q\ell\ell}$	SU3	249	$265 \pm 17 \pm 15 \pm 7$	1.0
$m^{\max}_{q\ell\ell}$	SU3	501	$501 \pm 30 \pm 10 \pm 13$	1.0

Table 1: Reconstructed endpoint positions. The first error of the expected value is the statistical error and the second is due to systematic from the lepton energy scale and β. In case of $m_{\tau\tau}$ the third error is due to the uncertainty in the tau polarization.

luminosity of 30 fb^{-1}, where already 10 fb^{-1} are sufficient to exclude the zero spin hypothesis at 99% CL [7]. In the case of SU1 far and near leptons are distinguishable on kinematic grounds. On the other hand, cross section times branching ratio of this decay chain is much lower than the SU3 case, so that 100 fb^{-1} are needed to exclude the zero spin hypothesis at 99% CL.

The slepton spin can be measured in direct di-slepton production $q\bar{q} \to \mathrm{Z}\gamma \to \widetilde{\ell\ell} \to \widetilde{\chi}^0\ell\widetilde{\chi}^0\ell$. In UED the corresponding process is $q\bar{q} \to \mathrm{Z}\gamma \to \ell_1\ell_1 \to \gamma_1\ell\gamma_1\ell$, where ℓ_1 and γ_1 are the KK-lepton and -photon, respectively. Both have spin $1/2$, the same as their SM partners. In both decay chains a SM lepton-pair is produced, all other particles escape undetected. Although the involved new particle masses can be the same, the slepton spin (0) and KK-lepton spin ($1/2$) are different. The angle θ^*, as defined between the incoming quark and the slepton/KK-lepton, can be used to discriminate between both model. The pure phase space (PS) distribution would be flat. In SUSY and UED models it is proportional to $1 + A\cos^2\theta^*$, where $A = -1$ for SUSY and $A = (E^2_{\ell_1} - m^2_{\ell_1})/(E^2_{\ell_1} + m^2_{\ell_1})$ for UED. However, θ^* is not directly accessible. Experimentally only $\theta^*_{ll} \equiv \cos\left(2\tan^{-1}\exp\left(\Delta\eta_{\ell^+\ell^-}/2\right)\right) = \tanh\left(\Delta\eta_{\ell^+\ell^-}/2\right)$, the angle between the two leptons, can be measured. Note, that θ^*_{ll} is invariant under boosts along the beam axis. Still, θ^*_{ll} has some correlation with θ^*. Events with two good leptons ($p_T^{l_1,l_2} > 40, 30\,\mathrm{GeV}$) and missing

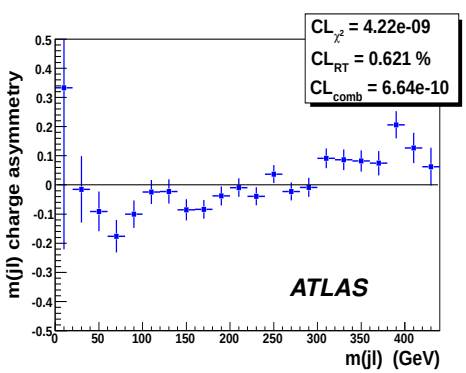


Fig. 3: Expected charge asymmetry A for SU3 and 30 fb^{-1}.

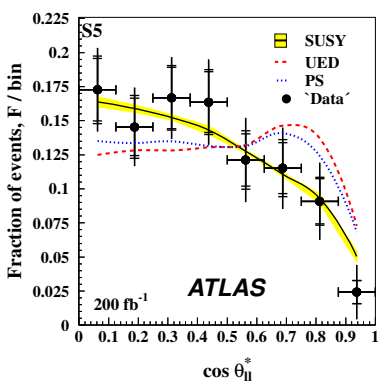


Fig. 4: Expected θ^*_{ll} distribution for the S5 bench mark point and 200 fb^{-1}.

$E_T > 100\,\mathrm{GeV}$ are selected. Further, events with b-jets and high p_T jets ($p_T > 100\,\mathrm{GeV}$) are rejected [8]. The expected θ^*_{ll} distribution for a luminosity of $200\,\mathrm{fb}^{-1}$ is shown in Fig. 4 including the predictions for the SUSY, UED and PS cases. Clearly, the difference between all three cases can be seen. For a five sigma significance $200\,\mathrm{fb}^{-1}$ are needed to distinguish between SUSY and UED and $350\,\mathrm{fb}^{-1}$ to distinguish between SUSY and PS.

3 Other Beyond the Standard Model Physics

The previous section was devoted to the measurement of masses and spins in the case of missing energy due to non detectable new particles within cascade decays. Without this complication the measurement of masses and spins of new particles is straight forward. As an example we will discuss the graviton case [9]. The graviton, which should be a spin 2 particle, can be produced directly in proton-proton collisions at the LHC. The decay channel $G \rightarrow \mathrm{e}^-\mathrm{e}^+$ can be cleanly selected. The mass of the graviton resonance can be directly measured from the di-electron invariant mass distribution. For a given luminosity of $100\,\mathrm{fb}^{-1}$ the graviton with m_G up to 2080 GeV can be discovered. θ^*, the angle between the electron and the beam axis, can be used to measure the spin of the observed resonance. The general form of the $\cos\theta^*$ distribution is $1 + A\cos^2\theta^* + B\cos^4\theta^*$. For graviton production via gluons or quarks the factors are $A = 0, B = -1$ and $A = -3, B = 4$, respectively. Further, the SM background is only flat ($A = 0, B = 0$) for electron-pair production via a scalar resonance. In the case of a vector resonance $A = \alpha, B = 0$, where $\alpha = 1$ in the SM. For a given luminosity of $100\,\mathrm{fb}^{-1}$ the spin 2 nature of the graviton can be determined at 90% CL up to graviton masses of 1720 GeV, which also means that the spin 1 case is ruled out.

4 Summary

Provided new particles are in the sub-TeV regime, already first LHC data will allow to perform a rough spectroscopy of these. In the case of no missing energy due to invisible particles at the end of a decay chain, the experimental methods for mass and spin measurements are very well established and can be applied at the LHC. In the case of missing energy the experimental methods to measure mass and spin of the new particles are quite advanced and will be needed to distinguish for example SUSY from UED. Clearly, some of the more difficult measurements need high luminosity.

References

[1] ATLAS Collaboration, G. Aad *et al.*, JINST **3**, S08003 (2008).

[2] CMS Collaboration, R. Adolphi *et al.*, JINST **3**, S08004 (2008).

[3] ATLAS Collaboration, *Expected Performance of the ATLAS Experiment, Detector, Trigger and Physics*. CERN-OPEN-2008-020, Geneva, 2008, to appear.

[4] P. Bechtle, K. Desch, and P. Wienemann, Comput. Phys. Commun. **174**, 47 (2006). hep-ph/0412012.

[5] R. Lafaye, T. Plehn, M. Rauch, and D. Zerwas, Eur. Phys. J. **C54**, 617 (2008). 0709.3985.

[6] A. J. Barr, Phys. Lett. **B596**, 205 (2004). hep-ph/0405052.

[7] M. Biglietti *et al.* ATL-PHYS-PUB-2007-004.

[8] A. J. Barr, JHEP **02**, 042 (2006). hep-ph/0511115.

[9] B. C. Allanach, K. Odagiri, M. A. Parker, and B. R. Webber, JHEP **09**, 019 (2000). hep-ph/0006114.

Chapter 7

Working Group Recent Developments

Crossover between hadronic and partonic phases and liquid property of sQGP †

XU Mingmei[1], *YU Meiling*[2], *LIU Lianshou*[1‡]
[1] Institute of Particle Physics, Huazhong Normal University, Wuhan 430079, China
[2] Department of Physics, Wuhan University, Wuhan 430072, China
Email: liuls@iopp.ccnu.edu.cn

DOI: http://dx.doi.org/10.3204/DESY-PROC-2009-01/90

Abstract

It is argued that, due to the existence of two vacua – perturbative and physical – in QCD, how to realize crossover between hadronic and partonic phases without contradiction with color confinement is a challenge. In order to solve this problem the assumption on molecule-like aggregation of hadron is proposed. A bond-percolation model is constructed basing on this assumption. The mechanism of crossover is then the appearance and growth up of hadron-clusters, resulting in a grape-shape QGP – gQGP. The pair-correlation function of gQGP is calculated, showing a short range correlation typical for liquid.

The theory of strong interaction – quantum chromodynamics QCD has a complicated phase structure [1]. It has been shown that the first order phase transition line ends at the critical point, above it is analytic crossover [2], cf. Fig. 1. But what really happens in crossover and in first order phase transition is still open question.

Let us take some examples.

Example-1 First order phase transition in QCD. Consider a nucleon gas. At high temperature and/or density some nucleons combine to a big bag, refereed to as QGP droplet. There is thus a co-existence of QGP and hadron gas with a boundary in between, which is typical for a first order phase transition, cf. Fig.2(a).

Example-2 Analytical crossover in QED. The atoms in an atomic gas can be ionized one by one and eventually turned to E.M. plasma. In the intermediate stage there is a mixture of electrons, positive-ions and neutral atoms without phase boundary and phase separation, cf. Fig.2(b).

Example-3 Analytical crossover in QCD. At zero temperature and high chemical potential there could happen an crossover between Bose-Einstein condensation BEC, due to the formation of di-quarks, and BCS superconducting, due to the existence of Cooper pairs. In the intermediate stage there is a mixture of di-quarks and Cooper pairs, cf. Fig.2(c), both of them being colored objects, mixed in perturbative vacuum, causing no problem.

However, if similar mechanism were applied to the crossover between hadron gas and QGP there would be in the intermediate stage a mixture of colored quarks and color-singlet hadrons, cf. Fig.2(d), which contradicts color confinement and is, therefore, unallowed.

† supported by NSFC under projects No. 10835005, 10775056 and 10847131.
‡ speaker

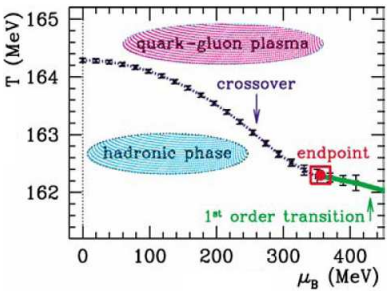


Fig. 1: (Color online) The phase diagram of QCD.

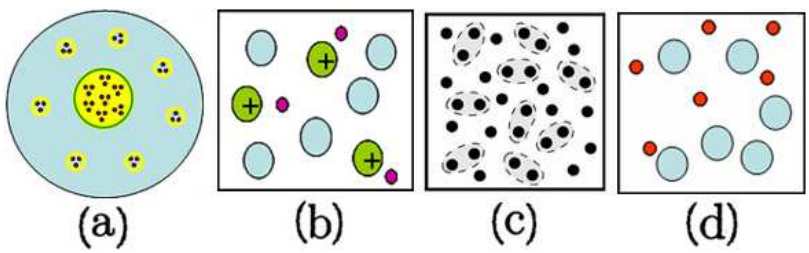


Fig. 2: (Color online) A comparison of the intermediate states in (a) first order phase transition between hadron gas and QGP in QCD and (b) crossover between neutral atomic gas and E.M. plasma in QED; (c) crossover between BEC and BCS superconductor in QCD; (d) a wrong mechanism for crossover between hadron gas and QGP in QCD.

How to solve this problem? Let us take still another example, i.e. the geometrical bond percolation model [3]. In this model hadrons connected by bonds form clusters, cf. Fig.3(a). When an infinite cluster, i.e. a cluster extending from one boundary to the other, cf. Fig.3(b), is formed, we say that the system turns to a new phase. Thus the crossover from one phase to the other is realized through the formation and growth up of clusters. No contradiction with color confinement anymore. But we have still to turn this geometrical model to a dynamical one, i.e. to provide the bond-formation with physical meaning.

In this respect we borrow the concept of delocalization from low energy nuclear physics [4] and propose the assumption on *molecule-like aggregation* [5] or MAM in short, i.e. in addition to the fusion of hadrons to QGP-droplet, cf. Fig.2(a), which is refereed to as *gas-like aggregation*, we assume that at high temperature the quarks in adjacent hadrons can tunnel through the potential barrier between the hadrons, cf. Fig.4, and bond the hadrons to cluster. Since color can flow through bonds, the hadrons in a cluster become colored objects, which will be referred to as *cells*, and only the cluster as a whole is color-singlet.

The average size of cluster increases as the increase of temperature. The appearance of infinite cluster marks the start of crossover, cf. Fig.3(b). The corresponding temperature is denoted by $T_{\rm c}$. When all the hadrons are combined to a unique cluster, crossover ends, cf. Fig.3(c), and the corresponding temperature is $T'_{\rm c}$.

In order to calculate the value of $T_{\rm c}$ and $T'_{\rm c}$ we need a dynamical model. An example is given in Ref. [5]. In this model there is a temperature dependent parameter. Using this parameter

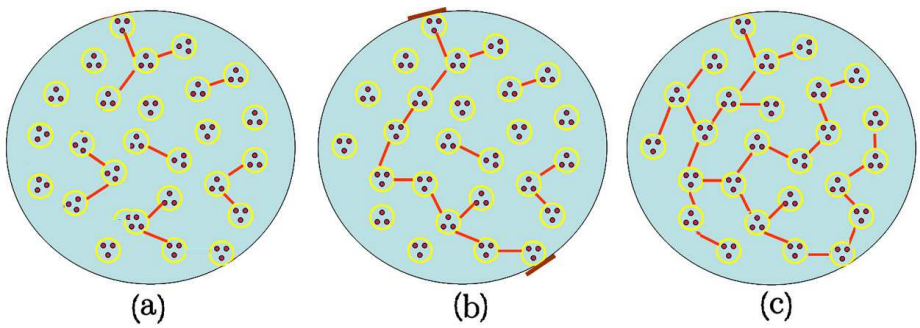


Fig. 3: (Color online) A schematic plot for the bond-percolation model. (a) Hadrons connected by bonds form clusters. (b) A cluster extending from one boundary to another is an infinite cluster. The appearance of infinite cluster is the start of crossover. (c) All the hadrons combined to a unique cluster is recognized as the end of crossover.

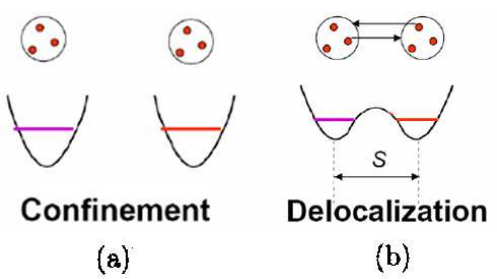


Fig. 4: (Color online) A schematic plot for confinement (a) and delocalization (b).

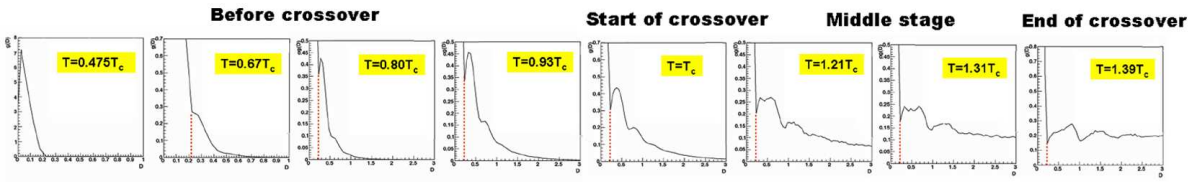


Fig. 5: (Color online) The evolution of $g(D)$. The head of the first highest peak in all the figures besides the leftmost one has been cut away.

the *maximum length of bond* $S(T)$ can be calculated. The quarks in two adjacent hadrons can tunnel through the potential barrier between hadrons, cf. Fig.4, forming bond when and only when the distance between these hadrons are nearer than $S(T)$. A bond-percolation model is constructed basing on the maximum bond-length $S(T)$ [5] and the crossover between hadron gas and QGP as well as the transition between sQGP and wQGP are successfully obtained.

In the molecule-like aggregation model MAM the QGP formed in crossover has a grape shape, cf. Fig.3(c), which will be refereed to as *grape-shape QGP*, or gQGP in short. The gQGP is a special form of strong-coupling QGP — sQGP. It is worthwhile noticing that the hot-dense matter produced in RHIC experiment is more like a perfect fluid rather than an ideal gas as previously expected. A question arises: does the gQGP posses liquid property?

To answer this question we make use of the *pair distribution function* defined as the probability of finding two atoms in the liquid at a distance r from each other [6],

$$g(r) = \frac{dN(r)}{2\pi\rho r dr}, \tag{1}$$

where $dN(r)$ is the number of atoms inside a ring with radius $(r, r+dr)$ apart from the selected center atom, ρ is the number density of the bulk homogeneous liquid. Applying to gQGP the distance between quarks in different cells should be measured along the bonds, which is refereed to as *chemical distance* and is denoted by D. So we define

$$g(D) = \sum_r \frac{dN(D,r)\cdot w}{2\pi\rho r dr}, \tag{2}$$

where w is a factor to correct for the boundary effect [7].

The resulting $g(D)$ at various temperatures are shown in Fig.5. The left 4 figures are before crossover, while the right 4 ones are during crossover. It can be seen that there is a high peak in all the figures, which is due to the intra-cell correlations among quarks. Long before crossover there is no correlation peak beside the first high one. Going nearer to crossover some shoulders appear, which develop to peaks, indicating short-range order typical for liquid at the start of crossover. This shows that the gQGP formed in crossover really possess liquid property. In the process of crossover, correlation peaks appears more and more and go farther and farther, indicating the reduction of viscosity in the process.

In summary, it is argued that how to realize crossover between hadron gas and QGP without contradiction with color confinement is a challenge. In order to solve this problem the assumption on molecule-like aggregation of hadron is proposed. A bond-percolation model is

constructed basing on this assumption. The mechanism of crossover is then the appearance and growth up of hadron-clusters, resulting in a grape-shape QGP — gQGP. The pair-correlation function of gQGP is calculated, showing a short range correlation typical for liquid.

References

[1] T.D. Lee, G.C. Wick, Phys. Rev. D **9**(1974)2291; T.D. Lee, Rev. Mod. Phys. **47** (1975) 267; E.V. Shuryak, Phys. Rept. **61** (1980) 71; for a recent review see e.g. T. Schäfer, lecture given at HUGS 2005, hep-ph/0509068.

[2] Aoki et al., Nature 443, 675-678 (2006).

[3] G. Baym, Physica 96A (1979) 131; T. Celik, F. Karsch and H. Satz, Phys. Lett. 97B (1980) 128; H. Satz, Nucl. Phys. A **642** (1998) 130c;

[4] F. Wang, G. H. Wu, L. J. Teng and T. Goldman, Phys. Rev. Lett. **69** (1992) 2901.

[5] Xu M M, Yu M L and Liu L S 2008 *Phys. Rev. Lett.* **100** 092301.

[6] March N H and Tosi M P 2002 *Introduction to liquid state physics* (World Scientific Publishing Co., Singapore); Ichimaru S 1982 *Rev. Mod. Phys.* **54** 1017.

[7] Yu Meiling, Xu Mingmei, Liu Zhengyou and Liu Lianshou, Arxiv: 0805.1588v2 (2008).

Nuclear Effects in High-p_T Hadron Production at Large x

J. Nemchik[1,2] *and M. Šumbera*[3†]
[1] Institute of Experimental Physics SAS, Watsonova 47, 04001 Košice, Slovakia,
[2] Czech Technical University, FNSPE, Břehová 7, 11519 Prague, Czech Republic,
[3] Nuclear Physics Institute ASCR, 25068 Řež, Czech Republic

DOI: http://dx.doi.org/10.3204/DESY-PROC-2009-01/91

Abstract
We demonstrate that strong suppression of the relative production rate $(d+Au)/(p+p)$ observed at forward rapidities in inclusive high-p_T hadron production at RHIC is due to parton multiple rescatterings in nuclear matter. The light-cone dipole approach-based calculations are in a good agreement with BRAHMS and STAR Collaborations data at large x_1. We predict similar suppression pattern also for regions where effects of parton saturation are not expected thus ruling out applicability of the models based on Color Glass Condensate.

1 Introduction

High-p_T hadron spectra at large forward rapidities are promising tool to study nuclear effects. Strong nuclear suppression of the spectra observed by the BRAHMS [1, 2] and STAR [3] Collaboration in deuteron-gold collisions at the Relativistic Heavy Ion Collider (RHIC) was tempting to call in the parton saturation [4, 5] or the Color Glass Condensate (CGC) [6] motivated phenomenology [7] as its most natural interpretation.

According to these models the parton coherence phenomena may reveal itself already at RHIC energies showing up first in the wave function of heavy nuclei. Kinematically most favorable region to access these effects is the fragmentation region of the light projectile nucleus 1 colliding with the heavy one 2. At large x_1 (i.e. at large Feynman x_F) one can simultaneously reach the smallest values of the light-front momentum fraction variable in nuclei $x_2 = x_1 - x_F$.

However, observed nuclear effects occur not only at forward rapidities [1–3] but, quite unexpectedly, also at midrapidities [8]. In this case they can not be explained in terms of CGC because at large p_T the data cover region of not too small $x_2 \gtrsim 0.01$ where effects of coherence are very unlikely.

It was shown in [9, 10] that a considerable nuclear suppression for any large x_1 reaction comes from the energy conservation applied to multiple rescatterings of the projectile partons. It was also demonstrated [9] that such a large-x_1 suppression is a leading twist effect, violating QCD factorization, a basic ingredient of the CGC-based models.

Analysis of nuclear suppression based on multiple parton rescatterings leads also to approximate x_1 (x_F)-scaling [9, 10]: similar nuclear effects occur also at smaller energies where the onset of coherence effects is expected to be much weaker.

† speaker

In this article we present another consequence of x_1-scaling and namely that the similar nuclear effects can be important also at midrapidities provided that the corresponding p_T-values are high enough to keep the same value of x_1 as that at forward rapidities.

2 High-p_T hadron production: Sudakov suppression, production cross section

Let us recall that in the limit $x_1 \to 1$ gluon radiation in any pQCD-driven hard scattering is forbidden by the energy conservation. For uncorrelated Poisson distribution of radiated gluons, the Sudakov suppression factor, i.e. the probability to have a rapidity gap $\Delta y = -\ln(1-x_1)$ between leading parton and rest of the system acquires a very simple form: $S(x_1) = 1 - x_1$ [9].

Suppression at $x_1 \to 1$ can thus be formulated as a survival probability of the large rapidity gap (LRG) process in multiple interactions of projectile valence quarks with the nucleus. Every additional inelastic interaction of the quarks contributes an extra suppression factor $S(x_1)$. The probability of an n-fold inelastic collision is related to the Glauber model coefficients via the Abramovsky-Gribov-Kancheli (AGK) cutting rules [11]. Correspondingly, the survival probability at impact parameter $\vec{b}$ reads,

$$W^{hA}_{LRG}(b) = \exp[-\sigma^{hN}_{in}\, T_A(b)] \sum_{n=1}^{A} \frac{1}{n!} \left[\sigma^{hN}_{in}\, T_A(b)\right]^n S(x_1)^{n-1}\,, \tag{1}$$

where $T_A(b)$ is the nuclear thickness function.

At large p_T, the cross section of hadron production in $d+A$ $(p+p)$ collisions is given by a convolution of the distribution function for the projectile valence quark with the quark scattering cross section and the fragmentation function,

$$\frac{d^2\sigma}{d^2p_T\, d\eta} = \sum_q \int\limits_{z_{min}}^{1} dz\, f_{q/d(p)}(x_1, q_T^2)\; \frac{d^2\sigma[qA(p)]}{d^2q_T\, d\eta}\bigg|_{\vec{q}_T = \vec{p}_T/z} \frac{D_{h/q}(z)}{z^2}, \tag{2}$$

where $x_1 = \frac{q_T}{\sqrt{s}}\, e^{\eta}$. The quark distribution functions in the nucleon have the form adopted the lowest order (LO) parametrization from [12]. Fragmentation functions have been taken from [13]. Summed over multiple interactions, the quark distribution in the nucleus reads,

$$f^{(A)}_{q/N}(x_1, q_T^2) = C\, f_{q/N}(x_1, q_T^2)\, \frac{\int d^2b \left[e^{-x_1\sigma_{eff}T_A(b)} - e^{-\sigma_{eff}T_A(b)}\right]}{(1-x_1)\int d^2b \left[1 - e^{-\sigma_{eff}T_A(b)}\right]} \tag{3}$$

where effective cross section $\sigma_{eff} = \sigma_{eff}(p_T, s) = \frac{\langle \sigma^2_{\bar{q}q}(r_T)\rangle}{\langle \sigma_{\bar{q}q}(r_T)\rangle}$ has been evaluated in [9] and normalization factor C in Eq. (3) is fixed by the Gottfried sum rule.

The cross section for quark scattering on the target $d\sigma[qA(p)]/d^2q_T d\eta$ in Eq. (2) is calculated in the light-cone dipole approach [14, 15]. We separate the contributions characterized by different initial transverse momenta and sum over different mechanisms of high-p_T hadron production. Details can be found in [9].

At midrapidities in the RHIC kinematic range, at small and moderate p_T, one should also take into account production and fragmentation of gluons. Details of calculation can be found

in [16]. Consequently, the cross section for hadron production, Eq. (2), should be supplemented by the gluon term with corresponding distribution function, parton scattering cross section and the fragmentation function. Including multiple parton interactions, the gluon distribution in the nucleus is given by the same formula as for quarks (see Eq. (3)), except σ_{eff}, which should be multiplied by the Casimir factor $9/4$.

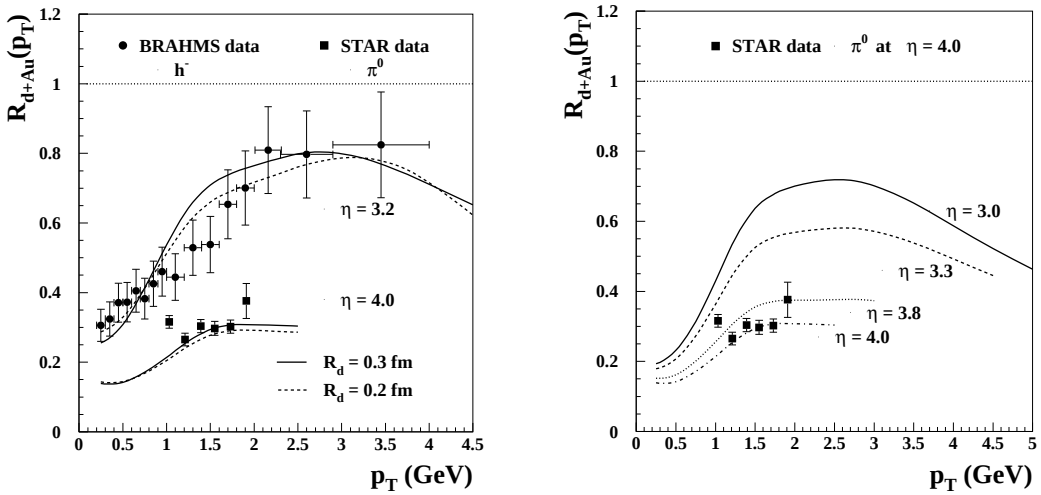


Fig. 1: Left panel: Ratio of negative hadron and neutral pion production rates in $d + Au$ and $p + p$ collisions as function of p_T at $\eta = 3.2$ and $\eta = 4.0$ vs. data from the BRAHMS [1] and STAR Collaborations [3], respectively. Right panel: Model predictions for nuclear attenuation factor $R_{d+Au}(p_T)$ as a function of p_T for production of π^0 mesons at $\sqrt{s} = 200\,\mathrm{GeV}$ and at different values of η from 3.0 to 4.0.

3 Comparison with data

In 2004 the BRAHMS Collaboration [1] found a significant nuclear suppression in production of negative hadrons at $\eta = 3.2$. Their measurements are plotted in the left panel of Fig. 1. Much stronger onset of nuclear effects was observed later on by the STAR Collaboration [3] for π^0 production at pseudorapidity $\eta = 4.0$ (left panel of Fig. 1). A huge difference in nuclear effects for different η is due to the energy conservation and reflects much smaller survival probability of the LRG in multiple parton interactions at larger x_1 [9, 10].

To demonstrate different onsets of nuclear effects as a function of pseudorapidity we present in the right panel of Fig. 1 predictions for nuclear suppression factor at different fixed values of η. Changing the value of η from 3.0 to 4.0, one can see a huge rise of nuclear suppression by a factor of 2 [10].

Fig. 2 clearly demonstrates x_1 (x_F)-scaling of nuclear suppression, i.e. approximately the same nuclear effects at different energies, $\sqrt{s} = 200, 130$ and $62.4\,\mathrm{GeV}$ accessible at RHIC, and pseudorapidities corresponding to the same values of x_1.

Let us note that observed x_1-scaling enables to predict similar nuclear effects also at midrapidities. However, in this case hadron transverse momenta should be high enough so that x_1 are as large as those at forward rapidities. This expectations seems to be confirmed by the recent PHENIX Collaboration $d + Au$ data at midrapidities [8] (see the left panel of Fig. 3).

If the effects of multiple parton rescatterings are not taken into account the p_T-dependence of the ratio $R_{d+Au}(p_T)$ is given by the thin dashed line shown in the left panel of Fig. 3. The model predictions with inclusion of multiple parton rescatterings are presented by the thin solid line. Obviously at moderate $3 \lesssim p_T \lesssim 7\,\text{GeV}$ our calculations underestimate the data. Nevertheless, quite a strong onset of nuclear suppression at large p_T is not in a disagreement with the corresponding experimental data points. At $p_T = 25\,\text{GeV}$ we expect $R_{d+Au}(p_T) \sim 0.9$.

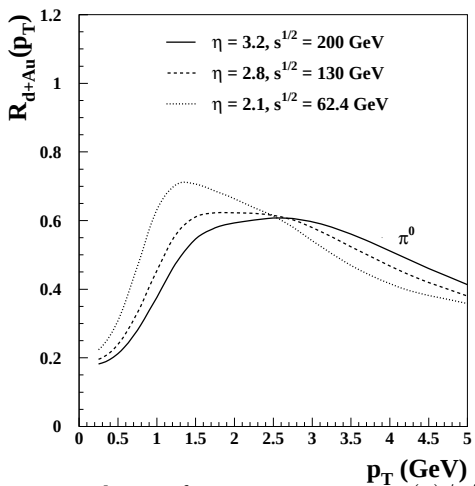


Fig. 2: Predictions for an approximate $\exp(\eta)/\sqrt{s}$-scaling of the ratio $R_{d+Au}(p_T)$ for π^0 production rates in $d + Au$ and $p + p$ collisions.

Let us note that midrapidity calculations in the RHIC energy range are most complicated since this is the transition region between the regimes with (small p_T) and without (large p_T) onset of the coherence effects. One can deal with this situation relying on the light-cone Green function formalism [17–19]. However, in this case the integrations involved become too complicated. Therefore, we present in the same Fig. 3 also corrections for finite coherence length by the linear interpolation performed by means of the so-called nuclear longitudinal form factor following the procedure from [16]. Such a situation is described by the thick solid and dashed lines reflecting the cases with and without inclusion of the multiple parton rescatterings, respectively. It brings the model predictions to a better agreement with data at moderate p_T.

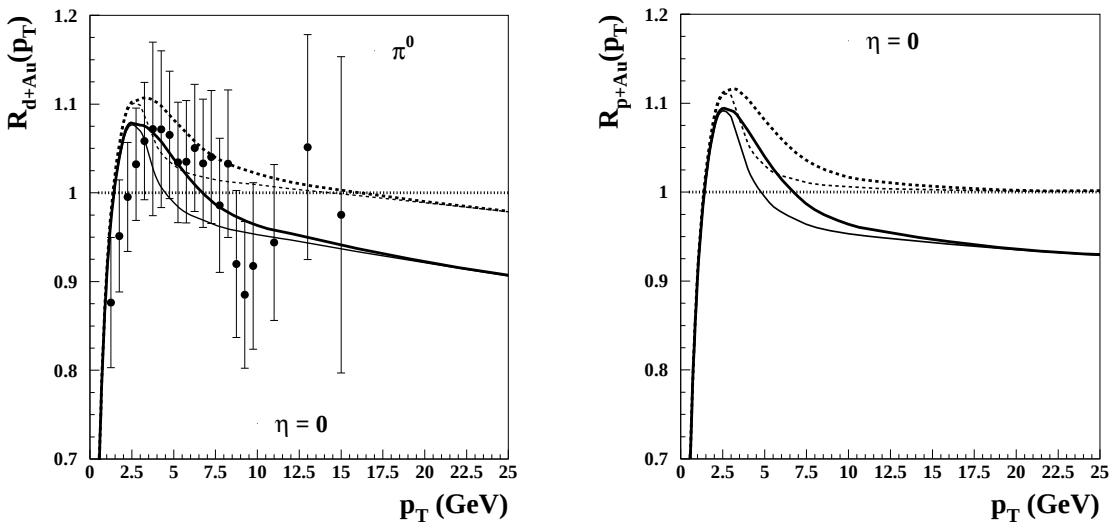


Fig. 3: (Left) Ratio $R_{d+Au}(p_T)$ as a function of p_T for production of π^0 mesons at $\sqrt{s} = 200\,\text{GeV}$ and $\eta = 0$ vs. data from the PHENIX Collaboration [8]. Thin solid and dashed lines represent the predictions calculated in the limit of long coherence length. Thick solid and dashed lines include corrections for the finite coherence length. (Right) The same as Fig. in the left panel but for the ratio $R_{p+Au}(p_T)$.

In order to minimize the isospin effects it is more convenient to study the nuclear effects in $p+Au$ collisions. Therefore, we present in the right panel of Fig. 3 also model predictions for R_{p+Au} as a function of p_T. At $p_T = 25\,\mathrm{GeV}$ we predict $R_{p+Au} \sim 0.93$.

4 Summary and conclusions

In this article we have analyzed implications of the x_1 (x_F)-scaling of nuclear suppression for production of high-p_T hadrons in $p(d) + Au$ collisions at RHIC. Using this scaling we predict considerable nuclear suppression at large x_1 at several very different kinematic regions: **i)** at large forward rapidities, **ii)** at smaller rapidities and smaller energies, **iii)** at midrapidity but at very large p_T.

Using a simple formula Eq. (3) based on Glauber multiple interaction theory and the AGK cutting rules, we have calculated hadron production at midrapidity and found an unexpectedly strong nuclear suppression at large p_T. This observation is not in a contradiction with the recent PHENIX Collaboration measurements [8].

To avoid the isospin effects, we have also studied large-p_T π^0 production in $p + Au$ collisions. With the same input parameters, we predict quite a strong nuclear suppression factor, $R_{p+Au} = 0.93$ at $p_T = 25\,\mathrm{GeV}$.

As a final remark let us note that in the RHIC kinematic region, investigation of hadron production in $p(d) + Au$ collisions at midrapidities is very important because at large p_T the data cover rather large $x_2 \sim 0.05 - 0.1$ where no effects of coherence are possible. It allows to exclude the models based on CGC from interpretation of observed nuclear suppression.

Acknowledgments

This work was supported in part by the Grant Agency of the Czech Republic, Grant 202/07/0079, Slovak Funding Agency, Grant 2/7058/27; and by Grants VZ MSM 6840770039 and LC 07048 (Ministry of Education of the Czech Republic).

References

[1] BRAHMS Collaboration, I. Arsene *et al.*, Phys. Rev. Lett. **93**, 242303 (2004).

[2] BRAHMS Collaboration, Hongyan Yang *et al.*, J. Phys. **G34**, S619 (2007).

[3] STAR Collaboration, J. Adams *et al.*, Phys. Rev. Lett. **97**, 152302 (2006).

[4] L.V. Gribov, E.M. Levin, and M.G. Ryskin, Nucl. Phys. **B188**, 555 (1981); Phys. Rep. **100**, 1 (1983).

[5] A.H. Mueller, Eur. Phys. J. **A1**, 19 (1998).

[6] L. McLerran, and R. Venugopalan, Phys. Rev. **D49**, 2233 (1994); Phys. rev. **D49**, 3352 (1994).

[7] D. Kharzeev, Y.V. Kovchegov, and K. Tuchin, Phys. Lett. **B599**, 23 (2004).

[8] PHENIX Collaboration, S.S. Adler et al., Phys. Rev. Lett. **98**, 172302 (2007).

[9] B.Z. Kopeliovich, *et al.*, Phys. Rev. **C72**, 054606 (2005).

[10] J. Nemchik, V. Petráček, I.K. Potashnikova, and M. Šumbera, Phys. Rev. **C78**, 025213 (2008).

[11] A.V. Abramovsky, V.N. Gribov, and O.V. Kancheli, Yad. Fiz. **18**, 595 (1973).

[12] M. Gluck, E. Reya, and A. Vogt, Z. Phys. **C67**, 433 (1995).

[13] D. de Florian, R. Sassot, and M. Stratmann, Phys. Rev. **D75**, 114010 (2007); Phys. Rev. **D76**, 074033 (2007).

[14] A.B. Zamolodchikov, B.Z. Kopeliovich, and L.I. Lapidus, *Pis'ma Zh. Eksp. Teor. Fiz.* **33**, 612 (1981); *Sov. Phys. JETP Lett.* **33**, 595 (1981).

[15] M.B. Johnson, B.Z. Kopeliovich, and A.V. Tarasov, Phys. Rev. **C63**, 035203 (2001).

[16] B.Z. Kopeliovich, J. Nemchik, A. Schäfer, and A.V. Tarasov, Phys. Rev. Lett. **88**, 232303 (2002).

[17] B.Z. Kopeliovich, J. Nemchik, A. Schäfer, and A.V. Tarasov, Phys. Rev. **C88**, 035201 (2002).

[18] B.Z. Kopeliovich, J. Raufeisen, and A.V. Tarasov, Phys. Rev. **C62**, 035204 (2000).

[19] B.Z. Kopeliovich, J. Nemchik, I.K. Potashnikova, and I. Schmidt, J. Phys. **G35**, 115010 (2008).

The nimbus of away-side jets

I.M. Dremin
Lebedev Physical Institute, Moscow, Russia
DOI: http://dx.doi.org/10.3204/DESY-PROC-2009-01/92

Abstract
The conical structure around the away-side jets is discussed. The equations of in-medium gluodynamics are proposed. Their classical lowest order solution is explicitly shown for a color charge moving with constant speed. For nuclear permittivity larger than 1 it describes the shock wave induced by emission of Cherenkov gluons. The values of real and imaginary parts of nuclear permittivity are estimated from fits of RHIC data. Specific effects at LHC energies are described.

The conical structure around away-side jets has been observed in high-energy central nucleus-nucleus collisions at RHIC [1–3]. It can be explained as the emission of Cherenkov gluons by a parton passing through a quark-gluon medium. The properties and evolution of the medium are widely debated. At the simplest level it is assumed to consist of a set of current quarks and gluons. The collective excitation modes of the medium may, however, play a crucial role. Phenomenologically their impact would be described by the nuclear permittivity of the matter corresponding to its response to passing partons. Namely this approach is most successful for electrodynamical processes in matter. Therefore, it is reasonable to modify the QCD equations by taking into account collective properties of the quark-gluon medium [4]. Strangely enough, this was not done earlier. For the sake of simplicity we consider here the gluodynamics only.

The classical lowest order solution of these equations coincides with Abelian electrodynamical results up to a trivial color factor. One of the most spectacular of them is Cherenkov radiation and its properties. Now, Cherenkov gluons take the place of Cherenkov photons [5, 6]. Their emission in high-energy hadronic collisions is described by the same formulae but with the nuclear permittivity in place of the usual one. Actually, one considers them as quasiparticles, i.e. quanta of the medium excitations leading to shock waves with properties determined by the permittivity.

Another problem of this approach is related to the notion of the rest system of the medium. It results in some specific features of this effect at LHC energies.

To begin, let us recall the classical in-vacuum Yang-Mills equations

$$D_\mu F^{\mu\nu} = J^\nu, \qquad F^{\mu\nu} = \partial^\mu A^\nu - \partial^\nu A^\mu - ig[A^\mu, A^\nu], \tag{1}$$

where $A^\mu = A^\mu_a T_a$; $A_a(A^0_a \equiv \Phi_a, \mathbf{A}_a)$ are the gauge field (scalar and vector) potentials, the color matrices T_a satisfy the relation $[T_a, T_b] = if_{abc}T_c$, $D_\mu = \partial_\mu - ig[A_\mu, \cdot]$, $J^\nu(\rho, \mathbf{j})$ a classical source current, the metric $g^{\mu\nu}$=diag(+,–,–,–).

The chromoelectric and chromomagnetic fields are $E^\mu = F^{\mu 0}$, $B^\mu = -\frac{1}{2}\epsilon^{\mu ij}F^{ij}$ or, as functions of the gauge potentials in vector notation,

$$\mathbf{E}_a = -\mathrm{grad}\Phi_a - \frac{\partial \mathbf{A}_a}{\partial t} + gf_{abc}\mathbf{A}_b\Phi_c, \quad \mathbf{B}_a = \mathrm{curl}\mathbf{A}_a - \frac{1}{2}gf_{abc}[\mathbf{A}_b\mathbf{A}_c]. \tag{2}$$

Herefrom, one easily rewrites the in-vacuum equations of motion (1) in vector form. We do not show them explicitly here (see [4]) and write down the equations of the in-medium gluodynamics using the same method as in electrodynamics. We introduce the nuclear permittivity and denote it also by ϵ, since this will not lead to any confusion. After that, one should replace $\mathbf{E}_a$ by $\epsilon\mathbf{E}_a$ and get

$$\epsilon(\mathrm{div}\mathbf{E}_a - gf_{abc}\mathbf{A}_b\mathbf{E}_c) = \rho_a, \quad \mathrm{curl}\mathbf{B}_a - \epsilon\frac{\partial\mathbf{E}_a}{\partial t} - gf_{abc}(\epsilon\Phi_b\mathbf{E}_c + [\mathbf{A}_b\mathbf{B}_c]) = \mathbf{j}_a. \quad (3)$$

The space-time dispersion of ϵ is neglected here.

In terms of potentials these equations are cast in the form

$$\triangle\mathbf{A}_a - \epsilon\frac{\partial^2\mathbf{A}_a}{\partial t^2} = -\mathbf{j}_a - gf_{abc}(\frac{1}{2}\mathrm{curl}[\mathbf{A}_b,\mathbf{A}_c] + \frac{\partial}{\partial t}(\mathbf{A}_b\Phi_c) + [\mathbf{A}_b\mathrm{curl}\mathbf{A}_c] - \epsilon\Phi_b\frac{\partial\mathbf{A}_c}{\partial t} - \epsilon\Phi_b\mathrm{grad}\Phi_c - \frac{1}{2}gf_{cmn}[\mathbf{A}_b[\mathbf{A}_m\mathbf{A}_n]] + g\epsilon f_{cmn}\Phi_b\mathbf{A}_m\Phi_n), \quad (4)$$

$$\triangle\Phi_a - \epsilon\frac{\partial^2\Phi_a}{\partial t^2} = -\frac{\rho_a}{\epsilon} + gf_{abc}(2\mathbf{A}_b\mathrm{grad}\Phi_c + \mathbf{A}_b\frac{\partial\mathbf{A}_c}{\partial t} + \epsilon\frac{\partial\Phi_b}{\partial t}\Phi_c) + g^2f_{amn}f_{nlb}\mathbf{A}_m\mathbf{A}_l\Phi_b. \quad (5)$$

If the terms with coupling constant g are omitted, one gets the set of Abelian equations, that differ from electrodynamical equations by the color index a only. The external current is due to a parton moving fast relative to partons "at rest".

The crucial distinction between the in-vacuum and in-medium equations is that there is no radiation (the field strength is zero in the forward light-cone and no gluons are produced) in the lowest order solution in vacuum, and it is admitted in medium, because ϵ takes into account the collective response (color polarization) of the nuclear matter.

Cherenkov effects are especially suited for treating them by classical approach to (4), (5). Their unique feature is independence of the coherence of subsequent emissions on the time interval between these processes. The lack of balance of the phase $\Delta\phi$ between emissions with frequency $\omega = k/\sqrt{\epsilon}$ separated by the time interval Δt (or the length $\Delta z = v\Delta t$) is given by

$$\Delta\phi = \omega\Delta t - k\Delta z\cos\theta = k\Delta z(\frac{1}{v\sqrt{\epsilon}} - \cos\theta) \quad (6)$$

up to terms that vanish for large distances. For Cherenkov effects the angle θ is

$$\cos\theta = \frac{1}{v\sqrt{\epsilon}}. \quad (7)$$

The coherence condition $\Delta\phi = 0$ is strictly valid independent of Δz. This is a crucial property specific for Cherenkov radiation only. The fields $(\Phi_a, \mathbf{A}_a)$ and the classical current for in-medium gluodynamics can be represented by the product of the electrodynamical expressions $(\Phi, \mathbf{A})$ and the color matrix T_a.

Let us recall the Abelian solution [7] for the current with velocity $\mathbf{v}$ along z-axis:

$$\mathbf{j}(\mathbf{r},t) = \mathbf{v}\rho(\mathbf{r},t) = 4\pi g\mathbf{v}\delta(\mathbf{r}-\mathbf{v}t). \tag{8}$$

In the lowest order the solutions for the scalar and vector potentials are related $\mathbf{A}^{(1)}(\mathbf{r},t) = \epsilon\mathbf{v}\Phi^{(1)}(\mathbf{r},t)$ and

$$\Phi^{(1)}(\mathbf{r},t) = \frac{2g}{\epsilon}\frac{\theta(vt-z-r_\perp\sqrt{\epsilon v^2-1})}{\sqrt{(vt-z)^2-r_\perp^2(\epsilon v^2-1)}}. \tag{9}$$

Here $r_\perp = \sqrt{x^2+y^2}$ is the cylindrical coordinate; z symmetry axis. The cone

$$z = vt - r_\perp\sqrt{\epsilon v^2-1} \tag{10}$$

determines the position of the shock wave due to the θ-function in (9). The field is localized within this cone and decreases with time as $1/t$ at any fixed point. The gluons emission is perpendicular to the cone (10) at the Cherenkov angle (7).

Due to the antisymmetry of f_{abc}, the higher order terms (g^3,...) are equal to zero for any solution multiplicative in space-time and color as seen from (4), (5).

The expression for the intensity of the radiation is given by the Tamm-Frank formula (up to Casimir operators) that leads to infinity for constant ϵ. The ω-dependence of ϵ (dispersion), its imaginary part (absorption) ϵ_2 and chromomagnetic permeability can be taken into account [4].

Recently, the experimental data of STAR and PHENIX [1, 2] were fitted [8] with account of the imaginary part of ϵ and emission of pions and ρ-mesons within the Cherenkov cone. The results are presented in Table 1 (for more details see [8]).

Table 1

Experiment	$\theta_{\max}$	ε_1	ε_2
STAR	1.04 rad	3.95	0.8
PHENIX	1.27 rad	9.5	1.8

The real parts ϵ_1 are quite large while the imaginary parts are small so that $(\epsilon_2/\epsilon_1)^2 \approx 0.04 \ll 1$. Different values of ϵ_1 for STAR and PHENIX are related to different positions of hump maxima in these experiments.

The theoretical attempts to estimate the nuclear permittivity from first principles are not very convincing [6, 9–12]. Therefore, I prefer to use the general formulae of the scattering theory for the nuclear permittivity. It is related to the refractive index n of the medium $\epsilon = n^2$ and the latter one is expressed [13] through the real part of the forward scattering amplitude of the refracted quanta $\mathrm{Re}F(0^\mathrm{o},E)$ by

$$\mathrm{Re}n(E) = 1 + \Delta n_R = 1 + \frac{6m_\pi^3\nu}{E^2}\mathrm{Re}F(E) = 1 + \frac{3m_\pi^3\nu}{4\pi E}\sigma(E)\rho(E). \tag{11}$$

Here E denotes the energy, ν the number of scatterers within a single nucleon, m_π the pion mass, $\sigma(E)$ the cross section and $\rho(E)$ the ratio of real to imaginary parts of the forward scattering amplitude $F(E)$.

Thus the emission of Cherenkov gluons is possible only for processes with positive $\mathrm{Re}F(E)$ or $\rho(E)$. Unfortunately, we are unable to calculate directly in QCD these characteristics of gluons and have to rely on analogies and on our knowledge of the properties of hadrons. The only experimental facts we get for this medium are brought about by particles registered at the final stage. They have some features in common, which (one may hope!) are also relevant for gluons as the carriers of the strong forces. Those, first, are the resonant behavior of amplitudes at rather low energies and, second, the positive real part of the forward scattering amplitudes at very high energies for hadron-hadron and photon-hadron processes as measured from the interference of the Coulomb and hadronic parts of the amplitudes. $\mathrm{Re}F(0^{\mathrm{o}}, E)$ is always positive (i.e., $n > 1$) within the low-mass wings of the Breit-Wigner resonances. This shows that the necessary condition for Cherenkov effects $n > 1$ is satisfied at least within these two energy intervals. This fact was used to describe experimental observations at SPS, RHIC and cosmic ray energies. The asymmetry of the ρ-meson shape at SPS [14] and azimuthal correlations of in-medium jets at RHIC [1,2] were explained by emission of comparatively low-energy Cherenkov gluons [15,16]. The parton density and intensity of the radiation were estimated. In its turn, cosmic ray data [17] at energies corresponding to LHC require very high-energy gluons to be emitted by the ultrarelativistic partons moving along the collision axis [5]. The specific predictions at LHC stemming from this observation were discussed elsewhere [18]. Let us note the important difference from electrodynamics, where $n < 1$ at high frequencies. The energy of the forward moving partons at LHC would exceed the thresholds above which $n > 1$. Then both types of experiments can be done, i.e. the 90°-trigger and non-trigger forward-backward partons experiments. The predicted results for 90°-trigger geometry are similar to those at RHIC. The non-trigger Cherenkov gluons should be emitted within the rings at polar angles of tens degrees in c.m.s. at LHC by the forward moving partons (and symmetrically by the backward ones) according to some events observed in cosmic rays [16, 17]. This is the new prediction for LHC.

To conclude, the in-medium gluodynamics leads quite naturally to the prediction of Cherenkov gluons emitted within the nuclear medium if $\epsilon > 1$. The experimental data about the nimbus of away-side jets obtained at RHIC have been well fitted by these formulae with complex nuclear permittivity. Quite large values of its real part are estimated from fits to experimental data. Therefrom one concludes that the density of scatterers ν is rather high (about 10-20 per a hadron). The imaginary part is comparatively small. The specific predictions at LHC energies are waiting for their verification.

Acknowledgement

This work is supported by RFBR grants 06-02-17051, 06-02-16864, 08-02-91000-CERN.

References

[1] N.N. Ajitanand, Nucl. Phys. A783 (2007) 519; PoS LHC07:001,2007.

[2] J.G. Ulery, PoS LHC07:036,2007; arXiv:0801.4904; 0807.1613.

[3] C.A. Pruneau, arXiv:0810.1461.

[4] I.M. Dremin, Eur. Phys. J. C56 (2008) 81.

[5] I.M. Dremin, JETP Lett. 30 (1979) 140; Sov. J. Nucl Phys. 33 (1981) 726.

[6] V. Koch, A. Majumder, X.N. Wang, Phys. Rev. Lett. 96 (2006) 172302.
[7] M.V. Kuzelev, A.A. Rukhadze, *Metody teorii voln v sredah s dispersiey*, M., Fizmatlit, 2007.
[8] I.M. Dremin, M.R. Kirakosyan, A.V. Leonidov, A.V. Vinogradov, arXiv:0809.2472.
[9] O.K. Kalashnikov, V.V. Klimov, Sov. J. Nucl. Phys. 31 (1980) 699.
[10] H.A. Weldon, Phys. Rev. D26 (1982) 1394.
[11] J.P. Blaizot, E. Iancu, Phys. Rep. 359 (2002) 355.
[12] M.K. Djongolov, S. Pisov, V. Rizov, J. Phys. G30 (2004) 425.
[13] M. Goldberger, K. Watson, *Collision Theory* (John Wiley and Sons Inc., 1964) Ch. 11, sect. 3, sect. 4.
[14] S. Damjanovic et al, Phys. Rev. Lett. 96 (2006) 162302.
[15] I.M. Dremin, V.A. Nechitailo, arXiv:hep-ph/0704.1081.
[16] I.M. Dremin, Nucl. Phys. A767 (2006) 233.
[17] A.V. Apanasenko et al., JETP Lett. 30 (1979) 145.
[18] I.M. Dremin, Int. J. Mod. Phys. A22 (2007) 3087.

Baryon stopping as a test of geometric scaling

Yacine Mehtar-Tani and Georg Wolschin[†]
Institut für Theoretische Physik der Universität Heidelberg,
Philosophenweg 16, 69120 Heidelberg
DOI: http://dx.doi.org/10.3204/DESY-PROC-2009-01/96

Abstract

We suggest to use net-proton rapidity distributions in central relativistic heavy-ion collisions at SPS, RHIC and LHC energies in order to probe saturation physics. Within the color glass condensate framework based on small-coupling QCD, net-baryon rapidity distributions are shown to exhibit geometric scaling. Excellent agreement with RHIC data in Au + Au collisions at $\sqrt{s_{NN}}$ = 200 GeV is found. Predictions for net-proton rapidity spectra in central Pb + Pb collisions at LHC energies of $\sqrt{s_{NN}}$ = 5.5 TeV are made.

Baryon stopping in relativistic heavy-ion collisions as a probe of QCD-matter at high parton density is of great current interest [1–4]. Theoretical QCD-based approaches usually focus on charged-hadron production. In the central rapidity region a reasonable understanding has been achieved in the color glass condensate (CGC) framework [5–8] through inclusive gluon production [9,10]. In this theory, due to the self-interaction of gluons, the number of gluons in the nuclear wave function increases with increasing energy and decreasing longitudinal momentum fraction x carried by the parton.

Unitarity requires that the gluon density saturates below a characteristic momentum scale, the so-called saturation scale Q_s. In this regime gluons form a coherent state. Presently the evidence for the existence of this state of matter is, however, not yet clear. Due to the dependence of the saturation scale on rapidity and mass number, it has been proposed that saturation effects should be studied with heavy nuclei and large rapidities at RHIC energies and beyond.

We have suggested in [11] to use the rapidity distribution of net protons ($p - \bar{p}$) in central heavy-ion collisions as a testing ground for saturation physics, cf. Fig. 1. In $A+A$ collisions, two distinct and symmetric peaks with respect to rapidity y occur at SPS energies [12] and beyond. The rapidity separation between the peaks increases with energy, and decreases with increasing mass number A reflecting larger baryon stopping for heavier nuclei, as has been investigated phenomenologically in the relativistic diffusion model [13].

The net-baryon number is essentially transported by valence quarks. During the collision the fast valence quarks in one nucleus scatter in the other nucleus by exchanging soft gluons, leading to their redistribution in rapidity space. Here we do not address the issue of the baryon transport mechanism in the fragmentation process [14] that is relevant for identified baryons.

We take advantage of the fact that the valence quark parton distribution is well known at large x, which corresponds to the forward and backward rapidity region, to access the gluon distribution at small x in the target nucleus. Therefore, this picture provides a clean probe of

[†] speaker

the unintegrated gluon distribution $\varphi(x, p_T)$ at small x in the saturation regime. Here p_T is the transverse momentum transfer.

We have two symmetric contributions, coming from the two beams. The contribution of the fragmentation of the valence quarks in the forward moving nucleus is given by the simple formula [15] for the rapidity distribution of hadrons:

$$\frac{dN}{dy} = \frac{C}{(2\pi)^2} \int \frac{d^2p_T}{p_T^2}\, x_1 q_v(x_1, Q_f)\, \varphi\,(x_2, p_T)\,, \tag{1}$$

where $x_1 = p_T/\sqrt{s}\exp(y)$, $x_2 = p_T/\sqrt{s}\exp(-y)$ are the longitudinal momentum fractions carried, respectively, by the valence quark in the projectile and the soft gluon in the target. The factorization scale is set equal to the transverse momentum, $Q_f \equiv p_T$. The contribution of valence quarks in the other beam nucleus is added incoherently by changing $y \to -y$. The gluon distribution is related to the forward dipole scattering amplitude $\mathcal{N}(x, r_T)$, for a quark dipole of transverse size r_T, through the Fourier transform

$$\varphi(x, p_T) = 2\pi p_T^2 \int r_T dr_T \mathcal{N}(x, r_T) J_0(r_T p_T). \tag{2}$$

In the fragmentation region of the projectile the valence quark parton distribution function (PDF) is dominated by large values of x_1. We integrate out the fragmentation function such that the hadron rapidity distribution is proportional to the parton distribution. The overall constant C depends on the nature of the produced hadron.

One important prediction of the color glass condensate theory is geometric scaling: the gluon distribution depends on x and p_T only through the scaling variable $p_T^2/Q_s^2(x)$, where $Q_s^2(x) = A^{1/3} Q_0^2\; x^{-\lambda}$, A is the mass number and Q_0 sets the dimension. This has been confirmed experimentally at HERA [16]. The fit value $\lambda = 0.2 - 0.3$ agrees with theoretical estimates based on next-to-leading order Balitskii-Fadin-Kuraev-Lipatov (BFKL) results [17, 18]. To show that the net-baryon distribution reflects the geometric scaling of the gluon distribution, we perform the following change of variables:

$$x \equiv x_1, \;\; x_2 \equiv x\; e^{-2y}, \;\; p_T^2 \equiv x^2 s\; e^{-2y}. \tag{3}$$

Thus, we rewrite Eq. (1) as

$$\frac{dN}{dy}(\tau) = \frac{C}{2\pi} \int_0^1 \frac{dx}{x}\; x q_v(x)\; \varphi(x^{2+\lambda} e^{\tau}), \tag{4}$$

where $\tau = \ln(s/Q_0^2) - \ln A^{1/3} - 2(1+\lambda)\, y$ is the corresponding scaling variable. Hence, the net-baryon multiplicity in the peak region is only a function of a single scaling variable τ, which relates the energy dependence to the rapidity and mass number dependence. In the fragmentation region, the valence quark distribution is only very weakly dependent on Q_f. From the equation for the isolines, $\tau = \text{const}$, one gets the evolution of the position of the fragmentation peak in the forward region with respect to the variables of the problem, $y_{\text{peak}} = 1/(1+\lambda)[(y_{\text{beam}} - \ln A^{1/6}] + \text{const}$, where $y_{\text{beam}} = 1/2 \cdot \ln[(E + p_L)/(E - p_L)] \simeq \ln\sqrt{s}/m_0$ is the beam rapidity at beam energy E and longitudinal momentum p_L with the nucleon mass m_0.

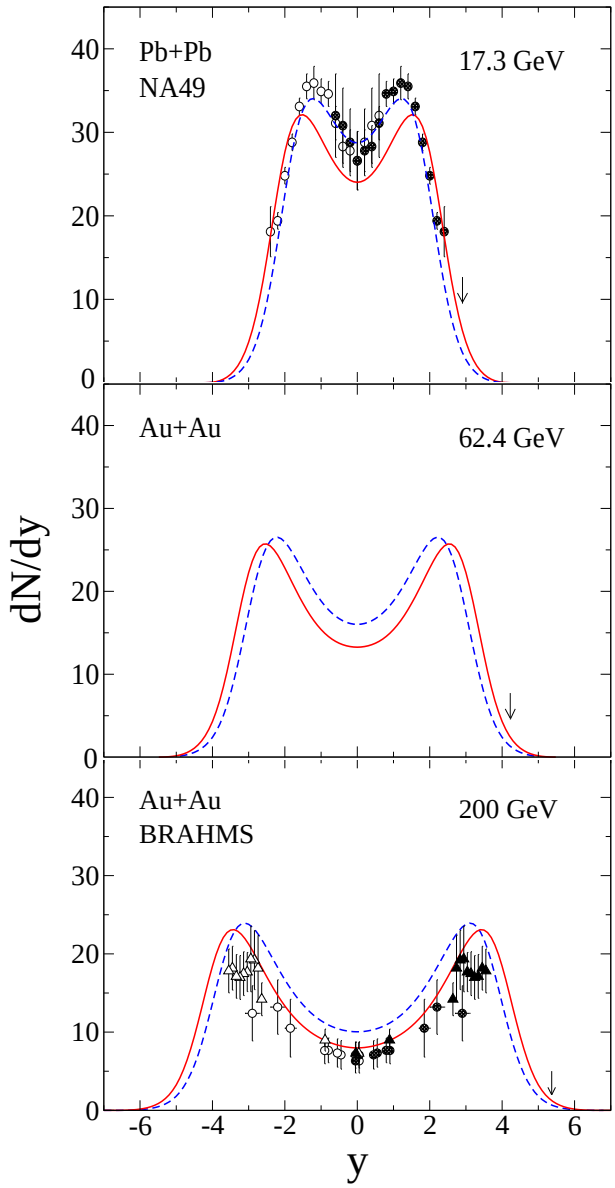


Fig. 1: Rapidity distribution of net protons in central (0 – 5%) Pb + Pb collisions at SPS energies of $\sqrt{s_{NN}}$ = 17.3 GeV (top frame). The theoretical results are compared with NA49 data [12]. Solid curves are for $Q_0^2 = 0.034$ GeV^2 and $\lambda = 0.288$, dashed curves are for $Q_0^2 = 0.068$ GeV^2, producing more stopping. At RHIC energies of $\sqrt{s_{NN}}$ = 62.4 GeV (middle frame) and 200 GeV (bottom frame) for central (0 - 5%) Au + Au, our corresponding theoretical results are shown, and compared with BRAHMS data at 200 GeV [1] (circles, 0 – 5%). Triangles are preliminary BRAHMS data points for 0 – 10% [19]. Arrows indicate the beam rapidities. From Y. Mehtar-Tani and G. Wolschin, arXiv:0811.1721 (2008).

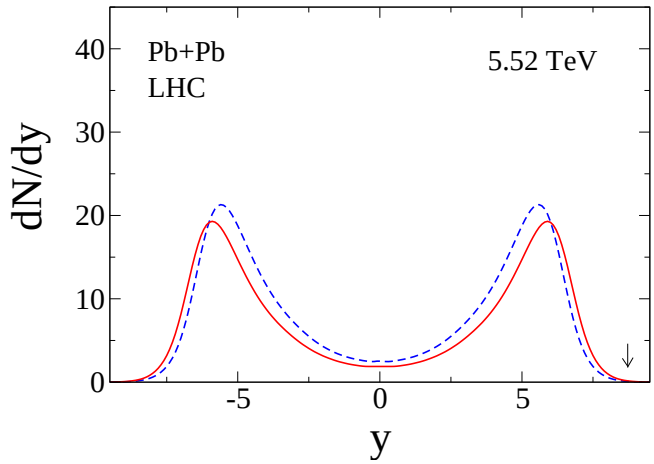


Fig. 2: Rapidity distribution of net protons in central Pb + Pb collisions at LHC energies of $\sqrt{s_{NN}}$ = 5.52 TeV. The theoretical distribution is shown for two values of the saturation scale as in Fig. 1.

To take into account saturation effects in the target we choose the Golec-Biernat-Wüsthoff model [20] for the forward dipole scattering amplitude $\mathcal{N}$. The valence quark parton distribution of the nucleus is taken to be equal to the valence quark PDF in a nucleon times the number of participants in the nucleus. We are focusing here on the forward rapidity region, and interpolate to mid-rapidity where small-x quarks are dominant, by matching the leading-order distributions and the Regge trajectory, $xq_v \propto x^{0.5}$, at $x = 0.01$ [3].

Our results for net-proton rapidity distributions in central Pb + Pb and Au + Au collisions are shown in Fig. 1. Solid curves are for $Q_0^2 = 0.034$ GeV^2 and $\lambda = 0.288$ [20]. Dashed curves are for twice the value of Q_0^2 producing slightly more stopping, as would also be the case for a larger value of A. These two values correspond to $Q_s^2 = 0.77$ GeV^2 and 1.54 GeV^2 at $x = 0.01$, respectively. We compare with SPS NA49 Pb + Pb data at $\sqrt{s_{NN}} = 17.3$ GeV [12], and BRAHMS Au + Au data at 200 GeV [1, 2]. Our prediction for central Pb + Pb at 5.52 TeV LHC energies is shown in Fig. 2, again for the above two values of the saturation scale. Here we have normalized the total yield to the number of proton participants, $N_p \simeq 140$ for both, central Au + Au and Pb + Pb. At LHC energies the mid-rapidity region is almost charge (baryon) free, and we obtain $dN/dy(y = 0) \simeq 1 - 3$ for net protons.

To summarize, we have presented a saturation model for net-baryon distributions that successfully describes net-proton rapidity distributions and their energy and mass dependence. The remarkable feature of geometric scaling predicted by the CGC is reflected in the net-baryon rapidity distribution, providing a direct test of saturation physics.

In particular, we have shown that the peak position in net-proton rapidity distributions of centrally colliding heavy ions at ultra-relativistic energies obeys a scaling law involving the mass number and the beam energy. Our result for the mean rapidity loss in $\sqrt{s_{NN}}$ = 200 GeV Au + Au [11] is significantly larger than the BRAHMS result, which contains an extrapolation to the unmeasured region. This emphasizes the importance of a detailed analysis at LHC energies.

This work has been supported by the Deutsche Forschungsgemeinschaft under Grant No. STA 509/1-1.

References

[1] I.G. Bearden *et al.* (BRAHMS Collaboration), Phys. Rev. Lett. **93**, 102301 (2004).

[2] H.H. Dalsgaard *et al.* (BRAHMS Collaboration), Int. J. Mod. Phys. E **16**, 1813 (2007).

[3] K. Itakura, Y.V. Kovchegov, L.D. McLerran, and D. Teaney, Nucl. Phys. **B730**, 160 (2004).

[4] J.L. Albacete, Y.V. Kovchegov, and K. Tuchin, Nucl. Phys. **A781**,122 (2007).

[5] L.V. Gribov, E.M. Levin, and M.G. Ryskin, Phys. Rep. **100**, 1 (1983); A.H. Mueller and J. Qiu, Nucl. Phys. **B268**, 427 (1986); J.P. Blaizot and A.H. Mueller, Nucl. Phys. **B289**, 847 (1987); L. McLerran and R. Venugopalan, Phys. Rev. D **49**, 2233 (1994).

[6] I. Balitsky, Nucl. Phys. **B463**, 99 (1996); Y.V. Kovchegov, Phys. Rev. D **60**, 034008 (1999).

[7] J. Jalilian-Marian, A. Kovner, A. Leonidov, and H. Weigert, Nucl. Phys. **B504**, 415 (1997); J. Jalilian-Marian, A. Kovner, and H. Weigert, Phys. Rev. D **59**, 014015 (1998); J. Jalilian-Marian, A. Kovner, A. Leonidov, and H. Weigert, Phys. Rev. D **59**, 034007 (1999); Erratum, 099903 (1999).

[8] E. Iancu, A. Leonidov, and L.D. McLerran, Nucl. Phys. **A692**, 583 (2001); Phys. Lett. B **510**, 133 (2001).

[9] D. Kharzeev, E. Levin, and M. Nardi, Nucl. Phys. **A730**, 448 (2004); Nucl. Phys. **A747**, 609 (2005).

[10] J.L. Albacete, Phys. Rev. Lett. **99**, 262301 (2007).

[11] Y. Mehtar-Tani and G. Wolschin, arXiv:0811.1721 (2008)

[12] H. Appelshäuser *et al.* (NA49 Collaboration), Phys. Rev. Lett. **82**, 2471 (1999).

[13] G. Wolschin, Eur. Phys. J. A **5**, 85 (1999); Europhys. Lett. **47**, 30 (1999); **74**, 29 (2006); Phys. Rev. C **69**, 024906 (2004); Prog. Part. Nucl. Phys. **59**, 374 (2007).

[14] G.C. Rossi and G. Veneziano, Phys. Rep. **63**, 153 (1980); D. Kharzeev, Phys. Lett. B **378**, 238 (1996); S.E. Vance, M. Gyulassy, and X.N. Wang, Phys. Lett. B **443**, 45 (1998).

[15] D. Kharzeev, Y.V. Kovchegov, and K. Tuchin, Phys. Lett. B **599**, 23 (2004); R. Baier, Y. Mehtar-Tani, and D. Schiff, Nucl. Phys. **A764**, 515 (2006); A. Dumitru, A. Hayashigaki, and J. Jalilian-Marian, Nucl. Phys. **A765**, 464 (2006).

[16] A. M. Staśto, K. Golec-Biernat, and J. Kwieciński, Phys. Rev. Lett. **86**, 596 (2001).

[17] L.N. Lipatov, Sov. J. Nucl. Phys. **23**, 338 (1976); E. A. Kuraev, L.N. Lipatov, and V.S. Fadin, Sov. Phys. JETP **45**, 199 (1977); I.I. Balitskii and L.N. Lipatov, Sov. J. Nucl. Phys. **28**, 822 (1978).

[18] D.N. Triantafyllopoulos, Nucl. Phys. **B648**, 293 (2003).

[19] R. Debbe *et al.* (BRAHMS Collaboration), J. Phys. G **35**, 104004 (2008).

[20] K. Golec-Biernat and M. Wüsthoff, Phys. Rev. D **59**, 014017 (1998).

[21] F. Videbaek and O. Hansen, Phys. Rev. C **52**, 2684 (1995); L. Ahle *et al.* (E802 Collaboration), Phys. Rev. C **60**, (1999) 064901. B.B. Back *et al.* (E917 Collaboration), Phys. Rev. Lett. **86**, 1970 (2001).

[22] A. Dumitru, L. Gerland, and M. Strikman, Phys. Rev. Lett. **90**, 092301 (2003).

Transport Coefficients for Non-Newtonian Fluids and Causal Dissipative Hydrodynamics

T. Kodama[†]*and T. Koide*
Instituto de Física, Universidade Federal do Rio de Janeiro, C. P. 68528, 21945-970, Rio de Janeiro, Brazil

DOI: http://dx.doi.org/10.3204/DESY-PROC-2009-01/93

Abstract
We discuss the roles of viscosity in relativistic fluid dynamics from the point of view of memory effects. We show that, depending on what quantity the memory effect is applied, different terms appear in higher order corrections. We generalize the application of the Green-Kubo-Nakano (GKN) to calculate transport coefficients when the memory effects are present.

1 Why should relativistic fluid be non-Newtonian?

The effect of dissipation in relativistic fluids is one of current topics in the physics of relativistic heavy-ion collisions [1]. Here, we discuss this problem focusing on the memory effect on irreversible current. First let us illustrate the basic idea of memory effect as the solution for the problem of relativistic hydrodynamics using the example of diffusion equation.

In the usual derivation of diffusion equation, we assume that the irreversible current $J(t)$ is simply proportional to the corresponding thermodynamic force $F(t)$,

$$J(t) = DF(t), \tag{1}$$

where D is a transport coefficient. The fluid with this current is referred to as a Newtonian fluid, and the evolution is described by, for example, the Navier-Stokes equation. However, exactly speaking, there should exist a time retardation effect (remember the linear response theory) and the expression (1) is justified only when there is a clear separation of microscopic and macroscopic scales. This assumption is obviously satisfied in fluids around us, where the velocity of molecules is around $10^2 - 10^3$ m/s but the speed of a fluid diffusion is much slower.

However, it is not clear if this is still true in relativistic fluids, because the fluid is accelerated up to the speed of light. Then it is natural to consider the retardation effect in the definition of relativistic irreversible currents,

$$J(t) = \int_{-\infty}^{t} G(t-s)F(s), \tag{2}$$

where $G(t)$ is a memory function which represents the retardation effect.

This is a natural extension of hydrodynamics to the relativistic region and, as a matter of fact, this extension is related to the problem of acausality. Let us consider a diffusion process [3].

[†] speaker

Then the thermodynamic force is given by the spatial derivative of a conserved density n and the linear relation (1) is called Fick's law. By substituting Fick's law into the equation of continuity, we obtain the diffusion equation. As is well known, the diffusion equation has a problem of infinite propagation speed. On the other hand, when we use Eq. (2) with a simple exponential memory function,

$$G(t) = \frac{D}{\tau_R} e^{-t/\tau_R}, \tag{3}$$

where τ_R is the relaxation time and D is the diffusion constant, we obtain a telegraph equation and then the maximum propagation speed is given by $\sqrt{D/\tau_R}$. It is also worth mentioning that what we can obtain from microscopic dynamics is not the diffusion equation but the telegraphic equation [3].

The same discussion is applicable to relativistic dissipative hydrodynamics [2]. In the relativistic Navier-Stokes (Landau-Lifshitz) equation, the viscous flows are defined by assuming Eq. (1). For example, in the bulk viscosity, the corresponding thermodynamic force is $\partial_\mu u^\mu$, where u^μ is the fluid velocity. Thus the bulk viscosity is given by

$$\Pi = -\eta \partial_\mu u^\mu. \tag{4}$$

On the other hand, in the hydrodynamics consistent with causality, it is given by

$$\pi(\tau) = \int_{-\infty}^{\tau} G(\tau - s) \partial_\mu u^\mu(s), \tag{5}$$

where τ is a proper time. As is shown in Ref. [4, 5], the propagation speed of signal exceeds the sped of light in the case of Eq. (4), and this acausality makes the hydrodynamic evolution unstable. On the other hand, causal dissipative hydrodynamics (5) is causal and stable. In this sense, it is impossible to solve the Landau-Lifshitz theory without using artificial tricks.

2 Memory Effects on Extensive Measures

Another important mechanism is the finite volume effect of fluid cells [6]. In the derivation of hydrodynamics, it is assumed that the local equilibrium is achieved in each fluid cell which has finite spatial extension. Then, the second law of thermodynamics and the memory effect should be applied on extensive measures associated with this finite volume. To introduce an extensive measure for the density of an additive quantity, let us consider a fluid cell of proper volume V. Due to the fluid flow, this volume changes in time and its time rate of change is given by

$$\frac{1}{V}\frac{dV}{dt} = \nabla \cdot \vec{v},$$

where $\vec{v}$ is the fluid velocity field. This equation can be written in a covariant form as

$$\partial_\mu (\sigma(\mathbf{r}, t) u^\mu(\mathbf{r}, t)) = 0, \tag{6}$$

where $\sigma(\mathbf{r}, t)$ is the inverse of the volume of the fluid cell at $\mathbf{r}$, and u^μ is the fluid velocity. Then the irreversible current is given by

$$\frac{J(t)}{\sigma(t)} = \int_{t_0}^{t} ds G(t - s) \frac{F(s)}{\sigma(s)} \tag{7}$$

This is equivalent to the solution of the following differential equation,

$$\tau_R \frac{d}{dt} J(t) + J(t) = DF(t) - \tau_R J(t) \partial_\mu u^\mu(t). \tag{8}$$

Noted that this result does not depend on the choice of the volume of the fluid cell $\sigma(t)$.

The last non-linear term is important not only for the physical concept but also for stability of relativistic fluids. There are two different instabilities in relativistic dissipative hydrodynamics. One is the instability induced by acausality. It is sometimes claimed that the problems of acausality and instability are not correlated and the relativistic Navier-Stokes equation is still available when we carefully remove unphysical signals caused by acausality. However, as is shown in Ref. [5], the instability of relativistic fluids is induced by acausality. Thus, the causal dissipative hydrodynamics will be a more appropriate theory to describe relativistic fluids.

The other instability appears in ultra-relativistic phenomena. In such an extreme situation, the bulk viscosity becomes very small and we can analytically show that the causal dissipative hydrodynamics is instable for such a small bulk viscosity. On the other hand, this instability is solved by considering the non-linear term, because the non-linear term prevents the bulk viscosity to have very small values and the minimum is given by [6]

$$\Pi_{min} = -\frac{\zeta}{\tau_R}, \tag{9}$$

where ζ is the bulk viscosity coefficient and τ_R is the corresponding relaxation time. Thus the causal dissipative hydrodynamics with finite size effect is stable even for ultra-relativistic phenomena. Another important fact is that, the so-called full Israel-Stewart theory can also be expressed in terms of a memory function, but in this case, a very peculiar form of thermodynamical quantity should be taken to apply the memory effect [6].

In Fig. 1, we show the shock formation with an initial velocity $\gamma = 5$. As is shown in the left panel, in this ultra-relativistic initial condition, the causal dissipative hydrodynamics without the finite size effect becomes unstable. On the other hand, if the finite size effect is taken into account, the instability disappears.

A very different scenario where relativistic fluid dynamics can be applied is found in astrophysics. The speed of flow becomes $\gamma \sim 100$ in the Gamma-raybursts. Thus, the construction of the dissipative hydrodynamics applicable to such an extreme situation is important for some astrophysical processes, too.

3 GKN formula: applicable to non-Newtonian fluids ?

As we have shown, it is more natural to consider that the relativistic fluid is a non-Newtonian fluid. It means that we cannot use various techniques which are known to analyse the Newtonian fluids. The Green-Kubo-Nakano (GKN) formula is one of them. The GKN formula has been used to calculate the viscosity coefficients and the heat conductivity of relativistic fluids. However, it should be noted that the assumption of Newtonian fluids is implicitly used in the derivation of the expressions. Thus the usual GKN formula is not applicable for calculation of relativistic fluids.

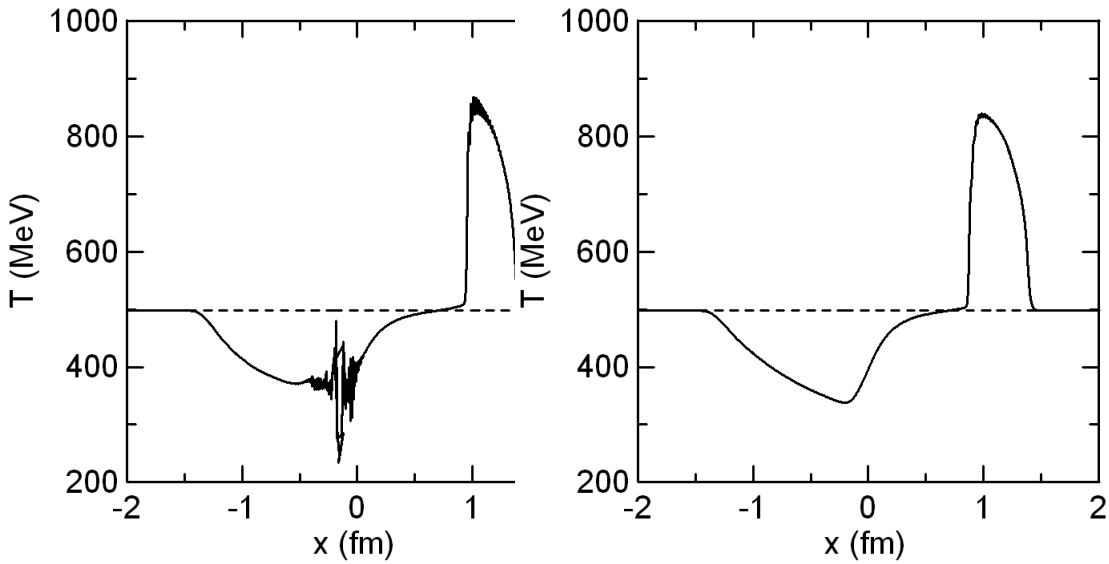


Fig. 1: The temperature in the shock formation calculated without the finite size effect (left) and with the finite size effect (right), starting from the homogeneous initial condition (dotted line) [6].

To show this, we consider the system whose Hamiltonian is given by H. By applying an external force, the total Hamiltonian is changed from H to $H + H_{ex}(t)$, with

$$H_{ex}(t) = -AF(t), \tag{10}$$

where A is an operator and $F(t)$ is the c-number external force.

We consider the current J induced by the external force. From the linear response theory, we obtain

$$\langle J \rangle = \int_{-\infty}^{t} ds \Psi(t-s) F(s), \tag{11}$$

where the response function is given by

$$\Psi(t) = \int_{0}^{\beta} d\lambda \langle \dot{A}(-i\lambda) J(t) \rangle_{eq}, \tag{12}$$

where β is the inverse of temperature. This is the exact result in the sense of the linear approximation. This formula is one of the expressions of the GKN formula. However, in particular, when we define transport coefficients of hydrodynamics, we do not use this expression.

In deriving the GKN formula for hydrodynamic transport coefficients, we assume a linear relation between currents and the external force, $J(t) = D_{GKN} F(t)$ with the transport coefficient D_{GKN}. One can easily see that this is nothing but the assumption of Newtonian fluids. And the formula to calculate this D_{GKN} is usually called the GKN formula of the shear viscosity, the bulk viscosity, heat conduction and so on. To derive the expression, we have to ignore the memory effect (time-convolution integral) in Eq. (11),

$$\langle J \rangle \approx \int_{0}^{\infty} ds \Psi(s) F(t). \tag{13}$$

Then the GKN formula is

$$D_{GKN} = \int_0^\infty ds \Psi(s). \tag{14}$$

In the shear viscosity, this is given by the time correlation function of the energy-momentum tensor.

In principle, we can derive the formula for non-Newtonian transport coefficients by assuming Eq. (8) instead of Eq. (1). From the exact result (11), we can derive the following equation,

$$\partial_t J(t) = \Psi(0) F(t) + \int_0^\infty ds \partial_s \Psi(s) F(t). \tag{15}$$

In the second term, we ignore the time-convolution integral. We further assume the usual GKN formula to reexpress the first term. Then we finally obtain

$$\partial_t J(t) = \frac{\Psi(0)}{D_{GKN}} J(t) + \int_0^\infty ds \partial_s \Psi(s) F(t). \tag{16}$$

By comparing this equation with Eq. (8) ignoring the non-linear term, we can derive the expressions for D and τ_R.

Exactly speaking, the shear viscosity is induced not by the external force but by the difference of the boundary conditions. Actually, the GKN formula of the shear viscosity is derived by using the nonequilibrium statistical operator method proposed by Zubarev. Thus the discussion that we developed here is not applicable to the problems discussed in this paper. The exact expression of the non-Newtonian transport coefficients are given in [7, 8].

We have investigated the viscous fluid dynamics emphasizing the memory effect. When a fluid posesses a non-Newtonian behavior, the use of GKN formula should be cautious.

References

[1] See for example, M. Luzum, P. Romatschke, Phys.Rev.C78, 034915, 2008; R. Baier, P. Romatschke, D. T. Son, A. O. Starinets and A. Stephanov, JHEP 0804, 100, 2008; P. Romatschke and U. Romatschke, Phys.Rev.Lett. 99, 172301, 2007; U. W. Heinz and Huichao Song, J.Phys.G35, 104126, 2008; T. Hirano, U.W. Heinz, D. Kharzeev, R. Lacey and Y. Nara, J.Phys. G35, 104124, 2008.

[2] T. Koide, G. S. Denicol, Ph. Mota, and T. Kodama, Phys. Rev. **C75**, 034909 (2007) .

[3] T. Koide, Phys. Rev. E**72**, 026135 (2005).

[4] G. S. Denicol, T. Koide, T. Kodama and Ph. Mota, Phys. Rev. **C78**, 034901 (2008).

[5] G. S. Denicol, T. Koide, T. Kodama and Ph. Mota, J. Phys. **G35** 115102 (2008).

[6] G. S. Denicol, T. Koide, T. Kodama and Ph. Mota, arXiv:0808.3170.

[7] T. Koide, Phys. Rev. E**75**, 060103(R) (2007).

[8] T. Koide and T. Kodama, Phys. Rev. E **78**, 051107 (2008).

Study of extremely high multiplicity events in the SVD-2 experiment

E. Kokoulina[1]†, *A. Kutov*[2] *and V. Ryadovikov*[3]
[1]JINR, Dubna, Russia and GSTU, Gomel, Belarus
[2]DM UrD RAS, Syktyvkar, Russia
[3]IHEP, Protvino, Russia

DOI: http://dx.doi.org/10.3204/DESY-PROC-2009-01/97

Abstract
The observation of hadronic and nuclear interactions producing high charged multiplicity events is presented. These events may be the manifestation of such collective phenomena as Bose-Einstein condensation, Cherenkov gluon radiation, clusterization and abundant soft photon yield. The status of "Thermalization" project at U-70 accelerator (IHEP, Protvino) is reported. The purpose of this project is to search for new phenomena leading to final states with extremely high multiplicity.

1 Introduction

This report is devoted to the study of events with extreme multiplicity (ExMu) [1]. We define those as an event sample with the number of secondary particles considerably bigger than mean multiplicity [2]. Such events occur very rarely and their registration is highly non-trivial task. Every advance requires significant increase of total statistics. Modern theoretical models and Monte Carlo event generators do not describe the existing experimental data in this region. We think this area is unknown to most of the researches.

SVD Collaboration carries out experimental study of ExMu at the accelerator U-70 of IHEP (Protvino, Russia) at $P_{\rm lab} = 50 - 70$ GeV. This experiment is unique, because the average charged multiplicity at these energies is about 5-6 and the apparatus can register almost all secondaries.

Here I would like to mention Pavel Ermolov who was an active leader of our program. He died this year. He was known at DESY as well, as a member of ZEUS Collaboration.

2 Status of the "Thermalization" project

SVD setup (Spectrometer with Vertex Detector) [3] consists of the following basic components: the hydrogen target, microstrip silicon vertex detector (MSVD), the drift tube tracker (DTT), the magnetic spectrometer equipped with the proportional chambers, the Cherenkov counter and electromagnetic calorimeter. To register the events with high multiplicity we have designed and constructed the scintillator hodoscope. It generates the trigger signal for events with the number of secondaries exceeding given level of multiplicity.

MSVD consists of 10 silicon planes with $50\ \mu m$ strip sensors. The planes have four different angular orientations: 0, $\pi/2$ and $\pm 10.5^{\circ}$. Hence we distinguish coordinates x, y, u

† speaker

(+10.5°) and v (-10.5°), respectively. The size of each plane is about $50 \times 50\ mm^2$. There were no oblique planes in 2006 run. In the year 2007 only one oblique plane has been added. It is necessary to have at least two such planes to disentangle tracks in space. This will be available in the next run. The MSVD has limited acceptance and does not allow to register all the secondaries. Therefore we have constructed also the drift tube tracker. It is located between MSVD and the magnetic spectrometer. DDT consists of three modules, each having three planes oriented under the following angles: +10.5° (u-plane), 0° (y-plane), -10.5° (v-plane). Each plane consists of two layers of the 6 mm diameter drift tubes. The length of the middle drift chamber is about 1 m.

The magnetic spectrometer consists of 16 proportional chambers located inside the magnet. It provides the momentum resolution of 1.5 % in the range from 300 MeV/c to 5 GeV/c. The electromagnetic calorimeter, or gamma detector, (DeGa) consists of 1536 full absorption Cherenkov counters. Their lead glass radiators have the volume $38 \times 38 \times 505\ mm^3$ and are read out by the photomultipliers PMT-84-3.

The prime purpose of the scintillator hodoscope is to provide selective recording of interesting events, i.e. to serve as high multiplicity trigger (HMT). It consists of 19 elements called "petals of camomile". They collect light and produce the trigger signal when the number of charged secondaries exceeds given fixed level. An example of the work of this trigger is given in Fig. 1 at different levels of HMT. It illustrates that indeed we can select high multiplicity events and suppress low multiplicity ones at high level of HMT.

An important task is the alignment procedure. It is vital to provide the correct geometry of complete setup for efficient track reconstruction in space and to achieve necessary precision in determination of track parameters. For these purposes we have developed the software package based on the ideas of Millepede program of V. Blobel [4] to determine both linear and nonlinear parameters in our alignment procedure.

Detector simulation is based on GEANT-3, while the Pyhia and other Monte Carlo programs are used as event generators.

Due to economical reasons the energy of proton beam was reduced from 70 GeV in year 2002 down to 50 GeV in the later runs. At the end of 2008 we plan data taking run with fully equipped detector to collect sufficient statistics for ExMu studies, and then continue the search for collective phenomena in this area. So far we already have reconstructed events with charged multiplicity higher than those obtained with the bubble chamber (more than 18 charged particles). The addition of two silicon oblique planes in MSVD will allow us to disentangle tracks in space and to obtain their multiplicity distribution (MD).

The DTT data processing is ongoing. We performed the calibration of every tube, i.e., determined the radial position as a function of drift time (Fig. 2, left). The resolution of DTT was detemined by using the sum of radii ($r_f + r_b$) of two neighboring tubes from forward and backward layers of the plane (Fig. 2, right). Presently we are developping the algorithms for the track reconstruction in DTT.

Our preliminary data from electromagnetic calorimeter allow to obtain the dependence of the mean multiplicity for neutral particles (γ and π^0) versus charged particle multiplicity. We observe significant correlation between these spieces. In the ExMu sample this dependence has tendency to grow.

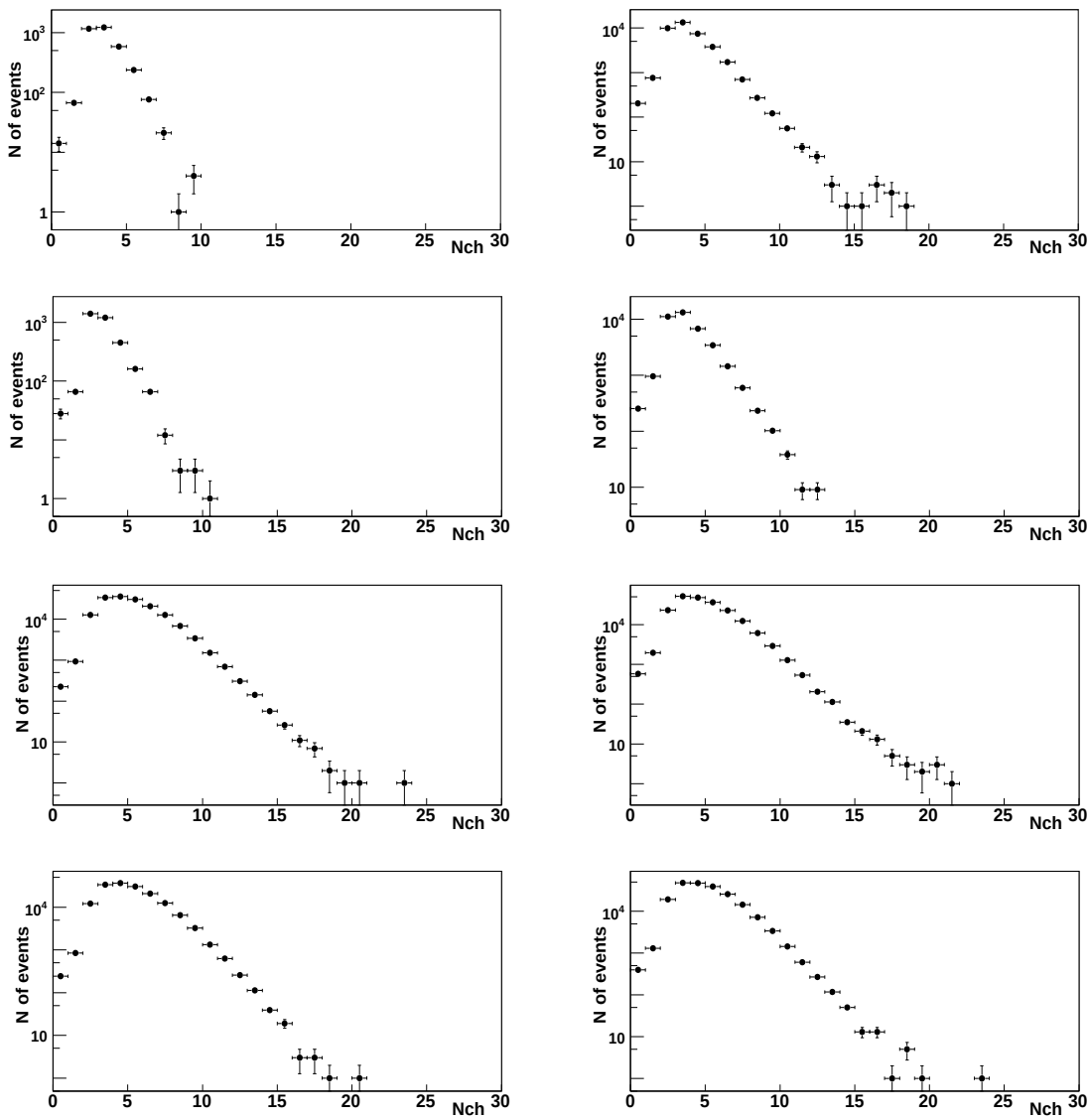


Fig. 1: MD at trigger-level 2, 4, 6 and 7 (from top to bottom). In the projections: (left) *XOZ* plane and (right)*YOZ* plane.

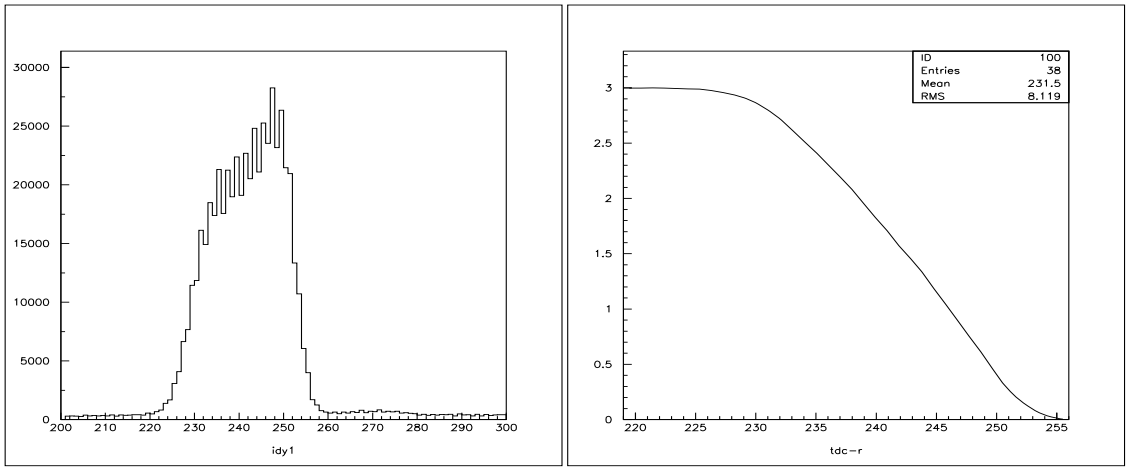


Fig. 2: Drift time distribution (left) and calibration function for drift tube (right).

3 Achievements and outlook of the ExMu studies

Our physical program is directed to the search for collective phenomena in ExMu area. At the beginning of this study we have analyzed the existing experimental and theoretical results on MD in hadronic and nuclear interactions. We have found that Monte Carlo event generators underestimate MD at 16 charged particles by about two orders of magnitude. Phenomenological models differ considerably in this region [5, 6]. To explain ExMu phenomenon we have developed the gluon dominance model (GDM) [6–8]. It is based on the main features of QCD and supplemented with phenomenological mechanism of hadronization. It states the dominant role of gluons in multiparticle production mechanism, while the valence quarks remain relatively passive. The behavior of the hadronization parameters points to this important conclusion. GDM confirms convincingly the recombination mechanism of hadronization in hadronic and nuclear interactions and fragmentation in lepton processes. We have shown [9] that with small modification the GDM is able to describe MD in $p\bar{p}$ annihilation. It also describes well MD in pp interactions from IHEP energies up to ISR and higher. Within the model two-shoulder structure of MD is explained by evaporation followed by hadronization of gluon groups, or clans consisted of single, double or more fission gluons. This can explain the nature of soft and semi-hard components in multiparticle production. We obtained the limits on the maximal observable number of charged and neutral particles at 70 GeV.

In the last years when RHIC data became available the multiparticle production mechanism was significantly revised. The CGC theory was developed and relativistic nuclear physics have got new concept. Our GDM agrees with this theory and helps to understand the nature of strong interactions.

The basic collective phenomena which we study in our project are: (1) Bose-Einstein condensation (BEC) of pions. (2) The ring events (the analogy of Cherenkov radiation). (3) The excess of soft photon yield. (4) The clusterization. (5) The turbulence phenomena.

The possibility of BEC formation in ExMu region has been demonstrated by Begun and Gorenstein [11] in the framework of the ideal hadron Bose-gas model. The pions (charged and

neutral) are copiously produced at 70 GeV. They are spin zero bosons. In ExMu events their momenta are approaching to zero. Hence the BEC may be formed. The fluctuation in the number of pions will be a prominent signal in the BEC-point. As temperature of the system decreases, the chemical potential is increasing at fixed particle number density, and become zero at $T = T_0$ (BEC-temperature). In this point pions reach its lower state. Authors predict that the scaled variance of neutral and charged pion-number fluctuations, $\omega^0 = \langle(\Delta N)^2\rangle/\langle N\rangle$, in the vicinity of BEC-line have an abrupt and anomalous increase. Our apparatus allows to check this prediction experimentally.

The ring-like structures in the angular distributions of secondaries have been observed in some nuclear collision experiments close to our energies [12]. Our preliminary data analysis shows the presence of two peaks in pseudorapidity distribution for ExMu events ($n_{ch} > 18$) in pA - interactions (A = Si, C, Pb) [3, 10]. In the inclusive sample these peaks are absent. This is an indication for the appearance of the ring events at ExMu.

The puzzle of soft photons is also part of our investigation program. In GDM we estimated the size of the emission region of soft photons. It is about $4 - 6$ fm [13]. In this region hadronization process is finished and the kinematical freeze-out is realized.

By visual scanning of ExMu events we have seen few groups of particles which fly under small angles (points to clusterization). An interesting hypothesis has been proposed by V. Nikitin [14] to explain this observation. His idea is that the turbulence phenomena may occur in hadron-nuclear interactions which could lead to groups of particles lying in one plane in ExMu events. We believe the realization of our scientific program will be successful and unique for multiparticle dynamics study.

Author (E.K.) would like to thank the ISMD 2008 Organizing Committee for the financial support and for the fruitful working atmosphere at the Symposium. These investigations have been partially supported by RFBR grant $08 - 02 - 90028 - Bel_a$.

References

[1] V. Avdeichikov *et al.*, Proposal *"Termalization"*. JINR-P1-2004-190, 45pp (2005).

[2] SVD Collaboration, A. Aleev *et al.*, in Proceedings of the 13th Annual Seminar "NPCS", Minsk, 83 (2006).

[3] E.S. Kokoulina and A.Ya. Kutov, Phys.At.Nucl. **71**, 1543 (2008).

[4] V. Blobel. Linear Least Squares Fits with a Large Number of Parameter. Version 0.999 - 17.10 2000. Institut fur experimentalphysik.Universitet Hamburg. 22pp. (2000) .

[5] O.G. Chikilev, P.V. Chliapnikov. Jad. Phys. (Rus), **55**, 820 (1992).

[6] E. S. Kokoulina, Acta Phys.Polon. **B35**, 295 (2004).

[7] E.S. Kokoulina and V.A. Nikitin. Proc. 17th ISHEPP, JINR, Dubna, 319 (2005) .

[8] P.F. Ermolov et al. Proc. 17th ISHEPP, JINR, Dubna, 327 (2005).

[9] E. S. Kokoulina, AIP Conf. Proc. **828**, 81 (2006).

[10] E. Kokoulina, A. Kutov and V. Nikitin, Braz. J. Phys. **37**, 785 (2007).

[11] V. V. Begun and M. I. Gorenstein, Phys. Lett. **B653**, 190 (2007).

[12] I.M. Dremin Eur.Phys.J. **C56**, 81 (2008).

[13] M.K. Volkov, E.S. Kokoulina and E.A. Kuraev. Phys.Part.Nucl.Lett. **1**, 235 (2004).

[14] V. Nikitin, private communications (2008).

Soft photon production in matter in two particle green's function consideration

A.V.Koshelkin
Moscow Institute for Physics and Engineering,
DOI: http://dx.doi.org/10.3204/DESY-PROC-2009-01/99

Abstract
The production of soft photons in dense matter is studied in terms of the two-particle Green's function in a non-equilibrium medium. The rate of photons is calculated and studied in detail.

1 Introduction

Production of soft photons in matter is studied in the context of the formalism of two-particle Green' functions in a non-equilibrium medium. The exact expression for such functions which determines completely the spectrum of soft photons in matter is derived in the diffusive approximation. On a basis of the calculated two-particle Green's functions the photon rate in equilibrium matter is obtained. The contribution of the bremsstrahlung, two-to-two particle process as well as inelastic pair annihilation is taken into account in the derived rate in the whole region of the emission spectrum of the soft photons which includes the :andau-Pomeranchu-Migdal (LPM) [1, 2] effect range. It is shown that the consistent consideration of both the elastic and inelastic collisions of in-matter particles leads to the additional suppression of the rate of photons as compared with the results obtained earlier in studying the Landau-Pomeranchuk effect [2]. The rate of soft photons from an equilibrium hot quark-gluon plasma is studied in detail. It is shown that the rate is suppressed along all range of the energies of soft photons due to multi-particle interaction between particles in the matter. In this way, the spectral distribution of the emitted photons has a maximum which shifts to the short-wave region of the spectrum with increasing temperature of the matter.

2 Two-particle Green's functions and photon production in the matter

The probability of photon production by the current j^ν is given by the following expression:

$$d^4w = \frac{4\pi}{\omega(k)} e_\mu e^*_\nu (1+n_\gamma) \int d^4x_1 d^4x_2 \exp\left(-ik(x_2-x_1)\right) \langle j^{\mu+}(x_2) j^\nu(x_1)\rangle \frac{d^3k}{(2\pi)^3} \tag{1}$$

where $k=(\omega,\vec{k})$ and e_α are the 4-vector of momentum and the polarization vector of a photon; n_γ is the occupancy number of photon states; $j^\nu(x)$ is the current of the particles generating photons. The angle brackets mean averaging over some state of the particles in matter; x are 4-coordinates. In the absence of a photon "bath" we have $n_\gamma = 0$.

When the energy of produced photons is not too large, so that the emission of them can not change the state of the matter, the bilinear combination of the currents in the last equation can be written as follows :

$$\langle j^{\mu+}(x_2)j^{\nu}(x_1)\rangle = \alpha_E \cdot \langle i|\Big(\hat{O}^{\mu}\Big)_{\alpha,\beta}\Big((\hat{O}^{\dagger})^{\nu}\Big)_{\gamma,\delta}|j\rangle\langle\Psi^{\dagger}{}_{\gamma}(x_2)\Psi_{\delta}(x_2)\Psi_{\alpha}(x_1)\Psi^{\dagger}{}_{\beta}(x_1)\rangle, \tag{2}$$

where $\langle i|\Big(\hat{O}^{\mu}\Big)_{\alpha,\beta}\Big((\hat{O}^{\dagger})^{\nu}\Big)_{\gamma,\delta}|j\rangle$ is the matrix element of some operator which is independent on 4-coordinates, $\Psi_{\alpha}(x)$ are the psi-operators in the Heisenberg picture; $\alpha,\beta,\gamma,\delta$ are the spin variables; α_E is the fine structure constant.

Thus, the problem of the calculation of the photon rate in matter is reduced to obtaining the two-particle Green's function since it is proportional to the product of four Ψ-functions.

We assume that the matter is such that the in-matter particles are ultrarelativistic ones and their spins are equal to $1/2$. Then, the influence of scattering in the matter on the spin states of the particles is negligible [1, 2]. Expanding the correlator $\langle\Psi^{\dagger}{}_{\gamma}(x_2)\Psi_{\delta}(x_2)\Psi_{\alpha}(x_1)\Psi^{\dagger}{}_{\beta}(x_1)\rangle$ over the whole set of plane waves, we can write the expression for the probability of photon production dW per unit volume as follows (see Eqs.(1)-(3)):

$$\begin{aligned} d^4W = \overline{d^4w} \;\; = \;\; & \frac{4\pi\alpha_E}{\omega(k)}\frac{d^3k}{(2\pi)^3}\Bigg\{\frac{(1+n_{\gamma})}{2}\cdot \\ & \int\frac{d^4p_1d^4p_2d^4p_3d^4p_4}{(2\pi)^8}\delta^4(p_2-p_1-k)\cdot\delta^4(p_3-p_4-k) \\ & Tr\Bigg[e_{\mu}e_{\nu}\Big\langle\overline{u}^{\beta}(p_2)\overline{u}^{\gamma}(p_3)\Big|\Big(\hat{O}^{\mu}\Big)_{\alpha,\beta}\Big((\hat{O}^{\dagger})^{\nu}\Big)_{\gamma,\delta}\Big|u^{\alpha}(p_1)u^{\delta}(p_4)\Big\rangle \\ & \cdot K^{-+,-+}_{\alpha\gamma,\beta\delta}(p_1;p_2|p_3;p_4)\Bigg], \end{aligned} \tag{3}$$

where $p_i=(p_i^0,\vec{p}_i)$ are the 4-momentum of the radiating particle, s is its spin, $u^{\alpha}(p)$ are the Dirac spinors. The line over d^4w means the averaging and summing over the corresponding spin states of the particles in the matter. In the case of the generation of photons by fermions with the spin $s=1/2$ the operator $\hat{O}^{\nu}$ is the corresponding Dirac matrix.

The function $K^{-+,-+}_{\alpha\gamma,\beta\delta}(p_1;p_2|p_3;p_4)$ is the so-called time-unordered two-particle Green's function $K(1(-),2(-)|3(+),4(+))$ in the momentum representation. Thus, the problem of the calculation of the photon production in matter is reduced to obtaining the non-chronological (time-unordered) two-point Green's functions $K(p_1(-);p_4(-)|p_3(+);p_2(+))$ [3].

3 Two-particle Green's functions in non-equilibrium matter in the diffusive approximation

According to [3] the Green's function $K^{ac,bd}_{\alpha\gamma,\beta\delta}(p_1;p_2|p_3;p_4)$ satisfies the Bethe-Salpeter-like equation which has the following form in the momentum representation ($\hbar=c=1$) in the case of the Fermi statistics:

$$
\begin{aligned}
K^{ac,bd}_{\alpha\gamma,\beta\delta}(p_1;p_2|p_3;p_4) &= (2\pi)^4\Bigg\{G^{ac}_{\alpha\gamma}(p_1)G^{bd}_{\beta\delta}(p_2)\delta(p_1-p_3)- \\
&\quad G^{ac}_{\alpha\delta}(p_1)G^{bd}_{\beta\gamma}(p_2)\delta(p_1-p_4)\Bigg\}-\Bigg\{G^{aa_1}_{\alpha\alpha_1}(p_1)G^{bb_1}_{\beta\beta_1}(p_2) \\
&\quad \int dq\Gamma^{a_1a_2,b_1b_2}_{\alpha_1\alpha_2,\beta_1\beta_2}(p_1;p_2,|p_1-q;p_2-q)\cdot \\
&\quad K^{a_2c,b_2d}_{\alpha_2\gamma,\beta_2\delta}(p_1-q,;p_2-q|p_3;p_4)\Bigg\}.
\end{aligned}
\tag{4}
$$

where the Roman letters are minus or plus sign, the Greek letters mean spin variables; where $\Gamma^{\cdots}_{\cdots}(...)$ is the exact two-particle vertex function consisting of all diagrams that can not be cut by a vertical line so that this line only intersects two lines which correspond to the exact or free one-particle Green's functions; $G^{ab}_{\alpha\beta}(p_1=p_3)$ is the exact 2-point Green's function in the momentum representation [4].

In the diffusive approximation the last equation is reduced to the corresponding differential equation which can be solved in the small angle approach with respect to elastic scattering of particles in matter.

When small angle scattering occurs it is convenient to introduce the angle vectors $\vec{\eta}$ and $\vec{\theta}$ [1, 2] which are connected with the velocity $\vec{v}$ of a particle and the wave vector of a photon $\vec{k}$ by means of the formulae:

$$
\begin{aligned}
\vec{v} &= \vec{v}_0\left(1-\frac{\vec{\eta}^2}{2}\right)+v_0\vec{\eta}; \qquad \vec{v}_0\perp\vec{\eta}; \qquad |\vec{\eta}|\ll 1 \\
\vec{k} &= \frac{k\vec{v}_0}{v_0}\left(1-\frac{\vec{\theta}^2}{2}\right)+v_0\vec{\theta}; \qquad \vec{v}_0\perp\vec{\theta}; \qquad |\vec{\theta}|\ll 1,
\end{aligned}
\tag{5}
$$

Then, the solution of the equation for the unordered two-particle Green's function in the momentum representation can expressed by the following formulae:

$$
\begin{aligned}
&K^{-+,-+}_{\alpha\gamma,\beta\delta}(p\,;p-k|p';p'-k)= \\
&(2\pi)^4\int d^2\vec{\zeta}\Bigg\{\delta_{\alpha\gamma}\delta_{\beta\delta}\cdot\delta(p-p')\cdot\delta\left(p^0-E(p)+\mu\right)\cdot F(p\,,p',\vec{\eta},\vec{\zeta}) \\
&\frac{\Gamma\cdot\left[n(p^0)\cdot\theta(p^0)+\left(1-n(p^0)\right)\cdot\theta(-p^0)\right]\cdot\left[\left(1-n(p^0)\right)\cdot\theta(p^0)+n(p^0)\cdot\theta(-p^0)\right]\delta\left(\vec{\eta}\right)}{\left(\Gamma^2+\left(E(p)-E(p-k)-\omega\right)\right)^2}\Bigg\},
\end{aligned}
$$

where $F(p\,,p',\vec{\eta},\vec{\zeta})$ is equal to:

$$F(p\,,p',\vec{\eta},\vec{\zeta}) = \frac{a}{\pi < \theta_s^2 >} \int\limits_0^{+\infty} \frac{d\tau}{\sinh(a\tau)} \exp\Bigg\{ -\frac{a\cdot\left(\vec{\eta}-\vec{\zeta}\right)^2}{< \theta_s^2 > \coth(a\tau)} + \tag{6}$$

$$\frac{2a}{q}\left(\vec{\eta}-\vec{\zeta}\right)\cdot\left(\vec{\theta}-\vec{\zeta}\right)\tanh\left(\frac{a\tau}{2}\right) - \frac{2a}{q}\left(\vec{\theta}-\vec{\zeta}\right)^2\tanh\left(\frac{a\tau}{2}\right) - \imath\Omega\tau(1-v)\Bigg\}\cdot\delta\left(\vec{\zeta}\right),$$

where Γ is the width with respect to inelastic processes.

Substituting Eqs.(6), (7) into the formulae (3) and carrying out the needed integrations, we derive the probability of the photon production in the absence of the photon "bath" ($n_\gamma = 0$):

$$\begin{aligned}\frac{dW}{d\omega} &= \frac{\alpha_E}{\pi}\int\frac{d^3\vec{p}}{(2\pi)^3}\cdot\int\limits_0^{+\infty}dz\exp\left(-\frac{z\left(\omega/ < \theta_s^2 >\right)^{1/2}}{2\gamma^2}\right)\cdot\Bigg\{\sin\left(\frac{z\left(\omega/ < \theta_s^2 >\right)^{1/2}}{2\gamma^2}\right)\\ &\cdot\coth(z) - \frac{1}{z}\Bigg\}\cdot\frac{\Gamma\cdot[n(E(p))\cdot\theta(E(p)) + (1-n(E(p)))\cdot\theta(-E(p))]}{\gamma^2\pi\left(\Gamma^2 + (E(p)-E(p-k)-\omega)\right)^2}\\ &[(1-n(E(p-k)))\cdot\theta(E(p-k)) + n(E(p-k))\cdot\theta(-E(p-k))]\end{aligned} \tag{7}$$

where $\gamma = E/M$ is the Lorenz-factor of the particle; $E(\vec{p})$ is the energy of a particle, M is its mass.

The products of the first and last terms in the square brackets in Eq.(8) are the contribution to the probability of photon production due to the particle-particle and antiparticle-antiparticle bremsstrahlung in matter. The products of the other terms in the square bracket results in the photon production via the annihilation of off-shell particles and antiparticles and on-shell antiparticles and particles, respectively.

4 Photon production in a hot equilibrium quark-gluon plasma

We illustrate the applicability of the developed method of the calculation of the photon rate in matter and consider a hot quark-gluon plasma. We assume that the plasma is in equilibrium at temperature $T \geq 300MeV$ and consists of light quarks mainly. In this case the quarks are ultrarelativistic ones, and they are scattered on small angles. The small angle elastic scattering in a hot quark-gluon plasma can be described by the t-channel-exchange diagrams [5]. In this case the mean square of the angle per unit path length is $< \theta_s^2 >= 8.5\cdot L_c\cdot {\alpha_s}^2\cdot\frac{T^3}{p^2}$ [5], where L_c is the Coulomb logarithm depending on ${\alpha_s}^2; T$ and p. Owing to the logarithm we set L_c as the constant of the order of unit.

Taking into account the flavor degeneracy in Eq.(8) we derive the following for the energy being escaped from the quark-gluon plasma via the photon emitted by the light quarks:

$$\frac{d\varepsilon}{d\omega} = 2\frac{\omega\cdot W}{d\omega} \tag{8}$$

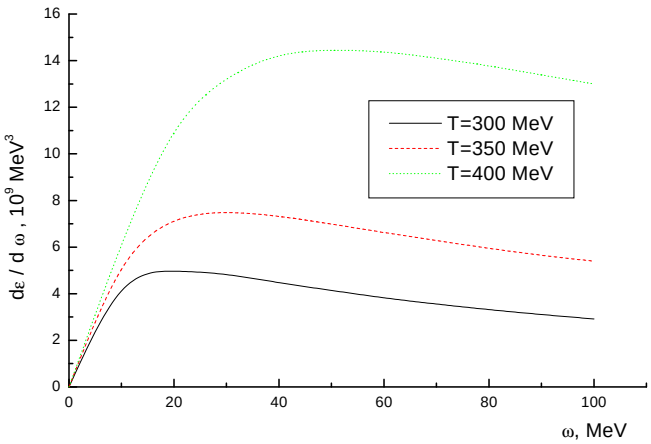


Fig. 1: Dependence of emission energy on the energy of photons at the fixed matter temperature.

The results of the numerical calculation of the photon rate according to Eq.(9) are presented in Figs.1. It follows from Figs.1. that the emission energy increases with increasing the temperature of the matter at any fixed frequency. In this way, the maximum of the spectral distribution of the emission energy shifts to the short wave range of the spectrum with increasing the temperature of the medium.

5 Conclusion

The photon production in matter in terms of the two-particles Green's functions in non-equilibrium matter is considered in the paper. The developed method of the calculation of photon rate allows us to take properly into account the contribution of all mechanism of forming the emission spectrum such as the particle (antiparticle) and antiparticle (particle) bremsstrahlung, particles and off-shell-antiparticle annihilation, two-to-two process. As an illustration of the applicability of the developed method, the energy emitted from a hot equilibrium quark-gluon plasma due quark emission is calculated for various temperatures of the matter.

References

[1] L.D. Landau, I.Ya. Pomeranchuk, Dokl.Akad.Nauk SSSR **92**, 735 (1953).

[2] A.B. Migdal, Phys. Rev, **103**, 1811 (1956).

[3] A.V. Koshelkin, Phys. Rev. **D77**, 025024 (2008).

[4] L.V. Keldysh, Sov.-JETP. **20**, 235 (1965).

[5] J. Cleymans, V.V. Goloviznin, K . Redlich, Phys. Rev. **D47**, 989 (1992).

New Scaling Behavior of low-p_T Hadron Production in proton-(anti)proton collisions at RHIC and Tevatron

M.Tokarev[1]†, *I.Zborovský*[2]
[1]Joint Institute for Nuclear Research, Dubna, Russia,
[2]Nuclear Physics Institute, Academy of Sciences of the Czech Republic, Řež, Czech Republic
DOI: http://dx.doi.org/10.3204/DESY-PROC-2009-01/94

Abstract
Data on inclusive cross sections of particles produced in high energy proton-(anti)proton collisions at ISR, RHIC, and Tevatron are analyzed in the framework of z-scaling. New properties of the scaling function $\psi(z)$ - flavor independence and saturation at low z, are established. The approach can be useful for searching for new physics phenomena in particle production at RHIC, Tevatron, and LHC.

1 Introduction

The search for new physics in soft- and high-p_T regions is one of the main goals of investigations at Relativistic Heavy Ion Collider (RHIC) at BNL and Large Hadron Collider (LHC) at CERN [1–4]. Experimental data on particle production at high energy and multiplicity provide constraints for different theoretical models. Processes with high transverse momenta of produced particles are suitable for a precise test of perturbative Quantum Chromodynamics (QCD). The soft regime is preferred for verification of non-perturbative QCD and investigation of phase transitions in non-Abelian theories.

One of the methods allowing systematic analysis of data on inclusive cross sections over a wide range of the collision energies, multiplicity densities, transverse momenta, and angles of the produced particles is based on the z-scaling observed in high energy proton-(anti)proton collisions (see Ref. [5] and references therein). Here we show [6] that in the high energy pp and $p\bar{p}$ collisions the shape of the scaling function $\psi(z)$ is independent of the hadron type including production of hadrons with heavy flavor content. A saturation of $\psi(z)$ is found at low z. The single parameter c which controls the behavior of $\psi(z)$ at low z is interpreted as a "specific heat" of the produced medium. The scaling in pp and $p\bar{p}$ collisions is consistent with a constant value of c. A possible change in this parameter could be an indication of a phase transition in the matter produced in high energy collisions.

2 z-Scaling

At sufficiently high energies, the collision of extended objects like hadrons and nuclei is considered as an ensemble of individual interactions of their constituents. The constituents are partons in the parton model or quarks and gluons in the theory of QCD. Multiple interactions are assumed to be similar. This property represents a self-similarity of the hadronic interactions at a constituent level. A single interaction of the constituents is illustrated in Fig. 1.

† speaker

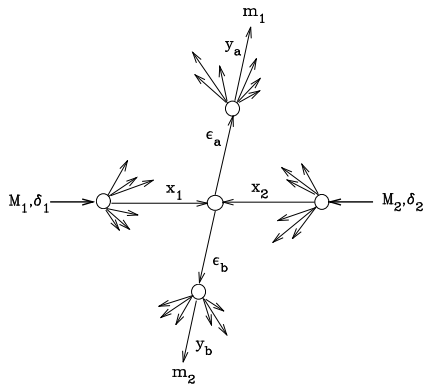


Fig.1. Diagram of the constituent subprocess.

The structures of the colliding objects (M_1) and (M_2) are characterized by parameters δ_1 and δ_2. The interacting constituents carry the fractions x_1, x_2 of the incoming momenta P_1, P_2. The inclusive particle (m_1) carries the momentum fraction y_a of the scattered constituent with a fragmentation characterized by a parameter ϵ_a. The fragmentation of the recoil constituent is described by ϵ_b and the momentum fraction y_b. The associate production of (m_2) ensures conservation of the additive quantum numbers.

The constituent subprocess is considered as a binary collision of the constituents (x_1M_1) and (x_2M_2) resulting in the scattered (m_1/y_a) and recoil $(M_X = x_1M_1 + x_2M_2 + m_2/y_b)$ objects in the final state. The momentum conservation law of the subprocess is connected with a recoil mass which we write as follows

$$(x_1P_1 + x_2P_2 - p/y_a)^2 = M_X^2. \tag{1}$$

This equation is expression of the locality of the hadron interaction at a constituent level. It represents a constraint on the fractions x_1, x_2, y_a, and y_b. The structure of the colliding objects and the fragmentation are characterized by the parameters $\delta_{1,2}$ and $\epsilon_{a,b}$, respectively. The structural parameters are connected with the corresponding momentum fractions by the function

$$\Omega(x_1, x_2, y_a, y_b) = (1 - x_1)^{\delta_1}(1 - x_2)^{\delta_2}(1 - y_a)^{\epsilon_a}(1 - y_b)^{\epsilon_b}. \tag{2}$$

The quantity Ω is proportional to relative number of all such constituent configurations which contain the configuration defined by the fractions $x_1, x_2, y_a,$ and y_b. We use $\delta_1 = \delta_2 \equiv \delta$, $M_1 = M_2$, $\epsilon_a = \epsilon_b \equiv \epsilon_F$, and $m_2 = m_1$ in the analysis of proton-(anti)proton interactions. The parameters δ and ϵ_F were found to have constant values. They are interpreted as fractal dimensions in the space of the momentum fractions. We determine the fractions x_1, x_2, y_a, and y_b in a way to maximize the function Ω under the condition (1). The maximal value of Ω is used in the definition of the scaling variable z which has the form

$$z = z_0\Omega^{-1}. \tag{3}$$

The part $z_0 = s_\perp^{1/2}/(dN_{ch}/d\eta|_0)^c$ is proportional to the transverse kinetic energy $s_\perp^{1/2}$ of the subprocess consumed on the production of (m_1) and (m_2). The charged multiplicity density

$dN_{ch}/d\eta|_0$ at $\eta = 0$ and constant c have thermodynamical interpretation. The scaling function

$$\psi(z) = -\frac{\pi s}{(dN/d\eta)\sigma_{inel}} J^{-1} E \frac{d^3\sigma}{dp^3}. \quad (4)$$

is expressed in terms of the inclusive cross section, multiplicity density $dN/d\eta$ of the particular hadron species, and total inelastic cross section. Here s is square of the center-of-mass energy, and J is the corresponding Jacobian. The function $\psi(z)$ is normalized to unity.

3 Properties of the scaling function

The z-dependence of data on inclusive spectra of hadrons produced in pp and $\bar{p}p$ collisions at ISR, $\mathrm{Sp\bar{p}S}$, RHIC, and Tevatron reveals the energy, angular, and multiplicity independence [5]. Here we analyze the experimental data (see [6] and reference therein) on the transverse momentum spectra obtained at RHIC and Tevatron. New properties of the scaling function $\psi(z)$ - the flavor independence and saturation at low z for different hadrons are established.

3.1 Flavor independence of $\psi(z)$

We exploit the transformation $z \to \alpha_F z,\ \ \psi \to \alpha_F^{-1}\psi$ for comparison of the shape of the scaling function $\psi(z)$ for different hadron species. The parameter α_F is a scale independent quantity. The transformation does not change the shape of $\psi(z)$. It preserves the energy, angular, and multiplicity independence of the z-presentation of particle spectra.

Figure 2(a) shows the z-dependence of the spectra of negative pions, kaons, antiprotons, and $\Lambda's$ produced in pp collisions over the range $\sqrt{s} = 19 - 200$ GeV and $\theta_{cms} = 3^0 - 90^0$. The analysis comprises the inclusive spectra measured up to very small transverse momenta ($p_T \simeq 45$ MeV/c for pions and $p_T \simeq 120$ MeV/c for kaons or antiprotons). The distributions of different hadrons are sufficiently well described by a single curve over a wide z-range ($0.01-30$). The solid lines and experimental data are shifted by multiplicative factors for reasons of clarity. The parameters ϵ_F and α_F are found to be independent of $\sqrt{s}, p_T$, and θ_{cms}. They are consistent with the energy, angular, and multiplicity independence of the z-scaling.

Figure 2(b) shows similar results for other hadrons ($\rho, \omega, \phi, K^*, \Xi$) produced in pp collisions at $\sqrt{s} = 200$ GeV and $\theta_{cms} = 90^0$. The data on inclusive spectra are compared with the pion distributions measured at RHIC. The shape of $\psi(z)$ is described by the same curve as depicted in Fig. 2(a). The black circle at the lowest $z \simeq 0.007$ corresponds to the STAR data on K^* resonances measured in the region where the scaling function is saturated. We conclude that RHIC data on pp collisions confirm the flavor independence of the z-scaling including the production of particles with small p_T.

The inclusive spectra of heavy hadrons ($J/\psi, D^0, B, \Upsilon$) obtained at the Tevatron energies $\sqrt{s}$ =1800 and 1960 GeV allow us to verify the new property of the z-scaling in $p\bar{p}$-collisions. The data include measurements up to small transverse momenta ($p_T \simeq 125$ MeV/c for charmonia, $p_T \simeq 290$ MeV/c for bottomia, and $p_T \simeq 500$ MeV/c for B-mesons). Figure 3(a) shows the spectra of $J/\psi, D^0, B$, and Υ mesons in the z-presentation. The scaling function is the same for hadrons with light and heavy flavors in the range $z = 0.001 - 4$. The corresponding values of the parameters α_F and ϵ_F are shown in Fig. 3(a). Figure 3(b) demonstrates results of the combined

analysis of the RHIC and Tevatron data on J/ψ-meson spectra measured in pp and $p\bar{p}$ collisions at $\sqrt{s} = 200, 1800, 1960$ GeV and $\theta_{cms} = 22^0, 90^0$ as a function of z.

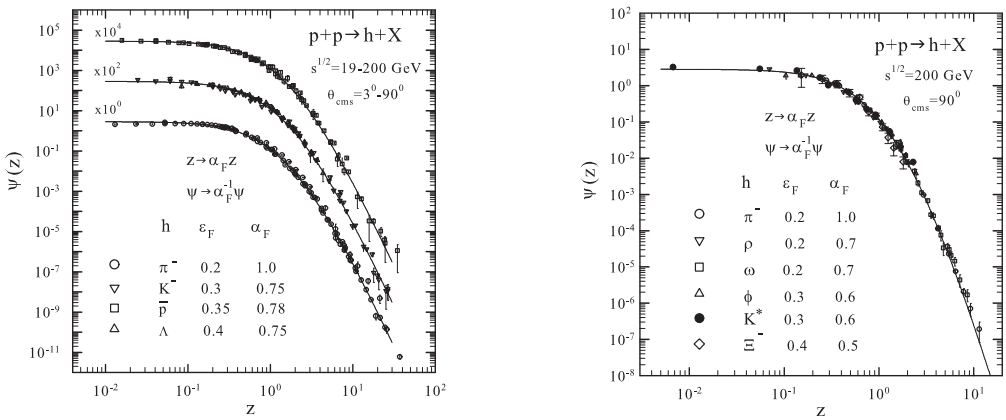


Fig. 2. The flavor independence of z-scaling. The spectra of π^-, K^-, $\bar{p}$, Λ (a) and ρ, ω, ϕ, K^*, Ξ (b) hadrons produced in pp collisions as a function of z. Data are obtained at CERN, FNAL, and BNL. The solid line is a fit of the data.

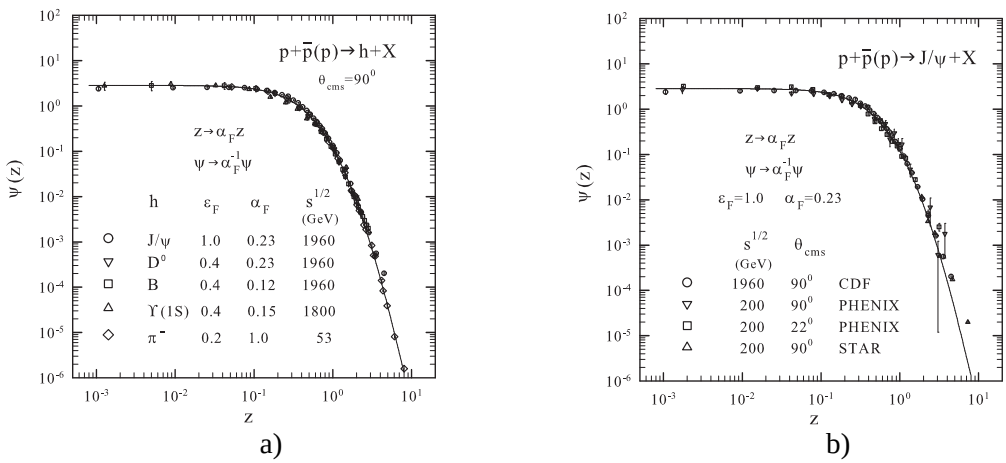


Fig. 3. The flavor independence of z-scaling. The spectra of $J/\psi, D^0, B, \Upsilon, \pi^-$ (a) and J/ψ (b) mesons produced in $pp/p\bar{p}$ collisions in z-presentation. Data are obtained at Tevatron and RHIC. The solid line is the same as shown in Fig. 2.

From this analysis we conclude that ISR, RHIC, and Tevatron data on inclusive spectra manifest the flavor independence of the scaling function $\psi(z)$ over a wide range of z. We would like to stress that the obtained result is based on p_T distributions of the cross sections $Ed^3\sigma/dp^3$ which reveal strong dependence on the energy, angle, multiplicity, and type of the produced particle.

3.2 Saturation of $\psi(z)$

As seen from Figs. 2 and 3, the z-presentation of hadron distributions demonstrates independence on the variable z in the soft (low p_T) region. The saturation is manifested by the pion, kaon, antiproton and especially J/ψ and Υ spectra in the range $z = 10^{-3} - 10^{-1}$. The similar independence is observed for other hadrons ($K^*, B, \rho, ...$) at low p_T. A characteristic of the saturation is the slope parameter β of the scaling function which is diminishing with the decreasing z. The value of $\beta = dln\psi(z)/dlnz$ is approximately zero for $z < 0.1$.

One can assume that the asymptotic behavior of $\psi(z)$ at $z \to 0$ is universal and reflects properties of the produced system consisting of its constituents (hadrons or quark and gluons). The universal scaling behavior in this region suggests that mechanism of particle production at low p_T is governed by soft self-similar processes which reveal some kind of a mutual equilibrium leading to the observed saturation.

4 Conclusions

The experimental data on inclusive cross sections of different hadrons measured at ISR, RHIC, and Tevatron were analyzed. The data cover a wide range of the collision energies, the transverse momenta, and the production angles. New properties of the z-scaling - the flavor independence and the saturation of $\psi(z)$ at low z, were established. The flavor independence of the z-scaling means that the shape of $\psi(z)$ is the same for different hadrons. A saturation regime of the function $\psi(z)$ was observed for $z < 0.1$. The approximate constancy of $\psi(z)$ was demonstrated up to $z \simeq 10^{-3}$ for charmonia and bottomia. The variable z depends on the parameters δ, ϵ_F, and c. The parameters δ and ϵ_F characterize structure of the colliding objects and fragmentation process, respectively. Their values are fixed by the energy, angular, and multiplicity independence of $\psi(z)$ in the high-p_T part of the spectra. The parameter c is interpreted as "specific heat" of the produced medium. The z-scaling is consistent with $c = 0.25$ and $\delta = 0.5$ for all types of the analyzed inclusive hadrons. The value of ϵ_F increases with the mass of the produced hadron. It was found that the parameters are independent of kinematical variables.

We conclude that soft and hard regimes of hadron production manifest self-similarity of particle production at a constituent level. The obtained results may be exploited to search for and study of new physics phenomena in particle production in the high energy proton-proton and proton-antiproton collisions at RHIC, Tevatron, and LHC.

The investigations have been partially supported by the IRP AVOZ10480505, by the Grant Agency of the Czech Republic under the contract No. 202/07/0079 and by the special program of the Ministry of Science and Education of the Russian Federation, grant RNP.2.1.1.5409.

References

[1] BRAHMS Collaboration, I. Arsene *et al.,* Nucl.Phys. **A757**, 1 (2005).

[2] PHOBOS Collaboration, B.Back *et al.,* Nucl.Phys. **A757**, 28 (2005).

[3] STAR Collaboration, J. Adams *et al.,* Nucl.Phys. **A757**, 102 (2005).

[4] PHENIX Collaboration, K. Adcox *et al.,* Nucl.Phys. **A757**, 184 (2005).

[5] I.Zborovský and M.Tokarev, Phys.Rev. **D75**, 094008 (2007).

[6] I.Zborovský and M.Tokarev, arXiv:0809.1033 (hep-ph).

Strongly Interacting Massive Particles at LHC

O.I. Piskounova[1]†, *A.B. Kaidalov*[2]
[1]P.N.Lebedev Physical Institute of Russian Academy of Science, Moscow, Russia,
[2]Institute for Theoretical and Experimental Physics, Moscow, Russia.

DOI: http://dx.doi.org/10.3204/DESY-PROC-2009-01/102

Abstract
The search for strongly interacting massive particles (SIMP) is one of the most promising ways to observe new physics phenomena at the LHC. This paper describes the propagation in matter of stable new hadrons containing a heavy exotic quark with new quantum number. The accuracy of any exclusion limit or cross-section measurement from a search depends on the degree to which the interactions of SIMPs with detector material can be quantified with phenomenological models of strong interactions. This paper outlines a model for scattering of heavy hadrons that is based on Regge phenomenology and the Quark Gluon String Model (QGSM). We discuss also some astrophysical constraints on the possibility of H-hadrons to be next to lightest supersymmetry particle (NLSP) that makes more interesting their discovery at the LHC.

1 Introduction

First it should be mentioned that new massive particles may explain the dark matter (DM) content of the Universe. Supersymmetry is the most elaborated theory that provides us with such particles, and according to it the dark matter may consist of the lightest supersymmetry partner of the known elementary particles (LSP). As long as the dark matter candidates must be neutral and stable, from the experimental point of view the discovery of next-to-lightest supersymmetry particles (NLSP) in new physics hierachy seems to be more promising at LHC searches. These particles from beyond the Standard Model are expected to be of relatively low masses and quasistable on distances of detectors.

Looking for such particles in various versions of SUSY we see that Minimal SUSY model expects neutralinos as LSP, while Supergravity theory predicts gravitino as DM candidate. In the latter type of models it is easy to presume quasistable NLSP since it decays into gravitino with very small cross section of gravitation interaction. On the other hand, supersymmetry models should have more sophisticated constructions in order to obtain light NLSP particles. An example of how this can be obtained in found Compressed SUSY model [2] where relatively light gluino and squarks allow to slot the dark matter cosmological parameter, Ω_{DM}, into the range of known observations with the help of neutralino pair annihilation to top quark-antiquark pair via stop quark exchange. The Split SUSY model [3] has been constructed to provide the possibility of light gluino NLSP. This idea has already been discussed in [1]. The model of Warped Extra Dimensions [4] gives weakly interacting massive particles (WIMP) as a candidate for dark matter.

† speaker

As one can see there exist good reasons to explore the possibility of discovery of some strongly interacting long living NLSP at LHC energies. Here we would like to consider the stop quarks as an example of strongly interacting massive particle (SIMP) [5]. ATLAS and CMS experiments have already developed search strategies for SIMPs, which usually assume that these particles are included into heavy exotic H-hadrons that behave in muon chamber like a slow-moving muons. The QGSM [8] is then used to construct a description of the collisions of those particles with the matter and to estimate average energy losses in such collisions. Finally, we discuss the impact of some astrophysical constrains on the prospects for detecting exotic hadrons at the LHC.

Considering the interactions with matter, it is important to know the mass hierarchy of exotic hadrons. This determines the states to which a heavy exotic hadron, produced either in the primary interaction or after scattering with matter, would rapidly decay. The lowest lying neutral and charged mesonic states should be stable since the mass difference between them is expected to be far smaller than the pion mass and the meson mass $m_{u'\bar{q}}$ is given by $m_{u'\bar{q}} \approx m_{u'} + m_q$, where m_q and $m_{u'}$ the constituent masses of the SM quark and exotic quark, respectively. This statement contradicts to the suggestion adduced in [6] that only neutral heavy hadrons survive in the first moments after hadronization of SIMP and rapid decays of charged H-hadrons. Another idea we should disprove here was figured out in [9]. Authors have suggested that SIMPs deposit smaller energy in the matter than muons. Although the energy losses of SIMP in matter are to be smaller than the losses of ordinary hadrons, their energy deposit in matter are still of the order of hadronic losses, so they have to be bigger than the losses of muons. In folowing sections we describe the basic formulas of the propagation of H-hadrons in matter, but will not have a room to show the results of experimental simulations. The recent complete publication [7] contains all necessary diagrams and resulting plots.

2 Interactions of Heavy Hadrons in Matter

Interactions of H-hadrons with protons of ordinary matter are rather specific. The heavy squark will be always a spectator due to the absence of antisquarks in the detector matter to annihilate with. Thus there is only the low energy light ordinary quark in the hadron that can interact. At the LHC, the light quark's kinetic energy will typically be around several GeV and the Regge phenomenology approach [8] can be employed to describe exotic hadron interactions with matter.

In our approach one can distinguish two classes of scattering processes: reactions mediated by (a) reggeon and corresponding to planar QCD diagrams and (b) pomeron exchange related to the cylinder-type diagrams in elastic scattering. Exotic hadrons containing a light constituent anti-quark interact via pomeron and reggeon exchanges, the latter processes are due to the annihilation of light antiquarks with the quarks of detector matter. Conversely, hadrons containing a light constituent quark can only interact via pomeron exchange. Let us consider the process of interaction of a heavy H-hadron with a nucleon of the target in the target rest frame. In this frame the light antiquark of H-hadron carries only a small fraction of the total energy E

$$E_q \approx \frac{E m_{q\perp}}{M_H} = \gamma m_{q\perp}$$

where $\gamma = E/M_H$ and $m_{q\perp}$ is the transverse mass of the light antiquark. It was shown in the framework of QGSM [8], that the planar diagram contribution to the total cross section $\sigma_R(s)$ is

universal for the same energy of the annihilating antiquark. This means that the contribution to the total cross section of reggeons can be written as:

$$\sigma_R(E) = K\sigma_{pl}(E = \gamma m_{q\perp}) = K g_R (2\gamma m_{q\perp}/E_0)^{\alpha_R(0)-1}, \quad (1)$$

where K is the number of possible planar diagrams, $E_0 = 1$ GeV. The vertex parameter g_R can be evaluated from the data on cross sections of hadronic interactions and the intercept of the exchange degenerate regge tragectories $\alpha_R(0)$ is equal to 0.5.

The pomeron contribution to the total cross section (σ_P) can be estimated as

$$\sigma_P \sim (2\gamma m_{q\perp}/E_0)^{\alpha_P(0)-1} \quad (2)$$

The reggeon contribution to the cross section for a H-meson and a nucleon within a nucleus, which consists of equal amounts of protons and neutrons, can be derived as the difference between the reggeon contributions to $\sigma(\pi^- p)$ and $\sigma(\pi^+ p)$ data multiplied by a factor 1.5.

3 Differential Cross Sections of H-hadron scattering

In determining the kinematics of the scattering process, we consider the inclusive process $H + N \to H' + X$, where H, H', N and X are the incoming exotic hadron, the outgoing exotic hadron, the target nucleon, and whatever else is produced in the interaction, respectively. The kinematics of such an interaction can be specified by three independent kinematic variables. Commonly used variables are t, the usual four-momentum transfer between the incoming and outgoing exotic hadrons, s, the center-of-mass energy squared of the interaction, and M_X, the mass of the final state X.

The final H'-hadron carries a fraction of energy x_F close to unity and only a small fraction of energy $1 - x_F \sim m_{q\perp}/M_H \ll 1$ is transferred to production of hadrons. This justifies the application of the triple-regge formulae to provide a description of inclusive cross sections. Strictly speaking the triple-regge description is valid for $m_X^2 \gg 1GeV^2$ and the rapidity difference between H' and rest hadrons $\Delta y > 1$. This is equivalent to the condition $2\gamma m_{q\perp} m_N/M_X^2 \gg 1$. In hadronic interactions, the triple-regge description works usually up to $\Delta y \sim 1$ and we will assume in the following that the same is true for interaction of H-hadrons. Expressions for the contributions of different triple-regge terms iik to inclusive cross sections is straightforward to obtain noting, that for reggeons i corresponds to the factor $\exp(2(\alpha_i(t)-1)\Delta y)$, while an exchange by the reggeon k leads to the factor $\exp((\alpha_k(0)-1)y_q)$. Here, $y_q = \ln(M_X^2/(m_{q\perp} m_N)$ is the rapidity interval covered by produced hadrons (the total rapidity $Y = \ln(2E/M_H) = \ln(2\gamma) = \Delta y + y_q$). As for the total cross section we consider here the pomeron P and secondary reggeons R as exchanged reggeons i, k. Thus we have the following triple-regge contributions: RRR,RRP,PPR and PPP.

Using the rules described above we can write inclusive cross sections for the corresponding triple-regge terms in the following forms:

$$\frac{d^2\sigma_{RRR}}{dtdM_X^2}(\gamma, M_X^2) = \frac{1}{M_X^2}\sigma_R^2(\gamma) C_{RRR} \exp[(2B_{RH} + B_{RRR} + 2\alpha'_R \ln(\frac{2\gamma M_0^2}{M_X^2}))t]$$

$$\times \left(\frac{M_0^2}{M_X^2}\right)^{\Delta_R} \quad (3)$$

$$\frac{d^2\sigma_{RRP}}{dtdM_X^2}(\gamma, M_X^2) = \frac{1}{M_X^2}\sigma_R^2(\gamma) C_{RRP} \exp[(2B_{RH} + B_{RRP} + 2\alpha'_P \ln(\frac{2\gamma M_0^2}{M_X^2}))t] \times \left(\frac{M_0^2}{M_X^2}\right)^{2\Delta_R - \Delta_P} \quad (4)$$

$$\frac{d^2\sigma_{PPR}}{dtdM_X^2}(\gamma, M_X^2) = \frac{1}{M_X^2}\sigma_P^2(\gamma) C_{PPR} \exp[(2B_{PH} + B_{PPR} + 2\alpha'_P \ln(\frac{2\gamma M_0^2}{M_X^2}))t] \times \left(\frac{M_0^2}{M_X^2}\right)^{2\Delta_P - \Delta_R} \quad (5)$$

$$\frac{d^2\sigma_{PPP}}{dtdM_X^2}(\gamma, M_X^2) = \frac{1}{M_X^2}\sigma_P^2(\gamma) C_{PPP} \exp[(2B_{PH} + B_{PPP} + 2\alpha'_P \ln(\frac{2\gamma M_0^2}{M_X^2}))t] \times \left(\frac{M_0^2}{M_X^2}\right)^{\Delta_P} \quad (6)$$

where $\Delta_R = \alpha_R(0) - 1$= -0.5, $\Delta_P = \alpha_P(0) - 1$= 0.12, $\alpha'_R = 0.9\ GeV^{-2}$, $\alpha'_P = 0.25\ GeV^{-2}$ [8] and $M_0^2 = m_N m_{q\perp} = 0.5\ GeV^2$.

The parameters, C_{iij}, and B_{iij} can be determined using Regge factorization from the triple-regge description of inclusive spectra in high-energy hadronic interactions. Let us emphasise that the RRR-term corresponds to the cutting of planar diagram or R-exchange, while the RRP-term corresponds to the cutting of the cylinder-type diagram. Due to conservation of H-hadrons integrals over M_X^2 and t give σ_R and σ_P contributions to the total cross section correspondingly.

The PPR and PPP-terms describe the diffractive dissociation of a nucleon and their cross sections can be calculated, using factorization from the corresponding cross sections extracted from pp-interactions

$$\sigma_{Hp}^{PPi} = \frac{\sigma_P(Hp)^2}{\sigma_P(pp)^2}\sigma_{pp}^{PPi} \quad (7)$$

Here, we neglected the small difference in t-dependence for Hp and PP vertices. Taking into account that $\frac{\sigma_P(Hp)}{\sigma_P(pp)} \approx 1/4$ and that the sum of PPR and PPP-contributions for pp-collisions in the relevant energy domain does not exceed 2mb, we obtain very small cross sections for diffraction dissociation of a nucleon in Hp-interactions: 0.12 mb. Thus these cross sections constitute only about 1% of the total cross section and can be safely neglected.

For parameters characterising the t-dependence of RRR and RRP-terms we take the same values as those which have been extracted from the analysis of pp-interactions: $2B_{RH} + B_{RRR} = 2B_{RH} + B_{RRP} = 4\ GeV^{-2}$.

4 The possible impact of SIMP discovery on astrophysical models

There are two astrophysical facts which resist to the hypothesis of new heavy quarks being NLSP: a) the success of big bang nucleosynthesis (BBN) model and b) the observation of perfect black-

body characteristics of cosmic microwave background (CMB). Both precise astrophysical calculations can dismiss SIMP-as-NLSP idea because the decays of new heavy quarks lead to hadronic showers that certainly destroy BBN scenario [10]. On the other hand, if the exotic quarks are living long enough, then the effect of their decay should produce a visible structure of CMB which gets in conflict with the above mentioned observations. All arguments show that detection of exotic quarks occurs intertwined between high energy particle physics and astrophysics and it may require more precise balance of observations and up-to-date physical models.

5 Conclusions

Strongly interacting massive particles are predicted by the number of scenarios of physics beyond the SM. This article presents a model for description of the interactions of exotic H-hadrons containing new heavy quarks with the matter of detector. QGSM formulas for energy dependence of cross sections and differential distributions of scattered H-hadrons were shown. Two statements follows from our recently developed approach: 1) the conversion of H-baryon into H-meson and back can be neglected in calculations due to the very small probability of nucleon trajectory exchange; 2) the processes with double charge exchange like a transition of H^+-mesons into H^- ones are also impossible. These admissions make significantly clearer the calculation of H-hadron propagation in the matter. The discovery of such strongly interacting new particles would have an important impact on modern astrophysical schemes.

References

[1] H. Baer, K. M. Cheung and J. F. Gunion, Phys. Rev. D **59** (1999) 075002 [arXiv:hep-ph/9806361];
A. Mafi and S. Rabi, Phys. Rev. D **62** (2000) 035003.

[2] Stephen P. Martin, [arXiv:hep-ph/0703097].

[3] N. Arkani-Hamed, S. Dimopoulos, G.F. Giudice, A. Romanino, Nucl.Phys. B709 (2005) 3, [arXiv:hep-ph/0409232].

[4] Lisa Randall, Raman Sundrum, Phys.Rev.Lett. 83 (1999) 3370, [arXiv:hep-ph/9905221].

[5] J. L. Diaz-Cruz, J. R. Ellis, K. A. Olive and Y. Santoso, JHEP **0705** (2007) 003, [arXiv:hep-ph/0701229].

[6] Yudi Santoso, [arXiv:0709.3952].

[7] Yt. R. de Boer , A.B. Kaidalov, D. A. Milstead and O. I. Piskounova, J. Phys. G: Nucl. Part. Phys. 35(2008)075009, [arXiv:0710.3930].

[8] A.B. Kaidalov,Z. Phys.**C3**(1979)329
A.B. Kaidalov, Phys. Lett.**B117**(1982)247
A.B. Kaidalov and K.A. Ter-Martirosyan, Sov.J.Nucl.Phys.**39**(1984)1545;
A.B. Kaidalov and O.I. Piskounova, Sov.J.Nucl.Phys.**41**(1985)1278;
O. Piskounova, Phys.At.Nucl. **66** (2003) 332.

[9] Shin'ichiro Ando, John F. Beacom, Stefano Profumo, David Rainwater, JCAP 0804 (2008) 029, [arXiv:0711.2908].

[10] T. Kanzaki, M. Kawasaki, K. Kohri, T. Moroi, [arXiv:0705.1200].

Saturation in lepton- and hadron induced reactions

L.L. Jenkovszky
Bogolyubov Institute for Theoretical Physics, National Academy of Sciences of Ukraine;
RMKI (KFKI), POB 49, Budapest 114, H-1525 Hungary
DOI: http://dx.doi.org/10.3204/DESY-PROC-2009-01/101

Abstract
Possible saturation of the matter density in two different classes of reactions, those induced by hadrons and leptons are studied. They may have common dynamical origin and be of the same nature.

1 Hadron-induced reactions: The Black Disc Limit at the LHC?

Unitarity in the impact parameter b representation reads:

$$\Im h(s,b) = |h(s,b)|^2 + G(s,b),$$

where $h(s,b)$ is the elastic scattering amplitude at the center of mass energy $\sqrt{s}$, $\Im h(s,b)$ is the profile function, representing the hadron opacity and $G(s,b)$, called the inelastic overlap function, is the sum over all inelastic channel contributions. Integrated over b, the above equation reduces to a simple relation between the total, elastic and inelastic cross sections $\sigma_{tot}(s) = \sigma_{el}(s) + \sigma_{in}(s)$.

Unitarity imposes the absolute limit

$$0 \leq |h(s,b)|^2 \leq \Im h(s,b) \leq 1,$$

while the so-called black disc limit $\sigma_{el}(s) = \sigma_{in}(s) = \frac{1}{2}\sigma_{tot}(s)$, or

$$\Im h(s,b) = 1/2,$$

is a particular realization of the optical model, namely it corresponds to the maximal absorption within the eikonal unitarization, when the scattering amplitude is approximated as

$$h(s,b) = \frac{i}{2}(1 - \exp\left[\mathrm{i}\omega(\mathrm{s},\mathrm{b})\right]),$$

with a purely imaginary eikonal $\omega(s,b)$.

Eikonal unitarization corresponds to a particular solution of the unitarity equation, with $\Re h(s,b) = 0$,

$$h(s,b) = \frac{1}{2}\left[1 \pm \sqrt{1 - 4G_{in}(s,b)}\right],$$

the one with the minus sign.

An alternative solution, that with a plus sign in front of the square root, is known and realized within the so-called U-matrix approach, where the unitarized amplitude is a ratio rather than an exponential typical of the eikonal approach:

$$h(s,b) = \frac{U(s,b)}{1 - i\,U(s,b)},$$

where U is the input Born term, the analogue of the eikonal ω.

In the U-matrix approach, the scattering amplitude $h(s,b)$ may exceed the black disc limit as the energy increases. The transition from a (central) black disc to a (peripheral) black ring, surrounding a gray disc, for the inelastic overlap function in the impact parameter space corresponds to the transition from shadowing to antishadowing.

The impact parameter amplitude $h(s,b)$ can be calculated either directly from the data (where, however, the real part of the amplitude was neglected) or by using a particular model that fits the data sufficiently well.

In the dipole Pomeron (DP) model [1], logarithmically rising cross sections are produced with a Pomeron intercept equal to unity, thus respecting the Froissart-Martin bound.

Apart from the conservative Froissart-Martin bound, any model should satisfy also s-channel unitarity. We show that both the D-L and DP models are well below this limit and will remain so for long, in particular will so at the LHC.

The elastic scattering amplitude corresponding to the exchange of a dipole Pomeron reads

$$\begin{aligned} A(s,t) = & \quad \tfrac{d}{d\alpha}\left[\mathrm{e}^{-i\pi\alpha/2}G(\alpha)(s/s_0)^\alpha\right] \\ = & \quad \mathrm{e}^{-i\pi\alpha/2}(s/s_0)^\alpha[G'(\alpha)+(L-i\pi/2)G(\alpha)]\ , \end{aligned}$$

where $L \equiv \ell n\dfrac{s}{s_0}$ and $\alpha \equiv \alpha(t)$ is the Pomeron trajectory.

The elastic amplitude in the impact parameter representation in our normalization is

$$h(s,b) \ = \ \frac{1}{2s}\int_0^\infty dq\ qJ_0(bq)A(s,-q^2)\ , \qquad q=\sqrt{-t}\ .$$

The impact parameter representation for linear trajectories is calculable explicitly for the DP model. We have

$$h(s,b) \ = i\ g_0\ [e^{r_1^2\delta}\ e^{-b^2/4R_1^2}\ -\ \epsilon\ e^{r_2^2\delta}\ e^{-b^2/4R_2^2}]\ ,$$

where

$$R_i^2=\alpha' r_i^2\ \ (i=1,2);\ g_0=\frac{a}{4b_p\alpha' s_0}\ .$$

Asymptotically (when $L \gg b_p$, i.e. $\sqrt{s} \gg 2.$ TeV, with the parameters quoted in Table 1) we get

$$h(s,b)_{s\to\infty} \to i\ g(s)\ (1-\epsilon)\ e^{-\frac{b^2}{4R^2}}\ ,$$

where

$$R^2=\alpha' L \qquad ;\ g(s)=g_0\left(\frac{s}{s_0}\right)^\delta\ .$$

It is important to note that the unitarity bound 1 for $Imh(s,b)$ will not be reached at the LHC energy, while the black disc limit 1/2 will be slightly exceeded, the central opacity of the nucleon being $\Im\mathrm{m}h(s,0)=0.54$.

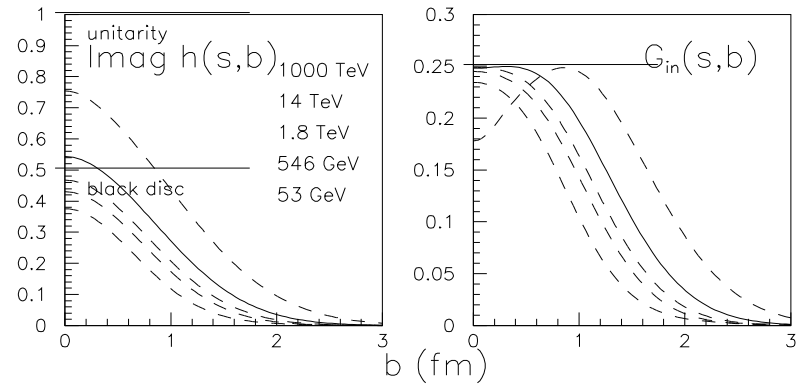


Fig. 1: A family of curves showing the imaginary part of the amplitude in the impact parameter-representation as well as the calculated inelastic overlap function $G(s,b)$ at various energies.

$\sqrt{s}$	53 GeV	546 GeV	1800 GeV
exp	0.36	0.420 ± 0.004	0.492 ± 0.008
th	0.36	0.424	0.461

Table 1: Central opacity of the nucleon $Imh(s,0)$ calculated at the ISR, SPS and Tevatron energies compared with experiment.

The black disc limit is reached at $\sqrt{s} \sim 2$ TeV, where the overlap function reaches its maximum $\frac{1}{4}$. While $Imh(s,b)$ remains central all the way, $G_{in}(s,b)$ is getting more peripheral as the energy increases starting from the Tevatron. For example at $\sqrt{s} = 14$ TeV, the central region of the antishadowing mode, obtained from the U matrix unitarization, below $b \sim 0.4$ fm is discernible from the peripheral region of shadowing scattering beyond $b \sim 0.4$ fm, where $G_{in}(s,b) = \frac{1}{4}$. The proton will tend to become more transparent at the center (gray, in the sense of becoming a gray object surrounded by a black ring).

The s channel unitarity limit will not be endangered until extremely high energies (10^5 for the Donnachie-Landshoff model and 10^6 GeV for the DP), safe for any credible experiment.

2 Lepton-induced reactions: DIS

An ansatz interpolating between the soft (VMD, Pomeron) Regge behavior and the hard (GLAP evolution) regime, given by the explicit solution of the DGLAP equation in the leading-log approximation, for the small-x singlet part of the proton structure function,

$$F_2 \approx \sqrt{\gamma_1 \ell n(1/x)\ \ell n \ell n Q^2}\ ,$$

with $\gamma_1 = \frac{16N_c}{(11-2f/3)}$ (for 4 flavours ($f = 4$) and three colours ($N_c = 3$), $\gamma_1 = 5.76$) was suggested in Ref. [2]

$$F_2^{(S,0)}(x,Q^2) = A\left(\frac{Q^2}{Q^2+a}\right)^{1+\widetilde{\Delta}(Q^2)} e^{\Delta(x,Q^2)},$$

with the "effective power"

$$\widetilde{\Delta}(Q^2) = \epsilon + \gamma_1 \ell n\left(1+\gamma_2 \ell n\left[1+\frac{Q^2}{Q_0^2}\right]\right),$$

and

$$\Delta(x,Q^2) = \left(\widetilde{\Delta}(Q^2)\ell n\frac{x_0}{x}\right)^{f(Q^2)},$$

where

$$f(Q^2) = \frac{1}{2}\left(1+e^{-Q^2/Q_1^2}\right).$$

At small and moderate values of Q^2, the exponent $\widetilde{\Delta}(Q^2)$ can be interpreted as a Q^2-dependent effective Pomeron intercept.

By construction, the model has the following asymptotic limits:

b) Low Q^2, fixed x:

$$F_2^{(S,0)}(x,Q^2\to 0) \to A\, e^{\Delta(x,Q^2\to 0)}\ \left(\frac{Q^2}{a}\right)^{1+\widetilde{\Delta}(Q^2\to 0)}$$

with

$$\widetilde{\Delta}(Q^2\to 0) \to \epsilon + \gamma_1\gamma_2\left(\frac{Q^2}{Q_0^2}\right)\ \to\ \epsilon,$$

$$f(Q^2\to 0)\to 1,$$

whence

$$F_2^{(S,0)}(x,Q^2\to 0) \to A\ \left(\frac{x_0}{x}\right)^{\epsilon}\ \left(\frac{Q^2}{a}\right)^{1+\epsilon} \propto (Q^2)^{1+\epsilon}\ \to 0\,,$$

as required by gauge invariance.

c) Low x, fixed Q^2:

$$F_2^{(S,0)}(x\to 0,Q^2)\ =\ A\left(\frac{Q^2}{Q^2+a}\right)^{1+\widetilde{\Delta}(Q^2)} e^{\Delta(x\to 0,Q^2)}.$$

If $f(Q^2)\sim 1$ i.e. when $Q^2 \ll Q_1^2$, we get the standard (Pomeron-dominated) Regge behavior (with a Q^2 dependence in the effective Pomeron intercept)

$$F_2^{(S,0)}(x\to 0,Q^2) \to A\ \left(\frac{Q^2}{Q^2+a}\right)^{1+\widetilde{\Delta}(Q^2)}\ \left(\frac{x_0}{x}\right)^{\widetilde{\Delta}(Q^2)}\ \propto x^{-\widetilde{\Delta}(Q^2)}.$$

Within this approximation, the total cross-section for (γ, p) scattering as a function of the center of mass energy W is

$$\sigma_{\gamma,p}^{tot,(0)}(W) = 4\pi^2\alpha \left[\frac{F_2^{(S,0)}(x,Q^2)}{Q^2}\right]_{Q^2\to 0} = 4\pi^2\alpha\, A\, a^{-1-\epsilon}\, x_0^{\epsilon}\, W^{2\epsilon}.$$

Accounting for large x :

$$F_2^{(S)}(x,Q^2) = F_2^{(S,0)}(x,Q^2)\,(1-x)^{n(Q^2)},$$

with

$$n(Q^2) = \frac{3}{2}\left(1 + \frac{Q^2}{Q^2+c}\right),$$

where $c = 3.5489$ GeV^2.

The non-singlet (NS) part of the structure function is also included:

$$F_2^{(NS)}(x,Q^2) = B\,(1-x)^{n(Q^2)}\, x^{1-\alpha_r} \left(\frac{Q^2}{Q^2+b}\right)^{\alpha_r}.$$

The free parameters that appear with this addendum are c, B, b and α_r. The final and complete expression for the proton structure function thus becomes

$$F_2(x,Q^2) = F_2^{(S)}(x,Q^2) + F_2^{(NS)}(x,Q^2)\,.$$

Of great interest are the slopes:

$$\frac{\partial F_2}{\partial(\ell n Q^2)} \text{ as a functionof } x \text{ and } Q^2$$

and

$$\frac{\partial \ell n F_2}{\partial(\ell n(1/x))}$$

as a function of Q^2 for x fixed, showing explicitly the onset of the saturation in x and Q^2, namely the inflection point near $Q^2 = 100$ GeV^2, followed by its flattening around $Q^2 = 4\times 10^3$ GeV^2 for $x \le 10^{-3}$ (see Figs. 5-7 in Ref. [2]).

I thank the Organizers of this Meeting for their hospitality. This work was supported by the "Fundamental Properties of the of the Physical Systems at Extreme Conditions Program" of the Department of Astronomy and Physics, Academy of Sciences of Ukraine.

References

[1] See: R. Fiore, L. Jenkovszky, R. Orava, E. Predazzi, A. Prokudin, and O. Selyugin, *Forward physics at the LHC; Elastic scattaring.* arXiv: hep-ph/0810.2902 and earlier references therein.

[2] P. Desgrolard, L. Jenkovszky, F. Paccanoni, EPJ **C7**, 263 (1999).

Multi-parton interactions and underlying events from Tevatron to LHC

Paolo Bartalini[1†], *Filippo Ambroglini*[2], *Livio Fanò*[3], *Rick Field*[4], *Lucia Garbini*[3], *Daniele Treleani*[2]
[1]National Taiwan University,
[2]University of Trieste,
[3]University of Perugia,
[4]University of Florida.

DOI: http://dx.doi.org/10.3204/DESY-PROC-2009-01/43

Abstract
We give a review of the Multiple Parton Interaction measurement plan at the LHC concentrating on the original Underlying Event and mini-jet feasibility studies. The Tevatron and SPS phenomenological legacies and the most popular Multiple Parton Interaction models are also briefly covered.

1 The QCD models and the Multiple Parton Interaction concept

In the years '80, the evidence for Multiple Parton Interaction (MPI) phenomena in the high-p_T phenomenology of hadron colliders [1] suggested the extension of the same perturbative picture to the soft regime, giving rise to the first implementation of the MPI processes in a QCD Monte Carlo model [2] which was very successfull in reproducing the UA5 charged multiplicity distributions [3].

On top of the general Minimum Bias (MB) observables these MPI models turn out to be particularly adequate to describe the Underlying Event (UE) physics at Tevatron [4], in particular they partly account for the pedestal effect (i.e. the enhancement of the Underlying Event activity with the energy scale of the interaction) as the effect of an increased probability of multiple partonic interactions in case a hard collision has taken place[1].

Examples of MPI models are implemented in the general purpose simulation programs PYTHIA [5], HERWIG/JIMMY [6] and SHERPA [7]. Other successful descriptions of UE and MB at hadron colliders are achieved by alternative approaches like PHOJET [8], which was designed to describe rapidity gaps and diffractive physics (relying on both perturbative QCD and Dual Parton Models). The purely phenomenological UE and MB description available in HERWIG [9] provides a very useful reference of a model not implementing multiple interactions. The most recent PYTHIA versions [10] adopt an optional alternative description of the colliding partons in terms of correlated multi-parton distribution functions of flavours, colors and longitudinal momenta.

[†] speaker

[1] A second important effect that can contribute to the pedestal effect is the increase in initial state radiation associated to the presence of a hard scattering

2 Progress in the study of the Underlying Events

CMS proposes [11] an original refinement to the standard CDF UE analysis in charged jets [4].

The strategy of the measurement is very much along the lines of the CDF one. Charged particle jets are defined using an iterative cone algorithm on charged particles only. The direction of the leading charged jet, which in most cases results from the hard scattering, is used to isolate different hadronic activity regions in the $\eta - \phi$ space and to study correlations in the azimuthal angle ϕ. The plane transverse to the jet direction is where the 2-to-2 hard scattering has the smallest influence and, therefore, where the UE contributions are easier to observe.

The ratios between (uncorrected) UE multiplicity (and momentum) density observables in the "transverse" region, for charged particles with $p_T > 0.9\,\mathrm{GeV/c}$ and with $p_T > 1.5$ GeV/c, are presented in Figure 1, for an integrated luminosity of 100 pb^{-1}. Ratios are shown here as obtained after track reconstruction, without applying additional reconstruction corrections; given the uniform performance of track reconstruction, the ratios presented here at detector level are similar to those at generator level. These ratios show a significant sensitivity to differences between the PYTHIA tunes DW [12], DWT [12] and S0 [13], thus providing a feasible and original investigation method.

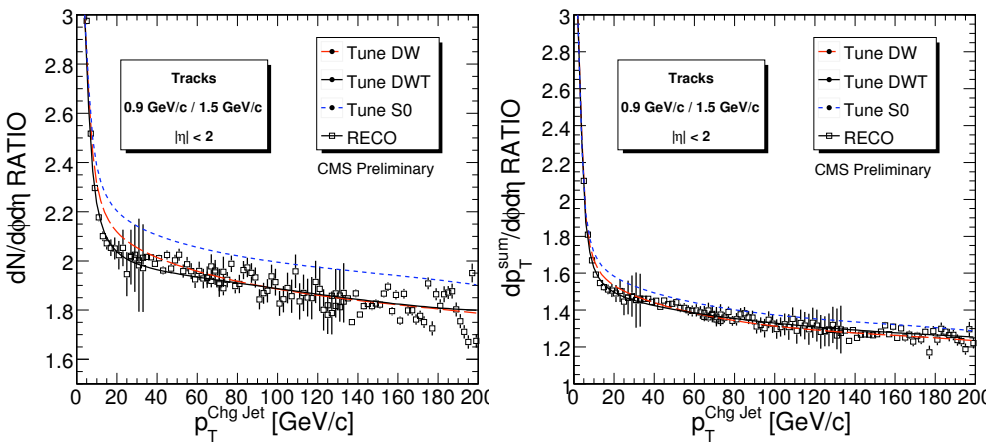


Fig. 1: Ratio of the UE event observables, computed with track transverse momenta $p_T > 1.5$ GeV/c and $p_T > 0.9\,\mathrm{GeV/c}$: densities $dN_{chg}/d\phi d\eta$ (*left*) and $dp_{T.sum}/d\phi d\eta$ (*right*), as a function of the leading charged jet P_T, in the transverse region, for an integrated luminosity of 100 pb^{-1} (uncorrected distributions). The input to the simulation is tune DWT.

3 The Direct Observation of Multiple Partonic Interactions

The final goal of the MPI study is to achieve a uniform and coherent description of MPI processes for both high- and the low-p_T regimes. Recent theoretical progress in this field has been reported [14]. The cross section for a double high-p_T scattering is parameterized as:

$$\sigma_D = \frac{m\sigma_A\sigma_B}{2\sigma_{eff}}$$

where A and B are 2 different hard scatters, m=1,2 for indistinguishable or distinguishable scatterings respectively and σ_{eff} contains the information about the spatial distribution of the partons [15] [16]. In this formalism $m\sigma_B/2\sigma_{eff}$ is the probability that a hard scatter B occurs given a process A and this does strongly depend on the geometrical distribution of the partons inside the interacting hadrons. The LHC experiments will perform this study along the lines of the CDF experiment [17], i.e. studying 3jet+γ topologies [18]. On top of that the extension to the study of same sign W production is also foreseen. Here we would like to propose an original study concentrating on the search for perturbative patterns in MB events looking for mini-jet pair production.

Let's introduce the formalism for the study of MPI in charged particle jet production. We re-write the inelastic cross section as the sum of one soft and one hard component.

$$\sigma_{inel} = \sigma_{soft} + \sigma_{hard} \tag{1}$$

with σ_{soft} the soft contribution to the inelastic cross section σ_{inel}, the two contributions σ_{soft} and σ_{hard} being defined through the cutoff in the momentum exchanged between partons, p_T^c. Notice that, differently from the case of the inclusive cross section (σ_S), which is divergent for $p_T^c \rightarrow 0$, both σ_{hard} and all exclusive contributions to σ_{hard}, with a given number of parton collisions, are finite in the infrared limit.

A simple relationship links the hard cross section to $\langle N \rangle$, i.e. the average number of partonic interactions:

$$\langle N \rangle \sigma_{hard} = \sigma_S \tag{2}$$

While the effective cross section σ_{eff} turns out to be linked to the dispersion $\langle N(N-1) \rangle$:

$$\frac{1}{2}\langle N(N-1) \rangle \sigma_{hard} = \sigma_D \tag{3}$$

These relationships can be used to express σ_{eff} in terms of the statistical quantities related to the multiplicity of partonic interactions:

$$\langle N(N-1) \rangle = \langle N \rangle^2 \frac{\sigma_{hard}}{\sigma_{eff}} \tag{4}$$

This last equation is particularly relevant from an experimental point of view. Indeed, even with a reduced detector acceptance and detection efficiency, one can always measure the physical ob-

servable $\sigma_{hard}/\sigma_{eff}$ that accounts for the probability enhancement of having additional partonic interactions above the scale p_T^c.

We propose to perform this measurement counting the charged particle jet pairs above a minimal scale p_T^c in MB events. Charged particle jets are reconstructed along the lines described in the previous section. First of all the charged jets are p_T-ordered. A pairing criteria is introduced which is based on the maximum difference in azimuth between the charged jets. The pairing algorithm starts from the leading charged jet and associates the first secondary jet in the hierarchy that respects the criteria. The highest p_T of the pair is assumed to be the scale of the corresponding partonic interaction. The paired charged jets are removed from the list and the remnant charged jets are re-processed following the same steps. One end-up with a list of paired charged jets. N is the number of charged pairs above the scale p_T^c.

Fig. 2 shows the difference in azimuth versus the p_T ratio between the first and the second charged jet in the event. Right plot shows the case when both MPI and radiation are switched off to study the sensitivity of the pairing algorithm in a clean hard process. Two cuts have been set to define the pairs: $\Delta\phi > 2.7$ and $p_T\ ratio > 0.25$.

Fig 3 reports σ_{eff} for two different pseudorapidity ranges $|\eta| < 5$ $(left)$ and $|\eta| < 2.4$ $(right)$. As expected σ_{eff} does not depend on the detector acceptance. In the same figures is shown the sensitivity of the pairing algorithm to radiation coming from initial and final state (red points refer to the no-radiation case).

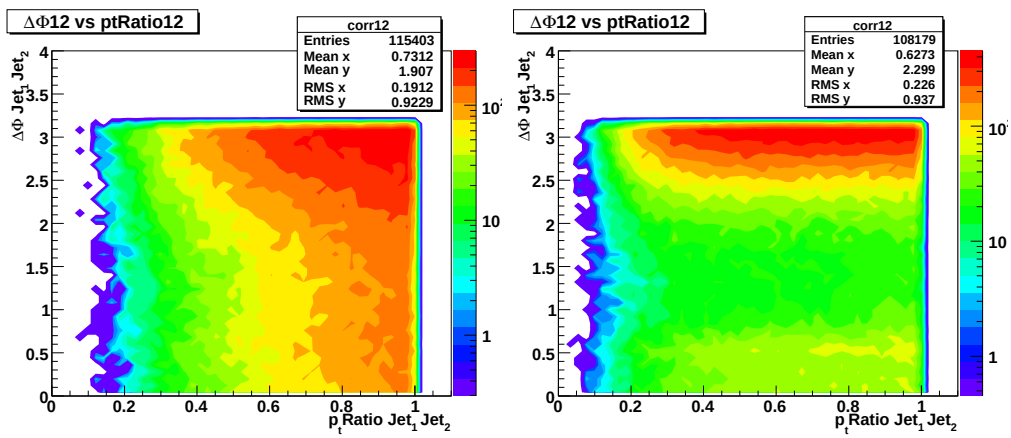


Fig. 2: Delta azimuth versus the p_T ratio between the first and the second charged jets in MB events at the LHC. Right plot is considered as a cross check for the pairing algorithm when Multiple Parton Interactions and radiation processes are switched off. PYTHIA Tune S0 is considered.

Notice that in the result of the simulation the effective cross section does not depend on the acceptance of the detector. One observes the same dependence of σ_{eff} on p_T^{min} also after switching off the radiation. It should be emphasized that this feature would not show up in the simplest model of multiparton interactions, where the distribution in the number of collisions, at fixed hadronic impact parameter, is a Poissonian. In this case one would in fact obtain that the effective cross section is constant not only as a function of the acceptance of the detector, but

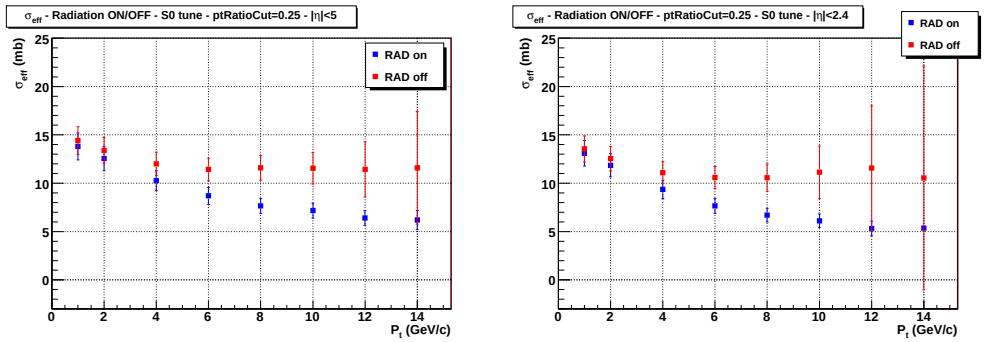


Fig. 3: Effective cross section in MB events at the LHC quoted for mini-jet processes in two different pseudorapidity ranges: $|\eta| < 5$ (left) and $|\eta| < 2.4$ (right) with and without radiation processes (blue and red). PYTHIA Tune S0 is considered.

also as a function of the cutoff. While the matter distribution in the transverse parton coordinates determines the dependence of the average number of multiparton collision on the impact parameter, a cutoff dependent effective cross section might be produced by a distribution in the number of collisions at fixed impact parameter different from a Poissonian. Observing a dependence of σ_{eff} on p_T^{min} one would hence provide evidence of further non trivial correlations effects between partons in the hadron structure. To trace back the origin of the dependence of σ_{eff} on p_T^{min}, observed in the simulation, one might notice that, in the simplest uncorrelated Poissonian model, the impact parameter is chosen accordingly with the value of the overlap of the matter distribution of the two hadrons and independently on value of the cutoff p_T^{min}. In Pythia, on the contrary, events are generated through a choice of the impact parameter which is increasingly biased towards smaller values at large p_T. The correlation induced in this way between the impact parameter of the hadronic collisions and the scale of the interaction has the result of decreasing the behavior of σ_{eff} at large p_T^{min}.

References

[1] Axial Field Spectrometer Collaboration, T. Akesson *et al.*, Z. Phys. **C34**, 163 (1987); UA2 Collaboration, J. Alitti *et al.*, Phys. Lett. **B268**, 145 (1991); CDF Collaboration, F. Abe *et al.*, Phys. Rev. **D47**, 4857 (1993).

[2] T. Sjostrand and M. van Zijl, Phys. Lett. **B188**, 149 (1987).

[3] UA5 Collaboration, G. J. Alner *et al.*, Z. Phys. **C33**, 1 (1986).

[4] CDF Collaboration, A. Affolder *et al.*, Phys. Rev. **D65**, 092002 (2002); CDF Collaboration, D. Acosta *et al.*, Phys. Rev. **D70**, 072002 (2004).

[5] T. Sjostrand *et al.*, Comput. Phys. Commun. **135**, 238 (2001). `hep-ph/0010017`.

[6] J. M. Butterworth, J. R. Forshaw, and M. H. Seymour, Z. Phys. **C72**, 637 (1996). `hep-ph/9601371`.

[7] T. Gleisberg *et al.*, JHEP **02**, 056 (2004). `hep-ph/0311263`.

[8] F. W. Bopp, R. Engel, and J. Ranft (1998). `hep-ph/9803437`.

[9] G. Corcella *et al.*, JHEP **101**, 010 (2001). `hep-ph/0011363`.

[10] T. Sjostrand *et al.*, JHEP **05**, 026 (2006). `hep-ph/0603175`.

[11] P. Bartalini *et al.*, HERA and the LHC - A workshop on the implications of HERA for LHC physics (2007-2008 edition). Proceedings Section WG5 (2009).

[12] CMS Collaboration, D. Acosta *et al.*, CERN CMS-NOTE-2006-067 (2006).

[13] P. Skands and D. Wicke, Eur. Phys. J. **C52**, 133 (2007). hep-ph/0703081.

[14] D. Treleani, Phys. Rev. **D76**, 076006 (2007). 0708.2603.

[15] N. Paver and D. Treleani, Nuovo Cim. **A70**, 215 (1982).

[16] L. Ametller and D. Treleani, Int. J. Mod. Phys. **A3**, 521 (1988).

[17] CDF Collaboration, F. Abe *et al.*, Phys. Rev. **D56**, 3811 (1997);
CDF Collaboration, F. Abe *et al.*, Phys. Rev. Lett. **79**, 584 (1997).

[18] F. Bechtel, HERA and the LHC - A workshop on the implications of HERA for LHC physics (2007-2008 edition). Proceedings Section WG5 (2009).

Multiplicities and the Underlying Event

Deepak Kar
For the CDF Collaboration
University of Florida
DOI: http://dx.doi.org/10.3204/DESY-PROC-2009-01/103

Abstract

CDF Run II data for minimum bias collisions and the underlying event associated with Drell-Yan lepton pair production are presented and how these measurements can give us better insights into the relative importance of the different contributing subprocesses to the 'softer' physics are discussed.

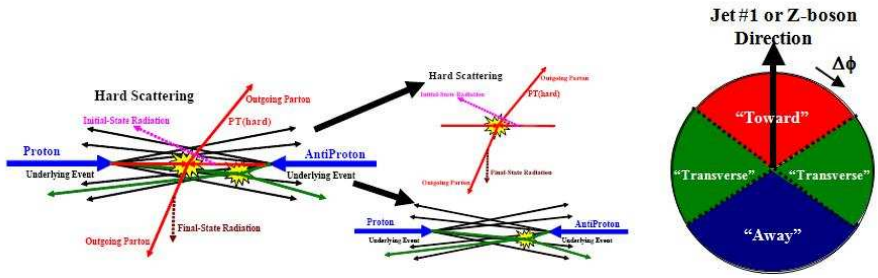
1 Introduction: Minimum Bias Events and the Underlying Event

In order to find 'new' physics at a hadron-hadron collider it is essential to understand and simulate accurately the 'ordinary' QCD hard-scattering events, so that we can discriminate new physics from the complicated background. To do this one must not only have a good model of the hard scattering part of the process, but also of the theoretically poorly understood softer part.

A typical 2-to-2 hard scattering event is a proton-antiproton collision at the hadron colliders as shown in the Figure 1(a), all happening inside the radius of a proton. In addition to the two hard scattered outgoing partons, which fragment into jets - there is initial and final state radiation (caused by bremsstrahlung and gluon emission), multiple parton interaction (additional 2-to-2 scattering within the same event), 'beam beam remnants' (particles that come from the breakup of the proton and antiproton, from the partons not participating in the primary hard scatter). We define the 'underlying event' [1] as everything except the hard scattered components, which includes the 'beam-beam remnants' (or the BBR) plus the multiple parton interaction (or the MPI). However, it is not possible on an event-by-event basis to be certain which particles came from the underlying event and, which particles originated from the hard scattering. The 'underlying event' (*i.e.* BBR plus MPI) is an unavoidable background to most collider observables. For example, at the Tevatron both the inclusive jet cross section and the b-jet cross section, as well as isolation cuts and the measurement of missing energy depend sensitively on the underlying event. A good understanding of it will lead to more precise measurements at the Tevatron and the LHC.

For Drell-Yan lepton pair production, we have the outgoing lepton anti-lepton pair in the final state and there would be no colored final state radiation. Hence it provides a very clean way to study the underlying event.

'Minimum bias event', although different from the underlying event, is another excellent place to look at the 'softer' physics. One selects (*i.e.* 'triggers' on) certain events to store onto tape. Minimum bias (or 'min-bias') is a generic term which refers to events that are selected with a 'loose' trigger. All triggers produce some bias and the term min-bias is meaningless until one specifies the precise trigger used to collect the data. The CDF 'min-bias' trigger consists of requiring at least one charged particle in the forward region $3.2 < \eta < 5.9$ and simultaneously



(a) (b)

Fig. 1: A typical 2-2 hard scattering process and dividing the central region

at least one charged particle in the backward region $-5.9 < \eta < -3.2$. In principle it contains all types of interactions proportionally to their natural production rate.

2 Comparing data with QCD Monte Carlo Models

2.1 Minimum Bias Events

Two of the observables that are experimentally accessible in the minimum bias (or MB) final state are presented here. They are the inclusive charged particle transverse momentum differential cross section $d^3\sigma/p_T dp_T dy d\phi$ and the event transverse energy sum differential cross section $d^3\sigma/dE_T d\eta d\phi$, in the range $p_T > 0.4\ GeV/c$ and $|\eta| < 1$. These two measurements provide some of the basic features of the inelastic inclusive particle production spectra. The measurement of the event transverse energy sum is new to the field and represents a first attempt at describing the full final state including neutral particles. In this regard, it is complementary to the charged particle measurement in describing the global features of the inelastic $p\overline{p}$ cross section.

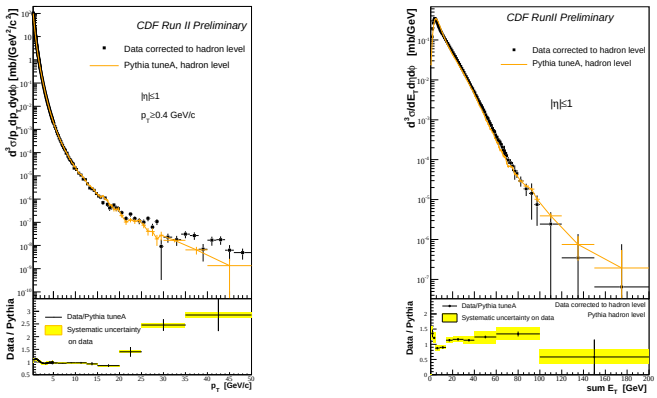
In Fig. 2(a), we show the track p_T differential cross section. PYTHIA tune A [2, 3] was the first model that comes close to describing a wide range of MB experimental distributions. It reproduces the data for inclusive charged particle p_T distribution within 10% up to $p_T > 20$ GeV/c but the data are above the prediction at high p_T. This implies that the tune probably does not have exactly the right fraction of hard 2-to-2 parton-parton scattering and, also, that there is more soft energy in the data than predicted.

In Fig. 2(b), we show the ΣE_T cross-section spectrum. The transverse energy is measured in the central region only as the sum of the E_T of each calorimeter tower in $|\eta| < 1$. This plot shows the fully corrected distribution. The MC generators tuned to reproduce charged particle production fail to reproduce this variable, especially at higher energy ($\Sigma E_T > 50$ GeV). This might be related to the observation that there is an excess of energy in the underlying event in high transverse momentum jet production over the prediction of PYTHIA tune A.

The lower plots show the ratio of data to simulation in each case.

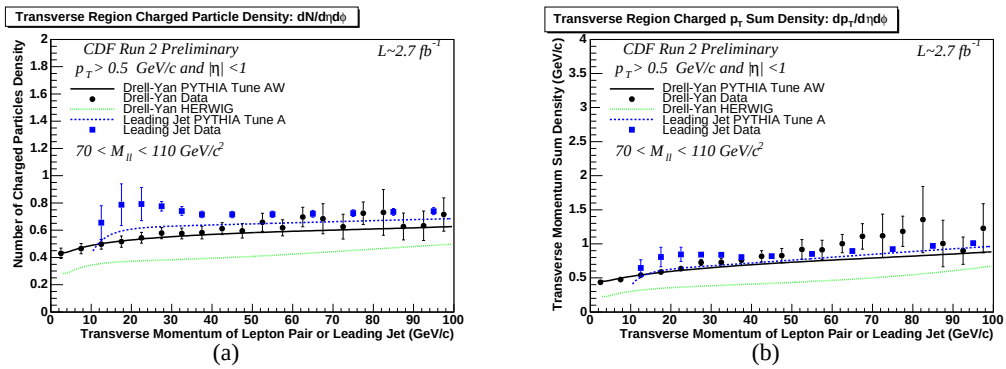
2.2 The Underlying Event with Drell-Yan

Here we study charged particles in the range $p_T > 0.5\ GeV/c$ and $|\eta| < 1$, at the region of Z-boson, defined as $70\ GeV/c^2 < M_{ll} < 110\ GeV/c^2$, in the 'toward', 'away' and 'transverse'



(a) (b)

Fig. 2: Min-bias plots, the track p_T differential cross section at the left and the ΣE_T cross-section on the right



(a) (b)

Fig. 3: Drell-Yan underlying event plots, charged particle multliplicity on the left and the charged p_T sum on the right

regions, as defined in Fig. 1(b). The underlying event observables are found to be reasonably flat with the increasing lepton pair transverse momentum in the transverse and toward regions, but goes up in the away region to balance the lepton pairs. In Fig. 3(a) and Fig. 3(b), we looked at the two observables corresponding to the underlying event, the number of charged particle density and the charged transverse momentum sum density in the transverse region, compared with PYTHIA tunes A and AW [3, 4], HERWIG [5] without MPI and a previous CDF analysis on leading jet underlying event results. We mostly observed very good agreements with PYTHIA tune AW Monte Carlo predictions (HERWIG produces much less activity), although the agreement between theory and data is not perfect. We also compared them with leading jet underlying event results and observed reasonably close agreement - which may indicate the universality of underlying event modeling.

3 Correlation Studies

The rate of change of $< p_T >$ versus charged multiplicity is a measure of the amount of hard versus soft processes contributing to collisions and it is sensitive to the modeling of the multiple parton interactions [6]. This variable is one of the most sensitive to the combination of the physical effects present in MB collisions and is also the most poorly reproduced variable by the available Monte Carlo generators. If only the soft beam-beam remnants contributed to min-bias collisions then $< p_T >$ would not depend on charged multiplicity. If one has two processes contributing, one soft (beam-beam remnants) and one hard (hard 2-to-2 parton-parton scattering), then demanding large multiplicity would preferentially select the hard process and lead to a high $< p_T >$. However, we see that with only these two processes $< p_T >$ increases much too rapidly as a function of multiplicity. Multiple-parton interactions provides another mechanism for producing large multiplicities that are harder than the beam-beam remnants, but not as hard as the primary 2-to-2 hard scattering.

Fig. 4(a) shows the data corrected to the particle level on the average p_T of charged particles versus the multiplicity for charged particles with $p_T > 0.5\ GeV/c$ and $|\eta| < 1$ for Z-boson events from this analysis. HERWIG (without MPI) predicts the $< p_T >$ to rise too rapidly as the multiplicity increases. For HERWIG (without MPI) large multiplicities come from events with a high p_T Z-boson and hence a large p_T 'away-side' jet. This can be seen clearly in Fig. 4(b) which shows the average p_T of the Z-boson versus the charged multiplicity. Without MPI the only way of getting large multiplicity is with high p_T(Z) events. For the models with MPI one can get large multiplicity either from high p_T(Z) events or from MPI and hence $< p_T(Z) >$ does not rise as sharply with multiplicity in accord with the data. PYTHIA tune AW describes the Z-boson data fairly well.

Fig. 4(d) shows the data corrected to the particle level on the average p_T of charged particles versus the multiplicity for charged particles with $p_T > 0.5\ GeV/c$ and $|\eta| < 1$ for Z-boson events in which $p_T(Z) < 10\ GeV/c$ and Fig. 4(c) shows the same distribution for minimum bias events, compared to some PYTHIA Min-Bias production tunings. Regardless of all the improvements in the comprehension of low-p_T production, the models are still unable to reproduce second order quantities such as final state particle correlations. We see that $< p_T >$ still increases as the multiplicity increases although not as fast. If we require $p_T(Z) < 10\ GeV/c$, then HERWIG (without MPI) predicts that the $< p_T >$ decreases slightly as the multiplicity increases. This is because without MPI and without the high p_T 'away-side' jet which is suppressed by requiring low $p_T(Z)$, large multiplicities come from events with a lot of initial-state radiation and the particles coming from initial-state radiation are 'soft'. PYTHIA tune AW describes the behavior of $< p_T >$ versus the multiplicity fairly well even when we select $p_T(Z) < 10\ GeV/c$. This strongly suggests that MPI are playing an important role in both these processes.

4 Summary and Conclusions

We are making good progress in understanding and modeling the softer physics. CDF tunes A and AW describe the data very well, although we still do not yet have a perfect fit to all the features of the CDF underlying event and min-bias data. Future studies should focus on tuning the

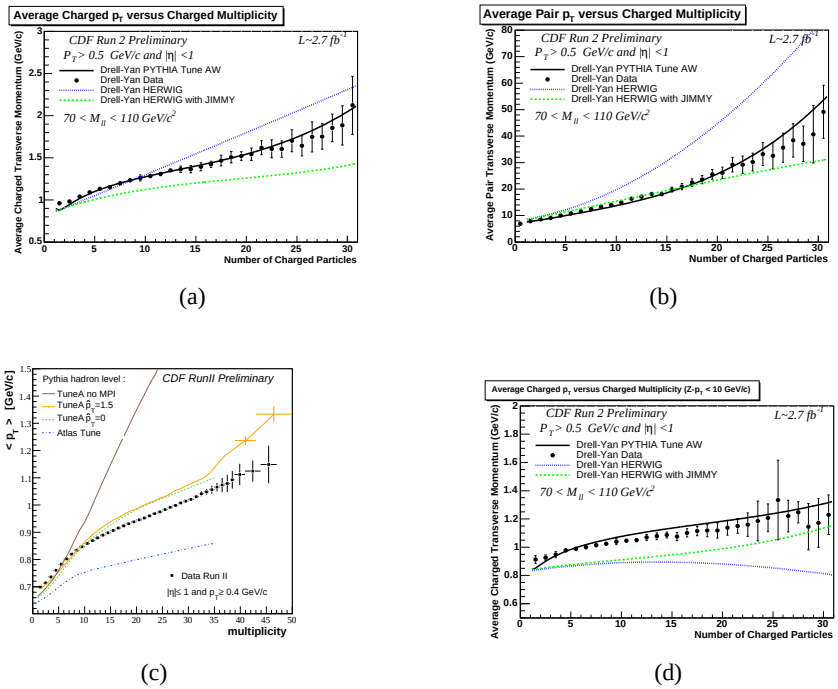


Fig. 4: Charged multiplicity against charged transverse momentum average correlation plots. While (a), (b) and (d) show Drell-Yan data, (c) comes from minimum-bias studies.

energy dependence for the event activity in both minimum bias and the underlying event, which at the moment seems to be one of the least understood aspects of all the models. The underlying event is expected to be much more active in LHC and it is critical to have sensible underlying event models containing our best physical knowledge and intuition, tuned to all relevant available data.

References

[1] CDF Collaboration, D. Acosta *et al.*, Phys. Rev. D **70**, 072002 (2004).

[2] T. Sjostrand *et al.*, Computer Physics Commun. **135**, 238 (2001).

[3] CDF Collaboration, R. Field and R. C. Group (2005). `hep-ph/0510198`.

[4] CDF Collaboration, R. Field. Proceedings of TeV4LHC 2006 Workshop 4th meeting, Batavia, Illinois, 20-22 Oct 2006, `hep-ph/0610012`.

[5] G. Corcella *et al.*, JHEP **1**, 10 (2001).

[6] P. Skands and D. Wicke, Eur. Phys. J. C **52**, 133 (2007).

Saturation effects in final states due to CCFM with absorptive boundary

Krzysztof Kutak[1†], *Hannes Jung*[1,2]
[1] DESY Notkestr 85, 22603, Hamburg, Germany
[2] University of Antwerp

DOI: http://dx.doi.org/10.3204/DESY-PROC-2009-01/112

Abstract
We apply the absorptive boundary prescription to include saturation effects in CCFM evolution equation. We are in particular interested in saturation effects in exclusive processes which can be studied using Monte Carlo event generator CASCADE. We calculate cross section for three-jet production and distribution of charged hadrons.

1 Introduction

At the dawn of LHC it is desirable to have tools which could be safely used to evolve colliding protons to any point of available in collision phase space. It is also desirable to have formulation within Monte Carlo framework because this allows to study complete events (see also contribution of E. Avsar to ISMD 08). At present there are two main approaches within pQCD which can be applied to describe evolution of the parton densities: collinear factorisation with integrated parton densities, with DGLAP as the master equation and k_T factorisation with unintegrated gluon density with BFKL as the master equation [1]. These two approaches resum different perturbative series and are valid in different regimes of the longitudinal momentum fraction carried by the partons. However, they tend to merge at higher orders meaning that one is a source of subleading corrections for the other. The economic way to combine information from both of them is to use the CCFM [2] approach which interpolates between DGLAP and BFKL and which has the advantage of being applicable to Monte Carlo simulation of final states. However, if one wants to study physics at largest energies available at LHC one has to go beyond DGLAP, CCFM or BFKL because all these equations were derived in an approximation of dilute partonic system where partons do not overlap or to put it differently do not recombine. Because of this those equations cannot be safely extrapolated towards high energies, as this is in conflict with unitarity requirements. To account for dense partonic systems one has to introduce a mechanism which allows partons to recombine. There are various ways to approach this problem [3], here we are interested in the one which can be directly formulated within k_T factorisation approach [4]. In this approach one can formulate momentum space version [5] of the Balitsky-Kovchegov equation [6] which sums up large part of important terms for saturation and which is a nonlinear extension of the BFKL equation. As it is a nonlinear equation it is quite cumbersome but one can avoid complications coming from nonlinearity by applying absorptive boundary conditions [7] which mimics the nonlinear term in the BK equation. Here, in order to have description of exclusive processes and account for saturation effects we use CCFM evolution equation together with absorptive boundary implemented in CASCADE Monte Carlo event generator [8].

[†] speaker

In section one we show description of F_2 data using CCFM equation. In section two we describe way to incorporate saturation effects. In section three we show results for angular distribution of three jets and distribution of charged particles.

2 CCFM evolution equation and F_2

The CCFM evolution equation is a linear evolution equation which sums up a cascade of gluons under the assumption that gluons are strongly ordered in an angle of emission. This can be schematically written as: $xA(x,k_T^2,q^2) = xA_0(x,k_T^2,q^2) + K \otimes xA(x,k_T^2,q^2)$ where x is the longitudinal momentum fraction of the proton carried by the gluon, k_T is its transverse momentum and q is a factorisation scale. The initial gluon's distribution $xA_0(x,k_T,\mu^2) = Nx^{Bg}(1-x)^4 exp\left[(k-\mu)^2/\sigma^2\right]$ parameters are to be determined by fit to data. At present we keep parameters μ and σ fixed and fit N and Bg. Using k_T factorisation theorem gluon density coming from the CCFM equation can be applied to calculate F_2 and compare with measurements. In the k_T factorisation approach the observables are calculated via convolution of an off-shell hard matrix element with gluon density. The appropriate formula in schematic form for F_2 reads: $F_2(x,Q^2) = \Phi(x,k_T^2,Q^2) \otimes xA(x,k_T^2,q^2(Q^2))$ where the convolution symbol stands for integration in longitudinal and transversal momenta. From Fig. 1 we see agreement with F_2 measurements. We should however note that at the LHC for processes in the forward region we will probe the gluon density at smaller x than at HERA and unitarity corrections could be visible.

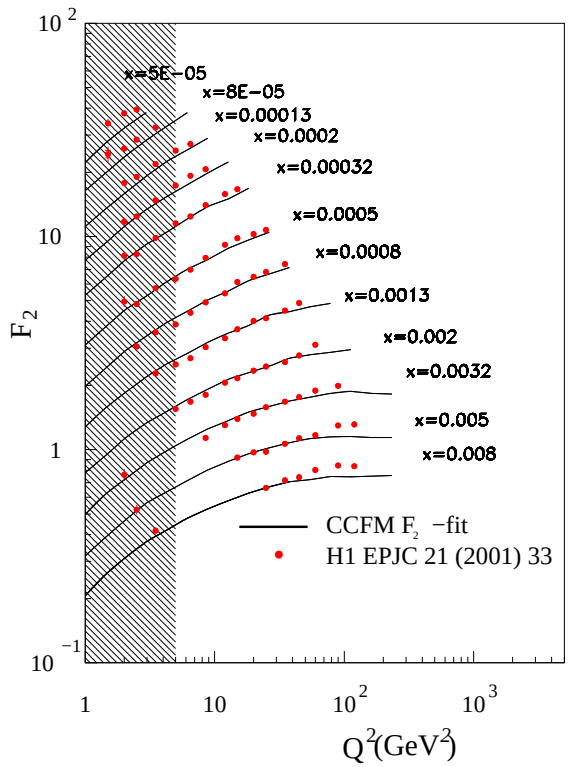


Fig. 1: *F_2 description of HERA data with CCFM evolution equation*

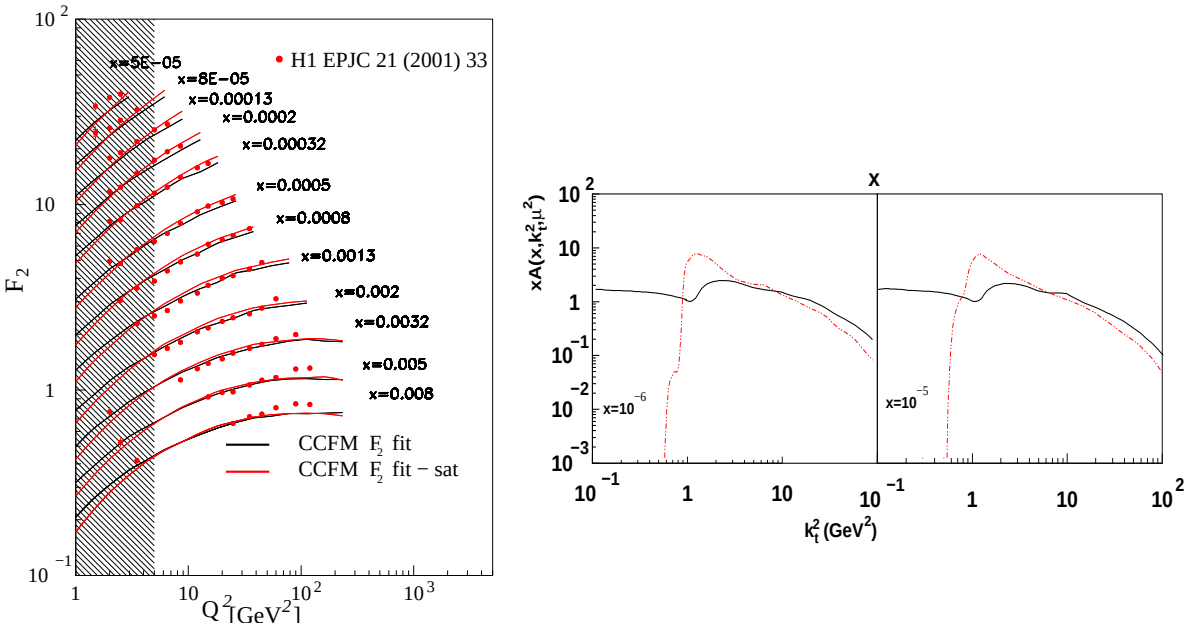


Fig. 2: *(left) F_2 calculated using CCFM with saturation compared to CCFM and to the data. (right) Comparison of gluon density obtained from CCFM with saturation to gluon density from CCFM as a function of k_T^2 for $x = 10^{-5}$, $x = 10^{-6}$*

3 F_2 from CCFM with saturation

The CCFM equation predicts the gluon density which behaves like $A(x, k^2, \mu^2) \sim x^\beta$ and this power like behaviour is in conflict with unitarity bounds. As it has been already stated the way to introduce part of unitarity corrections is to introduce nonlinear terms to the BFKL or CCFM evolution equation. The nonlinearity gives rise to the so called energy dependent saturation scale below which gluon density is suppressed. Following an idea of A. Mueller and D. Triantafyllopoulos we model the saturation effects by introducing an absorptive boundary which mimics the nonlinear term. In the original approach it was required that the BFKL amplitude should be equal to unity for a certain combination of k_T^2 and x. Here we introduce the energy dependent cutoff on transverse gluon momenta which acts as absorptive boundary and slows down the rate of growth of the gluon density. As a prescription for the cutoff we use the GBW [9] saturation scale $k_{sat} = k_0(x_0/x)^{\lambda/2}$ with parameters x_0, k_0, λ to be determined by fit. We are aware of the fact that this approach has obvious limitations since the saturation line is not impact parameter dependent and is not affected by evolution. However, it provides an energy dependent cutoff which is easy to be implemented in a Monte Carlo program, and therefore we consider it as a reasonable starting point for future investigations. We applied our prescription to calculate the F_2 structure function and we obtained good descriptions of HERA data, both in scenario with and without saturation, see Fig. 2. However, the gluon densities which are used in calculation of the F_2 structure function have very different shape and they may have impact on exclusive observables even in HERA range.

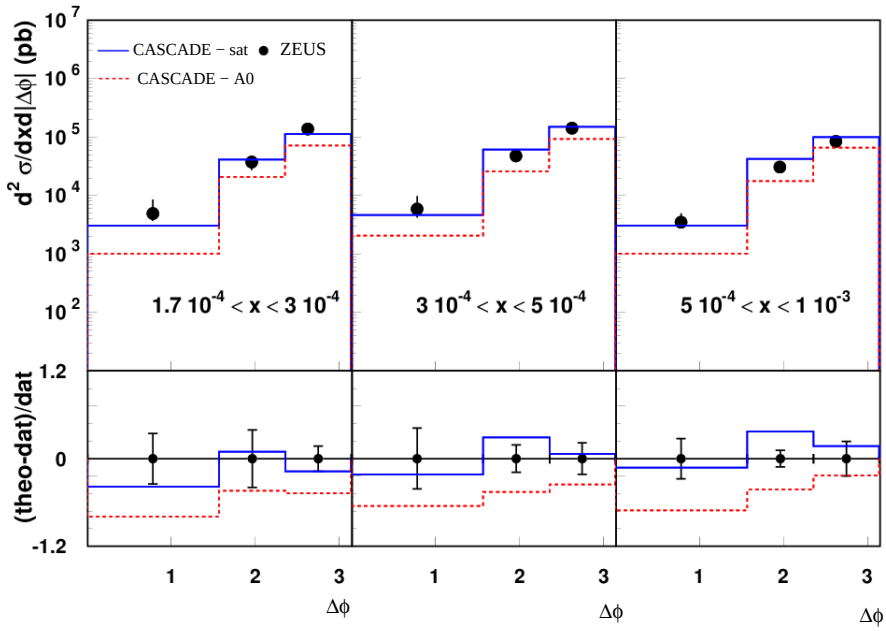


Fig. 3: *(up) Differential cross section for three jet event calculated within CCFM with saturation boundary (blue line) compared to CCFM without saturation (red line). (down) Ratio between theory prediction minus data divided by data*

4 Impact of saturation on exclusive observables

Using the gluon density determined by fit to F_2 data we may now go on to investigate the impact of saturation on exclusive observables. As a first exclusive observable we choose the differential cross section for three jet events in DIS [10]. Here we are interested in the dependence of the cross section on the azimuthal angle $\Delta\phi$ between the two hardest jets. This calculation is motivated by the fact that the produced hard jets are directly sensitive to momentum of the incoming gluon and therefore are sensitive to the gluon k_T spectrum. In the results we see a clear difference between the approach which includes saturation and the one which does not include it. The description with saturation is closer to data suggesting the need for saturation effects. Another observable we choose is the p_T spectrum of produced charged particles in DIS [11]. We compare our calculation with calculation based on CCFM and on DGLAP evolution equations. From the plots Fig. 4 we see that the CCFM with saturation describes data better then the other approaches. CCFM overestimates the cross-section for very low x data while DGLAP underestimates it. This is easy to explain, in CCFM one can get large contributions from larger momenta in the chain due to lack of ordering in k_T while in DGLAP large k_T in the chain is suppressed. On the other hand CCFM with saturation becomes ordered for small x both in k_T and rapidity and therefore interpolates between these two.

5 Conclusions

In this contribution we studied saturation effects in exclusive observables using a Monte Carlo event generator. Including saturation effects we obtained a reasonably good description of DIS data for $\Delta\phi$ distribution of jets Fig. 3 and p_T spectrum of produced charged hadrons Fig. 4. We compared prediction based on an approach with saturation to one which does not include

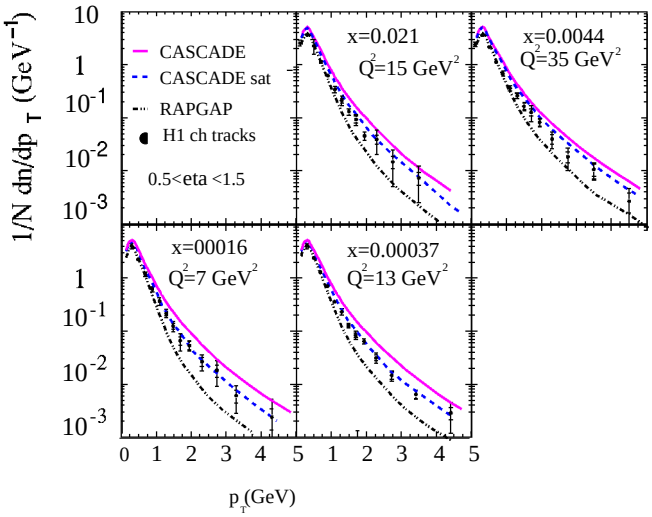


Fig. 4: *Differential cross section for transverse momentum distribution of charged hadrons calculated within CCFM (violet continuous line), CCFM with saturation (dashed blue line) and DGLAP (dotted black line)*

it, and we clearly see that the approach based on saturation gives a better description of the measurements.

Acknowledgments

We would like to thank E.Avsar, G.Gustafson, Al Mueller for useful discussions. Useful comments by G. Gustafson on the manuscript are kindly acknowledged.

References

[1] L. N. Lipatov, Sov. J. Nucl. Phys. **23**, 338 (1976);
E. A. Kuraev, L. N. Lipatov, and V. S. Fadin, Sov. Phys. JETP **44**, 443 (1976);
E. A. Kuraev, L. N. Lipatov, and V. S. Fadin, Sov. Phys. JETP **45**, 199 (1977);
I. I. Balitsky and L. N. Lipatov, Sov. J. Nucl. Phys. **28**, 822 (1978).

[2] M. Ciafaloni, Nucl. Phys. **B296**, 49 (1988);
S. Catani, F. Fiorani, and G. Marchesini, Phys. Lett. **B234**, 339 (1990);
S. Catani, F. Fiorani, and G. Marchesini, Nucl. Phys. **B336**, 18 (1990).

[3] L. V. Gribov, E. M. Levin, and M. G. Ryskin, Phys. Rept. **100**, 1 (1983);
A. H. Mueller and J.-w. Qiu, Nucl. Phys. **B268**, 427 (1986);
A. H. Mueller, Nucl. Phys. **B415**, 373 (1994);
A. H. Mueller and B. Patel, Nucl. Phys. **B425**, 471 (1994). `hep-ph/9403256`;
E. Iancu, A. Leonidov, and L. D. McLerran, Nucl. Phys. **A692**, 583 (2001). `hep-ph/0011241`;
E. Avsar, G. Gustafson, and L. Lonnblad, JHEP **01**, 012 (2007). `hep-ph/0610157`.

[4] S. Catani, M. Ciafaloni, and F. Hautmann, Nucl. Phys. **B366**, 135 (1991).

[5] J. Bartels and K. Kutak, Eur. Phys. J. **C53**, 533 (2008). `0710.3060`.

[6] I. Balitsky, Nucl. Phys. **B463**, 99 (1996). `hep-ph/9509348`;
Y. V. Kovchegov, Phys. Rev. **D60**, 034008 (1999). `hep-ph/9901281`.

[7] A. H. Mueller and D. N. Triantafyllopoulos, Nucl. Phys. **B640**, 331 (2002). `hep-ph/0205167`.

[8] H. Jung, Comput. Phys. Commun. **143**, 100 (2002). `hep-ph/0109102`.

[9] K. J. Golec-Biernat and M. Wusthoff, Phys. Rev. **D59**, 014017 (1999). `hep-ph/9807513`.

[10] F. Hautmann and H. Jung, JHEP **10**, 113 (2008). `0805.1049`.

[11] H1 Collaboration, C. Adloff *et al.*, Nucl. Phys. **B485**, 3 (1997). `hep-ex/9610006`.

Photoproduction total cross-sections at very high energies and the Froissart bound

Y. N. Srivastava[1]†, *A. Achilli*[1], *R. Godbole*[2], *A. Grau*[3], *G. Pancheri*[4]
[1]INFN and Physics Department, University of Perugia, I-06123 Perugia, Italy
[2] Centre for High Energy Physics, Indian Institute of Science,Bangalore, 560012, India
[3]Departamento de Física Teórica y del Cosmos, Universidad de Granada, 18071 Granada, Spain
[4]INFN Frascati National Laboratories, I-00044 Frascati, Italy

DOI: http://dx.doi.org/10.3204/DESY-PROC-2009-01/104

Abstract
A previously successful model for purely hadronic total cross-sections, based on QCD minijets and soft-gluon resummation, is here applied to the total photoproduction cross section. We find that our model in the γp case predicts a rise with energy stronger than in the $pp/\bar{p}p$ case.

1 Introduction

In this note, we shall describe (and apply to data) a model for the total cross-section [1, 2], based on the ansatz that infrared gluons provide the saturation mechanism in the rise of all total cross-sections (thus obeying the Froissart bound), with the rise calculated through the increasing number of hard collisions between low-x, but perturbative gluons. These collisions produce low p_t partons which hadronize in so called mini-jets. We assume that for $p_t \geq 1 \div 2\ GeV$ the parton-parton cross-section can still be calculated perturbatively and set a minimum p_t cut-off, p_{tmin} in the jet cross-section calculation. To make connection with actual phenomenological inputs, the mini-jet cross-sections are calculated [3, 4] using DGLAP evolved parton densities: for the proton we have used GRV [5], MRST [6] and CTEQ [7], for the photon GRS [8] and CJKL [9]. In our model we use only LO densities, as part of the NLO effects are described by soft gluon resummation and the use of NLO would result in some double counting. Similarly, we have opted for tree level parton-parton cross-sections and one loop α_s. As the c.m. energy increases, with fixed p_{min}, these mini-jet cross-sections increase and their contribution to the total cross-section becomes larger than any observed cross-section, violating unitarity. This has resulted in discarding the mini-jet model. Embedding the mini-jet cross-section in the eikonal representation, restores unitarity, but requires modelling of the matter distribution in the colliding particles via an impact parameter distribution. Convolution of the electromagnetic form factors is frequently used and more fundamental attempts exist in the framework of Reggeon calculus and perturbative QCD. Our model focuses on very soft gluons as the source of a dynamical description of the impact factor and its energy dependence. Thus the name Bloch Nordsieck (BN) underlies the infrared region and its resummation. We shall briefly present this model, show its results for purely proton processes, and then apply it to photoproduction processes.

† speaker

2 The Bloch-Nordsieck Model (BN)

Our BN model exhibits fractal behaviours for quantities such as (i) the energy rise of the mini-jet cross-sections for which $\sigma_{jet} \approx s^{\delta}$ with $\delta \approx 0.3$ and (ii) the very low momentum single gluon emission probability which we propose to be proportional to k_t^{-p-1} with $0 < p < 1$, for gluons of transverse momentum k_t .

This model, which was initially developed for purely hadronic total cross-section, incorporates QCD inputs such as parton-parton cross-sections, realistic parton densities, actual kinematics, and soft gluon resummation. We write, for a general process,

$$\sigma_{tot}^{AB} = 2 \int d^2\vec{b}[1 - e^{-n(b,s)/2}] \tag{1}$$

with the imaginary part of the eikonal related to the average number of inelastic collision $n(b, s)$. We isolate all hard perturbatively calculated collisions into

$$n_{hard}(b, s) = A(b, s)\sigma_{jet}(p_{tmin}, s) \tag{2}$$

and phenomenologically determine the remaining collisions which we call $n_{soft}(b, s)$. At present our model is unable to make an *ab initio* calculation of this quantity, and we use a QCD inspired modelling, described in [2].

The impact parameter distribution is obtained from the Fourier transform of the soft gluon transverse momentum, resummed, distribution, namely

$$A(b, s) = \mathcal{N} \int d^2\mathbf{K}_\perp \frac{d^2P(\mathbf{K}_\perp)}{d^2\mathbf{K}_\perp} e^{-i\mathbf{K}_\perp\cdot\mathbf{b}} = \frac{e^{-h(b,q_{max})}}{\int d^2\mathbf{b} e^{-h(b,q_{max})}} \equiv A(b, q_{max}(s)) \tag{3}$$

with

$$h(b, q_{max}(s)) = \int d^3\bar{n}_g(\vec{k})[1-e^{i\mathbf{k}_\perp\cdot\mathbf{b}}] = \frac{16}{3}\int_0^{q_{max}(s)} \frac{dk_t}{k_t}\frac{\alpha_s(k_t^2)}{\pi}\left(\log\frac{2q_{\max}(s)}{k_t}\right)[1 - J_0(k_t b)] \tag{4}$$

In the above equation, we need to extend the integral to zero momentum gluons, which supply the saturation effect of resummation. One needs then an ansatz for the single soft gluon distribution in Eq. 4, namely for $\alpha_s(k_t^2)$ as $k_t \to 0$. Our model for this behaviour is inspired by the Richardson potential, but in order to have a finite result for the integral in Eq. 4 we use

$$\alpha_s = \frac{12\pi}{33 - 2N_f}\frac{p}{\ln[1 + p(\frac{k_t}{\Lambda})^{2p}]}. \tag{5}$$

This expression gives the asymptotic freedom value for large k_t , and is singular (but integrable) at $k_t = 0$ (for $p < 1$). The closer p is to 1, the more the minijet cross-sections will be quenched at any given energy.

The energy dependence of the impact function $A(b, s)$ is introduced through the upper limit of integration in Eq. 4. As amply discussed in ref. [1], the function q_{max} is obtained through an averaging over the parton densities

$$q_{max}(s) = \sqrt{\frac{s}{2}}\frac{\sum\limits_{i,j}\int\frac{dx_1}{x_1}\int\frac{dx_2}{x_2}\int_{z_{min}}^1 dz f_i(x_1)f_j(x_2)\sqrt{x_1x_2}(1-z)}{\sum\limits_{i,j}\int\frac{dx_1}{x_1}\int\frac{dx_2}{x_2}\int_{z_{min}}^1 dz f_i(x_1)f_j(x_2)}, \tag{6}$$

Notice that in our model, the impact parameter distribution depends on the energy and the process under consideration through the parameter $q_{\max}(s)$, which is evaluated using the given parton densities.

The BN model thus described has been applied to proton-proton scattering, obtaining a total cross-section for LHC to be $\sigma(\sqrt{s} = 14\ TeV) = (100 \pm 12)\ mb$, where the error reflects various uncertainties as in the choice of densities, minimum parton p_t cut-off and the IR behaviour of the soft gluon coupling. Our results for proton-proton and proton-antiproton scattering are shown in Fig. 1 with labelling and references defined as in [4].

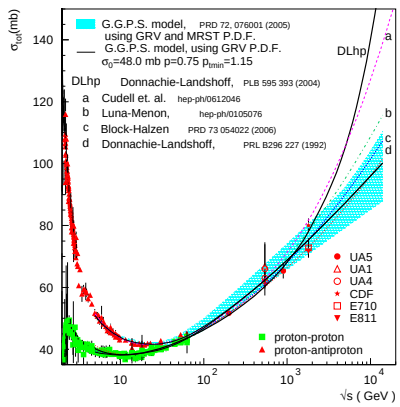


Fig. 1: Data and models for proton-proton and proton-antiproton total cross-section from ref. [4].

3 Photon processes and the total γp cross-section at high energies

Application to photons requires the probability that a photon behaves like a hadron. One possibility is to use Vector Meson Dominance (VMD) in the eikonal representation, as in [10, 11],

$$\sigma_{tot}^{\gamma p} = P_{\gamma \to hadron} \sigma_{tot}^{\gamma_{had} p} = 2 P_{had} \int d^2\vec{b} [1 - e^{-n(b,s)/2}] \tag{7}$$

with $P_{\gamma \to hadron} = 1/240$. As for the proton case, the average number of inelastic collisions, $n(b,s)$, is split between hard collisions calculable as QCD minijets, and a soft part. Hence, the average number of collisions is written as

$$n(b,s) = n_{soft}(b,s) + n_{hard}(b,s) = \frac{2}{3} n_{soft}^{pp}(b,s) + A(b,s)\sigma_{jet}(s)/P_{had} \tag{8}$$

with n_{hard} including all outgoing parton processes with $p_t > p_{tmin}$. The jet cross-sections are calculated using actual photon densities, which themselves give the probability of finding a given quark or gluon in a photon, and thus P_{had} needs to be canceled out in n_{hard}. For the soft part, a good description is obtained with $n_{soft}^{pp}(b,s)$ being the same as in the pp case [4].

The impact function $A(b,s)$ again supplies saturation and is calculated using photon and proton densities in Eq. 6. Once this energy parameter has been calculated, $A(b,s)$ is fully

determined. More fundamental attempts to obtain the impact function for photons can be found in ref. [12].

For γp we show in Fig. 2 both the saturation parameter q_{max} plotted as a function of the γp c.m. energy, as well as the resulting impact parameter function at four representative energies. Unlike other models, based on the convolution of the form factors of the colliding particles, the impact function in the BN model is energy dependent, with a shape shrinking with energy. Both

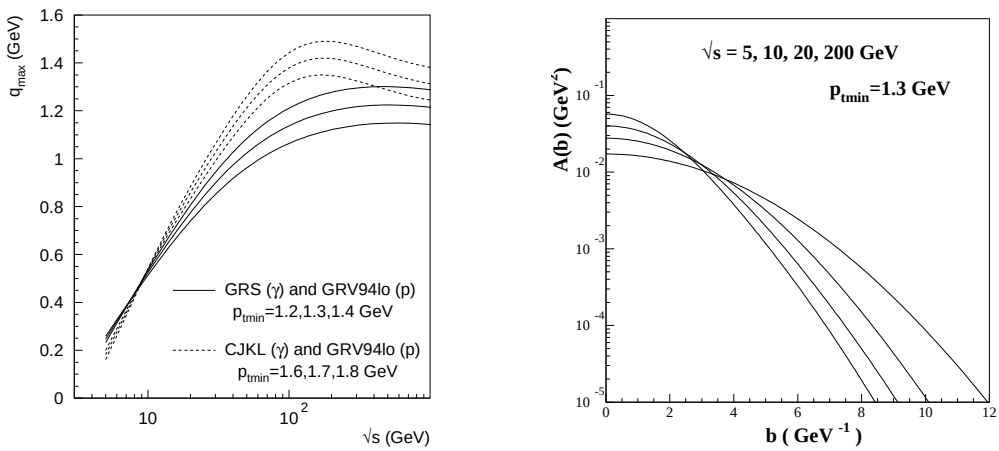


Fig. 2: Left: average maximum tramsverse momenttum allowed to single soft gluon emission in γp scattering. Right: Impact parameter distribution for γp scattering at various c.m. energies

the mini-jet cross-section and the impact function (the latter through q_{max}) for γp depend on the set of Parton Density Functions (PDFs). We choose GRV94 for the proton, GRS and CJKL for the photon, input them into the eikonal and compare the results with HERA data [13, 14], including a set of ZEUS BPC data extrapolated from $\gamma^* p$ to $Q^2_\gamma = 0$ [15]. These results for the BN model are shown in Table 1 for different parameters sets chosen so that all of HERA data are included in a band defined by the last two columns in table 1.

In ref. [16], we have observed that at very high γp energies, our results indicate a faster rise than is the case for proton inspired models. For energies beyond HERA, $q_{\max}(s)$, computed through the photon densities, no longer increases (unlike the proton case) thus blocking saturation earlier than for protons. As a result, since the mini-jet cross-sections keep on increasing, the photon cross-sections, past present accelerator energies, would grow faster than the purely hadronic ones. We have noted [16] that this prediction from our model finds independent support in the fit by Block and Halzen [17] which gives results close to ours in the very high energy region.

G. P. thanks the MIT LNS for hospitality while this work was being written. R.G. aknowledges support from the Department of Science and Technology, India, under the J.C. Bose fellowship. This work has been partially supported by MEC (FPA2006-05294) and Junta de Andalucía (FQM 101 and FQM 437).

Table 1: Values (in mb) for total cross-section for γp scattering evaluated in the c.m. energy of colliding particles, for different parameter sets

$\sqrt{s}$ GeV	EMM with Form Factors $p_{tmin} = 1.5$ GeV	BN_γ model GRS, p=0.75 $p_{tmin} = 1.2$	BN_γ model CJKL, p=0.8 $p_{tmin} = 1.8$	BN_γ GRS, p=0.75 $p_{tmin} = 1.15$
5	0.116	0.116	0.116	0.116
11.46	0.114	0.115	0.114	0.1155
48.93	0.122	0.130	0.121	0.132
112.14	0.139	0.155	0.140	0.16
478.74	0.238	0.228	0.203	0.236
1097.3	0.352	0.279	0.250	0.289
4684.6	0.635	0.384	0.338	0.395
10736.8	0.829	0.449	0.390	0.461
20000	0.985	0.499	0.429	0.512

References

[1] A. Corsetti , A. Grau, G. Pancheri and Y. N. Srivastava, Phys. Lett. **B 382** (1996) 282, hep-ph/9605314; A. Grau, G. Pancheri and Y.N. Srivastava, Phys. Rev. **D60** (1999) 114020, hep-ph/9905228;

[2] R.M. Godbole, A. Grau, G. Pancheri and Y. N. Srivastava, Phys. Rev. **D72** (2005) 076001, hep-ph/0408355.

[3] R.M. Godbole, A. Grau, R. Hegde, G. Pancheri, Y.N. Srivastava, Pramana **66** (2006) 657, hep-ph/0604214.

[4] A. Achilli et al., Phys. Lett. **B659** (2008) 137, hep-ph/0708.3626.

[5] M. Gluck, E. Reya and A. Vogt, Z. Phys. **C53** (1992), 127; Z. Phys., **C67** (1995) 433; Eur. Phys. J. **C5** (1998) 461, hep-ph/9806404.

[6] Martin, A. D. and Roberts, R. G. and Stirling, W. J. and Thorne, R. S., Phys. Lett. **B531** (2002) 216, hep-ph/0201127.

[7] H. Lai et al., Phys. Rev. **D51** (1995) 4763, hep-ph/9410404.

[8] M. Gluck, E. Reya and I. Schienbein, Phys. Rev. **D60** (1999) 054019, hep-ph/9903337.

[9] F. Cornet, P. Jankowski, M. Krawczyk, and A. Lorca, Phys. Rev. **D68** (2003) 014010, hep-ph/0212160.

[10] Raj Gandhi, Ina Sarcevic, Phys. Rev. **D44** (1991) 10-14.

[11] R.S. Fletcher, T.K. Gaisser and F. Halzen, Phys. Lett. **B298** (1993) 442; Phys. Rev. **D45** (1992) 377-381, Erratum-ibid.**D45** (1992) 3279.

[12] J. Bartels, D. Colferai, S. Gieseke, A. Kyrieleis, Phys.Rev. **D66** (2002) 094017. e-Print: hep-ph/0208130.

[13] H1 Collaboration, S. Aid et al., Zeit. Phys. **C69** (1995) 27, hep-ex/9509001.

[14] ZEUS collaboration, S. Chekanov et al., Nucl. Phys. **B627** (2002) 3, hep-ex/0202034.

[15] D. Haidt , *The transition from $\sigma(\gamma^* p)$ to $\sigma(\gamma p)$*, Prepared for 9th International Workshop on Deep Inelastic Scattering (DIS 2001), Bologna, Italy, 27 Apr - 1 May 2001. Published in *Bologna 2001, Deep inelastic scattering* 287-290, and refs. therein; ZEUS Collaboration, J. Breitweg et al., EPJC **7** (1999) 609, DESY-98-121, hep-ex/9809005v1; B. Surrow, DESY-THESIS-1998-004; A. Bornheim, in the *Proceedings of the LISHEP International School on High Energy Physics, Brazil, 1998*, hep-ph/9806021;

[16] R.Godbole. A. Grau, G. Pancheri and Y.N. Srivastava, *Total photoproduction cross-section at very high energy*, submitted to EPJC, hep-ph/0812.1065.

[17] M.M. Block and F. Halzen, Phys.Rev. **D70** (2004) 091901, hep-ph/0405174.

Monte Carlo and large angle gluon radiation

Giuseppe Marchesini
University of Milan–Bicocca and INFN Sezione di Milano–Bicocca, Milan, Italy
DOI: http://dx.doi.org/10.3204/DESY-PROC-2009-01/106

Abstract
I discuss the problem of incorporating recoil effects into the probabilistic QCD evolution scheme based on the picture of colour dipoles as done in recent Monte Carlo programs.

1 Introduction

Generation of events using Monte Carlo methods is an indispensable tool for planning, running and analysing the results of modern high energy experiments. A possibility to generate multi-particle production as a Markov chain of successive independent parton splittings is based on the general property of *factorization of collinear singularities*. For inclusive parton distributions this leads to the DGLAP evolution equations [1] whose generalisation to multi-particle distributions can be achieved in the spirit of jet-calculus [2], with additional account of soft gluon coherence [3–6]. This is done essentially by ordering the angles of successive gluon emissions, which ordering takes full care of the destructive interference contributions in the soft region and preserves the probabilistic parton multiplication picture. In particular, this procedure was applied to construct the HERWIG event generator [5].

An alternative way of dealing with soft gluon interference effects is provided by the "dipole scheme" [4, 7] in which an independently radiating *parton* is replaced by a colourless *dipole* formed by two partons neighbouring in the colour space. Gluon radiation off a dipole is automatically suppressed at angles exceeding the dipole opening angle thus reproducing the angular ordering. The dipole formulation offers a possibility to improve the treatment by taking into consideration logarithmically enhanced effects due to multiple emission of soft gluons at *large angles* with respect to jets. Non-collinear soft gluons dominate inter-jet particle flows in various hard processes. They also complicate the analysis of the so-called *non-global* QCD observables [8], i.e. in observables in which recorded radiation is confined in geometrically definite phase space regions. It is then interesting to involve these corrections into a Monte Carlo code based on dipole emission, including soft radiation away from jets.

In this talk, based on the paper [9] with Yuri Dokshitzer, I discuss a dipole scheme (in the large-N_c approximation) well suited for deriving improved analytic predictions for observables that incorporate large-angle soft gluon radiation effects. However we observe that, once one aims at *beyond the no-recoil (soft) approximation*, treating colour dipoles as independently evolving entities is likely to conflict the collinear factorization. Taking energy ordering as natural from the multi-parton distributions in [4] one does not obtain the correct DGLAP equation. However considering transverse momentum ordering one obtains the DGLAP evolution to leading order with important non-leading corrections. But this ordering does not really reproduce the multi-parton distributions [4].

2 Multiple soft gluons and Monte Carlo

Consider, for simplicity, the generation of quark-antiquark pair $p_a p_b$ plus an ensemble of n secondary *soft* gluons $\gamma^* \to p_a p_b\, q_1\, q_2\, \ldots q_n$. In the planar approximation [4, 10] the distribution is given by a sum of permutation of

$$\frac{(p_a p_b)}{(p_a q_1)\cdots(q_n p_b)}\,. \tag{1}$$

Selecting soft emission $\omega_i \ll E_a \simeq E_b \simeq E = Q/2$ (with E_a, E_b and ω_i the c.m. quark antiquark and gluon energies) one obtains for the generating functional

$$E\partial_E \mathcal{G}(p_a, p_b; E) = \int \frac{d\Omega}{4\pi} \bar{\alpha}_s \, \frac{\xi_{ab}}{\xi_{aq}\xi_{qb}} \Big[u(q)\, \mathcal{G}(p_a, q; \omega)\mathcal{G}(q, p_b; \omega) - \mathcal{G}(p_a, p_b, \omega) \Big]_{\omega = E} \tag{2}$$

with $\bar{\alpha}_s = \frac{N_c \alpha_s}{\pi}$ and $\xi_{ik} = 1 - \cos\Theta_{ik}$. The "source functions" u attached to each parton help to extract an arbitrary final state observable. The fully inclusive measurement, that is when one allows for production of any number of particles with arbitrary momenta, corresponds to setting all $u = 1$. This gives $\mathcal{G}(Q, u = 1) = 1$ corresponding to normalization to the total cross section. Iteration of this equation can be interpreted as parton branching which can be realised as a Monte Carlo (Markov) process. We now discuss first the multiplicities (large angle contributions are correctly included) then the distributions in which recoil is needed.

3 Mean multiplicity

In order to obtain an equation for the multiplicity of secondary partons, one applies to (2) the variational derivative over the probing function $u(q)$ and integrates over q, while setting $u \equiv 1$ for all remaining probing functions (one-particle inclusive measurement). We derive

$$E\partial_E \mathcal{N}(\xi_{ab}) = \int \frac{d\Omega}{4\pi}\, \bar{\alpha}_s \, \frac{\xi_{ab}}{\xi_{aq}\xi_{qb}} \Big[\mathcal{N}(\xi_{qa}) + \mathcal{N}(\xi_{qb}) - \mathcal{N}(\xi_{ab}) \Big]. \tag{3}$$

This formulation leads to the following results:

- resummation of collinear logs and large angle corrections are correctly included here;
- large angle $Q\bar{Q}$ emission in which soft singularities are important are correctly resummed (see [11]);
- non-global jet corrections [8] are correctly treated by (2).

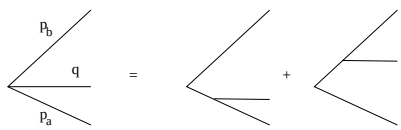
4 Attempt to include recoil in dipole multiplication

The dipole-based evolution equation (2) remains insufficient for building a realistic Monte Carlo event generator as we shall discuss in the following. The simplest observable to consider is the inclusive distribution of the final-state quark. This is obtained by studying the generating functional $\mathcal{G}_{ab}$ with $u = 1$ as function of the energy fraction x of the final-state quark p_a after the emission of any number of soft gluons y_i (here P_a is the incoming quark at the photon vertex)

$$p_a \simeq x\, P_a\,, \qquad x = 1 - \sum_i y_i\,, \qquad \omega_i = y_i\, E\,. \tag{4}$$

We shall restrict ourselves to configurations in which all radiated gluons have small emission angles with respect to the quark direction. This — quasi-collinear — approximation is sufficient for the analysis of the *anomalous dimension* which accumulates collinear singularities of the fragmentation function in all orders and describes the scaling violation. Here one has to consider recoil (see (4)). We start from the elementary process $P_a + P_b \implies p_a + p_b + q$. In order to properly formulate a recoil strategy, one must split the soft dipole radiation function into two pieces which incorporate the collinear singularity when $\vec{q}$ collinear to $\vec{p}_a$ or $\vec{p}_b$, respectively

$$\frac{\xi_{ab}}{\xi_{aq}\xi_{qp_b}} = \widehat{W}^{(a)}_{ab}(q) + \widehat{W}^{(b)}_{ab}(q)\,, \tag{5}$$

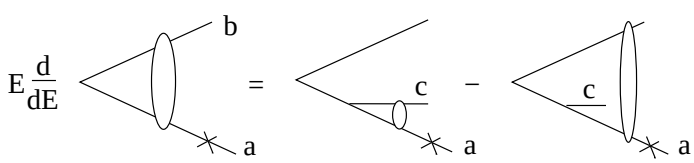


(6)

In the above final-state quark distribution one needs to consider only the splitting $\widehat{W}^{(a)}_{ab}(q)$ which is singular for $\xi_{aq} \to 0$. This distribution essentially becomes irrelevant when the emission angle ξ_{aq} exceeds the opening angle of the parent dipole, $\xi_{aq} > \xi_{ab}$, that is away from the angular ordered kinematics. Upon averaging over the azimuthal angle ϕ_{qa} of the gluon momentum $\vec{q}$ around the singular direction $\vec{p}_a$ one has

$$\int \frac{d\phi_{aq}}{2\pi}\widehat{W}^{(a)}_{ab}(q) = \frac{1}{\xi_{qa}} \cdot \vartheta(\xi_{ab} - \xi_{aq}). \tag{7}$$

Iterating this procedure for all splittings, for the final quark distribution one is left to consider



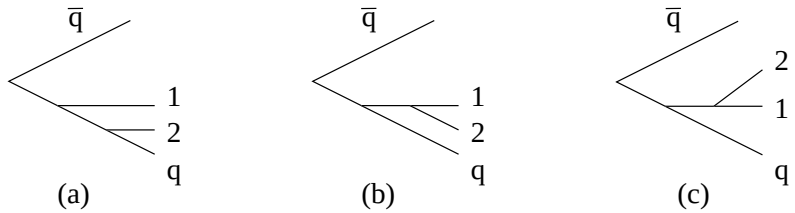
(8)

with only gluons emitted in the lower blob involving the parton a.

And here comes the crucial observation: the emission angle of the gluon c is essentially limited from above by the aperture of the parent dipole ξ_{ab}, see (7). Therefore, soft gluons generated by the evolution equation (8) turn out to be ordered, simultaneously, in energies *and* in angles with respect to the radiating quark. Instead we know that the DGLAP equation is obtained from ordering only in collinear variables, disregarding the relative energies of emitted partons.

The variation is already at two loop order. Consider the splitting (5). For the term $\widehat{W}^{(a)}_{ab}$, following the Catani–Seymour prescription [12], one has $p_b^{(a)} = (1-\eta)P_b$, $p_a^{(a)} = zP_a + (1-z)\eta P_b - k_t$ and $q = (1-z)P_a + z\eta P_b + k_t$ with k_t orthogonal to P_a and P_b. Here z is the light-cone fraction of the parent momentum P_a carried by the final quark p_a. In the collinear limit $\eta \to 0$. In the soft limit both $\eta \to 0$ and $z \to 1$. Consider now the emission of two soft gluons off the parton P_a. The antenna functions that potentially contribute in the collinear limit

(recall that we keep all gluon angles with respect to the quark P_a to be small) are displayed here:



(9)

The first two graphs correspond to the splitting of the dipole $(a1)$:

$$W_{a1}^{(a)}(2) \to \vartheta(\xi_{a1} - \xi_{a2}) \qquad \text{and} \qquad W_{a1}^{(1)}(2) \to \vartheta(\xi_{a1} - \xi_{12}),$$

while the third one is the relevant part of the large-aperture dipole $(1b)$:

$$W_{1b}^{(1)}(2) \to \vartheta(\xi_{1b} - \xi_{12}),$$

Due to the *local* recoil prescription used, only the contribution (a) affects the momentum of the quark q. In the two remaining ones, (b) and (c), the gluon 2 borrows its energy–momentum from the gluon 1 and does not produce any quark recoil. Therefore, these contributions cancel against corresponding virtual corrections in the inclusive quark measurement. In conclusion, within the adopted recoil strategy, only the graph (a) should be kept, and we obtain the following phase space for the two-gluon emission:

$$\xi_{a2} < \xi_{a1} < \xi_{ab} \qquad \text{and} \qquad \omega_2 < \omega_1 < E. \tag{10}$$

The first condition comes from the angular ordering in the graph (9(a)), and the second condition from the energy ordering of successive emissions. We know, however, that in order to obtain the DGLAP equation that properly resums collinear singular contributions, one needs to assemble angular (or, transverse momentum) ordered emissions (the first ordering), regardless to the order of gluon energies (the second one). At the same time, the dipole logic is leading us to the *double-ordered* gluon ensemble, according to (10). What is missing here is actually the coherence of QCD radiation. As well known, a soft gluon ω_2, with $\omega_2 \ll \omega_1 \ll E_a$, could be emitted at large angles ($\xi_{a2} \gg \xi_{a1}$) directly by the original parton $q + p_1 \simeq q$. In the language of Feynman amplitudes, such radiation occurs as a coherent sum of the graphs (b) and (c).

We compute directly the soft contribution (large N) to this second order distribution

$$D_N^{(2)}(Q) \sim \bar{\alpha}_s^2 \int_{1/N}^1 \frac{dy_1}{y_1} \int_{1/N}^{y_1} \frac{dy_2}{y_2} \int_{Q_0}^Q \frac{dq_{1t}}{q_{1t}} \int_{Q_0}^Q \frac{dq_{2t}}{q_{2t}}\, \Theta\left(\frac{q_{t1}}{y_1} - \frac{q_{t2}}{y_2}\right) \tag{11}$$

$$= \frac{\bar{\alpha}_s^2}{4} \ln^2 N \ln^2 \frac{Q}{Q_0} - \frac{\bar{\alpha}_s^2}{6} \ln^3 N \ln \frac{Q}{Q_0}\,,$$

Here the theta-function comes from averaging the distribution as in (7). As a result the first term does not provide the correct correction to the first order distribution $D_N^{(1)}(Q) \simeq -\bar{\alpha}_s \ln N \ln \frac{Q}{Q_0}$.

The situation changes if one considers transverse momentum ordering instead of energy ordering. This would give at two loop

$$D_N^{(2)}(Q) \sim \bar{\alpha}_s^2 \int_{1/N}^1 \frac{dx_1}{x_1} \int_{1/N}^1 \frac{dx_2}{x_2} \int_{Q_0}^Q \frac{dq_{1t}}{q_{1t}} \int_{Q_0}^{q_{1t}} \frac{dq_{2t}}{q_{2t}} \Theta\left(\frac{q_{t1}}{x_1} - \frac{q_{t2}}{x_2}\right) \tag{12}$$

$$= \frac{\bar{\alpha}_s^2}{2} \ln^2 N \ln^2 \frac{Q}{Q_0} - \frac{\bar{\alpha}_s^2}{6} \ln^3 N \ln \frac{Q}{Q_0} .$$

The first order term provides the correction to the leading order anomalous dimension. However the second term requires a compensation, possibly from Sudakov form factors, which are away from the leading order distribution (8). The relevant question here is that energy ordering does reproduce the multi-parton distribution (1) while transverse momentum ordering does not reproduce it, see [9].

5 Conclusions

Monte Carlo generation of QCD events is a quarter century old business, based on the structure of resummation of *collinear enhanced* Feynman diagram contributions. *Collinear-non-enhanced* ("large angle") soft gluon radiation provides significant corrections to global event characteristics (e.g., mean particle multiplicity) and determines the structure of various *non-global* observables [8]. Effects of multiple soft gluon radiation at large angles lie beyond the scope of the standard (collinear) approach and must be treated order by order in perturbation theory (while collinear enhanced contributions are resummed in all orders).

An elegant expression [4] for the multiple soft gluon production probability is valid for *arbitrary angles* and offers a possibility of improving the parton picture. The structure of multi-gluon distribution naturally suggests an interpretation in terms of a chain of *colour connected dipoles*. By using energy ordering of gluons this chain may be generated via a Markov process of successive dipole splittings, see [9]. The generating functional that we have constructed allows one to calculate specific effects due to multiple emission of soft gluons at large angles in the large-N_c approximation. In order to construct a realistic Monte Carlo generator for multi-parton ensembles it is imperative, however, to formulate an adequate recoil prescription which would ensure energy–momentum conservation at every successive step of the parton (dipole) multiplication. In the present paper we addressed the question, whether the "dipole factorization" extends beyond the no-recoil approximation. By keeping energy ordering as a prescription to generate the multi-parton distributions (1), we have shown that a naive implementation of the dipole recoil strategy results in violating the collinear factorization, see (11) and [9].

There exists a number of Monte Carlo implementations of the dipole picture, see [13], which use transverse momentum ordering. This formulation does not produces the multi-parton distribution (1). It satisfies collinear factorization, see (12), but generates non leading pieces which needs to be cancelled. We are looking forward to learning from the experts.

Acknowledgements

This paper is based on a work done with Yuri Dokshitzer [9]. We are especially grateful to Walter Giele, Gösta Gustafson, David Kosower, Hannes Jung, Leif Lönnblad, Zoltan Nagy, Gavin

Salam, Jim Samuelsson, Mike Seymour, Torbjorn Sjöstrand, Peter Skands, Davidson Soper, Stefan Weinzierl and Bryan Webber for illuminating discussions.

References

[1] V.N. Gribov, L.N. Lipatov, Sov.J.Nucl.Phys. 15 (1972) 438; G. Altarelli and G. Parisi, Nucl. Phys. B126 (1977) 298; Yu.L. Dokshitzer, Sov. Phys. JETP 46 (1977) 641.

[2] K. Konishi, A. Ukawa and G. Veneziano, Nucl. Phys. B157 (1979) 45.

[3] A.H. Mueller, Phys. Lett. 104B (1981) 161; B.I. Ermolayev and V.S. Fadin, JETP Lett. 33 (1981) 285; A. Bassetto, M. Ciafaloni, G. Marchesini and A. H. Mueller, Nucl. Phys. B 207 (1982) 189; Yu.L. Dokshitzer, V.S. Fadin and V.A. Khoze, Zeit. Phys. C15 (1982) 325; *ibid* C18 (1983) 37.

[4] A. Bassetto, M. Ciafaloni and G. Marchesini, Phys. Rept. 100 (1983) 201.

[5] G. Marchesini and B.R. Webber, Nucl. Phys. B238 (1984) 1, and B310 (1988) 461.

[6] Yu.L. Dokshitzer, V.A. Khoze, A.H. Mueller and S.I. Troian, *Basics of Perturbative QCD*, Editions Frontières, Gif-sur-Yvette, 1991.

[7] G. Gustafson, Phys. Lett. B175 (1986).

[8] M. Dasgupta and G.P. Salam, Phys. Lett. B512 (2001) 323 and JHEP 0203 (2002) 017; A. Banfi, G. Marchesini and G. Smye, JHEP 0208 (2002) 006; R.B. Appleby and M.H. Seymour, JHEP 0212 (2002) 063; C.F. Berger, T. Kucs and G. Sterman, Phys. Rev. D65 (2002) 094031 and Phys. Rev. D68 (2003) 014012; Yu.L. Dokshitzer and G. Marchesini, JHEP 0303 (2003) 040.

[9] Yu.L. Dokshitzer and G. Marchesini, *Monte Carlo and large angle gluon emission* [arXiv:0809.1749].

[10] S. J. Parke, T.R. Taylor, Phys. Rev. Lett. 56 (1986) 2459.

[11] G. Marchesini and A.H. Mueller, Phys. Lett. B575 (2003) 37; G. Marchesini and E. Onofri, JHEP 0407 (2004) 031.

[12] S. Catani and M. Seymour, Nucl. Phys. B485 (1997) 291, Erratum-ibid. B510 (1998) 503.

[13] T. Sjostrand, S. Mrenna, P. Skands, JHEP 0605 (2006) 026; L. Lonnblad, Comput. Phys. Cmmun.71 (1992) 15; Z. Nagy and D.E. Soper, JHEP 0803 (2008) 030 and JHEP 0807 (2008) 025; W.T. Giele, D.A. Kosower and P.Z. Skands, Phys. Rev. D78 (2008) 014026; M. Dinsdale, M. Ternick, S. Weinzierl, Phys.Rev. D76 (2007) 094003.

Production amplitudes in $N = 4$ SUSY and Mandelstam cuts

J. Bartels[1], *L.N. Lipatov*[2†]
[1] Hamburg University, Germany
[2] Petersburg Nuclear Physics Institute, Russia, Hamburg University, Germany

DOI: http://dx.doi.org/10.3204/DESY-PROC-2009-01/107

Abstract
Pomeron in QCD is a composite state of reggeized gluons. The BDS ansatz for production amplitudes in the planar approximation for $N = 4$ SUSY is not valid beyond one loop due to the presence of the Mandelstam cuts. The hamiltonian for the corresponding composite states in the adjoint representation coincides with the hamiltonian of an integrable open Heisenberg spin chain.

1 BFKL Pomeron and anomalous dimensions

In the leading and next-to-leading approximations fo QCD and the supersymmetreic gauge theories the high energy production amplitude in the planar approximation has the multi-Regge form [1–3], which gives a possibility to write a Bethe-Salpeter-type equation for the total cross-section σ_t. The corresponding Pomeron wave function satisfies the equation of Balitsky, Fadin, Kuraev and Lipatov (BFKL) [1]

$$E\,\Psi(\vec{\rho}_1,\vec{\rho}_2) = H_{12}\,\Psi(\vec{\rho}_1,\vec{\rho}_2)\;,\;\Delta = -\frac{\alpha_s N_c}{2\pi}\,E\;,\;\sigma_t \sim s^{\Delta_{max}}\,. \tag{1}$$

It is important, that the BFKL Hamiltonian H_{12} in the coordinate representation ρ is invariant under the Möbius transformations [4, 5].

One can write the Bartels-Kwiecinski-Praszalowicz (BKP) equation [6] for colorless composite states of several reggeized gluons and the correspondin hamiltonian in the large-N_c-limit has the separable form [7]

$$E\,\Psi = \frac{1}{2}(h + h^*)\,\Psi\;,\quad h = \sum_{k<l} h_{kl}\,, \tag{2}$$

$$h_{12} = \ln(p_1 p_2) + \frac{1}{p_1}\,\ln(\rho_{12})\,p_1 + \frac{1}{p_2}\,\ln(\rho_{12})\,p_2 - 2\psi(1)\,. \tag{3}$$

Apart from the Möbius invariance h has the duality symmetry [8]

$$p_k \to \rho_{k,k+1} \to p_{k+1} \tag{4}$$

and n integrals of motion q_r, q_r^* [9]. The operators h and h^* are local hamiltonians of the integrable Heisenberg spin model [10]. As usual, for the integrable system one can introduce the transfer (T) and monodromy (t) matrices according to the definitions [9]

$$T(u) = Tr\,t(u) = \sum_{r=0}^{n} u^{n-r}\,q_r\;,\quad t(u) = L_1(u)L_2(u)...L_n(u)\,, \tag{5}$$

† speaker

$$L_k(u) = \begin{pmatrix} u + \rho_k\, p_k & p_k \\ -\rho_k^2\, p_k & u - \rho_k\, p_k \end{pmatrix}, \quad t(u) = \begin{pmatrix} A(u) & B(u) \\ C(u) & D(u) \end{pmatrix}. \tag{6}$$

The matrix elements $A(u), B(u), C(u), D(u)$ satisfy some bilinear commutation relations following from the Yang-Baxter equation [9] which can be solved with the use of the Bethe ansatz and the Baxter-Sklyanin approach [11, 12].

One can calculate next-to-leading corrections to the BFKL equation [13]. The eigenvalue of its kernel $\Delta(n, \gamma)$ does not contain the non-analytic terms $\delta_{|n|,0}$ and $\delta_{|n|,2}$ only in $N = 4$ SUSY [3]. Further, all functions entering this expression have the property of the maximal transcendentality [14]. This property is valid also for the anomalous dimensions of twist-2 -operators in $N = 4$ SUSY [15, 16] contrary to the case of QCD [17]. One can calculate the higher loop corrections with the use of the effective action [18, 19].

The leading Pomeron singularity in $N = 4$ SUSY should be situated in the strong coupling regime near the point $j = 2$ coinciding with the graviton Regge pole. This conclusion is related to the AdS/CFT correspondence, formulated in the framework of the Maldacena hypothesis claiming, that $N = 4$ SUSY is equivalent to the superstring model living on the 10-dimensional anti-de-Sitter space [20–22]. In this case according to Ref. [21] the eigenvalue for the BFKL hamiltonian in the diffusion approximation coincides with the expression for the graviton Regge trajectory [16]. From the knowledge of this trajectory at large $\hat{a}$ and j [23] one can calculate the explicit expression for the Pomeron intercept at large coupling constants $j = 2 - \hat{a}^{-1/2}/2\pi$ [16, 24].

More then ten years ago it was argued [25], that for $N = 4$ SUSY the evolution equations for anomalous dimensions of quasi-partonic operators are integrable in LLA. Later such integrability was generalized to other operators [26] and to higher loops [27]. With the use of the maximal transcendentality and integrability the equation for the cusp anomalous dimension was constructed in all orders of perturbation theory [28, 29]. Later the anomalous dimension of twist-2 operators in four loops was calculated [30]. After taking into account the wrapping effects [31] the obtained expressions agree with the BFKL predictions [3, 14].

2 Two gluon production amplitudes and the Mandelstam cuts

For the case of the maximal helicity violation in $N = 4$ SUSY Bern, Dixon and Smirnov suggested a simple ansatz for the multi-gluon scattering amplitude in the planar limit $\alpha N_c \sim 1$ [32]. It can be expressed as a product of an infraredly divergent factor and some special functions.

Recently the BDS ansatz was investigated in the multi-Regge kinematics [33] (see also Ref. [34]). It turns out, that the elastic amplitude has the Regge asymptotics and the amplitude for one gluon production has the multi-Regge form in an agreement with the Steinman relations [33]. However, for two gluon production in the physical kinematical region, where $s, s_2 > 0$ but $s_1, s_3 < 0$ the Regge factorization for the BDS amplitude is broken [33]. A similar situation is valid for the BDS amplitude describing the transition $3 \to 3$ in the region, where $s, s_2 = t_2' > 0$ but $s_1, s_3 < 0$. The reason for the breakdown of the Regge factorization is that the production amplitudes in these regions should contain the Mandelstam cuts in the j-pane of the t_2-channel [33]. It means, that the BDS amplitudes are not correct beyond 1 loop.

In the elastic amplitude the cut in the j-plane appears only in the non-planar diagrams

because the integrals over the Sudakov variables $\alpha = 2kP_A/s$ and $\beta = 2kp_B$ for the reggeon momenta k and $q-k$ should have the singularities above and below the corresponding integration contours. For the case of planar diagrams this condition is fulfilled only for the multi-particle amplitudes starting from six external particles in the region $s, s_2 > 0$ and $s_1, s_3 < 0$. The imaginary part of the amplitude $A_{2\to4}$ in the s_2-channel can be written in terms of the BFKL-like equation for the state in the adjoint representation [33]. One can obtain the exact solution of this equation [35]

$$\Im M_{2\to4} \sim s_2^{\omega(t_2)} \sum_{n=-\infty}^{\infty} \int_{-\infty}^{\infty} \frac{d\nu}{\nu^2 + \frac{n^2}{4}} \left(\frac{q_3^* k_1^*}{k_2^* q_1^*}\right)^{i\nu - \frac{n}{2}} \left(\frac{q_3 k_1}{k_2 q_1}\right)^{i\nu + \frac{n}{2}} s_2^{\omega(\nu,n)} . \tag{7}$$

The eigenvalue of the reduced BFKL kernel is

$$\omega(\nu, n) = -a\left(\psi(i\nu + \frac{|n|}{2}) + \psi(-i\nu + \frac{|n|}{2}) - 2\psi(1)\right) . \tag{8}$$

This result is in a disagreement with the BDS ansatz starting from two loops. The leading singularity of the t_2-partial wave corresponds to $n = 1$ and is situated at $j - 1 = \omega(t_2) + a(4\ln 2 - 2)$.

3 Integrability for multi-gluon composite states

Here we shall discuss the Mandelstam cuts constructed from several reggeons [36]. The non-vanishing contribution from the exchange of $n+1$ reggeons appears in the planar diagrams only if the number of external lines is $r \geq 2n + 4$. The Green function describing the interaction of n reggeized gluons in the adjoint representation satisfies the BFKL equation with the integral kernel [36]

$$K = \omega(t) - \frac{g^2 N_c}{16\pi^2} H , \quad \omega(t) = a\left(\frac{1}{\epsilon} - \ln\frac{-t}{\mu_2}\right) , \quad t = -|q|^2 . \tag{9}$$

The reduced Hamiltonian H has the property of the holomorphic separability [36]

$$H = h + h^* , \; h = \ln\frac{p_1\, p_{n+1}}{q^2} + \sum_{l=1}^{n} h_{l,l+1} . \tag{10}$$

With the use of the duality transformations (cf. [8])

$$p_1 = z_{0,1} , \quad p_r = z_{r-1,r} , \quad q = z_{0,n} , \quad \rho_{r,r+1} = i\frac{\partial}{\partial z_r} = i\partial_r \tag{11}$$

one can present the holomorphic hamiltonian h in the form invariant under the Möbius transformations, which gives a possibility to put $z_0 = 0 , \; z_n = \infty$. For this choice of these coordinates one can present h as follows [36]

$$\ln(z_1^2\partial_1) + \ln(\partial_{n-1}) + 2\gamma + \sum_{r=1}^{n-2} h_{r,r+1} , \tag{12}$$

where $h_{r,r+1}$ coincides in fact with the expression (3) after the substitution $\rho_r \to z_r$.

One can verify the commutativity of h with the matrix element $D(u)$ of the monodromy matrix (6) introduced for the description of integrability of the BKP equations in the multi-color QCD [36]

$$[D(u), h] = 0\,. \tag{13}$$

Moreover, h coincides with the local hamiltonian of the open integrable Heisenberg model in which spins are generators of the Möbius group.

To solve this model we can use the algebraic Bethe ansatz. For this purpose it is convenient to go to the transposed space, where the pseudo-vacuum state Ψ_0 can be written in the simple form

$$\Psi_0 = \prod_{r=1}^{n-1} z_r^{-2}\,, \quad C^t(u)\Psi_0 = 0\,. \tag{14}$$

Here the operator $C^t(u)$ is the transposed matrix element $C(t)$ of the monodromy matrix (6). The eigenfunctions of h and $D(u)$ are constructed in the framework of the Baxter-Sklyanin approach by applying the product of the Baxter functions $Q(u)$ to the pseudovacuum state

$$\Psi = \prod_{r=1}^{n} Q^t(\hat{u}_r)\,\Psi_0\,, \tag{15}$$

where the operators $\hat{u}_r$ are zeroes of the matrix element $B(u)$ of the monodromy matrix $t(u)$. The Baxter function satisfies the Baxter equation which is reduced to the simple recurrent relation

$$\Lambda(u)\,Q(u) = (u+i)^{n-1}\,Q(u+i)\,. \tag{16}$$

The function $\Lambda(u)$ is an eigenvalue of the integral of motion $D(u)$ and can be written in terms of its roots

$$D(u)\,\Psi_{a_1,a_2,\ldots,a_{n-1}} = \Lambda(u)\,\Psi_{a_1,a_2,\ldots,a_{n-1}}\,, \quad \Lambda(u) = \prod_{r=1}^{n-1}(u - ia_r)\,. \tag{17}$$

As a result, one can present the solution of the Baxter equation in the form [36]

$$Q(u) = \prod_{r=1}^{n-1} \frac{\Gamma(-iu - a_r)}{\Gamma(-iu+1)}\,. \tag{18}$$

The composite state Regge trajectory has the additivity property

$$\omega_n(t) = \omega(t) - \frac{a}{2}\,E\,, \quad E = \sum_{r=1}^{n-1}\epsilon(a_r) + \sum_{r=1}^{n-1}\epsilon(\widetilde{a}_r)\,, \tag{19}$$

where

$$\epsilon(a) = \psi(a) + \psi(1-a) - 2\psi(1)\,, \quad a_r = i\nu_r + \frac{n_r}{2}\,. \tag{20}$$

For three gluon composite state in the adjoint representation one can find an explicit solution of these equations in the momentum space [36]

$$\Psi^t(\vec{p}_1,\vec{p}_2) = (p_1+p_2)^{-a_1-a_2}(p_1^*+p_2^*)^{-\widetilde{a}_1-\widetilde{a}_2}\int d^2u\,\phi(u,\widetilde{u})\,\left(\frac{p_1}{p_2}\right)^{-iu}\,\left(\frac{p_1^*}{p_2^*}\right)^{-i\widetilde{u}}\,, \tag{21}$$

where

$$-iu = i\nu_u + \frac{N_u}{2}\,, \quad -i\widetilde{u} = i\nu_u - \frac{N_u}{2}\,, \quad \int d^2u \equiv \int_{-\infty}^{\infty} d\nu_u \sum_{N_u=-\infty}^{\infty}\,. \tag{22}$$

and

$$\phi(u,\widetilde{u}) = u\,\widetilde{u}\,Q(u,\widetilde{u})\,, \tag{23}$$

where

$$Q(u,\widetilde{u}) \sim \frac{\Gamma(iu)\Gamma(i\widetilde{u})}{\Gamma(1-iu)\,\Gamma(1-i\widetilde{u})}\,\frac{\Gamma(-iu-a_1)\,\Gamma(-iu-a_2)}{\Gamma(1+i\widetilde{u}+\widetilde{a}_1)\Gamma(1+i\widetilde{u}+\widetilde{a}_2)} \tag{24}$$

in an accordance with the Baxter-Sklyanin representation [11].

Acknowledgments

I thank L.D. Faddeev and A. Sabio Vera for helpful discussions.

References

[1] L. N. Lipatov, Sov. J. Nucl. Phys. **23** (1976) 338;
V. S. Fadin, E. A. Kuraev, L. N. Lipatov, Phys. Lett. B **60** (1975) 50;
E. A. Kuraev, L. N. Lipatov, V. S. Fadin, Sov. Phys. JETP **44** (1976) 443 ; **45** (1977) 199;
I. I. Balitsky, L. N. Lipatov, Sov. J. Nucl. Phys. **28** (1978) 822.

[2] V. S. Fadin, R. Fiore, M. I. Kotsky, Phys. Lett. B **387** (1996) 593.

[3] A. V. Kotikov, L. N. Lipatov, Nucl. Phys. B **582** (2000) 19.

[4] L. N. Lipatov, Phys. Lett. B **309** (1993) 394.

[5] L. N. Lipatov, Sov. Phys. JETP **63** (1986) 904.

[6] J. Bartels, Nucl. Phys. **B175** (1980) 365;
J. Kwiecinski, M. Praszalowicz, Phys. Lett. **B94** (1980) 413.

[7] L. N. Lipatov, Phys. Lett. B **251** (1990) 284.

[8] L. N. Lipatov, Nucl. Phys. B **548** (1999) 328.

[9] L. N. Lipatov *High energy asymptotics of multi-colour QCD and exactly solvable lattice models*, Padova preprint DFPD/93/TH/70, hep-th/9311037, unpublished.

[10] L. N. Lipatov, JETP Lett. **59** (1994) 596;
L. D. Faddeev, G. P. Korchemsky, Phys. Lett. B **342** (1995) 311.

[11] H. J. de Vega, L. N. Lipatov, Phys. Rev. **D64** (2001) 114019; **D66** (2002) 074013-1;

[12] S. E. Derkachov, G. P. Korchemsky, A. N. Manashov, Nucl. Phys. **B617** (2001) 375.

[13] V. S. Fadin, L. N. Lipatov, Phys. Lett. B **429** (1998) 127;
M. Ciafaloni and G. Camici, Phys. Lett. B **430** (1998) 349.

[14] A. V. Kotikov, L. N. Lipatov, Nucl. Phys. B **661** (2003) 19.

[15] A. V. Kotikov, L. N. Lipatov, V. N. Velizhanin, Phys. Lett. B **557** (2003) 114.

[16] A. V. Kotikov, L. N. Lipatov, A. I. Onishchenko, V. N. Velizhanin, Phys. Lett. B **595** (2004) 521; [Erratum-ibid. B **632** (2006) 754].

[17] S. Moch, J. A. M. Vermaseren, A. Vogt, Nucl. Phys. B **688** (2004) 101.

[18] L. N. Lipatov, Nucl. Phys. B **452** (1995) 369; Phys. Rept. **286** (1997) 131.

[19] E. N. Antonov, L. N. Lipatov, E. A. Kuraev, I. O. Cherednikov, Nucl. Phys. B **721** (2005) 111.

[20] J. M. Maldacena, Adv. Theor. Math. Phys. **2** (1998) 231.

[21] S. S. Gubser, I. R. Klebanov, A. M. Polyakov, Phys. Lett. B **428** (1998) 105.

[22] E. Witten, Adv. Theor. Math. Phys. **2** (1998) 253.

[23] S.S. Gubser, I.R. Klebanov, A.M. Polyakov, Nucl. Phys. B **636** (2002) 99.

[24] R. C. Brower, J. Polchinski, M. J. Strassler, C. I. Tan, JHEP **0712** (2007) 005.

[25] L. N. Lipatov, talk at "Perspectives in Hadronic Physics", Proc. of Conf. ICTP. Triest, Italy, May 1997.

[26] J. A. Minahan, K. Zarembo, JHEP **0303** (2003) 013.

[27] N. Beisert and M. Staudacher, Nucl. Phys. B **670** (2003) 439.

[28] B. Eden, M. Staudacher, J. Stat. Mech. **0611** (2006) P014.

[29] N. Beisert, B. Eden, M. Staudacher, J. Stat. Mech. **0701** (2007) P021.

[30] A. V. Kotikov, L. N. Lipatov, A. Rej, M. Staudacher, V. N. Velizhanin, J. Stat. Mech. **0710** (2007) P10003.

[31] Z. Bajnok, R. Janik, T. Lukowski, arXiv:hep-th/0811.4448.

[32] Z. Bern, L. J. Dixon, V. A. Smirnov, Phys. Rev. D **72** (2005) 085001.

[33] J. Bartels, L. N. Lipatov, A. Sabio Vera, arXiv:hep-th/0802.2065.

[34] R. C. Brower, H. Nastase, H. J. Schnitzer, C.-I. Tan, arXiv:hep-th/0801.3891.

[35] J. Bartels, L. N. Lipatov, A. Sabio Vera, arXiv:hep-th/0807.0807.

[36] L. N. Lipatov, arXiv:hep-th/0807.0807 and in preparation.

High energy scattering in QCD vs. tiny black holes

L. Álvarez-Gaumé[1], *C. Gómez*[2], *A. Sabio Vera*[1†], *A. Tavanfar*[1,3] *and M. A. Vázquez-Mozo*[4]
1 Theory Group, Physics Department, CERN CH-1211 Geneva 23, Switzerland
2 Instituto de Física Teórica UAM/CSIC, Universidad Autónoma de Madrid E-28049, Spain
3 Institute of Theoretical Physics and Mathematics (IPM) P.O. Box 19395-5531, Tehran, Iran
4 Departamento de Física, Universidad de Salamanca, Plaza de la Merced s/n, E-37008, Spain
DOI: http://dx.doi.org/10.3204/DESY-PROC-2009-01/111

Abstract
We review the holographic conjecture which links the transition from a dilute to a dense system of partons in DIS with the formation of tiny black holes in the gravitational collapse of a perfect fluid. At small 't Hooft coupling and large center-of-mass energies the onset of unitarity in the Yang-Mills side is interpreted as the formation of a horizon due to nonlinear gravitational dynamics in the higher dimensional bulk. Recent progress in the study of critical behaviour present in the formation of closed trapped surfaces in the collision of gravitational shock waves is also presented.

1 Critical gravitational collapse of a massless scalar field and a perfect fluid

In Ref. [1] it was remarked that the critical exponent characterizing the formation of a small black hole in the gravitational collapse of a massless scalar field is quite similar to the critical exponent present in the saturation line of DIS. This line marks the onset of saturation effects in the evolution of parton distribution functions at very small values of Bjorken x. It should be indicated that the calculation of the critical exponent in the QCD side suffers from some intrinsic uncertainties even if one stays in the leading logarithmic approximation. If the calculation of the saturation line is performed using an effective absorptive barrier implemented in the integration over transverse momenta [2] one obtains a critical exponent ~ 2.44. Using other approaches where unitarity takes the form of a nonlinear

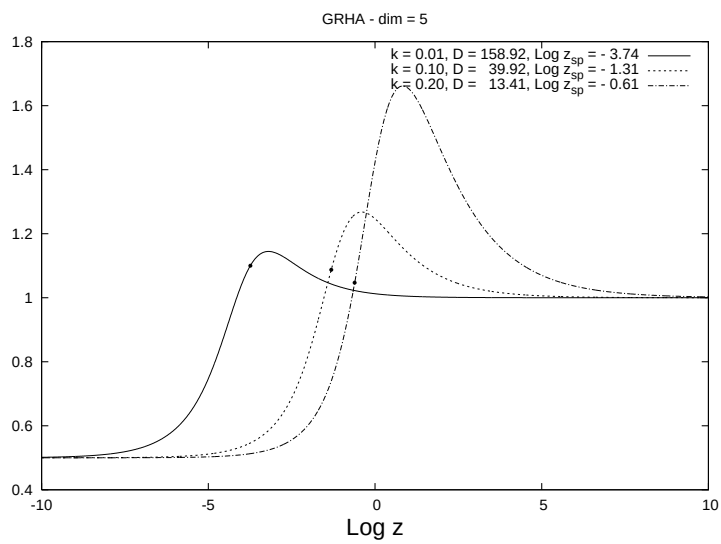


Fig. 1: Solutions for different CSS backgrounds.

† speaker

term in the evolution equation [3, 4] this number changes to ~ 2.28 [5]. Nevertheless it is encouraging that these are pure numbers independent of the value taken for the coupling and that they are quite similar to each other. Higher order corrections in the gauge theory side, such as next-to-leading order terms, are suppressed if we assume that the 't Hooft coupling is very small. The calculation of the so-called Choptuik exponent in the gravity side is robust and a recent study [6] has shown that its value for the scalar field in 5 dimensions is ~ 2.42.

There is a more serious complication to map perturbative saturation with the critical collapse of a scalar field. In this case the solutions to Einstein's equations for any scaleless quantity have a discrete self-similarity. This means that they reproduce themselves after a simultaneous fixed discrete rescaling in the time and radial components. Such a discrete scaling, also known as "echoing", is not present in the Yang-Mills side. However, not everything is lost since it is well known that DIS data for the total cross section in the collision of a virtual photon with a proton manifests what is known as "geometric scaling". This behaviour appears for a large range of values of the virtuality of the photon, Q^2, when Bjorken $x \simeq Q^2/s$ is smaller than 0.01, with s being the center-of-mass energy in the process. In this region the HERA data is a function only of the ratio of Q^2 over x to some power [7]. In this way we can consider this scaling as continuous self-similar (CSS) because the cross section is invariant under any shift in Q^2, compensated by a similar one in x. This CSS can be interpreted within perturbative QCD as a consequence of saturation effects where the parton multiplicity is so large that a simple linear evolution cannot hold any longer and recombination effects must be taken into account. These effects are of non-perturbative origin, in the sense that they are related to the dynamics of the formation of a high density system, but not related to confinement since the typical transverse scale in the problem is set by Q^2, always above $\Lambda^2_{\rm QCD}$.

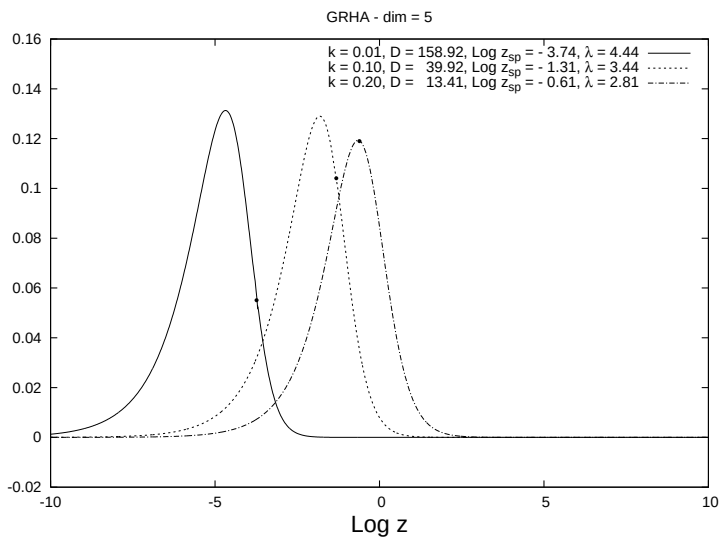


Fig. 2: Liapunov perturbations for different CSS backgrounds.

The natural question now is whether there exists any gravitational system with CSS collapse which is characterized by a similar critical exponent to that found in the case of the scalar field. This question motivated us to study [8] the critical gravitational collapse of a perfect fluid with barotropic equation of state $p = k\rho$ and spherical symmetry in arbitrary dimensions. In this type of collapse black hole singularities are formed with a radius given by

$$r_{\rm BH} \sim (p - p^*)^\gamma,$$

where p parameterizes generic values of the initial radial density of collapsing fluid. p^* denotes a critical region of densities for which, if p is above but close to p^*, a singularity appears. We are particularly interested in this system because the critical solutions at $p = p^*$ are CSS and can be directly calculated from Einstein equations sourced by the perfect fluid imposing that they depend only on the variable $z = -r/t$. For fine tuned values of p^* we numerically obtained these background solutions at different values of the speed of sound $\sqrt{k}$ in the fluid. An example of our numerical results is shown in Fig. 1 where we plot the ratio of the fluid local density at the point r over the global density up to that point. We show the behaviour of this function versus the variable z for different values of k in five dimensions. Note that D, which is related to p^*, has to be fine tuned in order to cross the so-called "sonic point", where the surfaces of constant z move at a speed equal to $\sqrt{k}$. The main constraint to select the correct value of D is to have analyticity at this sonic point, indicated by a dot in the figure.

The critical exponent γ in the formula for the radius of the black hole can be found by introducing a Lyapunov perturbation around the CSS critical line $y(z)$ of the form

$$y(t,z) = y(z)\left(1 + \epsilon\,(-t)^{-\frac{1}{\gamma}}\, y_1(z)\right).$$

To calculate the perturbations $y_1(z)$ it is again crucial to have analyticity at the sonic point. This condition fixes the value for the single unstable mode γ. The form of the perturbations can be seen in Fig. 2 where $\lambda = 1/\gamma$. The corresponding γ modes which we calculated for different dimensions are shown in Table 1. The results for dimension four coincide with those found in Ref. [9]. Thinking of a possible holographic interpretation we have also investigated how these critical exponents vary with the dimension. To match the numbers obtained in QCD we would be looking for a range of $\gamma \in (0.41, 0.44)$. Of course we now face the problem of selecting the correct k. A possible candidate would be that corresponding to a conformal fluid of traceless energy-momentum tensor for which $k = 1/(d-1)$. An heuristic motivation for this choice is that in the linear growth of parton distributions and in the transition vertex from two reggeized gluons to four reggeized gluons, which is a fundamental piece in the unitarization corrections, there is an associated $SL(2,C)$ invariance [10]. We are currently investigating the extension of Table 1 up to dimension ten since it is possible that the holographic dual might live in a $AdS_5 \times S^5$ geometry where all dimensions would be equally important since the critical black holes here discussed can be arbitrarily small. Preliminary studies show that γ is close to the QCD range of results in the conformal limit of ten dimensions.

Although these investigations show encouraging results we are still far from having a holographic picture of the problem at hand. There are many unanswered questions and probably the most pressing one is to find the geometry corresponding to the perturbative hard pomeron. In Ref. [11] this problem was addressed from the large 't Hooft coupling perspective arguing that the main features of the BFKL kernel cannot change too much in the transition from weak to strong coupling since it is protected by conformal invariance. Our research targets a more complicated problem, not only because we handle perturbative results in the Yang-Mills side but also because we are at the transition region from a single pomeron picture to a regime dominated by multiple pomeron exchanges.

k	$\gamma_{d=4}$	$\gamma_{d=5}$	$\gamma_{d=6}$	$\gamma_{d=7}$
0.01	0.114	0.225	0.290	0.330
0.02	0.123	0.233	0.296	0.336
0.03	0.131	0.241	0.303	0.342
0.04	0.140	0.248	0.309	0.348
0.05	0.148	0.256	0.316	0.353
0.06	0.156	0.263	0.322	0.359
0.07	0.164	0.270	0.328	0.364
0.08	0.172	0.277	0.334	0.369
0.09	0.180	0.284	0.340	0.375
0.10	0.187	0.291	0.346	0.380
0.11	0.195	0.298	0.352	0.385
0.12	0.203	0.304	0.358	0.390
0.13	0.210	0.311	0.364	0.396
0.14	0.218	0.318	0.369	0.401
0.15	0.225	0.324	0.375	0.406
0.16	0.232	0.330	0.381	0.411
0.17	0.240	0.337	0.386	0.416
0.18	0.247	0.343	0.392	0.421
0.19	0.254	0.347	0.397	0.426
0.20	0.261	0.356	0.403	0.431
0.21	0.259	0.362	0.408	0.435
0.22	0.276	0.368	0.414	0.440
0.23	0.283	0.375	0.419	0.445
0.24	0.290	0.381	0.425	0.450
0.25	0.297	0.387	0.430	0.454

Table 1: Values of the Choptuik exponent with precision ± 0.001 as a function of k for $d = 4$, 5, 6 and 7.

2 Closed trapped surfaces in shock wave collisions

Some light might be shed on these issues if we focus our attention on a related problem which shares some features with the physics of saturation. In Ref. [12] a gravity dual of a boosted Woods-Saxon nuclear energy density for heavy ions was proposed. For example, if we consider gold with a typical size L and energy E the corresponding energy momentum tensor on the gauge theory side, $T_{\mu\nu}$, is associated with a bulk gravitational source of the form $\rho(x_i, z) \sim E\delta(x_i)\delta(z-L)$, where x_i are the transverse coordinates and z the holographic direction in a H_3 space. The $R^{3,1}$ boundary lies at $z = 0$. The solution to the Einstein equations in this space

$$\left(\Box_{H_3} - \frac{3}{L^2}\right)\Phi(x_i, z) = \delta(u)\rho(x_i, z)$$

can be used to construct a five dimensional AdS shock wave bulk geometry with metric

$$ds^2 = \frac{L^2}{z^2}\left(-dudv + \sum_i dx_i^2 + dz^2 + \frac{z}{L}\Phi(x_i, z)\delta(u)du^2\right).$$

It is very interesting that in [12] when head-on collisions of heavy ions, which correspond to the gravitational collision of two shock waves, are considered, a closed trapped surface is formed. The area of the trapped surface is of the order of the entropy generated in the collision, which is itself related to the number of generated charged tracks. The total energy in the system can be written as $E \sim \int_{H_3}\rho(x_i, z)$. If a $O(3)$ symmetry in the H_3 plane is assumed then the source can be written as a function of the chordal coordinate $q(x_i, z) = \left(\sum_i x_i^2 + (z-L)^2\right)/(4zL)$. In this coordinate the trapped surface is characterized by a density function $\rho(q)$ describing the strong gravity collision region such that $E \sim \int_0^{q_c}\rho(q)$ with the horizon defined by the surface $q = q_c$.

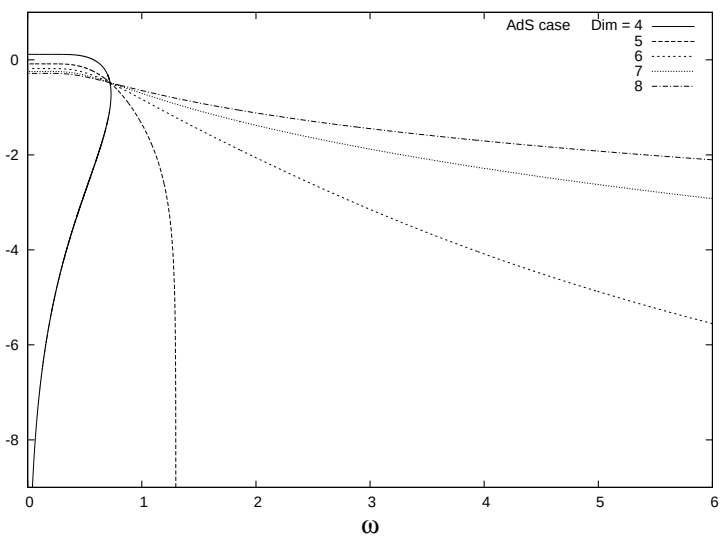


Fig. 3: Size of the trapped surface versus the diluting parameter ω.

It would be important to see if a similar set up could be used to describe DIS in the saturation region with the onset of nonlinear effects being related to the formation of a trapped surface. Indeed, we have found that in the formulation of [12] a critical phenomena resembling that found by Choptuik is present. In order to see this it is needed to smear the energy density in the chordal variable using, for example, a Gaussian distribution with width parametrized by a variable ω. With an AdS metric in different dimensions we have solved the equation to form a close trapped surface of size q_c as a function of ω. The results are plotted in Fig. 3.

We observe that in dimensions larger than five it is always possible to form an arbitrary small trapped surface by simply diluting the initial energy density. This is done by increasing ω while keeping the total energy constant. No critical behaviour is found in these dimensions. However, the situation is more interesting at $d = 4, 5$ since criticality kicks in. In both cases there exists a maximal $\omega = \omega_c$ beyond which it is not possible to form a trapped surface and in the region close to this point the relation

$$q_c \simeq q_c^* + (\omega_c - \omega)^\gamma$$

holds with q_c^* being different from zero in $d = 4$ and canceling for $d = 5$. The critical exponent γ is 1 in $d = 5$ and 0.5 in $d = 4$. When considering the same physics in a flat background we have found an equivalent behaviour, shown in Fig. 4. The only difference is that now the critical exponent γ is 0.5 in both dimensions 4 and 5. Further details on these results can be found in Ref. [13].

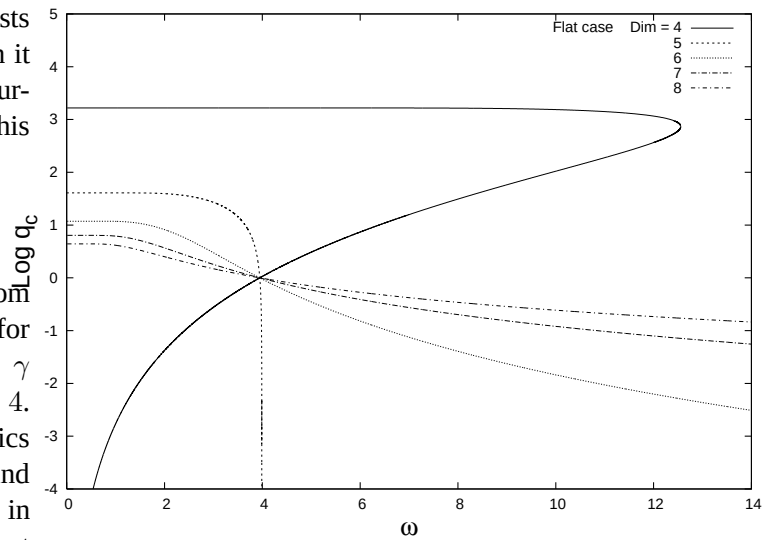


Fig. 4: Size of the trapped surface versus the diluting parameter ω.

References

[1] L. Alvarez-Gaume, C. Gomez and M. A. Vazquez-Mozo, Phys. Lett. B **649** (2007) 478.

[2] A. H. Mueller and D. N. Triantafyllopoulos, Nucl. Phys. B **640** (2002) 331.

[3] I. Balitsky, Nucl. Phys. B **463** (1996) 99.

[4] Y. V. Kovchegov, Phys. Rev. D **60** (1999) 034008.

[5] J. L. Albacete, N. Armesto, J. G. Milhano, C. A. Salgado and U. A. Wiedemann, Phys. Rev. D **71** (2005) 014003.

[6] J. Bland and G. Kunstatter, Phys. Rev. D **75** (2007) 101501.

[7] A. M. Stasto, K. J. Golec-Biernat and J. Kwiecinski, Phys. Rev. Lett. **86** (2001) 596.

[8] L. Alvarez-Gaume, C. Gomez, A. Sabio Vera, A. Tavanfar and M. A. Vazquez-Mozo, Nucl. Phys. B **806** (2009) 327.

[9] T. Harada and H. Maeda, Phys. Rev. D **63** (2001) 084022.

[10] J. Bartels, L. N. Lipatov and M. Wusthoff, Nucl. Phys. B **464** (1996) 298.

[11] R. C. Brower, J. Polchinski, M. J. Strassler and C. I. Tan, JHEP **0712** (2007) 005.

[12] S. S. Gubser, S. S. Pufu and A. Yarom, Phys. Rev. D **78** (2008) 066014.

[13] L. Alvarez-Gaume, C. Gomez, A. Sabio Vera, A. Tavanfar and M. A. Vazquez-Mozo, arXiv:0811.3969 [hep-th].

Chapter 8

Discussion Session

Discussion Session

G. Gustafson (summarizing the discussion session)
University of Lund, University of Hamburg

DOI: http://dx.doi.org/10.3204/DESY-PROC-2009-01/110

The applicability and limitations of collinear factorization, and of linear parton evolution

The program included a discussion session about the applicability and limitations of collinear factorization, and of linear parton evolution. Moderator was *J. Bartels*, and four speakers, *M. Diehl, K. Golec-Biernat, A. Cooper-Sarkar*, and *A. de Roeck*, were asked to act as "provocateurs", giving short introductory presentations of some essential open problems. In this short write-up we only present the most important points. The full discussion is video-recorded, and can be seen on the web page `http://ismd08.desy.de`. together with the slides from the provocateurs.

On the theory side strong emphasis was given to the problem to *cast NLO BFKL into dipole form*, and to study saturation and the *dipole model beyond leading* $\log(1/x)$. The dipole model has been successful in describing inclusive total cross sections and diffraction in DIS, and also quasi-elastic reactions like DVCS and $\gamma p \to Vp$. The dipole model and the impact parameter formalism is also the main tool for studies of saturation and multiple interactions. Thus studies of saturation also calls for dipole models beyond leading $\log(1/x)$, which includes *NLL BK equation phenomenology*.

The phenomenologically successful *Geometric Scaling* ought to be better understood. It has been expected in the deeply saturated region, but is observed also outside this regime. This problem is related to the question to what extent saturation is at work at HERA.

For *LHC physics* an understanding of nonlinear effects from saturation, pomeron loops, and multiple interactions will be very important. Besides including NLL effects in the dipole evolution, this also emphasizes the need for further studies of *pomeron interactions* and also *a dipole model for exclusive final states*. Saturation effects and the formation of pomeron loops are color suppressed compared to the splitting process in the dipole cascade. Therefore *effects beyond the large N_c approximation* and color reconnection are also very important subjects for further studies.

.

Have we seen anything beyond (N)NLO DGLAP at HERA?

Amanda Cooper-Sarkar
Oxford University

DOI: http://dx.doi.org/10.3204/DESY-PROC-2009-01/110

Abstract
The evidence from HERA for parton saturation, and other low-x effects beyond the conventional DGLAP formalism, is recalled and critically reviewed in the light of new data and analyses presented at the conference.

In the mid-90's the original surprise of the HERA Neutral Current e^+p scattering data was the strong rise of the structure function F_2 at low-x. This was taken to imply a strong rise of the gluon density at low-x which was widely interpreted as implying the possibility of gluon saturation and the need for non-linear terms in the parton evolution equations. Even somewhat more conservative interpretations suggested the need to go beyond the DGLAP formalism at small-x, resumming $ln(1/x)$ as in the BFKL formalism.

However, at low-x linear NLO DGLAP evolution itself predicts a rise in F_2, and in the gluon and sea PDFs, provided that Q^2 is large enough. One can begin parton evolution at a low Q^2 input scale, Q_0^2, using flat (or even valence-like) gluon and sea-quark input shapes in x and the DGLAP Q^2 evolution will generate a steep low-x rise of the gluon and sea at larger $Q^2 \gg Q_0^2$. The real surprise - seen in the data of the late 90's- was that steep shapes were already observed at rather low Q^2. Traditionally values of $Q_0^2 \sim 4\text{GeV}^2$ were used, but the data already show a steep rise of F_2 at low-x for lower Q^2 values, $Q^2 \sim 1\text{GeV}^2$, see Fig. 1 left-hand-side. To interpret these data in terms of conventional NLO DGLAP evolution we clearly need a low starting scale and thus we are forced into using perturbative QCD at a scale for which $\alpha_s(Q^2)$ is quite large- $\alpha_s(1.0) \sim 0.35$. Even if this is considered to be acceptable, we also need to use flexible input parton shapes, which can reproduce the steepness of the data. Surprisingly enough this does NOT imply that both the gluon and the sea input are already steep at $Q^2 \sim 1\text{GeV}^2$. The sea input is indeed steep, but the gluon input is valence-like, with a tendency to be negative at low-x!- see Fig. 1 right-hand-side. (Essentially the gluon evolution must be fast in order that upward evolution can produce the extreme steepness of high-Q^2 data, however this also implies that downward evolution is fast and this results in the valence-like gluon at low-Q^2).

Thus when statements are made that HERA has established that the low-x gluon is steep one must remember that this is only true for higher Q^2, $Q^2 \gtrsim 10\text{GeV}^2$, within the DGLAP formalism. However this formalism seems to work to much lower Q^2. Let us examine how the gluon and sea PDFs are extracted from the measurements. At low-x, the sea PDF is extracted fairly directly since, $F_2(x,Q^2) \sim xq(x,Q^2)$. However the gluon PDF is extracted from the scaling violations, $\partial F_2/\partial ln(Q^2) \sim P_{qg} xg(x,Q^2)$, such that the measurement is related to a convolution of the splitting function P_{qg} and the gluon distribution. Thus if the correct splitting function is NOT that of the conventional DGLAP formalism, or if a more complex non-linear realtionship is needed, then a turn over of the data $\partial F_2/\partial ln(Q^2)$ at low-Q^2 and low-x may not imply a turn

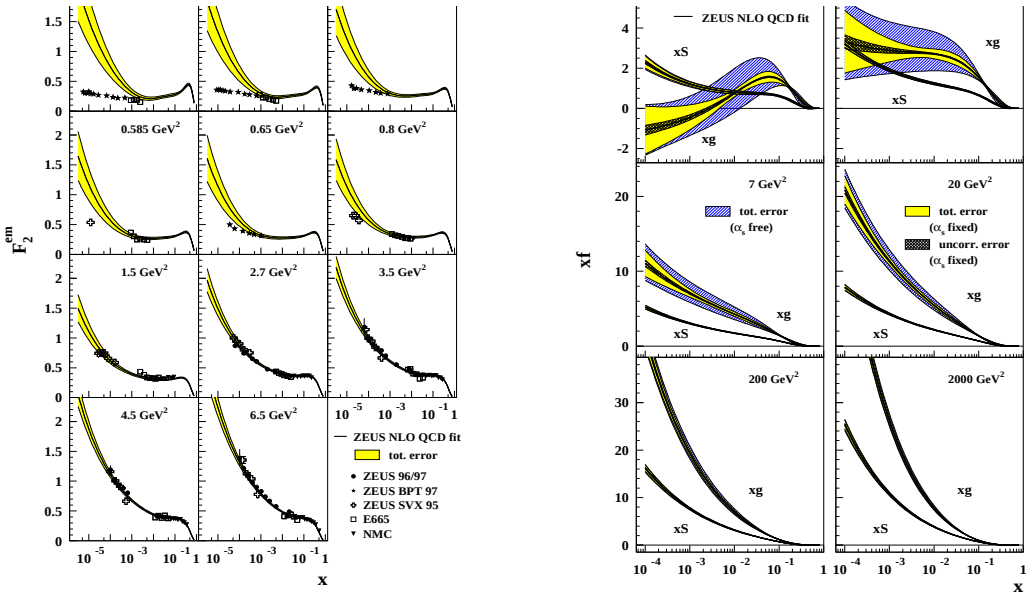


Fig. 1: Left plot: F_2 vs x for various low Q^2 values. Right plot: Sea and gluon PDF distributions extracted from a global PDF fit including these data.

over of the gluon distribution. It was suggested that measurements of other gluon related quantities could help to shed light on this question and the longitudinal structure function, F_L, and the heavy quark structure functions, $F_2^{c\bar{c}}, F_2^{b\bar{b}}$, are obvious candidates. All of these quantities have now been measured (see talks of K. Papageorgiou and P. Thompson in these proceedings) and, within present experimental uncertainties, they can be explained by the conventional NLO DGLAP formalism (with the heavy quark results shedding more light on the complexities of general-mass-variable-flavour number schemes than on the gluon PDF).

Other measurements of more exclusive quantities can also give information on the correctness of the conventional formalism at low-x. For example HERA forward jet mesaurements (see talk of A. Savin in these proceedings). DGLAP evolution would suppress the forward jet cross-section, for jets with $P_t^2 \sim Q^2$ and low-x, because LO DGLAP evolution has strong k_t ordering, from the target to the probe, and thus it cannot produce such events. The rate is also suppressed for NLO DGLAP. However BFKL evolution has no k_t ordering and thus a larger cross-section for such events at both LO and NLO. The data do indeed show an enhancement of forward jet cross-sections wrt conventional NLO DGLAP calculations. However this cannot be regarded as a definitive indication of the need for BFKL resummation because conventional calculations at higher order, $O(\alpha_s^3)$, do describe the data.

However, as we have already mentioned, even though conventional calculations do give reasonable fits to data, the peculiar behaviour of the low-x, low-Q^2 gluon gives us cause for some concern. Thorne and White have performed an NLL BFKL resummation and matched it to NLO DGLAP at high-x in order to perform a global PDF fit. When this is done the gluon shape deduced from the scaling violations of F_2 is a lot more reasonable and a good fit is found

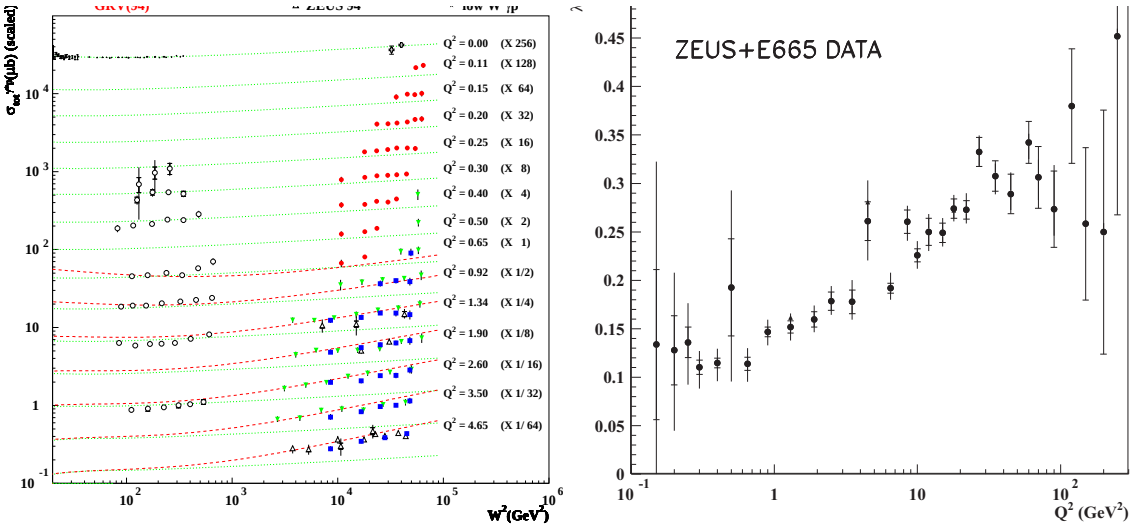


Fig. 2: Left plot: the photon-proton cross-section vs W^2 for various virtualities of the photon. Right plot: the slope $\lambda = \partial ln F_2 / \partial ln(1/x)$.

to global DIS data, see the talk of C. White in these proceedings. A similar improvement to the gluon shape is got by introducing a non-linear term into the evolution equations, as done by Eskola et al [1], but although this work has been widely used to give non-linear PDFs one must remember that it is limited to leading order.

These analyses make us suspect that the conventional formalism could be extended, but they are still not definitive. A different perspective comes from considering the low-x structure function data in terms of the virtual-photon proton cross-section: at low-x, $\sigma(\gamma^* p) \sim 4\pi\alpha^2 F_2/Q^2$. The data are presented in this way in Fig. 2 left-hand-side. A rise of $F_2(x) \sim x^{-\lambda}$, implies a rising cross-section with W^2, the centre-of mass energy of the photon-proton system, $\sigma(W^2) \sim (W^2)^\lambda$ (since $x = Q^2/W^2$ at low-x). However, the real-photon proton cross-section (and all high energy hadron-hadron cross-sections) rises slowly as $(W^2)^{\alpha-1}$, where, $\alpha = 1.08$, is the intercept of the soft-Pomeron Regge trajectory. Thus the data on virtual-photon proton scattering are showing something new - a faster rise of cross-section than predicted by the soft-Pomeron which has served us well for many years. In Fig. 2 right-hand-side we show the slope of this rise, $\lambda = (\alpha - 1)$, as calculated from the data, $\lambda = \partial ln F_2 / \partial ln(1/x)$. One can see a change in behaviour at $Q^2 \sim 0.8\,\mathrm{GeV}^2$ as we move out of the non-perturbative region -where the soft pomeron intercept gives a reasonable description of the data -to larger Q^2. Does this imply that we need a hard Pomeron as well?

Dipole models have given us a way to look at virtual-photon proton scattering which can model the transition from the non-perturbative to the perturbative region. The interaction can be viewed as the virtual photon breaking up into a quark-antiquark pair and this pair, or dipole, then interacts with the proton. At low-x, the lifetime of the $q\bar{q}$ pair is longer than the dipole-proton scattering time, such that the physics is contained in the modelling of the dipole-hadron cross-section. There are many dipole models but the simplest Golec-Biernat Wusthoff model [2] contains the essential features: $\sigma = \sigma_0(1 - exp(-r^2/(2R_0^2))$, where r is the transverse size of

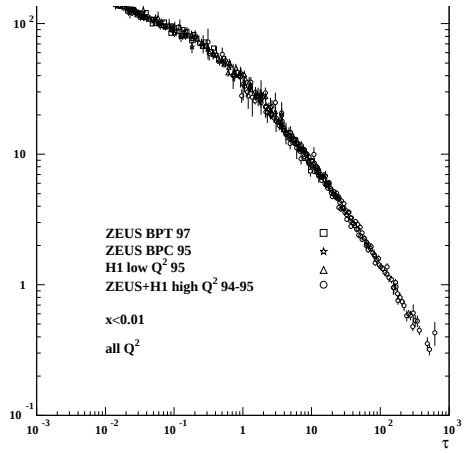


Fig. 3: $\sigma(\gamma^* p)$ vs the scaling variable $\tau = Q^2/Q_s^2$

the dipole and R_0 is the transverse separation of the gluons in the target, $R_0^2 = 1/Q_0^2(x/x_0)^\lambda$, where $x^\lambda \sim 1/(xg(x))$, is inverse to gluon density. Thus for small dipoles, $r < 1/Q$ and large Q^2, one obtains $\sigma \sim r^2 \propto 1/Q^2$ and Bjorken scaling (sophistications to the model correct this to give logarithmic scaling violation), whereas for large dipoles and small Q^2, one obtains $\sigma \sim \sigma_0$, ie a constant cross-section which corresponds to the correct photo-production limit. The reason that such dipole models have attracted attention in recent years is that the dipole-proton cross-section can be written in terms of a single scaling variable, τ, $\sigma = \sigma_0(1 - exp(-1/\tau)$, where $\tau = Q^2 R_0^2 = Q^2/Q_0^2(x/x_0)^\lambda$, rather than in terms of the two variables x, Q^2. This is known as geometric scaling, and evidence for it is shown by the low-x ($x < 0.01$) data in Fig. 3. Note that only low-x data show this scaling. Geometrical scaling is predicted by many theoretical approaches to the low-x regime which involve saturation and, $Q_s^2 = 1/R_0^2$, is interpreted as a saturation scale below which non-linear dynamics applies.

Note that the power $\lambda \sim 0.3$, which describes the gluon density, $xg(x) \sim x^{-\lambda}$, within many dipole-models, is fitted to the data. It cannot be trivially related to the measured slope, $\partial ln F_2/\partial ln(1/x)$, at any Q^2, and it is not justified by the steep slopes of the gluon distribution observed at HERA- because such steep slopes are not in fact observed but are derived within the DGLAP formalism- which is explicitly not the formalism of most dipole models- and a steep slope $\lambda \gtrsim 0.3$ is only found for $Q^2 \gtrsim 10$ GeV^2. However the saturation scale for HERA data is much lower, $Q_s^2 \sim 1 - 2$ GeV^2. Thus the steep slope of the gluon in the dipole models must be regarded as an input assumption.

Geometric scaling is not unique to non-linear approaches, it can be derived from solutions to the linear BFKL equation [3] and even from the DGLAP equation [4]. But note that such solutions do not extend into the low-Q^2 region and cannot give a picture of the transition from low to high-Q^2, as the dipole models do. Moreover, dipole models provide explanations for the constant ratio of the diffractive to the total cross-section data at HERA, and geometric scaling has also been observed in diffractive processes including vector meson production and deeply virtual compton scattering, see the talk of R. Yoshida in these proceedings. These observations

give hints that there is some truth to the dipole picture of saturation even though data at HERA are not definitive.

Even if the evidence for saturation at HERA is taken seriously the saturation scale is only, $Q_s^2 \sim 1-2\,\mathrm{GeV}^2$, such that the region of non-linear dynamics largely coincides with the strongly-coupled region (where α_s is large). That is why there is interest in results from RHIC, where the nuclear environment enhances the high-density of the partons by $A^{1/3}$, such that saturation scales are higher, see the talk of A. Dainese in these proceedings. But what of the LHC? Clearly ALICE data will be interesting, but even proton-proton data can be searched for signs of saturation if the large rapidity region is considered, since small x values are then accessed. For example, low-mass Drell-Yan data at LHCb can access $x \sim 10^{-6}$, see the talk of T. Shears in these proceedings.

If our conventional picture of DGLAP evolution in the HERA x region is significantly wrong then this will have implications even for classic Standard Model predictions, such as W and Z production in the central region of CMS and ATLAS. These bosons are produced at low-x, $5 \times 10^{-4} < x < 5 \times 10^{-2}$, in the central rapidity region, $-2.5 < y < 2.5$ and they are produced with enormous rate (even a modest 100 pb^{-1} luminosity produces 10^6 W events) such that very early low luminosity running could show up discrepancies with our predictions. Whereas rapidity spectra may not be much affected by unconventional Q^2 evolution [5], it should be fruitful to examine the boson p_t spectra, since lack of p_t ordering could affect these significantly [6].

In summary, it is unclear that HERA data have actually given any evidence for BFKL evolution, non-linear evolution or saturation, but there are hints in many places. The contribution of A. De Roeck to this discussion considers the possibilities for further progress at HERA, the LHC and at future facilities.

References

[1] C. Eskola et al., Nucl.Phys.B660 (2003)211.

[2] K. Golec-Biernat and M. Wusthoff, Phys.Rev.D59 (1999)014017.

[3] E. Iancu et al., Nucl.Phys.A708(2002)327.

[4] F. Caola and S. Forte, Phys.Rev.Lett.101(2008)022001

[5] R. D. Ball, Nucl.Phys.B706 (2008)137.

[6] S. Berge et al., AIP Conf.Proc:792 (2005)722.

Saturation: what do we need

Albert De Roeck[1] *and Hannes Jung*[2]
[1]CERN, 1211 Geneva 23 Switzerland and University of Antwerp
[2] DESY, Notkestr 85, 22603 Hamburg, FRG and University of Antwerp

DOI: http://dx.doi.org/10.3204/DESY-PROC-2009-01/110

Abstract
A discussion session was organized during the ISMD in Hamburg. This note describes a summary of open questions that were brought up to introduce this discussion session.

1 Introduction

Parton saturation has been a topic of considerable scientific interest since many years. It would allow to access a new QCD region where apart from simple parton branching diagrams also parton recombination will contribute. Thus one can probe a region of large parton densities, where one can still use a perturbative expansion to describe the system, due to the α_s value that remains small. Saturation has been predicted to occur at HERA in the bare proton for values of low-x but, while there is circumstantial evidence for it, the situation is still not clear.

In 2009 the LHC will turn on and will allow in principle for measurements to reach regions of lower x values than before, at high enough scales. It will be important to analyse data at the LHC with the objective of searching for saturation effects. This will require equiping the present detectors with better instrumentation in the forward regions, i.e. the regions at high pseudo-rapidity $\eta = -\ln\tan\theta/2$. Both ATLAS and CMS have studies ongoing to extend forward region instrumentation, and some of it is already being installed [1].

This short note reports on a few questions that served as an introduction for the discussion session at the symposium, and were in part already presented in [2].

2 Discussion

The program to investigate non-linear effects at HERA further, and to constrain the validity of linear evolution equations, is essential for any proper interpretation of small-x effects at LHC. HERA is the main place where these effects can systematically be studied in a clean and controllable environment, i.e. where precision measurements of these subtle QCD effects are possible. The results of such a program will have direct impact on measurements at RHIC and even more so at the LHC, where deviations from linear dynamics (saturation and multi-parton interactions) are expected to affect even the high p_t processes [3].

The following questions were put forward:

- What is a good and at the same time indisputable signature for parton saturation? There are definitely a number of hints in the HERA data, eg the observation of diffractive events and their interpretation in terms of the dipole picture. A strong signal for the onset of a dense region (or black disk limit) are the measured diffractive gluon PDFs, which indicate [4] that for $x \sim 10^{-4}$ and $Q^2 \sim 4$ GeV^2 the probability of diffraction in gluon induced processes

reaches $\sim 40\%$ which is close to the black disk limit of 50%. Now, the theoretical understanding of the dense region has received much support from measurements at RHIC, and new evolution equations (like the Balitsky-Kovchegov equation [5,6] (BK)), which include non-linear terms, are available. However, the BK equation is derived for a large nucleus and only approximately applicable to ep and pp. Although saturation is theoretically well motivated, a clear, clean and indisputable experimental signature for it is still missing. To decide if and where nonlinear dynamical effects become important at HERA is difficult, especially since some signatures of saturation can be mimicked approximately within the linear DGLAP or BFKL descriptions.

- What can HERA still contribute to clarify the situation on saturation? The k_t-dependence of the unintegrated PDF as a function of x could provide important information. In a linear scenario (BFKL) the parton density (for fixed k_t) is expected to increase with deceasing x, while in the case of saturation this density will first increase, then flatten for smaller and smaller x and will eventually decrease. As a function of k_t the parton density is expected to decrease for k_t below the saturation scale and the x-dependence of the saturation scale can thus be studied directly. High-precision data in a wide kinematic region for dedicated observables will certainly help. Are there other signatures? Proposals are to study F_L, $F^{2D}/F_2, F_2 - F_2^C$ (in terms of geometrical scaling), as also discussed in [7].
- Can the potential larger x-range of the LHC be used for saturation studies? The LHC offers the opportunity to reach smaller x values, perhaps even down to 10^{-7}. What are the most useful processes/variables to study to search for saturation effects? In the CMS/TOTEM common physics program LOI [8] the Drell-Yan process was proposed to study saturation. Are all theoretical tools for saturation analyses at the LHC in place?
- Nuclei versus protons studies? Nuclei are expected to amplify the saturation effect as a result of the overlap in the transverse projection of the nucleons, by an enhancement factor $A^{1/3}$ which is about 6 for heavy nuclei. The HERA collider program has been terminated and thus HERA will never run with heavy nuclei instead of protons, but future machines where this is an option are under study like EIC [9] and LHeC [10]. The kinematic reach of these facilities is shown in Fig. 1a. Still naively one could ask if the effects seen in nuclei can be interpreted directly for the dynamics of the single proton case.
- What is the Q^2, x region where non-linear effects become important ? A typical "saturation plane" is shown in Fig. 1b with the transition from dilute to dense systems. Where that transition exactly happens is however somewhat vague (see also below).

Clearly continuing and specific analyses of present data from e.g. HERA and future data at the LHC can shed more light on this topic. On the other hand on the theoretical side progress would be desirable on:

- the calculation of the evolution of unintegrated PDFs in the presence of saturation,
- the factorization and factorization breaking in the presence of saturation,
- the calculation of the change of the leading pion spectrum expected due to the onset of the saturation regime compared to the factorization prediction.

Furthermore, besides investigations on saturation, the range of validity of the linear evolution equations is not yet fully understood:

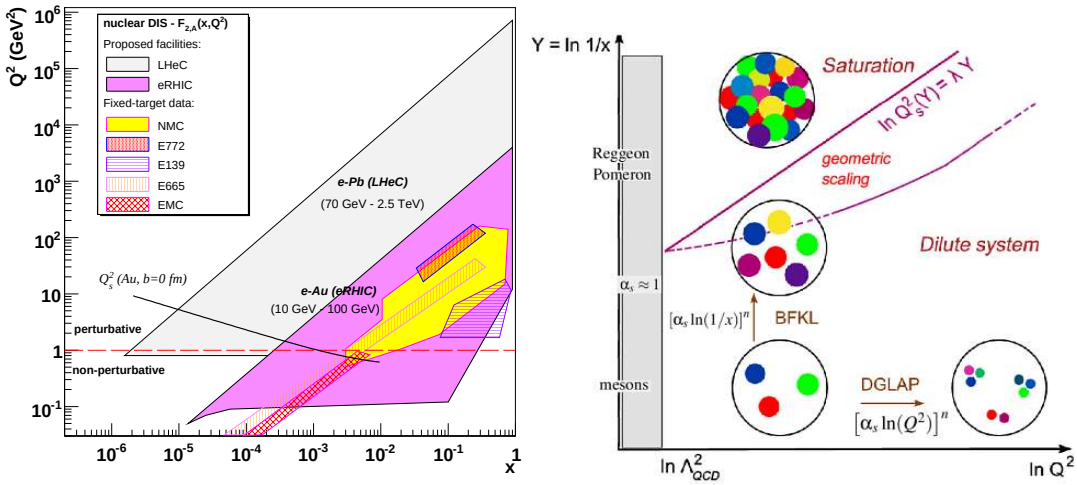


Fig. 1: (a) new proposed nuclear DIS facilities (right): LHeC and EIC/eRHIC (adapted from [11]; (b) saturation QCD "phase diagram" in the $1/x, Q^2$ plane (each dot represents a parton with transverse area $\sim 1/Q^2$ and fraction x of the hadron momentum). The different evolution regimes (DGLAP, BFKL, saturation) as well as the "saturation scale" and "geometric scaling" curves between the dense and dilute domains are indicated. Adapted from [12]

- in the moderate Q^2 region contributions from higher twist effects (multi-parton exchange processes) are expected. However they are suppressed by additional powers of $1/Q^2$ and therefore typically have only a small effect. At small x this contribution is increased by large $\log(1/x)$ terms. A systematic investigation of the higher-twist region would require measurements at the same Q^2 but with x varying over a larger range than available up to now. This can be achieved with F_2 measurements recorded at lower center-of-mass energies.
- in the large x region a breakdown of the collinear factorization ansatz is expected due to the transverse momentum as well as energy momentum conservation as advocated in [13].

3 Conclusion

Saturation in the proton is an important effect which still awaits to be established unambiguously in data. Here a number of questions and suggestions have been collected for further progress and developments on this interesting topic.

References

[1] E.g. A. De Roeck, Prospects for diffraction at the LHC, in "Hamburg 2007, Blois07, Forward physics and QCD" 181, May 2007.

[2] H. Jung et al., What HERA may provide? DESY-08-125, Sep 2008, arXiv:0809.0549.

[3] A. Del Fabbro and D. Treleani. A double parton scattering background to Higgs boson production at the LHC. *Phys. Rev.*, D61 077502, 2000.

[4] Leonid Frankfurt and Mark Strikman. Future small x physics with e p and e A colliders. *Nucl. Phys. Proc. Suppl.*, 79:671–687, 1999.

[5] I. Balitsky. Operator expansion for high-energy scattering. *Nucl. Phys.* B463 99, 1996.

[6] Yuri V. Kovchegov. Small-x F_2 structure function of a nucleus including multiple pomeron exchanges. *Phys. Rev.*, D60 034008, 1999.

[7] K. Golec-Biernat, these proceedings.

[8] M. Albrow et al. CERN-LHCC-2006-039, CERN-LHCC-G-124, CERN-CMS-NOTE-2007-002, Dec 2006.

[9] A. Deshpande, Physics and Status of the Electron Ion Collider, Proceedings of the 34th International Conference on High Energy Physics, Philadelphia 2008.

[10] M. Klein et al., Prospects for a Large Hadron Electron Collider (LHeC) at the LHC, EPAC08-WEOAG01, Jun 25, 2008. 3pp. In the Proceedings of 11th European Particle Accelerator Conference (EPAC 08), Magazzini del Cotone, Genoa, Italy, 23-27 Jun 2008, pp WEOAG01.

[11] D. G. d'Enterria, *In the Proceedings of 9th Workshop on Non-Perturbative Quantum Chromodynamics, Paris, France, 4-8 Jun 2007, pp 17* [arXiv:0706.4182 [hep-ex]].

[12] D. G. d'Enterria, Eur. Phys. J. A **31** (2007) 816 [arXiv:hep-ex/0610061].

[13] Stanley J. Brodsky and G. Peter Lepage. Structure functions and high twist contributions in pQCD. *AIP Conf. Proc.*, 68 805, 1981.

Chapter 9

Summaries

Experimental summary

Pierre Van Mechelen
Universiteit Antwerpen, Belgium
DOI: http://dx.doi.org/10.3204/DESY-PROC-2009-01/88

Abstract
A selection of experimental results contributed to the XXXVIIIth International Symposium on Multiparticle Dynamics is presented. Following the working group structure of the symposium, emphasis is put on dilute systems, the interpolation region, dense systems, strategies and analysis methods and new physics.

1 Dilute systems

In many cases, the proton is considered to be a dilute system of quarks and gluons, bound together by the strong interaction. This is because, to a good approximation, the densities of quarks and gluons inside the proton can be well described by linear QCD evolution equations, yielding the dependence of the parton densities on the resolution scale Q^2 and the fraction x of the proton momentum carried by the parton. This linear approximation should be valid if the probability for parton recombination or multiple scattering is small, as is the case in a dilute system.

The description of interactions with dilute protons in perturbative QCD can be factorised in two parts. First, the matrix element is an exact calculation of the partonic cross section up to a fixed order in perturbation theory. Nowadays, calculations up to $O(\alpha_S^3)$ are possible. Second, this partonic cross section is convoluted with the density of partons with certain kinematics, given by x and Q^2. The error made by neglecting higher orders in the calculation of the matrix element can be covered by so-called parton showers or evolution equations for the parton densities, which sum a subset of (leading) diagrams at each order. Which diagrams are leading depends on the kinematics of the process and different approaches therefore exist. The DGLAP approach [1] will resum terms proportional to $[\alpha_S \ln Q^2/Q_0^2]^n$, with Q_0^2 a fixed, low starting scale, and is therefore relevant to processes at large Q^2. The BFKL approach [2] on the other hand resums terms proportional to $[\alpha_S \ln 1/x]^n$ and should be used for process at low x. Other approaches, combining elements of the former two, like the CCFM approach [3], also exist.

This section reviews results, presented at ISMD08, on parton densities and linear parton dynamics. The extraction of parton densities is dominated by data on inclusive deep inelastic ep scattering. As will be shown, a standard DGLAP analysis of the data works well. Signals of different parton dynamics are best obtained by looking at specific final states by applying cuts to enhance the phase space for non-DGLAP dynamics.

1.1 Structure functions and parton distributions

The HERA experiments have studied the structure of the proton extensively through the measurement of the deep inelastic electron[1]-proton scattering cross section. As is well known, the

[1] "Electron" is used here as a generic name for both electrons and positrons.

differential cross section can be expressed as a function of the structure functions F_2, F_L and F_3:

$$\frac{d^2\sigma(e^{\pm}p)}{dxdQ^2} = \frac{2\pi\alpha^2}{xQ^4}Y_+\left[F_2(x,Q^2) - \frac{y^2}{Y_+}F_L(x,Q^2) \pm xF_3(x,Q^2)\right], \quad (1)$$

where the kinematic variables are defined as $Q^2 = -q^2 = -(k-k')^2$, $x = \frac{Q^2}{2P\cdot q}$ and $y = \frac{P\cdot q}{P\cdot k}$, with P, k, and k' the four-momenta of the incoming proton, incoming electron and scattered electron, respectively. For brevity, one further defines $Y_+ = \frac{(1+(1-y)^2)}{2}$.

The careful combination of HERA-I data obtained by the H1 and ZEUS collaborations has greatly improved the precision of the measurement of F_2 [4]. Some representative results are shown in Fig. 1 (left). Systematic uncertainties are now smaller than the statistical errors across the x, Q^2 plane. This combined data set has been subjected to a NLO DGLAP fit and yields parton density functions (PDFs) with impressive precision (shown in Fig. 1 (right)).

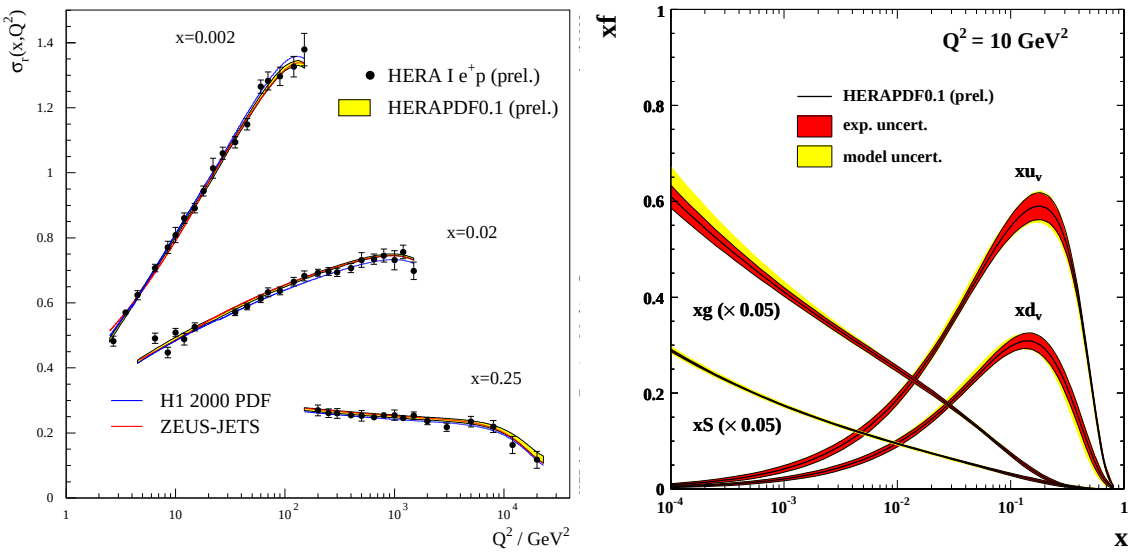


Fig. 1: (left) The neutral current reduced cross section $\sigma_r = \frac{xQ^4}{2\pi\alpha^2 Y_+}\frac{d^2\sigma(e^{\pm}p)}{dxdQ^2}$ vs. Q^2 for three x-bins. The prediction of the HERAPDF0.1 fit are superimposed, together with predictions of the H1PDF2000 and ZEUS-JETS PDFs as obtained in NLO QCD fits to the inclusive H1 data and to the inclusive and jet ZEUS data, respectively. (right) HERAPDF 0.1 PDFs from the analysis of the combined data set.

Figure 2 (left) shows a measurement of xF_3 [5], which is the parity-violating term in Eq. (1) arising from Z exchange. At HERA, this term is dominated by γ/Z interference rather than pure Z exchange. It can be experimentally extracted from the difference between the DIS cross section with electrons and positrons. F_3 should be approximately proportional to the valence quark density of the proton and thus peaks at relatively large fractional momenta x.

It should be noted that the HERA-I running period only corresponds to about one third of the total integrated luminosity. The final analysis of the proton structure by H1 and ZEUS will be based on some $1\ \mathrm{fb}^{-1}$ of data for both experiments together.

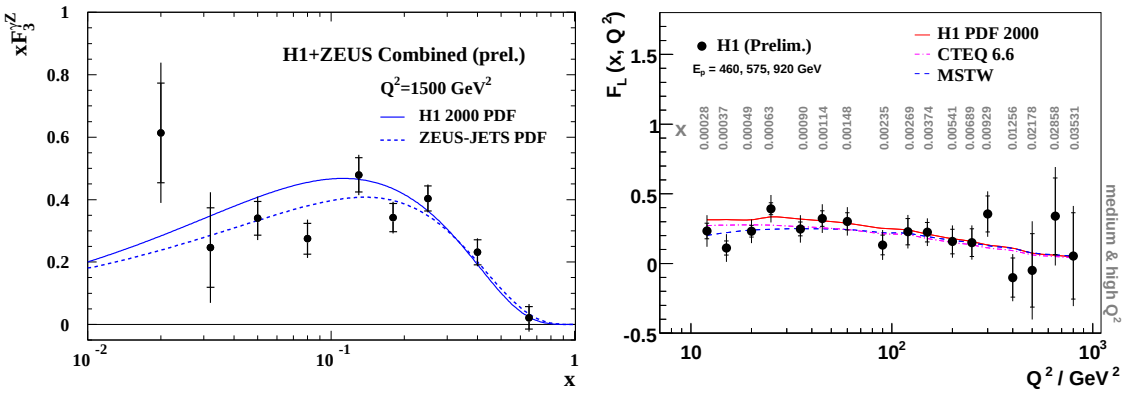


Fig. 2: (left) Combined H1/ZEUS measurement of the structure function $xF_3^{\gamma/Z}$. The curves describe the Standard Model predictions based on the H1PDF2000 and ZEUS-JETS PDFs. (right) The longitudinal structure function F_L averaged in x at given values of Q^2. The resulting x values of the averaged F_L measurements are given in the figure for each point in Q^2. The solid line represents a QCD prediction based on the H1PDF2000 fit. The dashed line represent the MSTW and the dashed-dotted line the CTEQ 6.6 predictions.

In order to extract the longitudinal structure function F_L, one needs to measure the DIS cross section at fixed x and Q^2, but different y. Because of the relation $Q^2 = sxy$, this is only possible with different centre-of-mass energies $\sqrt{s}$. At the end of the HERA-II running period, a special run was performed with a lower proton beam energy, with the aim to measure F_L directly. As F_L is proportional to the gluon density at higher orders, one expects a direct sensitivity to gluon dynamics. Some of the obtained results are shown in Fig. 2 (right) [6]. The results are consistent with expectations from global parton distribution fits at higher order pertubation theory.

Although the HERA measurements are very precise, TEVATRON data can still help to further constrain QCD fits of the PDFs. E.g., the production of jets in $p\bar{p}$ collisions occurs preferentially through the $gg \rightarrow jets$ or $qg \rightarrow jets$ processes, and the measurement of the inclusive jet cross section at moderate E_T is therefore mostly sensitive to the gluon density at large fractional momenta. In contrast, at HERA the gluon density is inferred from scaling violations of F_2 and this yields comparatively large uncertainties at large x.

D0 has measured the jet cross section in Run-II data at large E_T and in different intervals of rapidity, as shown in Fig. 3 (left) [7]. Whereas earlier jet data showed a preference for a large gluon density at high x compared to global fits without TEVATRON jet data, the new data now prefer smaller high-x distribution. The variance in the gluon distribution at high x however still remains large [8].

The production of weak bosons in $p\bar{p}$ collisions occurs through the fusion of quark-anti-quark pairs. Contrary to DIS where the quark charge squared enters the expression of the cross section, the cross section for weak boson production does not depend on the quark charge and treats the u- and d-quark equally. Therefore, the measurement of W and Z production at the TEVATRON will have the greatest impact on the d-quark density. Fig. 3 (right) shows the rapidity distribution of Z/γ^* bosons as measured by CDF [9]. In spite of better constraints using Run-II

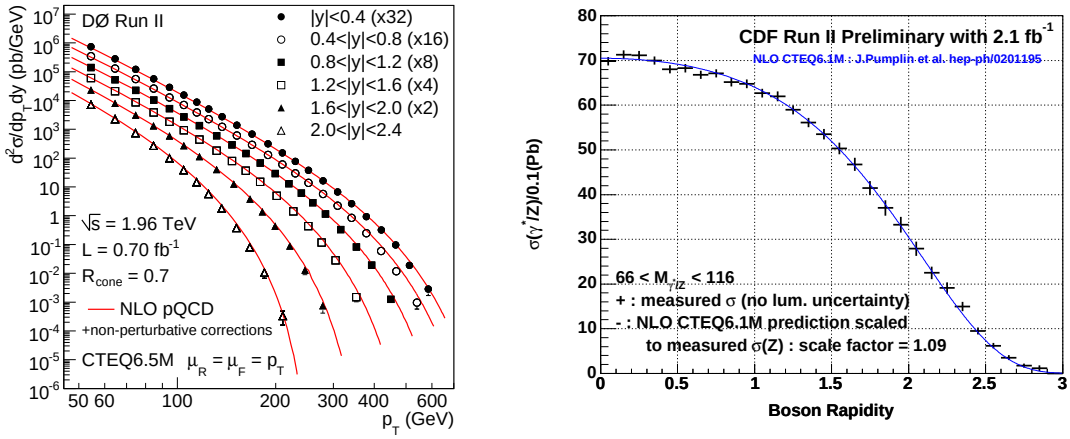


Fig. 3: (left) The inclusive jet cross section as a function of jet p_T in six $|y|$ bins. (right) Differential cross section $d\sigma/dy$ for $\bar{p}p \rightarrow Z^0/\gamma^* \rightarrow e^+e^-$. Data (crosses) are compared to a NLO calculation (solid line, scaled) based on the NLO CTEQ6.1 PDFs.

data, however, the variance of the extracted d-valance density is now larger than before due to more freedom in the d_v parametrisation that is being used [8].

Another possibility to exploit the measurement of W bosons in $p\bar{p}$ collisions is provided by the fact that the u-quark momentum in the proton is larger than the d-quark momentum. As a result, W^+-bosons in $p\bar{p}$ collisions are boosted along the direction of the incoming proton, while W^--bosons will prefer the antiproton direction. The resulting W charge asymmetry can be used to constrain PDFs further and, because antiquark terms are enhanced at low E_T, has the potential of differentiating between sea and valance contributions.

1.2 Final states

As discussed in the previous paragraph the quark-gluon structure of the proton can be well described by NLO DGLAP evolution equations. The parton density functions extracted from data are however by far dominated by measurements of the inclusive DIS cross section. It is therefore an important cross check to confront predictions based on these PDFs to final state measurements.

The production of heavy flavours in ep scattering boasts multiple scales: the photon virtuality Q^2, the heavy quark transverse momentum p_T and the heavy quark mass m_q. In NLO QCD, different approaches are used to calculate cross section for processes with heavy quarks in the final state. In the so-called Variable Flavour Scheme (VFS), one assumes that a heavy quark can be present in the initial state, giving the proton a heavy flavour content. This scheme resums terms proportional to $[\alpha_S \ln(Q^2, p_T^2/m_{c,b}^2)]^n$. In the Fixed Flavour Scheme (FFS), on the other hand, terms proportional to $[\alpha_S \ln(Q^2, p_T^2/m_{c,b}^2)]^n$ are neglected and heavy quarks are produced in the interaction itself. If calculations could be performed for all orders in perturbation theory, both schemes should yield the same result, as follows from the QCD factorisation theorem. Up to a fixed order in perturbation theory, however, differences occur and one has to choose a scheme that fits best with the kinematics of the process under study.

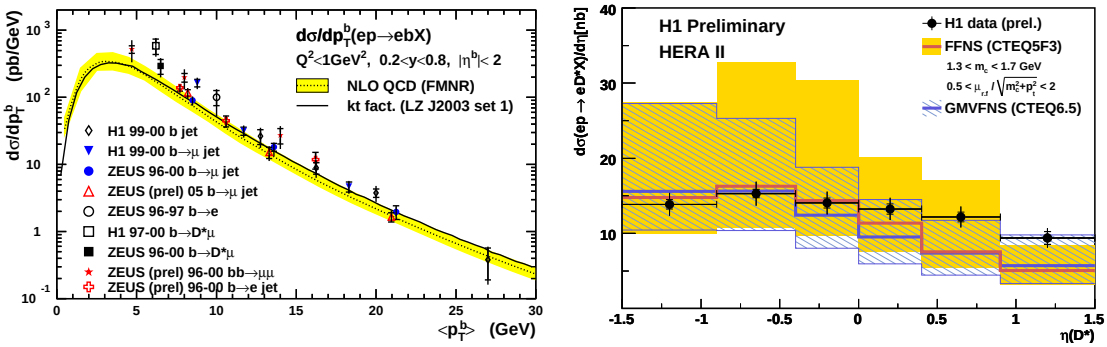


Fig. 4: (left) Differential cross section for $ep \to ebX$ as a function of p_T^b as obtained in various analyses. The result is compared to a Fixed Flavour Scheme calculation (FMNR). (right) Differential cross section for $ep \to eD^*X$ as a function of $\eta(D^*)$. The result is compared to a Fixed Flavour Scheme calcuation (FFNS) and a Variable Flavour Scheme calcuation (GMVFNS).

Figure 4 shows the transverse momentum and rapidity spectrum for bottom and charm quark, respectively, produced in photoproduction interactions at HERA [13]. Overall, NLO QCD provides a good description of the data, although the mass and scale uncertainties are often larger than the experimental errors. At forward rapidity ($\eta > 0$) there is a hint that higher order predictions might be needed to provide a better description of the data.

In general, the NLO pQCD description of jet production in ep scattering works well [10]. However, when looking at specific jet final states, one can show that higher orders and/or different evolution dynamics are needed to describe all corners of phase space. Typically, this involves looking at small-x processes where multiple gluon radiation is enhanced. Figure 5 shows dijet and trijet differential cross sections compared to NLO and NNLO pQCD calculations [11]. For dijets, the NLO ($O(\alpha_S^2)$) prediction clearly falls beneath the data, while the NNLO ($O(\alpha_S^3)$) calculation describes the data well. For trijets the NLO ($O(\alpha_S^3)$) calculation seems to suffice. However, when one or two of these jets are produced at forward rapidity, the fixed order QCD calculation again fail. It has been shown that different

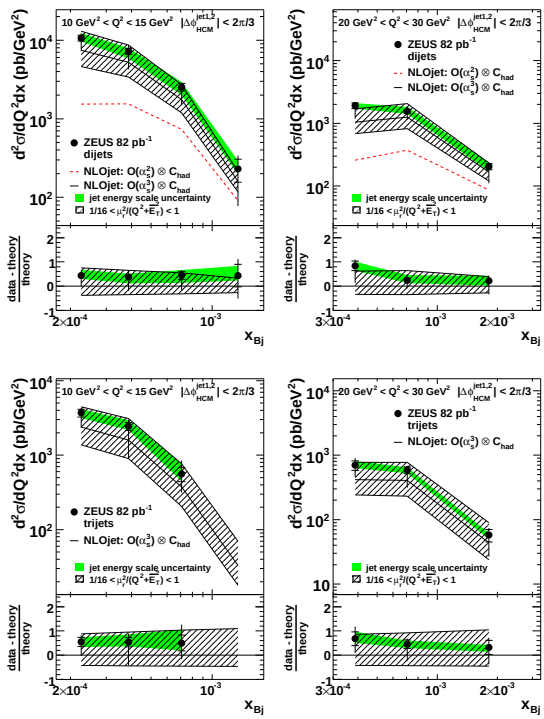


Fig. 5: The dijet and trijet cross section for events with $|\Delta\phi^{jet1,2}_{HCM}| < 2/3$ as functions of x_Bj in two different Q^2 bins. The NLOJET calculations at $O(\alpha_S^2)$ ($O(\alpha_S^3)$ are shown as dashed (solid) lines.

QCD dynamics (such as non k_T ordered parton showers) may accommodate the data well [12].

2 Interpolation region

A large part of the sessions on the interpolation region at the ISMD08 conference was dedicated to the study of diffractive interactions. In single diffractive dissociation (SDD), $pp \to pX$, one of the protons survives the interaction while the other dissociates in a hadronic system with invariant mass M_X, separated from the first proton by a large rapidity interval devoid of particles. In the presence of a hard scale, such interactions may be regarded as the result of the exchange of a colourless object with vacuum quantum numbers (e.g. a pomeron) consisting of quarks and gluons. One defines $\xi = 1 - \frac{P'_L}{P_L}$ as the fractional longitudinal momentum loss of the surviving proton and $t = (P - P')^2$, the squared four-momentum exchange at the proton vertex, with P and P' the four-momenta of the initial and scattered proton, respectively, measured in the initial state centre-of-mass frame.

In an optics analogon diffraction can also be called "shadow scattering" and is therefore inherently linked with the dense system upon which the incoming wave scatters. E.g. the t-slope of the diffractive cross section is related to the size of the dense system. Nevertheless to a large extend the description of diffractive interactions can be based on the same concepts as used for dilute systems and as such the study of diffractive interactions combines elements from both dense and dilute systems.

In this section, recent developments in diffractive scattering presented at ISMD08 are reviewed. The emphasis lies on the determination of the so-called "rapidity gap survival factor" and its implications on central exclusive production of various final states in pp scattering.

2.1 Measuring diffractive parton density functions

Diffractive deep-inelastic scattering (DDIS), $ep \to e\gamma^* p \to eXp$, occurs through the fusion of a virtual photon emitted by the electron and a colourless object exchanged by the proton (see Fig. 6a). Besides the usual deep-inelastic scattering variables, x and Q^2, and diffractive variables, M_X, ξ (here called $x_{I\!P}$) and t, one defines $\beta = x/x_{I\!P}$ as the momentum fraction of the pomeron carried by the struck quark.

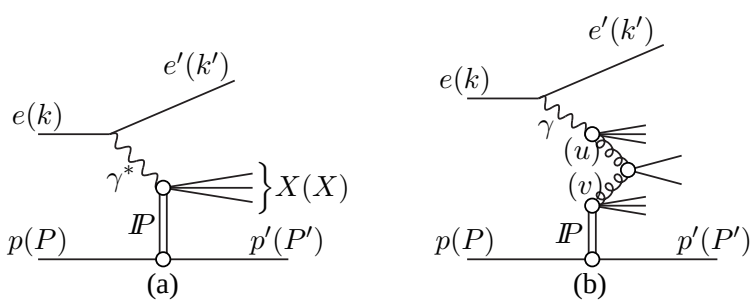


Fig. 6: (a) Diagram representing a diffractive deep-inelastic scattering interaction. (b) Diagram representing diffractive photoproduction. The four-momenta of the particles involved are given in parentheses

The HERA experiments use different methods for selecting diffractive interactions. In the rapidity gap method, one requires a large interval in rapidity devoid of particles. The kinematics of the event is then reconstructed from the dissociation system X. The four-momentum squared

t is not measured but integrated over. Another possibility is to extract a diffractive event sample from a fit to the M_X distribution. The non-diffractive background falls off exponentially towards low M_X and a fit of the form $D+C\exp(b\ln M_X^2)$ will yield the diffractive contribution D. As in the rapidity gap method, the kinematics of the event is measured from the X system and, again, one integrates over t. The most straightforward method is direct proton tagging with forward proton detectors. In this case, a pure single diffractive event sample is obtained without any contamination by proton dissociation events and a direct reconstruction of t is possible through the measurement of the proton four-momentum.

Figure 7 shows, as an example, the DDIS cross section obtained with the large rapidity gap method by the ZEUS and H1 experiments. Good agreement, within experimental uncertainties, is obtained between both experiments. A remaining normalisation difference of 13% is covered by the uncertainty on the proton dissociation correction (8%) and the relative normalisation uncertainty (7%). Results obtained with different selection methods also agree well.

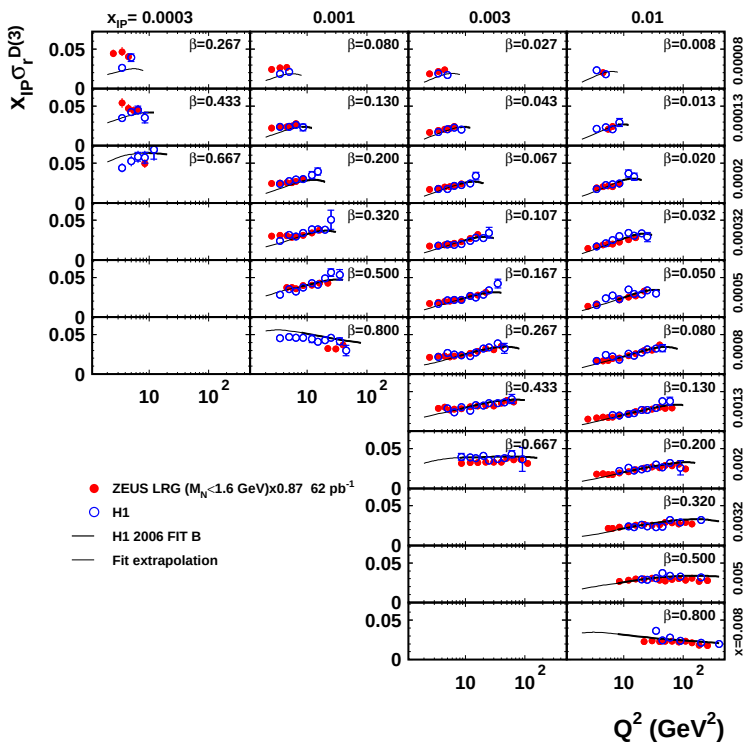


Fig. 7: The reduced cross section $\sigma_r^{D(3)} = \frac{d\sigma^D}{dx_{I\!P}\,dx\,dQ^2} / \frac{4\pi\alpha^2}{xQ^4}\left(1-y+\frac{y^2}{2}\right)$ is plotted against Q^2 in bins of x and $x_{I\!P}$. H1 and ZEUS data are compared to the H1 2006 Fit B (see futher in the text). A normalisation difference between ZEUS and H1 data is not shown (the ZEUS data points are scaled down by 13%).

In the QCD analysis of DDIS one assumes two different forms of factorisation. QCD hard scattering factorisation has been theoretically proven to hold in DDIS [15] and separates the partonic hard scattering cross section σ^{ei}, for the interaction between the electron and a quark i out of the proton, from a so-called diffractive parton density function (DPDF) f_i^D, which describes the probability to find a quark inside the proton under the condition that the proton survives the interaction with kinematics described by $x_{I\!P}$ and t:

$$\sigma^{ep\to eXY} = f_i^D(x, Q^2, x_{I\!P}, t)\cdot\sigma^{ei}(x, Q^2). \qquad (2)$$

Proton vertex (or Regge) factorisation on the other hand is only approximately satisfied. Nevertheless, it is used successfully in the parametrisation of the DDIS cross section. This fac-

torisation assumption expresses the DPDF as a superposition of pomeron and reggeon terms separating the flux factors $f_{I\!P/p}$ and $f_{I\!R/p}$ of pomerons and reggeons in the proton from their partonic structure $f_i^{I\!P}$ and $f_i^{I\!R}$:

$$f_i^D(x,Q^2,x_{I\!P},t) = f_{I\!P/p}(x_{I\!P},t)\cdot f_i^{I\!P}(\beta=\frac{x}{x_{I\!P}},Q^2)+n_{I\!R}f_{I\!R/p}(x_{I\!P},t)\cdot f_i^{I\!R}(\beta=\frac{x}{x_{I\!P}},Q^2). \quad (3)$$

Here $n_{I\!R}$ is factor describing the relative normalisation of reggeon to pomeron fluxes. The fluxes themselves are obtained from a parameterisation inspired by Regge Theory where the $x_{I\!P}$ dependence is governed by the parameter $\alpha_{I\!P}(0)$.

A NLO QCD fit can be performed yielding values for $\alpha_{I\!P}(0)$, $n_{I\!R}$ and a polynomial for the quark and gluon densities at a fixed starting scale Q_0^2. Usually, the reggeon flux is fixed and its parton density is taken to be equal to that of the pion.

The H1 collaboration obtained two fits (labelled A and B) using different polynomial forms for the gluon distribution at the starting scale (see Fig. 8) [16]. Both have similar good χ^2 values of 158/183 d.o.f. and 164/184 d.o.f., respectively. The quark distributions are found to be very stable in both fits, while the gluon distributions agree at low values of z but vary at high z.

One way of confirming the validity of the above approach and to differentiate between fit A and B is to take the parton distributions as obtained from a fit to the inclusive DDIS data and apply them to describe an exclusive channel such as DDIS dijet production. This channel is expected to be particularly sensitive to the gluon content of the pomeron, also at high z. Fit A is in good agreement with the DDIS dijet cross section at low $z_{I\!P}$, but overshoots the data at high $z_{I\!P}$. Fit B, however, is in good agreement with the data at all $z_{I\!P}$ [17]. This comparison therefore confirms QCD factorisation in DDIS and favours fit B obtained from inclusive data. Including the jet data in a combined fit of dijet and inclusive DDIS data yields a unique result with $\chi^2 = 196/218$ d.o.f., where both the quark and gluon distribution are constrained with similar good precision. The resulting parton densities lie close to Fit B and are the most precise to date.

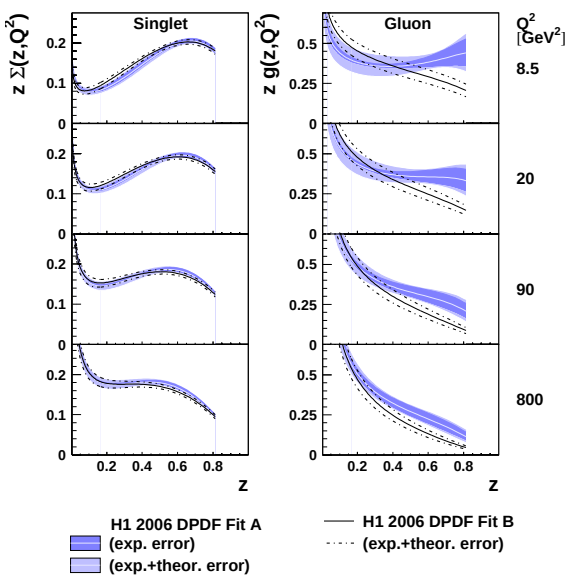


Fig. 8: The quark (singlet) and gluon densities as obtained in a NLO QCD fit are shown as function of fractional momentum z at different scales Q^2. Two fits are obtained based on different parametrisations of the gluon density at the starting scale Q_0^2.

2.2 Survival probabilities

Although the DPDFs extracted from a fit to inclusive DDIS data from HERA can be used to predict other DDIS channels such as dijet production, they fail to describe diffractive jet production

in proton-proton scattering at the TEVATRON by a factor of 10. This is to be expected, as QCD factorisation is not supposed to hold in proton-proton diffraction: multi-pomeron exchanges, remnant interactions or screening may lead to additional particle production, thereby destroying the rapidity gap. These effects can be parametrized as a rapidity gap survival probability and a lot of theoretical and experimental effort now goes to the determination of this factor.

One way to study the rapidity gap survival within one experiment is provided in electron-proton diffractive photoproduction (DPHP). In this process, $ep \to e\gamma p \to eXp$, a quasi-real photon emitted by the electron interacts diffractively with the proton (see Fig. 6b) to produce a central hadronic system X. If this system has a hard scale, one may define $x_\gamma = P \cdot u / P \cdot q$ as the fractional momentum from the photon entering the hard interaction and $z_{I\!P} = q \cdot v / q \cdot (P - P')$ as the fractional momentum from the colourless exchange transferred to the hard interaction. The four-momenta used in the above formulae are defined in the figure.

One can compare interactions where the quasi-real photon interacts as a whole to interactions where the photon is resolved in a hadron-like structure so that only part of the photon's momentum enters the dijet system. Experimentally, both cases can be distinguished by reconstructing the variable x_γ: direct photon interactions will have a reconstructed value of x_γ close to 1, while resolved photon interactions will have lower values for x_γ. One should note however that the separation between direct and resolved photon interactions in theoretical calculations is only possible at fixed order, as additional orders will move part of the direct photon cross section at lower order to the resolved photon cross section.

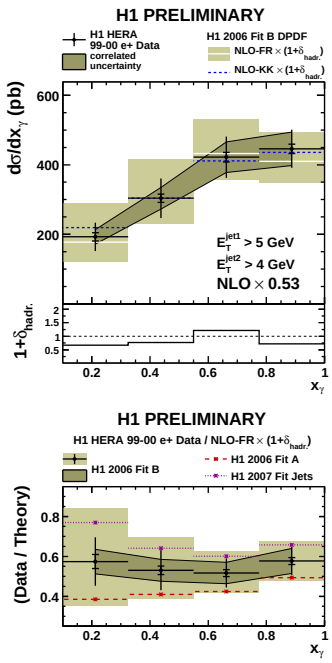


Fig. 9: Differential cross section and ratio of data over theory for diffractive photoproduction of dijets as function of x_γ measured by H1.

Both the H1 and ZEUS collaborations have studied the rapidity gap survival probability by measuring the x_γ dependence of the cross section for diffractive dijet production [18]. Surprisingly, although both experiments do observe a suppression of the measured cross section when compared to the theoretical prediction without survival factor, neither experiment finds a strong dependence on x_γ (see Fig. 9). As a result, no evidence has been found for any difference in survival probability for interactions mediated by resolved an direct photons. A difference in the observed survival factor between H1 and ZEUS has been traced back to different cutoffs in jet E_T and a harder E_T slope in data compared to NLO theory.

The measurement of diffractive production of vector bosons in pp collisions provides another possibility to study rapidity gap survival. Moreover, this process is also sensitive to the quark component of DPDFs.

2.3 Central exclusive production at the TEVATRON

Double pomeron exchange (DPE), $pp \rightarrow pXp$, is the process where both protons survive the interaction, whilst a central hadronic system with invariant mass M_X is produced through the fusion of two colourless objects (often assumed to be pomerons). In hard central exclusive production (CEP), the central hadronic system boasts a hard scale (transverse momentum, invariant mass,...) with no soft remnants present in the final state X.

Central exclusive production in pp collisions is a particularly interesting channel for the discovery or study of the Higgs because this channel has some advantages over inclusive channels: QCD $b\bar{b}$ backgrounds are suppressed due to the $J_z = 0$ spin selection rule, an accurate determination of the Higgs mass is possible through the measurement of the outgoing proton momenta and azimuthal angular correlations may shed information on the spin-parity of the Higgs-candidate. Given the large uncertainty on the rapidity gap survival factor, a data-driven calibration is however mandatory. Here the observation of central exclusive production of dijets, diphoton, χ_c particles, etc. may serve to calibrate models. The calculation in [20] predicts a CEP standard model Higgs cross section of 3 fb at the LHC. In particular scenarios of MSSM and NMSSM, CEP may be the most probable channel for a discovery [24].

The CDF collaboration searched for CEP of dijets by looking for an excess in the distribution of the dijet mass fraction $R_{jj} = \frac{M_{jj}}{M_X}$ in DPE events [19]. Events where dijets are produced exclusively should show up at $R_{jj} \approx 1$. In Fig. 10 the observed R_{jj} distribution is compared to the POMWIG Monte Carlo model. This model uses DPDFs extracted from data as input but does not include exclusive production of dijets. An excess of data over the POMWIG prediction is observed at high R_{jj}, indicating that exclusive dijet events are present in the data. As a cross-check, a similar search was made for an excess of b-tagged jets. Such an excess was not found, as is expected due to spin selection rules.

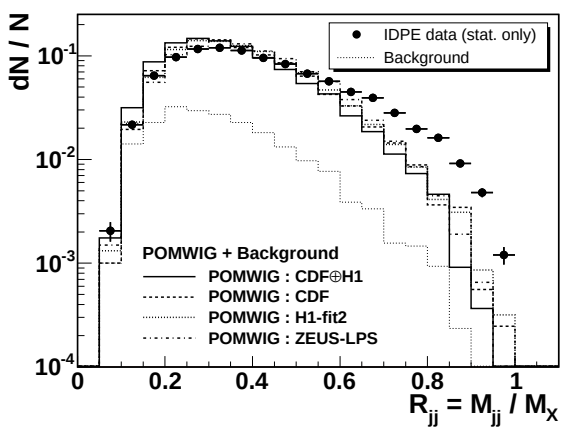


Fig. 10: (left) The R_{jj} distribution observed in DPE data (points) is compared to predictions by POMWIG (histograms) based on different DPDFs extracted from data.

After applying further selections to enhance the exclusive signal, a fit to the data distributions of R_{jj} was made using the sum of POMWIG and specific models for CEP of dijets with a free normalisation of the CEP models. Two models have been used: ExHuME, which is based on a LO pQCD calculation [20], and DPEMC, which is an exclusive DPE Monte Carlo model based on Regge Theory [21]. Both models are able to describe the excess at high R_{jj} well. However, when looking at the jet E_T distribution, the ExHuME model is favoured. This model also describes the M_{jj} distribution reasonably well.

Other CEP final states have also been investigated by the CDF Collaboration. In a sample

of $532\,\mathrm{pb}^{-1}$ of Run-II data, 3 exclusive diphoton events were found with $E_T^\gamma > 5\,\mathrm{GeV}$ and $|\eta^\gamma| < 1$ [22]. Exclusive production of dileptons can occur through two-photon exchange and is a nearly pure QED process. Using the same dataset as above, CDF found 16 candidate events with $E_T^e > 5GeV$ and $|\eta^e| < 2$, over an expected background of 1.9 ± 0.3 [23].

3 Dense systems

The approximations made for dilute systems will fail once the parton density becomes large enough. As observed at HERA, the proton structure function F_2 rises steeply towards small fractional momenta x. If continued unabided, this rise would violate unitarity conditions, even in the perturbative regime where $Q^2 \gg \Lambda^2$. One therefore expects new parton dynamics to show up at low x, resulting in a saturation of the growth of the parton density towards smaller x.

When parton densities become large, the linear approximation of Sec. 1 is no longer applicable. At high parton density, nonlinear fusion processes will start to balance parton branchings. Moreover, the collinear and k_T factorisation assumptions in perturbative QCD will become invalid, which means that higher twist contributions become important and that parton scatterings are no longer incoherent.

Saturation is expected to occur when partons are numerous enough and extended enough to overlap each other. This happens at low x and low Q^2. A simple estimate of the saturation scale is therefore given by the ratio of the parton density to the area of the target. Assuming the gluon density in the nucleus to be given by $G_A(x, Q^2) = Ag(x, Q^2)$, with A the atomic mass number and $g(x, Q^2)$ the gluon density inside the proton, the saturation scale for nuclei would be given by

$$Q_s^2 \propto \alpha_S \frac{xG_A(x, Q_s^2)}{\pi R_A^2} \propto A^{1/3} x^{-\lambda}, \tag{4}$$

where the last equation makes use of the fact that the nuclear radius $R_A \propto A^{1/3}$ and that the gluon density in the proton rises exponentially towards small x with exponent $\lambda \approx 0.3$.

From Eq. 4 one can deduce that saturation effects are amplified in heavy nuclei by a factor $A^{1/3}$. At RHIC, with d-Au collisions at 200 GeV, the saturation scale is given by $Q_s^2 \approx 2\,\mathrm{GeV}^2$. For p-Pb collisions at the LHC, with a centre-of-mass energy of 8.8 TeV, the saturation scale rises up to $5\,\mathrm{GeV}^2$.

3.1 Probing the matter created at RHIC

In a dense, strongly coupled medium, the propagation of high momentum, strongly interacting partons is expected to be impeded. This has been observed in heavy ion collisions at RHIC by looking at the nuclear modification factor $R_{AA}(p_T)$ which is defined as the ratio of particle yields in heavy ion collision to pp collisions, corrected for the number of collision partners [25]. As can be seen in Fig. 11 (left) a suppression is indeed observed for hadrons, but not for photons as should be the case because photons do not carry any colour charge. Moreover, the suppression for hadrons is not observed in periferal collisions where the medium is less dense. The same conclusion can be reached from Fig. 11 (right) where one looks for the away-side jet in proton and gold collisions [26]. While pp and p-Au data do show the presence of the away-side jet, it

dissappears in central Au-Au collisions indicating the effect of the dense medium. At high p_T, however, the away-side jet reappears, showing that it is possible to "punch through" the dense medium, as long as the initial momentum is high enough.

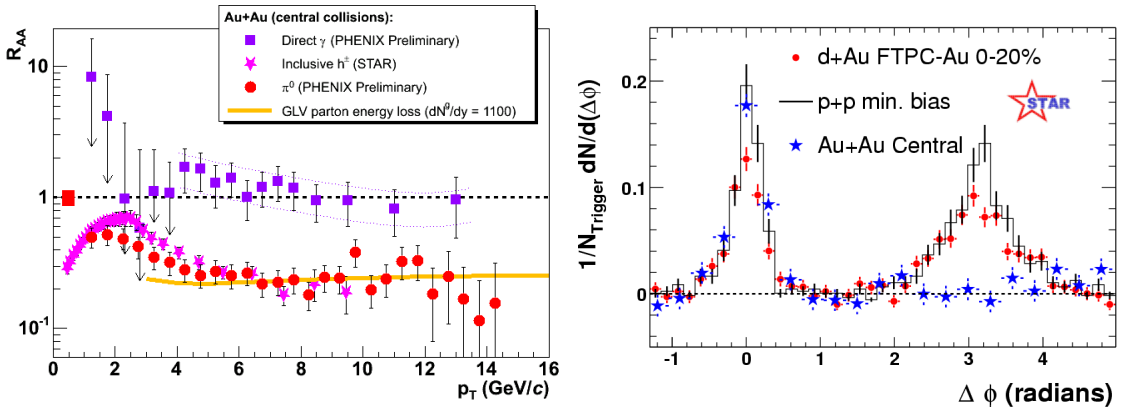


Fig. 11: (left) Nuclear modification factor as function of transverse momentum for direct photons, charged hadrons and neutral pions in central Au-Au collisions at 200 GeV centre-of-mass energy [27]. (right) Azimuthal correlation of charged hadrons with $p_T > 2$ GeV associated to a trigger particle with $4\ \mathrm{GeV} < p_T < 6\ \mathrm{GeV}$ [28].

For a quantitative understanding of these effects, one needs to constrain model parameters. Here the transport coefficient $\hat{q}$, defined as the average transverse momentum transferred per unit length, and gluon density dN_g/dy will play a major role. For this, more sofisticated observables are being used, such as di-hadron correlation function and fragmentation functions.

3.2 Saturation in heavy ion collisions from RHIC to LHC

The dense, strongly coupled nature of the medium probed in central heavy ion collisions at RHIC has thus been established. One has also found indications for the onset of saturation at RHIC. The charged hadron multiplicity at central rapidities is lower than predicted by all but a few models. Among those models giving a correct value are those which include saturation effects. The dependence of the charged hadron multiplicity on the centrality and centre-of-mass energy of the collision is consistent with geometrical scaling, which implies that the hadron multiplicity grows as the number of initally released gluons (assuming local parton-hadron duality) which is just proportional to the saturation scale [31]. Finally, Fig. 12 shows that, while d-Au collisions do not exhibit a suppression in R_{AA} for hadrons produced at central rapidities, a suppression does occur for hadrons produced at large rapidity [32]. This forward hadron suppression is well described by models based on saturation.

The rise of the saturation scale Q_s^2 from $2\ \mathrm{GeV}^2$ for 200 GeV d-Au collisions at RHIC to $5\ \mathrm{GeV}^2$ for 8.8 TeV p-Pb collisions at the LHC means that the LHC will be able to study saturation with perturbative probes. The ALICE Collaboration will study saturation effects with forward jets but also with low p_T open charm production at central rapidity.

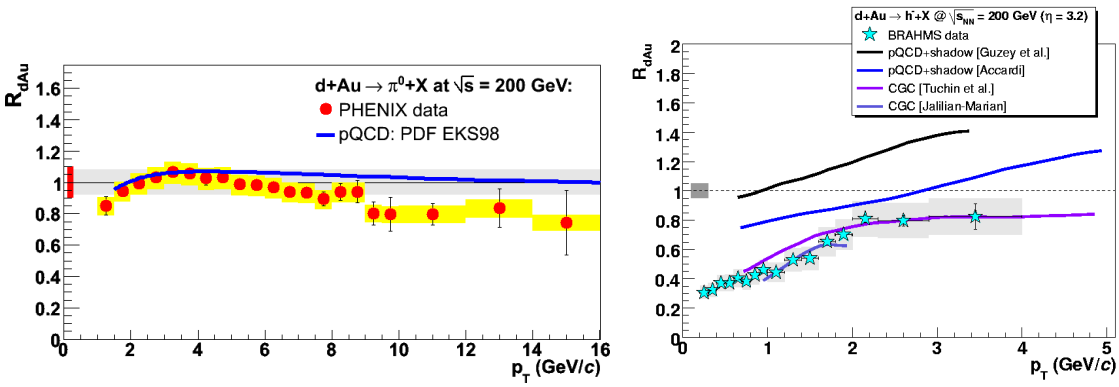


Fig. 12: Nuclear modification factors in deuterium-gold collisions for centrally (left) and forwardly (right) produced hadrons [29].

4 Strategies and analysis methods

In dense systems, the probability for additional activity besides the primary parton-parton interaction is large. One distinguishes two effects: the underlying event (UE) is caused by soft reinteractions between the remnants of the incoming particles, while multi-parton interactions (MPI) are due to multiple hard parton-parton interactions occuring in the same collision.

A good description of UE and MPI effects is crucial in the study of high energy hadron interactions. These effects may modify jet pedestals, mask missing energy or complicate isolation criteria. MPIs may even fake discovery signals, e.g. the MPI cross section for $pp \to Wb\bar{b}X$, where the W boson and $b\bar{b}$ pair are produced in separate parton-parton interactions, may constitute an important background to Higgs production at the LHC via W-Bremsstrahlung, $pp \to WHX$, with the Higgs boson decaying to a $b\bar{b}$ pair. Several models for UE and MPI effects exist in the form of tunes of the PYTHIA Monte Carlo program to TEVATRON data. However, the extrapolation to higher energy yields wide uncertainties on the magnitude of these effects at the LHC. It will therefore be of crucial importance to tune UE and MPI models with early LHC data

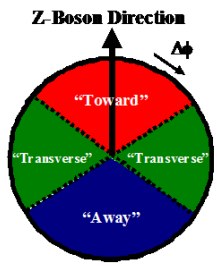


Fig. 13: Definition of "toward", "away" and "transverse" region in azimuth w.r.t. the direction of the Z-boson created in $p\bar{p} \to ZX$ interactions.

In the following, I will review some of the techniques, presented at ISMD08, which are used to study the effect of UE and MPI. As will be seen, detectors placed near the beamline in order to detect forward scattered particles play an essential role in the study of various high density effects, including QCD evolution and saturation.

4.1 Observables for studying underlying events and multi-parton interactions

The underlying event will produce additional soft particles next to the hard scattering component. It can therefore be beneficial to divide the phase space into different regions with respect to the direction of the hard scattering products and to look at various event properties in these

regions. In Fig. 13 this principle is applied to Drell-Yan production of lepton pairs via the process $p\bar{p} \rightarrow ZX$. One may then define observables like the charged particle multiplicity, the scalar transverse momentum sum of charged particles or the average or maximum transverse momentum of charged particles in each region. Some examples are given in Fig. 14. A excellent agreement with PYTHIA tune "AW" is observed. The close match with leading jet UEs is perhaps indicating a universality of underlying event models irrespective of the hard scattering event [33].

Multi-parton interactions will induce long range correlations in particle production: whereas in single interaction events the central particle multiplicity does not depend strongly on forward activity, one does expect a strong correlation between central particle multiplicity and forward energy [35]. Figure 15 shows the dependence of central particle multiplicity on forward energy depositions for different MPI scenarios. Clearly, in the absence of MPI, very little correlation is observed. A measurement of this correlation at the LHC may help to differentiate between different MPI tunes based on TEVATRON data.

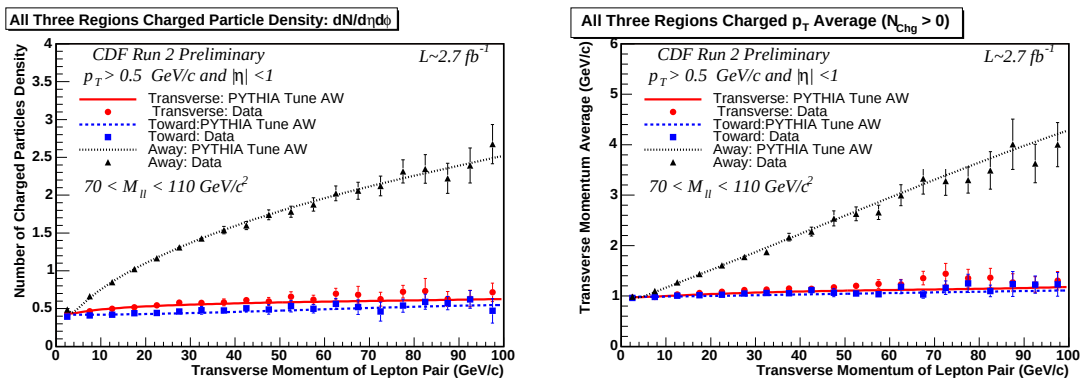


Fig. 14: Depedence of charged multiplicity (left) and average transverse momentum (right) on the p_T of the Z-boson created in $p\bar{p} \rightarrow ZX$ interactions in different region in azimuth. The effect of the recoil quark back-to-back to the Z-boson is clearly visible. Data are compared to the PYTHIA "AW" tune.

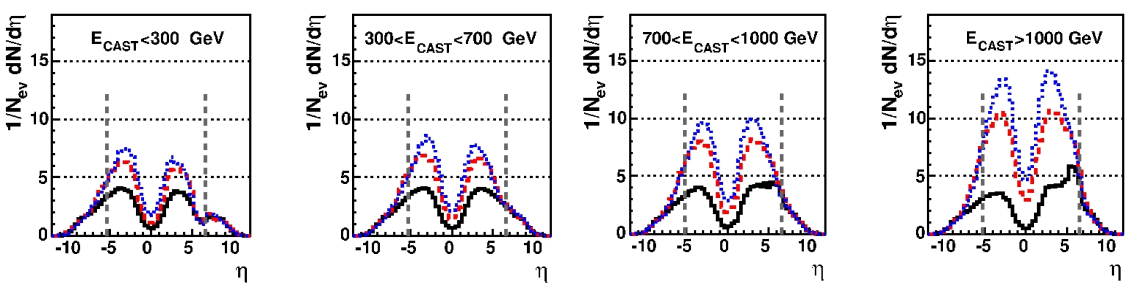


Fig. 15: Simulated rapidity distribution for particles in pp collisions produced at the LHC with different conditions on energy deposited in the forward region. E_{CAST} is defined as the energy sum of charged particles with $5.2 < \eta < 6.6$ and $p > 1$ GeV. The black histograms was obtained with MPI simulation turned off, while the coloured histograms represent different tunes for MPI implemented in PYTHIA.

4.2 Forward physics

Both the ATLAS and CMS Collaboration plan the installation of several detector near to the outgoing proton direction in order to detect forward scattered particles. The main detectors have calorimetric coverage up to values of pseudorapidity $|\eta| < 3$. Outside this range the ATLAS and CMS detector include foward calorimeters (FCAL and HF) covering the pseudorapidity range of $3 < |\eta| < 5$. Beyond this, the ATLAS Collaboration will install a luminosity detector (LUCID) covering $5.5 < |\eta| < 6.2$. In CMS, a similar pseudorapidity range, $5.2 < -\eta < 6.6$, will be covered by a calorimeter (CASTOR), albeit only on one side of the experiment. Both collaborations plan furthermore to install Zero Degree Calorimeters and Roman Pot detectors along the beam line. Also the TOTEM Collaboration, which shares the same interaction point as CMS, will install trackers and Roman Pot detectors close to the beam line. An overview of the coverage in pseudorapidity and transverse momentum is given in Fig. 16.

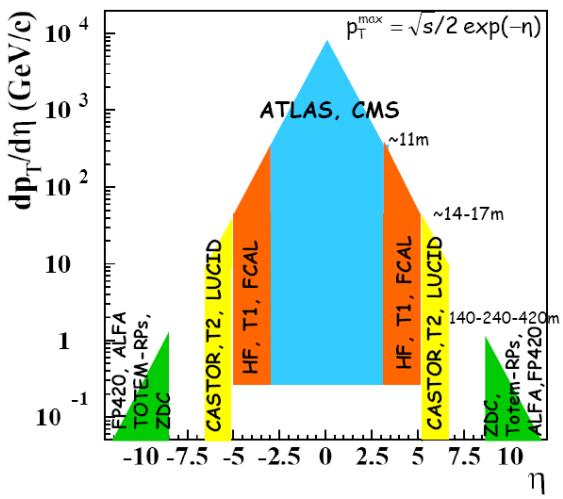


Fig. 16: Coverage in p_T and η of different subdetectors constructed and planned by the ATLAS, CMS and TOTEM Collaborations at the LHC.

At low Bjorken-x, partons may undergo long parton showers before they meet to form the hard scattering subsystem. Forward particles can then be produced in two ways: (i) a collision between a low-x and a high-x parton will boost the hard scattering subsystem forward; (ii) a collision between two low-x partons will produce a central hard scattering system while forward jets may result from gluons radiated in the parton shower.

A large imbalance in Bjorken-x will result in a hard scattering subsystem X that is produced forward. X can be jets, Drell-Yan pairs, prompt photons, heavy quark pairs, etc. The relation between the Bjorken-x of the low-x parton and the pseudorapidity of the hard scattering system is given by $x = \frac{Q}{\sqrt{s}} e^{-\eta}$, which yields $x \geq 10^{-6}$ for $Q \geq 10\,\mathrm{GeV}$ and $\eta = 6$ at the LHC. Figure 17 shows the kinematic plane of M vs. x for the production of forward Drell-Yan pairs with invariant mass M. CASTOR will be able to measure the energy deposits of Drell-Yan e^+e^- pairs with $M \lesssim 30\,\mathrm{GeV}$ and $x < 10^{-5}$. In this kinematic region one expects large shadowing effects in the proton parton densities. One calculation using the PYTHIA Monte Carlo generator based on a *saturated* parton density function [36] yields a reduction by a factor 2 w.r.t. the prediction based on the CTEQ5L parametrisation [37].

When both partons involved in the hard scattering have similar, low x, a dijet system will be produced centrally in the detector. Forward jets may then result from parton showers. BFKL-like QCD evolution will result in a larger cross section for high energy forward jets, as can be seen in Figure 17. Also jet-gap-jet or Mueller-Navelet jet topologies are particularly sensitive to different approaches for QCD evolution.

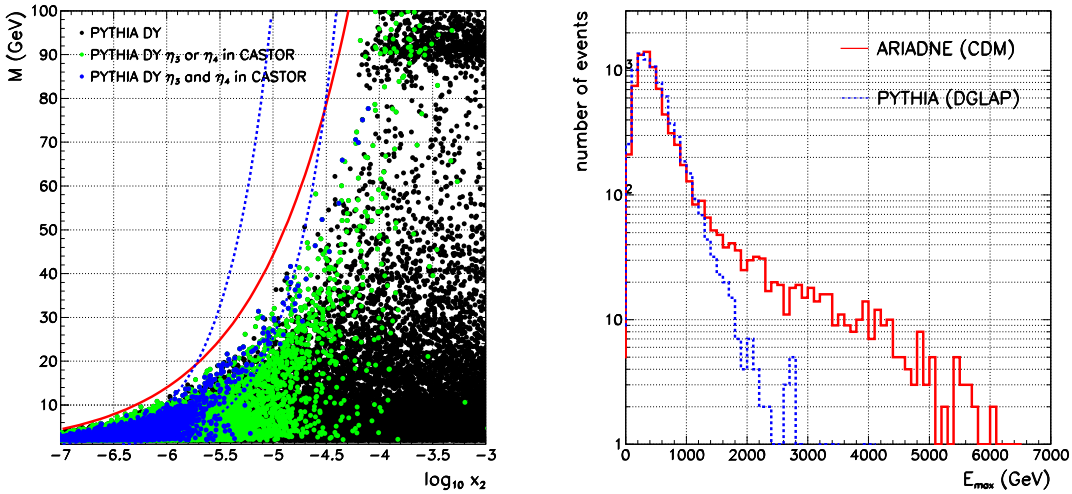


Fig. 17: (left) Kinematic plane of invariant mass M vs. x for Drell-Yan pairs at generator level. The full line gives the kinematic limit $M_{max} = \sqrt{x_2 s}$, while the dashed lines show the acceptance limits $M = x_2\sqrt{s}\exp^y, y \in [5.2, 6.6]$ of the CASTOR calorimeter. Green (blue) dots indicate Drell-Yan pairs where at least one (both) electron(s) are within the CASTOR acceptance. (right) Distribution of generator-level jet energy in CASTOR for events with hard central dijets ($p_T > 60$ GeV and $|\eta| < 3$) as obtained from a PYTHIA simulation using the standard DGLAP evolution [38] (dashed line) and the colour dipole model implemented in ARIADNE [39] (full line).

5 New physics

Many different scenarios exist for physics beyond the Standard Model, ranging from compositeness over supersymmetry to the existence of extra dimensions. It is cleary impossible to review all final states that are being scrutinized by running and future experiments in this experimental summary. For this, I refer to the relevant contributions to these proceedings. Here, I will focus on model independent searches for new physics and the status of Standard Model Higgs searches at the TEVATRON and the LHC.

5.1 Global search for physics beyond the Standard Model

Data collected in Run II of the TEVATRON have been searched for indications of new electroweak scale physics. Rather than focusing on particular new physics scenarios, CDF data have been analyzed for discrepancies with the Standard Model prediction. A model-independent approach (Vista) considers gross features of the data, and is sensitive to new large cross section physics. A quasi-model-independent approach (Sleuth) emphasizes the high-p_T tails, and is particularly sensitive to new electroweak scale physics. An algorithm has been developed to search invariant mass distributions for "bumps" that could indicate resonant production of new particles. As can been seen in Fig. 18, this combined global search for new physics in 2.0 fb^{-1} of $p\bar{p}$ collisions at $\sqrt{s} = 1.96$ TeV reveals no indication of physics beyond the Standard Model [40].

The H1 collaboration too has performed a model-independent search for deviations from

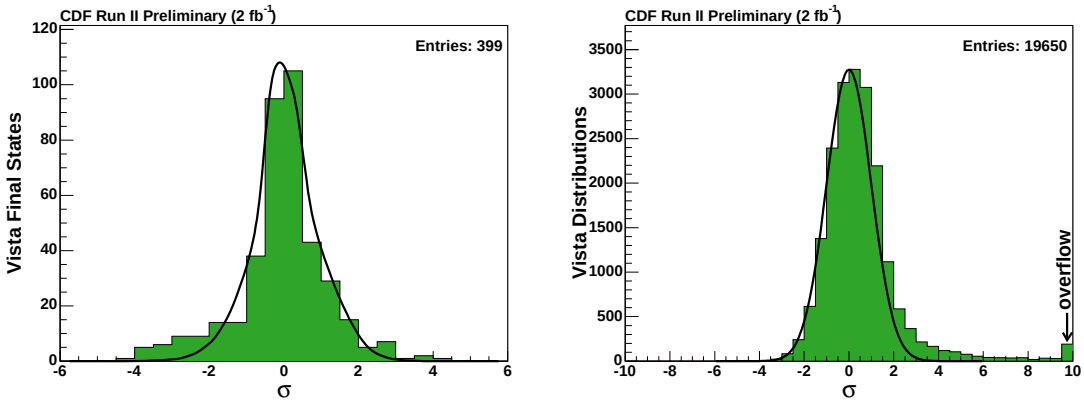


Fig. 18: (left) Graphical summary of Vista final state population discrepancies showing the number of standard deviations from the Standard Model prediction. No final state shows a significant population discrepancy, after accounting for the trials factor. (right) Graphical summary of Vista kinematic variable distribution discrepancies. Interest is focused on the outliers, representing distributions with significant discrepancy. However, after analysis, none of these discrepant distributions motivate a new physics claim.

the Standard Model. Both e^+p and e^-p collisions from the HERA II run are used, corresponding to $178\ \mathrm{pb}^{-1}$ and $159\ \mathrm{pb}^{-1}$, respectively. All event topologies involving isolated electrons, photons, muons, neutrinos and jets with high transverse momenta are investigated in a single analysis. Events are assigned to exclusive classes according to their final state. A statistical algorithm is used to search for deviations from the Standard Model in the distributions of the scalar sum of transverse momenta or invariant mass of final state particles and to quantify their significance. A good agreement with the Standard Model prediction is observed in most of the event classes. Figure 19 shows that no significant deviation is observed in the phase-space and in the event topologies covered by this analysis [41].

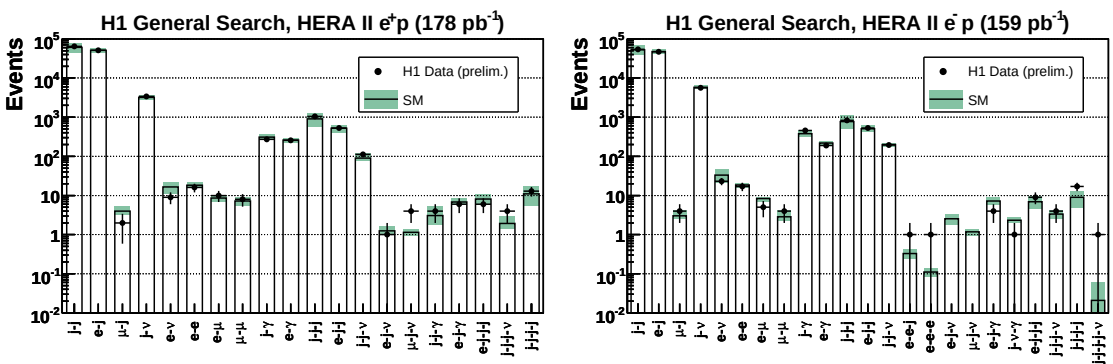


Fig. 19: The data and SM expectation for all event classes with observed data events or SM expectation greater than 1 event: (left) e^+p data, (right) e^-p data.

If new physics beyond the SM is around, the LHC experiments will see it in most of the

cases. The observation and identification of supersymmetric reaction channels will require as many measurements as possible, including cross sections, branching ratios, masses and spins. Various methods will be used and are thoroughly being prepared [42].

5.2 Standard Model Higgs searches at the TEVATRON and LHC

The CDF and D0 collaborations have each combined their search results in single full mass range exclusion plots. The 95% CL exclusion limits lie around 4 and 2 times the Standard Model cross sections for $m_H = 115\,\mathrm{GeV}$ and $m_H = 170\,\mathrm{GeV}$, respectively (see Fig. 20 (left-top)). A TEVATRON wide combination of low mass exclusion limits is challenging because of the large number of channels involved. An exclusion limit of around 3 times the Standard Model cross section at $m_H = 115\,\mathrm{GeV}$ is however expected if CDF and D0 results would be combined. At high mass, a Standard Model Higgs particle with $m_H = 170\,\mathrm{GeV}$ is now excluded at 95% CL by the combined CDF and D0 data, as is shown in Fig. 20 (left-bottom). A larger exclusion zone around 170 GeV will probably follow soon.

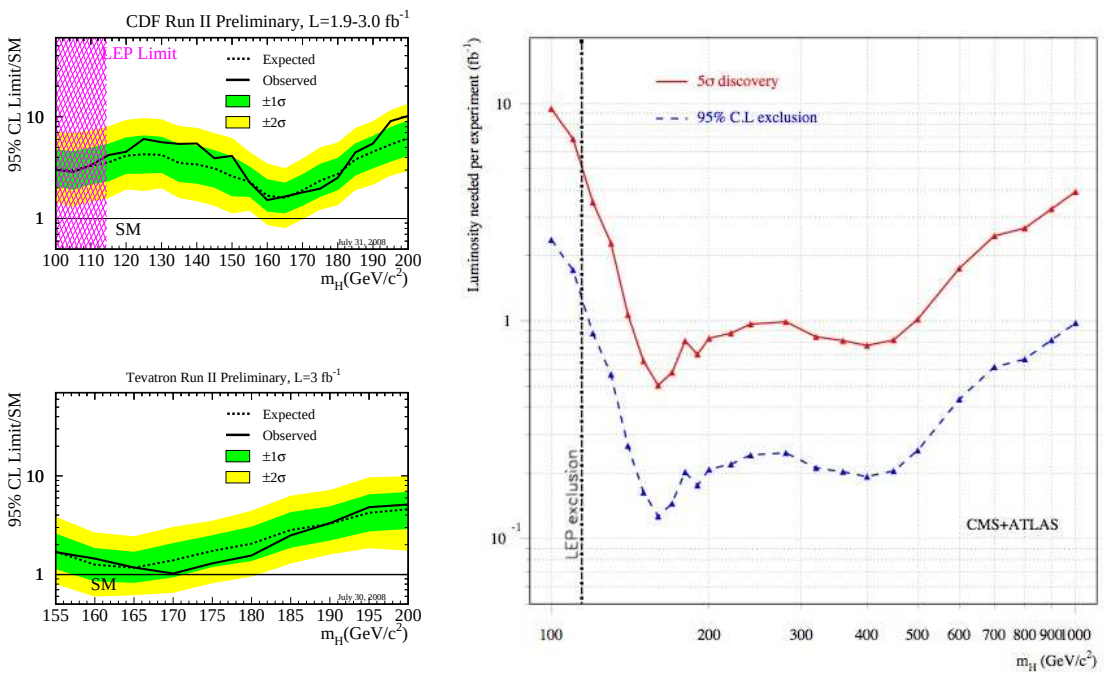


Fig. 20: (left-top) Observed and expected (median, for the background-only hypothesis) 95% CL upper limits on the ratios to the SM cross section, as functions of the Higgs boson mass between 100 and 200 GeV/c^2 for the combined CDF data. The bands indicate the 68% and 95% probability regions where the limits can fluctuate, in the absence of signal. (left-bottom) Observed and expected 95% CL upper limits at high masses as obtained from the combined CDF and D0 data. (right) The prospects for discovering a Standard Model Higgs boson in initial LHC running, as a function of its mass, combining the capabilities of ATLAS and CMS.

A light Standard Model Higgs particle therefore seems most likely. This happens to be the

most challenging region, also at the LHC. Figure 20 (right) shows the luminosity needed for a discovery or 95% CL exclusion at the LHC. 5 or 1 fb^{-1} are needed for a 5σ discovery or 95% CL exclusion, respectively [44].

Acknowledgments

I would like to thank the organisers of ISMD08 for their hospitality and the invitation to DESY, Hamburg. I acknowledge the hard work of all speakers and gladly refer to individual contributions in these proceedings for more detailed information on the topics presented during the symposium.

References

[1] V. N. Gribov, L. N. Lipatov, Sov. J. Nucl. Phys. 15 (1972) 438; ibid. 15 (1972) 675; L. N. Lipatov, Sov. J. Nucl. Phys. 20 (1975) 94; G. Altarelli and G. Parisi, Nucl. Phys. B126 (1977) 298; Yu. L. Dokshitzer, Sov. Phys. JETP 46 (1977) 641.

[2] E. A. Kuraev, L. N. Lipatov and V. S. Fadin, Sov. Phys. JETP 44 (1976) 443; ibid. 45 (1977) 199; I. I. Balitsky and L. N. Lipatov, Sov. J. Nucl. Phys. 28 (1978) 822.

[3] M. Ciafaloni, Nucl. Phys. B296 (1998) 49; S. Catani, F. Fiorani and G. Marchesini, Phys. Lett. B234 (1998) 339; ibid. Nucl. Phys. B336 (1990) 18; G. Marchesini, Nucl. Phys. B445 (1995) 49.

[4] A. M. Cooper-Sarkar, *Extraction of the proton parton density functions using a NLO-QCD fit of the combined H1 and ZEUS inclusive DIS cross sections*, Proc. of XVI Int. Workshop on Deep Inelastic Scattering and Related Topics, London, England, April 2008, http://dx.doi.org/10.3360/dis.2008.25.

[5] V. Chekelian, *Neutral Current DIS with polarized e^+/e^- at HERA*, Proc. of the XXXIII Int. Conference on High Energy Physics, Moscow, Russia, July-August 2006.

[6] V. Chekelian, *A measurement of the longitudinial proton structure function $F_L(x, Q^2)$ at high Q^2 at HERA*, Proc. of the XVI Int. Workshop on Deep Inelastic Scattering and Related Topics, London, England, April 2008, http://dx.doi.org/10.3360/dis.2008.39.

[7] D0 Collaboration, Phys. Rev. Lett. 101 (2008) 062001.

[8] G. Watt, A. D. Martin, W. J. Stirling, R. S. Thorne, *Recent Progress in Global PDF Analysis*, Proc. of the XVI Int. Workshop on Deep Inelastic Scattering and Related Topics, London, England, April 2008, http://dx.doi.org/10.3360/dis.2008.22.

[9] S. Malik, *PDF constraints from CDF*, Proc. of the XVI Int. Workshop on Deep Inelastic Scattering and Related Topics, London, England, April 2008, http://dx.doi.org/10.3360/dis.2008.26.

[10] M. Gouzevitch, *Jet cross sections and α_S in DIS*, Proc. of the XVI Int. Workshop on Deep Inelastic Scattering and Related Topics, London, England, April 2008, http://dx.doi.org/10.3360/dis.2008.171.

[11] ZEUS Collaboration, Nucl. Phys. B786 (2007) 152-180.

[12] H1 Collaboration, Eur. Phys. J. C46 (2006) 27-42.

[13] A. W. Jung, *D^* meson production in DIS and photoproduction with the H1 detector at HERA*, Proc. of the XVI Int. Workshop on Deep Inelastic Scattering and Related Topics, London, England, April 2008, http://dx.doi.org/10.3360/dis.2008.196. U. Samson, *Beauty photoproduction at ZEUS*, Proc. of the XVI Int. Workshop on Deep Inelastic Scattering and Related Topics, London, England, April 2008, http://dx.doi.org/10.3360/dis.2008.189.

[14] M. Ruspa, *Inclusive Diffraction in DIS with the ZEUS detector*, Proc. of the XVI Int. Workshop on Deep Inelastic Scattering and Related Topics, London, England, April 2008, http://dx.doi.org/10.3360/dis.2008.65.

[15] J. Collins, Phys. Rev. D57 (1998) 3051 [Erratum-ibid. D61 (2000) 019902]

[16] H1 Coll., Eur. Phys. J. C48 (2006) 715-748.

[17] H1 Coll., JHEP 0710:042, 2007.

[18] K. Černy, *Diffractive photoproduction of dijets in ep collisions at HERA*, Proc. of the XVI Int. Workshop on Deep Inelastic Scattering and Related Topics, London, England, April 2008, http://dx.doi.org/10.3360/dis.2008.69; ZEUS Coll., Eur. Phys. J. C55 (2008) 177-191.

[19] CDF Coll., T. Aaltonen et al., Phys. Rev. D77, 052004 (2008).

[20] J. Monk and A. Pilkington, Comput. Phys. Commun. 175, 232 (2006); V. A. Khoze, A. D. Martin and M. G. Ryskin, Eur. Phys. J. C14, 525 (2000).

[21] M. Boonekamp and T. Kucs, Comput. Phys. Commun. 167, 217 (2005); A. Bialas and P. V. Landshoff, Phys. Lett. B256, 540 (1991).

[22] CDF Coll., T. Aaltonen et al., Phys. Rev. Lett. 99, 242002 (2007).

[23] CDF Coll., A. Abulencia et al., Phys. Rev. Lett. 98, 112001 (2007).

[24] M. Tasevsky, S. Heinemeyer and V. Khoze *Central exclusive diffractive MSSM Higgs boson production by forward proton tagging at the LHC* and J. Forshaw, *NMSSM Higgs Boson Production with Tagged Protons*, Proc. of the XVI Int. Workshop on Deep Inelastic Scattering and Related Topics, London, England, April 2008, http://dx.doi.org/10.3360/dis.2008.84 and http://dx.doi.org/10.3360/dis.2008.86.

[25] STAR Coll., Phys. Rev. Lett. 91 (2003) 072304

[26] STAR Coll., Phys. Rev. Lett. 90 (2003) 082302; ibid. 97 (2006) 162301.

[27] D. G. d'Enterria, Eur. Phys. J. C **43** (2005) 295 [arXiv:nucl-ex/0504001].

[28] C. Adler *et al.* [STAR Collaboration], Phys. Rev. Lett. **90** (2003) 082302 [arXiv:nucl-ex/0210033].

[29] D. G. d'Enterria, J. Phys. G **34** (2007) S53 [arXiv:nucl-ex/0611012].

[30] H. Caines, these proceedings.

[31] N. Armesto, C. A. Salgado, U. A. Wiedemann, Phys. Rev. Lett. 94 (2005) 022002.

[32] A. Dainese, these proceedings.

[33] D. Kar and R. Field, CDF/PUB/CDF/PUBLIC/9351, July 24, 2008.

[34] CDF Coll., Phys. Rev. Lett. 79, 584 (1997)

[35] Z. Rurikova, *Underlying event studies with Castor calorimeter in CMS experiment*, at "HERA and the LHC A workshop on the implications of HERA for LHC physics", CERN, May 2008.

[36] A. Dainese et al., *Small-x effects in heavy quark production*, Proc. of the HERA and the LHC workshop, March 2004 - March 2005; K. J. Eskola et al., Nucl. Phys. B660 (2003) 211.

[37] H. L. Lai et al., Eur. Phys. J. C12 (2000) 375 - 392.

[38] T. Sjöstrand, S. Mrenna and P. Skands, JHEP 05 (2006) 026.

[39] L. Lönnblad, Comput. Phys. Commun. 71 (1992) 15.

[40] C. Henderson, *Results of a model-independent global search for new physics at CDF*, Proc. of the XLIIIth Rencontres de Moriond: QCD and High-Energy Interactions, La Thuile, Italy, March 2008, arXiv:0805.0742v1 [hep-ex].

[41] E. Sauvan, *A general search for new phenomena at HERA*, Proc. of 15th Int. Workshop on Deep-Inelastic Scattering and Related Subjects, Munich, April 2007, http://dx.doi.org/10.3360/dis.2007.73.

[42] W. Ehrenfeld, *Supersymmetry and other beyond the Standard Model physics: Prospects for determining mass, spin and CP properties*, these proceedings, ATL-PHYS-PROC-2008-075.

[43] CDF and D0 Collaborations, *Combined CDF and D0 upper limits on Standard Model Higgs boson production at high mass (155–200 GeV^2/c^2) with 3 fb^{-1} of data*, Proc. of the XXXIV International Conference on High Energy Physics, ICHEP08, July 29-August 5, Philadelphia, USA, arXiv:0808.0534v1 [hep-ex].

[44] J.-J. Blaising et al., *Potential LHC contributions to Europe's future strategy at the high-energy frontier*, CERN Council Strategy Group, Briefing Book Volume 2, http://council-strategygroup.web.cern.ch.

Theory Summary: International Symposium on Multiparticle Dynamics 2008

Yuri V. Kovchegov
Department of Physics, The Ohio State University, Columbus, OH 43210, USA
DOI: http://dx.doi.org/10.3204/DESY-PROC-2009-01/89

Abstract
I summarize the theory talks presented at the International Symposium on Multiparticle Dynamics 2008.

1 Introduction

The XXXVIII International Symposium on Multiparticle Dynamics (ISMD 2008) covered a wide variety of topics in nuclear and particle physics. The organizers had an interesting idea of arranging all the topics on a single plot in the $(\ln Q^2, \ln 1/x_{Bj})$-plane, as shown in the conference poster. I think the idea of such classification on such a broad scale is new and interesting: in Fig. 1 I present my own version of the classification proposed by the organizers with some slight modifications as compared to the original. Fig. 1 gives the summary of the topics covered during the conference: below I will discuss each of the topics shown in Fig. 1 in a separate Section.

Indeed no classification can adequately reflect all the subtleties of each of the topics discussed. The classification of Fig. 1 is no exception. Many of the subjects shown have a lot more dimensions to them (in some cases literally so) than shown in Fig. 1.

The idea of mapping out the $(\ln Q^2, \ln 1/x_{Bj})$-plane comes from the physics of parton saturation at small Bjorken x, also known as the Color Glass Condensate (CGC) (for a review see [1]). It appears that this approach could be generalized beyond small-x physics. One of the main concepts of CGC is that at small enough x the gluon density in the proton or nuclear wave functions gets so high that non-linear effects, such as parton mergers, become important leading to saturation of gluon and quark distribution functions. The transition to this saturation regime is described by the saturation scale Q_s, which is a function of x. Q_s increases as x decreases. Saturation region is schematically represented by a yellow triangle in Fig. 1. Indeed strong interaction physics below the confinement scale, at $Q^2 < \Lambda^2_{\rm QCD}$, is non-perturbative. The non-perturbative large-coupling region is denoted in Fig. 1 by a blue rectangle. At small enough x the saturation scale becomes larger than $\Lambda_{\rm QCD}$: therefore the saturation regime lies in the perturbative region to the right of $\Lambda_{\rm QCD}$.

The large-Q^2 region with not very small x is the domain of linear DGLAP evolution equation [2–4]. This is the region where collinear factorization applies. The approaches based on collinear factorization, such as parton cascade simulations and jet physics in general, also belong in that region. Some of the topics discussed in that subfield will be described in Sect. 2 below. As one moves towards smaller x (and somewhat lower Q^2) the logarithms of $1/x$ become important. Such logarithms are resummed by the BFKL equation [5, 6]. Progress in our understanding of BFKL will be reviewed in Sect. 3. Moving on toward even lower x one crosses the saturation line and enters the saturation/CGC region. Here the nonlinear JIMWLK [7, 8]

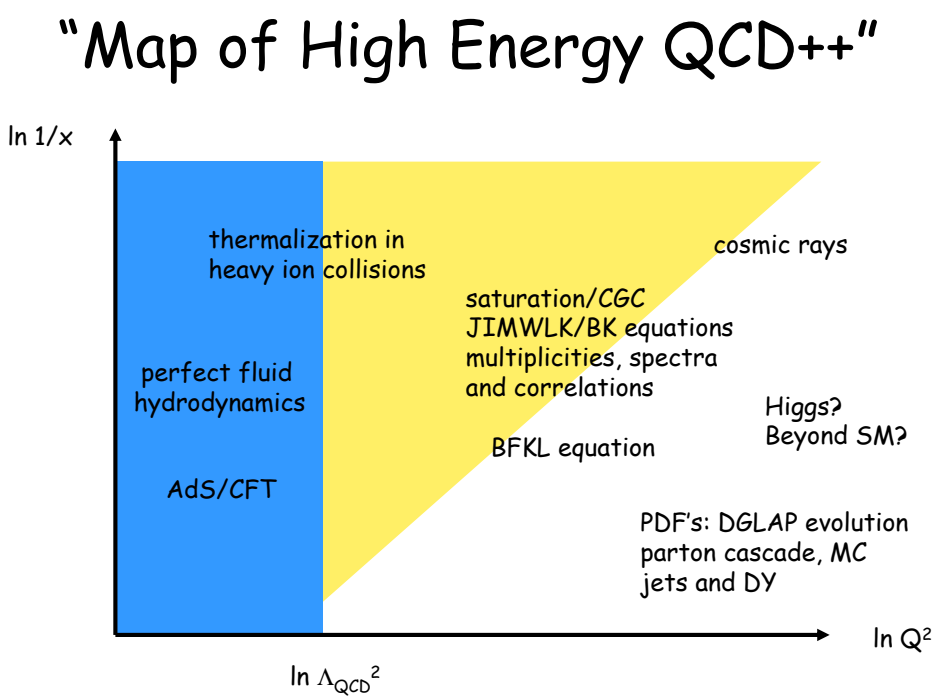


Fig. 1: My own version of arranging all the topics covered during the conference in the $(\ln Q^2, \ln 1/x_{Bj})$-plane. The idea was borrowed from the conference poster with the topics somewhat modified and moved around.

and BK [9, 10] evolution equations apply. I have also grouped in this region of the map the predictions of CGC physics for various AA, pA and pp observables. The talks on this topic will be discussed in Sect. 4. All the small-x machinery should be directly applicable to cosmic ray physics: the progress in this direction will be mentioned in Sect. 5. Heavy ion physics poses a number of important questions for theorists. Over the past several years a consensus has been reached in the heavy ion community that heavy ion collisions at RHIC lead to the creation of a strongly-coupled quark-gluon plasma (QGP). The challenges facing the heavy ion theory community include understanding of the creation of such medium: how do the particles produced in a collision thermalize to form the strongly-coupled QGP? The mechanism leading to the creation of strongly-coupled QGP may or may not be perturbative, as reflected in Fig. 1. The talks on this subjects will be reviewed in Sect. 6. The subsequent evolution of the produced medium governed by the perfect fluid or viscous hydrodynamics will be discussed in Sect. 7. Developments in Anti-de Sitter/Conformal Field Theory (AdS/CFT) correspondence, which can shed light on many topics in heavy ion collisions, deep inelastic scattering (DIS), and hadronic scattering, will be reviewed in Sect. 8. Finally, the Higgs boson and physics beyond Standard Model are placed at large Q^2 and at large energy/small-x in Fig. 1: they will be mentioned in Sect. 9.

ISMD 2008 featured a large number of very interesting talks. I have to apologize before-

hand for not being able to cover all of them due to space limitations. Also, when describing work presented at ISMD 2008 I will not provide explicit citations to the corresponding publications, assuming that interested readers could find the needed references in the Proceedings contributions of the corresponding speakers. Finally, as this is not a review article, in presenting the topics I will not spend much time recounting many important successes in each subfield, but will concentrate instead on open problems at the forefront of research.

2 PDF's, parton cascades and jets

Much of our knowledge about QCD at high energies comes from and could be summarized in parton distribution functions (PDF's). Our current knowledge of PDF's was summarized in the talk by Stirling. Fig. 2 presents the proton PDF's at $Q^2 = 10$ GeV^2 given by the MSTW 2007 parameterization.

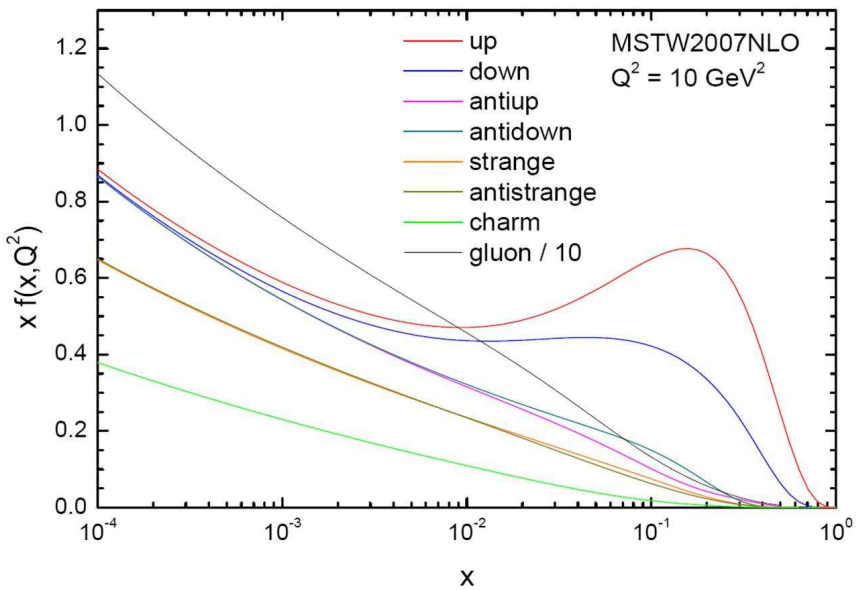


Fig. 2: PDF's in the MSTW 2007 parameterization (from the talk by Stirling).

There has been much improvement in our understanding of PDF's in recent years. Error analysis have been carried out and now many PDF's come with error bars, as demonstrated in Fig. 3 shown in the talk by Rojo-Chacon. Fig. 3 shows singlet and gluon distribution functions at $Q_0^2 = 2$ GeV^2 due to CTEQ, MRST/MSTW, Alekhin and NNPDF collaborations [11–14] along with the error bars. We see that in the small-x region PDF uncertainties are large. They appear to increase as we go toward lower Bjorken x into the region where there is no data.

The lower panel of Fig. 3 also shows that at small-x and small-Q^2 the gluon distribution function becomes *negative*. This issue had been discussed a lot over the past years, and received a lot of attention at ISMD 2008 as well. The question is whether a negative gluon distribution necessarily implies a breakdown of the approach based on the linear DGLAP evolution equation. The standard argument against DGLAP breakdown is that at small Q^2 the expectation value of

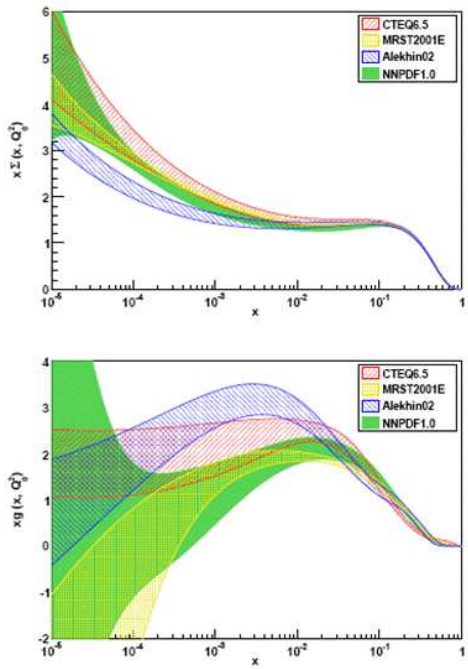


Fig. 3: Singlet and gluon distribution function at $Q_0^2 = 2$ GeV^2 due to different PDF collaborations with the error bars shown (from the talk by Rojo-Chacon).

the operator identified with the gluon distribution function does not anymore count the number of gluons. Therefore no fundamental law is violated if it goes negative. As was brought up in the discussion session by Cooper-Sakar, one has to look at the structure function F_L, which is closely related to the gluon distribution function. F_L is indeed a physical observable expressible in terms of scattering cross sections: it has to be positive. If F_L resulting from the gluon distribution functions in the lower panel of Fig. 3 remains positive, then one could argue that there is no problem with the negative gluon distribution function. As indeed the F_L's obtained from the gluon distribution functions in Fig. 3 appear to be positive one indeed can argue that negative xG are allowed.

To me such arguments sound a bit like epicycles in Ptolemaic astronomy: some of our colleagues are trying to rescue a theory in trouble. Strictly-speaking it is true that there is nothing requiring xG to be positive definite everywhere. However, I spent many years calculating xG at small-x in the perturbative (saturation) framework and never saw it go negative. It would be interesting and convincing if the proponents of negative xG could come up with a (purely theoretical) model for gluon distribution, where everything is perturbative and under calculational control, and where xG does become negative at small-x and small-Q^2. For instance one could study gluon distribution in a very heavy quarkonium. Large quark masses would insure small coupling allowing to calculate xG perturbatively from first principles. If negativity of xG at low-x and low-Q^2 is a natural property of the gluon distribution operator, it should come out straightforwardly in such a calculation.

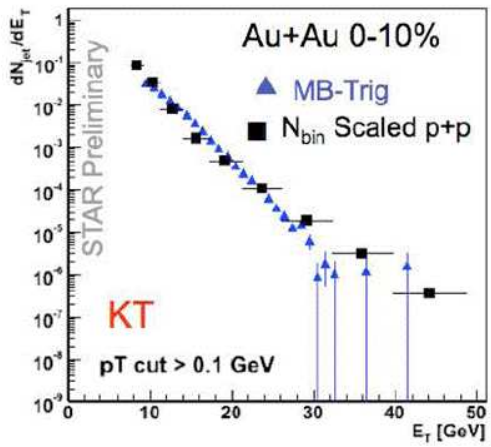


Fig. 4: Preliminary STAR collaboration data on the number of jets as a function of E_T of the jet for central $Au + Au$ collisions (triangles) and for proton-proton collisions scaled up by the number of binary collisions (squares). (Picture is from the talk by Rojo-Chacon, originally taken from [15].)

Parton cascades as the way to model actual collisions on the event-by-event basis received a lot of attention at ISMD 2008 as well with a nice review talk by Z. Nagy. The ideas of going beyond collinear factorization and including k_T-dependent effects into parton cascades were discussed by Hautmann. Problems with Monte Carlo simulations of small-x coherent effects were discussed in the talk by Marchesini. There is a difficult problem that arises when one tries to include recoil effects into the color-dipole parton cascades in a probabilistic QCD picture.

There were several good talks on jet analysis and algorithms. I was particularly interested to see jet analyses coming to RHIC. The suppression of high-p_T hadrons produced in $Au + Au$ collisions at RHIC as compared to $p + p$ collisions scaled up by the number of binary collisions is believed to be one of the smoking guns for the creation of a hot and dense medium in heavy ion collisions, likely to be a thermalized quark-gluon plasma (QGP) [16–18]. The suppression is quantified with the help of the nuclear modification factor R^{AA}. The suppression was observed in RHIC experiments at $\sqrt{s} = 200$ GeV and attributed to parton energy loss also known as jet quenching. However one should not forget that in the R^{AA} measurements one measures individual high-p_T hadrons, and not proper jets. A jet analysis with a jet cone definition has recently been carried out by the STAR experiment. The preliminary results are shown in Fig. 4, which was shown at ISMD 2008 by Rojo-Chacon with a similar figure shown by Caines. Fig. 4 depicts the number of jets as a function of E_T of the jet. In Fig. 4 the triangles denote the data for $Au + Au$ collisions, while the squares denote the $p + p$ data scaled up by the number of binary collisions. It is curious and a bit puzzling that no visible suppression of jets in $Au + Au$ compared to scaled-up $p + p$ was found (within error bars). One could speculate that the energy deposited by the hard parton into the medium is not simply absorbed by the medium, but instead travels along with the parton in the form of softer partons, such that the net energy in the jet cone does not change and the jet as a whole does not get suppressed. Indeed more work is needed to understand the data in Fig. 4.

3 The BFKL equation

The status of the linear BFKL evolution equation has been reviewed in the talk by White. The main problem with the linear BFKL evolution is the large and negative NLO BFKL correction to the pomeron intercept, which one obtains by using the NLO BFKL results of [19, 20] evaluated at the LO saddle point. The correction is so large that it makes the gluon distribution function fall off with decreasing x.

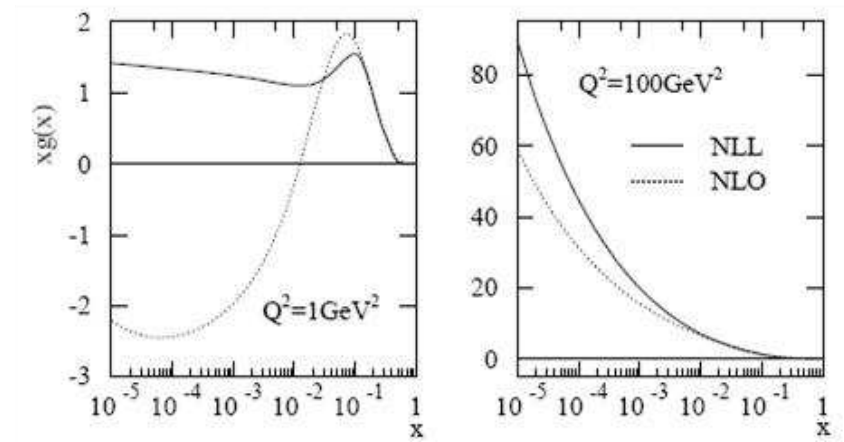


Fig. 5: Gluon distribution function due to NLO BFKL corrections resummed in the TW prescription (solid lines) compared to the NLO DGLAP results (dotted lines). (Pictures are from the talk by White.)

Several ways to remedy this problem have been proposed. It was observed that going beyond the saddle point approximation, e.g. by solving the NLO BFKL equation numerically, significantly reduces the NLO correction to the intercept, making the resulting BFKL Green function rise with decreasing x [21]. An alternative/complimentary way out involves resumming DGLAP transverse logarithms in the NLO BFKL kernel: one such procedure, pioneered by Ciafaloni, Colferai, Salam, and Stasto (CCSS) [22] also gives a positive pomeron intercept albeit somewhat smaller than the LO BFKL intercept. Other procedures involved are due to Altarelli, Ball, and Forte (ABF) [23] and Thorne and White (TW). The results of the TW resummation for the gluon distribution function are shown in Fig. 5 (solid lines) compared to the NLO DGLAP results (dotted lines). One can see that TW resummation cures the problem of the negative gluon distribution at low-Q^2 and low-x that NLO DGLAP has. Still the gluon distribution in the left panel of Fig. 5 corresponding to $Q^2 = 1$ GeV^2 is almost flat as one goes toward lower x: it is unclear what physical mechanism would make xG behave in such a way in the absence of saturation effects in the approach used.

Other problems of the linear BFKL evolution include violation of unitarity bound (or, more precisely, the black disk limit) and diffusion into the infrared. Those problems are remedied by the physics of parton saturation, to be discussed next.

4 Saturation/Color Glass Condensate

The talks by Golec-Biernat and by Marquet gave a nice introduction to the physics of parton saturation/CGC and the non-linear evolution equations involved [7–10]. While the theoretical framework behind CGC is solid, the question of unique experimental detection of CGC is still debated. CGC prediction of hadron suppression at forward rapidities in the $d + Au$ collisions at RHIC [24–26] shown here in Fig. 6 were spectacularly confirmed by the data [27–30]. The CGC prediction involved the conventional *shadowing* effects, which redistribute the partons through multiple rescatterings from lower p_T to higher p_T, leading to low-p_T suppression (shadowing) and high-p_T enhancement (anti-shadowing) shown in the upper curve in Fig. 6. (The high-p_T enhancement of produced particles is known as Cronin effect.) The effects of small-x BFKL/JIMWLK/BK evolution equations (the *saturation* effects) lead to decrease of the number of produced particles (as compared to the $p+p$ reference) at all p_T, as shown by the dash-dotted, dashed, and the lower solid curves in Fig. 6 (for a review see [1]).

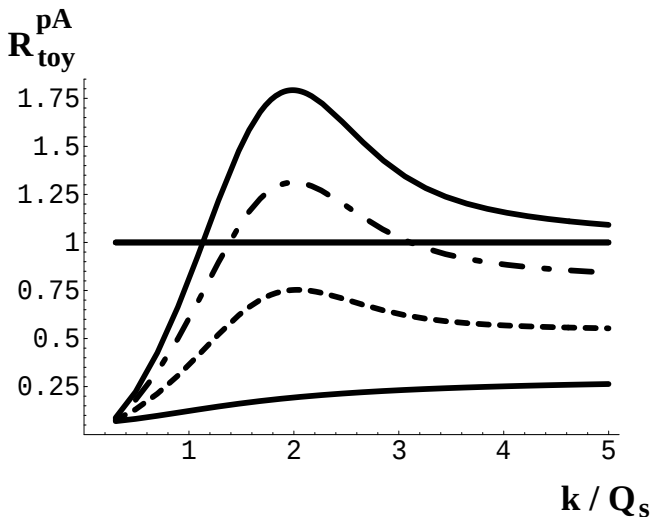


Fig. 6: A sketch of the nuclear modification factor R^{pA} as a function of the transverse momentum of the produced particle k_T in the units of the saturation scale from [25]. The upper curve corresponds to the lowest energy/rapidity, while the other curves show what happens as the energy/rapidity increases.

However, as conventional approaches based on collinear factorization with significantly *ad hoc* modified nuclear shadowing have been able to describe the data *a posteriori* [31], the need arose for new experimental tests to uniquely disentangle between the collinear factorization scenario with shadowing included and the physics of CGC. One of such CGC predictions for a two-particle correlation function was shown by Marquet and is presented here in Fig. 7, which shows a two-hadron correlation function plotted versus the opening azimuthal angle between the two hadrons $\Delta\phi$. The trigger particle has rapidity $y_1 = 3.5$ and $p_{T1} = 5$ GeV. The associate particle has rapidity $y_2 = 2$. The transverse momentum of the associate particle p_{T2} is different for different curves, as explained in Fig. 7. The CGC prediction is that as p_{T2} gets lower and comes closer to the saturation scale Q_s (which is of the order of $1 - 2$ GeV at RHIC), the saturation effects would "wash out" the back-to-back azimuthal correlations, leading to a decrease in the

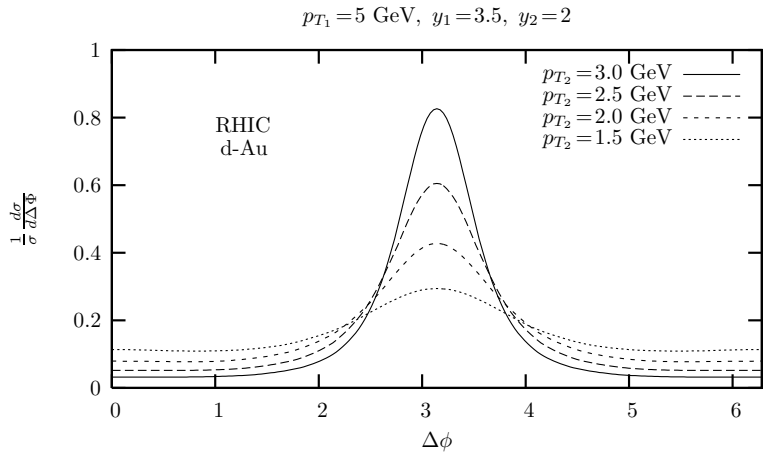


Fig. 7: CGC prediction for the azimuthal dependence of the two-hadron correlation function for different values of the p_T of the associate particle (from the talk by Marquet).

correlation function as predicted in Fig. 7. The experiments currently running at RHIC will be able to test this prediction.

Another test of CGC will come from the upcoming LHC heavy ion experiments. In heavy ion collisions it is hard to construct a rigorous CGC prediction, as the problem of particle production in CGC for the collision of two nuclei have not been solved analytically. One therefore constructs models based on k_T-factorization formula (proven for $p+A$ collisions in CGC in [32] but not proven for $A+A$) trying to mimic as close as possible the true CGC physics (see e.g. [33]). One of the less model-dependent predictions of such an approach is for the total charged hadron multiplicity in heavy ion collisions. Predictions for total charged hadron multiplicity in $Pb+Pb$ collisions at the LHC from the work of Albacete [34] were shown by Marquet and are reproduced here in Fig. 8. The plot in Fig. 8 resulted from using the k_T-factorization formula also used in [33]. However, the dipole scattering amplitudes which enter that formula were evolved using the BK evolution equation with running coupling corrections, which have been recently calculated in [35–37]. Thus at least one of the ingredients used in arriving at Fig. 8 comes form a fairly rigorous CGC analysis, which has became available very recently and never has been used before. Based on that I believe that the prediction in Fig. 8 is the best theoretically-founded one. Unfortunately, due to limitations of our understanding of CGC mentioned above (concerning the applicability of the k_T-factorization formula to nucleus-nucleus collisions), the prediction in Fig. 8 still involves some degree of modeling that we can not control, and should thus be still taken with care.

RHIC experiments continue to surprise us with an amazing quantity of interesting results. We now know the two-hadron correlation function as a function of both azimuthal angle between the hadrons and the rapidity interval between them, as shown in Fig. 9. The correlation function in Fig. 9 has at least one interesting unexplained feature: it has long-range rapidity correlations on the same azimuthal side ($\Delta\phi \approx 0$), known as "the ridge". While many explanations were proposed, the feature remains largely unexplained. At ISMD 2008 McLerran proposed that "the ridge" could be due to long-range rapidity correlations inherent to CGC. Indeed CGC predicts

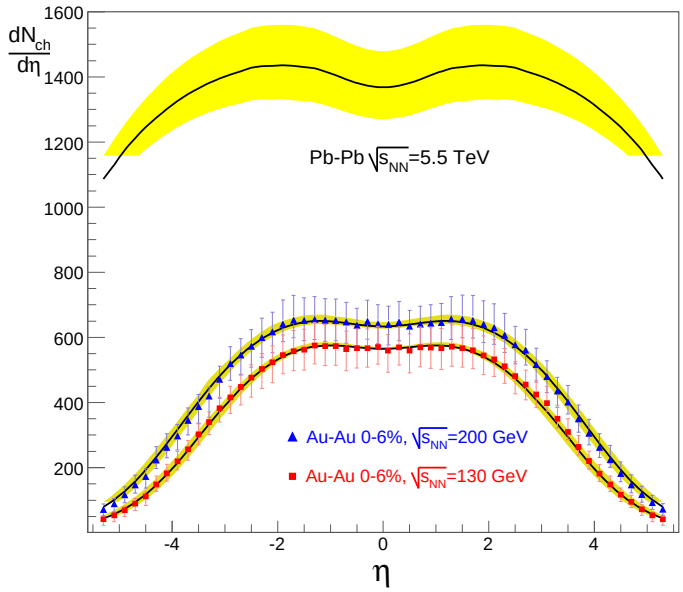


Fig. 8: CGC prediction from [34] for the total charged hadron multiplicity in $Pb + Pb$ collisions at LHC, along with successful fits of the same quantity measured by RHIC at two different center-of-mass energies. The yellow band around the LHC prediction indicates the error bars.

rapidity correlations over the intervals of the order of $\Delta y \sim 1/\alpha_s$, which could be large if the strong coupling constant α_s is small. The radial flow would then boost the correlations, confining them to small azimuthal opening angles, thus creating a ridge-like structure. This is indeed a plausible explanation, but I feel more detailed theoretical work is needed to determine whether this is a unique prediction of CGC.

Another important feature of the two-hadron correlation function in $Au + Au$ collisions at RHIC is the double-hump structure shown in Fig. 10. Fig. 10 depicts the two-particle correlation function measured by PHENIX collaboration plotted as a function of the azimuthal angle between the two hadrons. As one can see from Fig. 10 the distribution of the associate particles as a function of azimuthal angle at low transverse momentum of the associate particle has two maxima. Assuming that the trigger particle travels through a relatively thin medium layer, one concludes that the associate particle is likely to travel through a thicker layer of the medium. The double-hump structure could therefore be caused by a Mach cone produced by a particle moving through a strongly-coupled medium [39]. Alternative explanation could be due to non-Abelian (QCD) Cherenkov radiation, as discussed in the talk by Dremin. To describe such radiation one has to solve classical Yang-Mills equations in a medium with some dielectric tensor. (While indeed Cherenkov radiation is a medium effect, the methods applied to the analysis are those of CGC, and hence I placed it in the CGC section.) Cherenkov radiation allows one to describe both STAR and PHENIX azimuthal correlations data by an appropriate choice of the dielectric tensor in the medium.

A possible signal of the creation of QGP in heavy ion collisions is the mass shift for the

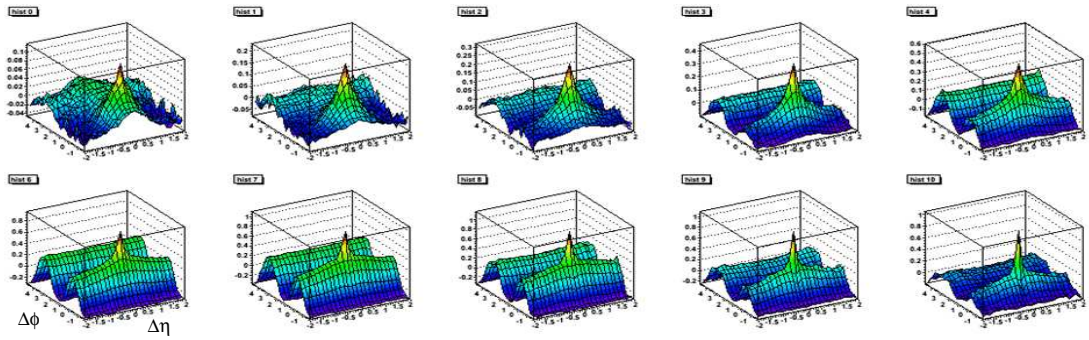


Fig. 9: Two-hadron correlation function measured in $Au + Au$ collisions at RHIC as a function of rapidity interval between the two hadrons $\Delta\eta$ and the azimuthal angle between them $\Delta\phi$. Each panel corresponds to a different centrality of the collision. The data are from the STAR collaboration [38].

produced mesons due to medium effects. Padula suggested that a cleaner way to measure the shift would be by studying two-particle correlations of $\phi\phi$ and K^+K^- pairs. Presence of the mass shift will be signaled by the appearance of back-to-back correlations in the $\phi\phi$ and K^+K^- correlators.

Another interesting CGC prediction is for the rapidity distribution of the net baryon number produced in heavy ion collision. In the talk by Wolschin it was shown how CGC ideas allow one to successfully describe baryon number rapidity distribution at SPS and RHIC, and to even make predictions for LHC. It would be really interesting and important to measure this quantity at LHC.

A sign of the fact that CGC physics is entering a new era is the construction of event generators based on CGC concepts and ideas. In the talks by Avsar and Kutak we have heard about event generators using CCFM evolution equation with an infrared cutoff mimicking saturation/CGC effects, similar to how one can mimic the BK equation by using the BFKL equation with an infrared cutoff. Interesting results and fits were shown in those talks.

5 Cosmic rays

Ultra-high energy cosmic ray data and the accompanying theory was presented in the talks by Ostapchenko and Pierog. It was suggested that the existing discrepancy between the cosmic ray data and the conventional models may be explained by saturation/CGC effects. This is indeed an exciting prospect which needs to be pursued by CGC practitioners. The progress in this direction can however be marred by the fact that when extrapolating from current collider energies to the cosmic ray energies a large uncertainty arises due to the non-perturbative diffusion of the black disk. As was argued in [41] in perturbative CGC approach the diffusion of black disk at high energies is very fast: the radius of the disk grows as a power of energy due to the lack of a mass gap in perturbative approaches. Any attempt to non-perturbatively model the diffusion by introducing a mass gap into the problem leads to the radius of the black disk growing as a logarithm of energy. As the non-perturbative models are not under the same degree of theoretical control as the perturbative CGC calculations, the potential theoretical uncertainty associated with extrapolation to cosmic ray energies could be very large, leading to uncertainty both in total

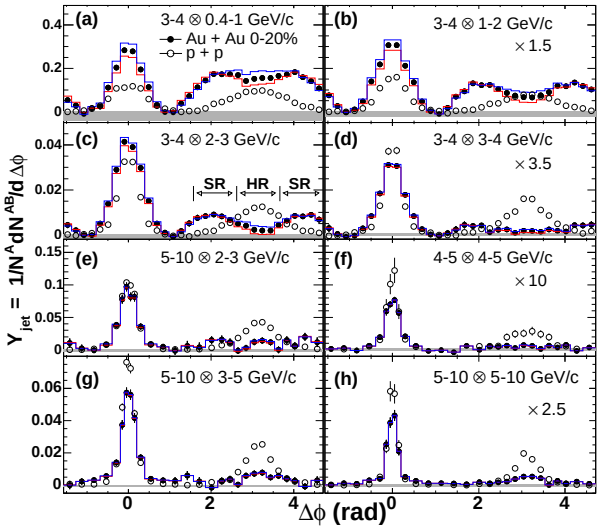


Fig. 10: Two-hadron azimuthal correlation function as measured by PHENIX experiment (taken from [40]).

scattering cross sections and particle production cross sections calculated in CGC.

6 Thermalization in heavy ion collisions

Understanding the mechanism of thermalization and isotropization of the medium produced in heavy ion collisions is a very important open problem in the field. The space-time structure of a

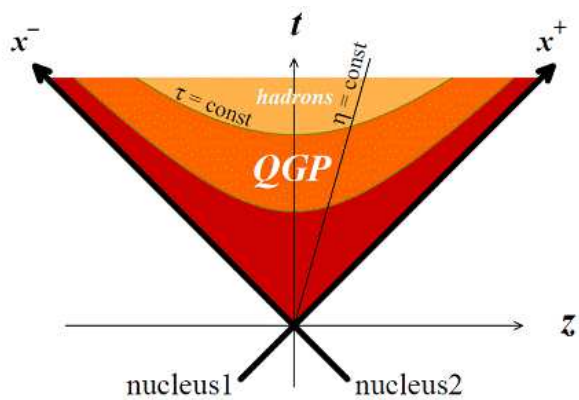


Fig. 11: Space-time structure of a heavy ion collision (from the talk by Itakura).

heavy ion collision is depicted in Fig. 11. The time immediately after the collision is dominated by particle production. In that region CGC applies, such that the production of particles is described by perturbative CGC techniques. This stage of the evolution of the medium is sometimes referred to as “Glasma” [42], the term which combines the Color Glass physics (“Glas”) with the creation of quark-gluon plasma at later stages of the collision (“lasma”), as shown in Fig. 11. However the CGC dynamics by itself leads to a very anisotropic distribution of the produced

matter in momentum space: the end result of CGC dynamics is a free-streaming "medium" with zero longitudinal pressure component. Indeed a thermalized medium should have all pressure components (transverse and longitudinal) equal, as it should be *isotropic*. Hence Color Glass itself does not lead to thermalization, or, more importantly, isotropization of the produced medium. (Isotropization is a necessary, but not a sufficient condition of thermalization.)

So how does Color Glass turn into a Glasma? One of the more popular scenarios was presented in the talk by Itakura and involves magnetic instabilities in the produced medium (see also [43, 44]). The main physical idea is that the momentum space anisotropy of the medium produced in heavy ion collisions would generate instabilities, which would rapidly isotropize the system leading to a hydrodynamic behavior of the medium. This indeed is a plausible scenario of thermalization/isotropization.

Since the saturation/Color Glass approach gives us a consistent framework in which all diagrams can be classified and resummed order-by-order, it is not at all clear why one has to separate the perturbative dynamics into a part which is incorporated in CGC and into everything else. From this standpoint the dynamics of instabilities would correspond to some higher order (quantum) corrections to the diagrams which we already know how to resum in the CGC approach. Such corrections would also be a part of CGC, just at some higher order. The magnetic instabilities could then be viewed as some higher order corrections to CGC which somehow got "out of control" and became very large (infinite?). Frankly I am skeptical whether such corrections exist: all our experience calculating CGC diagrams, both in the classical framework [45–47] and including (LO and NLO) quantum evolution and running coupling corrections [32, 48], never led to any uncontrolled infinities which would dominate the resulting production cross sections and the energy-momentum tensor. Perhaps the proponents of the instability-driven scenario should identify and resum diagrams with instabilities (starting from the very collision of two nuclei), and show that their contributions are really important (numerically or parametrically) and that these diagrams do lead to isotropization of the medium at late times. Implications of such diagrams on what we know in the standard perturbation theory in, say, proton-proton collisions would also have to be understood. One should also identify what those new instability diagrams have that was absent in the multitude of quantum corrections to the classical picture calculated over the years [32, 48].

Alternatively, as the medium created at RHIC is believed to be strongly-coupled, it is possible that thermalization and isotropization in heavy ion collisions are essentially non-perturbative (large-coupling) effects. Such a scenario can not be quantified in a controlled manner in QCD. However, AdS/CFT correspondence [49, 50] allows us to try to analyze this problem for the $\mathcal{N} = 4$ Super Yang-Mills (SYM) theory. In my talk in the Dense Systems session I have presented one of the efforts in this direction. One could model a heavy ion collision as a collision of two shock waves in AdS_5. Solving Einstein equations in AdS_5 one can find the energy-momentum tensor of the resulting medium. It has been argued in [51] using AdS/CFT correspondence that if one assumes that the produced medium distribution is rapidity-independent, the strong-coupling dynamics would inevitably lead at late proper times to an isotropic medium described by Bjorken hydrodynamics [52]. However, it is not yet clear whether such a rapidity-independent distribution would result from a collision of two shock waves. Our result was that in a strongly-coupled theory the colliding shock waves would stop shortly after the collision. This

seems like a natural result of the strong coupling effects. If the coupling is strong enough to stop the colliding nuclei, it is likely to quickly thermalize the system. However, a thermal system resulting from stopping of the nuclei is more likely to be described by rapidity-dependent Landau hydrodynamics [53], instead of the rapidity-independent Bjorken one. Hence the strong-coupling effects, if dominant throughout the collision, would not lead to Bjorken hydrodynamics. On top of that we know from the RHIC data on net baryon rapidity distribution that valence quarks in the nuclei do not stop in the collision, and instead (mostly) continue moving along the beam line [54]. Indeed the early stages of the collisions have to be described by the weak coupling effects, and are thus outside of the realm of the AdS/CFT correspondence. We presented a way of mimicking these weak-coupling effects in the dual AdS geometry. However, the question of what leads to Bjorken hydrodynamics still remains open.

7 Hydrodynamics

Regardless of our lack of understanding of thermalization in heavy ion collisions, the success of perfect-fluid hydrodynamics description of particle spectra and elliptic flow v_2 measured in the $Au + Au$ collisions at RHIC [55, 56] allows us to conclude that the medium created in the collisions is probably strongly coupled and that a hydrodynamic description of such medium is adequate.

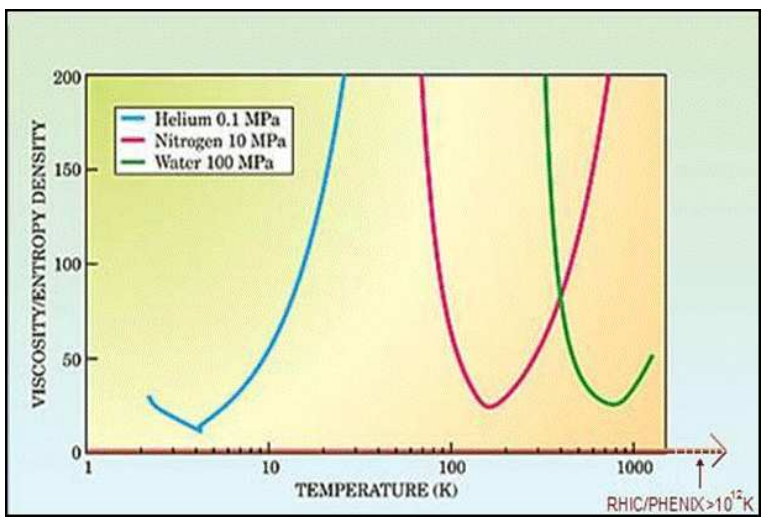


Fig. 12: The shear viscosity-to-entropy density ratio (in units of $1/4\pi$) for various media (from the talk by Csörgő).

The Kovtun, Son, Starinets, Policastro (KPSS) [57, 58] lower bound on the ratio of shear viscosity η to the entropy density S derived from AdS/CFT correspondence was discussed in the talk by Csörgő. The KPSS bound postulates that for any medium (or, more precisely, for any theory with a gravity dual) one has $\eta/S \geq 1/4\pi$. Fig. 12 shows the ratio of η/S plotted as a function of temperature for several different media with the KPSS bound shown by a straight horizontal line at the bottom. Csörgő pointed out that as RHIC data is consistent with a very low value of η/S, it is likely that RHIC fluid is more perfect than any other known fluid. This

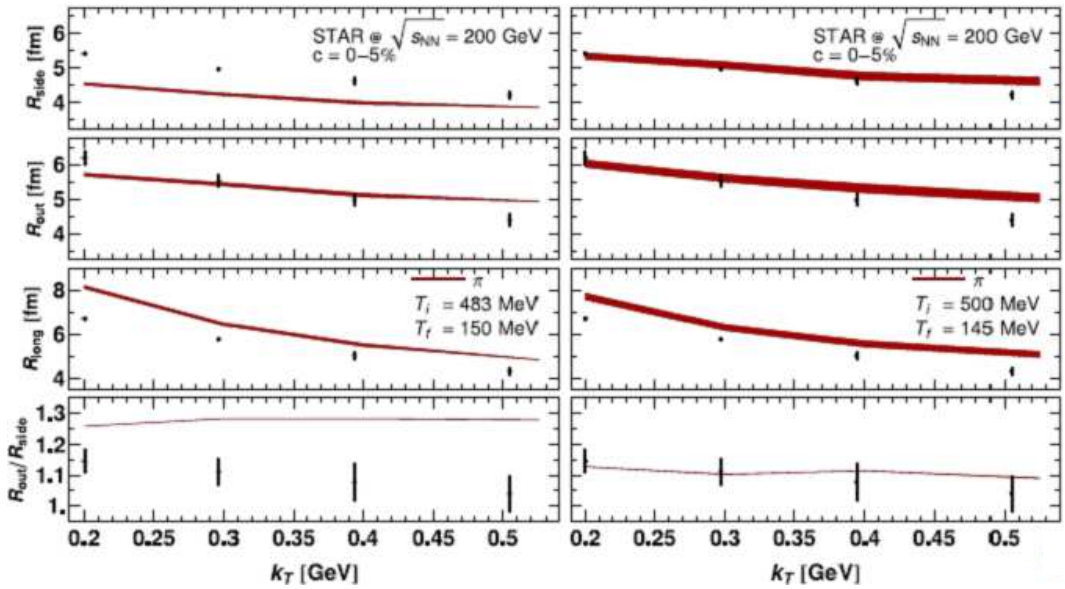


Fig. 13: HBT radii at RHIC compared to hydrodynamic simulations with the standard (Glauber) initial conditions (left panels) and the Glauber initial conditions proposed by Florkowski (right panels). (The picture is taken from the talk by Florkowski.)

superfluidity also takes place at an extremely high temperature, characteristic of the QGP. However it is still possible that RHIC data allows for higher values of η/S than $1/4\pi$: by varying the initial conditions for hydrodynamics one can accommodate somewhat larger values of η/S, though the exact values are still under investigation. There have also been some recent results in string theory suggesting that the KPSS bound might be violated in some theories due to stringy (mostly $1/N_c$) corrections. Regardless of that, the low viscosity of the RHIC QGP still strongly suggests that the medium created in the collisions is strongly-coupled.

Hydrodynamics is an exciting subfield by itself, allowing for many interesting exact solutions describing possible evolutions of RHIC fireball. Many of those solutions have been reviewed in the talk by M. Nagy, and fall into two main categories: relativistic and non-relativistic ones.

There are still open problems with the hydrodynamic description of the medium produced in RHIC collisions. One is the early thermalization proper time of $\tau_0 = 0.3 \div 0.5$ fm/c required for hydrodynamics to describe the data: this problem is related to our (lack of) understanding of thermalization/isotropization in heavy ion collisions. Another problem concerns the HBT radii. While hydrodynamics is successful in describing particle spectra and v_2 [55, 56], it has been having problems describing HBT radii. This has been known as the RHIC HBT puzzle (see e.g. [59]). At ISMD 2008 Florkowski suggested that one could modify the standard Glauber initial conditions for hydrodynamics simulations: he suggested starting the simulations with a smaller Gaussian source, which would generate faster initial expansion. Apparently this approach

worked, allowing to describe the HBT radii, as shown in Fig. 13, using a rather small set of free parameters. The obtained value for one of the parameters, the thermalization time τ_0, turns out to be $\tau_0 = 0.25$ fm/c, which is rather close to some recent estimates based on AdS/CFT approaches [60].

While the approach presented by Florkowski works very well, as can be clearly seen from Fig. 13, one may worry that the initial size of the Gaussian fireball used is rather small to adequately describe realistic $Au + Au$ collisions. Therefore in my opinion the conclusion one can draw from the Gaussian initial conditions analysis is that in the simulations of Fig. 13 it mimics some initial time dynamics which leads to hydrodynamics being initialized with a pretty strong radial flow. It appears then that in order to describe the HBT radii one needs the initial conditions for hydrodynamics simulations to contain large flow in them. The exact nature of such initial dynamics still needs to be identified: it might be given by the CGC physics.

The perfect fluid hydrodynamics appears to do a good job at RHIC. It is possible though that in heavy ion collisions at LHC the plasma that will be created will start out at higher temperature. This would lead to smaller coupling constant, thus possibly making the resulting plasma less strongly coupled. The viscous corrections in such case would get larger: one therefore needs to construct viscous hydrodynamics simulations to describe the dynamics of the medium to be produced in heavy ion collisions at the LHC. But what if viscous corrections are not enough? What if higher fluid velocity gradients would also become important? The dynamics of strongly coupled medium described by AdS/CFT correspondence contains the exact result, including all gradients of fluid velocity. While obtaining this exact solution from AdS/CFT correspondence appears to be rather complicated, one could calculate the viscosity and higher order coefficients in fluid velocity gradient expansion using AdS/CFT approach. The results of the project to calculate the coefficients needed to construct causal viscous hydrodynamics using the AdS/CFT correspondence were presented in the talk by Baier. The obtained coefficients could be used to construct strong-coupling predictions for LHC.

8 AdS/CFT correspondence

AdS/CFT correspondence [49, 50] is a very powerful new tool for studying non-perturbative aspects of gauge theories coming from string theory (for a review see [61]). AdS/CFT correspondence [49, 50] postulates a duality between the $\mathcal{N} = 4$ SYM theory in 4 space-time dimensions and the type-IIB string theory in $AdS_5 \times S^5$. The more widely used and better tested gauge-gravity duality suggests that $\mathcal{N} = 4$ SYM theory in the large-N_c large-$\lambda = g^2\, N_c$ limit is dual to classical super-gravity on AdS_5 (λ is 't Hooft's coupling constant, g is the gauge coupling). What this means practically is that in order to find expectation values of various operators in $\mathcal{N} = 4$ SYM theory at large N_c and λ one has to perform classical super-gravity calculations in a curved 5-dimensional space-time.

A number of talks at ISMD 2008 used the methods of AdS/CFT: some of these talks I have already mentioned in other Sections.

A talk by Iancu addressed the question of deep inelastic scattering on a thermal medium (plasma). In AdS such medium is modeled by the black brane metric. In the absence of bound states in a conformal theory, a thermal medium provides a fine target to scatter on. Iancu sug-

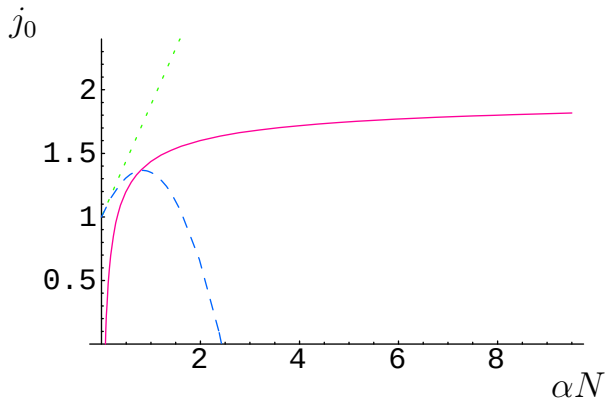


Fig. 14: The pomeron intercept j_0 in $\mathcal{N}=4$ SYM as a function of the coupling $\alpha\, N$. The dotted line represents the perturbative LO BFKL pomeron intercept, the dashed line is the LO+NLO BFKL intercept, and the solid line is the strong-coupling AdS result. (The picture is taken from the talk by Tan.)

gested calculating a correlator of two R-currents in order to find the structure functions of the plasma. One of the important results is that DIS at strong coupling also exhibits the feature of parton saturation, just like the weakly coupled CGC. The saturation scale in the theory at strong coupling was found to be equal to $Q_s \sim L\,T^2$, with L the part of the distance separating the two R-currents immersed in the medium and T the temperature of the medium. If the two currents are inside the medium, then L is the distance separating the currents, and for DIS $L \sim 1/(xT)$ with x the Bjorken x variable. This gives $Q_s \sim T/x$, i.e. the saturation scale would grow very strongly as Bjorken x decreases.

However, in a realistic high energy DIS scattering the incoming virtual photon splits into a quark–anti-quark pair very much in advance of the system hitting the proton or nuclear target. Hence a more realistic scenario would involve a finite-size medium, such that $L = 2R$ with R the radius of the target proton/nucleus. Then one gets $Q_s \sim R\,T^2$, i.e. the saturation scale is independent of Bjorken x, or, equivalently, of energy. In this regime the conclusions presented by Iancu agree with the results of other groups [62,63]. It is rather interesting to observe that at large coupling the saturation scale becomes independent of energy. It seems that the classical supergravity gives results similar to those given by the classical Yang-Mills fields in the McLerran-Venugopalan (MV) model [64]: there the saturation scale is also independent of energy. In the MV model we know that quantum corrections lead to energy-dependence of Q_s [9, 10]. It is possible that quantum (order $1/\sqrt{\lambda}$) corrections in AdS would make the saturation scale energy-dependent at strong coupling.

AdS/CFT correspondence allows one to try to understand other related quantities, such as the intercept of the pomeron and the pomeron trajectory. The results of such investigations were presented by Tan. He explained how an AdS/CFT calculation gives the pomeron intercept $j_0 = 2 - \frac{2}{\sqrt{\lambda}}$ for a strongly-coupled $\mathcal{N}=4$ SYM theory. His results are summarized in Fig. 14, where the intercept is plotted as a function of the gauge coupling α times the number of colors in the theory N. The dotted and dashed lines represent the perturbative LO and LO+NLO BFKL intercepts correspondingly. One can see that the NLO BFKL correction is indeed large

and threatens to make the intercept less than 1 at not very large αN. The solid line in Fig. 14 represents the AdS strong-coupling result of $j_0 = 2 - \frac{2}{\sqrt{\lambda}}$: the picture suggests that an interpolation between the two results is possible, leading to an intercept which is greater than 1 at all values of the coupling.

At the same time I have to point out that the result of a recent AdS investigation [62] suggests that at high energies multiple exchanges of the intercept-2 pomerons lead to a somewhat unphysical behavior of the cross section and violate the black disk limit. In [62] an alternative solution was proposed with the strong coupling pomeron having an intercept of $j_0 = 1.5$ and with multiple exchanges of such a pomeron giving cross sections which are unitary and do not violate the black disk limit. More investigations may be needed to understand the differences between the two results.

Lipatov talked about another important result related to AdS/CFT correspondence — the BDS amplitude ansatz [65]. He has argued that the ansatz is violated in the Regge limit, when one calculates the diagrams contributing to the BFKL evolution. The violation is relatively minor and only manifests itself in some channels. This allows one to hope that a modification of the BDS ansatz is possible which would take into account the discrepancy presented by Lipatov.

9 Higgs boson and physics beyond the Standard Model

LHC had turned on just before the start of ISMD 2008, but had to be shut down soon after due to a malfunction of the superconducting magnets. Nevertheless, despite the delay, LHC era is upon us and a number of talks at ISMD 2008 were dedicated to what one could discover at LHC. While some aspects of the LHC heavy ion program have been mentioned above, here I will concentrate on the search for new particles in proton-proton collisions.

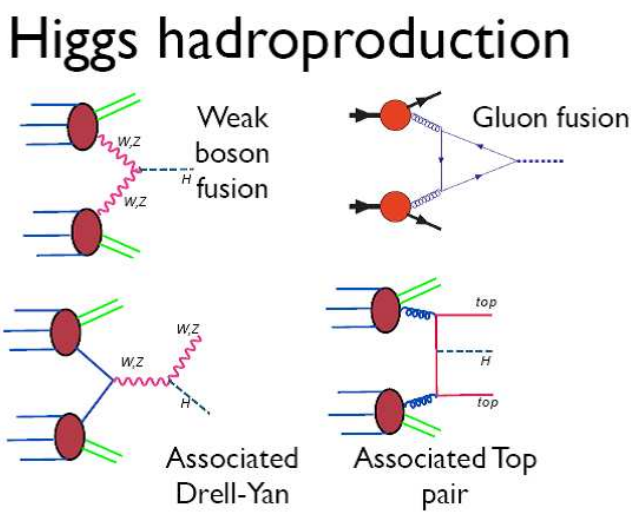


Fig. 15: Various possible channels of Higgs boson production at LHC (from the talk by Anastasiou.)

First of all, if the Standard Model is correct, one expects to be able to find the Higgs boson at the LHC. Anastasiou gave a talk reviewing various channels of Higgs production, which are

demonstrated in Fig. 15. Hopefully many (or at least one) of these channels would be observed at LHC.

It is possible however that backgrounds at LHC would be too high making the events shown in Fig. 15 hard to detect. In this case a possible cleaner signature of the Higgs would be the double diffraction production process illustrated in Fig. 16, which was discussed in the talks by Kaidalov and V. A. Khoze. In such process there will be rapidity gaps between the produced Higgs boson and each of the protons, allowing for a clean detection of the products of the Higgs boson decay, and thus for an unambiguous identification of the Higgs boson.

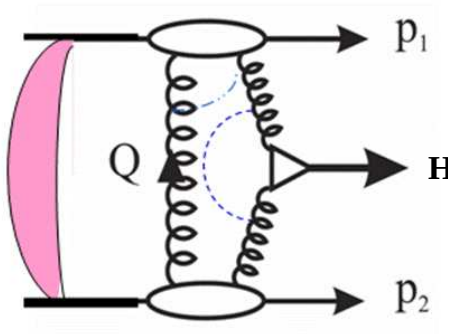


Fig. 16: Double diffractive Higgs boson production mechanism at the LHC (from the talk by V.A. Khoze.)

Unfortunately, as often happens when the soft QCD interactions are involved, theoretical predictions for the cross sections of the process shown in Fig. 16 at LHC vary quite significantly [66–68]. Two of the existing approaches [67, 68] were reviewed in the talk by Kaidalov. Among other things he outlined the approximations made for the triple pomeron vertex made in each of the approaches. Both approaches reproduce the existing Tevatron double diffractive data reasonably well, but differ significantly in their extrapolation to LHC energies. Since it is not clear from first principles which approximation of the triple pomeron vertex is better justified, it seems that error analyses similar to those done for PDF's may be needed to reconcile the differences between the two approaches in question.

Physics beyond the Standard Model was discussed in the talks by V.V. Khoze and Strassler dedicated to different supersymmetric models. While the former talk presented a minimal approach to introducing SUSY, the latter talk featured a broader range of possibilities. V.V. Khoze talked about the ISS scenario [69] in which the Universe lives in a metastable vacuum in which SUSY is broken. At the same time there exists a hidden sector of the theory with a true vacuum which is supersymmetric. The ISS model gives a concrete example of SUSY breaking, allowing to calculate the mass spectrum of the supersymmetric particles using the messenger fields. Strassler in his talk argued that minimalistic approach to physics beyond Standard Model is not necessarily what happens in nature and we should prepare for big surprises at the LHC. He therefore talked about hidden valleys and unparticles, both of which would lead to spectacular hadronic shower events at the LHC, which unfortunately would be hard to analyze and understand due to the large number of particles produced. Indeed both minimal and non-minimal SUSY scenarios are quite possible at LHC.

Acknowledgments

I would like to acknowledge helpful discussions with Ulrich Heinz, William Horowitz, Abhijit Majumder, and Heribert Weigert.

This work is sponsored in part by the U.S. Department of Energy under Grant No. DE-FG02-05ER41377.

References

[1] J. Jalilian-Marian and Y. V. Kovchegov, Prog. Part. Nucl. Phys. **56**, 104 (2006). hep-ph/0505052.

[2] Y. L. Dokshitzer, Sov. Phys. JETP **46**, 641 (1977).

[3] V. N. Gribov and L. N. Lipatov, Sov. J. Nucl. Phys. **15**, 438 (1972).

[4] G. Altarelli and G. Parisi, Nucl. Phys. **B126**, 298 (1977).

[5] Y. Y. Balitsky and L. N. Lipatov, Sov. J. Nucl. Phys. **28**, 822 (1978).

[6] E. A. Kuraev, L. N. Lipatov, and V. S. Fadin, Sov. Phys. JETP **45**, 199 (1977).

[7] J. Jalilian-Marian, A. Kovner, A. Leonidov, and H. Weigert, Phys. Rev. **D59**, 014014 (1998). hep-ph/9706377.

[8] E. Iancu, A. Leonidov, and L. D. McLerran, Nucl. Phys. **A692**, 583 (2001). hep-ph/0011241.

[9] I. Balitsky, Nucl. Phys. **B463**, 99 (1996). hep-ph/9509348.

[10] Y. V. Kovchegov, Phys. Rev. **D60**, 034008 (1999). hep-ph/9901281.

[11] CTEQ Collaboration, H. L. Lai *et al.*, Eur. Phys. J. **C12**, 375 (2000). hep-ph/9903282.

[12] A. D. Martin, W. J. Stirling, R. S. Thorne, and G. Watt, Phys. Lett. **B652**, 292 (2007). 0706.0459.

[13] S. Alekhin, Phys. Rev. **D68**, 014002 (2003). hep-ph/0211096.

[14] NNPDF Collaboration, R. D. Ball *et al.* (2008). 0808.1231.

[15] STAR Collaboration, S. Salur (2008). 0809.1609.

[16] PHENIX Collaboration, S. S. Adler *et al.*, Phys. Rev. Lett. **91**, 072303 (2003). nucl-ex/0306021.

[17] STAR Collaboration, J. Adams *et al.*, Phys. Rev. Lett. **91**, 072304 (2003). nucl-ex/0306024.

[18] BRAHMS Collaboration, I. Arsene *et al.*, Phys. Rev. Lett. **91**, 072305 (2003). nucl-ex/0307003.

[19] V. S. Fadin and L. N. Lipatov, Phys. Lett. **B429**, 127 (1998). hep-ph/9802290.

[20] M. Ciafaloni and G. Camici, Phys. Lett. **B430**, 349 (1998). hep-ph/9803389.

[21] J. R. Andersen and A. Sabio Vera, Nucl. Phys. **B679**, 345 (2004). hep-ph/0309331.

[22] M. Ciafaloni, D. Colferai, G. P. Salam, and A. M. Stasto, Phys. Rev. **D68**, 114003 (2003). hep-ph/0307188.

[23] G. Altarelli, R. D. Ball, and S. Forte, Nucl. Phys. **B575**, 313 (2000). hep-ph/9911273.

[24] D. Kharzeev, E. Levin, and L. McLerran, Phys. Lett. **B561**, 93 (2003). hep-ph/0210332.

[25] D. Kharzeev, Y. V. Kovchegov, and K. Tuchin, Phys. Rev. **D68**, 094013 (2003). hep-ph/0307037.

[26] J. L. Albacete, N. Armesto, A. Kovner, C. A. Salgado, and U. A. Wiedemann, Phys. Rev. Lett. **92**, 082001 (2004). hep-ph/0307179.

[27] BRAHMS Collaboration, I. Arsene *et al.*, Phys. Rev. Lett. **93**, 242303 (2004). nucl-ex/0403005.

[28] PHENIX Collaboration, S. S. Adler *et al.*, Phys. Rev. Lett. **94**, 082302 (2005). nucl-ex/0411054.

[29] PHOBOS Collaboration, B. B. Back *et al.*, Phys. Rev. **C70**, 061901 (2004). nucl-ex/0406017.

[30] STAR Collaboration, J. Adams *et al.*, Phys. Rev. Lett. **97**, 152302 (2006). nucl-ex/0602011.

[31] K. J. Eskola, H. Paukkunen, and C. A. Salgado, JHEP **07**, 102 (2008). 0802.0139.

[32] Y. V. Kovchegov and K. Tuchin, Phys. Rev. **D65**, 074026 (2002). hep-ph/0111362.

[33] D. Kharzeev, E. Levin, and M. Nardi, Phys. Rev. **C71**, 054903 (2005). hep-ph/0111315.

[34] J. L. Albacete, Phys. Rev. Lett. **99**, 262301 (2007). 0707.2545.

[35] Y. V. Kovchegov and H. Weigert, Nucl. Phys. **A784**, 188 (2007). hep-ph/0609090.

[36] I. Balitsky, Phys. Rev. **D75**, 014001 (2007). hep-ph/0609105.

[37] J. L. Albacete and Y. V. Kovchegov, Phys. Rev. **D75**, 125021 (2007). 0704.0612.

[38] STAR Collaboration, M. Daugherity, J. Phys. **G35**, 104090 (2008). 0806.2121.

[39] J. Casalderrey-Solana, E. V. Shuryak, and D. Teaney, J. Phys. Conf. Ser. **27**, 22 (2005). hep-ph/0411315.

[40] PHENIX Collaboration, A. Adare *et al.*, Phys. Rev. **C77**, 011901 (2008). 0705.3238.

[41] A. Kovner and U. A. Wiedemann, Phys. Lett. **B551**, 311 (2003). hep-ph/0207335.

[42] T. Lappi and L. McLerran, Nucl. Phys. **A772**, 200 (2006). hep-ph/0602189.

[43] S. Mrowczynski, Phys. Lett. **B314**, 118 (1993).

[44] P. Arnold, J. Lenaghan, and G. D. Moore, JHEP **08**, 002 (2003). hep-ph/0307325.

[45] A. Kovner, L. D. McLerran, and H. Weigert, Phys. Rev. **D52**, 6231 (1995). hep-ph/9502289.

[46] Y. V. Kovchegov and D. H. Rischke, Phys. Rev. **C56**, 1084 (1997). hep-ph/9704201.

[47] A. Krasnitz, Y. Nara, and R. Venugopalan, Nucl. Phys. **A727**, 427 (2003). hep-ph/0305112.

[48] Y. V. Kovchegov and H. Weigert, Nucl. Phys. **A807**, 158 (2008). 0712.3732.

[49] J. M. Maldacena, Adv. Theor. Math. Phys. **2**, 231 (1998). hep-th/9711200.

[50] E. Witten, Adv. Theor. Math. Phys. **2**, 253 (1998). hep-th/9802150.

[51] R. A. Janik and R. B. Peschanski, Phys. Rev. **D73**, 045013 (2006). hep-th/0512162.

[52] J. D. Bjorken, Phys. Rev. **D27**, 140 (1983).

[53] L. D. Landau, Izv. Akad. Nauk SSSR Ser. Fiz. **17**, 51 (1953).

[54] BRAHMS Collaboration, I. G. Bearden *et al.*, Phys. Rev. Lett. **93**, 102301 (2004). nucl-ex/0312023.

[55] P. Huovinen, P. F. Kolb, U. W. Heinz, P. V. Ruuskanen, and S. A. Voloshin, Phys. Lett. **B503**, 58 (2001). hep-ph/0101136.

[56] D. Teaney, J. Lauret, and E. V. Shuryak (2001). nucl-th/0110037.

[57] G. Policastro, D. T. Son, and A. O. Starinets, Phys. Rev. Lett. **87**, 081601 (2001). hep-th/0104066.

[58] P. Kovtun, D. T. Son, and A. O. Starinets, Phys. Rev. Lett. **94**, 111601 (2005). hep-th/0405231.

[59] M. A. Lisa and S. Pratt (2008). 0811.1352.

[60] Y. V. Kovchegov and A. Taliotis, Phys. Rev. **C76**, 014905 (2007). 0705.1234.

[61] O. Aharony, S. S. Gubser, J. M. Maldacena, H. Ooguri, and Y. Oz, Phys. Rept. **323**, 183 (2000). hep-th/9905111.

[62] J. L. Albacete, Y. V. Kovchegov, and A. Taliotis, JHEP **07**, 074 (2008). 0806.1484.

[63] F. Dominguez, C. Marquet, A. H. Mueller, B. Wu, and B.-W. Xiao, Nucl. Phys. **A811**, 197 (2008). 0803.3234.

[64] L. D. McLerran and R. Venugopalan, Phys. Rev. **D49**, 2233 (1994). hep-ph/9309289.

[65] Z. Bern, L. J. Dixon, and V. A. Smirnov, Phys. Rev. **D72**, 085001 (2005). hep-th/0505205.

[66] J. Bartels, S. Bondarenko, K. Kutak, and L. Motyka, Phys. Rev. **D73**, 093004 (2006). hep-ph/0601128.

[67] E. Gotsman, E. Levin, U. Maor, and J. S. Miller (2008). 0805.2799.

[68] V. A. Khoze, A. D. Martin, and M. G. Ryskin, Phys. Lett. **B650**, 41 (2007). hep-ph/0702213.

[69] K. A. Intriligator, N. Seiberg, and D. Shih, JHEP **04**, 021 (2006). hep-th/0602239.

Participants

ALBROW, Michael Fermi National Accelerator Laboratory Batavia, UNITED STATES OF AMERICA
ALEXANDER, Gideon Tel-Aviv University Tel-Aviv ISRAEL
ANASTASIOU, Charalampos ETH Zurich SWITZERLAND
AVSAR, Emil CEA/Saclay Gif Sur Yvette FRANCE
BAIER, Rudolf Universitaet Bielefeld, Fakultaet Physik Bielefeld GERMANY
BARTALINI, Paolo NTU Taipei TAIWAN
BARTELS, Jochen University Hamburg Hamburg GERMANY
BIALAS, Andrzej Inst. Nucl.Phys. Krakow POLAND
BOPP, Fritz W. UniversitŁt Siegen Siegen GERMANY
BORRAS, Kerstin DESY Hamburg GERMANY
BUESCHING, Henner University of Frankfurt Frankfurt GERMANY
BUNYATYAN, Armen MPI,Heidelberg/YerPhI, Yerevan Hamburg GERMANY
BUSZA, Wit Massachusetts Institute of Technology Cambridge UNITED STATES OF AMERICA
CHOLEWA, Axel DESY Hamburg GERMANY
CHYLA, Jiri Institute of Physics, Academy of Sciences Prague CZECH REPUBLIC
CIOCCA, Claudia INFN and University of Bologna Bologna ITALY
COOPER-SARKAR, Amanda (Mandy) Oxford University OXFORD OX1 3RH UNITED KINGDOM
CSANAD, Mate Etvs Universty Budapest Budapest HUNGARY
CSORGO, Tamas MTA KFKI RMKI Budapest XII HUNGARY
DAINESE, Andrea INFN Legnaro Legnaro (PD) ITALY
DE ROECK, Albert CERN Geneva SWITZERLAND
DE WOLF, Eddi University of Antwerpen Antwerpen BELGIUM
DIEHL, Markus DESY Hamburg GERMANY
DREMIN, Igor Lebedev Physical Institute Moscow RUSSIA
EBERHARD, Wuensch DESY Hamburg GERMANY
EGGERS, Hans University of Stellenbosch Stellenbosch SOUTH AFRICA
EHRENFELD, Wolfgang DESY Hamburg GERMANY
EISENBERG, yehuda Weizmann Institute Rehovot ISRAEL
ESKREYS, Andrzej Institute of Nuclear Physics PAN Krakow POLAND
FIALKOWSKI, Krzysztof Jagellonian University Krakow POLAND
FLENSBURG, Christoffer Lund University Lund SWEDEN
FLORKOWSKI, Wojciech IFJ PAN Krakow / UJK Kielce / Poland Krakow POLAND
GAYLER, Joerg DESY Hamburg GERMANY
GEISER, Achim DESY Hamburg GERMANY
GOLEC-BIERNAT, Krzysztof Institute of Nuclear Physics Krakow/ Rzeszow University Krakow POLAND
GRABOWSKY, Alla DESY Hamburg GERMANY
GREBENYUK, Anastasia DESY Hamburg GERMANY
GREBENYUK, Julia DESY Hamburg GERMANY
GROTHE, Monika U Wisconsin Madison UNITED STATES OF AMERICA
GUSTAFSON, Gosta Lund Univ./Hamburg Unv. Hamburg GERMANY
HAMA, Yogiro University of Sao Paulo Sao Paulo BRAZIL
HATAKEYAMA, Kenichi Rockefeller University New York, NY UNITED STATES OF AMERICA

HATTA, Yoshitaka University of Tsukuba Tsukuba JAPAN
HAUTMANN, Francesco University of Oxford Oxford UNITED KINGDOM
HELEN, Caines Yale University New Haven UNITED STATES OF AMERICA
HOMMA, Kensuke Hiroshima University Higashi-hiroshima JAPAN
HURTH, Tobias CERN, Theory Group Geneva SWITZERLAND
IANCU, Edmond Institut de Physique Theorique de Saclay Gif-sur-Yvette Cedex FRANCE
ITAKURA, Kazunori IPNS, KEK Tsukuba JAPAN
JENKOVSZKY, Laszlo Bogolyubov Institute for Theoretical Physics Kiev UKRAINE
JUNG, Hannes DESY Hamburg GERMANY
KAIDALOV, Alexei Institute of Theoretical and Experimental Physics (ITEP) Moscow RUSSIA
KAR, Deepak University of Florida Gainesville UNITED STATES OF AMERICA
KATZY, Judith DESY Hamburg GERMANY
KHAN, Mariam Saleh Uni. Hamburg, DESY Hamburg GERMANY
KHOZE, Valentin V IPPP, Durham University Durham UNITED KINGDOM
KHOZE, Valeri IPPP, University of Durham Durham UNITED KINGDOM
KNEUR, Jean-Loic Lab. Physique Theorique et Astroparticules Montpellier FRANCE
KODAMA, Takeshi Fed. Univ. Rio de Janeiro Rio de Janeiro BRAZIL
KOKOULINA, Elena Joint Institute for Nuclear Research Dubna Moscow region RUSSIA
KOLAR, Karel Institute of Physics, Academy of Sciences Prague CZECH REPUBLIC
KOSHELKIN, Andrew MOSCOW INSTITUTE FOR PHYSICS AND ENGINEERING Moscow RUSSIA
KOVCHEGOV, Yuri The Ohio State University Columbus, OH UNITED STATES OF AMERICA
KROPIVNITSKAYA, Anna ITEP Moscow RUSSIA
KULESZA, Anna DESY Hamburg GERMANY
KUTAK, Krzysztof DESY Hamburg GERMANY
KUVSHINOV, Viacheslav Joint Institute for Power and Nuclear Research Minsk BELARUS
LANCASTER, Mark UCL London UNITED KINGDOM
LEVONIAN, Sergey DESY Hamburg GERMANY
LI, Gang LAL Orsay FRANCE
LIPATOV, Artem SINP MSU Moscow RUSSIA
LIPATOV, Lev Petersburg Nuclear Physics Institute, Hamburg University St. Petersburg RUSSIA
LIU, Lianshou Institute of Particle Physics, Huazhong Normal University Wuhan CHINA
MACHADO, Magno Universidade Federal do Pampa Bag BRAZIL
MARCHESINI , Giuseppe Dept Physics Milano ITALY
MARQUET, Cyrille Columbia University New York UNITED STATES OF AMERICA
MARTI MAGRO, Lluis DESY Hamburg GERMANY
MCLERRAN, Larry Riken Brookhaven Center and BNL Upton, NY UNITED STATES OF AMERICA
METZGER, Wesley Radboud University Nijmegen NETHERLANDS
MEYER, Arnd RWTH Aachen University, III. Phys. Inst. A Aachen GERMANY
MEYER, Hinrich DESY Hamburg GERMANY
MNICH, Joachim DESY Hamburg GERMANY
MOCH, Sven-Olaf DESY Zeuthen GERMANY
MOTYKA, Leszek Hamburg University / Jagellonian University Hamburg GERMANY
NAGY, Mrton MTA KFKI RMKI Budapest HUNGARY
NAGY, Zoltan DESY Hamburg GERMANY

OSTAPCHENKO, Sergey Norwegian University of Physics and Technology (NTNU) Trondheim NORWAY
PADULA , Sandra S. Instituto de Fisica Teorica-State University of Sao Paulo Sao Paulo, SP BRAZIL
PAPAGEORGIOU, Kostas University of the Aegean Chios GREECE
PIEROG, Tanguy Forschungszentrum Karlsruhe, IK Karlsruhe GERMANY
PISKUNOVA, Olga Lebedev Physical Institute Moscow RUSSIA
PLATZ, Sabine DESY Hamburg GERMANY
ROJO CHACON, Juan LPTHE, UPMC Paris VI Paris FRANCE
SABIO VERA, Agustin CERN Geneve SWITZERLAND
SAVIN, Alexander University of Wisconsin and Hamburg GERMANY
SCHMITZ, Norbert Max-Planck-Institut fuer Physik Muenchen GERMANY
SESKUTE, Lilija Hamburg University Hamburg GERMANY
SHEARS, Tara University of Liverpool Liverpool UNITED KINGDOM
SHEHZADI, Ramoona Physikalishes institut, Universitaet Bonn Bonn GERMANY
SIMAK, Vladislav FNSPE CTU Prague CZECH REPUBLIC
SRIVASTAVA, Yogendra University of Perugia Perugia ITALY
STIRLING, James University of Cambridge Cambridge UNITED KINGDOM
STRASSLER, Matthew Rutgers University Piscataway UNITED STATES OF AMERICA
SUMBERA, Michal Nuclear Physics Institute ASCR Praha CZECH REPUBLIC
TAN, Chung-I Brown University Providence UNITED STATES OF AMERICA
THOMPSON, Paul University of Birmingham BIRMINGHAM UNITED KINGDOM
TOKAREV, Mikhail Joint Institute for Nuclear Research Dubna RUSSIA
TOLL, Tobias DESY Hamburg GERMANY
TRAVNICEK, Petr Institute of Physics, Academy of Sciences Prague CZECH REPUBLIC
TSILEDAKIS, Georgios University of Heidelberg Heidelberg GERMANY
TSUKERMAN, Ilya Institute for Theoretical and Experimental Physics Moscow RUSSIA
VAN MECHELEN, Pierre Universiteit Antwerpen Antwerpen BELGIUM
VON DEN DRIESCH, Martin Hamburg University Hamburg GERMANY
VON SAMSON, Federico DESY, Hamburg Hamburg GERMANY
WEGENER, Dietrich TU Dortmund Dortmund GERMANY
WEIGLEIN, Georg IPPP Durham Durham UNITED KINGDOM
WERNER, Klaus Univ. of Nantes Nantes FRANCE
WHITE, Chris Nikhef Amsterdam NETHERLANDS
WICKE, Daniel Bergische UniversitŁt Wuppertal Wuppertal GERMANY
WING, Matthew UCL/DESY/UHH London UNITED KINGDOM
WOLSCHIN, Georg Heidelberg University Heidelberg GERMANY
YOSHIDA, Rik Argonne National Laboratory Argonne, IL UNITED STATES OF AMERICA